



**ARCTIC
RESPONSE
TECHNOLOGY**
OIL SPILL PREPAREDNESS

January 20, 2016

W. Scott Pegau, Prince William Sound - Oil Spill Recovery Institute
Jessica Garron, University of Alaska Fairbanks
Leonard Zabilansky, U.S. Army Corps of Engineers, Cold Regions Research
and Engineering Laboratory

**DETECTION OF OIL ON-IN-AND-UNDER ICE –
FINAL REPORT 5.3**



ARCTIC OIL SPILL RESPONSE TECHNOLOGY – JOINT INDUSTRY PROGRAMME

The oil and gas industry has made significant advances in the ability to detect, contain, and cleanup oil spills in Arctic environments (Potter et al., 2012). Ongoing research continues to build upon more than fifty years of examining all aspects of oil spill preparedness, oil spill behaviour, and available options for oil spill response in the Arctic marine environment. This research has included hundreds of studies, laboratory and basin experiments, and field trials, conducted in the United States, Canada, and Scandinavia. To build on existing research and improve technologies and methodologies for Arctic oil spill response, members from the IPIECA-Oil Spill Working Group, Industry Technical Advisory Committee (ITAC) and the American Petroleum Institute-Emergency Preparedness and Response Programme Group formed a joint committee in 2009. The committee's task was to review the oil and gas industry's prior and future work scope on prevention and response to oil spills in ice in order to identify and prioritise technology advances and research needs. One outcome was the recommendation to establish the Arctic Oil Spill Response Technology Joint Industry Programme (JIP) that would undertake targeted research projects identified to improve industry capabilities and coordination in the area of Arctic oil spill response.

The JIP was launched in January 2012 and over the course of the programme is carrying out a series of advanced research projects in six key areas: dispersants, environmental effects, trajectory modelling, remote sensing and in situ burning (ISB).

PREPARED BY

W. Scott Pegau, Oil Spill Recovery Institute

Jessica Garron, University of Alaska Fairbanks

Leonard Zabilansky, Cold Regions Research and Engineering Laboratory

With content from

Christopher Bassett, Job Bello, John Bradford, Regina Carns, Zoe Courville, Hajo Eicken, Bruce Elder, Peter Eriksen, Andone Lavery, Bonnie Light, Ted Maksym, Hans-Peter Marshall, Marc Oggier, Donald Perovich, Pawel Pocwiardowski, Hanumant Singh, Dajun Tang, Chris Wiggins, Jeremy Wilkinson

Detection of oil on-in-and-under ice.

FINAL REPORT 5.3

Report from Joint Industry Programme on oil spill detection and mapping in low visibility and ice: experimental results.

Project Team

Project Managers

Scott Pegau – Oil Spill Recovery Institute

Jessica Garron – University of Alaska Fairbanks

Leonard Zabilansky – Cold Regions Research and Engineering Laboratory

Contractors

Boise State University

Cold Regions Research and Engineering Laboratory

EIC Laboratory

Inland Gulf Maritime

Norbit

Polar Ocean Services

University of Alaska Fairbanks

University of Washington

Woods Hole Oceanographic Institution

Project Team

Participants and Contributors

John Bradford – BSU – GPR and radar modelling
Hans-Peter Marshall – BSU – FMCW radar
Zoe Courville – CRREL – Ice structure
Donald Perovich – CRREL – Optical measurements
Bruce Elder – CRREL – Ice structure and optical measurements
Keran Claffey – CRREL – Ice structure and IR imagery
Nathan Lamie – CRREL – Instrumentation operator
Marie Darling – CRREL – Outreach and logistics
Jesse Stanley – CRREL – Carriage operator
Ben Winn – CRREL – Construction and operation
Troy Arnold – CRREL – Oil injection and removal
Job Bello – EIC – Fluorosensors
Christina Gasbarro – EIC - Fluorosensors
Chris Wiggins – IGM – Above-ice optical and IR imagery
Barry Lavoie – BAE – Above-ice optical and IR imagery
Pawel Pocwiardowski – Norbit – Multibeam sonar
Peter Eriksen – Norbit – Multibeam sonar
Jeremy Wilkinson – POS – Narrowband sonar
Iris Rankin – PWSSC – Report review
Marc Oggier – UAF – Ice properties, ice modelling, and optical imagery
Hajo Eicken – UAF – Ice modelling
Meibing Jin – UAF – Ice modelling
Andone Lavery – WHOI – Broadband acoustics and acoustical modelling
Christopher Bassett – WHOI – Broadband acoustics and acoustical modelling
Ted Maksym – WHOI – Broadband acoustics and Fluorosensor
Hanumant Singh – WHOI – Underwater imagery
Dajun Tang – UW – Acoustic modelling
Bonnie Light – UW – Optical modelling
Regina Carns – UW – Optical modelling

TABLE OF CONTENTS

EXECUTIVE SUMMARY	12
1. INTRODUCTION.....	20
1.1 The Ice Environment.....	20
1.2 Above Ice Remote Sensing Technologies	24
1.3 Below Ice Remote Sensing Technologies	27
1.4 Modelling.....	31
2. GOALS AND OBJECTIVES	34
3. TEST DESIGN AND METHODS.....	35
3.1 Facility and Layout.....	35
3.2 Instrument Mounting.....	36
3.3 Experimental Design.....	40
3.4 Health and Human Safety.....	42
3.5 Oil and Oil Injection.....	43
3.6 Sampling Sequence.....	45
3.7 Ice Conditions in Individual Hoops.....	45
3.8 Instrumentation.....	52
3.9 Modelling	80
4. Results.....	88
4.1 Ancillary Measurements	88
4.2 Sensor Results	123
4.3 Modelling	190
4.4 Radar Modelling	206
5. DISCUSSION.....	226
5.1 General Comments.....	226
5.2 Laboratory Performance	226
5.3 Expected Field Performance	230
5.4 Sensor Readiness	232
5.5 Deployment Considerations.....	234
5.6 Sensor Suite	235
6. NEXT STEPS.....	238
7. BIBLIOGRAPHY	240
8. APPENDICES	245
Appendix I. Problems encountered.....	245
Appendix II. Sea ice properties comparison between the 2014 CRREL oil-in-ice experiment and first year Arctic sea ice	246
Appendix III. Tabulation of first-year sea-ice properties representative of the annual cycle as relevant to 2014 CRREL oil-in-ice experiments.....	251
Appendix IV. Radar modelling runs not presented in the main report.....	265
Appendix V. Surface GPR data not presented in the main report.....	289
Appendix VI. Additional aerial GPR plots.....	302
Appendix VII. Single-beam narrowband sonar.....	318
Appendix VIII. Health and Human Safety Plan	370
GLOSSARY OF TERMS	375

FIGURES

Figure ES1. View down the length of the CRREL cold basin showing the test hoops frozen in.....	14
Figure ES2. Schematic of the experimental design.	14
Figure 1. Oil behavior in ice (Potter et al., 2012, adapted from A.A. Allen).....	23
Figure 2. Top left, a view along the length of the tank.	35

Figure 3. The conceptual layout of the experiments.	36
Figure 4. The aerial sensors mounted on the carriage (Top).....	38
Figure 5. Top left, the rail system with the chain between the rails run down the center of the tank. Top right, the sensor plate mounted to the carriage underwater.	39
Figure 6. Containment hoops being placed into the tank at the beginning of freeze up. The lines were used to align the hoops within the tank.	40
Figure 7. Oil injection system from above the ice..	44
Figure 8. The oil injection system as seen from below the ice prior to oil injection.	44
Figure 9. Oil and ice mixture from the first injection into Hoop 1 as seen from above (left) and below (right) one day after the injection.	46
Figure 10. Hoop1 near the end of the second injection..	46
Figure 11. Hoop 2 lit from below to show final distribution of oil..	47
Figure 12 Oil distribution in Hoop 3 showing oil that reached the surface along the edges.	48
Figure 13. Top. A back lit picture of Hoop 4 showing the final oil distribution. Bottom. The migrated oil distribution as seen from above one day after the oil injection.	49
Figure 14. Backlit picture showing the distribution of oil after the injection.	50
Figure 15. Oil distribution in Hoop 6.....	50
Figure 16. Snow and oil on the surface of Hoop 5B under the ceiling mounted FMCW.	51
Figure 17. Position of radar systems. Snow can be seen along the edge of Hoop 6.	52
Figure 18. Example transmitted and received FMCW wavelets for one reflector.....	54
Figure 19: Photo of the 1000 MHz, surface-coupled GPR.....	56
Figure 20. An image collected by the webcam on the side of the tank viewing down the tank. On the left side of the image is Hoop 5 and Hoop 1 is on the far right.	58
Figure 21. Picture of Hoop 4 from above from the time lapse camera.	58
Figure 22. Infrared image from the camera mounted near the webcam with Hoop 5 in the foreground. ...	59
Figure 23. The aerial FP sensor is in the black case.	60
Figure 24. The top photograph shows the sun illuminating a hoop.....	61
Figure 25. Pictured is the scanning fluorescence polarization instrument mounted on the instrumentation plate of the underwater carriage.	63
Figure 26. The fixed focus FP sensor mounted on the bottom of the tank.....	64
Figure 27. The low-light cameras are circled. The light source is next to the multibeam sonar.	65
Figure 28. Still image of oil in Hoop 5 from the camera on the underwater carriage.....	65
Figure 29. Layout of the AQUAscat on the carriage (Left). Example of the mounting of the four transducers (Right).....	66
Figure 30. Schematic showing the approximate acoustic return in a multilayer system.	69
Figure 31. Raw data from each of the four frequencies showing oil under Hoop 1.....	69
Figure 32: Left: Raw time series of data showing the acoustic returns over the logging period of 180 seconds. Right: Processed data showing the calculated average return from the measurements made over 180 seconds.	70
Figure 33. Multibeam sonars mounted on the underwater instrument plate..	73
Figure 34. A sample of a snippet showing return strength.....	74
Figure 35. Example of backscatter angular response data from Hoop 2..	75
Figure 36. The sonar distance return, in meters, from the nadir direction showing an oil thickness of about 6 cm.	76
Figure 37. Photograph of the electrical resistivity array.	80
Figure 38. (a) Typical profile of mostly level first-year ice at Barrow (data come from winter 2006) ; (b) Position of the MBS (Druckenmiller et al., 2009).....	82
Figure 39. Interannual variability and long-term change as shown in ice growth/melt conditions.	84
Figure 40. Definition of angular coordinates, adopted from “High-Frequency Seafloor Acoustics” by Jackson and Richardson, Springer (2007).	85
Figure 41. The four-layer model for the water/oil/ice medium.....	86
Figure 42. Air temperature is the continuous blue line.....	88
Figure 43. Water temperature below the ice through the growth phase of the experiment.....	89

Figure 44. The light colour line shows air temperature and the dark line the water temperature during the melt phase.....	89
Figure 45. Evolution of the ice sheet thickness over time.....	90
Figure 46. Variation of average standard deviation of multiple thickness measurements made on the same day.	91
Figure 47. Freeboard values for the test basin throughout the experiment.....	92
Figure 48. Ice growth under injections into Hoop 4 (left) and Hoop 5 (right) as seen by the Aquascat system.	93
Figure 49. Evolution of the density of the ice top, ice bottom, and average density over the entire ice thickness.	94
Figure 50. Evolution of density profiles over time, each sampling date is represented by different colour.	94
Figure 51. Evolution of top, middle, average density values over time in relation to the air temperature in the test facility.....	95
Figure 52. Evolution of salinity of top, bottom and average over the ice thickness of melted ice sections.	95
Figure 53. Evolution of salinity profiles over time.....	96
Figure 54. Salinity variation over 5 days (November 12 th to 17 th , top) and within the hoops on January 8 th (bottom).	97
Figure 55. Salinity and temperature variation over time.....	98
Figure 56. Temperature in top, bottom and over average of the cores.....	99
Figure 57. Evolution of temperature profiles measured in cores over time.....	99
Figure 58. Evolution of temperature profiles measured by the resistance thermal devices over time. Distances are given downward from the original water level.....	100
Figure 59. Clean ice core taken just outside of Hoop 6 on January 6 th , 2015.....	101
Figure 60. Clean ice core taken on Center Line between Hoops 5 & 6 on February 12 th , 2015.....	101
Figure 61. Images of the Hoop 1A cores. The top of the cores are to the left. Entire core (top), thick sectioned core (middle), thin sectioned core (bottom).....	102
Figure 62. Images of core 3A (top) and core 3A thick sections (bottom) show the small amount of oil intrusion above the oil gap. The top of the cores are to the left.....	102
Figure 63. Cross sections of the Hoop 3A core at, (from left to right) 5 cm, 10 cm, 15 cm, 20 cm, 25 cm deep.	103
Figure 64. Core taken from Hoop 1 at end of the experiment.....	104
Figure 65. Thin and thick section photos of core from Hoop 1 showing oil locations and crystal structure.	104
Figure 66. Core from Hoop 2 taken on February 11 th	105
Figure 67. Hoop 2 thin and thick sections showing location of oil and crystal structure.....	105
Figure 68. Thin and thick sections of a core from Hoop 4 taken in area of melt within hoop.....	106
Figure 69. Thin and thick sections of a core taken from dry area of Hoop 4.....	107
Figure 70. Core from Hoop 6 taken at end of experiment.....	107
Figure 71. Hoop 6 thin and thick sections showing location of oil and crystal structure.....	108
Figure 72. Example of a slab taken from the Hoop 3A January 12 th , 2015 looking at the vertical face of the slab – top is up in the photo.....	109
Figure 73. Bottom of the slab from Hoop 3A. Top of the ice is at the bottom of the photo.....	110
Figure 74. Close-up looking at the side of a slab at the oil-ice interface.....	110
Figure 75. Slab from inside Hoop 1A drilled January 13 th	111
Figure 76. Images of the ice immediately below the oil lens from Hoop 4.....	112
Figure 77. Clean ice slab removed from outside Hoop 4A (left) and 1 (right). Top of ice slab is up.....	113
Figure 78. Core from December 3 rd (left), and December 9 th (right), showing skeletal layer structure. ...	114
Figure 79. Schematic of core locations taken from 1.3m radii around acoustic sensor.	114
Figure 80. Variations in skeletal layer on meter-scale from December 9 th	115
Figure 81. Temporal variation of skeletal layer from micro-CT scans.	116

Figure 82. Thickness of skeletal layer (vertical extent) over time, in cm.	116
Figure 83. Thickness of lamellae structures (blue diamonds) and the spacing between lamellae (red squares) over time.	117
Figure 84. Evolution of skeletal layer structure over the course of the experiment as visualized by micro-C, at 60micron resolution.	117
Figure 85. Sound speed of oil from -10 to 20 C.	118
Figure 86. November 20, 2014 minimum (top) and maximum (bottom) resistivity orientation perpendicular to long axis of tank.	120
Figure 87. December 10, 2014 minimum resistivity orientation 135 degrees CW to long axis of tank.	120
Figure 88. December 10, 2014 maximum resistivity orientation 45 degrees CW to long axis of tank.	120
Figure 89. January 15, 2015 minimum resistivity orientation perpendicular to long axis of tank.	121
Figure 90. January 15, 2015 maximum resistivity orientation parallel to long axis of tank.	121
Figure 91. 3D GPR data volume acquired on January 10, 2015.	122
Figure 92. Base-of-ice topography measured using 3D GPR on November 18, 2014 and January 10, 2015, when the ice had roughly doubled in thickness.	123
Figure 93. Pictures of Hoop 4 just after (left) and a day after (right) injection of oil.	124
Figure 94. Hoop 4 after the onset of melt.	124
Figure 95. Snow from the cooling system covers sections of Hoops 4 and 5. Hoop 5 is in the bottom left of the frame.	124
Figure 96. EO and LWIR pictures without the addition of experimental solar heating.	125
Figure 97. Artificial sun applying solar heat (left); resulting LWIR signature 8 hours after removing solar radiation (right).	125
Figure 98. Oil being injected into Hoop 6. The picture is lit from above by the room lights.	126
Figure 99. Encapsulated oil in Hoop 5 (top) and Hoop 3 (bottom), as seen on January 6, 2015. Hoop 3 covers the top half of this image.	127
Figure 100. A pile of snow on the surface of the ice is present in the upper right section of the photograph.	128
Figure 101. Transmitted radiance on November 7, 2014 showing Hoop 1 after oil injection and Hoop 2 with no oil injected.	128
Figure 102. Hoop 3 albedo and transmitted radiance after the November 17 th oil injection at Hoop 3.	129
Figure 103. Spectral albedo (left) and transmitted radiance (center) on November 21 st and 22 nd for Hoop 4 before and after oil injection.	130
Figure 104. Albedo (left) and transmitted radiance (right) at Hoop 5 prior to the oil injection that occurred on December 9 th	131
Figure 105. Transmitted radiance through Hoop 6 prior to the oil injection and just after the oil injection on January 6 th	132
Figure 106. Photographs of the six hoops taken on December 8, 2014.	134
Figure 107. Albedo (left panel) and transmitted radiance (right panel) on February 9, 2015 under all 6 hoops, after the ice warmed.	135
Figure 108. The 1300/700 nm albedo ratio for all six hoops on 9 February 2015.	135
Figure 109. Time series of the ratio of the albedo at 1300 nm and 700 nm for all six hoops.	136
Figure 110. Time series of transmitted spectral radiance at Hoop 4.	137
Figure 111. Scan results from the aerial FP instrument over Hoop 1.	138
Figure 112. Photographs of Hoop 1 with frazil ice before and after the oil injection.	138
Figure 113. Scanning FP Hoop 1 results.	139
Figure 114. Scanning FP Hoop 2 results.	139
Figure 115. Scanning FP Hoop 3 results.	139
Figure 116. Scanning FP Hoop 4 results.	139
Figure 117. Scanning FP Hoop 5 results.	140
Figure 118. Scanning FP Hoop 6 results.	140
Figure 119. Plot of oil fluorescence intensity as a function of ice encapsulation thickness for Hoop 4 scanning FP data.	140
Figure 120. Images of laser beam after oil injection in Hoop 3 (left) and after ice encapsulation (right). ..	141
Figure 121. Fixed focus FP instrument result of the continuous monitoring of oil injected under Hoop 4B.	141
Figure 122. Plot of oil fluorescence intensity as a function of ice encapsulation thickness of oil injected under Hoop 4B.	142

Figure 123. Shown are data from the stationary FMCW over Hoop 5B before and after snow and oil was added to the top surface of the ice on January 7, 2015.	143
Figure 124. FMCW profile across length of tank, on November 24 th and December 23 rd	144
Figure 125. Ice sheet temperature profile from the West Probe thermistor string.....	145
Figure 126. Pre and post-spill profiles over Hoop 2.....	147
Figure 127. Pre- and post-spill profiles for the 2 cm oil injection into Hoop 5..	148
Figure 128. Pre and post-spill profiles for the injection in Hoop 6.....	149
Figure 129. The full tank profile from November 24 th , three days after the injection into Hoop 4.....	150
Figure 130. The full tank profile from January 6 th	150
Figure 131. 1GHz radar expanding spread gather acquired on January 5, 2015.	151
Figure 132. 500 MHz polarimetric GPR data acquired on January 10, 2015 after the Hoop 6 injection. .	152
Figure 133. Plot of reflection strength for the profile acquired on January 10, 2015 and shown in Figure 132.	153
Figure 134: Acoustic returns from the 1 MHz transducer.....	154
Figure 135. Pre-oil injection: Acoustic signature of the sea ice bottom about 20 minutes before the oil injection, as seen by the different transducers..	155
Figure 136. Post-oil injection: Acoustic signature of the oil located on the ice bottom, as seen by the different transducers.	155
Figure 137. Plot of the raw acoustic signal over the 300 second record of the four transducers 30 minutes after the oil release.	156
Figure 138. Plot of the average acoustic signal seen by the four transducers, both pre (blue line) and post (black line) oil deployment..	156
Figure 139. Plot of the raw acoustic signal from the four transducers during transit of Hoop 1.	157
Figure 140. One hour time series displaying the raw output from the 5 MHz (top left), 1 MHz (top right), 0.5 MHz (bottom left), 0.3 MHz (bottom right) transducers. Main features are:.....	158
Figure 141: These profiles are from the 1 MHz transducer.	159
Figure 142. Time-series of acoustic returns under Hoop 3, from 17:00 on the November 19 th to 08:00 on the November 20 th	160
Figure 143. This figure displays the mean Acoustic return for the 5 MHz (top left), 1 MHz (top right), 0.5 MHz (bottom left), 0.3MHz (bottom right) transducers.	161
Figure 144 Graphic showing the potential acoustic reflection points for oil that encapsulated within sea ice.	162
Figure 145 Average acoustic return, calculated from returns obtained between 17:00 on November 19 th and 08:00 on November 20 th , for the 0.3 MHz transducer.	163
Figure 146. Ice draft as seen by the location of the bottom of the sea ice in the 1 MHz transducer.	164
Figure 147. Acoustic returns under Hoop 4.	165
Figure 148. Time series of the raw acoustic returns from November 21 st to December 1 st	167
Figure 149. Blue trace shows the location of the ice bottom before the oil was deployed.	168
Figure 150. Raw acoustic returns from the moving trolley under Hoop 6.	169
Figure 151. This figure shows the slow draining of oil under Hoop 6, from an initial thickness of about 9 cm to final thickness of around 2 cm.	170
Figure 152. Mean acoustic return from the 1 MHz transducer over a 3 min recording cycle	171
Figure 153. Hoop 1. Low-frequency channel (black), mid-frequency (gray), high-frequency (red).	173
Figure 154. Hoop 2. Mid-frequency channel (gray), high-frequency channel (red).....	174
Figure 155. Hoop 3. Low-frequency channel (black), mid-frequency channel (gray), high-frequency channel (red).	175
Figure 156. Hoops 4 and 5. Low-frequency channel (black), mid-frequency channel (gray), high-frequency channel (red)..	177
Figure 157. Hoop 4 spill map.	178
Figure 158. Encapsulation data from Hoop 5.	179
Figure 159. Bubbles on under-ice surface, under Hoop 4..	180
Figure 160. Hoop 6. Low-frequency channel (black), mid-frequency channel (gray), high-frequency channel (red).	181

Figure 161. Temporal and frequency domain results from Hoop 6 while monitoring the melt-out stage..	182
Figure 162. Before injection (left) and after injections (right)	183
Figure 163. The nadir beam in the point (left) referenced by a surface difference map (right) showing possible double reflection from the oil and ice.....	183
Figure 164. Before injection (left) and after injections (right).....	184
Figure 165. Nadir beam snippets at the same location over eight days.....	184
Figure 166. The equalized comparison of the Backscattered Angular Response (BAR) based on the relative intensity.	185
Figure 167. Multibeam data during the second injection into Hoop 1.	185
Figure 168. The change in bottom scattering strength associated with the presence of oil.....	186
Figure 169. FLS observations before oil (left) and after oil injection (right).....	187
Figure 170. Map of acoustic return showing Hoops 2 and 3 after injection into Hoop 3 (left).	187
Figure 171. The nadir beam snippets from the 200 kHz unit show a double return associated with the oil layer that is observed 24 hours after injection.	188
Figure 172. The FLS observations before, after, and one day after oil injection.	189
Figure 173. Nadir beam returns showing the oil and ice returns were detected over a nine day period...	189
Figure 174. Signal from the oiled and clean ice surfaces was observed over time.....	190
Figure 175. Ice core length as a function of the number of freezing or thawing degree days.	191
Figure 176. 2000 to 2500 K-days	192
Figure 177. 2500 - 3000 K-days (growth season).....	193
Figure 178. 2500 - 3000 K-days (growth season).....	193
Figure 179. 3000-3500 K-days (growth season).....	194
Figure 180. -25/-35 K-days (melt season)	195
Figure 181. Model/data comparison for normal incidence (left) and at 20 degree oblique angle without oil layer (right).	196
Figure 182. Model/data comparison for normal incidence (left) and at 20 degree oblique angle (right) with oil layer.	197
Figure 183. Modeled scattered intensity at a 20 degree incident angle for different thicknesses of ice grown after oil injection. In the absence of oil, the intensity is 25 dB.....	199
Figure 184. Model prediction for normal incidence (nadir) scattered intensity with 1 cm of new ice growth underneath a 4 cm oil layer.	200
Figure 185. Model prediction for normal incidence (nadir) scattered intensity with 5 cm of new ice growth underneath a 4 cm oil layer.	201
Figure 186. Model prediction for normal incidence (nadir) scattered intensity with 10 cm of new ice growth underneath a 4 cm oil layer.	201
Figure 187. Bare ice with an initial thickness of 5 cm at the time of the spill, a 2 cm spill, and various amounts of ice growth. The version on the right was computed at higher spatial resolution.	202
Figure 188. A 2 cm thick oil patch below 129 cm of ice with ice growth to 140 cm.	203
Figure 189. A 20 m diameter, 2 cm thick oil patch below 150 cm of ice with ice growth to 160 cm.	203
Figure 190. A 10 cm thick oil patch below thin ice with various encapsulation thicknesses.....	204
Figure 191. (Left) A 2 cm thick oil patch below 28 cm of ice with the ice surface conditions representative of weathered snow or rotten ice. (Right) The same oil and ice but with the oil below 111 cm of ice.....	204
Figure 192. Transmission spectra for various ice thicknesses below a patch of oil at 5 cm depth (left) and 111 cm depth (right).	205
Figure 193. Transmission spectra for various ice thicknesses below a 2 m patch of dry snow on the surface (left) and a 2 cm thick patch of oil of the same size under 28 cm of ice (right).	206
Figure 194. A) Simple sea ice model with oil spill at the base varying in thickness from 0 to 24 cm. B) Simulated pulse radar data for the model in A. C) Maximum reflection amplitude, D) instantaneous frequency and E) instantaneous phase as a function of oil layer thickness extracted from the data in B.....	208
Figure 195. Before and after FMCW radar simulations for 5 injections in the test basin experiment.....	209
Figure 196. Before and after pulse radar simulations for 5 injections in the test basin experiment.	210

Figure 197. Simulations showing the evolution of the FMCW radar response for the injections into Hoops 2 – 5.	212
Figure 198. Simulations showing the evolution of the pulse radar response for the injections into Hoops 2 – 5.	213
Figure 199. Evolution of the FMCW radar response to an oil spill in January.	215
Figure 200. Evolution of the pulse radar response to an oil spill in January.	216
Figure 201. Ice electrical property models for the real world airborne radar simulation.	218
Figure 202. Pulsed radar model runs for the real world airborne radar simulation.	220
Figure 203. Reflection strength extracted from the simulated data shown in Figure 202.	221
Figure 204. Amplitude along the base-of-ice reflection for the simulations shown in Figure 203.	222
Figure 205. FMCW model data plots for the models shown in Figure 201.	223
Figure 206. Amplitudes for the base-of-ice reflection from the FMCW radar.	224

TABLES

Table 1. Planned injection conditions in primary hoops.	41
Table 2. Injection conditions in primary hoops along the centerline.	41
Table 3. North Slope Crude oil properties as analyzed by SL Ross.	43
Table 4. Summary of optical measurements.	62
Table 5. Settings used during this experiment.	67
Table 6. Transducer and signal parameters.	70
Table 7. Dates and Physical Properties Data.	78
Table 8. Standard deviation of ice thickness measurements made at the same location on the same day.	91
Table 9. Table showing the location and distance between each separate peak seen by the 0.3 MHz Transducer (see accompanying Figure 145).	163
Table 10. Model parameters.	196
Table 11. Model parameters when oil layer is added.	197
Table 12. Signal: noise ratios for acoustically modeled oil thickness.	198
Table 13. Sensor performance during the laboratory experiments.	228
Table 14. The expected field performance in level first-year ice of instrumentation tested during this experiment, based on laboratory and modelling results.	230
Table 15. Technical readiness level evaluation criteria used.	232

EXECUTIVE SUMMARY

The ability to unambiguously detect spilled oil is critical for responding to a spill. The presence of sea ice increases the complexity of detecting the oil. Depending on the nature of the spill, the time of year, and the time elapsed since the spill, oil can potentially be found on, under, around, or in ice. Recent efforts focus on developing and testing new sensors for detecting oil in ice covered seas.

In 2012, nine international oil and gas companies began a joint industry programme (JIP) to improve the technologies and methodologies to respond to oil spills in Arctic waters. Six key areas of research were identified for further experimentation and study: dispersants, environmental effects, trajectory modelling, remote sensing, mechanical recovery, and in situ burning. This report is a contribution to the remote sensing part of the programme.

The overall goal of the remote sensing (RS) component of the JIP is to expand the oil industry's detection and monitoring capabilities for spills in ice-covered waters including darkness and low visibility conditions. Scenarios include four specific oil in ice configurations: 1) oil on water and/or located in brash and frazil ice between ice floes; 2) oil located on the ice surface with and without snow cover; 3) oil located under ice soon after rising from the discharge point; and 4) encapsulated oil in ice with a layer of new ice grown beneath the oil. This current project looks at some aspects of all these scenarios.

In the first RS phase, the JIP commissioned two state-of-knowledge reports assessing sensor capabilities above and below the ice. These reports are on the Arctic JIP website (www.arcticresponsetechnology.org). A key finding from these studies was that industry already has access to a wide range of space, airborne and surface-imaging systems used from a variety of platforms such as satellites, helicopters, fixed-wing aircraft, drones, vessels and drilling platforms. While these systems were originally developed and tested for the "oil on open water scenario", it was found that many systems could potentially provide effective sensing in a broad range of ice conditions as well.

The second phase reported on here covers a fully integrated experiment, testing a variety of RS tools for detecting oil from above and below sea-ice. The experimental data were integrated into functional models to determine the potential applicability of different sensors to real sea-ice conditions.

Specifically, the Phase 2 RS programme aimed to:

- Acquire spectral, hydro-acoustic, thermal, and electromagnetic signatures of oil on, within, and underneath a level sheet of sea ice.
- Determine the capabilities of various sensors to detect oil in specific ice environments created in the test tank, including freeze-up, growth and melt.
- Model the potential performance of the sensors under more realistic field conditions using the test data for validation.
- Recommend the most effective sensor suite for detecting oil in the ice environment.

The laboratory based sensor testing began in November 2014 and spanned a two-month ice growth phase and a one-month decay/melt period. An 80-centimeter thick sheet of level salt-water ice was grown in the Geophysical Research Facility at the US Army Corps of Engineers Cold Regions Research and Engineering Laboratory (CRREL) in Hanover, New Hampshire. The basin ice was representative of natural level sea ice grown under quiescent conditions. This created a controlled baseline environment to compare different sensors with a manageable

number of variables. It was not the intent of this project to test in other much more complex ice environments such as drift ice, deformed ice or multi-year ice.

The controlled-environment test basin (see photo below) is 37 m long, 9 m wide, and 2.4 m deep. Six containment hoops were placed along the length of the tank to make up the primary experimental area. The hoops were numbered one to six from west to east. Six smaller hoops received the same treatment as the primary hoops to allow for coring to examine ice properties. Another four hoops were provided for additional experiments.

During the growth phase the cold basin temperature was brought down and held near -24°C. At predetermined stages Alaska North Slope crude oil at 0°C was injected into each of the experimental hoops from below. Camera systems were used by CRREL personnel to ensure proper placement of oil within the hoops. Within two days following injection, ice would begin to form below the oil. The combination of oil thicknesses and ice thicknesses, above and below the oil, presented a series of realistic oil detection scenarios. Overall, the combination of injections provided seven different experiments in which to quantify the detection of oil by sensors mounted above and below the sea ice.

After each injection, the oil in the hoop was monitored daily for at least three days with a suite of sensors, from both above and below the ice (listed below). An underwater carriage was parked under the oil and sensors allowed to make continuous observations. A weekly transect was made both above and below the ice to allow sensors to collect data along the length of the ice sheet.

Above-ice sensors were mounted on a 5 m long boom mounted on the carriage 2 m above the ice and included:

- Frequency modulated continuous wave (FMCW) radars,
- Ground penetrating radars (GPR, 2 frequencies),
- Visible and infrared cameras,
- Laser fluorescence polarization (FP) sensor.
- GPR and optical measurements were also collected at the ice surface.

Below-ice sensors were mounted on a trolley running on rails mounted on the tank bottom at a depth just over 2 m, and included:

- Spectral radiance and irradiance sensors,
- FP sensors,
- Optical cameras,
- Broadband acoustics (3 frequency bands),
- Narrowband acoustics (4 frequencies), and
- Multibeam acoustics (3 sensors).



Figure ES1. View down the length of the CRREL cold basin showing the test hoops frozen in.

The simplified schematic below shows a longitudinal cross section through the basin showing the two sensor carriages, above and below the ice, and the result of spilling oil at different stages in the ice growth cycle – not to scale. Note: solid blue lines are the individual hoop (see photo above) containment skirts hanging through the ice, and the black lines are oil layers of different thicknesses.

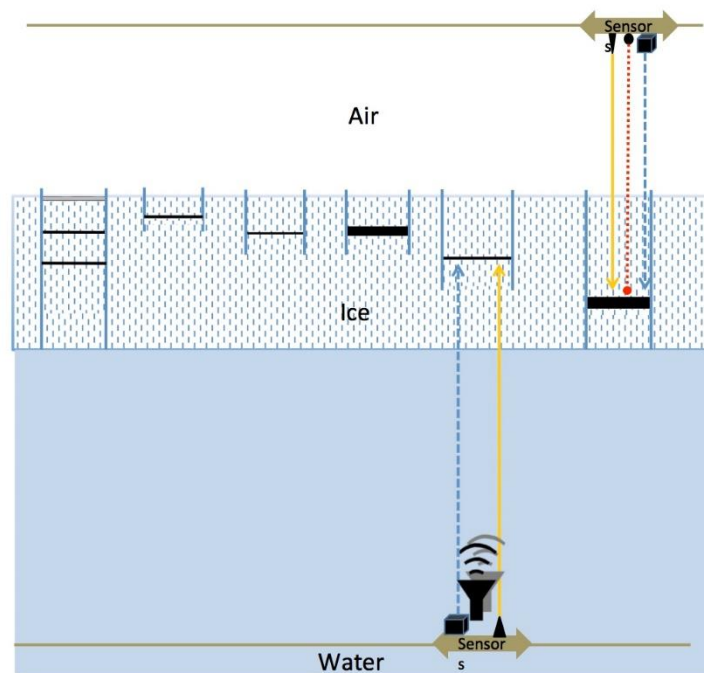


Figure ES2. Schematic of the experimental design.

Underwater sensors were connected to power and data logging computers and a dedicated server provided data archive and access to investigators outside of CRREL. Room lighting was used for all camera systems while an artificial sun (see below) was used for the on-ice and below-ice radiometric measurements.

After two months, when the ice reached its maximum thickness of 80 cm, the basin air temperature was raised to near 0°C and later raised further to accelerate ice melt. An artificial sun (high intensity lighting in the correct spectral band) was placed over one hoop and turned on for several hours for a week to examine how the simulated solar input changed the melt characteristics.

Oil-in-ice detection modelling was implemented to address a set of field scenarios based on two diameters of oil pools (2 and 200 m) and monthly ice growth. Specific ice parameters, such as temperature and salinity, were used to determine optical, acoustical, and radar properties of the ice in various situations and times of year. In addition, models also used the test-basin ice characteristics and the measured sensor performance in the laboratory for model validation.

The detailed test ice properties were determined from ice cores and in-situ temperature probes. Temperature, salinity, density, crystal characteristics, and skeletal layer shape provided the information necessary for understanding sensor performance and as inputs into the subsequent modelling. Three-dimensional CT scans provided detailed information on brine and air inclusions, along with the crystal structure of the boundary layer.

Results and Conclusions

All sensor types used during this experiment showed an ability to detect oil on, in, or below ice under certain conditions.

The ice-coupled (operated from the surface) GPR demonstrated the known potential of commercial radar systems in this application, detecting both fresh and encapsulated oil. In addition, the GPR was able to detect encapsulated oil in an airborne mode when the ice was cold, confirming previous model predictions. The FMCW airborne system had difficulties in terms of reliability and noise that are to be expected from a prototype device, but the limited data obtained in these tests demonstrated the capability of detecting an encapsulated oil layer. Modelling indicates the further potential of this system to expand the detection capabilities of airborne radar systems in the future.

The optical sensors (cameras, radiometers, and fluorescence) were able to detect oil on top of bare ice and at the bottom surface of the ice, and were the only technologies able to reliably detect oil in the brash ice from either above or below.

From above, the near-infrared spectra showed potential for discriminating oil from other dark targets. The thermal infrared sensors were also able to detect “solar” heating of oil at the surface of the ice.

From below, the cameras and radiometers could detect oil at various depths in the ice, and the FP sensor was able to detect oil with up to six centimeters of ice below the oil.

The acoustics systems were able to not only detect the presence of oil but also to measure the thickness of oil below the ice. Systems using frequencies in the 200 – 400 kHz range were able to detect oil through six centimeters (or less) of new ice grown beneath.

Major advances in RS oil in ice as a result of this project include:

- First-ever proof that acoustic and FP sensors can detect oil even after it is encapsulated by a new ice layer. While this ability rapidly declines once the layer thickness exceeds 6 cm, this finding is significant in that it means responders have a working window of approximately a week to ten days (depending on time of year) to reach a spill site and still detect oil.
- First confirmation that the recently developed FMCW radar designed specifically for airborne use for oil in ice has the potential to detect encapsulated oil layers when suspended above the ice.
- First comparison of sensors looking at oil in brash ice, an important scenario in late season drilling.
- First overall concurrent comparison of a wide range of sensors operated below and above the ice under controlled conditions.

Based on the results of this project and the state of knowledge of oil in ice RS, the expected field performance of different sensors is provided in the following table.

Not surprisingly, the capability matrix shows that in pack or drift ice offshore, below-ice sensors are best at detecting fresh oil under the ice and existing airborne sensors are best at detecting oil on the surface or buried under snow. The greatest limitation is in consistently detecting oil that is encapsulated in the ice sheet with more than 6 cm of new ice growth beneath the oil. This synopsis of capability assumes that on-ice methods using GPR only apply to scenarios involving oil spilled under stable fast ice that provides safe working conditions near shore.

Using the Beaufort Sea as a benchmark location, in a field environment almost all oil will be on the melting ice surface during the summer months, making below ice methods not applicable (N/A). On-ice activities are also N/A throughout these months due to safety considerations, leaving only airborne methods. Airborne radar systems will have difficulties in fall or spring when the ice is generally too warm and conductive. Provided there is sufficient light from above, under-ice optical methods can detect oil under ice, in the interior of ice (when encapsulation thickness is relatively small compared to the oiled area), and on top of thin ice. FP is possible for oil on new and young ice (with minimal snow cover). IR should work with oil on top of the ice during the early part of the ice season as long as there is enough daylight to create detectable temperature differences (October and early November). IR utility should return in spring with increasing sunlight.

Table of the expected field performance in level first-year ice of instrumentation tested during this experiment, based on laboratory and modelling results. Sensors include Ground Penetrating Radar (GPR), Frequency Modulated Continuous Wave Radar (FMCW), Optical (cameras and radiometers), Fluorescence Polarization (FP), Thermal Infrared (IR), and Acoustic systems. The P (for possible) rating indicates that there are conditions that may allow the system to work, and others when it is expected to fail. A yellow P2 rating indicates that there is still insufficient data fully assess performance. N/A indicates that sensor application in this scenario is not relevant – e.g. using below ice sensors to detect exposed oil on the surface.

Location	Airborne	On ice ¹	Below ice
----------	----------	---------------------	-----------

Sensor	GP R	FMC W	Optical	FP	IR	GPR	Optical ⁴	FP	Acoustic
Fall-Winter-Spring									
Exposed oil on ice	Y	P2	Y	Y	P2 ³	Y	P2	N/A	N/A
Snow covered oil on ice	Y	P2	N	N	N	Y	P2	N	N
Fresh oil under ice or with up to 6 cm new growth)	P2	P2	N	N	N	Y	Y	Y	Y
Encapsulated oil (more than 6 cm new growth)	P	P2	N	N	N	Y	P ⁵	N	P2 ⁶
Summer²									
Exposed oil on ice	P2	P2	Y	Y	Y	N/A	N/A	N/A	N/A

Notes to Table:

¹On-ice operations apply only to stable ice

² Snow covered oil on ice, oil beneath ice, or encapsulated oil is unlikely in summer

³ As long-wave IR detection depends on measurable temperature differences oil vs. ice related to solar input, there will be periods during the winter when detection is unlikely. Further testing is required to define the operating limits. .

⁴The performance of optical systems is based on sufficient sunlight penetrating through the snow and ice.

⁵ The ability will depend on the thickness of ice below the oil and the width of the pool of oil.

⁶ The low signal to noise ratio in the tank environment prevented the sonar systems from operating at full power. In a field setting, acoustic systems may be able to detect oil that is encapsulated by more than 6 cm new ice.

This project confirms the overall conclusion of previous work including RS Phase 1: that no one sensor has the capability of detecting oil in all situations. Rather, systems of sensors that complement each other in terms of, detection capabilities, oil thickness resolution, area coverage, or swath width are needed. Future operational systems will likely employ suites of different sensors operating from various platforms under, on and above the ice surface to provide the means to detect oil in a range of ice environments at different times of the year.

Based on the results of this study, an effective underwater detection suite should have a low light camera, broadband and/or multibeam sonar, and possibly a spectral radiometer or FP. While the various sonar units had similar levels of performance, the multibeam type of sonar provides the added ability to create a 3D map of the underside of the ice that may help identify priority locations for oil to accumulate and narrow the search area (oil will naturally seek the highest spots in the under ice surface – thinnest ice).

The study results suggest that aerial sensors should include visible and thermal infrared imagers. Presently available radar technology provides the greatest opportunity for aerial mapping of oil on the ice surface or under snow, but requires future development to lead to an operational airborne tool to detect oil encapsulated within ice. Ground penetrating radar operating from the ice surface is an appropriate tool as long as there is a stable and safe working environment.

The research conducted in this project points to several avenues of work that could continue to develop our ability to detect and map oil in different ice environments. Examples are:

- Conduct blind tests where the operators are unaware of oil location – this could also be done by having a group that is unaware of the oil locations analyse the data.
- Evaluate capabilities of infrared systems (short to long-wave) at different times of the year.
- Test a modified FMCW system with improved signal/noise performance.
- Redo encapsulated oil tests with acoustics in a test setup that permits the sonar systems to transmit at full power.
- Plan, permit and execute a deliberate oil injection in ice to test different systems in a field environment.

The Arctic Technology JIP Remote Sensing Technical Working Group will consider these and other ideas in developing a Phase 3 RS study package early in 2016.

THIS PAGE LEFT BLANK

INTRODUCTION

Increased interest in the potential for oil and gas exploration and development in the Arctic, coupled with increasingly ice-free waters and subsequent increases in shipping activity (Humpert, 2014), highlights the imperative to effectively respond to an oil spill in the waters of the Arctic. One of the challenges of an Arctic marine spill response is to be able to detect and track oil in the extreme environmental conditions often encountered. Safely mapping spilled oil throughout the year, in open-water as well as the various ice-covered water scenarios and within a wide range of visibility conditions, is an essential component of spill response in the Arctic.

Innovative remote sensing systems proposed for surveying both above and below the ice have the potential improve our ability to detect oil and to reduce human risk in oil spill response activities. Advances in the capabilities of underwater vehicles and aircraft as platforms to support a range of sensors expand the capacity for mapping remote areas of the Arctic ice environment that are otherwise inaccessible (Bradford et al., 2008; Brown, 2011; Dickins et al., 2012; Fingas & Brown, 2013b; Maksym et al., 2014 and others). What remains to be demonstrated are the capabilities of individual sensors to specifically detect oil under a range of conditions in an Arctic field environment. No one sensor will be most effective for all conditions; therefore, it is important to identify a suite of sensors that maximize the range of conditions in which the oil can be detected.

In January 2012, members of the international oil and gas industry launched a collaborative effort to enhance Arctic oil spill capabilities under the auspices of the International Association of Oil and Gas Producers (IOGP). This collaboration, called the Arctic Oil Spill Response Technology Joint Industry Programme (JIP) was designed to expand industry knowledge of, and proficiencies in Arctic oil spill response. Six key areas of research were identified for further experimentation and study: dispersants, environmental effects, trajectory modelling, remote sensing (oil spill detection and mapping in low visibility and ice), mechanical recovery and in situ burning.

1.1 The Ice Environment

Understanding when specific technologies are likely to work in sea ice requires an understanding of some fundamental characteristics of sea ice. For instance, radar attenuation depends on the salinity, optical propagation depends on the number and size of air and brine inclusions, and sonar can depend on the fine-scale roughness of the bottom of the ice sheet.

1.1.1 Sea Ice

Sea ice properties, many of which are heavily influenced by sea ice formation, will affect the behavior of oil within the sea ice ecosystem and the ability to detect it. As new sea ice develops, the liquid fraction of the ice decreases as brine is rejected through brine channels. This rejection process reduces the salinity of the ice and creates a discrete ionic layer below the advancing ice front of greater salinity and supercooled water. The growth of new ice will eventually pinch off brine channels, the spacing of which depends on the growth rate of the ice. Sea ice growth rate, which influences the ice porosity and microstructure, depends on temperature and salinity (Thomas & Dieckman, 2010). Under natural conditions, variables such as water temperature, ocean currents, wind and air temperature, also influence the growth rate of the ice. This ionic and thermodynamically variable growth process dictates the dendritic growth pattern of sea ice as seen in the skeletal layer.

The skeletal layer is the advancing growth front of the sea ice. It consists of ice lamellae or dendrites of developing ice crystals that orient vertically at the ice/water interface. These lamellae tend to have a sub millimeter thickness and are a few millimeters wide. The skeletal layer can range up to a few centimeters in length during active salt exudation and ice growth. Exuded brine, enriched in salt expelled by the growing ice crystals, fills the thin spacing between the lamellae. New ice crystals enlarge the lamellar structures, which effectively pinch off the brine layers, or channels between the dendritic lamellae, into closed pockets. As new sea ice develops, the liquid fraction of the ice continues to decrease as remaining brine is rejected from the brine channels. The growth of new ice eventually pinches off brine channels that retain some brine or air in the vacated brine channels and pockets. Spacing of brine channels depends on the growth rate of the ice, which in turn also depends on temperature and salinity. These brine channels can “open” or “shut” depending on temperature, salinity, and the pressure stress the ice is under.

Sea ice crystals play a large role in the definition of the brine channels. Typical Arctic sea ice formation begins with individual needle, spicule, or platelet shaped ice crystals in suspension. As the crystals continue to develop, wave action aggregates the crystals together to create grease ice. This congregated ice has a granular structure that extends approximately 10 cm below the surface and functions as substrate for ice growth of the underlying columnar ice. Ice crystals exhibit a hexagonal crystal structure for which the preferential growth is oriented in the basal plane, perpendicular to the primary axis (C axis) (Thomas & Dieckman, 2010). Sea ice crystals under natural ocean conditions may display multiple growth orientations, resulting in a mixture of vertical and horizontal growth axes of ice crystals; however, a growth advantage is observed in those ice crystals maintaining the horizontal orientation, which is often parallel to any present oceanic currents, creating anisotropy in the crystal structure (Kovacs & Morey, 1978; Babcock et al., 2013; Dickins et al., 2011; Thomas & Dieckman, 2010). Whichever way the crystals are oriented and spaced during initial growth of the skeletal layer, that orientation and porosity will be maintained throughout the growth process.

In multi-year ice (sea ice that has remained for more than one season), brine channels and pockets are smaller due to multi-season ice pack stressors, though any newly forming ice at the base of these sheets displays the same properties of growing first year ice. Snow on the surface of already developed ice decreases the new ice growth rate of developing ice below by insulating the surface from cold air temperatures. Multi-year ice has lower bulk salinity values from multiple freshwater flushing events and is generally less thermodynamically active than first-year ice (Thomas & Dieckman, 2010). Once the ice attains certain porosity and the water drains from the surface, ice above the freeboard is full of air pockets creating conditions that are difficult for sensors to see through.

Melting sea ice has higher water content than growing or stable sea ice. As air temperatures increase, heat is conducted downward, and depending on the permeability of the ice, so does any fresh water that pools on the surface (Untersteiner, 1968). The heat flux from the water, as well as the thickness of the ice, influences the melt rate (Perovich et al., 2003). Convective forces resulting from heat fluxes in the sea ice cause brine channels to reopen, filling with the underlying brine that gets flushed upwards through the ice sheet (Thomas & Dieckman, 2010), carrying microbes and potential contaminants with it. This additional moisture influences sea ice properties important to remote sensing tools. Just as air pockets in the ice create different scattering signatures for optical sensors, water influences scattering characteristics radar relies upon for imaging into the ice sheet, reducing this sensor's functionality to periods of the year when the ice is considered “dry” (Bradford et al., 2008).

1.1.2 *Optical Properties*

Optical properties of sea ice depend on scattering mechanisms within the ice and from the ice surfaces. The presence and distribution of the brine pockets and channels dictate how much of the incoming light reflects, within or back out of the ice, or is absorbed (Perovich, 1996). The structure of the sea ice influences the Inherent Optical Properties (IOPs), specifically the absorption, scattering, and attenuation coefficients. These properties are also dependent on the quantity and type of organic and inorganic inclusions in the ice that are seasonally variable (Light et al., 2008). The highly reflective presence of snow on the ice surface obscures ice attributes. Sea ice typically reflects between 60-90% of incoming sunlight (Light et al., 2008). Attenuation of light in water is a function of scattering and absorption characteristics, which in turn are a function of wavelength (Phase I – Subsea).

As with ocean water, there is seasonality to the light scattering properties of sea ice. Newly forming sea ice has high water content compared to fully developed mid-winter ice or multi-year ice, dampening signal scattering through the ice. As sea ice becomes older, air and brine pockets and residual salts are more influential scattering mechanisms, and corresponding increases in signal scattering can be observed (Perovich 1996; Light et al., 2004; Thomas & Dieckman, 2010). Microbiota influences light absorption, especially in the case of algal blooms in the Arctic spring. In the summer, the ice becomes more porous and the surface layer drains, creating numerous air pockets that are strong light scatterers.

1.1.3 *Acoustic Properties*

Longitudinal wave sound speed, reflectivity, and absorption are the key acoustical properties that determine sound propagation through sea ice (Williams et al., 1992). Sound waves originating from an underwater vehicle are directed upward and bounce from the underside of the ice (Fricke, 1993) to create acoustical maps of the underside of the ice. Scattering from discrete roughness elements on the undersurface of the ice, such as the skeletal layer and large-scale ice thickness variability, influence sound propagation into ice. Scattering from the surface of the ice can be a large portion of the signal detected by acoustic sensors. Frequency dependencies and the properties of the media through which the acoustical signal passes also influences how much of the acoustic signal (described in decibels or dB) penetrates into the ice sheet itself (Fricke, 1993).

Salinity, porosity, shear speed, and incidence angle are also influential to the way sound signal propagates through ice (Williams et al., 1992). Frequency range of the acoustic signal in highly porous ice is very important for quality acoustic measurements (Williams et al., 1992). Whether interest is in ice surface properties or deep in the ice sheet determines at which frequency of acoustic signals are useful.

The implication of the sound-speed profile is that direct-path propagation will be supported at ranges that depend on spreading and absorption loss. If the profile is much warmer at the bottom, the sound bends away from it, refracting back toward the surface where it reflects from the ice and undergoes some loss due to scatter; however, the underside of this first-year ice is relatively smooth in most places, and that loss is less than what would occur in highly ridged ice or multi-year ice (Maksym et al., 2014).

1.1.4 *Radar Properties*

Radar typically operates by detecting the range from a source to a phase interface via emission of a short energy pulse and observing the return time of flight from the target. Within the sea ice, the interface of varying dielectric constants encountered is typically between sea ice and sea

water. Radar technologies vary in the signal frequency, wavelength, propagation techniques, and efficiencies. Longer wavelength radar signals tend to penetrate deeper into the ice, but may not be as sensitive to smaller details. The electric conductivity heavily influences penetration of radar signals into the sea ice (Bradford et al., 2008; Bradford et al., 2015). These dielectric properties largely control radar signal propagation speed, as well as the reflectivity of that signal (Bradford et al., 2008).

The electrical properties of sea ice highly depend on temperature and salinity (Bradford et al., 2015). Brine in sea ice increases the conductivity, which in turn reduces radar signal penetration, while simultaneously increasing attenuation through the ice (Bradford et al., 2008). When ice warms above -5°C , the brine volume of the ice becomes highly conductive, severely limiting the penetration of the radar signal into the ice (Bradford et al., 2008). Similarly, brine pockets and their seasonal changes impact radar attenuation through sea ice.

1.1.5 Interactions of Oil and Ice

Oil released during initial freeze up conditions will likely be incorporated into developing sea ice as frazil ice crystals begin to form ice floes. The presence of oil may depress these initial ice development rates as its effects on water temperature, waves, and microsalinity would be temporarily significant. Direct effects on ice crystal growth structure may weaken the ice sheet until sufficient ice grows below the oiled area.

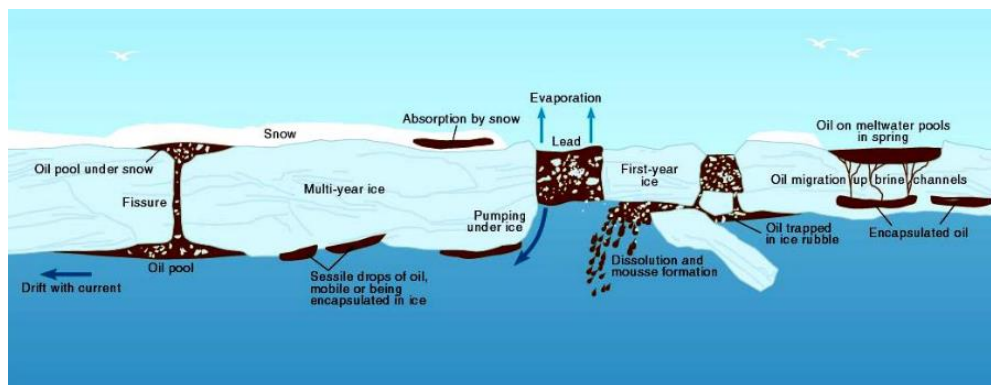


Figure 1. Oil behavior in ice (Potter et al., 2012, adapted from A.A. Allen).

Below continuous sea ice the topography of the underwater ice surface tends to contain oil, unless influenced by dynamic properties such as convection and ocean current (Fingas & Hollebone, 2003). The porosity of the ice and whether the ice was actively growing limits migration into the ice sheet from oil below. Oil spilled below forming sea ice will likely be encapsulated (Norcor, 1975; Dickins and Buist, 1981; Potter et al., 2012), though the amount entrained into ice beyond the encapsulation layer is variable (Karlson et al., 2011).

Oil can appear on the sea ice surface by convection up through brine channels during warming events or by direct deposition on the surface. Oil within the sea ice matrix displays some of the same characteristics as brine in the brine channels. The melt season releases oil that may have been trapped below the ice or encapsulated during the freeze-up process to the sea ice surface in the spring (Petrich et al., 2013). The possibility exists that when the spring flush of surface meltwater is forced through the deteriorated ice sheet via hydrostatic pressure (Petrich & Eicken, 2009; Holt & Digby, 1985; Untersteiner, 1968), oil will travel down in the ice or to the water column below with it.

1.2 Above Ice Remote Sensing Technologies

Airborne and satellite-borne sensors have proven their utility for monitoring the baseline of earth's conditions, and for mapping and tracking large-scale disasters from an aerial vantage. Swaths of imagery available from aerial platforms allow for efficient decision-making when putting people on the ground or in the water for direct observations is too challenging or dangerous. Some aerial sensors with these capabilities can also detect oil on the water surface, on snow and on ice-covered surfaces common to the Arctic. The advantages of aerially deployable sensors are primarily the relative safety of data collection (no requirement to be on the ice surface) and the large areas that can be imaged in a short amount of time.

The Remote Sensing Phase I report to the JIP titled, "Oil Spill Detection and Mapping in Low Visibility and Ice: Surface Remote Sensing" (2013) contains an extensive evaluation of known surface-based remote sensing technologies that may be useful in a spill response scenario. Some of the evaluated sensors and methodologies had been tested in experimental settings for the effectiveness in mapping oil spilled in, on, or under sea ice. Other sensors had never been tested in Arctic-like conditions, but are thought to have a high potential for success. The review included a discussion of the most appropriate conditions for which the given technologies could be useful for oil detection in Arctic conditions, which functionally serves as a guide for future research and development for oil detection experiments.

The Phase II team identified the most promising of these surface-based technologies for detecting oil below the ice or encapsulated within the ice to test their effectiveness at detecting oil in and under a controlled ice sheet. The above-ice sensors tested during Phase II included both passive** sensors (digital cameras, infrared cameras, spectroradiometer), and active** sensors (fluorosensors, frequency modulated continuous wave radar [FMCW], ground penetrating radar [GPR]). ** *Note: Active remote sensing systems require the emittance and receipt of energy, whereas passive systems make observations without the addition of energy.*

1.2.1 Cameras

Cameras are the most common optical remote sensors operating in the visible light range, and can be very effective and intuitive for interpretation. Presence and absence of oil can usually be detected on water when weather conditions are calm and during daylight using a camera. If these calm conditions persist, rough estimates of oil volume can be gleaned from the oil sheen appearance (Bonn agreement, 2009). Similarly, oil can be detected on the surfaces of snow and ice with the use of cameras during daylight. All applications of cameras in the Arctic field environment are weather dependent, as these are passive systems. If the instrument (i.e. camera) does not have the capability to image through clouds, precipitation events, smoke or night (no light source), the utility is diminished.

Advances in precision and resolution of digital cameras continue to increase, while the weight and size decrease, allowing for additional applications for both satellite-based and airborne camera operations. Cameras can provide information as single frames (pictures) or as movies. High-resolution photographs allow for image mosaicking to achieve a larger image of the area of interest. Image mosaicking is the process of digitally stitching together multiple images (optical or non-optical) to create larger areas of available imagery.

1.2.2 Infrared Sensors

Infrared (IR) sensors and cameras are passive optical systems that have demonstrated their utility in many different scientific fields. Near infrared (NIR) senses energy in the 700-1000 nm range

of the electromagnetic spectrum, whereas thermal infrared (TIR) senses energy in the 1000 nm to the 1 mm range. The IR sensor detects the heat (black-body radiation) emitted from any surface. The effectiveness of IR imaging remains weather dependent, as systems cannot detect IR signals through clouds. However, IR sensors are inexpensive and can be mounted to multiple airborne platforms and satellites, reducing barriers to acquiring these kinds of data.

The IR signal between water and oil can be significantly different allowing for discernment during both day and night. Dark oil heated by the sunlight during daylight hours, retains this heat energy after the sun sets, allowing for IR signatures from the oil to remain distinct from the water until temperature equilibrium between the oil and water is reached some hours later (Dickins & Anderson, 2010; Fingas & Brown, 1997). Positive correlations have been shown between measured oil thickness and the IR signature of that oil, though these signatures depend on daytime or nighttime observations (Svejkovsky & Muskat, 2009; Svejkovsky et al., 2012).

1.2.3 *Spectroradiometers*

Spectroradiometers measure spectral radiance or irradiance across various spectral ranges, but most typically in the 380nm to 1000nm range. By using spectroradiometers to measure incoming solar radiation and the energy reflected off of the earth's surface (albedo and remotely sensed reflectance [RSR]), scientists make inferences about the amount of radiance that a surface absorbs. Spectroradiometers are ideal for use in the field where accurate measurements need to be taken under real world conditions, due to their simplicity and resulting durability. Albedo can be measured aerially as well as directly on foot. Aerial averaging of spectral albedos has the benefit of analyzing more area than field measurements taken on foot, but is less sensitive to changes in the signal. (Perovich et al, 2002).

The spectral albedo of sea ice is seasonal in the Arctic and is dominated by the scattering mechanisms in the top few centimeters of ice (Perovich et al, 2002). Albedo signatures from these ice and snow-covered surfaces are typically high (much energy reflected) in comparison to the signal measured from water, which is highly absorptive (low albedo). Oil is also a highly absorptive media, with the potential to radically alter the measured albedo from a given surface. If oil is present on the surface of sea ice, albedo values will be low. If oil is incorporated into the sea ice sheet, it is possible that albedo signatures of the ice would decrease, but would likely be a function of how close the oil is to the sea ice surface. One of the potential advantages of using a spectroradiometer over a visible camera to locate oil in the Arctic ice environment is the ability of the sensor to discriminate oil from other naturally dark features on and in the ice due to the distinct spectral signatures that oil provides (Liu et al., 2015; Praks et al., 2004).

1.2.4 *Fluorosensors*

Fluorosensors are active sensor systems that use UV or visible light to excite a material and then measure the emission energy (fluorescence). The fluoresced light passes through a refracting telescope containing filters to narrow the spectrum of returns, before detectors within the instrument quantify the signal. Aromatic components of oil fluoresce when excited by UV light (300-400 nm). By selecting the excitation and emission wavelengths carefully, oil can be discriminated from naturally occurring materials.

One method used to discriminate oil with fluorosensors is to examine the polarization of the detected signal, the result of which is a fluorescence polarization (FP) measurement (Bello et al., 2012). It has also been proven that laser fluorosensors can discriminate between unoiled and oiled ice (Dick and Fingas, 1992). Many of the natural elements with similar fluorescing properties

to crude oil (algae, etc.) do not have the same polarized return as oil components, thus FP measurements reduce signal interference and false positive readings from naturally occurring substances in the water column (Bello et al, 2012; Fingas & Brown, 2000). Another benefit of polarizing the fluorosensor signal is that the resulting signature obtained by fluorosensors is unique enough to discern specific oil types, primarily due to the specific viscosity of the given oil (Bello et al, 2012; Turner Designs, 2012). In addition, thin slick thickness can be inferred from the relative intensity of the fluorosensor signal, as increased volumes of oil cause a reduced intensity signal (Brown, 2011). These sensors are limited by weather conditions in that they are unable to effectively image through clouds, fog, and other precipitation events that attenuate the excitation and emission signals.

1.2.5 Radar

Radar is an active sensor system that detects the range to a target by emitting a short pulse and observing the time of flight of the target echo. Radar technologies are able to profile areas through snow and ice and are a useful tool for detecting phase interfaces, whether that of oil/water, water/ice, oil/ice, or snow/ice. These radar distinctions between media are based upon the differences in the dielectric values of water, ice and snow as measured by backscatter fluctuations resulting from increased liquid content (Marshall & Koh, 2008). Another advantage is that radars can image large areas in a short amount of time, especially when mounted to either an aerial platform or a swift land-based vehicle (snowmobile). These clear distinctions in return signal from different media have encouraged researchers to examine the radar efficacy in detecting encapsulated oil and oil under the sea ice.

1.2.5.1 Ground Penetrating Radar (GPR)

GPR is a proven technology for detecting oil below the snow surface (Bradford et al., 2010) and below sea ice (Bradford et al., 2008). This radar operates by detecting the range to a phase interface via emission of a short energy pulse and observing the return time of flight from the target. The data consist of a collection of return pulses corresponding to reflections at interfaces where the dielectric permittivity or electrical conductivity change. The dielectric permittivity ratio of sea ice: sea water (~5:88) is far greater than the ratio of sea ice: oil (~5:2.2), allowing for GPR to distinguish oil in ice (Bradford et al., 2008). From these data, 3D cross-sections of the ice profile are created, highlighting the interfaces where phase shift is observed, including those indicative of oil in or below the ice. Though it has been demonstrated that GPR can detect oil slicks as thin as 2 cm under smooth ice, this technology may be limited in its capabilities for determining oil thickness under field conditions where the ice is often deformed into rubble and ridges (Bradford et al., 2008).

The GPR signal is influenced primarily by the brine volume in the sea ice, and also by the scattering and absorptive properties of the ice crystal structure. The anisotropic nature of sea ice can confound radar signal penetration into the ice, a condition that can be reduced by emitting radar energy to the surface using multiple polarizations (Babcock et al., 2013). GPR normally operates in the microwave region, typically ranging from 250 MHz to 1 GHz, and is optimized for detecting oil under ice at 500 MHz (Bradford et al., 2008). This technology is well suited for “cold ice” measurements, but becomes limited under “warm ice” conditions, when the ice is approximately -5°C, and gaining moisture content. Excessive moisture in the ice can create additional ice/liquid interfaces that can combine with the modifying effects of water on ice structure and deformations ultimately alter the conductivity of the ice. Highly conductive ice can cause extensive attenuation of the radar signal in the ice (Bradford et al., 2008), and reduce its utility for detecting oil in warm ice conditions.

Although GPR was designed to be in direct contact with the earth's surface, an aerial trial of GPR was conducted in 2010 to test the applicability of this technology to detect oil in snow from an aerial platform (Bradford et al., 2010). In this study, the GPR was suspended from a helicopter 5-20 m above the snow, below which was a layer of oil. The vehicle flew at speeds varying from 2.5-10.25 m/s, while the GPR was operating primarily in the 1300 MHz range. This experiment proved that GPR can detect oil in and under snow from variable altitudes and speeds. Sea ice is a more challenging material than snow for airborne GPR imaging due to the reduced penetration into the ice. The desire to increase the energy penetrating the ice surface encouraged investment into FMCW radar as a more effective means of detecting oil under ice from an airborne platform.

1.2.5.2 Frequency Modulated Continuous Wave Radar (FMCW)

Unlike traditional radar, the FMCW radar produces a sinusoidal waveform with frequency that varies linearly as a function of time, with a sweep time as small as 0.05 s. In other words, FMCW radar range to the target is found by detecting the frequency difference between the received and emitted radar signals. The range to the target is proportional to this frequency difference. Frequency differences of interest are typically in the kHz range, allowing for a reduced sampling rate required to record the data, compared to that required for a GHz pulsed radar. This reduced sampling rate as compared with traditional radar can reduce energetic costs and complexity in the electronic components. In practice, the transmitted sweep is multiplied by (mixed with) the received signal prior to analog to digital conversion (Marshall & Koh, 2008). After this process, the measured signal is given by

$$M_f = \frac{AR}{2} \cos(2\pi\Delta F)$$

Where A is the source amplitude, R is the received amplitude and ΔF is the frequency difference between the source and received signal at any given time. The frequency difference for any particular reflector remains approximately constant and is linearly related to the travel time from the source to the reflector. These units use microwave frequencies and are able to make observations in darkness and other low visibility conditions. These attributes result in high vertical resolution (1-3 cm), low power requirements, bandwidth flexibility and antennas that can be directionalized, indicating FMCW is a promising technique for identifying oil in an ice matrix (Dickins et al., 2011; Dickins et al., 2012).

FMCW radar can be operated on the ice surface or suspended above the ice (Marshall & Koh; 2008; Dickins et al., 2011; Dickins et al., 2012). This technology is being refined to not only more clearly discern oil under and encapsulated in ice, but to be able to deploy it from an airborne platform (Dickins et al., 2011; Dickins et al., 2012).

1.3 Below Ice Remote Sensing Technologies

There is a potential for using underwater sensors to detect oil by looking up from below the ice rather than down from above it. Current below ice oil detection is mostly performed by people standing on the ice surface, drilling holes into the ice, and placing lights or cameras below the ice. These and other remote sensing tools have also been mounted to submarines and AUVs to survey the underside of Arctic sea ice. These trials demonstrate the promise and challenges of

using traditionally bathymetric sensors to define sea ice and represent the possibility of their use in under-ice oil spill detection (Wilkinson et al. 2015).

Limitations of underwater remote sensing technologies are different than those above the ice surface. Weather plays a much less critical factor in the deployment of these sensors throughout the year, though support vehicles/vessels for AUVs or ROVs would be subjected to surface conditions including ice and storms. Mechanical limitations are tied to the platform on which the sensors are mounted, and typically are payload weight, power, and communications hurdles. Currents and water column properties pose the greatest hindrance to accurate detection of sea ice bathymetry and the potential to detect oil under or encapsulated in the sea ice. Underwater platforms such as ROVs and AUVs are much slower than aerial systems and there can be issues with identifying the location of oil in a timely manner.

In the 2013 ART JIP Phase I report, “Capabilities for Detection of Oil Spills Under Sea Ice from Autonomous Underwater Vehicles” (Phase I: Subsurface), a thorough investigation of below-ice sensors with the potential for detecting oil in and under a suite of sea ice and low visibility conditions was conducted. These investigations focused on a review of available literature and expertise of the reviewers about sonars, fluorosensors, cameras, and multispectral radiometers to provide a set of recommendations for further field-testing of these sensors with oil in ice.

Underwater sensors have been proven in their various capabilities to describe the underside of sea ice, sea ice thickness, features from the seafloor, and components of the water column; however, their full capability in detecting oil under or in ice was only hypothesized until recently as limited tests of these technologies had been attempted in the laboratory and small-scale, field-like settings (Wilkinson et al., 2015). One of the key recommendations from this report was to conduct these tests to determine the ability of each of these sensors to detect oil in and under ice. Addressing this specific recommendation, the Phase II team identified a set of sonar systems, fluorosensors, cameras, and multispectral radiometers to test with oil under and within the sea ice matrix in a large-scale laboratory setting.

1.3.1 Cameras

Camera technology is intuitive, accessible, and constantly evolving to be lighter in weight, higher in resolution, and broader in dynamic range (light sensitivity). Cameras are used from above and below ice to identify potential oil spills and, when using natural light, are inhibited by light blocking scenarios like clouds, snow, night-like conditions, and other processes that attenuate light in the water column. Artificial lighting can be used to augment natural lighting for cameras, though cameras will remain limited by the reflective properties of the surfaces imaged and attenuation of light within portion of the water column where the camera is operating.

When low-light conditions limit the effectiveness of traditional digital cameras, those with large dynamic ranges may provide the contrast between light and dark to discern specific features under the water or ice, including oil. The dynamic range of a camera describes the ratio of maximum (white) and minimum (black) light intensities. This ratio is greatest when both the reflectivity of a surface is high and there are strong non-reflectors in the image, such as a pool of oil against a backdrop of ice. Just like other remote sensing technologies, these digital camera images can become saturated with light or darkness, limiting their use. As a general rule, the larger the pixel size that is achievable with a digital camera, the larger the dynamic range of the camera.

Using images from high caliber digital cameras allows for the creation of quality 2D maps of the underside of ice and the oil beneath it, if present. Mosaicking digital images together allows for

broader data fusion possibilities with other underwater mapping techniques, but like other underwater mapping tools, is limited in the amount of processing time and energy required. The ease of oil detection using cameras will cause these technologies to continue to be included in most underwater sensor packages designed for ice and oil surveys.

1.3.2 *Spectroradiometers*

The versatility of spectroradiometers allows for measurements of reflectance and radiance on the earth's surface, and also measures light transmission through a given medium. In the Arctic, spectroradiometers have been used to measure light attenuation through ocean water, sea ice, and through sea ice covered with snow (Wozniak & Dera, 2007; Perovich, 1996). The amount of light that can be detected depends on the absorption and scattering properties of the medium through which it passes and the wavelength being measured. Arctic Ocean water has seasonality to its optical properties, as sediment load, biological activity, freeze/thaw activity, and overturning events influence the clarity of the water column (Wilkinson et al. (Phase I), 2013; Wozniak & Dera, 2007). As with ocean water, there is seasonality to the light scattering properties of sea ice. Wet ice of the fall and late spring absorbs more light than the more reflective, dry winter sea ice that has more scatterers as air pockets, indicating that moisture content is correlated with the light penetration depth into the ice. These and other variables (e.g. ice thickness, microbiota, sunlight availability) influence the utility of spectroradiometers to function below the ocean or ice surface.

Spectroradiometers have shown to be effective at measuring light transmitted through up to 7 feet of snow-free sea ice (Perovich, 1996). These below-ice measurements demonstrate the variability of light transmittance through the sea ice and the sunlight-dependent nature of the sensor. Success using this sensor to detect oil in or under ice is dictated by the thickness of the oil, as any appreciable volume of oil in the ice matrix obscures the detectable light signal. Thin layers of oil may allow some light to transmit through the ice, but it is unclear how this signal would mimic naturally occurring light blockade, such as an algal bloom just below the ice or in the ice matrix itself, or the variable blocking effects of undulating snow cover.

1.3.3 *Fluorosensors*

The known capability of laser fluorosensors to detect oil on water may provide the same benefits for the detection of oil from below the water surface. Underwater fluorosensors operate on the same principles as described for above-ice sensors. Algae, microbiota, dissolved organic matter (DOM), refined oil products, and other components of the ocean water column can also fluoresce in the same spectral region as crude oil or attenuate the excitation and emission light, though the clear peak of chlorophyll-a containing biologics does allow for refined discrimination (Hoge & Swift, 1981). By adjusting the excitation and emission nm used with the fluorosensor system or adding a polarization component (Hansen et al., 2009), it may be possible to eliminate a number of these false positives, thus reducing uncertainty of this technology in situ.

The main hurdles to the integration of this technology are limited to testing under different water, ice, and oil conditions from below the surface (Wilkinson et al., 2013). The capability to detect encapsulated oil from below using fluorosensors has not been proven in the subsea environment (Wilkinson et al., 2013). The effective depth range for this sensor to operate under the ice or ocean surface is also unknown.

1.3.4 *Sonar*

Acoustic systems use the reflectivity of the oil/water and oil/ice interfaces to identify the presence of oil below the ice (Bassett et al., 2014; Wilkinson et al., 2015; Wilkinson et al., 2014) and in

some cases provide a measure of oil thickness (Wilkinson et al., 2015). Initial testing indicates that it is also possible to detect oil encapsulated within the ice (Wilkinson et al., 2015).

The choice of acoustic frequency and the ice conditions determine the penetration depth and the minimum resolvable oil thickness (Maksym et al., 2014; Fingas & Brown, 2013; Wilkinson et al., 2013). In general, the lower the sonar frequency, the lower the resolution, larger the transducer, and longer the maximum range (Wilkinson et al., 2015; Chu & Stanton, 1998). The higher the sonar frequency, the greater the resolution, the smaller the transducer, and the shorter the maximum range. The beam width, shape, and side lobes generated by the instrument, as well as the bandwidth in which the system operates, also influences sonar resolution (Wilkinson et al., 2013). Sonars also vary in whether they scan individual points or as a scanning beam with a wider swath width.

1.3.4.1 *Single-beam narrowband*

Single-beam narrowband sonars operate at a single frequency, so frequency selection determines the ice penetration and layer resolution capabilities. The narrowband systems use the shape of the temporal return to identify changes in reflectivity associated with interfaces between oil, ice, and water. Experiments show that operation of the transducers in the frequency range of 300 kHz- 5 MHz allows for ice characteristic detection, oil detection under the ice (Wilkinson et al., 2014; Wilkinson et al., 2015), as well as estimates of under-ice oil thickness (Wilkinson et al., 2015). Furthermore, recent tests reveal that these systems, especially those at lower frequencies (< 1 MHz), have the ability to detect oil encapsulated within the ice itself (Wilkinson et al., 2015).

1.3.4.2 *Multibeam*

Multibeam sonar is best known for its exemplary 3D mapping capabilities (Rutledge & Leonard, 2001), which can be used to determine ice thickness. Multibeam sonar is unique in that the data collected over multiple incidence angles simultaneously over a given area are combined at the receiver, via a process called “beamforming”. The signals emitted from the transducer are in a fan shape, allowing for swath imaging of the object or surface of interest. This fan shape dictates calculations to correct for the refraction of the various incidence angles, which relies upon accurate sound speed and water depth. Multibeam sonars can be configured to operate in either a first return mode or alternately to fully reveal the backscatter characteristics of the surface being imaged (Wilkinson et al., 2013; Rutledge & Leonard, 2001).

Signal fidelity and range resolution of multibeam systems can vary significantly. Frequencies used for sampling with a multibeam sonar are chosen based upon the water depth in which the instrument will be operating. In other words, if imaging the seafloor, how far away the vehicle mounted multibeam sonar is from the seafloor. The choice of frequency allows for a direct comparison with the single beam sonar.

Multibeam systems may provide greater mapping capabilities, but also require significant processing effort. Operators of these sonars are quickly approaching the goal of real-time processing for mapping the underside of an ice surface on-board underwater vehicles, which would expand the utility in application of these sensors to real world scenarios.

In the case of an oil spill, multibeam sonar may be able to directly image the oil present under the sea ice or on the water surface when imaged from below. In addition to direct observation, using the 3D maps created from multibeam sonar data, scientists can predictively model the most likely locations for oil to migrate to on the underside of the sea ice.

1.3.4.3 *Broadband*

Similar to the FMCW, broadband sonar transmits a pulse containing a linearly varying frequency. Broadband sonar systems provide detailed scattering signatures of targets over a range of frequencies, allowing for detailed analyses about the specific scattering mechanisms imaged (Chu & Stanton, 1998). The scattered broadband signal is comprised of a coherent and incoherent component. If the interface roughness is very small compared to the wavelength, then the scattering is dominated by the coherent component. However, if the roughness is large compared to the wavelength, then the incoherent component of the scattering dominates (DJ Tang, personal communication). In broadband, the strength of the signal from the target is defined in terms of the differential backscattering cross section and the backscattered amplitude (Clay & Medwin, 1977). These sonar techniques were refined to identify zooplankton in the ocean, but can be applied to detect other scatterers as small as 2 mm depending on pulse lengths employed (Chu & Stanton, 1998). Broadband sonar signals can be analyzed in either the frequency domain or the time domain, a choice based on the given application. These sonars are more sensitive to ambient noise in the medium, typically water, as well as the electrical noise of the system itself, the effects of which can be diminished by increasing the transmit power of the sonar. The greater range resolution of these sonars is achieved by frequency modulating the energy pulse, the “chirp,” when operating at low frequencies (200-565 kHz), thus achieving greater penetration depth and uniform coverage through water (Chu & Stanton, 1998). Additional pulse compression techniques during data processing can be used to enhance the signal to noise ratio of the information, and the temporal resolution of the data (Chu & Stanton, 1998; Bassett et al., 2015).

Broadband sonar systems may be the most effective at detecting encapsulated oil due to the high range resolution allowing for greater penetration into the ice (Wilkinson et al., 2013). A variety of broadband transducers (with different beamwidths and center frequencies) and signals can be used to optimize the parameters for detection and quantification of oil under and in ice. Experiments using broadband transducers at frequencies 200-300 kHz and 350-565 kHz have identified the ability of these sonars to detect encapsulated oil as well as being able to precisely characterize the sea ice (Bassett et al., 2015). These experiments also revealed the difficulties in image interpretation at these frequencies due to scattering from the sea ice microtopography. The balance between low and high frequency broadband transducer selection for detecting oil pivots on the range resolution of the transducers. Low frequency transducers allow for deeper penetration of the signal into the ice, but higher frequencies allow for better characterization of small amounts of oil and small ice characteristics. The impact of beam width and the corresponding acoustical footprint varies by frequency and transducer, the full range of which has not been defined for oil detection in sea ice.

Broadband systems remain to be tested in a field setting for the detection of oil, though they have the potential of providing better penetration and detection capabilities than narrowband systems that are more commonly available.

1.4 Modelling

Modelling the effectiveness of remote sensing tools in Arctic conditions helps to determine the appropriate usage of these tools in specific, real-life scenarios. By testing remote sensing tools in a controlled environment, modelers can use the collected information to validate sensor response to the specific environmental conditions of the testing chamber. Through comparing model predictions to observed data, the demand on various model input parameters can clarify the

critical needs from the environment. In addition, model/data comparisons and model refinement can foster new science, and help identify practical indicators and engineering procedures to detect oil in ice.

The purpose of the modelling component of this project is to provide an expected response curve of the various sensors under expected field conditions.

1.4.1 Sea Ice Property Modelling

High-resolution, 1-D ice growth models can be used to simulate seasonal sea ice conditions, providing ice thickness, temperature and salinity as prognostic variables (Eicken 2003). A single-column enthalpy-conserving ice growth/decay model developed for coupled ice-ocean and climate model applications provides ice thickness and temperature (CICE, Hunke and Lipscomb 2010) and has also been proven effective in describing temperature, sound propagation, salinity, density, light regime, ice structure, and acoustic attenuation.

Due to the lack of a comprehensive ice microstructural model (see, e.g., Petrich and Eicken 2010), it is not possible to explicitly model the full range of microstructural parameters (such as volume densities of brine pockets or brine pocket shape) needed for, e.g., optical or dielectric property modelling. However, based on work carried out in UAF laboratories (Pringle et al. 2009; O'Sadnick, Oggier and Eicken, unpublished data) and available field data (e.g., Stierle and Eicken 2002) for samples from the Barrow ice observatory site, a simplified description of relevant microstructural parameters can be derived from a synthesis of these datasets for temperature and salinity intervals relevant in scenario simulations. Output variables include number density, pore elongation, and pore size as constrained by the resolution/scale of the respective measurements, which can in turn be used as input in optical and acoustical model simulations.

1.4.2 Acoustic Modelling

Sea ice is a complex medium that reflects, refracts, and scatters sound waves in complicated manners. The presence of oil adds additional complexity to this system. Capitalizing on the known benefits of broadband and multibeam radar systems to make predictions about sound behavior though oil and ice can aid in the detection, as well as understanding the fate and transport of, oil through the Arctic sea ice ecosystem.

Currently there are no acoustic models that address sound wave propagation through sea ice beyond treating the ice system as suites of reflectors. Most of the existing acoustic scattering models for sea ice are broadly based on the Eckart (1953) formulation, which treats the surface as stochastic with a roughness parameter and a two-dimensional correlation function, equivalent to a "roughness" spectrum. In developing an acoustic model to address the detection of oil beneath or within sea ice, one possible method is to treat the sea ice as an isotropic, heterogeneous elastic medium with a rough boundary. When modelling underwater remote sensing tools, specifically modes of sonar, important parameters to account for include frequency, range, beamwidth, angle of incidence, ice thickness, ice interface root mean square (rms) roughness, and roughness spectrum. A complete model would be able to make quantitative predictions, given environmental input, of sound energy scattered to all angles at a wide band of frequencies.

Broadband acoustic backscattering measurements could be used to provide a time-series of data on the oil thickness and the water/ice and oil/ice scattering, including both the reflection coefficient and echo statistics. The reflection coefficient and echo statistics are parameters used to guide the development of the acoustic scattering models and the evaluation of those models. By using

observed broadband sonar scattering data over a range of frequencies, it is possible to capitalize on the scattering regimes to infer the interface roughness parameter, as well as to better test acoustic models. The resulting acoustic models would allow for predictions of scattering mechanisms that could be extended to environmental parameters outside of the laboratory setting, as well as more comprehensive analysis of the optimum frequencies, beamwidths, ranges, and other parameters pertinent to field operations.

1.4.3 Optical Modelling

Numerical models for simulating the optical responses of light to a sea ice cover infiltrated or underlain by oil is key to understanding the value of optical remote sensing tools in a response situation. Structural-optical models incorporating parameters such as ice porosity, elasticity, ice-front topography, and ice microstructure, also need to include the disturbance of these parameters by layers of oil within or below the sea ice. Additional IOPs of oil in ice may be significant if the oil is released as a thin layer or migrating through the ice sheet. These detailed oil-in-ice IOPs are not readily available in the literature, but determinations of oil IOPs in seawater (Otremba et al. 2003) can be substituted in these models until observed properties can be reported. 2D optical scattering models have an advantage over 1D models in that they can better account for vertical as well as horizontal variability in the modeled ice (Light et al., 2008). The output from these models can be compared to measurements made under laboratory as well as field conditions, allowing for predictions beyond empirical data.

Local radiation transfer through the ice can also be incorporated for correlation to natural lighting conditions. Though thick oil layers would drastically change the extinction coefficient of an ice sheet, thin layers of oil may behave like other organic impurities in the ice. By using optical models to simulate the two defined experimental spill scenarios, understanding of thin oil layer IOPs under Arctic light conditions may be definable.

1.4.4 Radar Modelling

Numerical models for both pulsed GPR and FMCW radar systems operating in the sea ice environment have been developed (Bradford et al., 2015; Dickins et al., 2011; Dickins et al., 2008). Connectivity of pores and the temperature/salinity dependence of permeability, electrical conductivity, and potential dielectric permittivity, were described by Pringle et al. (2009), Golden et al. (2007) and Jones et al. (2012), and reliance upon these explicit property models is accepted. These property models express the variable under consideration as a function of the brine volume fraction, which in turn is determined by the temperature, salinity and – where relevant – density of the ice. The radar propagation modelling is done entirely in the frequency domain and includes frequency dependent material properties to enable study of second-order frequency dependent wave propagation effects that may prove to be useful indicators of oil. Modelling exclusively in the frequency domain also has the benefit of minimizing the digital sampling rate and results in greater computational efficiency. Testing of the pulsed radar model for numerous real ice conditions has been undertaken, and revealed the model reproduces real radar measurements under known ice condition but a well-controlled field comparison for the FMCW model is still needed.

2. GOALS AND OBJECTIVES

The overall goal of the remote sensing portion of the JIP is to expand the industry's remote sensing and monitoring capabilities in darkness and low visibility conditions, in broken ice and under ice. In the first phase of work to address this goal, the JIP sought state-of-knowledge reports for remote sensing capabilities above and below the ice. The second phase was to conduct laboratory experiments to detect oil using a suite of potential sensors and a modelling effort to infer how those sensors may perform in the field.

To address the second phase of the remote sensing portion of the JIP, a fully integrated experiment, testing remote-sensing tools for detecting oil from above and below an experimental oil spill in artificial sea-ice was designed. The data collected from the above- and below-ice sensor suites were integrated into functional models to determine their potential applicability under real sea-ice conditions. Specifically, the effort in the second phase aims to:

- Acquire spectral, hydro-acoustic, thermal, and electromagnetic signatures of oil on, within, and underneath a flat sheet of sea ice.
- Determine the capabilities of various sensors to detect oil in a specific ice environment created in the test tank.
- Model potential performance of the sensors under realistic field conditions.
- Recommend the most effective sensor suite for detecting oil in the ice environment, based on modelling the expected sensor performance in a wider range of real life scenarios.

This report discusses sea ice properties as they relate to oil management, experimental, and modelling efforts addressing the remote sensing portion of the JIP, and how these efforts can be applied to Arctic spill response scenarios.

3. TEST DESIGN AND METHODS

3.1 Facility and Layout

The experiment took place in the CRREL's Ice Engineering Research Facility Test Basin. This is an indoor facility with a basin 37 m long x 9 m wide and 2.4 m deep (Figure 2). Temperature in the room can be lowered to -24°C using refrigeration air units mounted to the ceiling along the centerline of the tank. A door at one end of the tank provides the ability to separate out a small portion of the tank (referred to in this document as the prep area) and the air temperature in that area can be maintained just above freezing. Two gantry-like, wheeled carriages and a ceiling-mounted rail system provide means for deploying sensors above ice and access to the ice when it is not safe to walk on. A rail system mounted on the bottom of the tank provides a means for deploying a carriage for underwater instruments. The rails continue into the prep area where ice can be removed, allowing cable access to the underwater carriage. The tank also has two ports that provide a means to connect to instruments mounted at fixed locations in the tank, and pocket underwater lighting for backlighting the ice. A heated instrumentation room runs along the length of the tank and provides space for control and logging computers. Access ports and network connections between the test basin and the instrumentation room provide means for connecting to instruments.



Figure 2. Top left, a view along the length of the tank. Windows to the instrumentation room can be seen on the left. Top right, a view back towards the prep area. The door that separates the prep area from the ice tank and the blue carriage is at the end of the rail. Bottom, the tank without water with underwater instrument platform in the foreground and rails for the underwater carriage visible in the tank.

The surface area of tank was subdivided into test areas using rectangular confinement hoops as depicted in Figure 3. Hoops were fabricated using 4" PVC pipes with a vertical hanging curtain fabricated from 13 oz. vinyl coated polyester tarps. The curtains in Hoop 2-5 were trimmed so they extended 15 cm below the anticipated ice thickness when the oil injection occurred to avoid

oil migration beyond the curtain. Hoops 1, 6 and all “A” hoops had skirts that extended down 1 m from the surface. The primary hoops were placed along the centerline of the tank to allow both the submerged and surface sensors to monitor the same areas. These centerline hoops were 3m long (X axis) by 2.5m wide (Y axis) except for Hoop 1, which were 3m long by 6m wide. The wider Hoop 1 was designed to evaluate the side looking capability of the multi-beam sensor. To preserve the ice structure in the primary hoops, secondary hoop designated with “A” suffix received the same oil treatment as the corresponding primary hoop. The off centerline “A” hoops were 1.5m square and outside the detection region of the submerged sensors. Special purpose hoops designated with a “B” suffix were placed off center and used for specialized experiments using a portion of the sensors. A large area of ice along the south side of the basin was left clear to provide a space to remove ice cores during the experiment. An area at the west end of the tank was used for resistivity measurements. The space between Hoops 5 and 6 provided an area clean ice for the instruments to acquire control measurements of the ice sheet.

Ancillary sensors installed in the ice-included thermistor strings (T) for measuring air-ice-water temperatures, ice sound speed (S), rotating broadband transducers (BB) for measuring ice anisotropy effects on sonar, and an electrical resistivity array (R) to examine ice anisotropy effects on radar. The two thermistor strings were installed approximately 10m from each end of the tank near the south side.

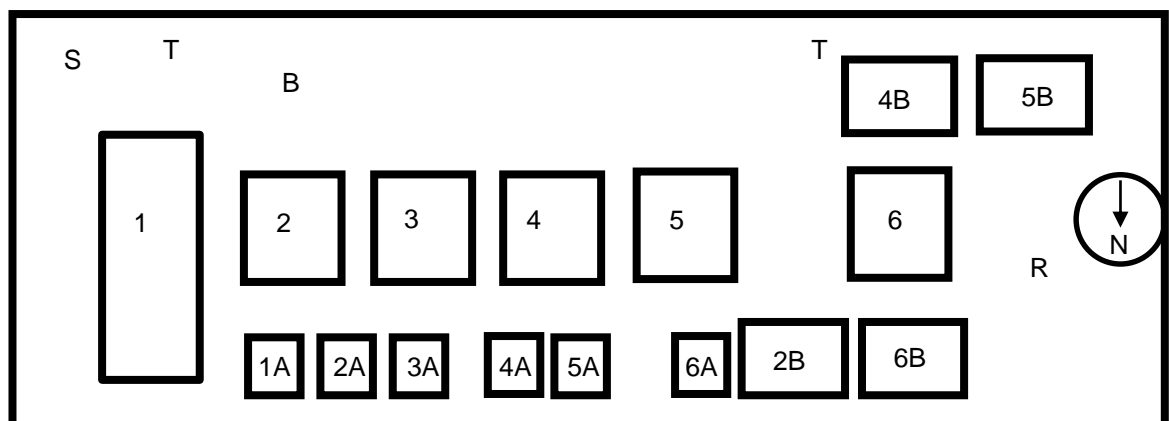


Figure 3. The conceptual layout of the experiments. Thermistor strings were placed at the locations marked with a T. The area marked by R was used for ice resistivity measurements. S represents ice sound speed measurement equipment, and a rotating set of broadband transducers were located at BB.

3.2 Instrument Mounting

Mobile aerial sensors were mounted to the blue (main) carriage that spans and travels the length and width of the tank (Figure 4). The carriage used a rack and pinion drive with variable frequency drive for speed control to facilitate scanning the ice while traversing down the tank (X axis). Radars (FMCW and GPR), EO/ IR cameras and a laser fluorosensor were mounted approximately 2 m above the ice on a boom that allowed the sensors to be 5 m ahead of the carriage to reduce signal noise associated with the carriage itself. The recorded position was at the carriage centerline, the GPR at the end of the boom was 7.15 m and the FMCW 5.85 m beyond the recorded position. Electronics for the aerial sensors were located in a heated control room on the carriage with network access. The blue carriage was also used to support the deployment of oil throughout the experiment. When not in use, the instrument extension was retracted, and the carriage stored in the prep area. A second yellow carriage of similar design

and function was used for mounting an incandescent light array used to simulate the sun and to provide access to the ice surface when the ice was unsafe.

For portions of the experiment several additional aerial sensors were mounted from the ceiling at fixed locations. Fixed sensors included an FMCW radar over Hoop 5B, time-lapse cameras over Hoops 4-6, and two IR cameras. One IR camera was mounted with the surveillance camera along the side of the tank and the other positioned over different areas in the tank during melt-out. Two other surveillance cameras were mounted with different views of test area.

Underwater measurements utilized a motorized carriage that could travel the length of the tank on two parallel rails on the bottom and was accessible from the prep area of the tank (Figure 5). A submerged servomotor moved the carriage along a stationary chain on the bottom of the tank with positioning accuracy within a centimeter. Submerged sensors were mounted to an intermediate sensor plate and then connected to the underwater carriage using alignment pins, allowing for removal of the instrumentation suite from the tank to service the sensors. This put the instruments just over 2 m below the water surface at the beginning of the experiment. A cable bundle for the carriage and a second bundle for the instruments were fed and retrieved by hand in the prep area during operations. The underwater carriage location was controlled from a computer located in the prep area. The instrument cables fed from the prep room through an access port into the instrumentation room for power and data archiving.

Sensors were arranged on the sensor plate to maximize overlap in observation locations. However, physical constraints and signal interference required the instruments to have some separation. Position of the underwater carriage was determined from the servomotor, and set to zero when the CRREL camera reached the border between the prep area and the main tank. Position accuracy was one centimeter and not dependent on the direction of travel. The center position of each hoop was programmed into the servo motor controller at the beginning of the experiment so the carriage could be repeatedly sent to those points. Positions were recorded during each of the transits. Using the start time of the transit the location as a function of time was determined. Offsets in centimeters to the center of the instruments are as follows: EIC laser fluorometer (15), Trios radiometer (10), Aquascat transducers (-10), Broadband transducers (-11), low light cameras (-37), Norbit 400 kHz (-43), Norbit 200 kHz (-64), and Norbit Forward Looking Sonar (FLS) (-102). A negative offset indicates the position is east of the recorded position. There was expected overlap of the measurement area for all except the multibeam sensors, which was not an issue as they traversed the entire tank during observations and sampled the same locations at a slightly later time. The FLS was mounted 60 degrees from the vertical so the actual measurement footprint is far from the platform and dependent on ice thickness.

A fixed set of broadband transducers and two laser fluorometer systems were mounted to the bottom of the tank under Hoop 4B, and the cables run through an underwater access port into the instrumentation room. A pair of transducers were mounted facing each other and frozen into the ice for measuring the sound speed in ice. A set of broadband transducers were also mounted on a 1 m long arm that was manually rotated in an arc along the bottom of the tank to document any spatially variation of the acoustic return as a result of ice crystal growth alignment.



Figure 4. The aerial sensors mounted on the carriage (Top). The control room on the right provided warm space for data recording computers. The sensors mounted on the boom (Bottom).



Figure 5. Top left, the rail system with the chain between the rails run down the centre of the tank. Fixed sensors can be seen on the right side of the image. Top right, the sensor plate mounted to the carriage underwater. (A) The servo motor, (B) CRREL PTZ camera system on the carriage, and (C) the instrument plate. Bottom, The instrument plate out of the water. (D) Trios spectral radiance and irradiance sensors, (E) EIC Labs scanning laser fluorosensor, (F) broadband acoustic transceivers, (G) narrow band acoustic transceivers, (H) low light camera, (I) light source for the cameras, (J) Norbit 400 kHz multibeam sonar, (K) Norbit 200 kHz multibeam sonar, (L) Norbit FLS.

3.3 Experimental Design

One aim of this experiment was to simulate natural sea ice conditions in a controlled environment. It was therefore important to use saltwater for the ice formation. Once the tank was filled, table salt (NaCl) was added to the tank and mixed using submerged pumps and a bubbling system to achieve a starting salinity of 27 PSU. The starting salinity was chosen to achieve a final salinity as close to realistic as possible. Salinity was monitored throughout the experiment, but not controlled after ice growth was initiated. As salt was rejected during the freezing process, the salinity increased throughout the experiment to a value of 37.4 PSU at the completion of the ice growth phase.

Once the salt was added, the room temperature was brought down to cool the water near the freezing point. Chilled glycol was circulated in a loop along the bottom of the tank to provide additional cooling. As the water temperature decreased, all instruments were provided an opportunity to be tested or collect measurements in ice-free conditions. Once the water temperature reached the freezing point, the containment hoops were added to the tank and positioned using lines to the tank sides (Figure 6). The tank was seeded with ice crystals by using fine water droplets sprayed into the air that formed small ice crystals and initiated ice growth.

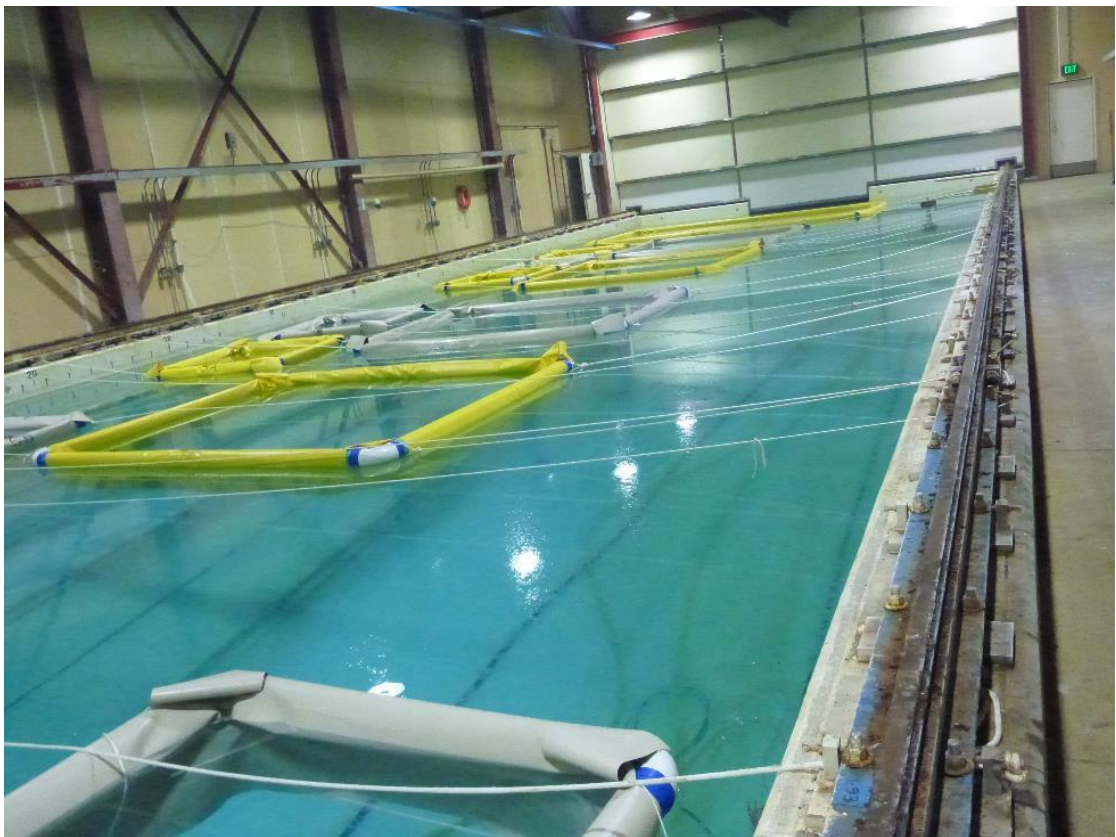


Figure 6. Containment hoops being placed into the tank at the beginning of freeze up. The lines were used to align the hoops within the tank.

The three-month experiment consisted of a two-month ice growth phase during which the air temperature was kept cold to promote ice growth. That was followed by a one-month decay phase during which the air temperature was allowed to warm and the ice to melt.

The test design was to use the six primary hoops for a series of experiments that would test the ability of sensors above and below ice to remotely sense oil through a series of ice thicknesses. Various amounts of oil were to be injected into the hoops at different times throughout the growth phase. The planned ice conditions and injection amounts are provided in Table 1. Hoop 1 was wider than other primary hoops to allow more complete testing of the multibeam sonar units. Experiments were designed to allow detecting the same thickness of oil through different ice thicknesses or to vary oil thickness while holding ice thickness constant. The ice sheet was grown as flat as possible so injected oil would uniformly fill the hoop to a nominal thickness that could be determined from the area of the hoop and the volume of oil injected.

For above-ice sensors, the ice growth between each injection led to varying ice thicknesses to test oil detection below the ice. After the oil injections, ice growth continued, eventually leading to oil encapsulation. For the below-ice sensors, these scenarios created several repeated experiments where the encapsulation process was observed and sensors were allowed to record data until the oil signal was no longer detectable.

Table 1. Planned injection conditions in primary hoops. During stair step injects the oil was added in 1 cm depth increments to allow for measurements as a function of thickness and for the oil to settle in the hoop.

Oil Confinement Hoop Configuration CRREL Basin								
Updated		5/3/2014						
Hoop ID	Dimension (L x W)	Curtain Depth	Surface Ice @ Freeze up	Ice Thickness @ Oil Injection	Nominal Oil Thick	Oil Injection Method	Snow	Remarks
	m	cm		cm	cm			
1	3 x 6	100	grease	5cm Frazil+	0.5	Spray on Surface and mixed		test multi-beam system. Start with grease ice spray oil in surface and mix. See Recycle of Hoop 1
2	3x2.5	35	columnar	20	2	single		thin ice with oil encapsulation
3	3x2.5	50	columnar	35	1	single		mid-thickness ice with thin layer of oil that will be encapsulated. Compare with 3,4,and 4b
4	3x2.5	50	columnar	35	5	stair step		mid-thickness ice with thick layer of oil that will be encapsulation. Compare with 3,4,and 4b
5	3x2.5	70	columnar	55	2	single		Thicker ice with encapsulation . Compare with 2 and 5b
6	3x2.5	100	grease	80	4	stair step	Snow in steps stay thru melt out	Thick ice thick oil prior to melt out

There were some deviations from the planned injections as the experiment progressed. The actual conditions are provided in Table 2. Insulation was added above Hoops 3-6 to create a 10cm wide border of thicker ice inside to curtain to bias the oil toward the center of the hoop and avoid oil migrating up the ice-curtain interface. The dome on the underside of the ice resulted in non-uniform ice thickness with the thinner ice in the middle of the hoop. Thus the ice thickness is less than originally planned during the injection and the oil thickness was not constant within the hoop.

Table 2. Injection conditions in primary hoops along the centerline. "A" hoops were injected on the same day as the primary hoop. Ice thickness was estimated from the distance to a sonar transducer plus

an estimated freeboard height. The curvature of the ice bottom in Hoops 3-6 led to oil and ice thickness differences of several centimeters.

Hoop ID	Injection Date & Start Time	Ice Thickness	Injection Amount	Sonar Measured Oil Thickness	Remarks
		cm	l	cm	
1	5-Nov-14 16:37	5 - 15	90	1	Mix of broken ice and slush
2	12-Nov-14 13:39	16	150	1	Oil lost out one side of the hoop over a day
3	17-Nov-14 13:24	26	75	2	
4	20-Nov-14 12:45	29	225	4	Three injections over an hour to build oil slowly.
1	4-Dec-14 10:37	46	360	5	
5	9-Dec-14 11:40	54	150	6	
6	6-Jan-15 13:50	68	300	9	

Additional hoops designated by a “B” in Figure 3 were used for instrument specific experiments. Warmer oil was injected into Hoop 2B to examine with IR. However the IR sensor did not operate during the injection. Oil was injected into Hoops 4B and 5B to approximately 2 cm thickness. Hoop 4B had stationary sensors mounted below the ice to allow a time series from a fixed location. Hoop 5B had a FMCW mounted above it to provide a time series. At the end of the experiment Hoop 5B was also used to do a surface addition of oil and snow.

3.4 Health and Human Safety

In support of the months of testing that took place at CRREL, an extensive Health, Safety and Environment (HSE) Plan (Appendix VIII) was developed by the hosts of the tests at the US Army Corps of Engineers, Engineering Research and Development Center, Cold Regions Research and Engineering Laboratory in Hanover, New Hampshire. The vetted HSE Plan identified all potential hazards associated with the RSOI testing performed, the mitigation of those hazards, and the resulting standard operating protocols of the elaborate experiments. The primary objectives of the HSE Plan were to conduct all aspects of the RSOI tests with no accidents or lost-time incidents resulting from safety violations, with specific focus on,

- Safety of technical staff during daily assembly, operation and disassembly of the testing equipment
- Safety of researchers, staff and observers during ice observations, oil injections and facility tours
- Safe storage and handling of unweathered crude oil

Throughout the duration of the four-month experimental period, the only violations of the HSE Plan were by visiting researchers wearing inappropriate footwear. In both cases the researchers

were removed from the testing area and provided with approved footwear in which they could continue to fulfill the research objectives.

3.5 Oil and Oil Injection

Alaska North Slope (ANS) crude oil was used for this experiment. The oil was characterized and the properties are given in Table 3. The oil for injection was stored on the blue carriage that the above-ice sensors were mounted to. This carriage was parked in prep area of the basin room when measurements were not being collected, which kept the oil near zero degrees Celsius. To introduce the oil within a containment hoop, a hole was drilled outside of the containment hoop, and a wand attached to the injection hose was guided through the hole and into the containment area using underwater cameras. The injection hose was attached to a variable speed lobe pump that was used to inject a known volume of oil under the ice within the containment hoop (Figures 7, 8). Water was drawn from the tank thru the injection hose and collected in a waste tank on the carriage. Confident the air was purged from the system, the direction of the pump was reversed and fixed volume of oil was injected. At the end of the injection the waste water in the collection tank was pumped through the injection system to clear the oil from the injection system. In addition to the CRREL PTZ camera a second underwater video camera was lowered through a separate hole outside of the containment area to monitor the oil injection from a different perspective. The amount injected was determined by calculating the required change in oil level in the tote of ANS on the carriage.

Table 3. North Slope Crude oil properties as analyzed by SL Ross.

ANS 2014	API=29.8		
Evaporation (Volume %)	0	23.27	31.44
Density (g/cm³)			
0 °C	0.889	0.929	0.942
20 °C	0.874	0.924	0.928
Dynamic Viscosity (mPa.s) at approx. 180 s⁻¹ except 31.4% evap 0 °C at 120 s⁻¹			
0 °C	40	686	2778
20 °C	13	91	224
Kinematic Viscosity (mm²/s)			
0 °C	45	738	2948
20 °C	15	99	242
Interfacial Tension (dyne/cm)			
Oil/Air	27.0	30.4	31.8
Oil/Seawater	15.9	17.7	19.6
Pour Point (°C)	-18	-3	3
Flash Point (°C)	<-10	66	119



Figure 7. Oil injection system from above the ice. The oil tote is in the blue mesh cage behind the wooden supports for the radar. The lobe pump is to the left of the tank. The green pipe is used to feed the oil hose and wand under the ice. At the other corner a video camera mounted on a stick was used to monitor the injection progress.



Figure 8. The oil injection system as seen from below the ice prior to oil injection.

3.6 Sampling Sequence

A detailed above- and below-ice sampling scheme was developed for each injection. Two primary measurement methodologies were used. “Point” measurements were collected by holding the carriages at a fixed location and collecting data with sensors capable of point data collection. “Sweep” data was collected by activating the scanning sensors and performing a transect of the test basin, collecting data as the carriage was moving. A “hoop sweep” started at the center of the hoop prior to the one of interest and ended in the center of the hoop following the one of interest. For example, to perform a hoop sweep on Hoop 3, sensors would be activated in the middle of Hoop 2 and remain active while collecting data until the carriage reached the middle of Hoop 4. “Basin sweeps” were measurements made of the full length of the test tank.

Prior to the oil injection, a set of baseline measurements were made with all sensors above and below the ice. The aerial instruments were turned on and the above-ice carriage completed a baseline hoop sweep. A set of underwater instruments were turned on and a hoop sweep completed. Multiple underwater hoop sweeps were required to reduce instrument interference with each other. After the initial underwater sweep, a different configuration of instruments was activated and a second hoop sweep in the opposite direction completed. This process was repeated until all underwater instruments had documented the initial conditions. After the hoop sweeps were complete, the underwater carriage was parked under the hoop to be injected to collect point measurements of the clean ice. A set of instruments would remain on under the hoop as oil was injected. They were allowed to measure the injection area for up to an hour after the injection. During that hour the aerial sensors completed post injection hoop sweeps. After an hour the underwater instruments were cycled to allow all instruments to collect point measurements of the fresh oil and hoop sweeps were conducted with all instruments. At the conclusion of the post injection hoop sweeps, the underwater carriage was parked under the hoop and a set of sensors monitored the oil over time.

Hoop sweeps were conducted with aerial and underwater sensors each day for the next three days. Throughout the experiment, basin sweeps with all sensors were completed once a week. When not being used to make sweep measurements, the underwater carriage and sensors were parked under the center of the hoop that had most recently been injected. The aerial carriage and sensors were parked in the prep area once measurements were completed.

3.7 Ice Conditions in Individual Hoops

3.7.1 Hoop 1

Two injections were completed on Hoop 1 during the testing period. One of these was the first injection of the experiment, and was designed to represent Arctic freeze-up conditions. The second was when the ice was approximately 45 cm thick to allow for additional analyses by the underwater sensors.

For the first Hoop 1 injection, slush ice was generated in a separate area to supply the desired slush ice for Hoop 1. After two days of freezing in the basin, the ice in Hoop 1 was broken into small chunks and the slush mixed into the space to create a brash ice environment that had a nominal thickness of 5 cm. On November 5th, ninety liters of oil was injected under the ice mixture and allowed to mix and freeze in place (Figure 9). Oil was observed rising through the ice which continued through the next day.



Figure 9. Oil and ice mixture from the first injection into Hoop 1 as seen from above (left) and below (right) one day after the injection.

Oil was injected into Hoop 1 a second time on December 4th. This injection was designed to allow the multibeam sonar to view the largest oiled area possible during the experiment. Oil from the first injection remained on the surface. The ice thickness was 46 cm and 360 liters of oil was injected. The injection did not fill the hoop evenly (Figure 10). The pictures available only show a portion of the hoop.



Figure 10. Hoop 1 near the end of the second injection. This picture contains a little more than half of the hoop.

3.7.2 Hoop2

One hundred and fifty liters of oil was injected into Hoop 2 on November 12th when the ice thickness was 16 cm. It was later noticed that a corner of the containment hoop had frozen up into the ice and the oil migrated out of the hoop over the following day. Initial measurements were expected to see oil, but little remained after 24 hours (Figure 11). A small volume of oil was captured in the natural undulations and skeletal layer, which migrate up through the ice.

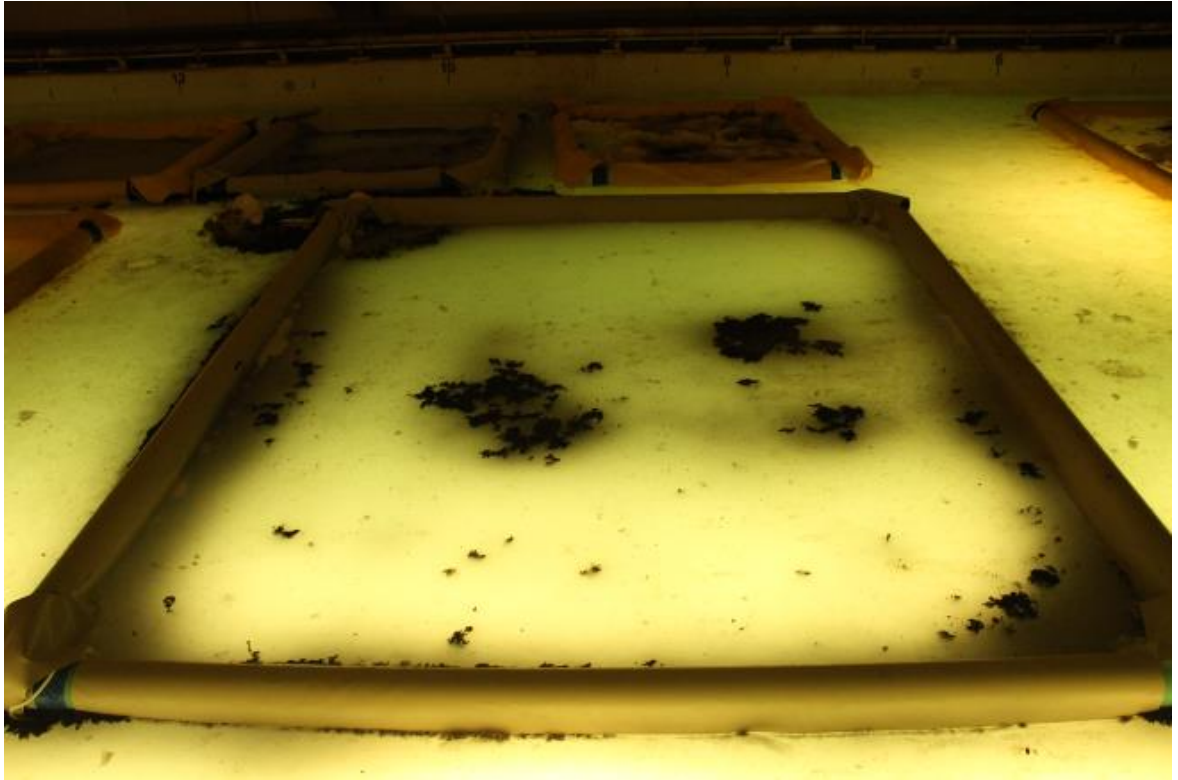


Figure 11. Hoop 2 lit from below to show final distribution of oil. The dark shadow along the edge of the hoop is the containment curtain extending downward through the ice. The oil migrated along the perimeter of the hoop and leaked out of the hoop in the upper left corner.

3.7.3 Hoop 3

Because of the loss of oil in Hoop 2, foam insulation was added to the surface in Hoops 3 to 6 to retard ice growth in the center and thereby create a dome in the ice to act as an additional containment measure. This led to an oil distribution that favors the center of the hoop and leaves un-oiled ice along the edges (Figure 12). Seventy-five liters of oil was injected on November 17th and was observed to remain within the containment hoop. Ice thickness in the center of the hoop was 26 cm. Over the next 24 hours, oil was observed migrating to the ice surface (Figure 12). A large air bubble was accidentally introduced into the hoop during the oil injection. Attempts were made to remove the air prior to oil injection, however, the video of the injection indicates significant amounts of air remained. While gas bubbles are expected from a subsea blowout, the addition of air was not part of the experiment design.

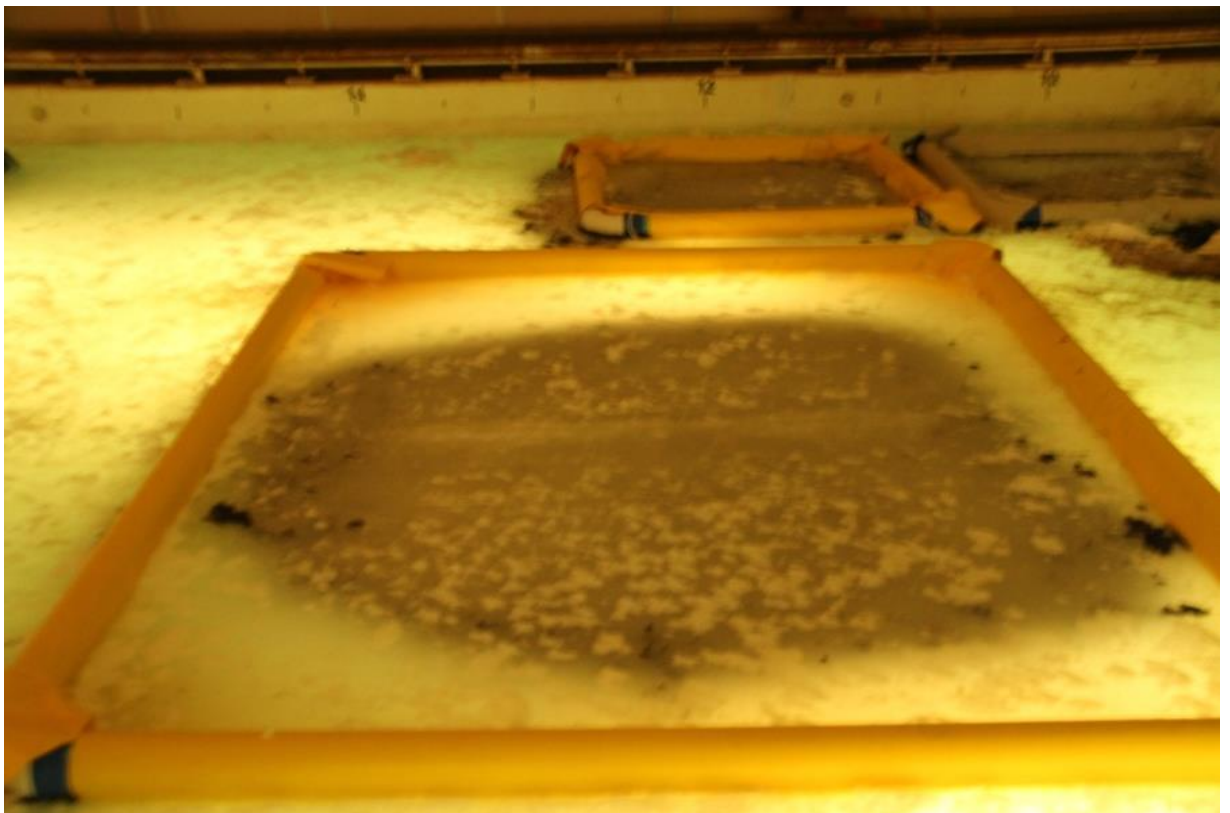


Figure 12 Oil distribution in Hoop 3 showing oil that reached the surface along the edges.

3.7.4 Hoop 4

The injection into Hoop 4 occurred on November 20th when the ice thickness was 29 cm. A stepped injection was used with a target thickness of 1 cm per injection (75 liters per injection). The test plan defined five injections for this hoop; however, oil was observed to begin to leak out of containment at the end of the third injection so the process was stopped at that point. Some bare ice remained around the edges (Figure 13). Because of the oil migration to the surface in previous hoops, a time-lapse camera was installed over the hoop to observe any oil migration. Again oil was observed to migrate up over a 24-hour period (Figure 13).



Figure 13. Top. A back lit picture of Hoop 4 showing the final oil distribution. Bottom. The migrated oil distribution as seen from above one day after the oil injection.

3.7.5 Hoop 5

One hundred and fifty liters of oil was injected into Hoop 5 on December 9th. The ice thickness at the center of the ice was 54 cm. The oil remained near the center of the containment skirt (Figure 14). As with the earlier hoops oil was observed migrating towards the surface over time, although it took longer to reach the surface.



Figure 14. Backlit picture showing the distribution of oil after the injection.

3.7.6 Hoop 6

Three hundred liters of oil was injected on January 6th when the ice thickness was 68 cm. The oil did not completely fill the hoop (Figure 15). Since the room temperature was raised soon after this injection the oil did not become encapsulated in ice.



Figure 15. Oil distribution in Hoop 6.

3.7.7 Hoop 4B

Ninety liters of oil was injected under Hoop 4B on November 20th for detecting encapsulation by broadband sonar and underwater fluorosensors.

3.7.8 Hoop 5B

Ninety liters of oil was injected under Hoop 5B on December 17, 2014 with a target oil thickness of 2 cm. Most of the oil collected in the center of the hoop so the actual oil thickness is expected to be greater than targeted. On January 07, 2015 the equivalent of 2 cm of oil was added to 8 cm of snow (Figure 16). After measurements another 8 cm of snow was added to the hoop.



Figure 16. Snow and oil on the surface of Hoop 5B under the ceiling mounted FMCW.

3.7.9 Snow pile

In December, a snow pile was placed along the edge of Hoop 6 that faced Hoop 5 (Figure 17). The snow was brought in from outdoors in buckets and piled on the ice surface of the basin to make a bank that extended the width of the hoop, about 1 m wide, and 40 cm high at the peak. The purpose of the snow was to provide an opportunity to examine the effect of snow on the light field observed from below.



Figure 17. Position of radar systems. Snow can be seen along the edge of Hoop 6.

3.8 Instrumentation

3.8.1 Above Ice

3.8.1.1 Frequency Modulated Continuous Wave (FMCW) Radar

The Frequency Modulated Continuous Wave (FMCW) radar used for this project was Prototype version 3. The FMCW radar was mounted on the boom of the blue carriage (Figure 17) that allowed for data collection over the main hoops. A separate FMCW radar system measured continuously from a stationary position over Hoop 5B. The FMCW systems performed continuous frequency sweeps from 500 MHz-2 GHz, with a sweep duration of 0.01 seconds, and approximately constant amplitude across the frequency band. Due to the size, weight, and cost of the directional horn antennas, only one polarization was used with each system, which was horizontal and orthogonal to the long axis of the tank. The FMCW radar systems were custom designed and built to maximize performance for detection of oil in ice, and consisted of surface mounted components on a printed circuit board. One of the big improvements in Prototype 3 was the use of a double balanced mixer, with Q ports, and I, which allowed a direct measurement of both amplitude and phase. This system is the same prototype used in previous sea ice experiment at CRREL and tested in the BSU cold laboratory on freshwater ice (Dickins et al. 2012). For this project, a complete backup system was fabricated to protect against the possibility of a complete system failure during the experiment. As this did not occur, this backup system was opportunistically used to perform continuous stationary measurements, although this was not planned in the original proposal.

FMCW radars operate in a significantly different way compared to commercial GPR systems. Rather than emitting a short impulse with a time duration approximately equal to the inverse of the bandwidth (~1 ns for 1 GHz bandwidth), a continuous wave is transmitted over a duration which is many orders of magnitude longer (0.01 seconds). The system is designed to transmit at a frequency, which varies extremely linearly, and the received signal is mixed with (i.e. multiplied by) a sample of the transmitted pulse within the analog hardware. This signal contains the sum and the difference of the frequency content between the transmitted and received wavelets. An analog low pass filter removes the unwanted frequency sum before digitization, such that the measured digital signal contains power at frequency differences between the two analog signals.

Due to the linear frequency sweep, and under the reasonable assumption in this experiment that there is no dispersion (wave velocity is constant with frequency), for a given reflection the frequency difference is constant across the entire band. Since the slope of the linear frequency sweep is known, the frequency differences can be converted to travel-time to the reflectors (e.g. Marshall and Koh, 2008). An example for one reflector is shown in Figure 18. The advantages of this technique are larger total integrated power, broader bandwidth, and more control over the transmitted wave. In addition, the signal can be digitized at speeds orders of magnitude lower than impulse GPR systems, reducing end cost. Horn antennas can be used, which are more directional than typical shielded dipole antennas typically used with GPR systems. Currently, FMCW systems in the frequency band required for sea ice penetration are not commercially available, therefore these radars had to be custom designed and fabricated for this application. While this resulted in a large R/D cost over the past 5 years, the system can now be replicated at a fraction of the cost of commercial GPR systems.

In data processing, the digitized mixed signal is formed by combining the I and Q channels from the double balanced mixer, filtered in the frequency domain, and internal reflections are removed by subtracting a calibration measurement made with no reflectors present. This step is tested and tuned using measurements made while the distance to a known reflector is changed continuously. The signal is transformed to the frequency domain using a windowed and zero-padded Fast Fourier Transform (FFT). A Kaiser-Bessel window is used, which allows optimizing the transform by providing control between amplitude accuracy and resolution. A range gain is applied to the signal, and if subsections of the frequency sweep contain obvious noise they are removed. Finally, migration is applied in an approach similar to that normally used with commercial GPR systems.

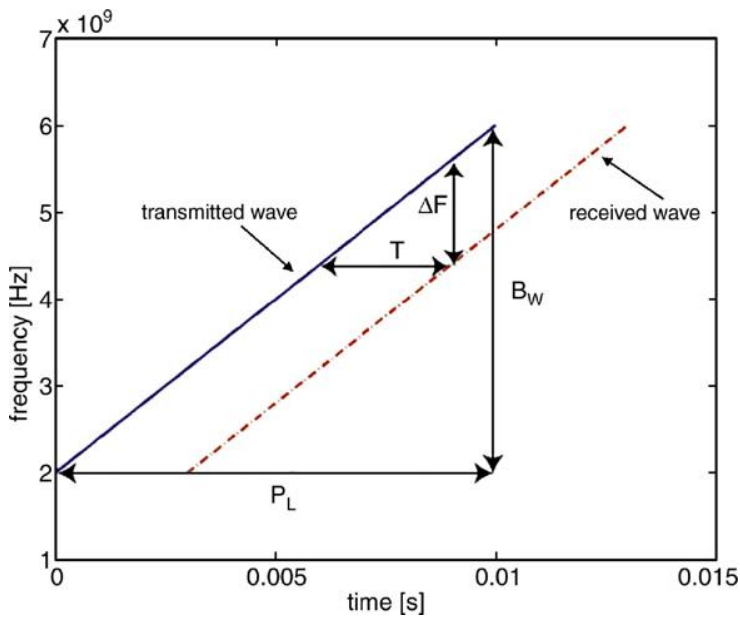


Figure 18. Example transmitted and received FMCW wavelets for one reflector, showing constant frequency difference and relationship between travel time to reflector, frequency difference, bandwidth, and pulse length (from Marshall and Koh, 2008).

Previous work by this group included the development and testing of earlier prototypes, which used directional couplers and detectors to mix the received signal with a sample of the transmitted waveform. These systems were not phase-stable and could measure only amplitude, not the phase of a reflection from the ice/oil/water interface. The newest prototype measures both the real and imaginary components of the mixed signal, and the software to leverage the phase information was developed. In addition to phase information, this approach allows an estimate of the background noise. Both positive and negative frequencies can be estimated, with one containing reflections of the transmitted wavelet, and the other a measure of the background noise internal to the radar and noise in the environment.

To reduce system noise, dedicated ruggedized PCs were placed in the electronics boxes adjacent to the antennas. This improved overall system noise. A control computer communicated with the radar PC units via an Ethernet cable, with remote desktop software. A low noise amplifier was improved and added to both systems to increase the transmit power.

3.8.1.2 Ground Penetrating Radar

A PulseEKKO Pro sensor and software system was used for all GPR measurements and acquired data with both 1000 MHz and 500 MHz antenna sets. These systems produce a broadband pulse with a 2-3 octave bandwidth approximately centered on the dominant reported frequency of the antenna when coupled to the ice, but a frequency roughly 50% higher when deployed in the air. The 1000 MHz aerial sensors were at too high a frequency to penetrate the ice and are not reported on. The 1000 MHz antenna measurements shown were acquired on the ice surface while the 500 MHz antennas were deployed from the boom over the primary hoops and on the ice surface. Radar profiles were acquired in two horizontal but orthogonal polarizations – one perpendicular to the long axis of the tank and the other parallel to the long axis. This mode of acquisition enabled the evaluation of azimuthal anisotropy in the electrical properties of the ice and to process the data to eliminate the effect of spatially variable attenuation anisotropy.

Off-ice measurements

Aerial GPR measurements were made to provide a comparison of off-the-shelf radar to our purpose-built FMCW radar under the experimental conditions. We acquired measurements with the 500 MHz GPR antennas mounted at the end of the boom in a custom built bracket (Figure 17), which utilized two GPR antenna pairs arranged in orthogonal horizontal polarization. The GPR was placed to ensure that reflections from the carriage did not have the same arrival time as reflections from the base of the ice. However, reflections from the boom and various other objects in the facility still produced significant interference with this system.

The phase center of the antennas was approximately 2 m above the ice surface to ensure that all reflections from the ice surface and below would be in the far-field region of the antennas. The lower bound of the far-field region is generally accepted to be the Fraunhofer distance, which is defined as $2D^2/\lambda$ where D is the length of the dipole antenna and λ is the wavelength of the signal. Radiating in air with a nominal frequency of 500 MHz, we have $\lambda = 0.6$ m. The antenna length was 0.18 m giving a Fraunhofer distance of 11 cm, so the ice surface at a distance of 2 m was well beyond the far-field transition.

The system was configured so that traces could be acquired in rapid succession from the two orthogonal antenna pairs with a trigger received from the FMCW control computer. Data from the two antenna pairs were acquired simultaneously using multichannel acquisition. Since the FMCW and GPR operate in the same frequency band, there was potential for interference between the two signals. To avoid this interference, trigger timing was set to ensure that the FMCW and GPR signals were not overlapping. With the carriage moving along a profile at approximately 2 cm/second, the trigger interval resulted in a nominal GPR measurement spacing of 5 cm, which is more than adequate spatial sampling for the purposes of this test.

Finally, 256 GPR pulses were recorded and vertically summed for each polarization at each measurement location to achieve a factor of 16 improvement in the signal to random noise ratio.

Data processing

Because of high levels of coherent noise and significant scattering from surface objects (e.g. the snow pile evident in Figure 17, the hoops themselves, etc.), the data processing flow for the above ice measurements differed substantially from the surface coupled processing flow. Processing included 1) a high pass filter (DEWOW) designed to attenuate the low frequency transient typical of surface coupled radar; 2) a time-zero shift to correct for temperature drift and recording start lag; 3) Median trace background subtraction to attenuate high levels of coherent noise caused by scattering from the carriage and boom; 4) geometric spreading correction; 5) vector summation of the orthogonal polarizations; 6) phase-shift wave field migration (focusing) to place scattered energy at its point of origin; 7) computation of instantaneous attributes (phase, frequency, and amplitude).

On-ice measurements

Surface-coupled (on-ice) measurements were acquired with both 1000 MHz antennas and 500 MHz antennas. The 1000 MHz data provide a high resolution (cm scale) measure of the sub-ice topography. The 500 MHz ground-coupled data are analogous to data we have acquired in previous tests at CRREL and Svalbard where oil in and under ice was successfully detected (Bradford et al., 2006). Confidence in this mode of acquisition encourages the use of these data as baseline measurements for comparison and evaluation of the above ice radar performance.

1000 MHz measurements

The 1000 MHz antennas utilized a custom built frame similar to that of the 500 MHz airborne system (Figure 19). Two horizontal orthogonal polarizations were acquired simultaneously using a multi-channel system. Repeat measurements were acquired in two types of surveys with the 1000 MHz system. These consisted of long 2D profiles along the centerline of the tank and traversing containment cells 2-6. The primary objective of these surveys was to test ice penetration and oil detection in the higher frequency band and to provide a cm-scale measure of under ice topography. An odometer wheel trigger was used to acquire a polarimetric measurement every 5 cm along the 2D profiles and stacked 8 pulses per position to attenuate random noise.

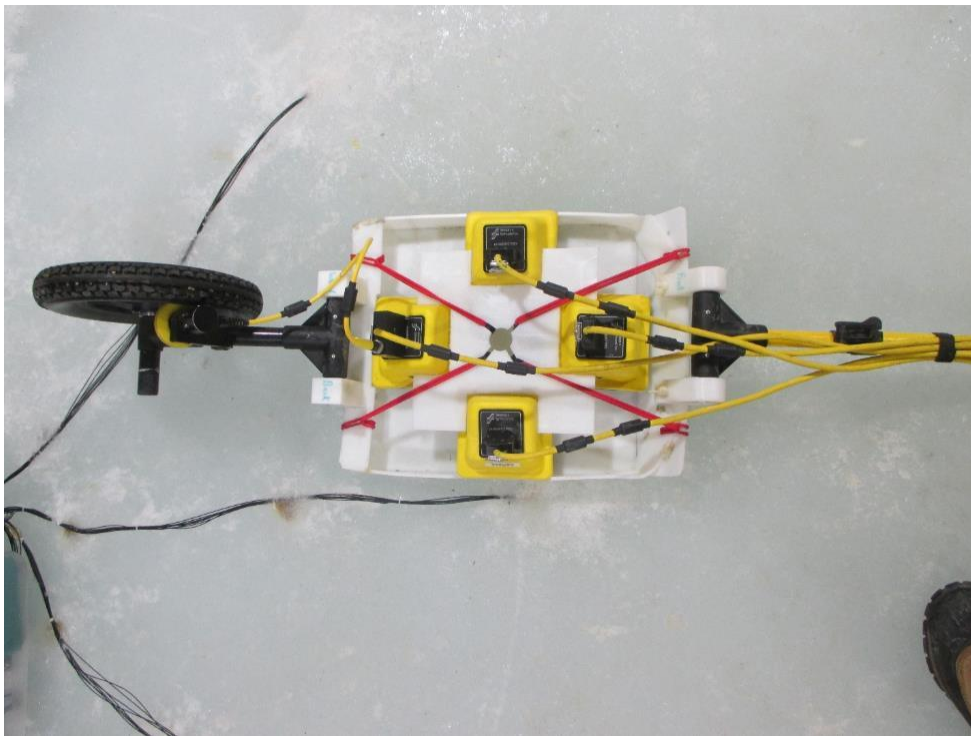


Figure 19: Photo of the 1000 MHz, surface-coupled GPR.

Common-midpoint measurements

During each 3D survey, an expanding spread, common-midpoint (CMP) record centered within the 3D survey template was recorded. The CMP was acquired in each orthogonal polarization. A CMP record is obtained by incrementally increasing the distance between the transmitting and receiving antennas about a common central point. As the antennas move further apart, the reflected wave must travel a greater distance and has a correspondingly greater travel time. From the travel time vs. separation distance curve, it is possible to calculate the bulk propagation velocity through the ice. Using velocity, data can be converted from the travel time domain to the depth domain. Additionally, this data allows for the calculation of the sea ice permittivity for validation and calibration of the ice property model.

500 MHz measurements

For the on-ice 500 MHz profiles, only one set of antennas was available. The single antenna resulted in the acquisition of the two orthogonal polarizations in two separate passes. Care was taken to ensure that the start position for the antenna phase center was the same for both

polarizations. The profile traversed along the center of the tank and crossed containment Hoops 2-6. Traces were collected every 5 cm along the profile and stacked 8 pulses per position to attenuate random noise.

Processing

The data processing flows for the 500 MHz and 1000 MHz datasets were the same and included 1) a high pass filter (DEWOW) designed to attenuate the low frequency transient typical of surface coupled radar; 2) a time-zero shift to correct for temperature drift and recording start lag; 3) geometric spreading correction; 4) vector summation of the orthogonal polarizations; 5) computation of instantaneous attributes (phase, frequency, and amplitude); 6) ice bottom picking to map ice thickness. For the CMP analysis, travel times were picked for the ice-bottom reflection then fit with normal move out equation ($t^2 = t_0^2 + d^2 / v^2$) using linear regression in the t^2 vs d^2 domain to find the velocity.

3.8.1.3 *Cameras*

Several camera systems were used for above ice measurements. HD Internet cameras were mounted along the side of the tank and on both carriages to document a majority of the test activity (Figure 20). Webcams provided a live feed in addition to archiving images every ten minutes throughout the duration of the experiment. Digital cameras were mounted from the ceiling above Hoops 4, 5, and 6. The cameras provided a direct view of the hoops (Figure 21), and were programmed to collect an image every minute from just prior to injection of oil in the hoops until the melt period was completed. A BAE combined visible/IR camera system was mounted on the instrument boom and video was collected during the sweeps of the tank. This system suffered from the cold environment and collected limited amounts of data. During the melt out phase, two infrared cameras were deployed in the tank. One was mounted near the webcam on the side of the tank and collected images once a minute (Figure 22). A second IR camera was deployed for short periods of time, viewing directly down on specific hoops.



Figure 20. An image collected by the webcam on the side of the tank viewing down the tank. On the left side of the image is Hoop 5 and Hoop 1 is on the far right.

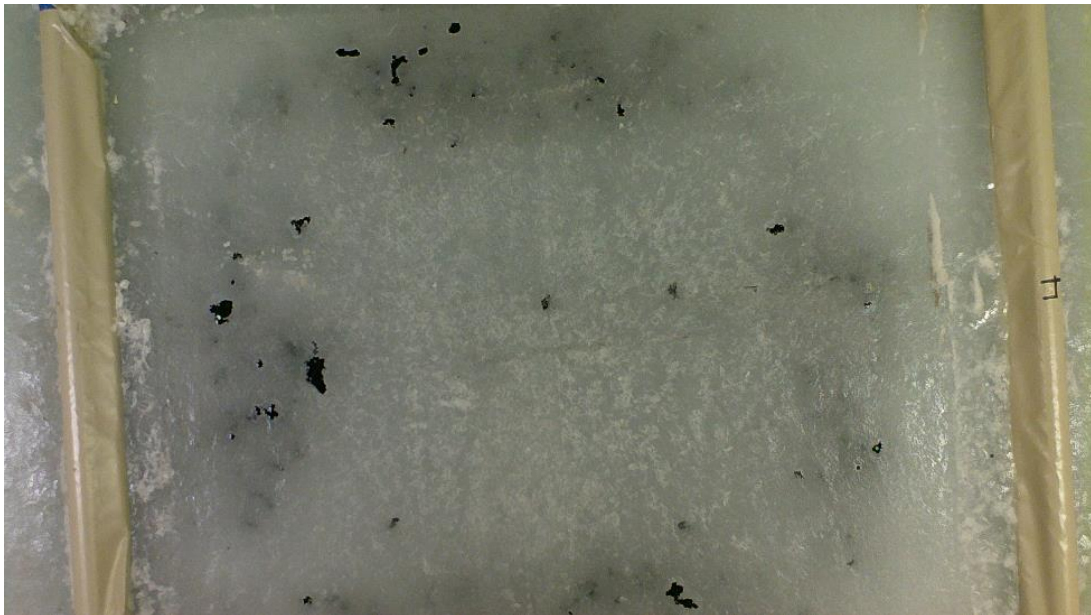


Figure 21. Picture of Hoop 4 from above from the time-lapse camera.

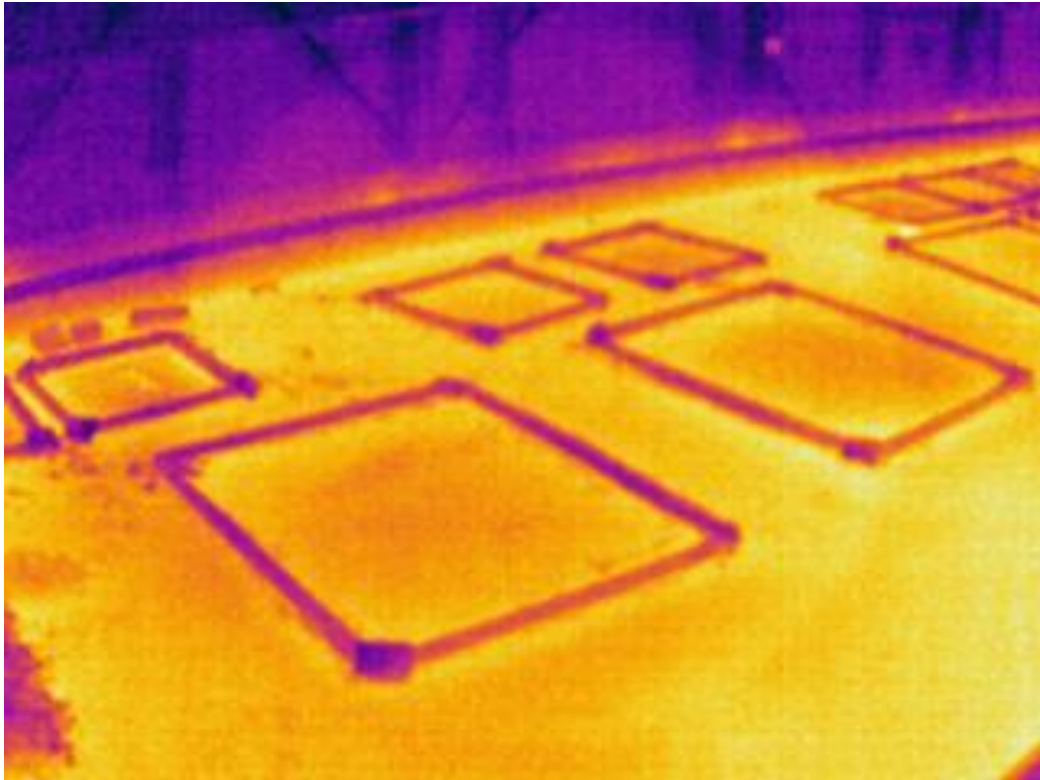


Figure 22. Infrared image from the camera mounted near the webcam with Hoop 5 in the foreground.

3.8.1.4 *Fluorescence Polarization Sensor*

Fluorosensors that detect fluorescence polarization (FP) were deployed above and below the ice. The sensors used a range of configurations. The above-ice unit is described here and the others will be described in the below-ice section.

The FP instrument used a laser projected telescopically outwards from the instrument body to detect fluorescence at a standoff distance. The laser beam was remotely focused onto the target via software. Fluorescence from the focused, polarized laser source was collected in 180° backscatter by the same telescopic optics and separated optically into its vertically and horizontally polarized components. After passing through wavelength selective filters, the intensity of these components was measured using separate photomultiplier detectors. An embedded computer allowed the FP instrument to be programmed or remotely controlled with another computer. The laser was modulated to allow a phase detection technique employing a lock-in amplifier to be implemented. The phase detection scheme discriminated against ambient light background and allowed operation of the instrument during daylight.

The aerial FP used a 405nm wavelength laser for a source and a 3" diameter telescope objective lens. The aerial FP was installed above the tank looking down in order to interrogate the surface of the ice. It was mounted on the above-ice boom, which allowed the instrument to be translated in a fixed, straight line on the ice surface. An umbilical cord provided power and serial communication links from the aerial FP to a laptop computer located in the carriage control room. Figure 23 shows the aerial FP sensor. The instrument was housed in a small pelican case modified with a telescope port on its side. A GoPro camera was attached to the aerial FP housing with its lens directed downward so that its field of view overlapped with the aerial FP. The GoPro camera was turned on during the aerial FP scans to provide a visual image of the interrogated area. Data was recorded as the carriage moved along the ice sheet.



Figure 23. The aerial FP sensor is in the black case. The lens for transmitting and gathering light can be seen along the bottom.

3.8.1.5 Spectral Albedo

The CRREL optical measurement programme was directed at measuring the spectral albedo and transmittance of the ice cover at all 6 hoop sites throughout the duration of the experiment. Table 4 summarizes the optical measurements that were made. Typically, a few measurements were made at each hoop. Spectral albedos could not be safely measured until the ice was thick enough to walk on.

The light source for the optical measurements was a 183 cm diameter faux sun, with 29 equally spaced, 150 W incandescent light bulbs (Figure 24). The total power of the sun was 4350 W. The laboratory sun used incandescent light bulbs and thus had a cooler colour temperature than the actual sun. The spectral shift of the light source was not a major issue, since our primary interest was in differences between ice with and without oil. The sun provided ample light to measure incident irradiance, reflected irradiance, transmitted irradiance, and transmitted radiance. Because of the spatial distribution of light from the artificial sun, the measured incident irradiance was disproportionately large and the observed albedos were too small. However, the spectral shapes of the albedos were representative of observations made in the field.

Spectral albedos were measured using an Analytical Spectral Devices Fieldspec Pro. The instrument is field portable and has a full spectral range from 350 to 2500 nm, with resolution ranging from 3 nm in the ultraviolet and visible and 10 nm in the near infrared. The instrument

has a rapid response time and can measure a full spectrum in only a few seconds. Spectral irradiance was measured using a cosine collector that consisted of a Spectralon diffuser mounted on a plate (Figure 24). The fiber optic probe from the spectroradiometer was mounted at a 45° angle aimed at the diffuser. The diffuser and plate were attached to a 1.5 m long aluminum arm for the measurements. This configuration has been shown to have a good cosine response and to be an effective fore-optics for albedo measurements (Grenfell and Perovich, 2004, 2008). Data processing was supervised and performed after the observations were made, typically taking about an hour.

Measurements were collected with the basin room lights off and the artificial sun on. Measurements were made at several locations within a hoop. In hoops with oil at the surface, measurements were made in areas with and without oil visible.

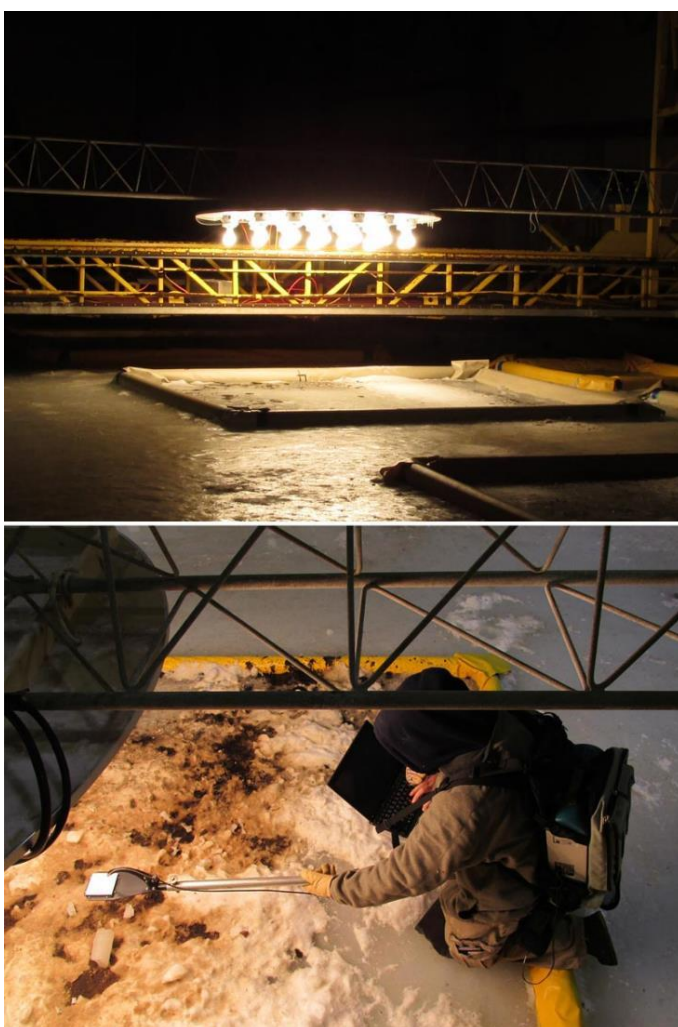


Figure 24. The top photograph shows the sun illuminating a hoop. The bottom photograph shows an incident reading being made as part of an albedo measurement. The white square is the Spectralon cosine collector.

3.8.2 *Below Ice*

3.8.2.1 *Spectral Transmission*

Measurements of transmitted radiance and irradiance were made using spectroradiometers made by Trios Science. Transmitted spectral irradiance was measured using a Ramses-ACC-VIS Hyperspectral Irradiance Sensor. This sensor had a full range of 320 to 950 nm, with 190 usable channels and a spectral resolution of 3.3 nm. Transmitted spectral radiance was measured

using a Ramses-ARC- Hyperspectral UV-VIS Radiance Sensor. The spectral characteristics of this sensor were the same as the irradiance sensor. The only difference was in the fore-optics. Instead of a cosine collector, this instrument has a 7° field of view in air. Both sensors were mounted on the underwater carriage in a way that gave them an unobstructed view of the ice bottom. Data processing was supervised and performed after the observations were made, typically taking about an hour.

Data was collected with the basin room lights off, the artificial sun on, and in most cases with the laser fluorosensor parked so the laser was not simultaneously transmitting. A measurement sequence included measurements in hoops with oil and at least one hoop without oil (Table 4).

Table 4. Summary of optical measurements. Measurements were made at the time and locations denoted by the blue cells. Multiple measurements were made at each location.

Date	Albedo						Transmittance					
	Hoop 1	Hoop 2	Hoop 3	Hoop 4	Hoop 5	Hoop 6	Hoop 1	Hoop 2	Hoop 3	Hoop 4	Hoop 5	Hoop 6
7-Nov-14												
12-Nov-14												
13-Nov-14												
14-Nov-14												
17-Nov-14												
18-Nov-14												
20-Nov-14												
21-Nov-14												
24-Nov-14												
25-Nov-14												
1-Dec-14												
3-Dec-14												
4-Dec-14												
5-Dec-14												
8-Dec-14												
9-Dec-14												
10-Dec-14												
11-Dec-14												
12-Dec-14												
16-Dec-14												
17-Dec-14												
22-Dec-14												
23-Dec-14												
30-Dec-14												
6-Jan-15												
7-Jan-15												
8-Jan-15												
9-Jan-15												
13-Jan-15												
15-Jan-15												
20-Jan-15												
22-Jan-15												
26-Jan-15												
28-Jan-15												
30-Jan-15												
3-Feb-15												
3-Feb-15												
5-Feb-15												
9-Feb-15												

3.8.2.2 Fluorescence Polarization Sensors

Two laser fluorescence polarization (FP) sensors were used below the ice. The FP instruments used employ a 405 nm laser projected telescopically outwards from the instrument body to detect fluorescence at a standoff distance. The laser beam was remotely focused onto the target via software. Fluorescence from the focused, polarized laser source was collected in 180° backscatter by the same telescopic optics and separated optically into its vertically and horizontally polarized components. After passing through wavelength-selective filters, the intensity of these components was measured using separate photomultiplier detectors. An embedded computer allowed the FP instrument to be programmed or remotely controlled with another computer. The laser was modulated so that a phase detection technique employing a

lock-in amplifier could be implemented. The phase detection scheme discriminates against ambient light background and allowed operation of the instrument during daylight.

A scanning FP sensor was mounted on the underwater carriage. The scanning capability allowed the instrument to interrogate an area without physically moving the instrument. This was accomplished by the integration of a scanning mirror assembly to the instrument that allowed the laser beam to raster scan a target area. The area scanned depended on the distance of the instrument to the object. Figure 25 shows a photograph of the scanning FP oil sensor. An umbilical cable carried both power and serial communication connected the underwater instrument to a laptop computer and a power supply. The laptop computer was used to send acquisition commands to the instrument embedded computer and to store acquired data.

Data was collected at fixed locations outside and inside of the oil containment hoops. Data was collected daily from each hoop until the oil was no longer observable by the FP instrument.

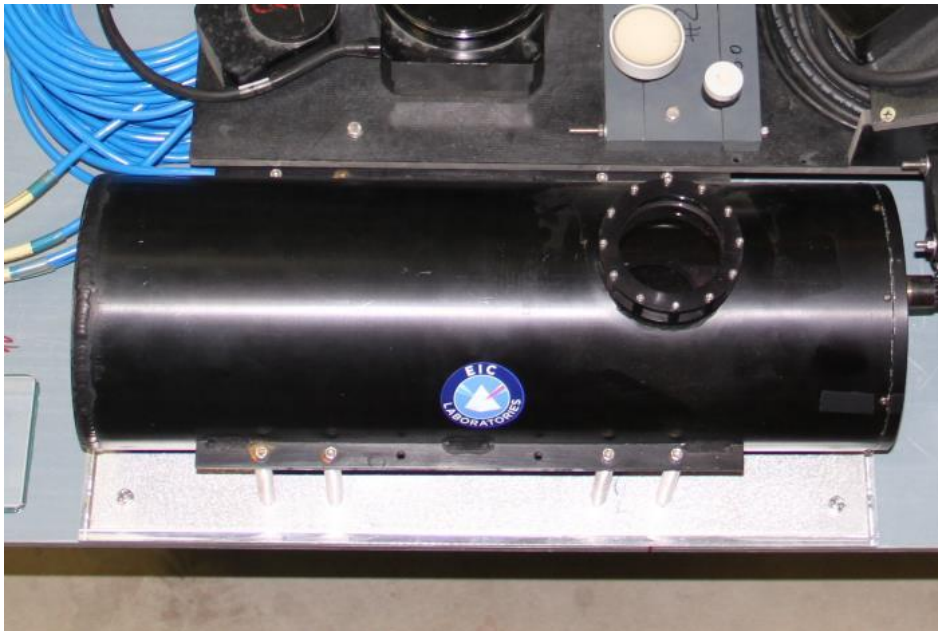


Figure 25. Pictured is the scanning fluorescence polarization instrument mounted on the instrumentation plate of the underwater carriage.

A fixed focus FP instrument was mounted on the bottom of the tank under Hoop 4B with the optical window oriented up to allow for the interrogation of the oil in the bottom of the ice during the oil injection and the encapsulation period (Figure 26). The instrument focus was varied remotely via software. For the CRREL oil in ice testing, the instrument focus was fixed at approximately 7 feet away from the ice, which corresponds to the distance that the oil was injected under the ice. An umbilical cable carried both power and serial communication from the instrument to a power supply and a laptop computer. The laptop computer sent commands to the embedded computer and stored data. The fixed focus FP instrument was operated continuously during the Hoop 4B-monitoring period.

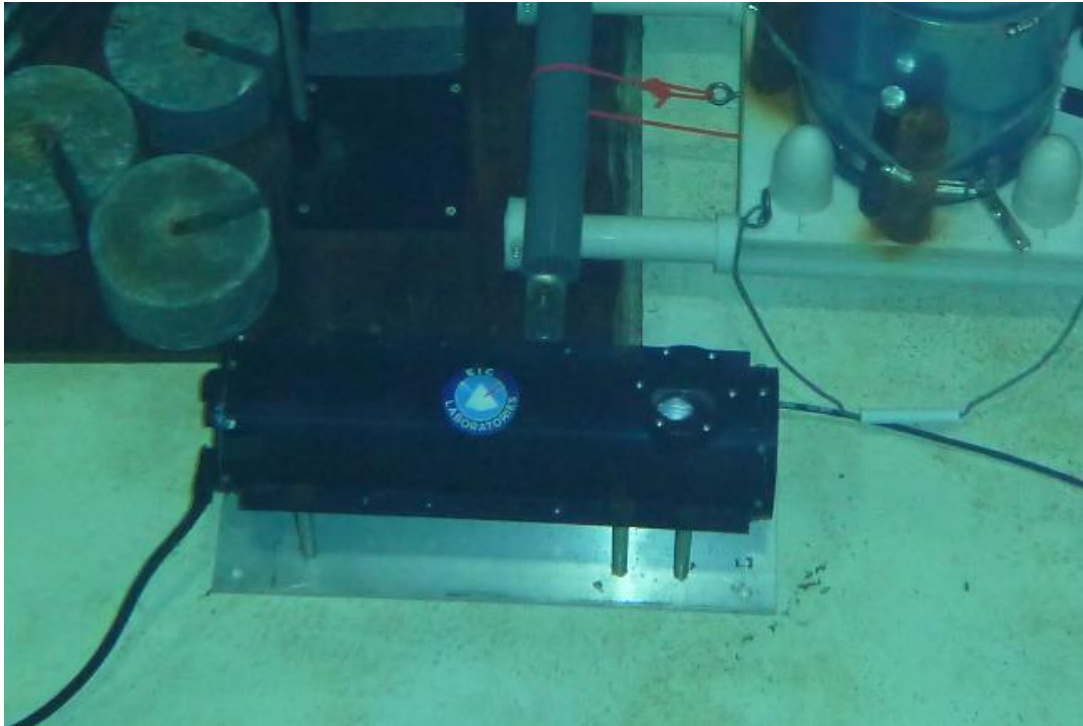


Figure 26. The fixed focus FP sensor mounted on the bottom of the tank.

3.8.2.3 *Camera*

Two camera systems were used on the underwater carriage. A pair of fixed-focus, low-light, black and white cameras were mounted on either side of the instrument platform (Figure 27). A light was mounted between the cameras, but the room lights were sufficient for operating the cameras. Images were collected every two seconds.



Figure 27. The low-light cameras are circled. The light source is next to the multibeam sonar.

A second camera system mounted on the underwater carriage and not the scientific payload provided an excellent alternative to the low-light cameras. The underwater camera was pan-tilt-zoom (PTZ) mount with HD camera with 360 degree of pan, 210 degree of tilt and 28 times zoom capabilities. The camera used Power over Ethernet (POE) with the submersible cable connected to the control console on the surface. Real-time images from the underwater camera were used to position the oil injection system and verify oil flow. Video segments were recorded during the injection and visually documented the underside of the ice during the periodic basin sweeps. Still images of items of interest were also captured (Figure 28).



Figure 28. Still image of oil in Hoop 5 from the camera on the underwater carriage.

3.8.2.4 Single-Beam Narrowband Sonar

During this experiment an AQUAscatter 1000 single-beam, narrowband sonar unit was used on the underwater instrument platform. The AQUAscatter transmitted pulses of high frequency sound on up to four transducers, each of which were operate at a different frequency. It measured the returned sound at discrete spatial intervals programmable from 2½ millimeters to 4 centimeters.

Frequencies were chosen based on earlier experiments at CRREL in May 2013. Those experiments showed that the range selected will capture the practical range of penetration depths into the ice (so that encapsulated oil can be detected) while balancing differing range resolution and practical range limitations for use on AUVs and ROVS. The frequencies chosen were:

- i. 5.0 MHz
- ii. 1.0 MHz
- iii. 0.5 MHz
- iv. 0.3 MHz,

The 0.3 MHz transducer was custom made by request to enable it be compared to the lower frequency broadband systems. These frequencies were chosen because of their resolution properties (i.e. 5 MHz) through to their ice penetrating properties (i.e. 0.3 MHz). The full echogram profile was recorded so multiple interfaces could be resolved, and the returned echogram compared to theoretical predictions.

The AQUAscatter system was located on two regions of the instrument platform of the underwater carriage. The transducers (0.3MHz, 0.5 MHz, 1 MHz, and 5 MHz) were located in the centre of the underwater carriage (Figure 29), whilst the electronics pod was located near the side of the trolley (Figure 29). A 200 ft. cable connected the base unit to a laptop. The laptop was situated in the warm room that is adjacent to the tank.

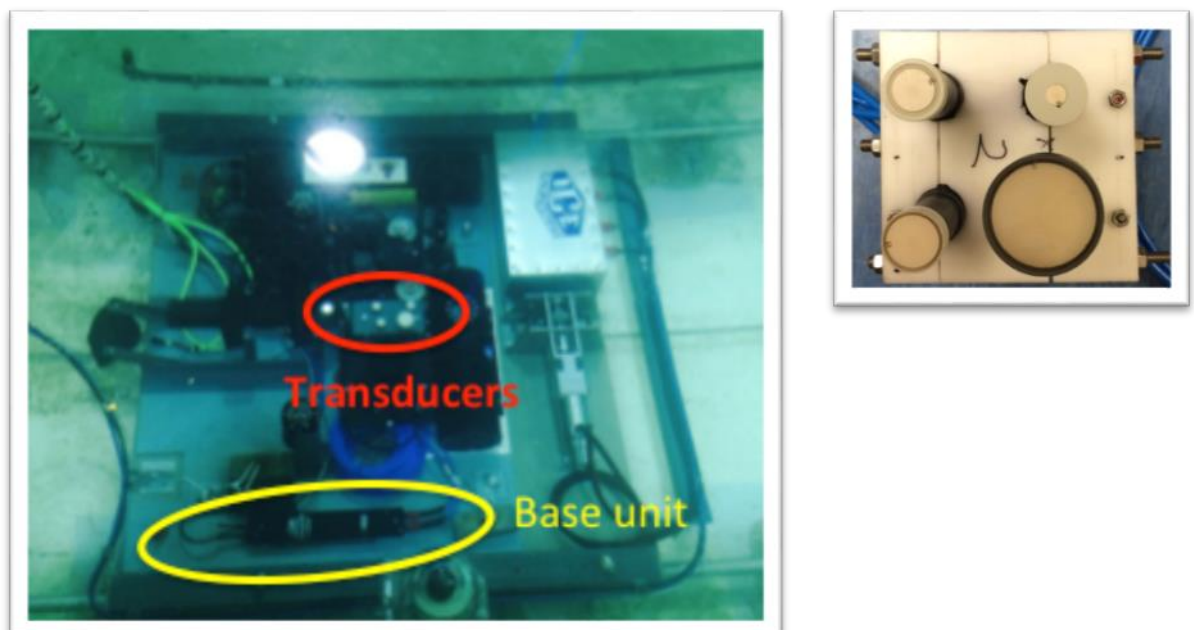


Figure 29. Layout of the AQUAscatter on the carriage (Left). The base unit was placed near the side and the transducers near the centre. Example of the mounting of the four transducers (Right).

In order to better understand the sonar return from the sea ice bottom and the spilled crude oil, there was a need to calibrate the sonars under calm conditions. Calibrations occurred when the water in the tank was fully quiescent (no ice).

The tests stepped through the five different pulse lengths. These were 2.5 mm, 5 mm, 10 mm, 20 mm and 40 mm. Each of these five calibration tests were performed over a 300 second period, with all transducers active (5 MHz, 1 MHz, 0.5 MHz, 0.3 MHz).

The calibration also provided the distance to the water surface from each transducer allowing the vertical differences in transducer height to be determined.

Several sensor parameters are configurable and the settings used are provided in Table 5.

Table 5. Settings used during this experiment. The bottom two rows are parameters that could be varied during the experiment.

Parameter	Channel 1	Channel 2	Channel 3	Channel 4
Samples to average	1	1	1	1
No of Bins	256	256	256	256
Beam Width	3	0.9	3.75	2.4
Power Level	0	0	0	0
Profile Rate	1 Hz	1 Hz	1 Hz	1 Hz
Transducer Frequency	0.3 MHz	5 MHz	0.5MHz	1MHz
Gain	0	0	0	0
Transducer Radius	0.025 m	0.052 m	0.012 m	0.009 m
Ping rate (second)	1	1	1	1
Ping length (2.5, 5, 10, 20, & 40 mm are possible)	Generally 10 mm	Generally 10 mm	Generally 10 mm	Generally 10 mm
Number of Pings in a file (Fully changeable)	180 seconds, but user changeable.	180 seconds, but user changeable	180 seconds, but user changeable	180 seconds, but user changeable

The sampling strategy involved three modes of operation;

- (a) User-controlled (stationary),
- (b) User-controlled (moving carriage) and
- (c) Autonomous measurements.

These sampling strategies are described below.

User-controlled measurements (stationary)

This sampling strategy was performed when the trolley was stationary under an area of interest, i.e. the oil spill. The sampling regime was entered and controlled from the Aquascats software on the PC. Five back-to-back logging runs were collected. These are:

- (1) 3 minute run, all Transducers active with pulse length 2.5 mm.
- (2) 3 minute run, all Transducers active with pulse length 5 mm.
- (3) 3 minute run, all Transducers active with pulse length 10 mm.

- (4) 3 minute run, all Transducers active with pulse length 20 mm.
- (5) 3 minute run, all Transducers active with pulse length 40 mm.

The aim of this sampling strategy was to better understand the influence of pulse length of the detection of oil.

User-controlled measurements (moving)

It was not practical to perform the five different pulse lengths runs when the trolley was moving. Therefore the pulse length was set to 10 mm for all four transducers during moving event (hoop and basin sweeps).

Autonomous measurements (stationary)

When the carriage was parked and not in use, i.e. outside working hours, the sampling regime was set to automatically perform readings every few hours. This prevented runs at different pulse lengths; therefore the pulse length was fixed at 10 mm for all four transducers.

During the experiment a problem occurred with the communications tether. After the problem was diagnosed a new cable was ordered and installed. During the period that cabled communications was not possible, the system was set to collect data in the autonomous mode on the hour every hour for 5 minutes.

The AQUAScat records the return waveform for each transmitted pulse, which allows the temporal signal from each transducer to be used in the detection of oil. With a multilayer system of seawater, oil, and ice, some acoustic energy is reflected from the first interface, whilst the remainder is transmitted across the interface into the overlying medium (the encapsulated oil). From there it continues on to the next interface whereby some acoustic energy will be reflected and the remainder transmitted and so on (Figure 30). Reflections from the ice/water, ice/oil/water, and ice/oil/ice/water interfaces were used to determine the presence of oil, oil layer thickness, and encapsulating ice thickness.

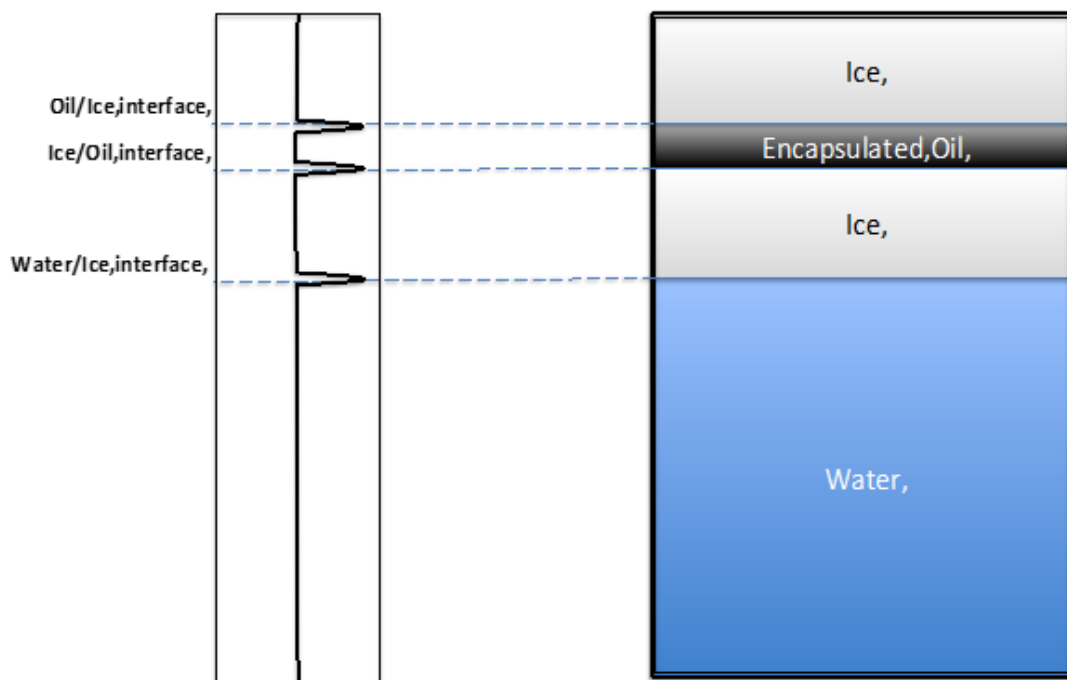


Figure 30. Schematic showing the approximate acoustic return in a multilayer system. The first acoustic return is from the water/ice interface, the second return from the oil/ice interface and the third return from the ice/oil interface. Note: This schematic does not take into account differences in sound speed, scattering or absorption properties of each medium or the acoustic pulse length. Peak return heights from the different interfaces are not expected to be equal.

Data processing of the Aquascat data was completed using a simple 3-step process.

Step 1: Download data from the Aquascat unit.

Step 2: Run custom MATLAB script to change the Aquascat data from a priority '.aq' file to a MATLAB based '.mat' file.

Step 3: Run another custom MATLAB script to plot data. The exact script used depends on whether the dataset is from (1) a moving trolley or (2) a stationary trolley. These are explained below:

Processing for a moving trolley:

No filtering or additional processing of data was required after acquisition. Raw data was collected at one reading per second. This raw data was adequate to detect oil. Examples of the raw data from a moving trolley under Hoop 1 can be seen below (Figure 31).

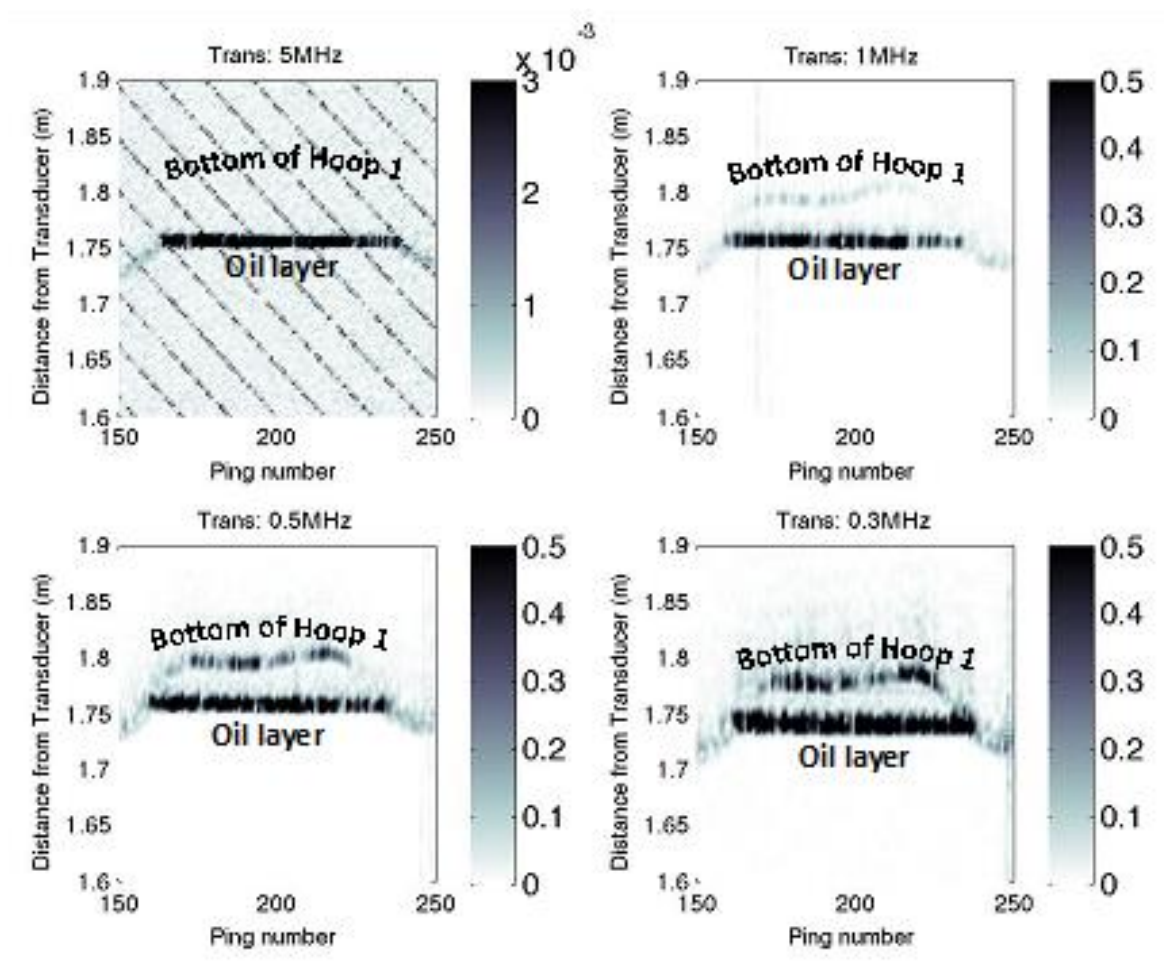


Figure 31. Raw data from each of the four frequencies showing oil under Hoop 1.

Processing for a stationary trolley:

Raw data was collected at one reading per second over a set period of time, usually over a three-minute period. The ensemble of measurements was averaged to determine a mean return. Example of the raw data set and the processed dataset that delivers the resultant average return can be seen below (Figure 32).

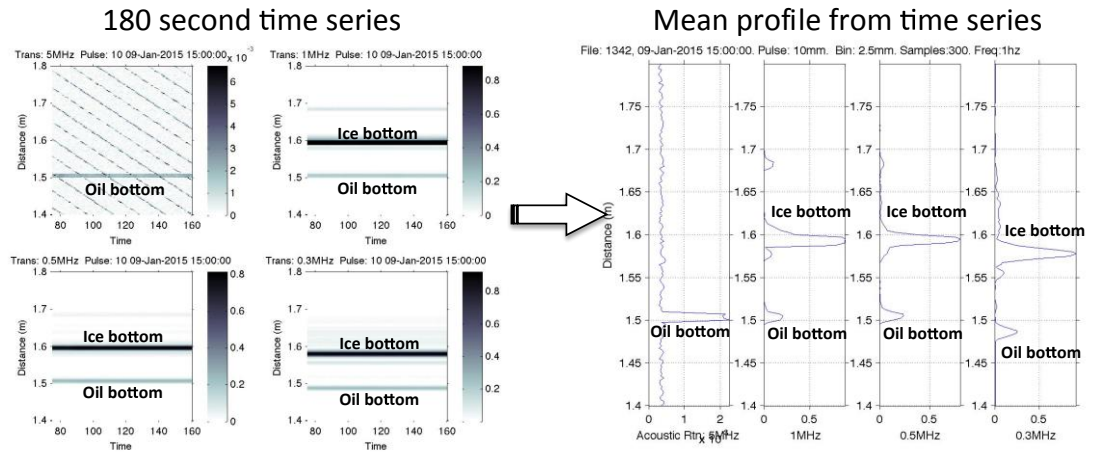


Figure 32: Left: Raw time series of data showing the acoustic returns over the logging period of 180 seconds. The oil bottom and ice bottom can clearly be seen. Right: Processed data showing the calculated average return from the measurements made over 180 seconds. Distance shown is the distance from the transducer head.

3.8.2.5 Broadband Sonar

The broadband acoustic scattering system consisted of a custom-modified six-channel Edgetech 2200- sidescan sonar system, described in detail in Lavery et al. (2010). This system was mounted on the underwater carriage and cabled to a computer in the adjacent instrument room allowing real time data collection and visualization. Two identical sets of three transducers were mounted on the instrument platform. The first set of transducers (each with a different center frequency) was mounted upward looking at normal incidence to the ice/water interface and the other set was mounted at a 20 degree angle from normal incidence. The transducers were octave-bandwidth, piston-transducers custom-developed by Airmar Technology Corporation (35 Meadowbrook Drive, Milford, NH, USA). The transmitted signals were 250us duration, linearly modulated chirps (Table 6). There was significant overlap between the transducer footprints throughout the experiment. In order to use the system in a laboratory setting without saturating the received signals, additional resistors were added to modify the amplifier output impedance of each channel. The amplitudes of the transmitted signals were maintained at a constant level throughout the experiment and calibration.

Table 6. Transducer and signal parameters. The footprint radius (normal incidence transducers) is calculated at 1.8 m. All parameters use a sound speed of 1437 m/s.

Operational Parameter	Low	Mid	High
-----------------------	-----	-----	------

Center Frequency, f_c (kHz)	100	160	500
Wavelength at f_c (cm)	1.44	0.9	0.29
Frequency Range (kHz)	75-130	115-225	370-590
Bandwidth (kHz)	55	110	220
Spatial Resolution (cm)	1.2	0.7	0.4
Full Beamwidth (-3 dB at f_c)	9.6	6.0	3.4
Footprint Radius (cm)	19.6	13.8	7.9

Two types of acoustic sampling measurements were performed. First, time series sampling was performed prior to, during, and following oil injections in each hoop to identify the crude oil layers and to monitor the encapsulation process. During time series sampling, the sensor platform was located under the center of the hoops and the ping rate was 0.1 Hz. The signal-to-noise ratio was sufficiently large throughout the experiment that little ping-to-ping variability was observed in the compressed-pulse output, obviating the need for further averaging. Second, spatial sampling was performed along the axis of the tank (hoop and basin sweeps) for the purpose of obtaining statistical scattering data from the ice and to map the oil layers. During spatial sampling, the ping rate on each channel was 10 Hz. The velocity of the underwater carriage during the transects was 2 m/min. Given the ping rate, the cart moved approximately 3 mm between pings, resulting in significant overlap in the acoustic footprints. In both the time series and spatial sampling, there were 20 ms delays between pings on different channels to avoid frequency contamination and cross talk between channels.

The air/water interface, prior to the formation of ice, was used to calibrate the broadband acoustic system. Reflections from the pressure-release air/water interface are, in the absence of significant surface disturbances, phase-shifted replicas of the transmitted signals. Using the pressure release surface for calibration accounts for the combined transmit and receive sensitivities in addition to any distortion of the signals introduced by the system (e.g., filters and amplifiers). Once the tank was filled and the surface had settled, calibration measurements were performed for each transducer. Each transducer transmitted 1000 pings for the calibration. The received echoes during calibration were stable, suggesting minimal surface disturbances. Nonetheless, the temporal domain output was obtained by coherently averaging the compressed pulse output and the calibration spectrum was determined by averaging the individual spectra.

Data analysis

Temporal domain

Backscattering measurements were analyzed in the time domain using pulse compression techniques (Turin, 1960; Stanton et al., 1998; Chu and Stanton, 1998; Stanton et al., 2010; Bassett et al. 2014). In comparison to traditional narrowband techniques, which have a temporal resolution proportional to the pulse length, broadband signals analyzed using pulse compression techniques have a temporal resolution proportional to $1/B$, where B is the bandwidth of the pulse (Chu and Stanton, 1998). The cross-correlation of the transmitted and received signals results in the pulse compressed output. This analysis was performed in the Edgetech electronics bottle and the complex compressed-pulse output is saved to a computer in the laboratory. The results are presented in terms of the envelope of the compress-pulse output, E_{CP} . Subsequent post-processing accounted for the calibration.

Assuming that the first significant arrival in E_{CP} is associated with the bottom interface, the range is given by $r=cw*t/2$, where cw is the sound speed of the water determined from CTD measurements and t is the delay time to the first interface peak in E_{CP} . Once injected, the buoyant oil forms a layer under the ice. When the oil layer is sufficiently thick, E_{CP} contains peaks from both interfaces. The thickness of the oil is then given by $h_{oil} = C_{oil} (t_{oil,ice} - t_{w,oil})/2$, where C_{oil} is the sound speed of the oil, and $t_{oil,ice}$ and $t_{w,oil}$ are the time delays that correspond to from the oil/ice and water/oil interfaces, respectively. Any regularly spaced peaks beyond the first two returns are associated with multiple interface reflections from the oil layer. Additional lower amplitude peaks that are not consistent with the processing side lobes are often present and are attributed to inhomogeneities within ice.

Frequency domain

The frequency spectra are presented in terms of a ratio of the scattered pressure to the incident pressure field, $R_p(\theta)$, where θ is the angular acoustic frequency (a slightly modified form of Eq. 10 in DiPerna and Stanton, 1991), in which the range dependence of the incidence pressure is accounted for, but not necessarily the range dependence of the scattered pressure, depending on the exact scattering processes involved (Lavery and Ross, 2007; Bassett et al., 2014, 2015). As a result, direct comparisons between $R_p(\theta)$ at different ranges are only appropriate under some circumstances. There are two limiting cases for the range dependence of the scattered pressure. In the first case, the smooth interface scattering case, the roughness (typically described by the root-mean-square surface height) of a scattering interface is small relative to the acoustic wavelength and the scattered pressure has a $1/r$ range dependence. In this case, $R_p(\theta)$ is analogous to a reflection coefficient. When any interfaces are not smooth relative to the acoustic wavelength, a direct comparison of $R_p(\theta)$ at different ranges may be inappropriate. Under these conditions, the range dependence of the scattered pressure can be as large as $1/r^2$. It is worth noting, however, that the limited ranges under consideration in this study (1.6-2.0 m) result in a maximum difference between the amplitude as presented and the limiting case with a $1/r^2$ range dependence of approximately $\pm 0.7/2.6$ dB (assuming the calibration pressure release surface is smooth). Due to the limited size of the tank, it was not possible to directly study the range dependence of the scattered pressure from the ice or oil. Here, in all cases, $R_p(\theta)$ is presented in log space and attenuation has been accounted for, following Francois and Garrison (1982a, 1982b).

To obtain the scattered spectrum from the compressed-pulse output, the time series data were time gated to include the main peaks and side lobes from all interfaces with the exception of the surface (ice/air). Furthermore, for consistency the spatial extent of the time gating was equal for all transducers for all data presented here including the calibration. As described in the following section, the inclusion of multiple interfaces, if present, leads to spectral structure that can be used to infer the distance between the interfaces if the properties are known (Stanton et al., 1994). Noting that the spatial length of the transmitted signal in the water was 0.36 m long and that the maximum oil thickness analyzed here was 9 cm, the time-delay between arrivals from the interfaces is much less than the length of the transmitted signals. A consistent time gate of 0.42 ms (length of 0.6 m in water) was applied to capture the full echo.

3.8.2.6 Multibeam Sonar

Two different multibeam sonar types were used: a) a forward-looking sonar (FLS), and b) vertical oriented sonar (bathymetric configuration) with a narrow transmit pattern in the along track

direction and a wide swath coverage in across track direction (Figure 33). The FLS was oriented 30° from the horizontal plane.

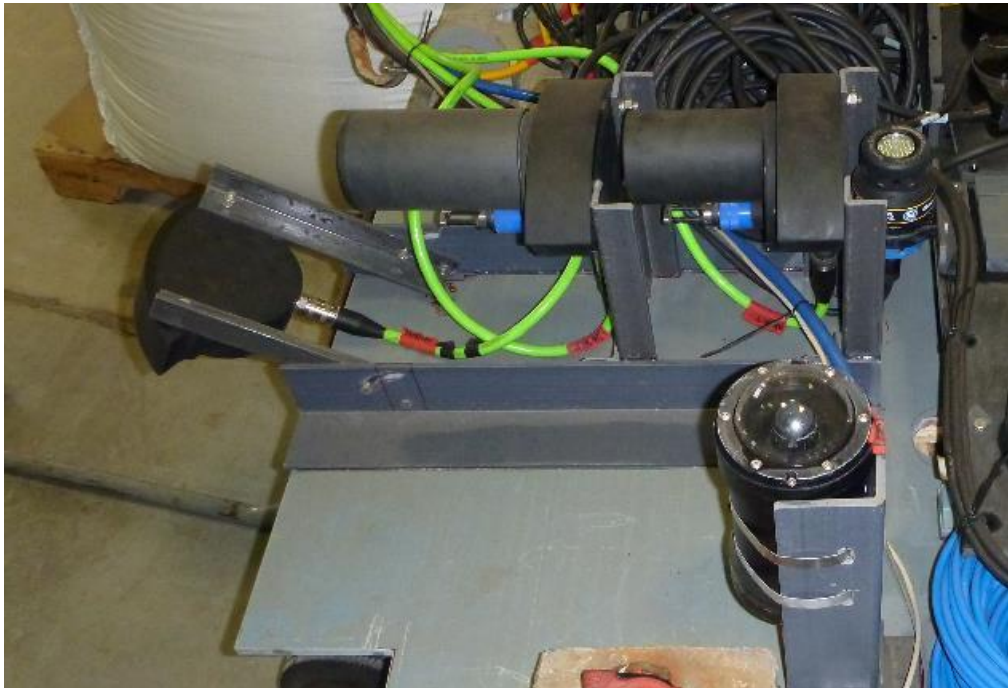


Figure 33. Multibeam sonars mounted on the underwater instrument plate. The unit on the far left that is pointed at an angle is the FLS, the two units orientated vertically are the 200 and 400 kHz bathymetric multibeam units.

The vertically oriented bathymetric sonar units used a narrow transmit beam pattern (<2 degree) illuminating a small footprint on the bottom/ice/water interfaces. This pattern was needed in order to provide sufficient information to perform reliable backscatter processing for classification of potential patches of oil on/in the water/bottom/ice interface region. The systems transmit a broadband signal with linear sweep around the central frequency of 80 kHz. The multibeam sonar utilized focused field-programmable, gate-array based beam forming and circular array topography. This provided a swath width up to 180° and an angular resolution typically less than 1°. Processing of multibeam acoustic signals included spatial filtering (beam forming) and bottom detection, as well as the generation of snippets. Snippets are a portion of the water column around the detected target that are used to detect presence of hydrocarbons in the water column. Snippets further enhance the flexibility in the processing of the water column, as only the portion of the water column of interest is being transmitted and stored if necessary.

Data was collected from one sonar unit at a time to prevent interference between sensors. Two sampling schemes were used: sweeps and fixed location collections. Full basin and hoop sweeps provided profiles of the underside of the ice. Short time series at fixed locations were collected to provide additional opportunities to examine the ability to detect the presence of oil.

Bathymetric data was provided in real time using the on-board computer for raw data processing. The reflectance data can potentially be used to detect and describe oil within the ice, and for automated classification of oil using standard bottom classification approaches. The sonar outputs the portion of the bottom around the detection points for each beam, called snippets. A sample snippet is shown in Figure 34.

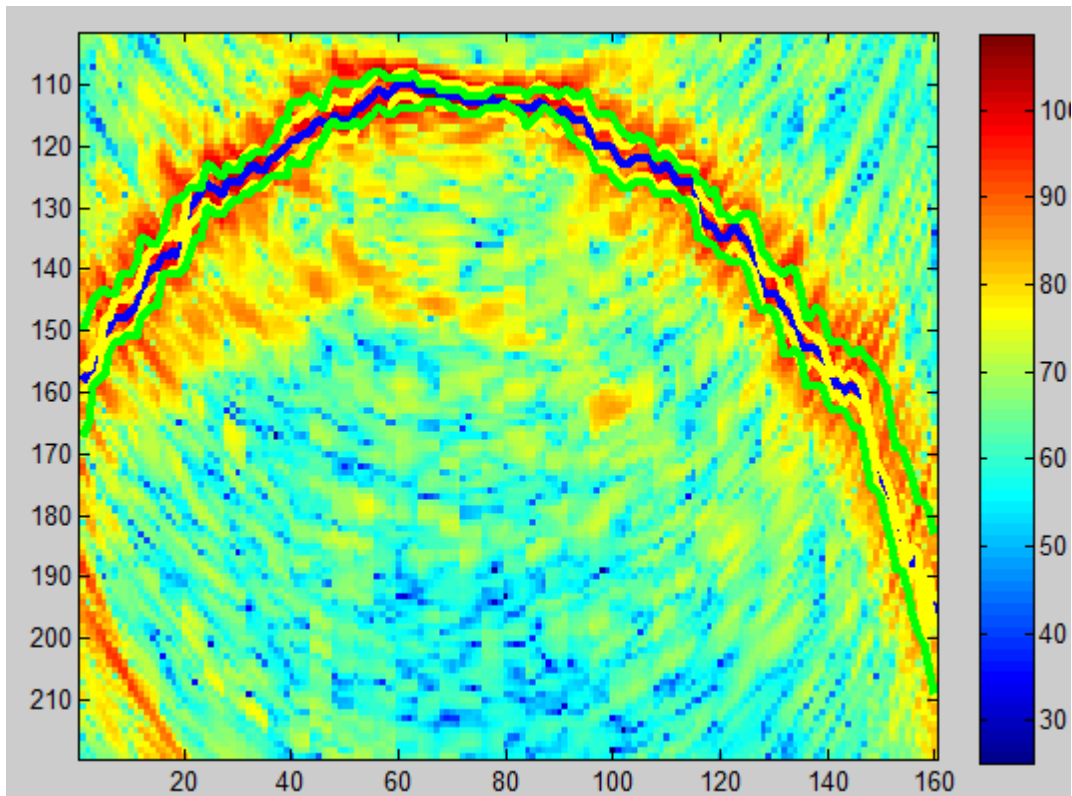


Figure 34. A sample of a snippet showing return strength. The blue line is the detection point, yellow is the extent of the pulse footprint, and green is the extent of the beam 6dB footprint.

The pulse footprint represents the scattering. The back scattering strength was computed based on the surface reverberation theory:

$$BSS = RL - SL + TL - 10\log A$$

Where the BSS is the backscattering strength, RL is reverberation level, SL is sonar source level, TL is two-way transmission losses and A is the reverberating area expressed by:

$$A = \min[\frac{c\tau}{2\sin(\phi)}\Psi R, \frac{\Phi}{\cos(\phi)}\Psi R^2]$$

The c is the speed of sound, the τ effective pulse length, Φ is the equivalent across track beam width, Ψ is the equivalent along track beam width, R is the range to the detection.

The two-way transmission losses TL are expressed as usual by:

$$TL = 40\log(R) + 2\alpha R/1000,$$

Where the α is sound absorption (rather negligible), which for these frequencies is around 40 and 100 dB/km for 200kHz and 400kHz, respectively.

The reverberation level RL is computed from the sonar beam intensity after subtracting the native sonar TVG gain applied during the signal acquisition:

$$RL = BL - TVG - G,$$

Where TVG is the time varied gain, BL is the beam level of the sonar data taken at the bottom detection instance.

The constant gain G represents the total constant gain of the system (the physical sensor, processing gain, array gain, etc.), relating the physical echo level to the actual signal received by the sonar.

In this experiment the sonar was not calibrated for the gain G and source level SL , therefore the absolute reverberation levels cannot be computed, but the relative values and the dependence on the incident angle could be derived.

The backscattering dependence on the incident angle is especially an interesting quantity as it can be used as a characteristic feature of the oil scattering strength. Therefore we will denote the backscatter angular response (relative to sonar total gain) as a feature of the true backscattering strength and call it,

$$BAR (= BSS + SL + G).$$

In a final form the Backscatter Angular Response (BAR) is simply:

$$BAR(\phi) = BL(\phi) - TVG + TL(\phi) - 10\log(\sigma / 2/\sin(\phi\Psi R)),$$

An example of BAR is shown below (Figure 35):

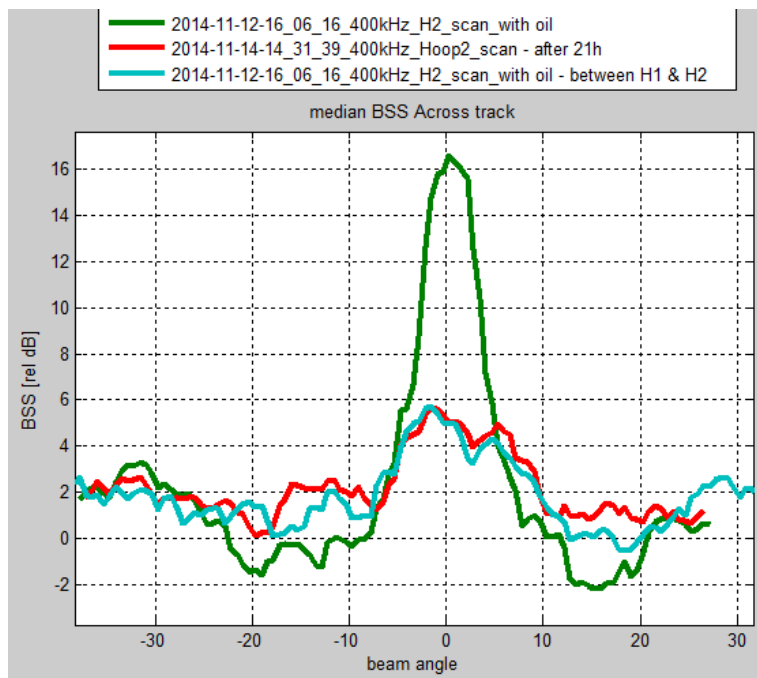


Figure 35. Example of backscatter angular response data from Hoop 2. The green line represents the backscattering strength when oil is present.

Oil thickness was detectable using the nadir direction return. The oil thickness determination procedure consists of two steps. The first step is to determine which portion of the ice is directly facing the multibeam sonar. For smooth ice (tank measurements) this ice will be directly above the sonar (nadir). Then use the waveform of the specular return from the oil surface and return from ice surface to measure the oil thickness (Figure 36).

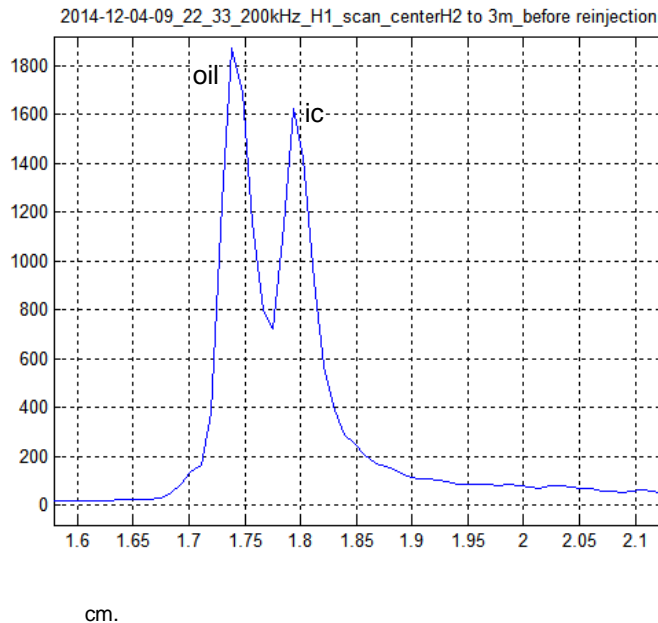


Figure 36. The sonar distance return, in meters, from the nadir direction showing an oil thickness of about 6

3.8.3 Ancillary

3.8.3.1 Temperature Monitoring

Two thermistor strings were used to measure air, ice, and water temperature in the tank, approximately 10 m from either end of the tank. Thermistors were placed at 5cm increments starting 10 cm above the surface to 90 cm below the surface and 10 cm spacing to 160 cm depth. The thermistor strings were fabricated by drilling holes in a root of a fiberglass angle and inserting 1% thermistors through the hole. Fiberglass was used as the support material to minimize any thermal conductivity influence. Water temperature data for the temperature strings was recorded with a Campbell Scientific data logger with Internet capabilities and provided in real-time to the sensor team.

3.8.3.2 Carriage Position

Above-ice

The position of the blue carriage was recorded at 500 Hz. Information recorded includes time since start of file, carriage speed, and carriage position in meters. The start time was recorded in the filename. Position is measured from the centerline of the carriage and is set to read 0 m at the edge of the tank adjacent to the prep tank. Because the instruments were mounted on a long boom the slope of the boom was measured and recorded using a tilt meter. With the instrument packages approximately 5 m in front of the carriage the offset needed to account for the absolute position for the respective instrument. For example to center the GPR in the respective hoop, the carriage had to be parked at the following positions H1 -2.31 m, H2 4.32 m, H3 6.21 m, H4 10.75 m, H5 14.84 m, H6 20.78 m. Using these positions it was possible to programme the carriage to ensure it returned to the same location for each series of measurements.

Below-ice

The underwater carriage position was determined from the position of the servomotor that pulled the carriage along the stationary chain on the bottom of the tank. The position was set to be zero

when the underwater camera on the carriage was centered on the edge of the prep tank. The software to capture the position recorded a limited number of points and recorded the time since the start of the record, position in centimeters and the velocity command in rpm. The start time of the record was programmable so the carriage was programmed to start at a specific time that was recorded in the file name. By combining the start time with the recorded time since start the actual time and position could be determined.

3.8.3.3 *Ice Properties*

Ice core samples were drilled from the ice sheet nominally every 10 cm of ice growth and prior to oil injection events. The cores were recovered with the CRREL core drill with a barrel diameter of 3"/7.5 cm. The hole was started by hand, and then a power drill was used to drill through the remaining ice. Care was taken to prevent the drill from punching through the ice at the bottom of the ice sheet at the bottom of the core. Generally, three to four cores per coring session were retrieved for salinity, temperature, photographs, stratigraphy, thickness, micro CT scanning, and thin and thick sectioning. In addition to core information, the air temperature, hole depth, freeboard, water temperature and salinity were measured, along with information about the surface of the ice where core sampling was conducted. Coring was restricted to ice outside of the hoops until the ice growth phase was completed. Once the ice growth phase was completed cores were collected inside the "A" hoops to characterize the distribution of oil through the melt out phase. Inside the hoops, slabs were also retrieved in order to examine spatial variation within the hoops. The date the data were collected is noted in Table 7.

Salinity cores were cut into 5cm segments, unless breaks in the core prevented 5cm sectioning, and placed into labeled bags. These segments were later melted and salinity was measured using a YSI 30 salinity/conductivity/temperature probe. Salinity and temperature of the melt water was noted.

Immediately following the recovery of the core designated for the temperature profile, holes were drilled every 5 cm along the core length and a thermocouple probe inserted. Holes were also drilled into the top and bottom of the core along the vertical axis, in order to obtain temperatures near the top and bottom of the core. The top and bottom were measured first, and the remaining holes measured working towards the center of the core. Temperatures were also recorded in situ as the thermistors in the thermistor string froze into the ice as it thickened.

Photographs of all the cores were taken both with and without a light, with a scale for reference. Photographs of the slabs were also taken, both with and without backlighting.

Stratigraphy and thickness notes were taken for each core.

Micro CT cores were sectioned so that the bottom 10-11 cm of the core was first cut, then placed right-side up in a container, suspended with the bottom of the core ~5cm from the container bottom in order to allow brine to drain out of the sample. The bottom of the core was taken to the micro CT facility immediately after drilling, cutting, and draining, and the outer diameter was shaved so that the core had a final diameter of 5cm. The bottom of the core was scanned upside down in order to prevent destruction of the skeletal layer. Settings of the micro-CT were 65kV, 125 uA at 65 microns resolution. The bottom sections of the cores were scanned as an oversized scan with 3 subsections, and typically took 90 min to complete. The rest of the core was bagged and scanned in 10 cm sections, typically the same day or the following day. All core samples were subjected to storage at colder temperatures, likely resulting in some freezing of the brine in the brine channels.

Thin and thick sections of the core were made for horizontal and vertical sections of the core, with photographs taken of each section both with and without polarized filtering for the thin sections.

Table 7. Dates and Physical Properties Data

Date	Location	Temp	Salinity	Photos	Thin Section	MicroCT	Density
7-Nov	Near Hoop 1			X			
8-Nov	Near Hoop 1			X		X	
10-Nov	Near Hoop 1	X	X	X		X	X
12-Nov	Near Hoop 2	X	X (2)	X		X Full core	
13-Nov							
14-Nov	Near Hoop 2	X	X	X			
17-Nov	Near Hoop 3	X	X (2)	X		X	
20-Nov	Near Hoop 4	X	X (2)	X		X (2)	X
3-Dec	Near Hoop 4	X	X	X		X Full core	X
4-Dec	Near Hoop 1	X	X				X
9-Dec	Near Hoop 5	X	X			X Full core	X
10-Dec	Near Hoop 2					X (4)	
18-Dec			X			X	X
30-Dec	Near Hoop 3	X	X	X	X	X Full core	X
6-Jan	Near Hoop 6	X	X	X	X	X Full core	X
8-Jan	Transects		X (5)				X (5)
12-Jan	Hoop 3A		to do			X	
13-Jan	Hoop 1A		X			X	X
16-Jan	Btwn 4/5	X	X (6)			X	X (6)
20-Jan	Hoop 4	X	X (2)			X	X (2)
21-Jan	Hoop 4A					X	
23-Jan	Hoop 6A/Btwn 6A/5A	X	X (2)				X (3)
2-Feb	Btwn Hoops 5/4	X	X			X Full core	X
10-Feb	All Hoops	X	to do			X Full core	X

3.8.3.4 Sound Speed

A sound speed sensor system consisting of a pair of transducers facing each other was frozen into the ice. Unfortunately, it was not able to make measurements of the sound speed of ice.

Another effort examined the sound speed of oil as a function of temperature. A pair of transducers facing each other were submerged in oil. The transducers were placed 30 cm apart and a

broadband (250-750 kHz) signal transmitted. The sound speed was determined based on the transit time between transducers. Sound speed measurements were collected continuously as the oil temperature varied from -10 to 20 °C.

3.8.3.5 3D GPR

A second type of surface ice 1000 MHz GPR survey consisted of a 3.66 m x 2.03 m 3D area located in an undisturbed section of the tank that was continuously observed throughout the experiment. The primary objective of the 3D surveys was to provide a high-resolution measure of the 3D under ice topography as a function of ice growth. We constructed a survey template by drawing the survey lines on sheets of plywood that could be pieced together for each survey. Position of the template was fixed with spikes placed at each corner of the plywood sheets and driven into the ice – these positions were fixed throughout the survey to ensure that the same patch of ice was measured over time. It was important to minimize the amount of time the survey template remained on the ice to ensure that the insulating effects of the plywood did not impact ice growth. The template was typically in place for less than two hours with several weeks between each survey and it is not believed to have a significant impact on ice growth. In-line trace spacing for the 3D survey was 3 cm and cross-line spacing was 5 cm.

3.8.3.6 Electrical Resistivity Measurements

A high-density 3D electrical resistivity dataset was acquired, primarily for comparison and validation of the ice property model and to evaluate anisotropy in the electric conductivity of the ice. This was accomplished using a 72 electrode SysCal Pro system with a custom-built electrode array. The array (Figure 37) consisted of 4 lines of electrodes arranged in a 2m diameter, wagon wheel configuration with 45° separation between each spoke of the wheel (Figure 37). Each line contained 18 electrodes with 6 electrodes on the surface spaced 40 cm apart. The remaining electrodes were equally distributed on two vertical strings at either end of the line. Vertical spacing between electrodes was 15 cm so the total depth of the vertical strings was 90 cm. The vertical strings were placed by first drilling a 3.8 cm diameter hole through the ice, then hanging a light weight from the end of the electrode string, inserting it through the hole, then allowing the ice to refreeze around the vertical string. Surface electrodes were placed by drilling a shallow hole (2.5 cm deep) in the surface of the ice, placing the electrode in the hole, then filling with salt water and allowing to refreeze. The electrodes consisted of marine grade stainless steel wool to maximize surface area and minimize grounding contact resistance with the ice.

Measurements were collected in dipole-dipole mode, with two adjacent electrodes acting as a current source and sink and measuring the potential across all other adjacent electrode pairs. The measurement was repeated for all possible dipole-dipole pairs.

Data processing used the commercial software package Res2DInv. 2D subsets of the data were extracted along each electrode profile and analyzed separately. The survey design made it so that full 3D processing was possible, however, this requires future development of a 3D anisotropic inversion package that is not presently available.



Figure 37. Photograph of the electrical resistivity array.

3.9 Modelling

The RSOI modelling team addressed two primary modelling tasks. One task was to model the conditions in the CRREL test facility to predict the laboratory performance of the instruments tested in the RSOI experiment. The second major modelling effort was to model a range of field conditions to provide an expected response curve of the different sensors.

Modelling of sea ice, optical, acoustic, and radar properties were done separately and the modelling approaches are described below. The models used the measured ice properties from the basin for understanding laboratory measurements. A sea-ice characterization modelling component provided monthly ice properties appropriate for the North Slope of Alaska to be used by the other modelling efforts.

3.9.1 Modelling Scenarios

First year sea ice temperature, salinity, and thickness properties for the months from October to July were provided to all modelling teams. These values will be used by the instrument modelling as the basic characteristics of the sea ice. Then the modelers were asked to address a set of scenarios to examine conditions that were outside the bounds of laboratory measurements. The modelling scenarios were for flat, first-year ice. This extends the laboratory experiments, but does not address the many forms of deformed ice.

Underwater Detectors

Modelling will be conducted on a matrix of conditions. Variables to be considered include:

- Month (October – July)
- Oil pool diameters (2 and 200m)
- Oil layer thickness (1, 2, 5, 10, and 15 cm)
- Ice thickness below the oil (1, 5, and 10 cm then monthly expected total ice thickness from the ice conditions). This assumes that the oil does not alter the growth characteristics of the ice. The thin layers are meant to represent detection within the first few days to a week after release.

Above-Ice Detectors

Modelling will be conducted on a matrix of conditions. Variables to be considered include:

- Month (October – July)
- Oil pool diameters (2 and 200m)
- Oil layer thickness (1, 2, 5, 10, and 15 cm)

Scenario 1 - 2m D oil pool, October – July, Oil thickness (1, 2, 5, 10, and 15 cm), ice thickness below oil layer (1, 5, and 10 cm then monthly expected total ice thickness)

Scenario 2 - 200m D oil pool, October – July, Oil thickness (1, 2, 5, 10, and 15 cm), ice thickness below oil layer (1, 5, and 10 cm then monthly expected total ice thickness)

3.9.2 Sea Ice Properties

Numerical model simulations and synthesis of field data representative of field conditions were completed by the UAF team to (1) provide other members of the modelling team with input for their model simulations, and (2) provide a reference framework for fundamental ice property data (in particular salinity, microstructure, permeability, dielectric properties) against which measurements of properties for ice obtained in tank experiments can be compared.

Numerical simulations employed a high-resolution, 1-D ice growth model providing ice thickness, temperature and salinity as prognostic variables (Eicken 2003), and a single-column enthalpy-conserving ice growth/decay model developed for coupled ice-ocean and climate model applications providing ice thickness and temperature (CICE, Hunke and Lipscomb 2010). Both models were forced with observed data (northern Alaska, Svalbard and as applicable the CRREL site), but can also be driven by reanalysis data or climatology for a broader range of conditions. Neither CICE nor other comparable models are currently able to predict ice salinity. While work is underway to address this shortcoming (Turner et al. 2013), salinity profiles for the CICE simulations are based on a large ice property dataset collected at Barrow, Alaska (Druckenmiller et al. 2009), complemented by data from the Barents Sea (Gerland et al., unpubl. data). As a result, two data sets were generated, one based on model simulations alone, and the other through synthesis of a large field data set.

Ice Core Data

Barrow

Data have been derived from ice-core and in-situ temperature measurements at the Mass Balance Station installed on homogeneous, undeformed land fast sea ice near Point Barrow from the 1999/2000 to the 2013/14 ice season (Eicken et al., 2014). While the position of the station varies slightly from year to year, observations are representative of first-year sea ice grown under quiet conditions in the North American Arctic. A typical annual cycle of ice growth and melt is displayed in figure 38. Sampling dates depend on field work timing, which is scheduled to capture and follow the important changes in sea ice throughout the winter and spring: young first-year sea ice in January, mature sea ice in April and mid-May, desalination and melt through mid-June.

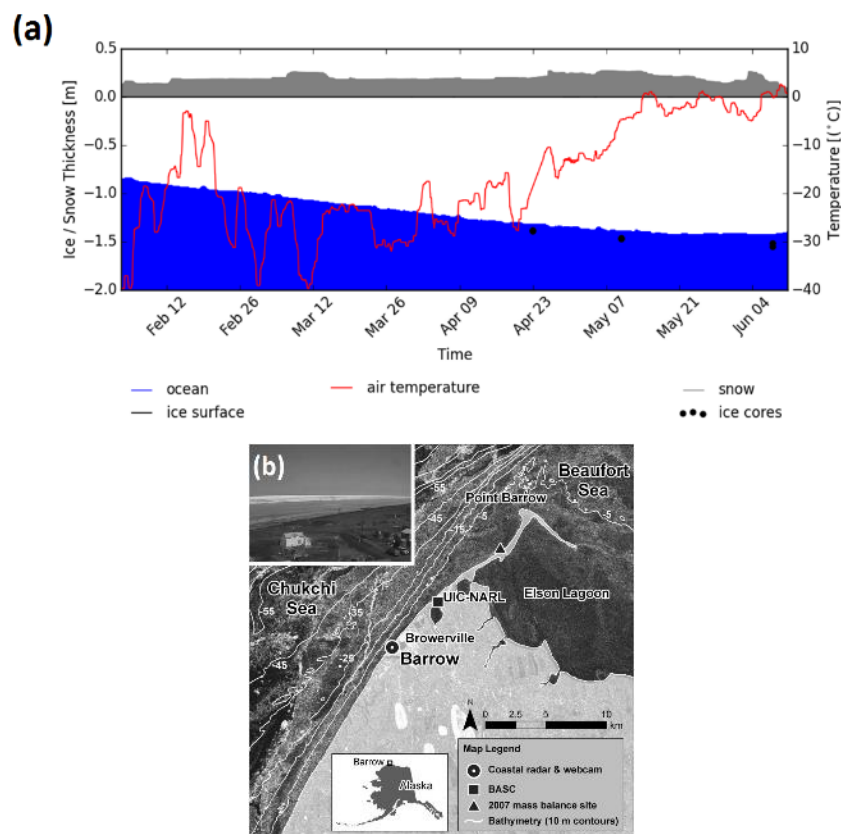


Figure 38. (a) Typical profile of mostly level first-year ice at Barrow (data come from winter 2006) ; (b) Position of the MBS (Druckenmiller et al., 2009)

For a coring event, the sampling scheme consists of measuring the vertical temperature profile on one core with a probe thermometer inserted in a sequence of holes drilled at 5 or 10 cm intervals from the bottom. The sea ice bulk salinity profile is determined on adjacent cores, cut into 5 or 10 cm thickness segments, melted at room temperature in the laboratory in a sealed container. Salinity is measured with a conductivity probe. The number of cores collected for salinity measurements at each site varies from 1 to 3.

Temperature profiles recorded with an in-situ thermistor array at the mass balance station from 2006 through 2014 are used to supplement the ice-core measurements. The mass balance station is an automated site installed annually, which provides measurements every four hours of temperature profiles, thickness information for ice and snow, sea-level measurements, temperature and relative humidity of the local atmosphere (2m above sea-level) (Druckenmiller et al., 2009). Temperature profiles are measured throughout the water/ice/snow/air at 10cm vertical intervals. Installation and removal dates are dependent on the time when the ice becomes

securely land fast in the beginning of the calendar year and the melt advance and break-up in June.

Svalbard

The only ice core time series representative of oil and gas extraction regions in the Eurasian Arctic that we were able to locate was of ice cores retrieved at Kongsfjorden in Svalbard at the end of the growth season between May 5 and June 9, 1998 (Gerland et al., 1999; Gerland and Hass, 2004). Each of the 10 coring events consists of two cores retrieved, one for temperature, and one for salinity profile measurement. This dataset is representative for thin first year sea ice (up to 80cm in thickness). Due to the lack of observations, no information on the interannual variability as well as ice conditions in early winter are available.

Data Processing

First, each salinity and temperature profile is discretized with a 5-cm layer thickness, ranging from 2.5 cm depth to the full core length, rounded to the closest 5 cm. Erroneous and missing data are replaced by linear interpolation between the two nearest points.

Ice cores are typically grouped into different categories based on ice thickness, salinity curve shape, and seasonal stage. Monthly grouping of ice property data does not provide as meaningful results as data presented in daily values, since curve collections do not take into account the interannual variability in timing of the growth and melt season. Grouping by a given date and a given temporal spread around it, to aggregate cores from the same field campaign period (beginning January, April, early-May,) improve the result, but do not perform well in spring when desalination of the top layer is highly dependent on the number of days with surface thaw.

Hence, in this analysis the ice cores were into different groups based on a degree-day approach. This index is defined as the difference between the daily average air temperature and a reference temperature. The latter was set to -1.8°C , the freezing point of seawater, rather than 0°C , to take into account sea ice thermodynamics. When the temperature falls below the reference, the index is positive and referred to as Positive Degree Days or Freezing Degree Days (FDD). The cumulative value of FDD calculated from the initiation of freezing to the coring date of a given core provides a measure of both the duration and severity of cooling during the ice season. Similarly, the cumulative thawing degree days (TDD) indicate the extent of potential melt that the ice sheet and the core extracted from it may have experienced. Furthermore, classifying the ice cores by FDDs and TDDs, rather than specific dates reduced interannual variations due to seasonal timing rather than genuine differences in ice properties (Figure 3).

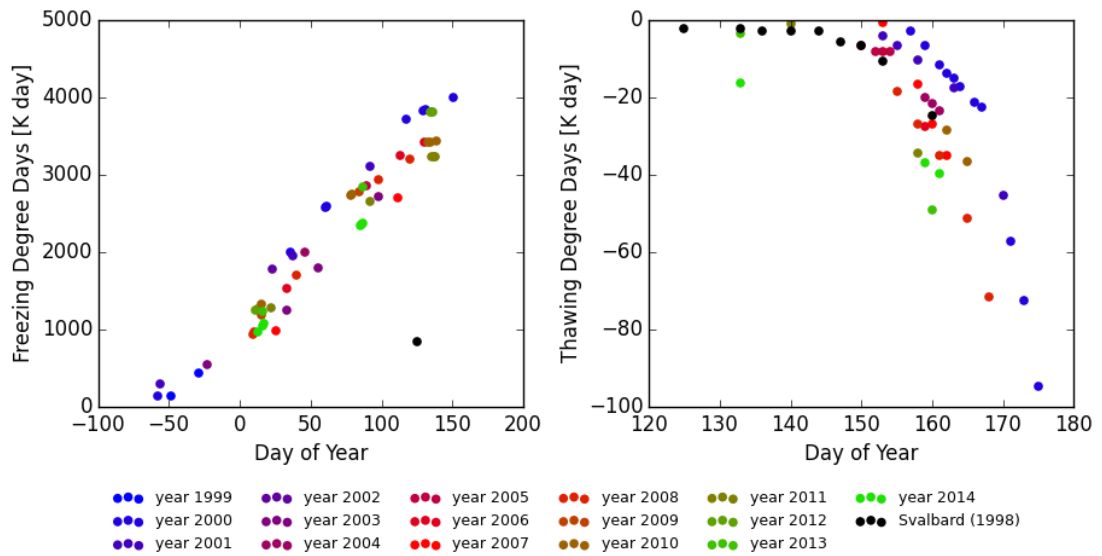


Figure 39. Interannual variability and long-term change as shown in ice growth/melt conditions: for the same day of the year, the number of freezing degree-days has decreased steadily. Each point describes a date when one or several ice cores have been sampled. Coloured data points represent ice cores collected at Barrow, black data points are ice cores collected in Svalbard.

Finally, mean and standard deviation are computed for each group. The resulting statistical envelope is a measure of the spread of sea ice properties.

3.9.3 Acoustics

The acoustic modelling was designed to enable data interpretation for data collected in the laboratory and to anticipate the performance of the model in arctic field conditions. Capitalizing on the under ice sonar system data and the oil acoustic characterization information, the changes in the measured reflection coefficient and echo statistics from the oil/ice interface were used to guide the model development, which is based on the Eckart (1953) formulation modified previously by Stanton et al. (1986). If the oil was very thin, then effects due to multiple reflections between the water/oil and oil/ice interface were considered, following an appropriately modified approach introduced in Lavery et al. (2007). The thin oil scenarios tend to result in possible constructive and destructive interference patterns. Predictions of scattering from oil under ice were compared to the data collected during the CRREL laboratory experiments. These measurements were used to test the integral equation model developed for the defined ice and oil scenarios. The integral equation model is an exact, but computationally inefficient model, which was adapted to the Kirchhoff Approximation. This method takes into account the topography of the oil/ice interface, as opposed to modelling the surface statistically. The statistical modelling approach, based on the Eckart method, is highly practical and computationally efficient, but may not encompass the details of all ice/oil conditions. Thus, these two complementary approaches allow for better verification of details necessary for quality modelling and to successfully extend the accuracy of the predictions to scenarios not tested in the laboratory measurements.

The key parameter to acoustic modelling is scattering strength (SS). The SS parameter is defined as:

$$SS = 10 \log_{10}(\sigma(\theta_i, \theta_s, \phi_s))$$

Where σ is the scattering cross section per unit area per unit solid angle for given frequency, θ_i is the incident grazing angle, θ_s the scattered grazing angle, and ϕ_s the bi-static angle (Figure 40).

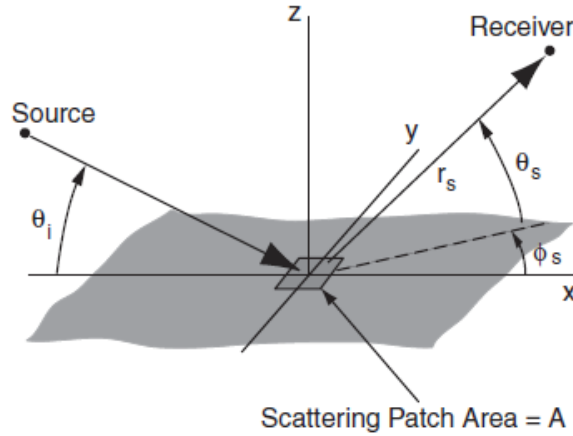


Figure 40. Definition of angular coordinates, adopted from “High-Frequency Seafloor Acoustics” by Jackson and Richardson, Springer (2007).

The model consists of four interfacing layers, as depicted in figure 41. The first is a homogeneous half-space of water. The second is a layer of oil that is heterogeneous and can scatter sound. The third and fourth layers are both for ice, which are divided into two parts: a thin skeletal layer at the leading edge of the water/ice interface and a thick ice layer. The skeletal layer is allowed to have very different properties from the ice layer. All the interfaces at the boundaries of the layers are assumed to be rough with the ability to scatter sound. The model is a modification based on the GABIM sediment acoustics model (Jackson et al. 2010). The modification uses the scattering cross sections to predict scattering sound intensity as a function of time, in order to directly compare to intensity data in the time domain. This is achieved by integrating the various volume (for heterogeneity) and interface roughness scattering sections in the following manner:

For volume scattering:

$$I(t) = \int I_0(t) B \frac{\sigma_v}{r^4} e^{-2\alpha r} dv$$

For roughness scattering:

$$I(t) = \int I_0(t) B \frac{\sigma_s}{r^4} e^{-2\alpha r} ds$$

where $r = c*t/2$, and c is the local sound speed, and α is local attenuation coefficient. B is the combined beam pattern of the source and receiver, and I_0 is the source intensity at 1 m from the source. σ_v is the volume scattering cross section and σ_s the roughness scattering cross section. Straight ray propagation is assumed. Integration is performed by dividing the entire scattering region into small pixels/voxels, each having an angular- and frequency-dependent scattering cross section.

Rough interfaces:

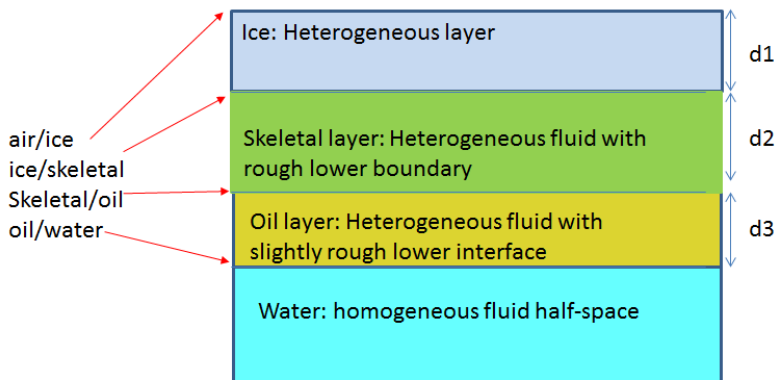


Figure 41. The four-layer model for the water/oil/ice medium.

3.9.4 Optics

Two numerical models were used for computing radiative transport in sea ice. One uses the Discrete Ordinates Method (Grenfell 1991) to solve the 1-D radiative transfer equation. The other uses a Monte Carlo solution (“2DMCRT”; Light et al. 2003). The 2DMCRT treats radiative transport in a 2-dimensional, azimuthally symmetric domain, and thus is easily tailored to simulating unique sensors and domains with unique geometry. This model does not rely on the domain being plane-parallel, or horizontally infinite, so would be ideally suited for simulating a patchy distribution of an absorbing compound, as would be expected for oil in ice.

Model simulations were compared with apparent optical property measurements.

3.9.5 Radar

The purpose of the radar modelling effort is to evaluate the change in radar response with increasing flight height above the ice. In particular, the radar footprint increases as a function of height above the target. Thus it is key to operational practice to evaluate how radar height above the sea ice impacts our ability to identify a small-scale spill. The project parameters dictate the evaluation of radar response to a 2 m diameter pool and a 200 m diameter pool. The 200 m diameter pool is well above the radar footprint at any reasonable flight height, so the 1D model is an adequate representation for this case and we refer to the 1D model results.

The signal response to a 2 m diameter pool was modeled using a 2D finite difference algorithm that operates using the exploding reflector principle. The exploding reflector principle states that the data recorded by a series of coincident sources and receivers at the surface is approximately equivalent to the data recorded as one way propagation by a line of receivers at the surface and an array of sources at all subsurface discontinuities. The sources have amplitude equal to the reflection coefficient at that point in the subsurface. This approach enables the simulation of an entire radar profile in a single model run which greatly reduces the model run time, but at the cost of some reduced accuracy. Regardless, the model remains computationally intensive and model runs are on the order of days, even for the small models simulated here.

Give the long run time; simulations were limited to a single scenario – the January ice model with 5 cm of oil at the base of the ice. The model is 6 m long, with the 2 m oil pool placed in the center.

4. RESULTS

Results are provided from ancillary measurements to help set the stage for the measurements collected by the various instrument systems. The instrument results are presented by the hoop number. Modelling results include modelling of the experimental conditions and expected field conditions.

4.1 Ancillary Measurements

4.1.1 Environmental Properties

Environmental conditions, primarily temperature and salinity, determine ice porosity and growth rate, which influenced the various measurements that were collected. Air temperature during the growth phase is provided in figure 42. In the early stages of the experiment, the room was warmed during oil injections for better working conditions and because the cooling system required defrosting. These warming events affected the radar measurements and were stopped before the last three injections. Water temperature remained at the freezing point throughout the experiment until melt-out. Because the salinity of the water increased as brine was rejected during ice formation, there was a corresponding slow decrease in the water temperature (Figure 43). While not shown, the tank salinity can be estimated from the freezing point of water and the water temperature.

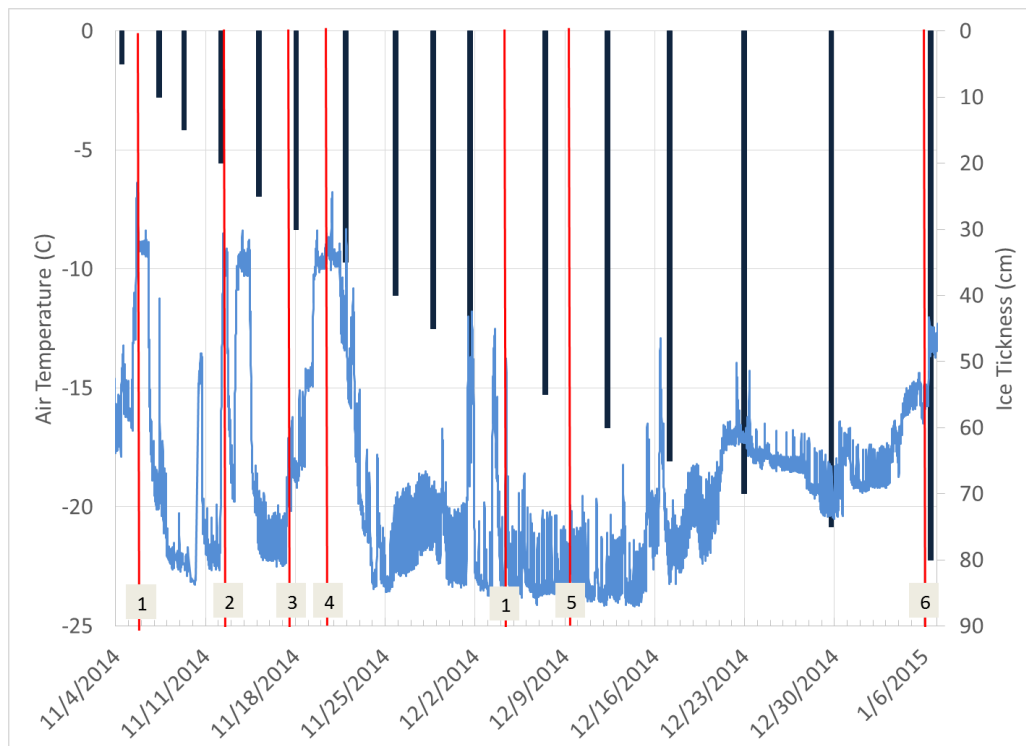


Figure 42. Air temperature is the continuous blue line. Injection dates are shown in vertical red lines with the hoop number provided at the bottom of the line. The blue bars represent ice thickness determined from the eastern thermistor array.

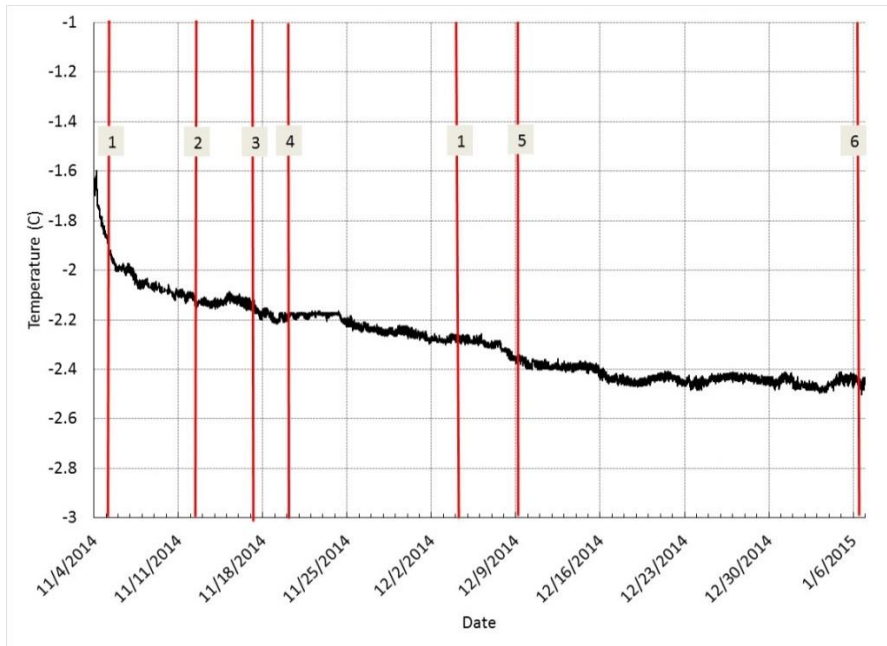


Figure 43. Water temperature below the ice through the growth phase of the experiment.

During the decay phase the air temperature was initially brought to near -2°C on January 12th and later warmed further to enhance the ice decay (Figure 44). The ice was above -5°C on January 15th and isothermal on January 28th. Temperature data indicated that most of the ice loss was from the upper surface. This is also evident in photographs that show the experiment hoops above the outside ice level.

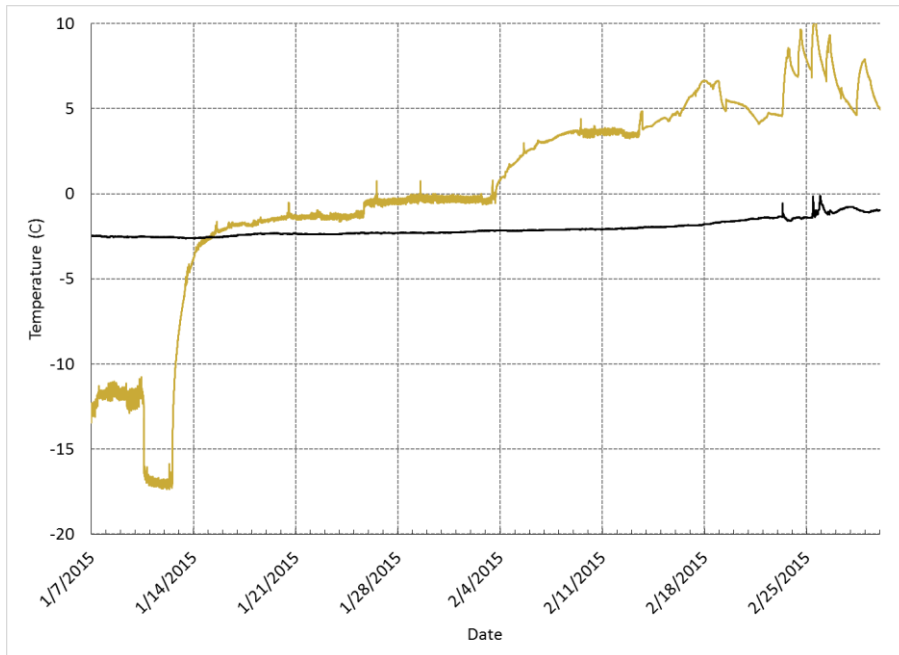


Figure 44. The light colour line shows air temperature and the dark line the water temperature during the melt phase.

4.1.2 Ice Properties

4.1.2.1 Ice Thickness

Ice thickness measurements were determined using three methods. Thickness was measured when ice cores were collected (Figure 45). In the figure, cores taken from the same location are grouped by circles. The largest distributions in measured thicknesses occurred in cores taken from within the hoops; the ice was also thinner in the hoops than ice taken outside the hoops in the same time frame. Table 8 presents the analysis of the variation of thickness within and outside of hoops. The ice thickness increased over time until the temperature in the test basin increased on January 13, 2015.

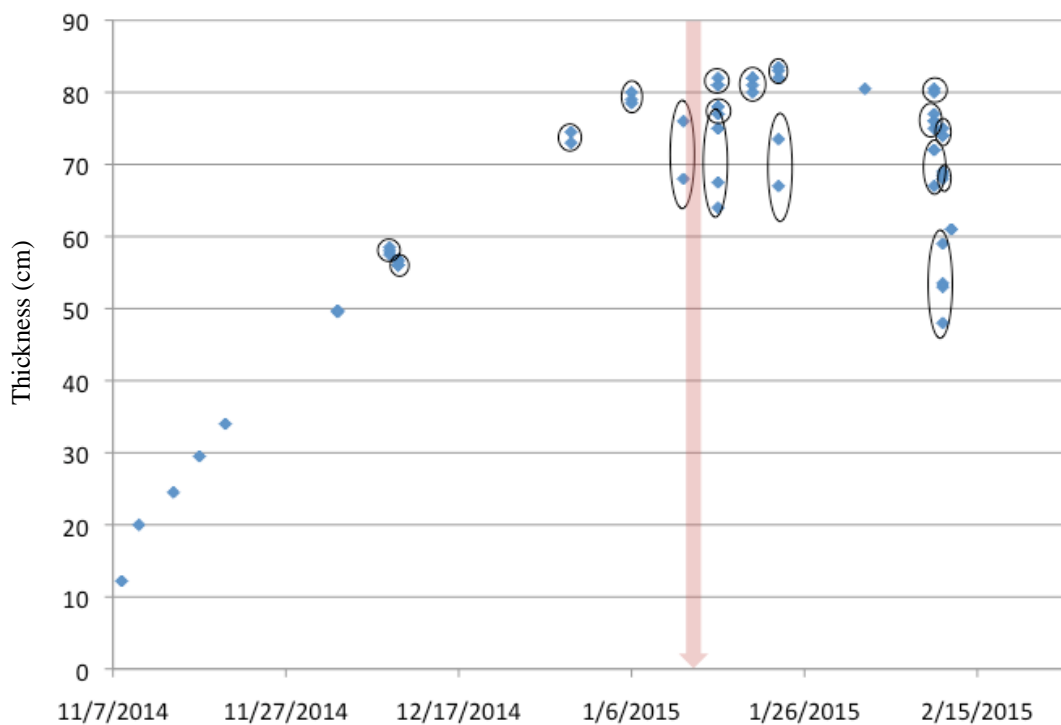


Figure 45. Evolution of the ice sheet thickness over time. Circles group cores drilled in the same area on the same day. Red line indicates start of warm up.

Figure 46 illustrates the variation in standard deviations of ice thickness over the course of the experiment. The variation is generally low, <1cm, except for times during the experiment when cores were retrieved from inside the hoops (January 12th, 16th, 23rd and February 10th and 11th). Table 8 compares values of the standard deviations of ice thicknesses measured from outside and inside the hoops. The standard deviation is higher for thickness measurements made inside the hoops. This was also reflected in measurements of thickness variations in slabs removed from inside hoops, which had dome-like bottom topographies, and showed on a range of about 10 cm in thickness.

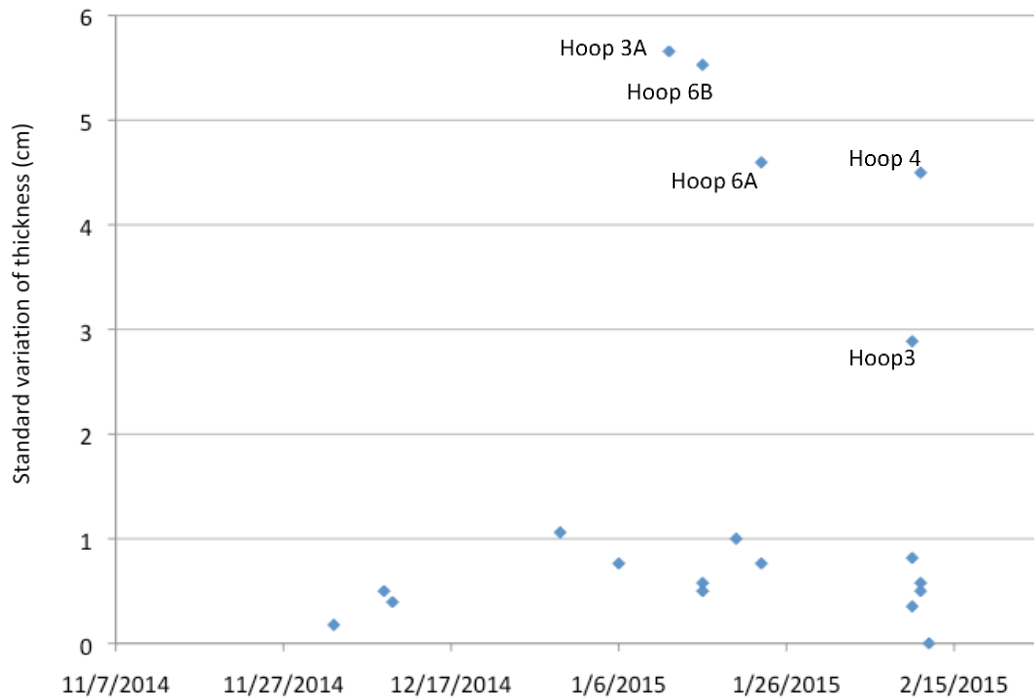


Figure 46. Variation of average standard deviation of multiple thickness measurements made on the same day. Values >1 are from multiple cores taken within the same hoop.

Table 8. Standard deviation of ice thickness measurements made at the same location on the same day. Comparison of thickness variation in and outside hoops.

Date	Location	Thickness (cm)	Stand. Dev. (cm)	% Variation
3-Dec-14	Outside Hoop 4	49.6	0.2	0.4
9-Dec-14	Outside Hoop 5	58	0.5	0.9
10-Dec-14	Outside Hoop 2	56.3	0.4	0.7
30-Dec-14	Outside Hoop 3	73.8	1.1	1.5
6-Jan-15	Outside Hoop 6	79.2	0.8	1.0
16-Jan-15	Outside Hoop 2/3	79.4	2.1	2.6
16-Jan-15	Outside Hoop 5	81.3	0.5	0.6
20-Jan-15	Outside Hoop 4	81	1	1.2
23-Jan-15	Outside Hoop 5A/6A	82.8	0.8	1.0
10-Feb-15	Outside Hoop 5/6	80.3	0.4	0.5
12-Jan-15	Inside Hoop 3A	72	5.7	7.9
16-Jan-15	inside Hoop 6B	70.4	5.5	7.8
23-Jan-15	Inside Hoop 6A	70.3	4.6	6.5
12-Feb-15	Inside Hoop 1	61	0	0.0
12-Feb-15	Inside Hoop 2	76	0.8	1.1
10-Feb-15	Inside Hoop 3	70.3	2.9	4.1
11-Feb-15	Inside Hoop 4	53.4	4.5	8.4
11-Feb-15	Inside Hoop 5	74.3	0.6	0.8
11-Feb-15	Inside Hoop 6	68.5	0.5	0.7
16-Jan-15	Slab in Hoop 6	72	4	5.6
20-Jan-15	Slab in Hoop 4	82		
23-Jan-15	Slab in Hoop 6A	65	5	7.7
11-Feb-15	Slab in Hoop 6	68.3	0.8	1.2

Thickness was also estimated from the thermistor strings embedded in the ice (Figure 42). The measured ice thickness and ice thickness estimated from temperature are in good agreement. Both of those measurements were outside of the experimental hoops, which was important

because the ice growth was intentionally retarded in hoops three through six. The determination of ice thickness within the hoops was estimated from ice draft measurements using sonar systems or from radar measurements. A more complete thickness estimate was available from sonar when it was able to image the upper ice surface, or conversely when the radar systems were able to image the bottom of the ice.

In estimating the ice thickness from sonar measurements of ice draft it is necessary to know the ice freeboard. Freeboard values measured in the boreholes from the core sampling are shown in Figure 47.

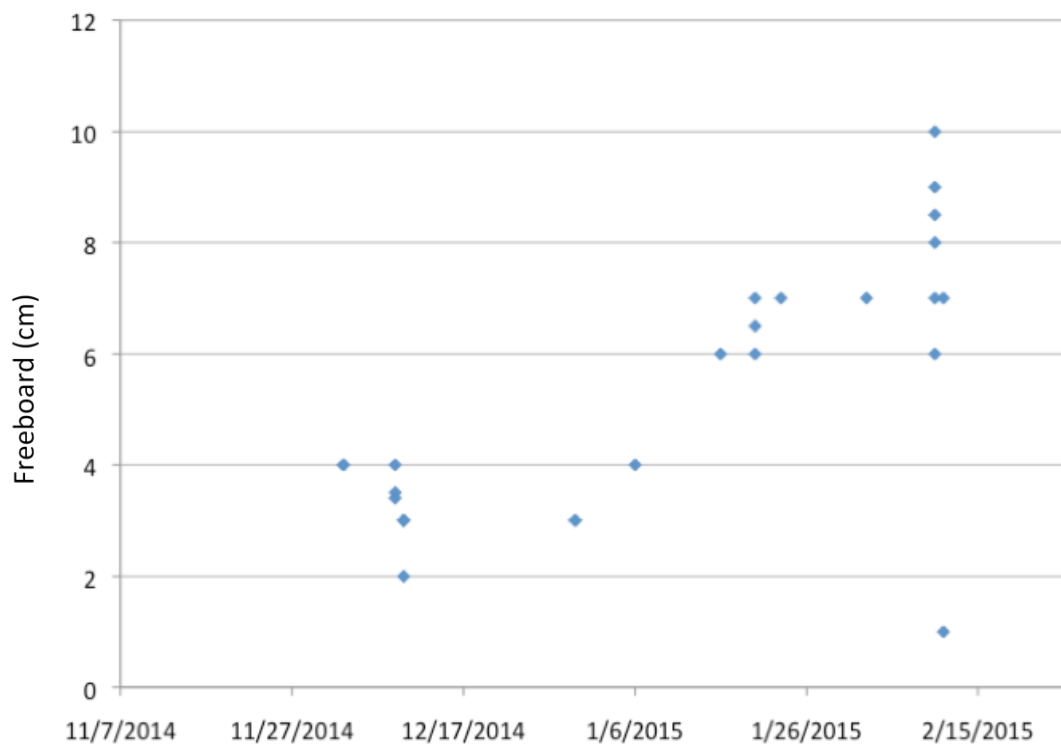


Figure 47. Freeboard values for the test basin throughout the experiment.

The presence of oil slowed the growth of ice between one and three days depending on the air temperature (Figure 48). Afterward the growth rate matches that of the surrounding ice.

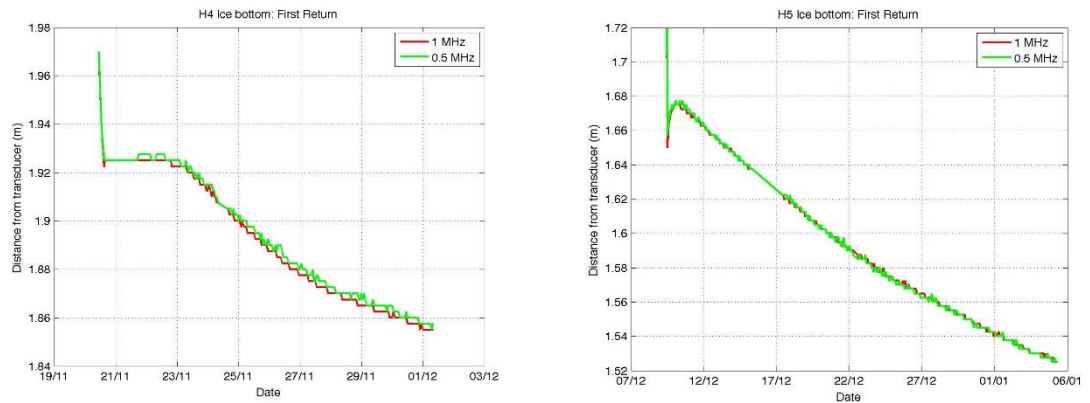


Figure 48. Ice growth under injections into Hoop 4 (left) and Hoop 5 (right) as seen by the Aquascat system. The steep gradient (almost vertical) at the start of the graph relates to the injection of the oil. After the injection, the ice growth initially slows and then returns to a rate similar to surrounding ice.

4.1.2.2 Ice Density

The evolution of the ice sheet density in top 5 cm, bottom 5 cm (skeletal layer) and the average of the entire ice sheet thickness is shown in Figure 49. The density of the top and bottom sections and of the average thickness stayed relatively constant during the course of the experiment, with a notable decrease at the onset of the warming phase on January 13th. There is also a slight decrease in density that occurred after an unscheduled warming phase on December 20th, after which the ice became denser after the temperature was decreased in the test facility. The top 5 cm generally had higher density than the bottom 5 cm, which comprised a large portion of the skeletal layer. The high variability in the bottom density values is due to brine drainage from the skeletal layer samples during the extraction process; brine drainage from the bottom layers is also indicated by the low-density values. The evolution of the density profiles over time are shown in Figure 50, which reflect relatively constant density values over the entire thickness of the ice sheet until the end of warming phase was approached (February 2-12, 2015). Figure 51 shows the evolution of the top, bottom and average density values in relation to the average daily air temperature as recorded by the temperature sensors located on the east side of the test basin. The correlation coefficient calculated between the average density and the air temperature is -0.64.

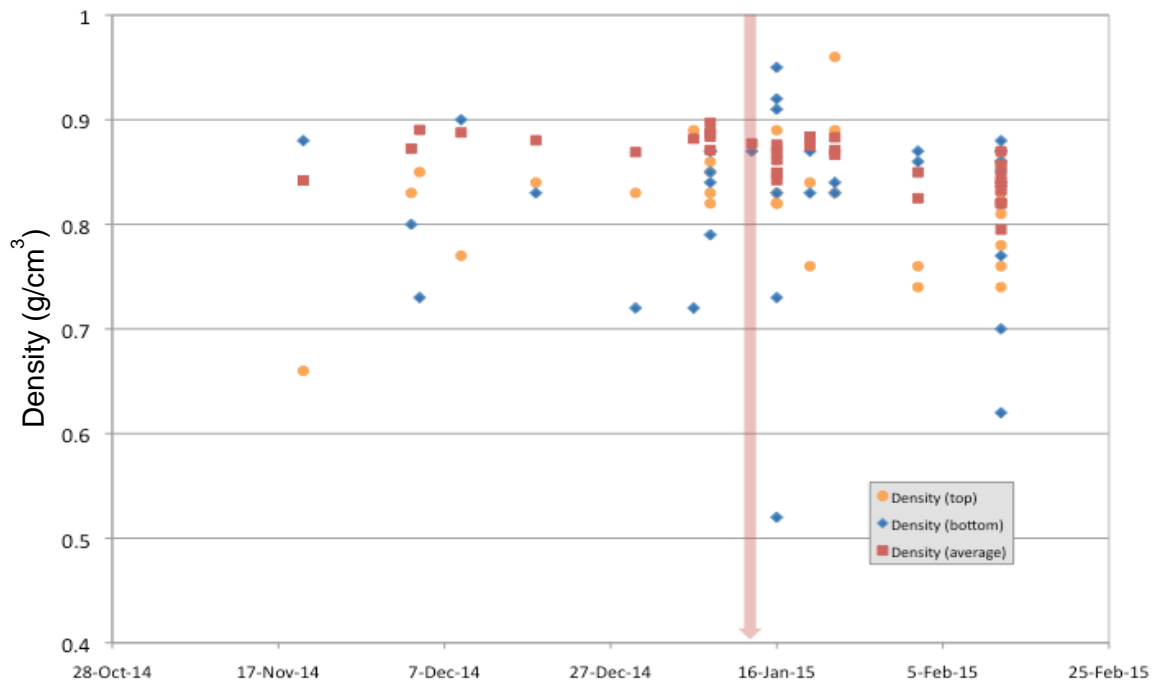


Figure 49. Evolution of the density of the ice top, ice bottom, and average density over the entire ice thickness. Red line indicates start of warm up.

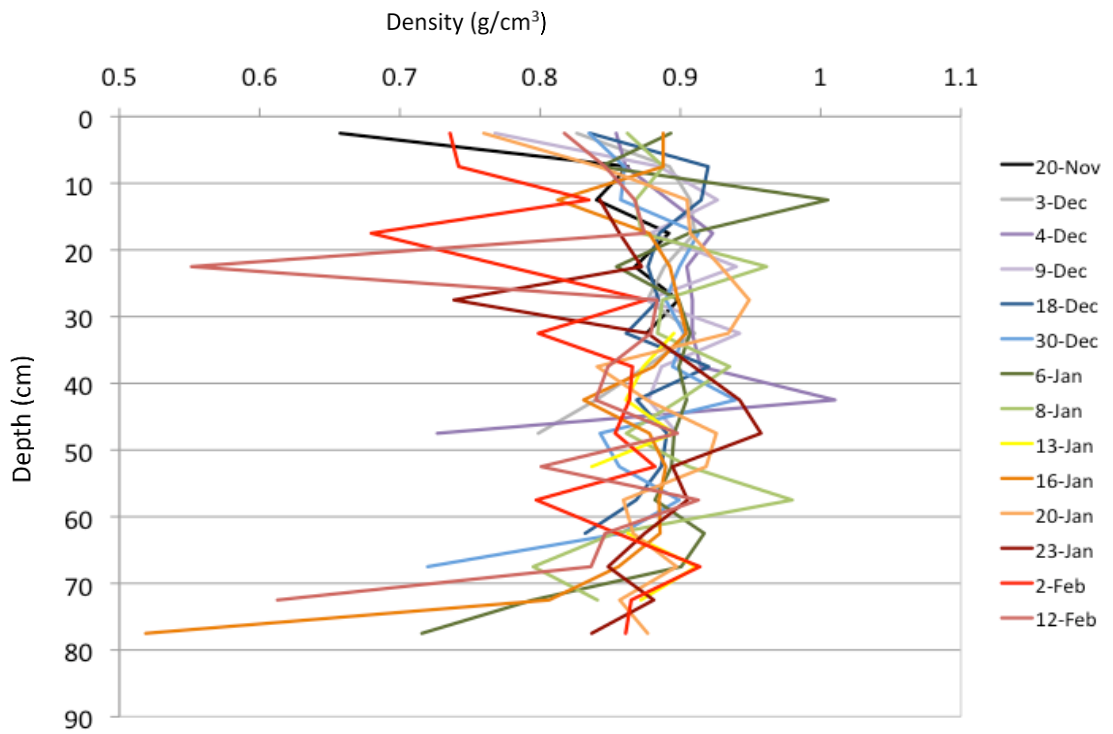


Figure 50. Evolution of density profiles over time, each sampling date is represented by different colour.

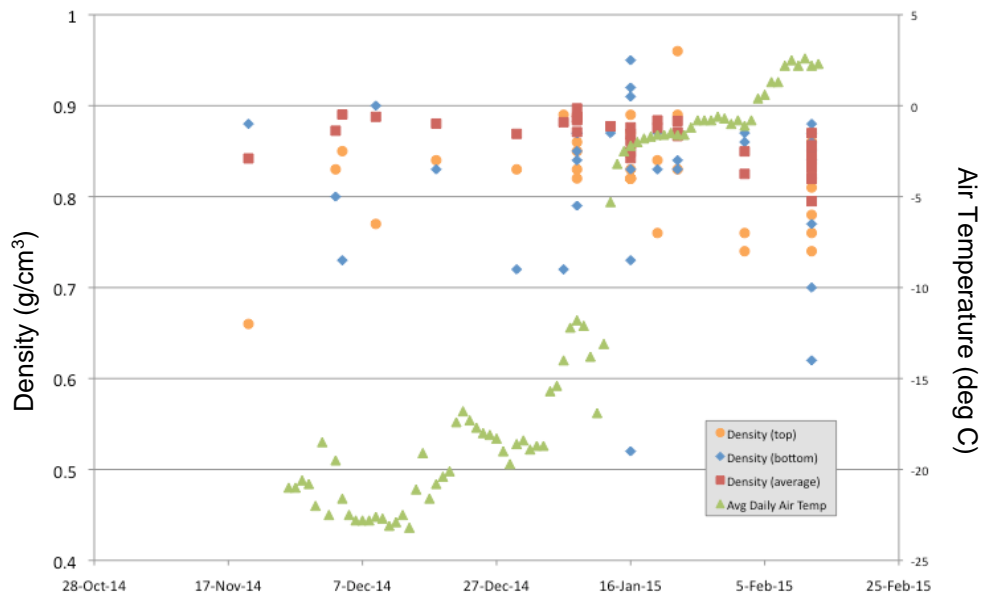


Figure 51. Evolution of top, middle, average density values over time in relation to the air temperature in the test facility.

4.1.2.3 Salinity

The evolution of the salinity in the top 5 cm of the ice, the bottom 5 cm of the ice, and the average salinity values over the entire ice thickness is shown in Figure 52. The evolution of the salinity profiles over the range of the ice thickness is shown in Figure 53. A distinct freshening of the top of the ice sheet began to occur after the warm-up phase on January 13th (marked by the red line in the figure 52), while the bottom 5 cm of the ice increased in salinity. The overall average salinity also decreased after the warm up phase began.

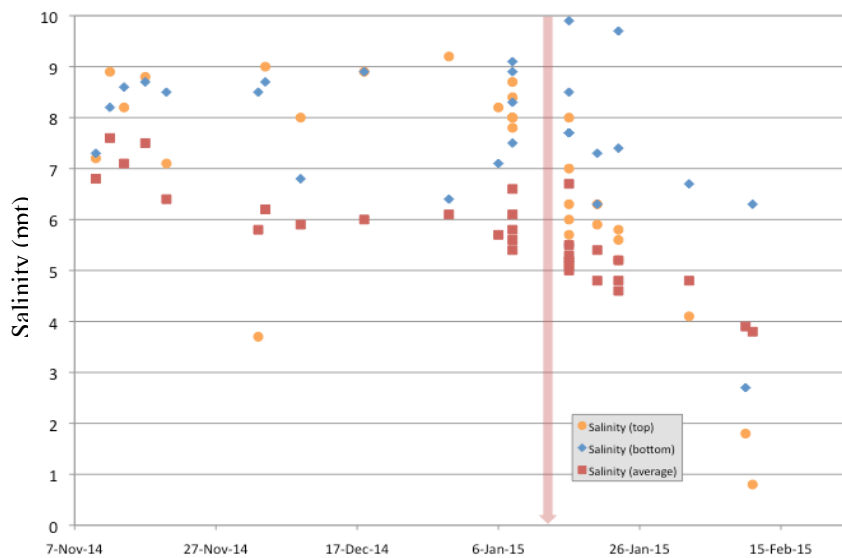


Figure 52. Evolution of salinity of top, bottom and average over the ice thickness of melted ice sections.

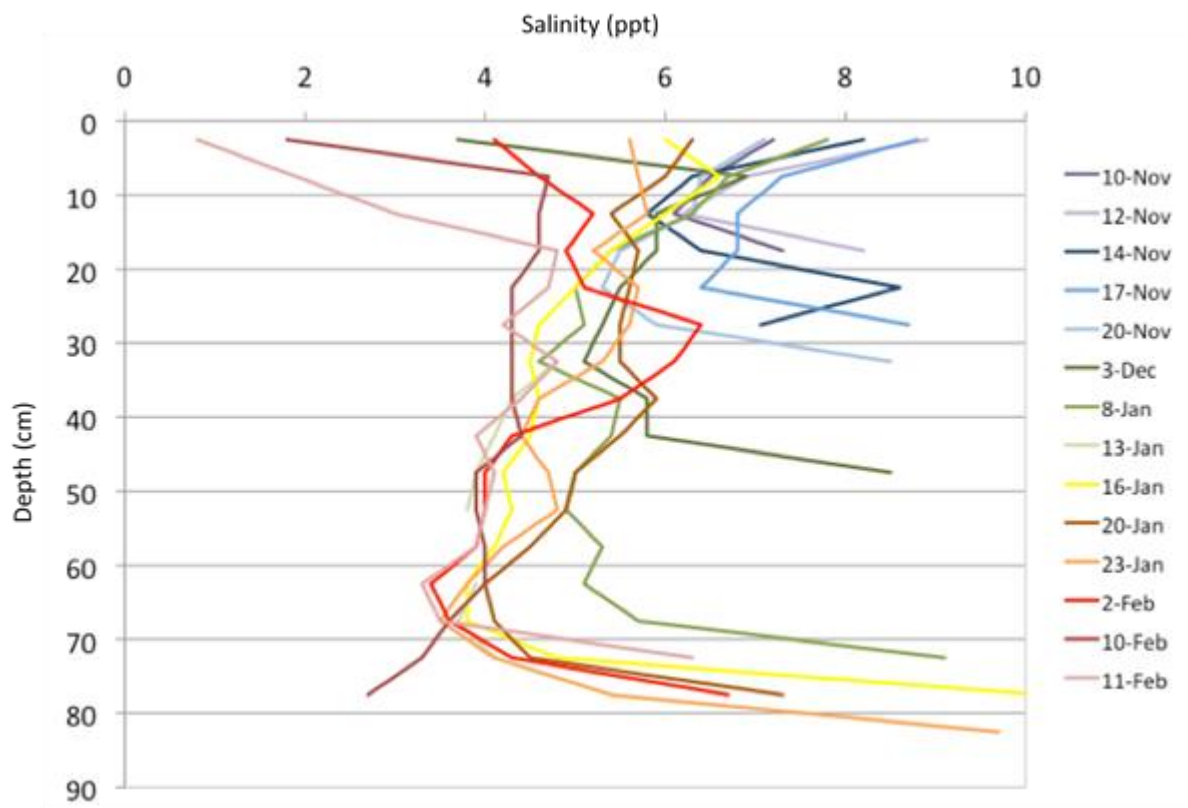


Figure 53. Evolution of salinity profiles over time.

Spatial and short-term temporal variation in the salinity at various times in the experiment is demonstrated in Figure 54. Figure 54 shows salinity profiles over a span of five days and different locations on the ice sheet and shows salinity profiles from a single day. Both short-term temporal variation during cold periods and spatial variability were minimal, particularly in the top of the ice sheet.

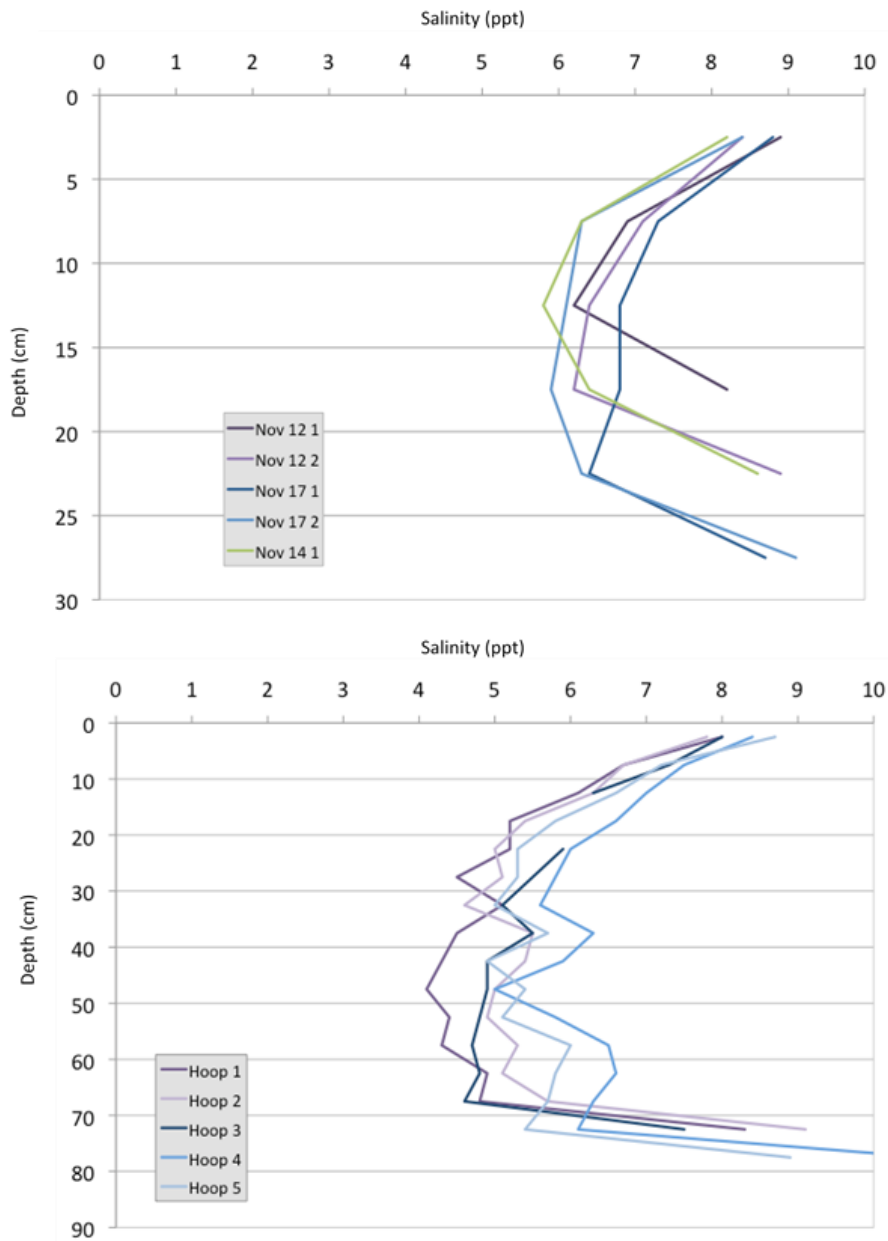


Figure 54. Salinity variation over 5 days (November 12th to 17th, top) and within the hoops on January 8th (bottom).

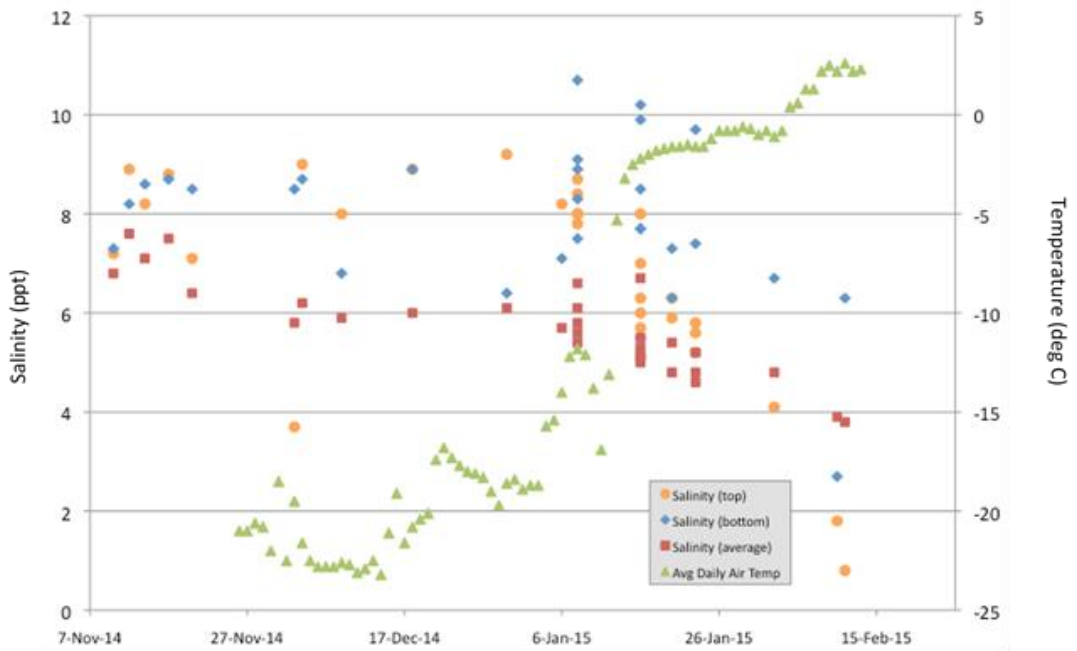


Figure 55. Salinity and temperature variation over time.

The variation of the salinity over time with respect to air temperature is shown in Figure 55. The calculated correlation coefficient of the average salinity values over the thickness of the ice and air temperature is -0.69.

4.1.2.3 Ice Temperatures

Temperatures measured in shallow holes drilled into the cores shortly after retrieval using a thermistor probe are shown in Figures 56 and 57. Figure 56 shows the temperature measured in the top of the core, the bottom of the core, and the average temperature of the entire core over time. Figure 57 shows the evolution of the temperature profiles at depth. The temperature profile from December 9th was particularly noisy, most likely due to the temperature sensors cooling in the colder air of the test facility between temperature readings on the cores, an issue with all the measurements made in this manner. Care was taken to make the measurements as quickly as possible, but some necessary delay was involved in drilling the probe holes and taking the temperature measurements.

A more detailed time series of temperature as a function of depth in the ice is provided in Figure 58. The nearly linear variation from air temperature to water temperature through the ice is evident.

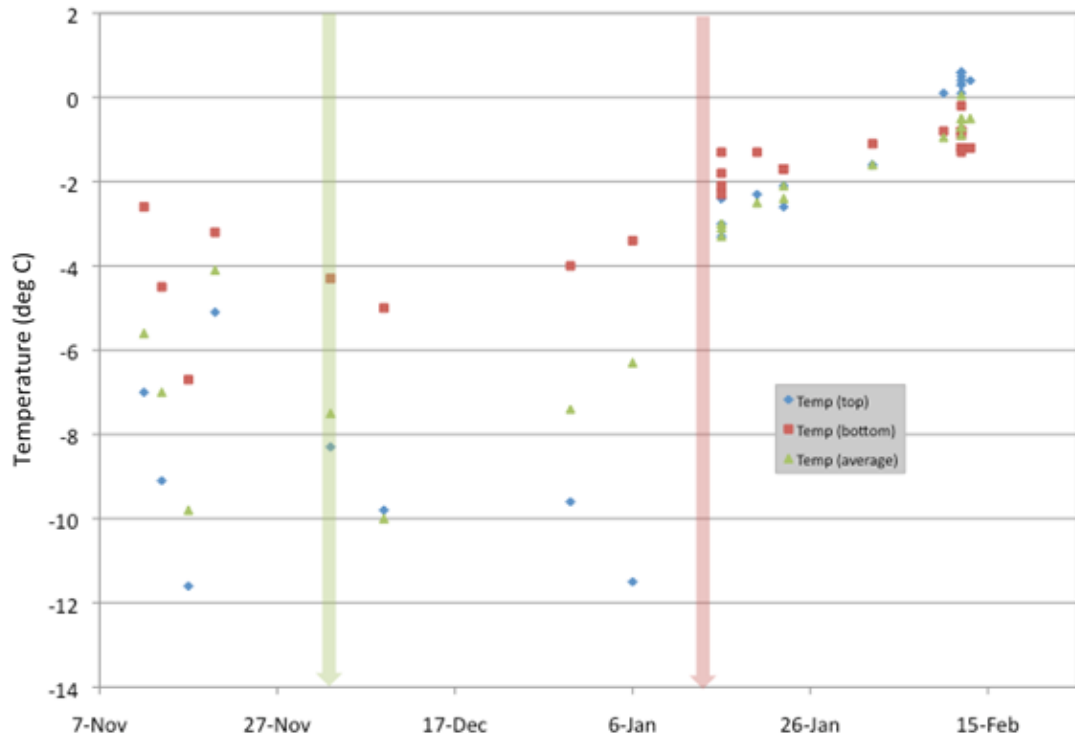


Figure 56. Temperature in top, bottom and over average of the cores.

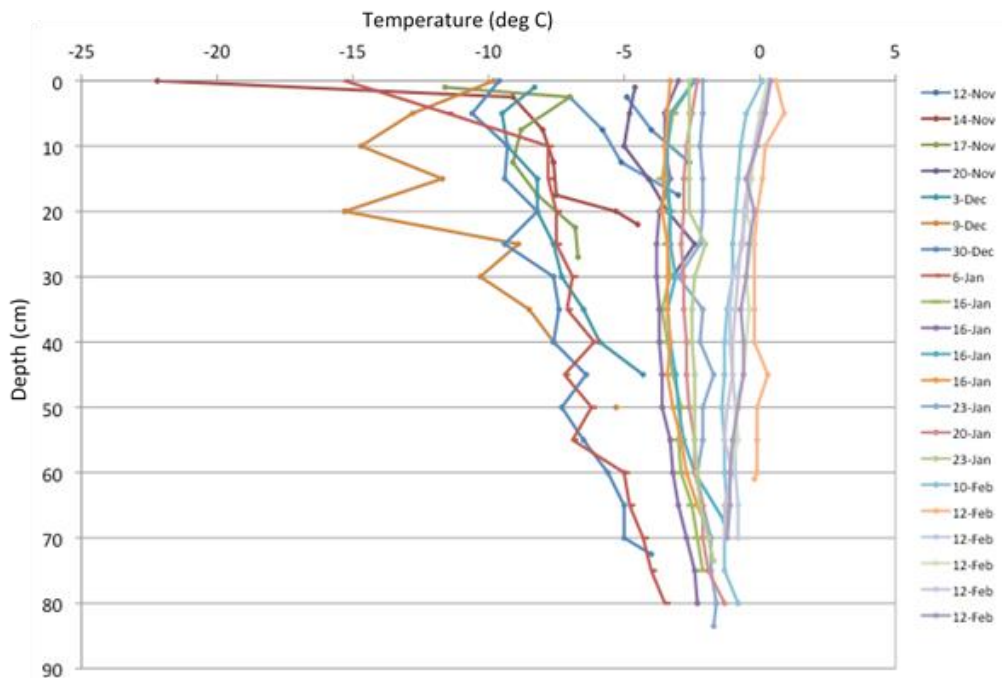


Figure 57. Evolution of temperature profiles measured in cores over time.

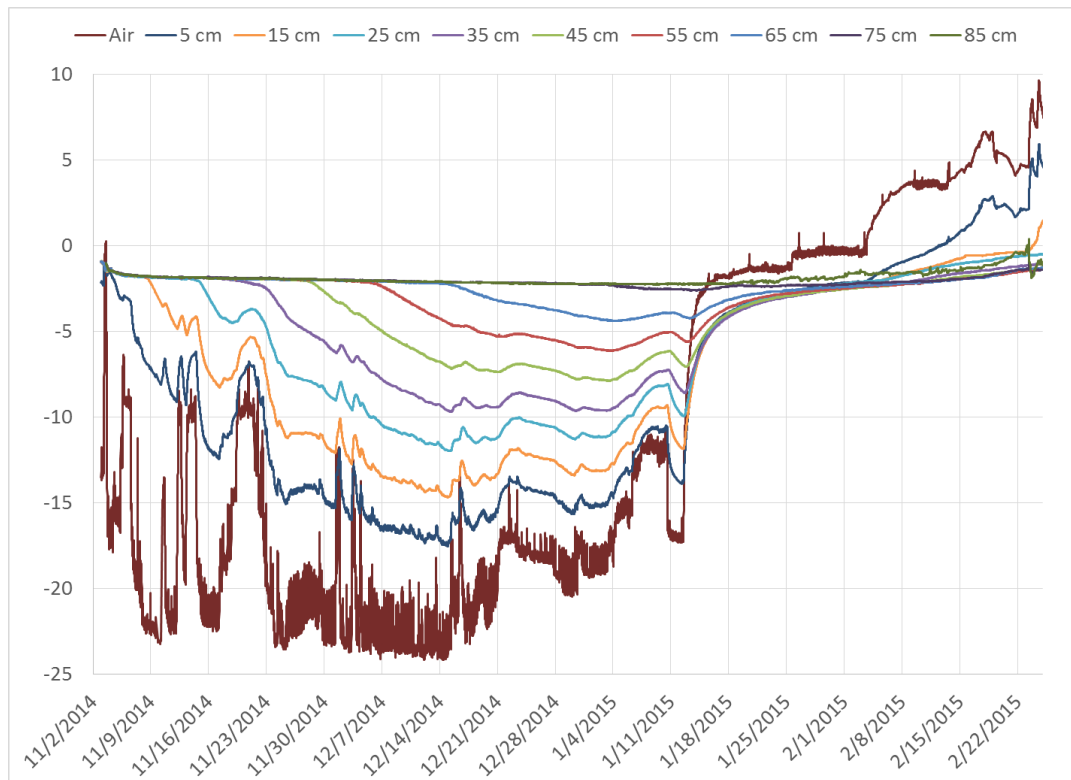


Figure 58. Evolution of temperature profiles measured by the resistance thermal devices over time. Distances are given downward from the original water level.

4.1.2.4 Ice Structure

Ice cores for structure analysis were taken at the end of the experiment on February 11th and 12th, one month after the warm-up phase of the experiment began. Several cores were taken inside every hoop, and in a clean (undisturbed from oil injection) area between Hoop 5 and Hoop 6. Images of thick sections (1cm thick vertical and horizontal cross sections) show internal macro brine and ice structure and thin sections (1mm vertical by 3mm thick) demonstrate crystal structure. Additional images are available at polar.ercd.dren.mil/Ice_Properties.html

Analysis of the ice cores showed growth patterns typical of sea ice grown in calm waters. The top of the ice contained small granular crystals changing to long columnar crystals a few centimeters below the ice surface. Due to the laboratory-setting imposed calm water in the tank, crystal sizes are, to a first order, larger than those experienced in natural sea ice. There are no growth rate changes to create many visible bands in the ice and no current changes to alter the preferred crystal orientation, which results in the crystals growing larger over time. This is not uncommon in calm water areas of sea ice growth (i.e. fast ice zone) where crystals tend to be larger than crystals formed in open pack. Typically, ice sheets in the Arctic would have a smaller columnar structure than seen in this experiment (thinner and shorter columnar crystals), as the ice sheet would have been exposed to ocean currents and wind driven movements as it developed. In general, the laboratory ice grown is similar to that of natural Arctic sea ice grown in calm conditions.

Clean cores

Clean (non-oiled) ice cores for structure analysis were collected throughout the ice growth period. The ice structure looked typical of sea ice growth in very calm conditions. The clean ice core had a small granular structure at the very top that quickly transitioned into columnar crystals that persisted the rest of the way down the core. This is typical of what would be seen in Arctic ice sheets that grow in very calm conditions. The core in Figure 59 was collected on January 6th, 2015, before the refrigeration to the room was turned off. The second core (Figure 60) was collected on February 10th, 2015, after a month of the room being allowed to warm up.

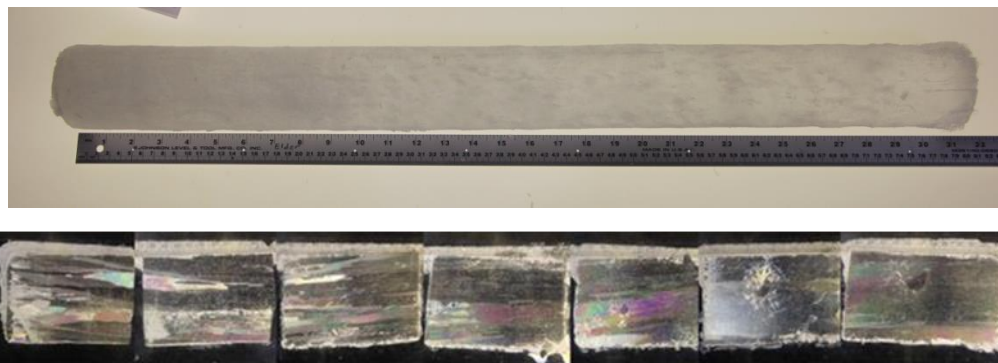


Figure 59. Clean ice core taken just outside of Hoop 6 on January 6th, 2015

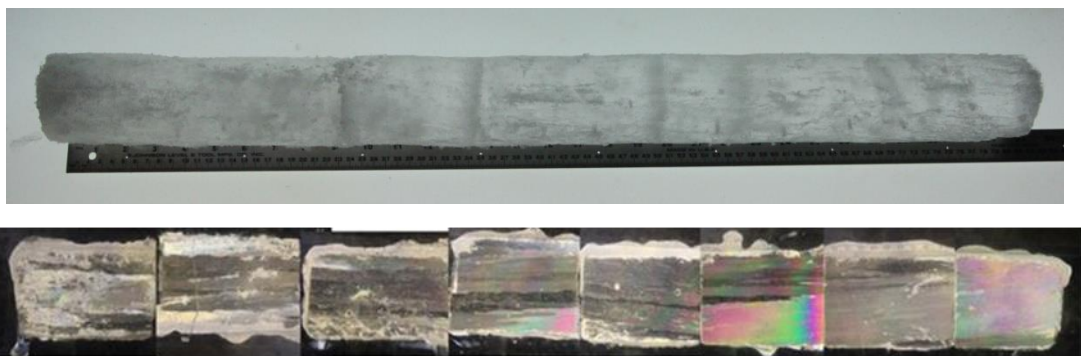


Figure 60. Clean ice core taken on Centre Line between Hoops 5 & 6 on February 12th, 2015

Oiled cores

Hoops 1A and 3A were used for coring and other analyses during the growth phase, and were cored before the room temperature rose to above freezing (on January 12th and 13th, 2015). Hoop 1A (along with Hoop 1), the first hoop injected, was injected while the ice was still in a frazil state, thus the oil was mixed into the top part of the ice very well. The ice core and thick/thin section shows this mixing clearly (Figure 61). The thin sections also show that the ice transitioned from granular to columnar below the oil injection depth.

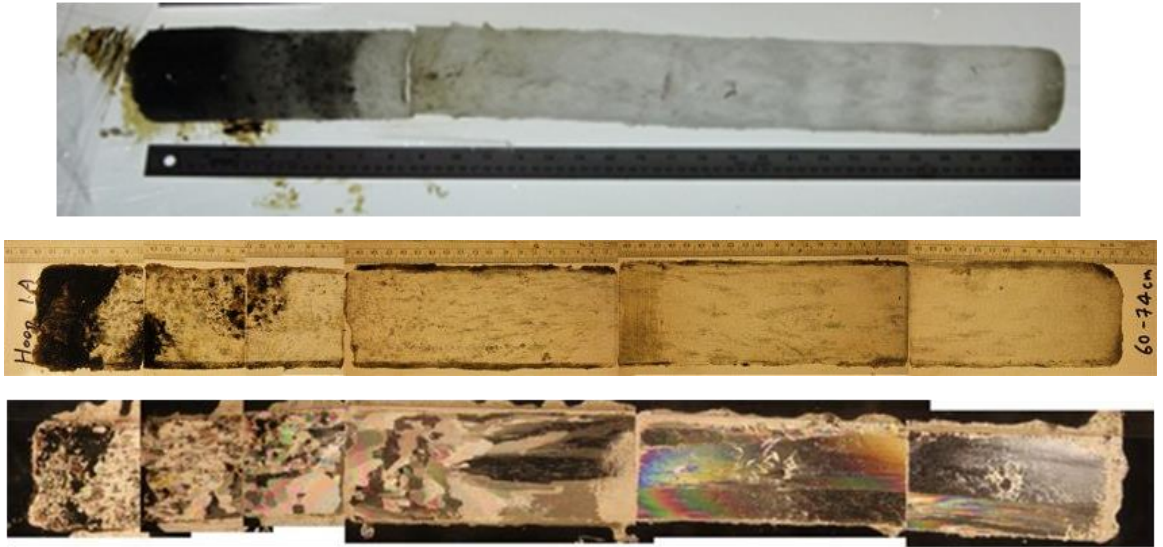


Figure 61. Images of the Hoop 1A cores. The top of the cores are to the left. Entire core (top), thick-sectioned core (middle), thin sectioned core (bottom).

Hoop 3A represented a more typical injection. During the coring process, an approximately 1 cm gap in the ice was noted at the level the oil was injected. Hoop 3A was cored before the room temperature reached above freezing. The images below indicate oil intrusion into the ice above the oil gap via the brine channels, between 7-14 cm from the top of the core (Figure 62). There was virtually no oil intrusion in the top 7 cm of the ice core (Figure 63).

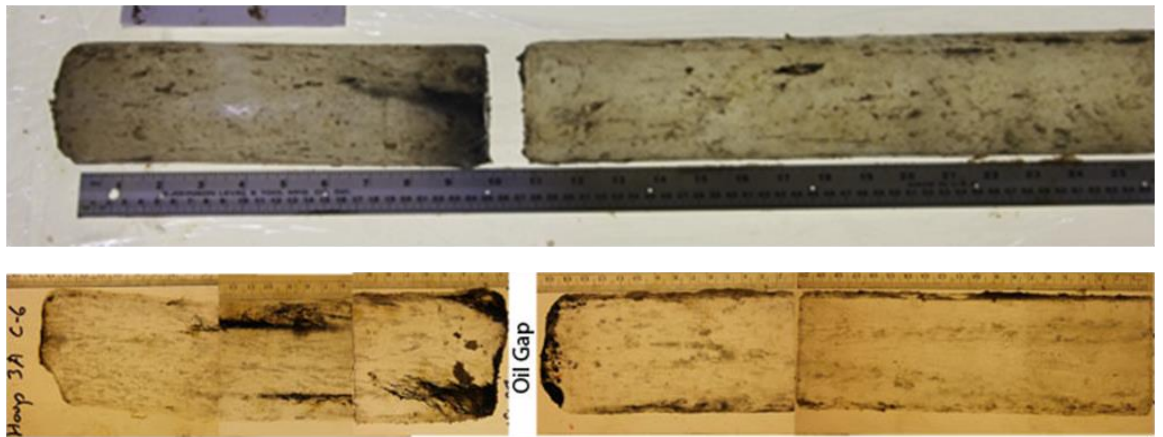


Figure 62. Images of core 3A (top) and core 3A thick sections (bottom) show the small amount of oil intrusion above the oil gap. The top of the cores are to the left.



Figure 63. Cross-sections of the Hoop 3A core at, (from left to right) 5 cm, 10 cm, 15 cm, 20 cm, 25 cm deep. Notice that the oil can only be seen intruding about 10 cm above the oil gap.

At the end of the experiment, ice cores for structure analysis were extracted from the inside of all the hoops on February 10th and 11th, approximately one month after the warm-up phase of the experiment began.

Analysis of the ice cores taken inside the hoops showed the same typical growth patterns of sea ice in calm waters as seen in the non-oiled ice cores discussed above. Normally, the columnar crystals in these ice cores would extend all the way to the bottom of the ice sheet. However, in the cores from Hoops 1 through 4, a 1 to 2 cm gap containing oil was found in the ice at the level where the oil was injected. Below this gap, a 1 to 2 cm layer of clear ice with very low salinity was found. We are uncertain if this layer formed during the oil injection or during the melt period prior to when the cores were collected. The thin sections showed the ice below the gap was granular, changing to long columnar crystals within a couple of centimeters, similar to the pattern seen at the top of the ice core. In Hoop 6, no gap in the ice core was noted. Hoop 6 was injected after the cooling of the room was turned off (beginning of melt phase), therefore no ice growth occurred under the oil that was injected.

The images of the cores and thick/thin sections below show the oil infiltrated the ice above the oil injection gap, while the ice below the oil injection gap remained mostly oil free.

Hoop 1

Hoop 1 had a 2cm thick oil-filled gap at 40cm, underneath the gap, the ice was oil free. The images of the cores and thick/thin sections below show the oil infiltrated the ice above the oil injection gap, while the ice below the oil injection gap remained mostly oil free (Figure 64). After the ice had reached a thickness of 40 cm, oil from the injection migrated up through the thickness of the ice. The large amount of oil present in the top portion of the core was due to the ice conditions during the first injection. The Hoop 1 oil injection was into a slush ice pack 5-15cm thick, through which oil percolated to the top of the ice sheet almost immediately. Also, more oil was injected into Hoop 1 (two injections) at this location than in any of the other locations, increasing the volume of oil in the top portion of the Hoop 1 cores.

In the thin sections of the core in Figure 65 (center and right) the same pattern in the top of the core can be seen: granular ice changing to columnar ice just a few centimeters below the oil injection gap.

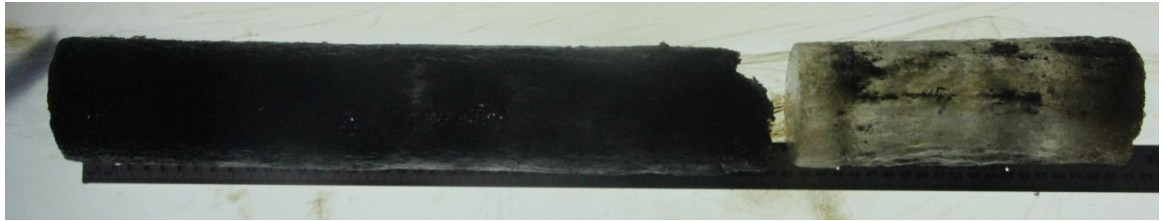


Figure 64. Core taken from Hoop 1 at end of the experiment. Top of the core is to the left. The difference in the ice above and below the oil injection can clearly be seen.

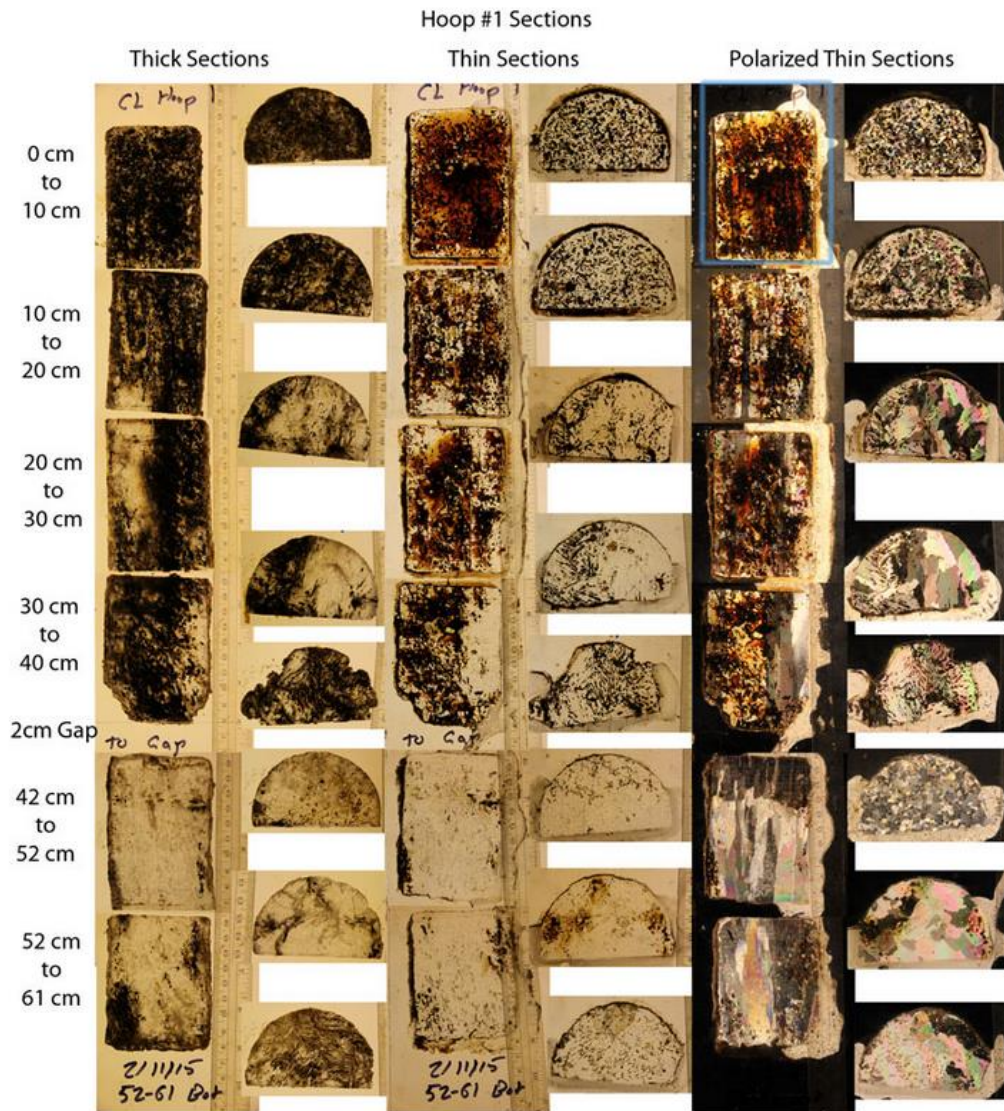


Figure 65. Thin and thick section photos of core from Hoop 1 showing oil locations and crystal structure. The oil in the ice makes it is hard to see the granular to columnar transition in the top part of the ice core. The granular to columnar transition a few centimetres below the oil gap is clearly visible.

Hoop 2

Hoop 2 had a 1 cm-thick, oil-filled gap at 19 cm. The core and thin/thick section images show the same transition above and below the oil injection gap (Figures 66 and 67) that can be seen in the Hoop 1 core.



Figure 66. Core from Hoop 2 taken on February 11th.

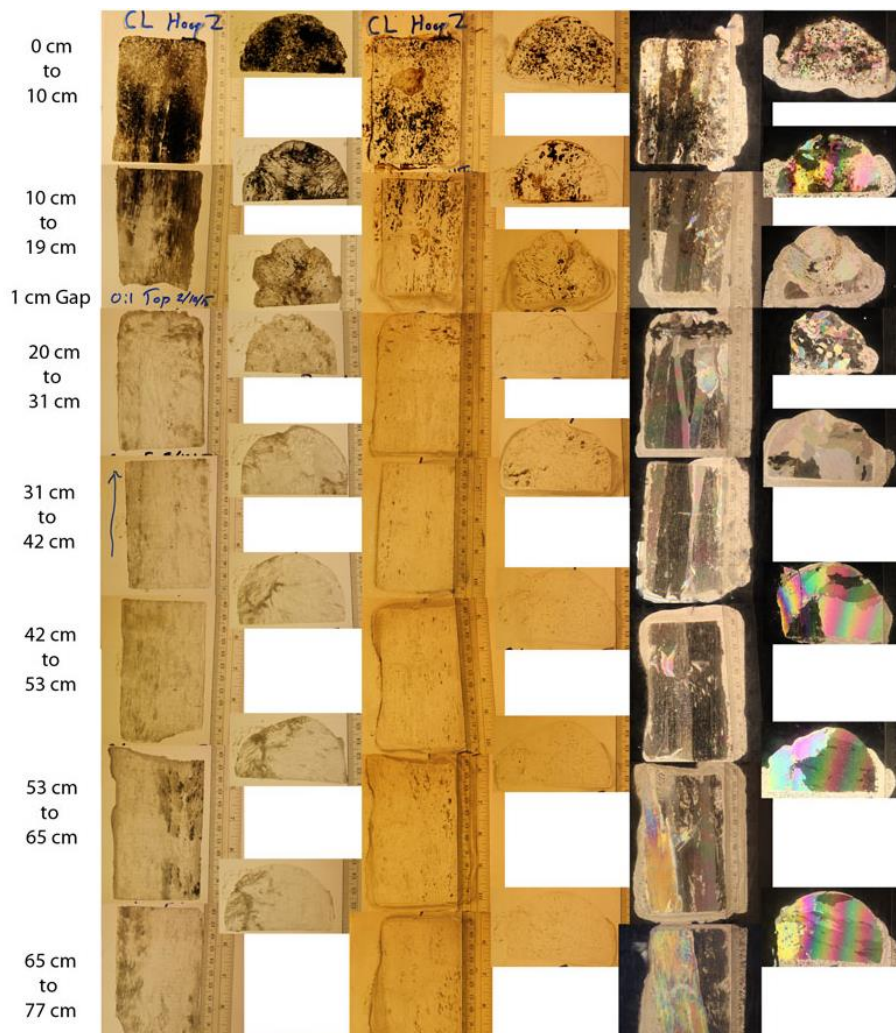


Figure 67. Hoop 2 thin and thick sections showing location of oil and crystal structure.

Hoop 4

The structure of two cores drilled in Hoop 4 is shown in Figures 68 and 69. The first core was drilled in an area of melt water that formed and ponded on the surface in an area exposed to the false sun approximately 4 hours per day during the course of the melt period of the experiment. The second core was taken from an area inside Hoop 4 that was dry in and away from the melt pond area inside the hoop. Observationally, it appears as though there is slightly more oil intrusion into the ice above the oil gap in the area of ice that had been exposed under the heat lamp (in the melt pond) then from the ice core taken from the unexposed area of the sheet (in the dry area). The heat from false sunlight may have caused the brine channels to open. In both cores from Hoop 4, we saw the same patterns: granular transitioning to columnar at the ice surface and granular transitioning to columnar ice just under the oil gap.

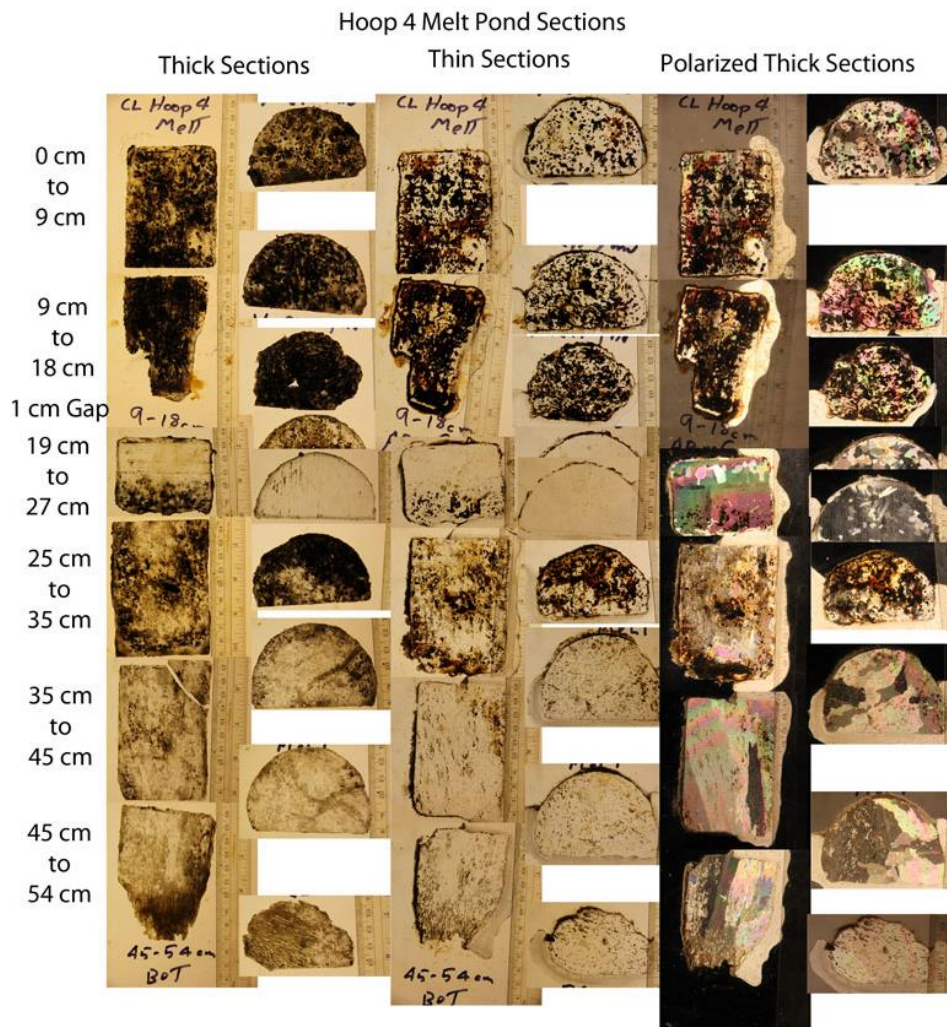


Figure 68. Thin and thick sections of a core from Hoop 4 taken in area of melt within hoop.

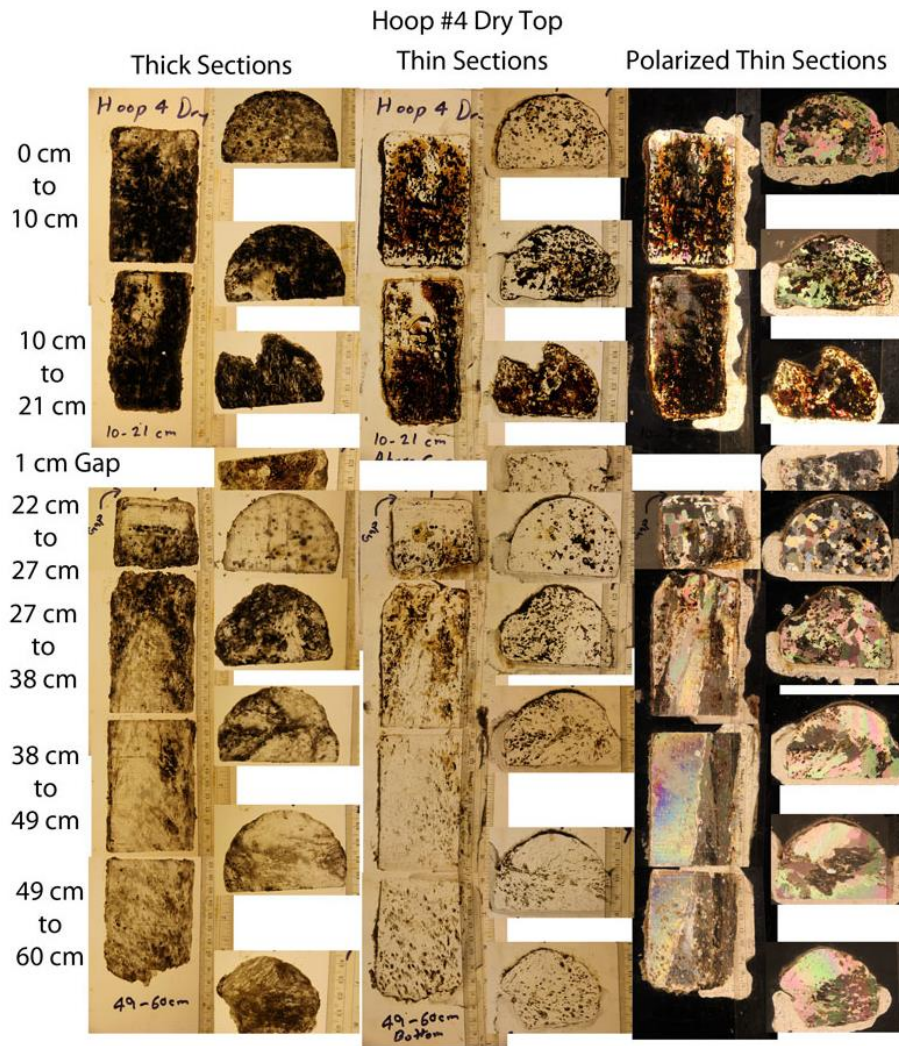


Figure 69. Thin and thick sections of a core taken from dry area of Hoop 4.

Hoop 6

In Hoop 6, the oil was injected underneath the ice at the end of the cooling period, so no ice formed under the oil, thus no oil gap was formed. Oil infiltrated the entirety of the core (Figure 70). The thin section crystals show the granular crystals at the surface of the ice sheet, transitioning to columnar crystals in the first few centimeters of the surface and remaining columnar to the bottom of the ice core (Figure 71).



Figure 70. Core from Hoop 6 taken at end of experiment.

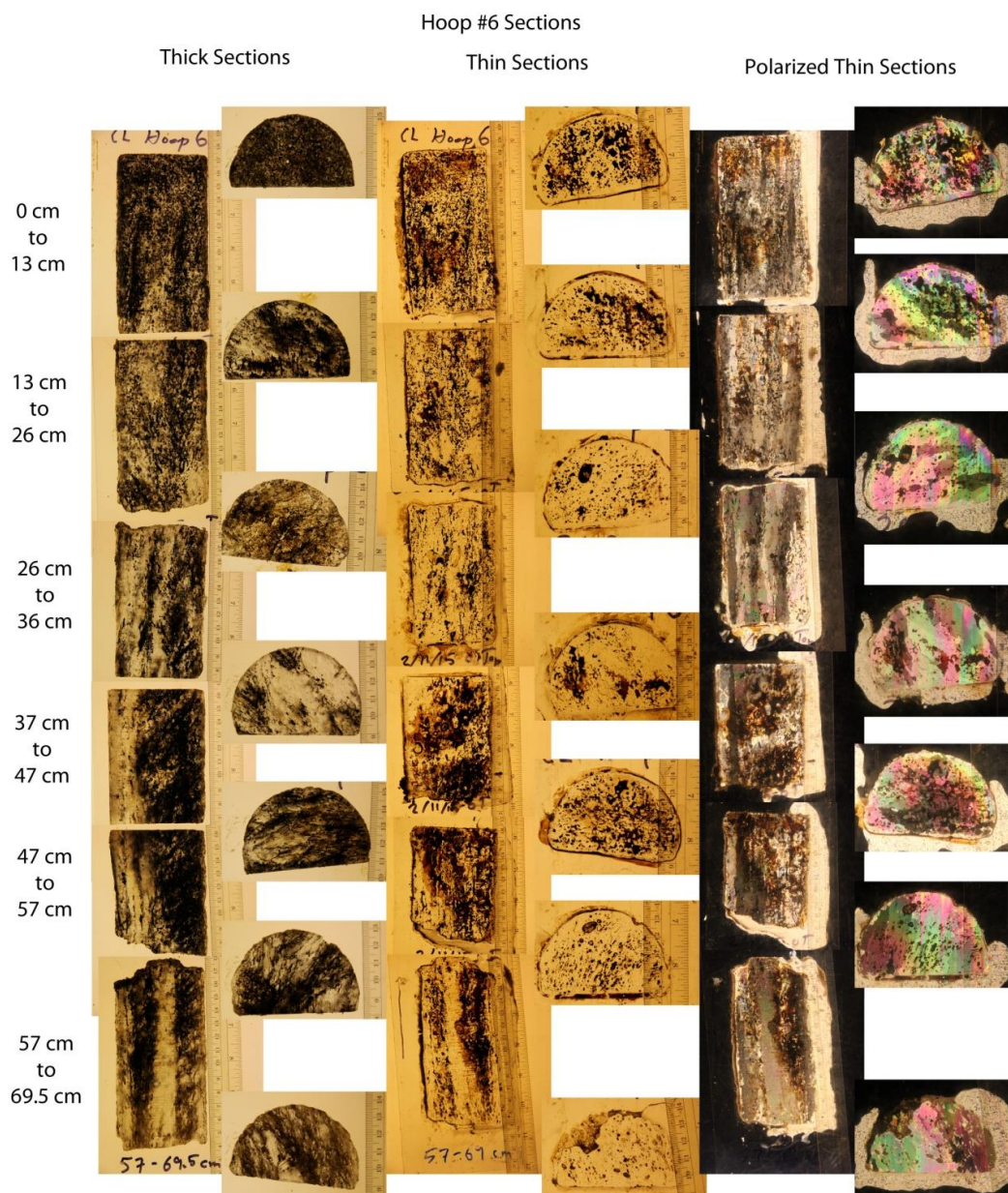


Figure 71. Hoop 6 thin and thick sections showing location of oil and crystal structure.

4.1.2.5 Spatial Variability Within Hoops from Ice Slabs

Ice slabs were taken from each of the hoops at the end of the experiment in order to investigate oil distribution in the ice. Figure 72 is of a slab drilled in the growth phase of the experiment from Hoop 3A showing the oil migration up through the brine channels. The brine drainage channels act as an avenue for the oil migration. Because oil is more buoyant than the seawater in the brine channels, the oil infiltrates up into the sea ice. The brine drainage systems naturally are larger with depth in the ice sheet. The oil migrates up through the ice to where the channels are narrower and also the ice is colder but will not necessarily come to the surface at the terminus of every brine drainage tube. Due to the spatial variability in the drainage systems, and the tendency for

some brine drainage channels to close off as they approach the surface, it is difficult to determine where oil has concentrated when looking down from the surface. As is shown in Figure 72, not all oil present in the brine channels migrates to the surface and/or has any surface expression.



Figure 72. Example of a slab taken from the Hoop 3A January 12th, 2015 looking at the vertical face of the slab – top is up in the photo

Figure 73 shows the variability in the bottom surface of the ice slab from Hoop 3A in Figure 72. Note the brine drainage systems exiting the ice sheet at the bottom surface (at top of image) have high spatial variability. There is not uniform uptake of the oil up into the ice cover. Figure 74 is a close-up view of the oil-infiltrated brine channel system shown in the above photo. This picture demonstrates how the oil infiltrates the ice sheet until the brine channel closes off as the channel approaches the surface. The samples taken here resemble natural samples collected during the 1974/75 winter on the Canadian Arctic coast, Norcor (1975).



Figure 73. Bottom of the slab from Hoop 3A. Top of the ice is at the bottom of the photo.

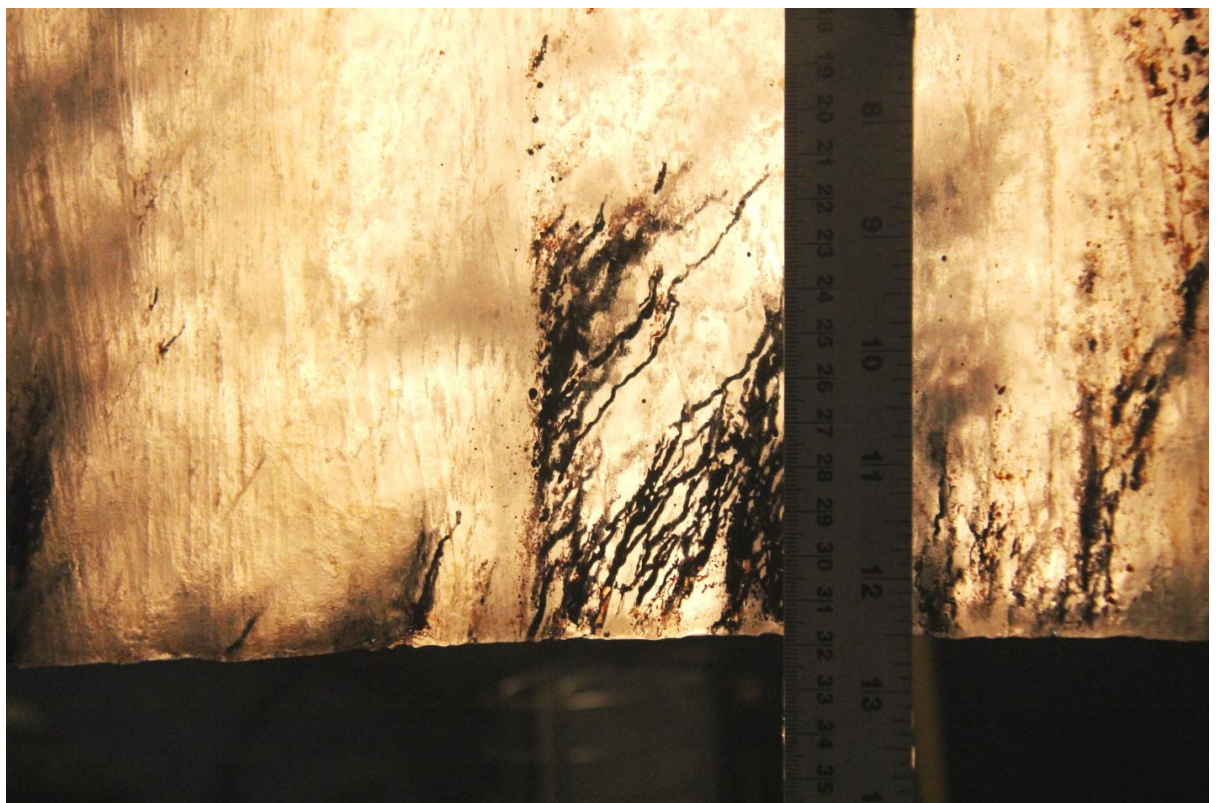


Figure 74. Close-up looking at the side of a slab at the oil-ice interface. Slab is from Hoop 3A, the top of the slab is up in the photo.

Figure 75 shows a slab taken from inside Hoop 1A on January 13th. Average thickness was 72cm with an uneven vertical distribution of vertical infiltration into the ice sample.

Figure 75. Slab from inside Hoop 1A drilled January 13th. Top of ice slab is up. The backlit view (right) shows the brine



channel system, which is angled slightly off from vertical.

At the end of the experiment while removing the slabs from Hoop 4, it was noted that the ice immediately beneath the oil injections was clear and almost bubble free, as shown in Figure 76. This layer was a few cm thick (usually thicker than the oil injection). The artificial sun had been turned on for several hours each day over this hoop. We postulate that melt from the surface drained through the ice/oil and was trapped beneath the oil lens above the next section of sea ice below the oil. The fresh water caused by the melt then refroze to the ice, thus creating the thin fresh lens of ice beneath the oil.



Figure 76. Images of the ice immediately below the oil lens from Hoop 4. Any oil seen in the ice is the result of sampling – as the oil was injected at a level higher than this sample.

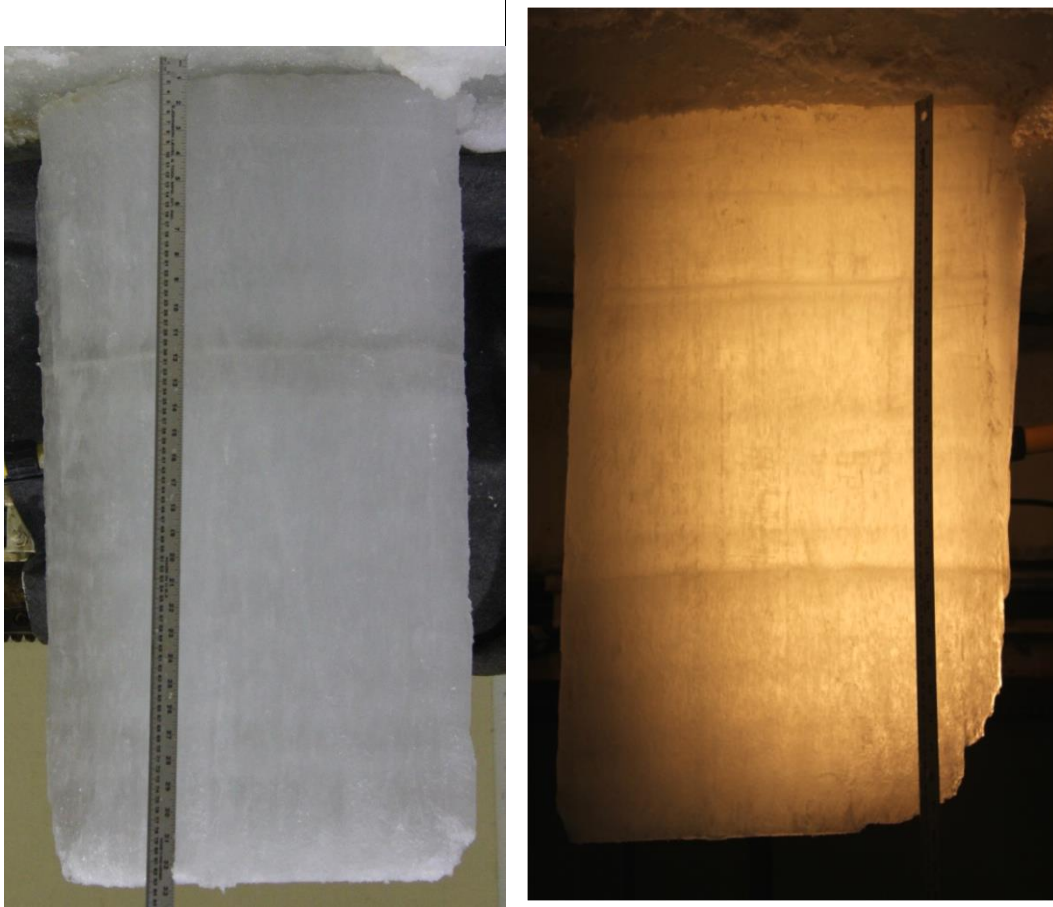


Figure 77. Clean ice slab removed from outside Hoop 4A (left) and 1 (right). Top of ice slab is up

Note that there was very little banding seen in the ice. There were lighter bands seen in the clean ice cores but their depth varied with location in the tank, as shown in Figure 77 with bands at different depths from slabs taken from Hoops 4A and 1.

4.1.2.6 *Micro-CT Data*

Reconstruction of micro-CT data into 3D images of ice core structure is used to measure skeletal layer thickness, structure (lamellae thickness and spacing), brine channel size, and also reveals oil and brine inclusions. Figure 78 shows two examples of micro-CT data displaying several structural characteristics.

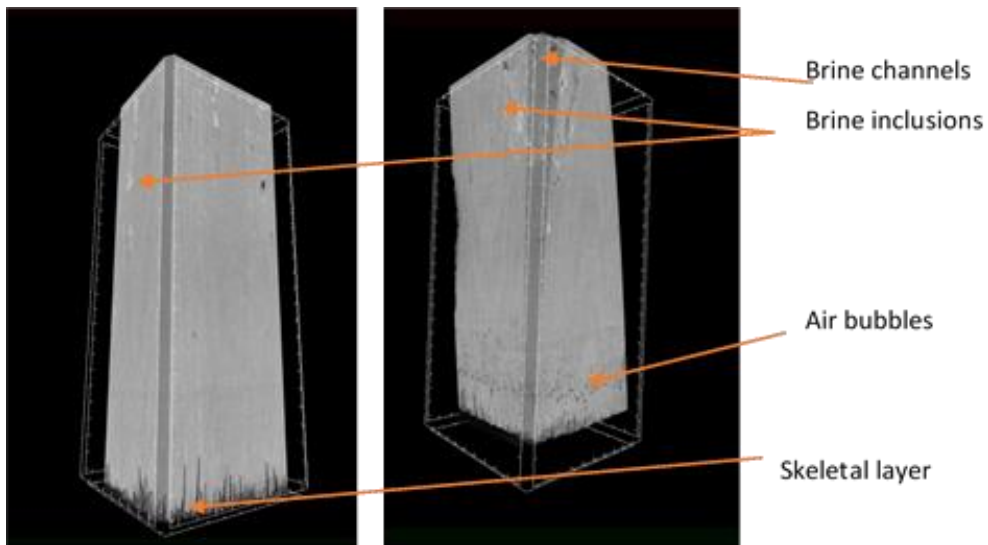


Figure 78. Core from December 3rd (left), and December 9th (right), showing skeletal layer structure.

Spatial variability of skeletal layer and thickness on meter-scale

A series of cores were collected on December 10th centered around the Woods Hole Oceanographic Institute (WHOI) acoustic sensor (see Figure 79 for location of cores). The skeletal layer was scanned to examine variations in skeletal layer thickness, lamellae structure, and lamellae spacing. Figure 80 shows the micro-CT for three of the cores.

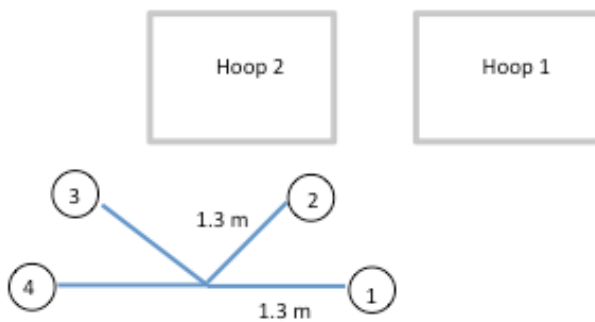
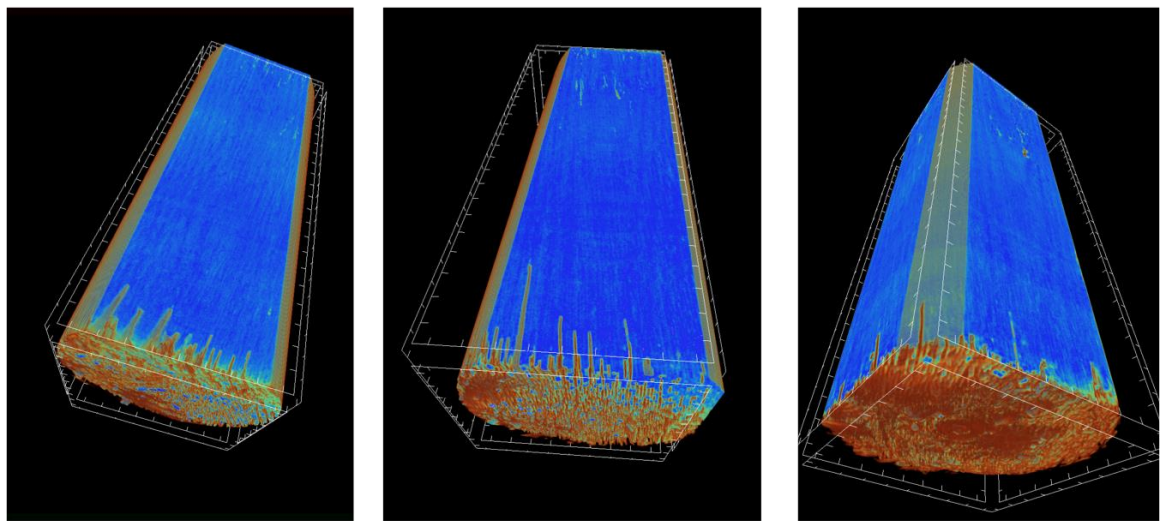


Figure 79. Schematic of core locations taken from 1.3m radii around acoustic sensor. Numbers correspond to core locations.



Core 1

Core 2

Core 3

Figure 80. Variations in skeletal layer on meter-scale from December 9th. Tick marks equal 5 mm in length. Dimensions of core sections shown here are 4 cm in diameter, 11 cm in length.

The variation in skeletal layer thickness between individual cores spaced at 1m+ intervals around the acoustic sensor is nearly equivalent to the variation in thickness that occurs within the 4cm diameter footprint of the core samples.

Skeletal layer thickness varies from 1-2 cm. In Core 1, average thickness is 1 cm. Core 2 has an average thickness of 1.5 cm, and Core 3 has an average thickness <1cm.

Temporal variation in skeletal layer

The thickness of the skeletal layer increased over time, as shown in micro-CT 3D reconstructed images of cores taken at various times throughout the experiment (Figure 81). The November 10th and December 30th cores were taken before the warm-up phase, while the February 2nd and February 10th were after the onset of melt. The evolution of the skeletal layer thickness as measured from micro-CT reconstructed images of the cores is shown in Figure 82. The skeletal layer is the portion of the image where the growing ice lamellae are interspaced with air. The thickness of the lamellae, and the distance between lamellae over time is shown in Figure 83. By February 2nd, the lamellae became more rounded and much thicker (Figure 84).

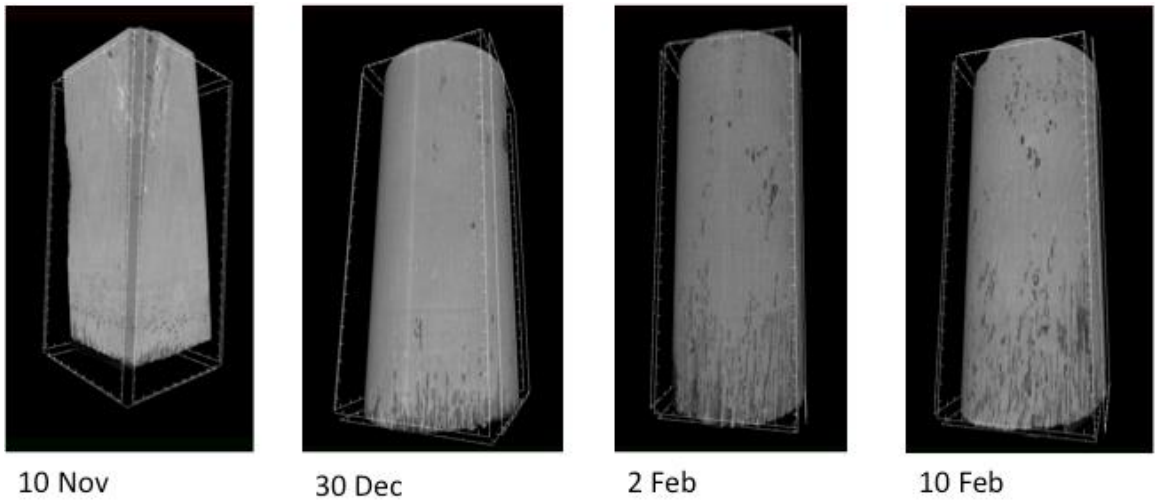


Figure 81. Temporal variation of skeletal layer from micro-CT scans. Tick marks equal 5mm.

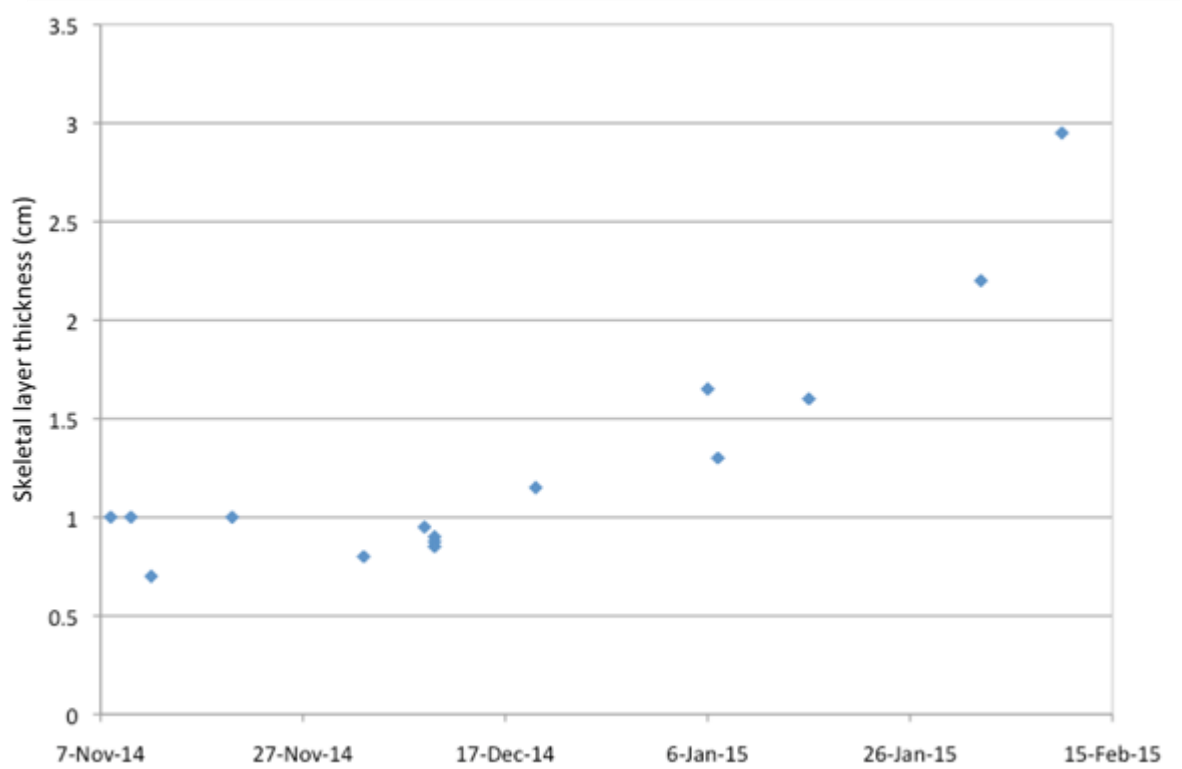


Figure 82. Thickness of skeletal layer (vertical extent) over time, in cm.

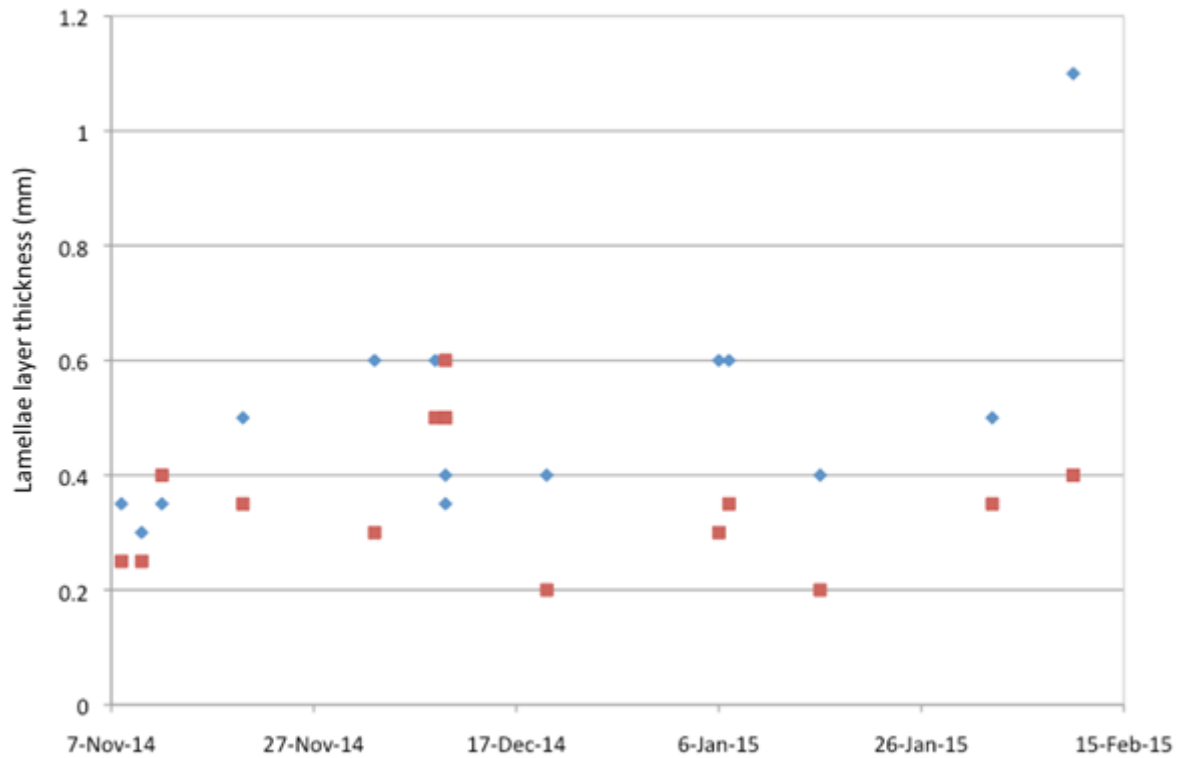


Figure 83. Thickness of lamellae structures (blue diamonds) and the spacing between lamellae (red squares) over time.

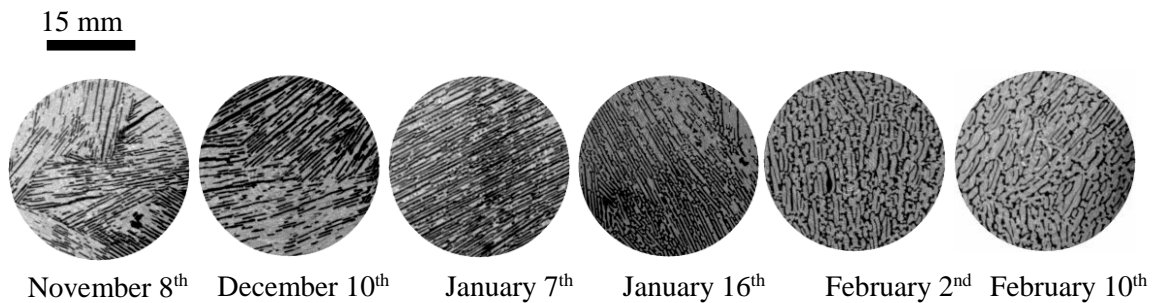


Figure 84. Evolution of skeletal layer structure over the course of the experiment as visualized by micro-C, at 60micron resolution.

4.1.3 Other Ancillary Measurements

4.1.3.1 Sound Speed

The sound speed of oil is used to interpret the acoustic return to aid in the determination of the thickness of oil layers. The sound speed changed linearly over the temperature range tested, and decreased with decreasing oil temperature (Figure 85). The sound speed in oil is similar to the sound speed of seawater at 0 °C.

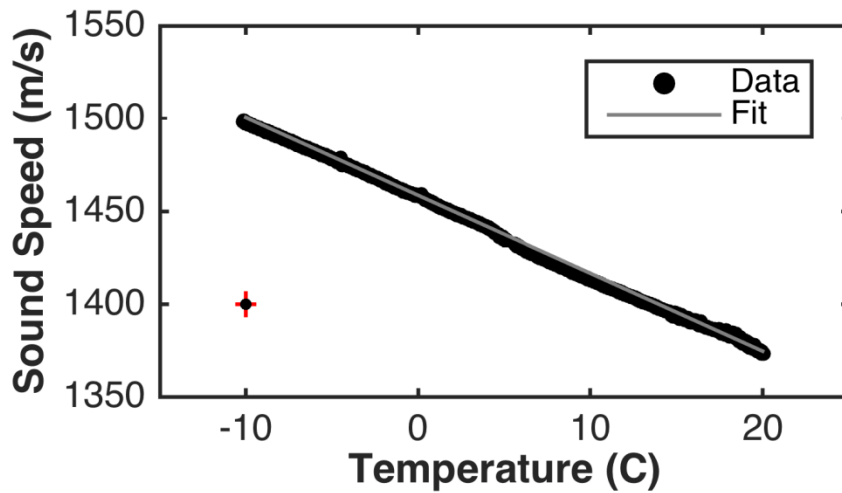


Figure 85. Sound speed of oil from -10 to 20 C.

4.1.3.2 Resistivity Array

Due to many sources of noise within the resistivity data, a custom workflow was developed in MATLAB to identify and remove each component of noise. The simplest filtering algorithm only allowed measured apparent resistivities with the range of: $0.01 \Omega m < \rho_a < 700 \Omega m$. For a given quadripole, 4-16 measurements were acquired depending on the variability of the values measured. From these multiple measurements, the filter also removed any data with a standard deviation greater than 5%.

The electrodes were made of 316 marine-grade stainless steel wool, which was specifically chosen to resist corrosion from exposure to salt water over extended periods of time; however, some electrodes showed visible evidence of corrosion within a few weeks after the survey was installed. These corroded electrodes significantly increased the contact resistance between the electrode and the sea ice/water, which resulted in artificially elevated resistivity measurements. A second filter was designed to remove this type of noise. This filter removed all quadrupoles that contained at least one electrode below the sea ice where $\rho_a > 100 \Omega m$.

Different geometric factors were much more sensitive to noise than others. Noise within the measurements from these quadrupoles was amplified enough, due to abnormally large geometric factors, that Res2dinv would yield negative resistivity values within the inversion process. A filter was developed to calculate the geometric factor for both surface and borehole electrodes. For surface only electrode configuration the geometric factor is:

$$k = \frac{1}{\frac{1}{dx_{AM}} - \frac{1}{dx_{BM}} - \frac{1}{dx_{AN}} + \frac{1}{dx_{BN}}}$$

$$dx_{AM} = x_A - x_M$$

Whereas the geometric factor for both surface and borehole electrodes is given by:

$$k = \frac{1}{\frac{1}{r_{AM}} - \frac{1}{r_{BM}} - \frac{1}{r_{AN}} + \frac{1}{r_{BN}} + \frac{1}{r'_{AM}} - \frac{1}{r'_{BM}} - \frac{1}{r'_{AN}} + \frac{1}{r'_{BN}}}$$

$$r_{AM} = \sqrt{dx_{AM}^2 + dz_{AM}^2}$$

$$r'_{AM} = \sqrt{dx_{AM}^2 + Dz_{AM}^2}$$

$$Dz_{AM} = z_A + z_M$$

Once the geometric factor for each quadripole was determined, the filter removed geometric factors greater than 25.

The electrode combination for each dataset was acquired for 3D processing/analysis, however, anisotropy in the data produced significant artifacts using the standard 3D isotropic inversion software. A simpler approach was taken by separating the data into four 2D profiles along each line. Each line of data was separated from the 3D dataset and processed as a 2D profile.

Once the data were filtered and separated, the data were processed using the Res2dinv inversion commercial software package. Due to the presence of a spatially sharp resistivity contrast present at the boundary between sea ice and seawater, the inversions were allowed to have a discontinuity across this boundary. For each dataset acquired on a given date, ice thickness measurements were inferred from the temperature probe data. Additionally, we allowed the inversion to apply a stronger smoother in the lateral direction than the vertical direction since we are primarily interested in obtaining an estimate of the conductivity profile with depth. Finally, we weighted the inversion by the standard deviation in each measurement; noisy measurements have less influence on the inversion result.

Figures 85-90 provide the final results. Figures 85-86 are the maximum and minimum orientations of the Electrical Resistivity Tomography (ERT) results acquired during November 20, 2014. During this time, the sea ice thickness was about 34cm. The orientation with minimum resistivity within the sea ice was parallel to the long axis of the tank, whereas the orientation of the maximum resistivity in the sea ice was perpendicular to the long axis of the tank. Figures 87-88 are the maximum and minimum orientations of the ERT results acquired from December 10, 2014 with a sea ice thickness around 57cm. The orientation with minimum resistivity within the sea ice was 135 degrees CW to the long axis of the tank, whereas the orientation of the maximum resistivity in the sea ice was 45 degree CW to the long axis of the tank. Figures 89-90 are the maximum and minimum orientations of the ERT results acquired on January 15, 2015 when the ice began to warm and at the maximum ice thickness of approximately 80 cm. The orientation with minimum resistivity within the sea ice was perpendicular to the long axis of the tank, whereas the orientation of the maximum resistivity in the sea ice was parallel to the long axis of the tank. This type of distinct electrical anisotropy has been observed in most previous radar trials at CRREL in both the indoor and outdoor test basins. The only exception was the 2003 trial which was conducted with urea ice and no measurements were made to test for anisotropy.

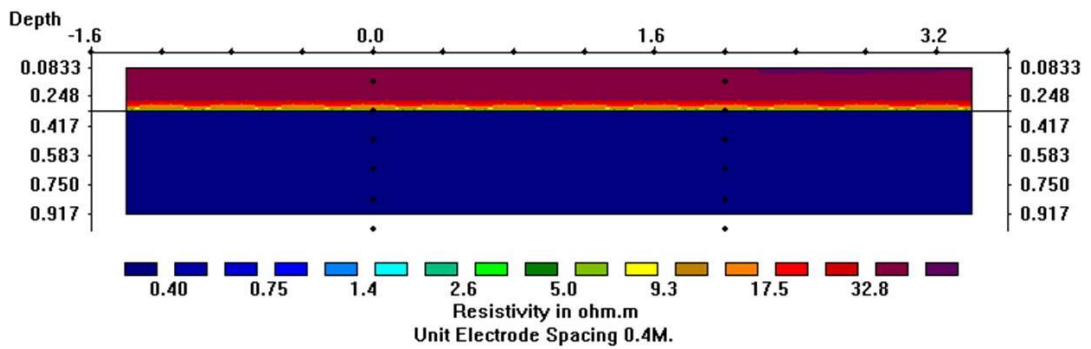
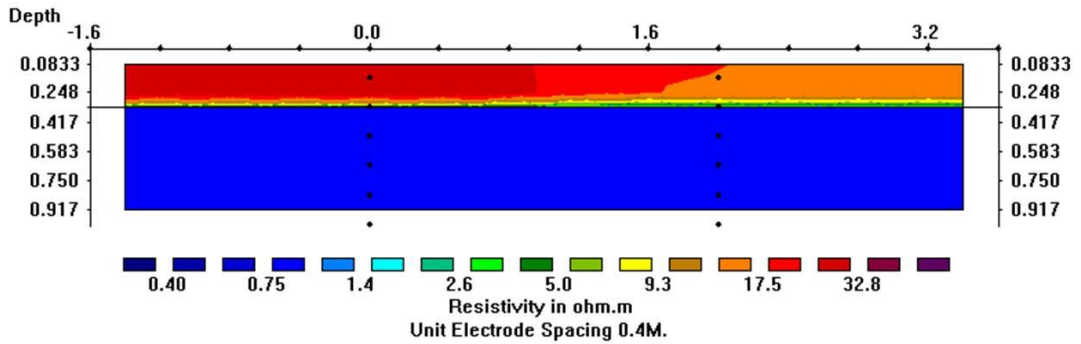


Figure 86. November 20, 2014 minimum (top) and maximum (bottom) resistivity orientation perpendicular to long axis of tank.

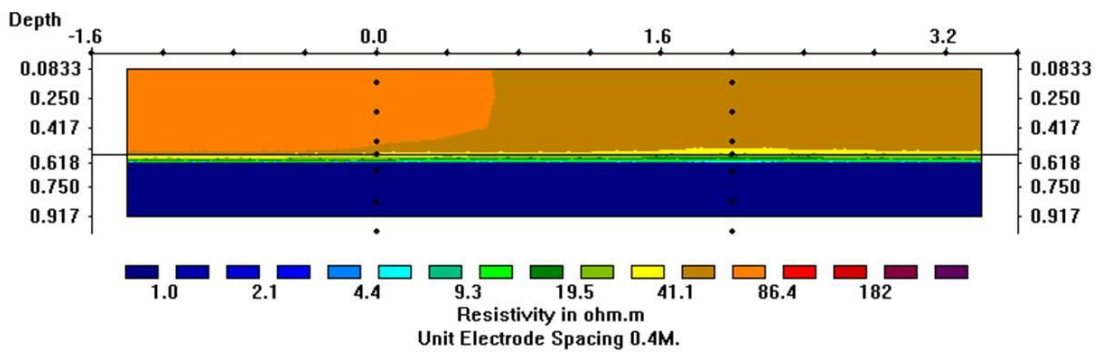


Figure 87. December 10, 2014 minimum resistivity orientation 135 degrees CW to long axis of tank.

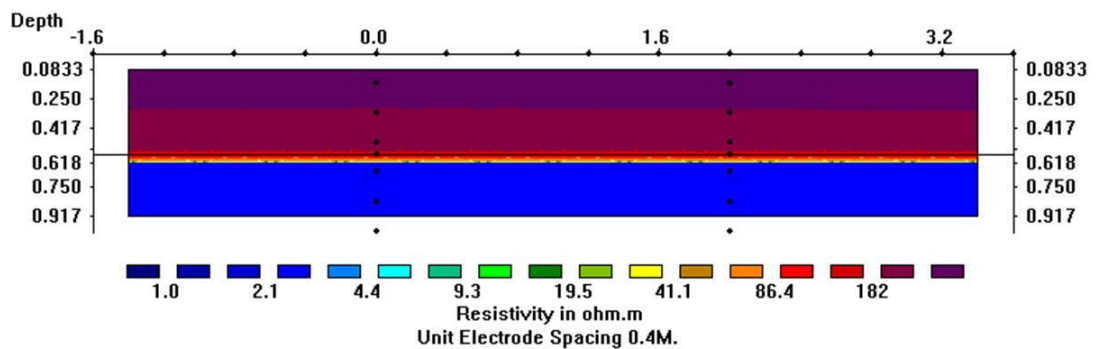


Figure 88. December 10, 2014 maximum resistivity orientation 45 degrees CW to long axis of tank.

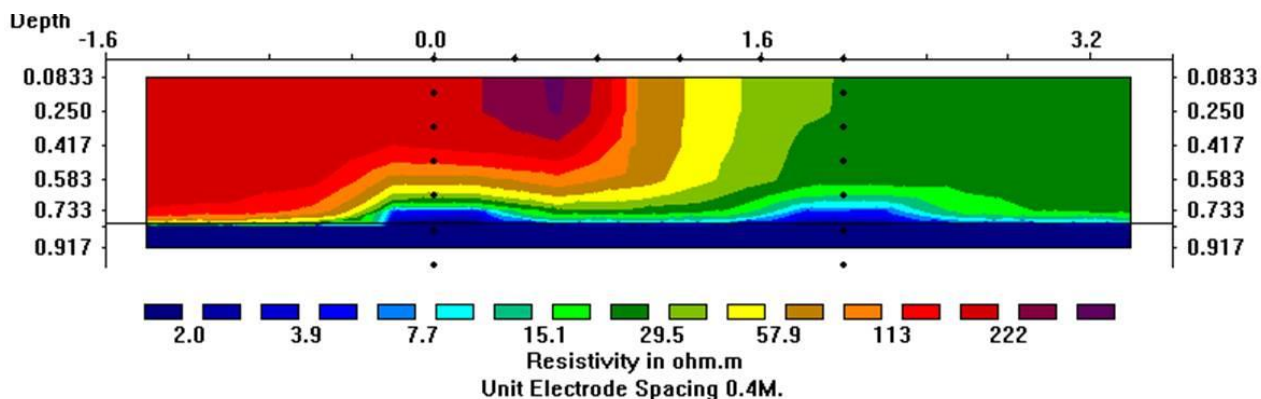


Figure 89. January 15, 2015 minimum resistivity orientation perpendicular to long axis of tank.

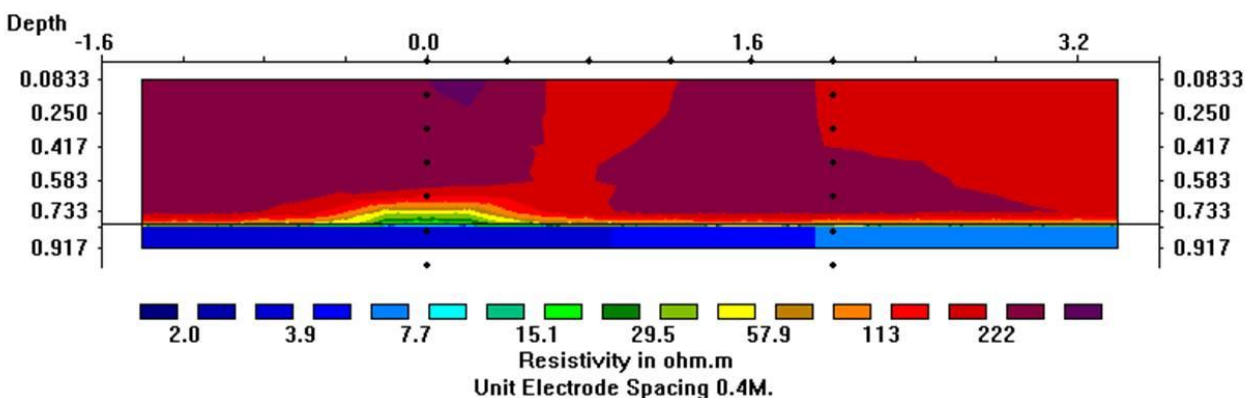


Figure 90. January 15, 2015 maximum resistivity orientation parallel to long axis of tank.

4.1.3.3 GHz 3D GPR Surveys

The 3D radar surveys acquired in the northwest portion of the tank produced excellent images of the ice bottom (Figure 91) and enabled measurement of cm scale variability in ice thickness (Figure 92). In the data acquired on January 10, 2015, when the ice had reached its greatest thickness, two roughly horizontal reflecting horizons are present in the ice that are consistent with ice thickness at the time of Hoop 3 & 4 (~35 cm) and hoop 5 (~60 cm) were injected. Ice cores from near the survey area did not show sheens of oil at these depths, however.

In both the early phase of ice growth on November 18, 2014 and late phase on January 10, 2015, the total variation of ice thickness was 4-5 cm over the 2 m x 3.6 m region of the survey area west of Hoop 6 (Figure 92). However, on January 10, 2015, the variability had increased substantially. The standard deviation from the mean on November 18, 2014 was 0.39 cm while on January 10, 2015 it was 0.62 cm, indicating that roughness had nearly doubled.

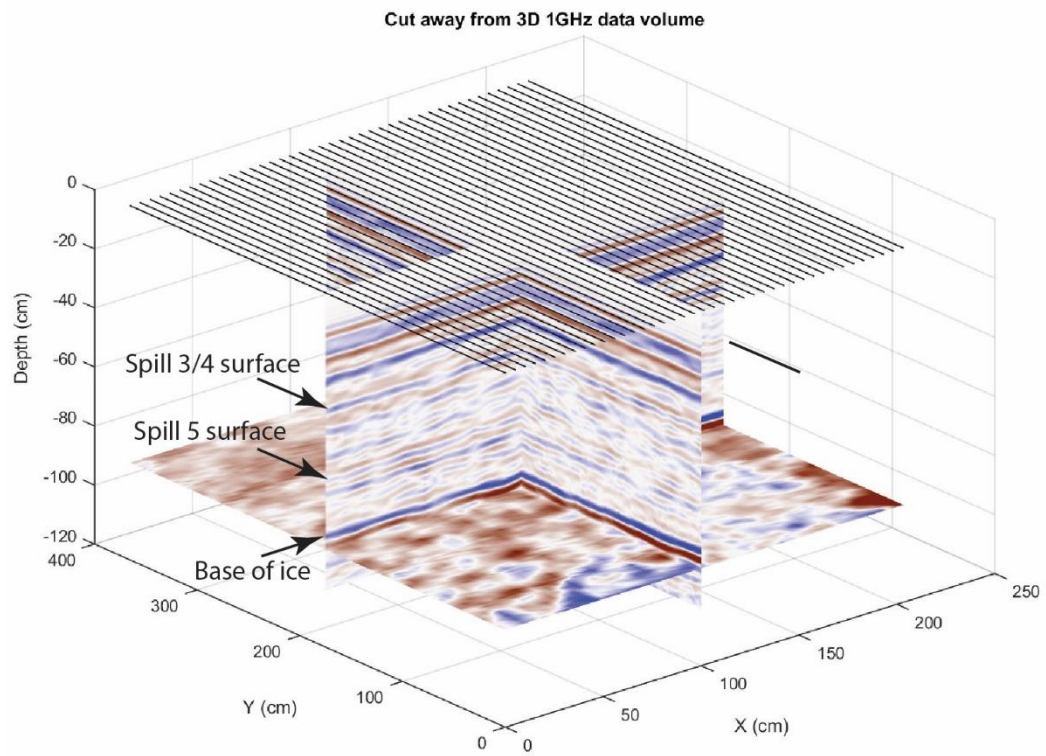


Figure 91. 3D GPR data volume acquired on January 10, 2015. A clear, well-defined reflection from the base-of-ice enables measurement of cm scale variability in ice thickness. Reflecting horizons are present in the ice at the depth of the Hoops 3, 4 and Hoop 5 injections. These may have been caused by a thin sheen of oil that was released during injection.

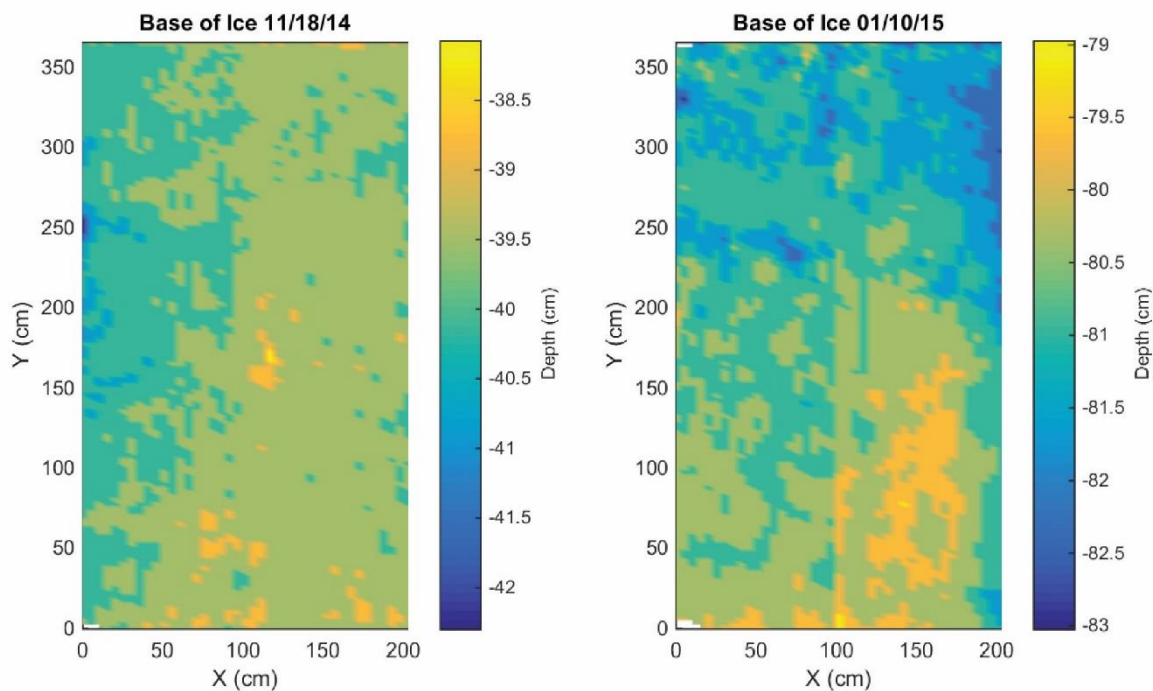


Figure 92. Base-of-ice topography measured using 3D GPR on November 18, 2014 and January 10, 2015, when the ice had roughly doubled in thickness. In both cases, the ice thickness generally thins in the positive y direction (westward). However, the variability had substantially increased in the thicker ice pack on January 10.

4.2 Sensor Results

4.2.1 Cameras

4.2.1.1 *Electro Optical / Visible – Above Ice*

Throughout this document there are pictures from above of oil in the hoops. Time series images from above the hoops show the migration of oil through the ice after injection (Figure 93). Oil can be seen at the surface and a darkening in many areas is evidence of oil within the ice at an unknown depth. When the ice was lit from below, the full extent of the oil distribution could be determined. With the onset of melt, two things are evident, oil begins to migrate vertically, and the surface ice becomes more opaque as it drains (Figure 94). Very small amounts of snow could hide any evidence of oil. In Figure 95, snow from the cooling system covers sections of the oiled hoops.

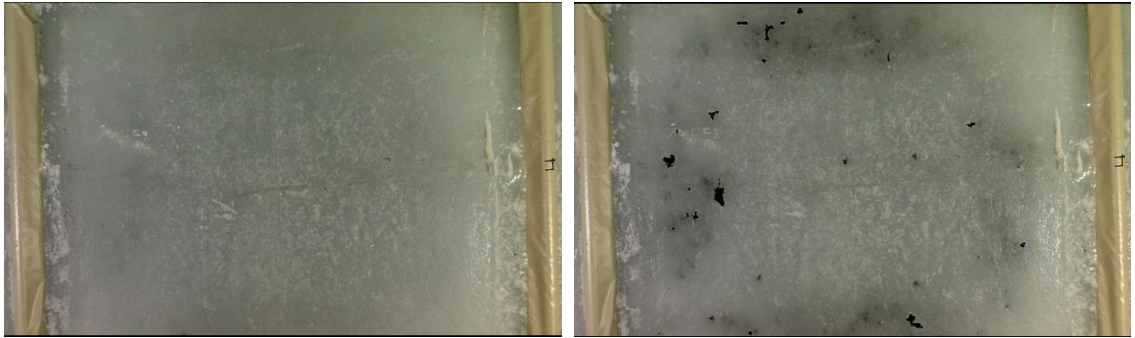


Figure 93. Pictures of Hoop 4 just after (left) and a day after (right) injection of oil.

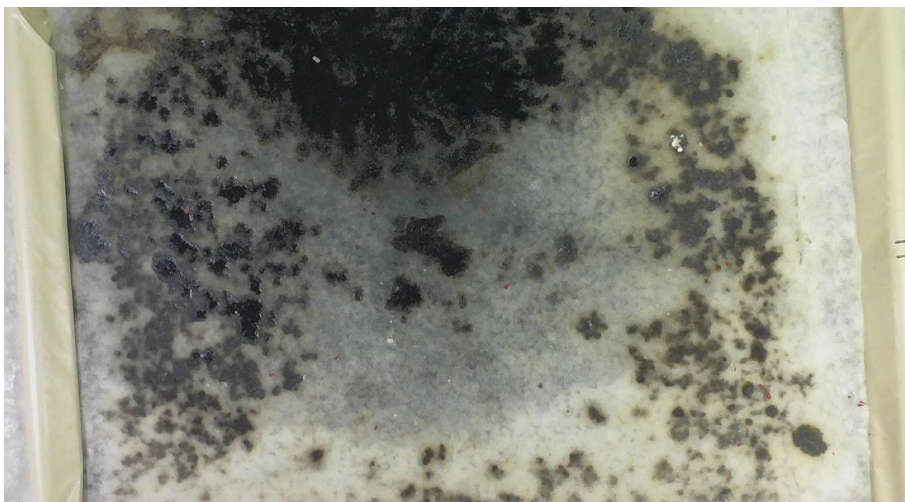


Figure 94. Hoop 4 after the onset of melt.

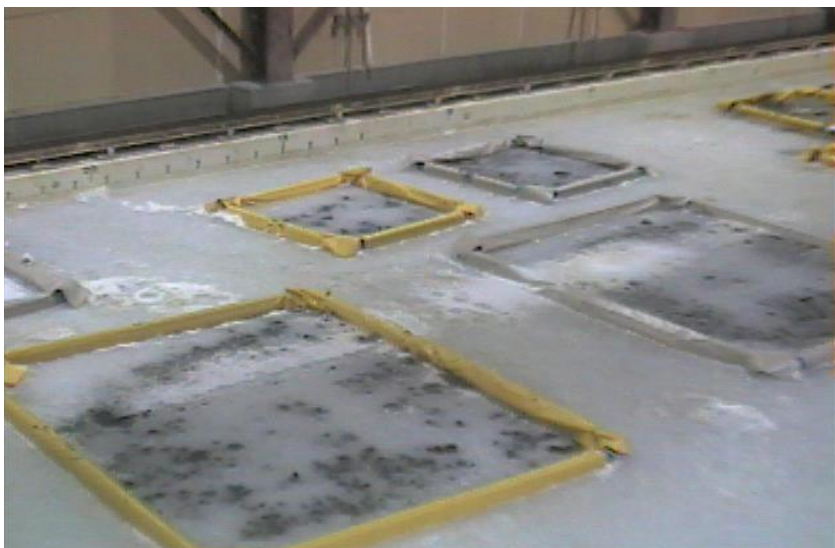


Figure 95. Snow from the cooling system covers sections of Hoops 4 and 5. Hoop 5 is in the bottom left of the frame.

4.2.1.2 Thermal Infrared

The two sets of images below were both taken on January 16, 2015 with an EO (Electro Optical, visible daylight), and LWIR (Long Wave Infrared, thermal) FLIR type camera. In the first two pictures (Figure 96), with the absence of a radiant heat source, the oil appears to be the same temperature as the ice and was undetected by a thermal camera.

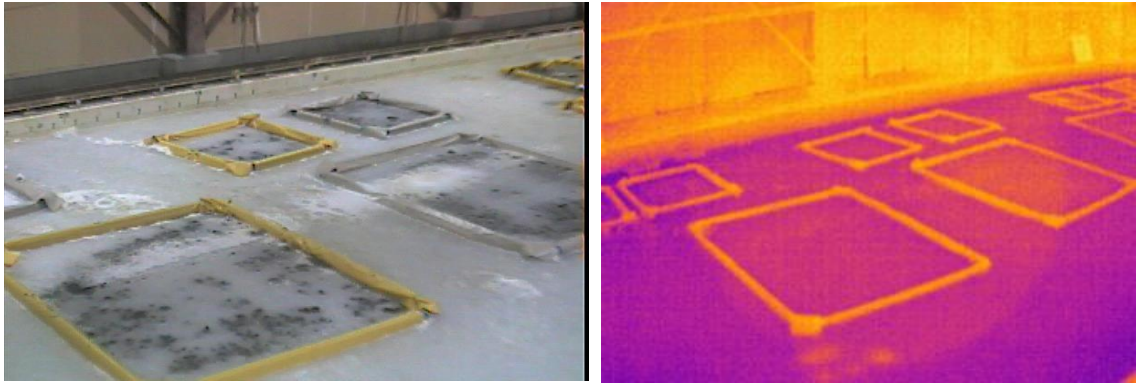


Figure 96. EO and LWIR pictures without the addition of experimental solar heating.

The next two images (Figure 97) indicate the effect of sunlight and demonstrate the LWIR sensor can detect and easily identify the presence of oil with the addition of solar heating. The LWIR image of Figure 97 was captured 8 hours after the radiant heat source (artificial sunlight) was removed.

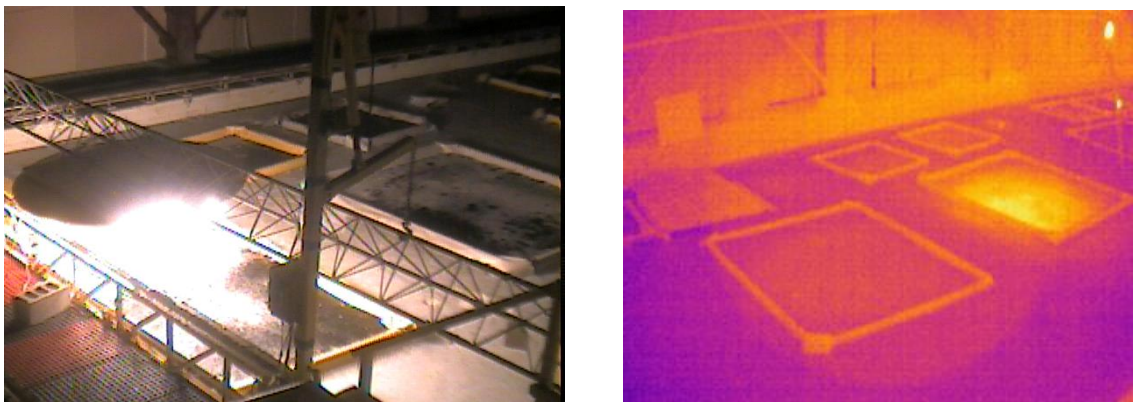


Figure 97. Artificial sun applying solar heat (left); resulting LWIR signature 8 hours after removing solar radiation (right).

4.2.1.3 Electro Optical / Visible – Below Ice

The presence of fresh oil below the ice is evident as black oil on white ice, using light from below or above the ice (Figure 98). As ice encapsulated the oil and continued to grow, it was still possible to see the oiled hoops in the cameras (Figure 99); however, the thicker the ice, the more light scattering below the oil degraded the ability to detect the edges of the oil patch. On January 6, 2015, the ice thickness below the oil in Hoop 5 was approximately 15 cm and below the oil in Hoop 3 it was approximately 40 cm. At that point, the edges of Hoop 5 were distinct, but Hoop 3 appeared as a darker area under the ice (Figure 99). A pile of snow on the ice surface also appeared as a dark area, as seen from below (Figure 100). The auto gain feature of the CRREL camera on the underwater carriage would adjust when under an oil layer in an attempt to lighten the picture. This feature made it more difficult to interpret the presence of encapsulated oil if no clean ice was within the frame.



Figure 98. Oil being injected into Hoop 6. The picture is lit from above by the room lights.



Figure 99. Encapsulated oil in Hoop 5 (top) and Hoop 3 (bottom), as seen on January 6, 2015. Hoop 3 covers the top half of this image.



Figure 100. A pile of snow on the surface of the ice is present in the upper right section of the photograph.

4.2.2 Spectral Albedo and Transmission

Hoop 1 Injection 1

Figure 101 presents transmitted radiance measured at Hoops 1 and 2 on November 7, 2014, illustrating the impact of injected oil on light transmission. Light transmission through the oil-injected Hoop 1 was much less than the oil-free Hoop 2. Light transmission through the ice and oil of Hoop 1 was roughly two and a half orders of magnitude less than the oil free ice at Hoop 2. Light levels at Hoop 1 were near the minimum detection limit of the spectroradiometer. The ice thickness was comparable at these two sites.

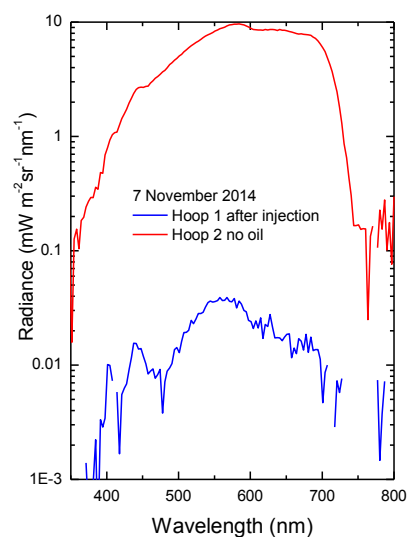


Figure 101. Transmitted radiance on November 7, 2014 showing Hoop 1 after oil injection and Hoop 2 with no oil injected.

Hoop 3

Figure 102 presents spectral albedos and transmitted radiance from the Hoop 3 injection on November 17th. As was the case with the Hoop1 injection, values of transmitted radiance are quite small. Albedo observations show no evidence of the presence of injected oil.

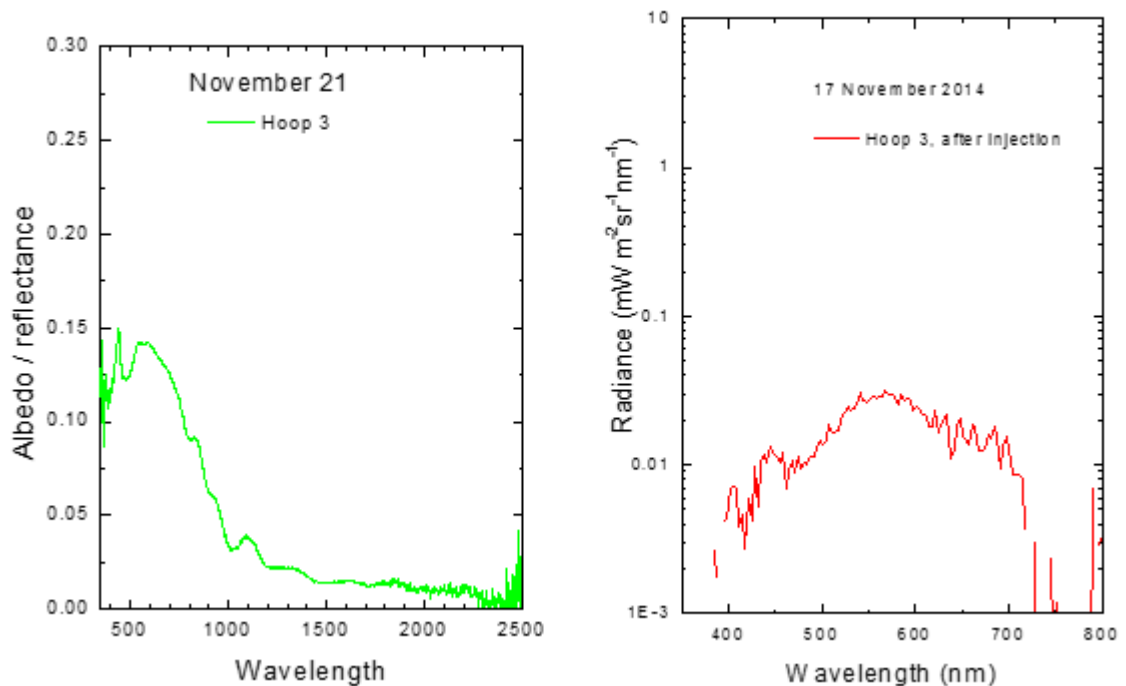


Figure 102. Hoop 3 albedo and transmitted radiance after the November 17th oil injection at Hoop 3.

Hoop 4

On November 20th three injections of oil were made under Hoop 4. Figure 103 presents spectral albedos and transmitted radiances for Hoop 4. Spectral albedos show no influence of the presence of the oil injected under the ice. The spike in albedo at 440 nm is due to a contribution from the LED overhead lights in the Test Basin. This is not surprising, since the water under the ice did not contribute to the albedo either. Transmitted radiances measured before and after the injection show the large impact of oil on light transmission. The presence of oil decreases the transmission by as much as three orders of magnitude.

The impact of oil injections on transmitted radiance is further explored in Figure 103, which presents transmitted radiances through all six hoops on December 1st. The largest values of transmitted radiance were in Hoops 5 and 6, where no oil was injected. Next largest was Hoop 2 which had an oil injection, but where much of the oil had leaked out of the hoop. The smallest transmitted radiances were observed at Hoops 1, 3, and 4, which had full injections of oil. Radiances at these hoops were near the detection limit of the instrument.

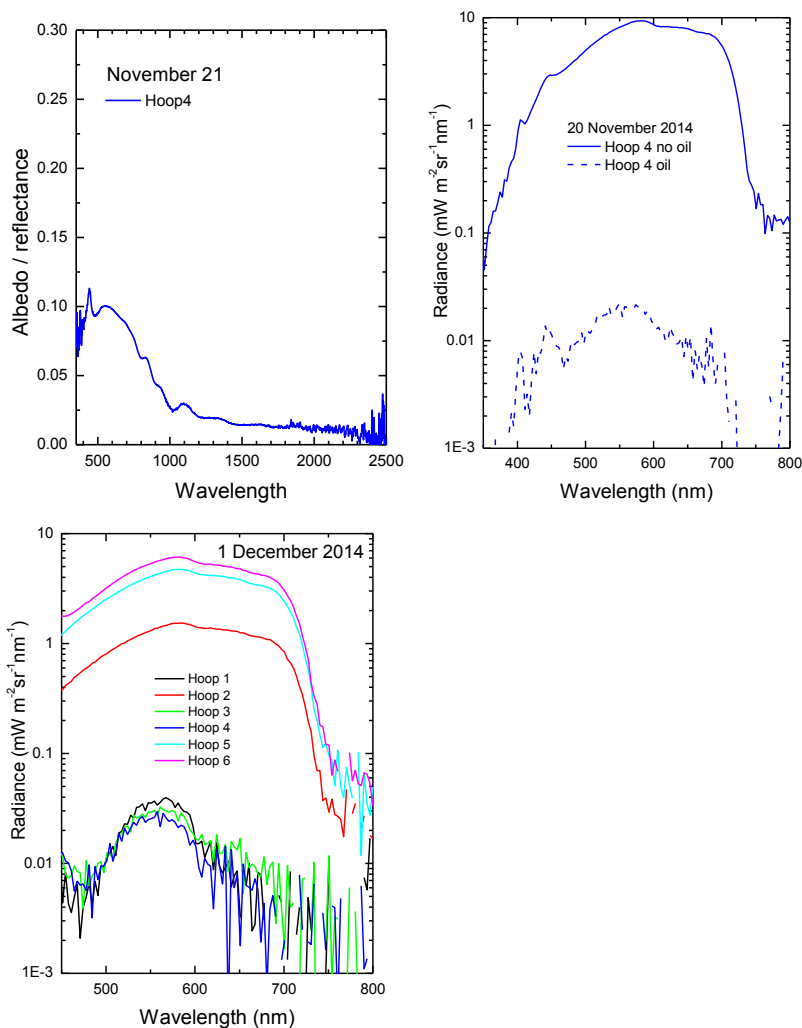


Figure 103. Spectral albedo (left) and transmitted radiance (centre) on November 21st and 22nd for Hoop 4 before and after oil injection. The right panel shows transmitted radiance through all hoops measured on December 1st. The spike in albedo near 440 nm is due to a contribution from the overhead LED lights in the Test Basin.

Hoop 5

An oil injection was made into Hoop 5 on December 9th. The ice was about 0.56 m thick at this time. The left panel of Figure 104 presents albedos measured on December 9th before and after the injection and a third albedo measured on the following day. All three albedos are virtually identical, indicating that the presence of oil at the bottom of the cold 0.56 m thick ice was undetectable in the albedo even a day after the injection.

The transmitted radiances plotted in the right panel of Figure 104. The results reinforce the earlier observation that an oil injection has a major impact on transmitted light causing a decrease of two to three orders of magnitude.

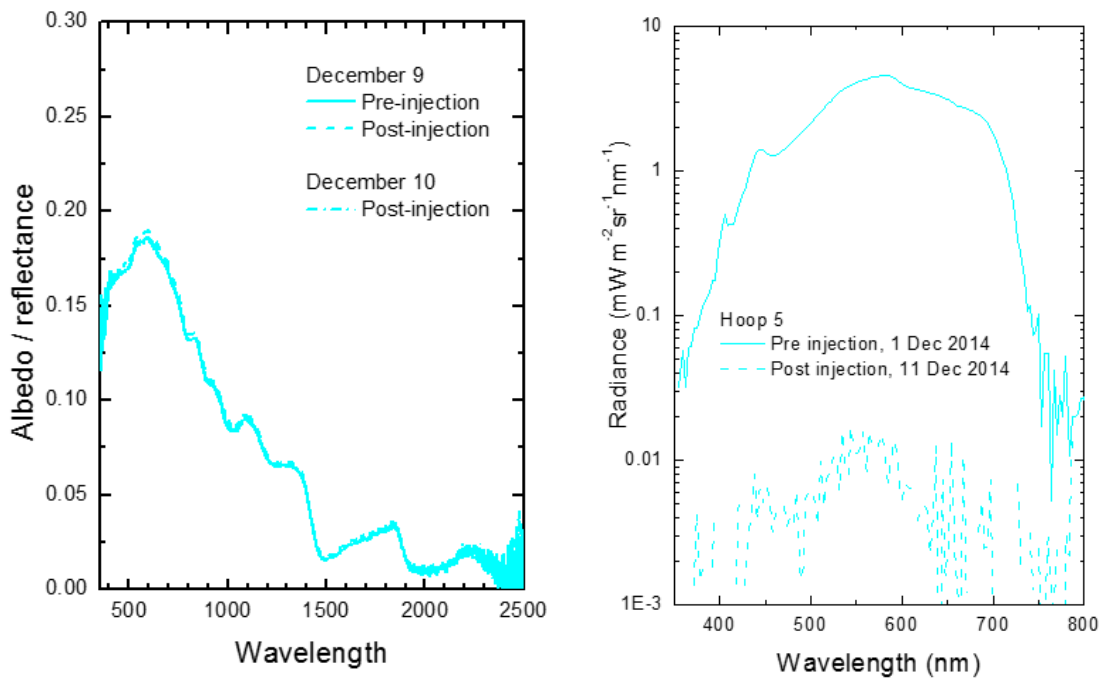


Figure 104. Albedo (left) and transmitted radiance (right) at Hoop 5 prior to the oil injection that occurred on December 9th.

Hoop 6

Oil was injected into Hoop 6 on January 6, 2015, when the ice was about 0.80 m thick. A thicker layer of oil was injected than in the earlier injections. The left panel of Figure 105 presents albedos measured before and directly after the injection. The before and after albedos were virtually identical, indicating that the presence of oil at the bottom of the cold 0.80 m thick ice was undetectable in the albedo. This was consistent with observations from earlier injections at other hoops.

The transmitted radiances plotted in the right panel of Figure 105. Here the impact of the oil layer is even more pronounced than in the earlier injections. The transmitted radiance is at the noise level of the instrument and cannot be reliably detected.

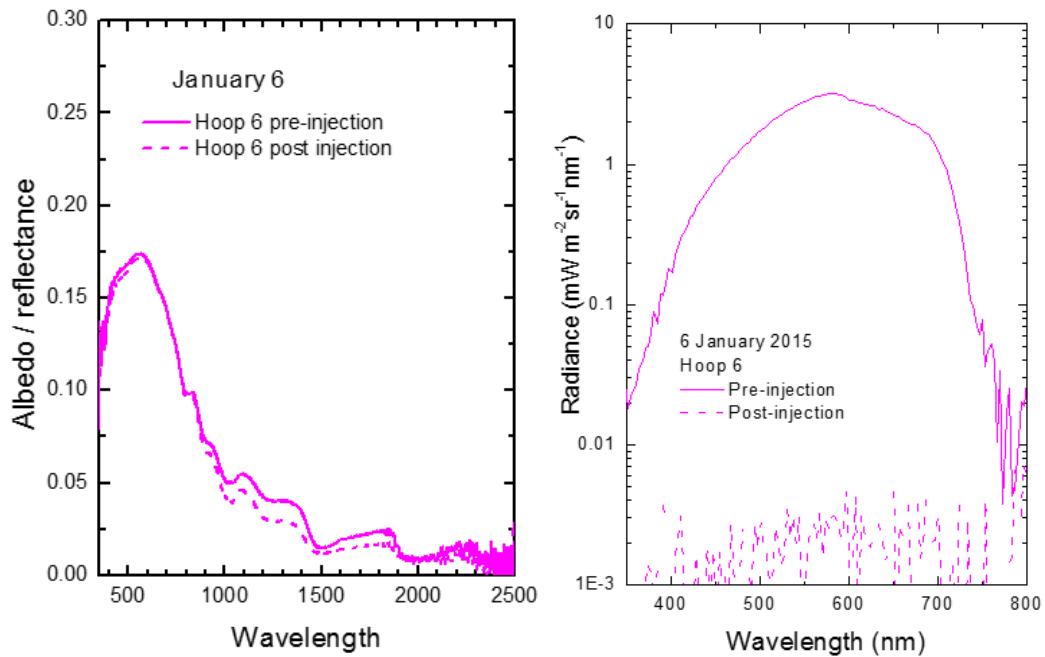


Figure 105. Transmitted radiance through Hoop 6 prior to the oil injection and just after the oil injection on January 6th.

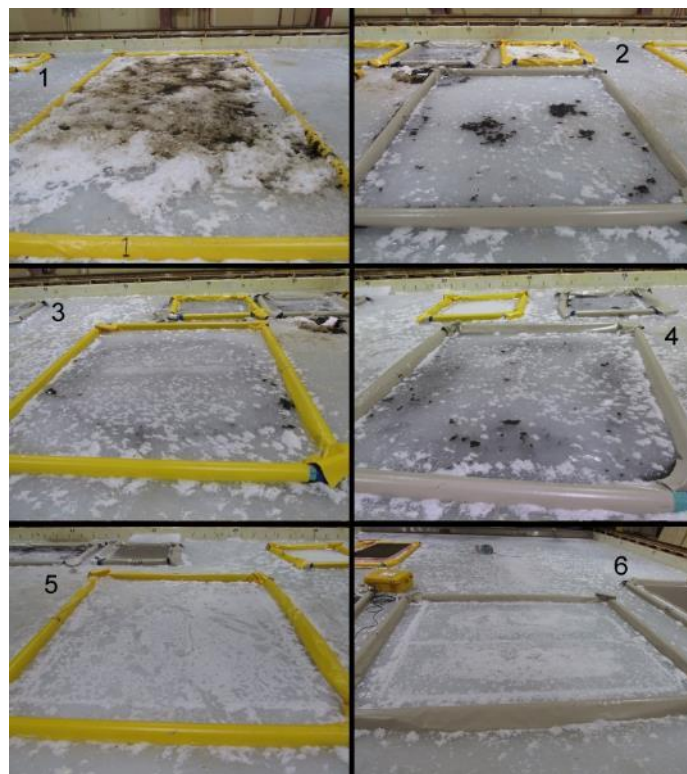
The results from the various hoop injections provide insight on the impact of oil on albedo and transmitted radiance, and on the utility of using albedo and transmitted radiance to detect oil in ice covered waters. Snow also reduces the light transmittance, but field measurements indicate that transmittance through the snow remains orders of magnitude greater than that through oil.

Figure 106 illustrates the impact of oil on spectral albedo and transmitted radiance with results from December 8th. Photographs of the surface of the six hoops are presented along with graphs of spectral albedo and reflectance. Hoop 1 has the darkest, most oil-rich appearance. Oil was injected into Hoop 1 when the ice was thin and broken, so there was a considerable amount of oil on the surface. The presence of this oil is evident in the different shape of the Hoop 1 albedo. There are small amounts of oil visible in Hoops 2, 3, and 4 and Hoops 5 and 6 were still oil-free at the time. Even though the oil had been injected into the hoops a few weeks earlier, the cold ice temperatures limited the percolation of oil upward to the ice surface. Hoops 5 and 6 had the largest albedos, with a typical bare ice spectral shape. Albedos from Hoops 2, 3, and 4 were dominated by bare ice, but showed the influence of small amounts of oil in the reduced magnitude.

The largest transmitted radiance was in Hoop 6, which had not yet had an injection of oil. The second largest was Hoop 2, which had an injection of oil where most of the oil leaked out of the hoop. Transmitted radiances at hoops 1, 3, and 4 were at least two orders of magnitude less than Hoop 6. Even though the oil had been injected up to a month earlier, its impact was still evident in the transmitted radiance.

Figure 107 provides a similar presentation of results for February 9, 2015. This was after all of the oil injections and the ice had warmed to the melting point. The warm, porous ice allowed oil to percolate up through the ice and collect on the surface. Changes in the state of the surface are evident in the photographs. Brown coloured oil covered the entire surface of Hoop 1, while Hoops 4, 5, and 6 were largely black with oil. The spectral albedo also manifested these changes. Hoops 2 and 3 have the largest albedos, as well as the least amount of oil. The black surfaces in hoops 4, 5, and 6 have smaller albedos with a spectral peak in the near infrared. The brown surface in Hoop 1 has a distinctly different spectral shape than all the other albedos. Transmitted

irradiance remained small for all cases except Hoop 2, with values near the noise level. Radiances were larger under Hoop 2, where most of the injected oil leaked out of the hoop.



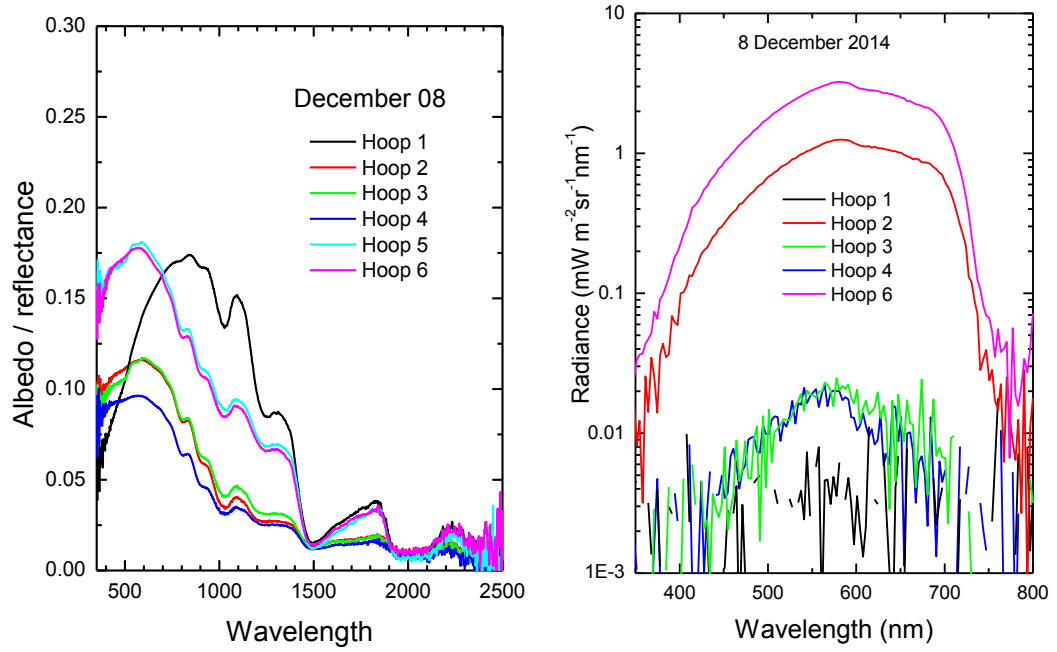
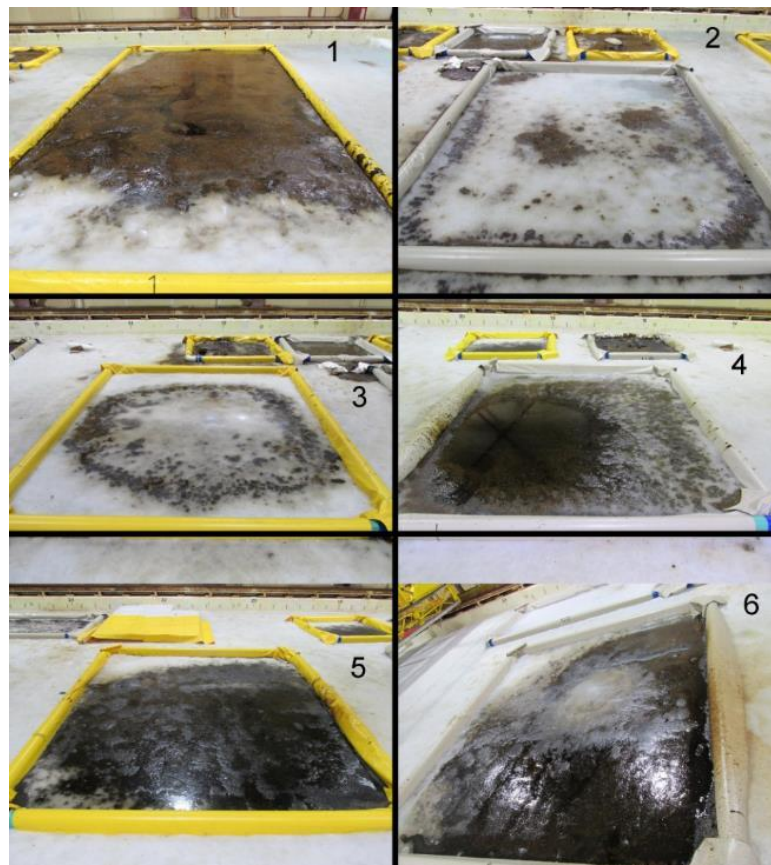


Figure 106. Photographs of the six hoops taken on December 8, 2014. Albedo (left panel) and transmitted radiance (right panel) measured at the six hoops on December 8th.



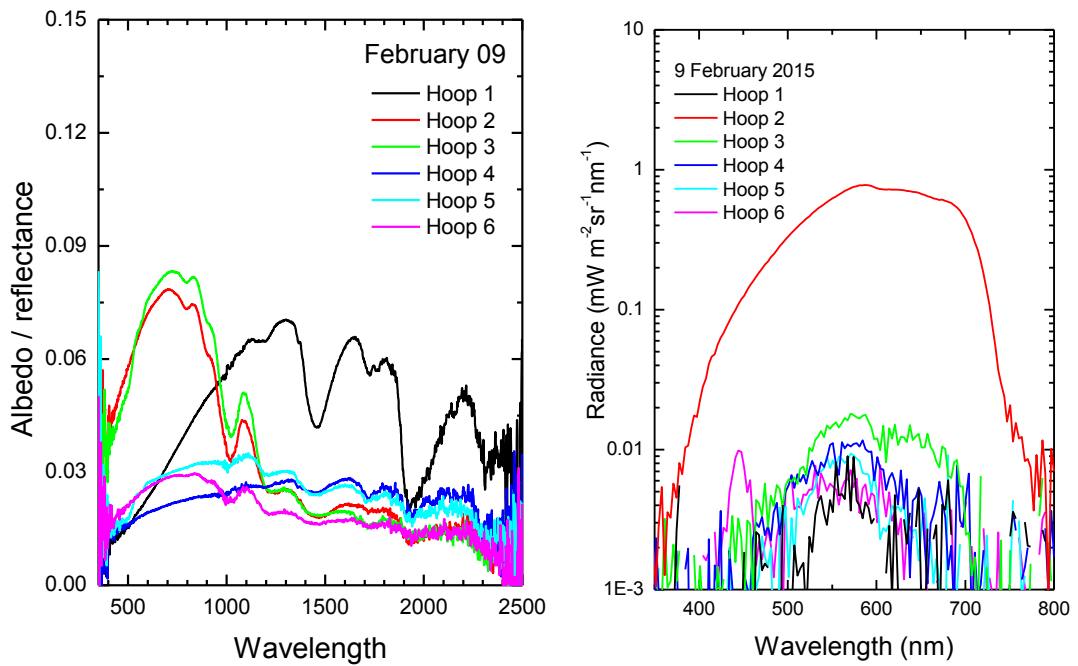


Figure 107. Albedo (left panel) and transmitted radiance (right panel) on February 9, 2015 under all 6 hoops, after the ice warmed.

The differences in spectral shape can be quantified by examining the ratio of albedo at different wavelengths. Figure 108 displays the ratio for the wavelength pair 1300 nm to 700 nm for the six hoops on February 9th. The results indicate the more oil present at the surface, the larger the value of the ratio.

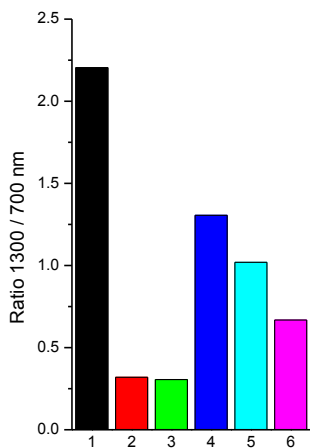


Figure 108. The 1300/700 nm albedo ratio for all six hoops on 9 February 2015.

Figure 109 examines the utility of the 1300/700 albedo ratio for discerning the presence of oil, which presents the time series of the ratio for all six buoys. Values for oil free ice surfaces are typically less than 0.3. Ratios remained less than 0.5 for most of the experiment, with the exception of Hoop 1; however, there was an increase in the ratio at all hoops towards the end of the experiment. This was a direct result of warming the ice, which increased the brine volume and

the ice porosity. The change allowed the oil to percolate up through the ice to the surface, markedly darkening the ice.

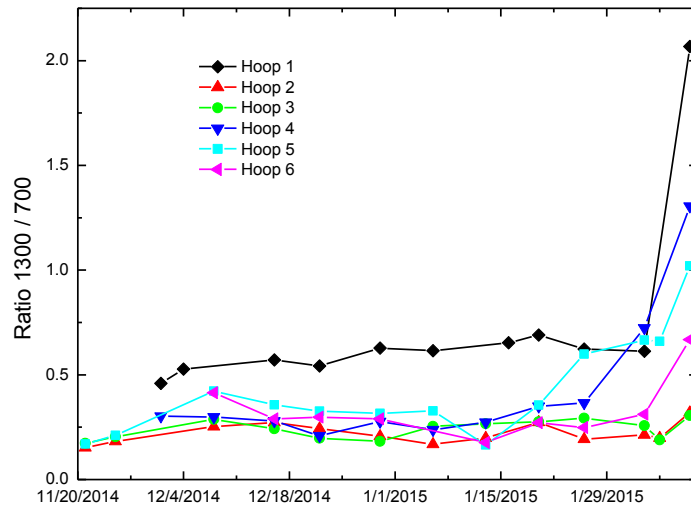


Figure 109. Time series of the ratio of the albedo at 1300 nm and 700 nm for all six hoops.

Figure 110 presents the time series of transmitted radiance in Hoop 4. The graph presents two significant findings: i) the addition of oil reduces transmission by roughly three orders of magnitude compared to the oil-free ice and ii) after the oil injection, the transmitted radiance remains small for the entire experiment. Values of transmitted radiance remained small after the Hoop 4 oil injection as the ice continued to grow, encapsulating the injected oil. Radiances remained small even at the end of the experiment, when the ice warmed and oil percolated to the surface. After an injection, the presence of oil was easily detectable throughout the entire experiment.

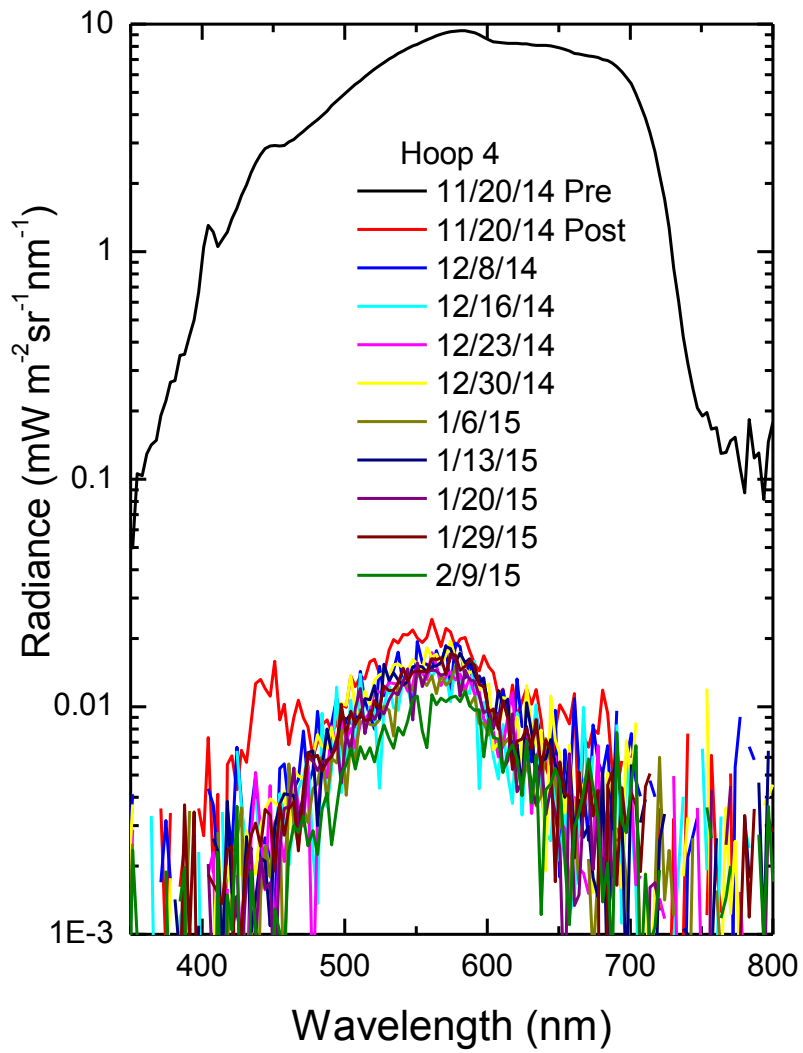


Figure 110. Time series of transmitted spectral radiance at Hoop 4.

4.2.3 Fluorescence Polarization

4.2.3.1 Aerial FP

Figure 111 shows a scan taken with the aerial FP instrument over Hoop 1. Figure 112 shows photographs of Hoop 1 with frazil ice before and after the oil injection. A baseline scan was taken before injection (labeled in blue) in Figure 111. The baseline scan shows that no fluorescence was detected from the ice surface of Hoop 1 prior to injection. After injection of oil under the ice, the oil began to percolate through the frazil ice and into the surface of Hoop 1. A scan of the centerline of Hoop 1 was performed a day after oil injection using the aerial FP instrument. The above-ice carriage traveled from the park position to the end of Hoop 1 at a rate of 1cm/sec. In a significant portion of the scan, the oil fluorescence signal was detected. The fluorescence intensity was very intense and it saturated the photomultiplier tube detectors of the FP instrument, indicated by the flat response on the graph, which is a typical result of the aerial FP instrument in all of the hoops that were scanned with the aerial FP instrument.

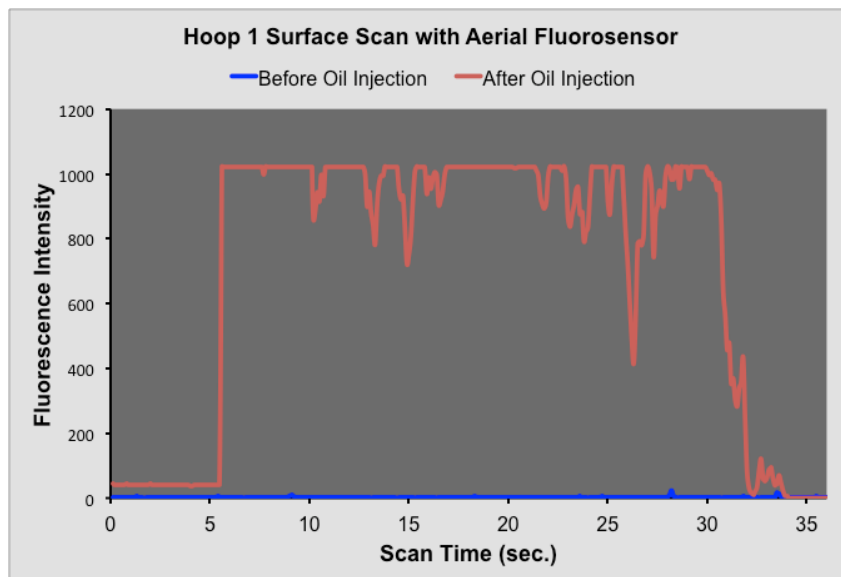


Figure 111. Scan results from the aerial FP instrument over Hoop 1.



Figure 112. Photographs of Hoop 1 with frazil ice before and after the oil injection.

4.2.3.2 Below-Ice Scanning FP

Figures 113-118 present data taken using the scanning FP instrument in all of the 6 hoops. For each scan, the underwater carriage containing the instruments was positioned under the centerline of the hoop being injected with oil. FP scans were taken right after injection and several hours after, when the oil had settled under the ice. Data were collected periodically each day while the ice continued to grow under the oil until the intensity went back down to the baseline. The graphs in Figures 113-118 show the fluorescence intensity scans recorded after oil injection and for subsequent days during ice encapsulation. Prior to oil injection, a scan of the clean ice under the hoop was also taken to establish a baseline measurement. Figures 113-118 also present baseline scans. The scanning FP results show that all hoops display a similar pattern. Freshly injected oil had a very strong fluorescence. The oil fluorescence intensity continued to increase until after the injection stopped and the oil had time to equilibrate in the hoop. As ice encapsulated the oil over several days, the oil fluorescence intensity decreased. The decrease in fluorescence intensity was the result of the ice encapsulating the oil. The ice encapsulation reduced the intensity of the laser beam impinging on the oil underneath. As a result, the oil fluorescence intensity decreased as the thickness of the ice under the oil increased.

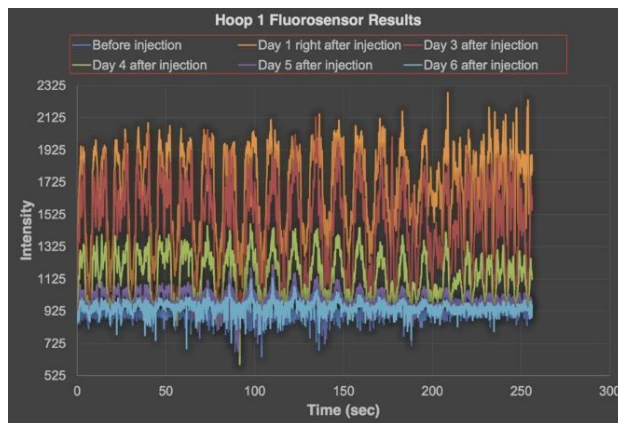


Figure 113. Scanning FP Hoop 1 results.

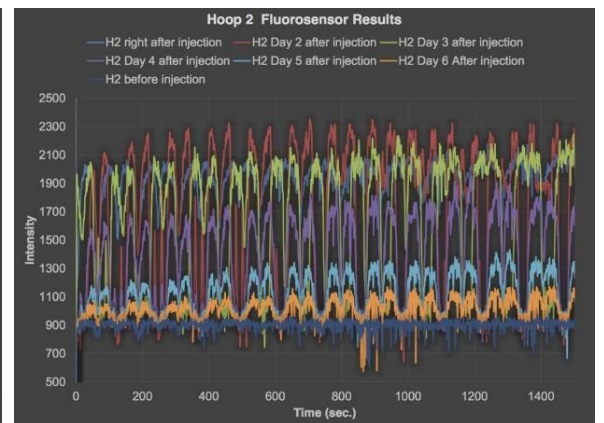


Figure 114. Scanning FP Hoop 2 results.

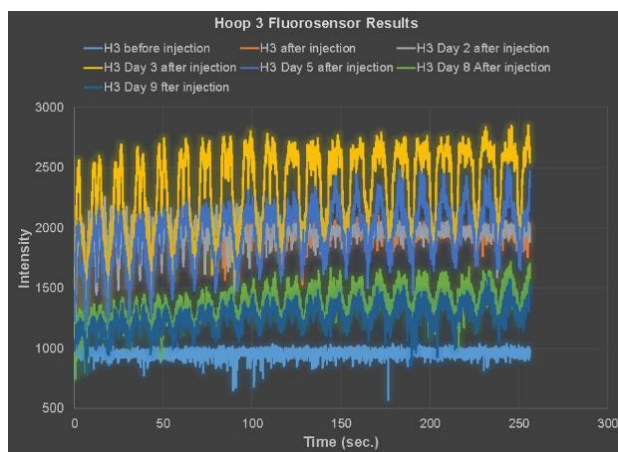


Figure 115. Scanning FP Hoop 3 results.

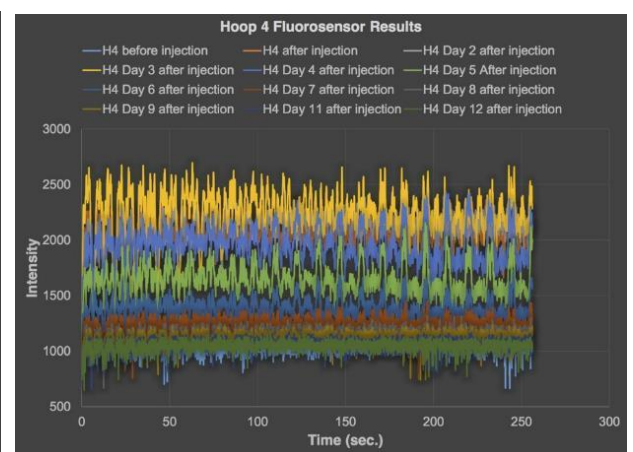


Figure 116. Scanning FP Hoop 4 results.

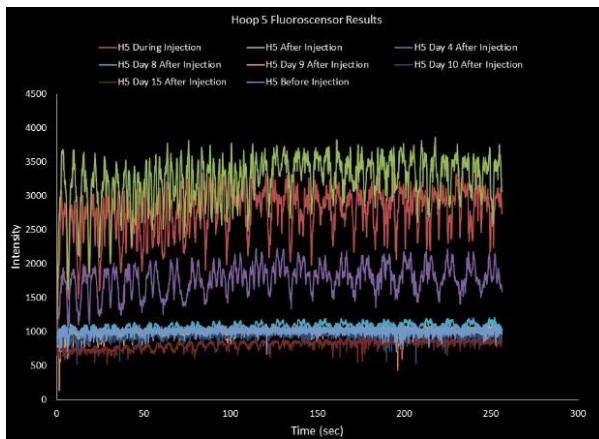


Figure 117. Scanning FP Hoop 5 results

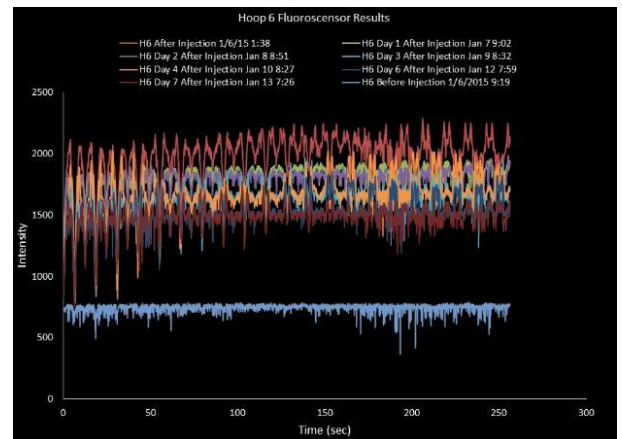


Figure 118. Scanning FP Hoop 6 results.

Figure 119 shows a plot of fluorescence intensity as a function of ice encapsulation thickness for Hoop 4 results. WHOI provided the ice encapsulation thickness data, which was calculated from the sonar instrument in the underwater carriage. For each fluorescence data in Figure 119, the baseline intensity value was subtracted. The graph indicates that as the thickness of the ice increased, the intensity decreased. The decrease in fluorescence intensity was the result of ice that encapsulated the oil scattering the laser beam, which resulted in less excitation energy impinging on the oil. Less fluorescence emission occurred as a result. Also, the fluorescence emitted by the oil was scattered, which further degraded the fluorescence intensity that was collected by the instrument telescope. Figure 119 shows that the scanning FP instrument is capable of detecting oil encapsulated in ice up to 6 cm of ice thickness. Figures 120 illustrate the effect of the laser as it scanned through un-encapsulated oil and through encapsulated oil in Hoop 3. Figure 120 shows the laser beam finely focused in the oil and through the encapsulation ice. The fluorescence intensity of the liquid oil scan was much stronger than when ice is present.

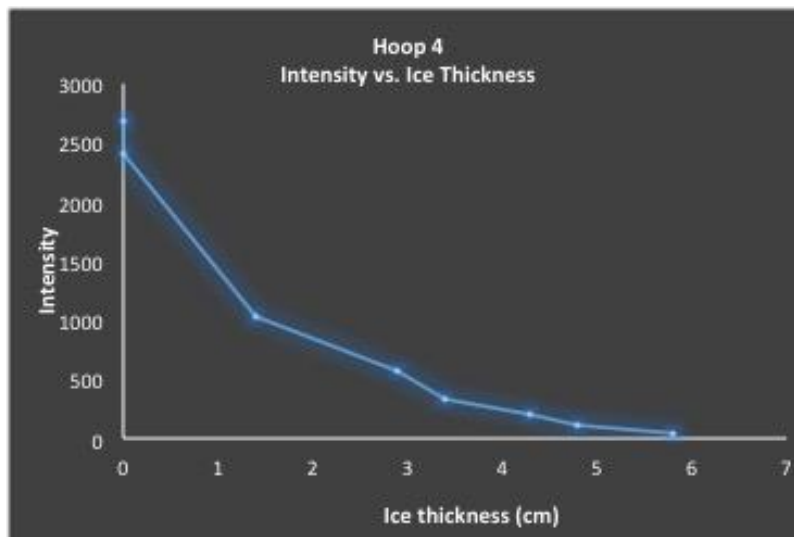


Figure 119. Plot of oil fluorescence intensity as a function of ice encapsulation thickness for Hoop 4 scanning FP data.



Figure 120. Images of laser beam after oil injection in Hoop 3 (left) and after ice encapsulation (right).

4.2.3.3 *Below-Ice Fixed Focus FP*

Figure 121 shows the results for the fixed focus FP instrument, which was mounted in a fixed location under the center of Hoop 4B. The instrument was turned on prior to oil injection and left on to continuously acquire data after the oil was injected and during ice growth under the oil. The result shows that after oil injection there was a spike in the recorded fluorescence intensity. The fluorescence intensity slowly decreased over time at a slow rate and then began to drop at a faster rate. Three days after oil injection, the instrument still showed a response, indicating that the fluorescence from the encapsulated oil was detected. However, after five days, the instrument no longer could detect any fluorescence response from the oil, indicating that the ice encapsulation thickness was too thick for the laser beam to penetrate. Under Hoop 4B, WHOI installed a sonar. Ice encapsulation thickness data from the WHOI sonar was plotted against the fixed focus FP instrument response. Figure 121 shows the result of the plot. The result shows that the oil fluorescence intensity decreased as the encapsulation ice thickness increased, which follows a similar trend as the result of the scanning FP shown in Figure 119. The fixed focus FP instrument proved that it could detect oil encapsulated in ice to thicknesses up to 6 cm.

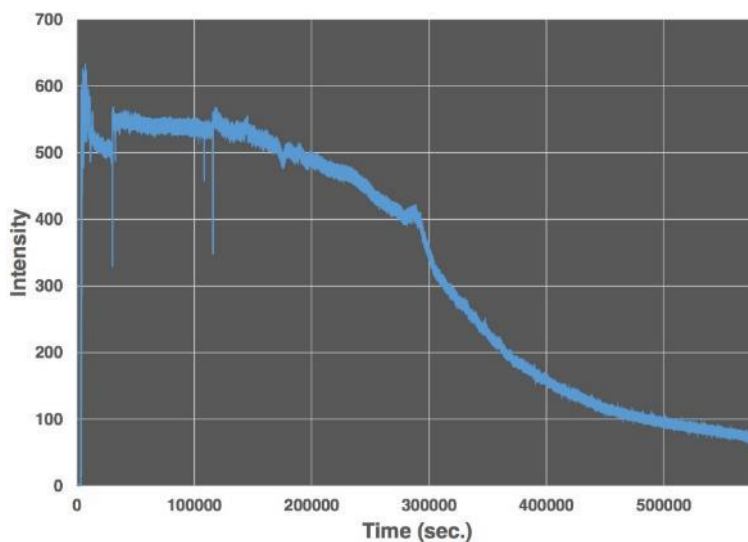


Figure 121. Fixed focus FP instrument result of the continuous monitoring of oil injected under Hoop 4B.

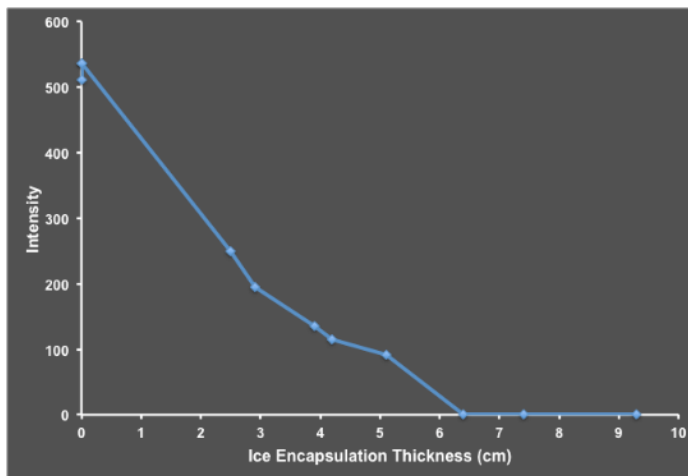


Figure 122. Plot of oil fluorescence intensity as a function of ice encapsulation thickness of oil injected under Hoop 4B.

4.2.4 FMCW

One FMCW system was mounted to the moving gantry to profile the ice before and after oil injections, and the other system was stationary and monitored the ice in Hoop 5B. Both radar systems showed signals associated with oil injections. Data was collected throughout the entire 3-month experiment, however, unfortunately, noise in the system, electromagnetic noise in the facility, and connection problems corrupted most of the measurements. This was the first long-term test of this kind with this prototype. While this prototype shows some promising results (see following), more R/D is required to make both the hardware and control software robust and to develop software from which an end-user can make interpretations.

4.2.4.1 Stationary FMCW

The stationary FMCW system experiment was added during the project as an opportunistic use of the backup FMCW radar system. As this was not an originally proposed deliverable, this radar didn't start operating until halfway through the experiment and hung by a metal chain over Hoop 5B. Good quality data was collected before and after the oil and snow addition on the ice surface, which showed an increase in amplitude of the ice/water interface return of approximately a factor of 3. Figure 123 shows results before (left panel) and after (right panel) the surface oil injection in Hoop 5B.

The reflection from the ice surface was very consistent throughout the experiment and was set to a depth of 0 in Figure 123. A snow surface reflection occurs just above this depth, and the ice/water interface is estimated at approximately 60 cm. This ice depth is shallower than that measured by the surface based radar along the majority of the tank on January 6, and it is most likely due to insulation placed on the hoop to slow ice growth.

Unfortunately, the radar PC continually crashed after approximately 20 hours of data collection, and therefore was restarted manually when BSU personnel were present. The restart required opening the electronics enclosure, which may have caused some inconsistent connections. As real-time software was still under development, these connection issues were not identified until after the experiment. More work is required to make this system more robust for Arctic environments.

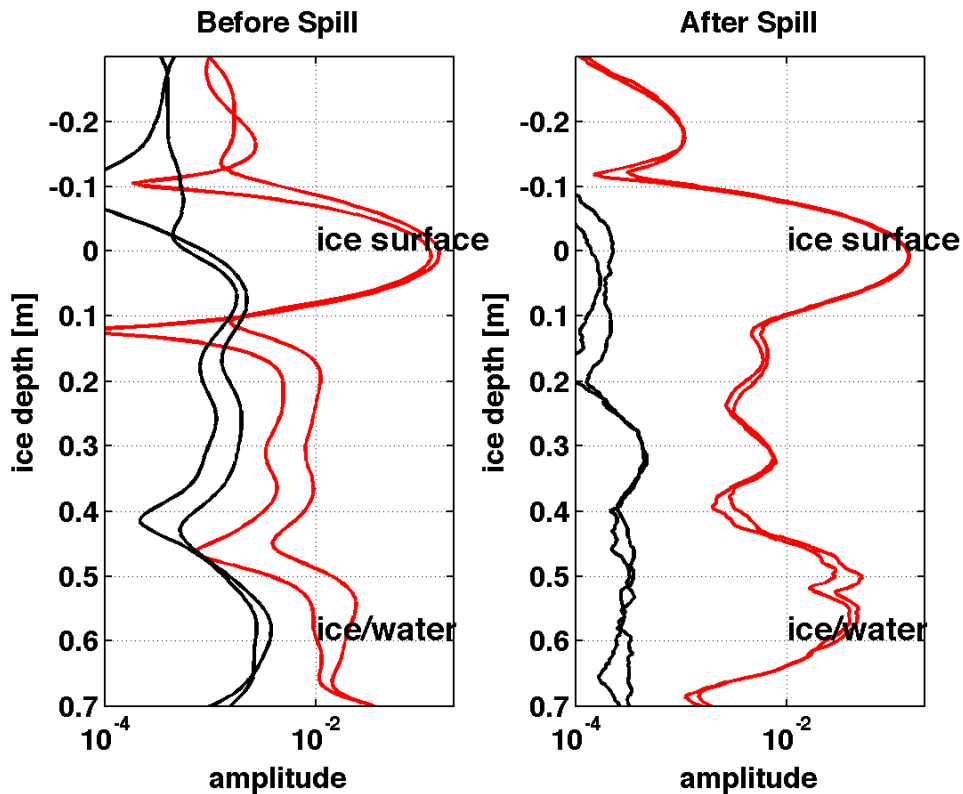


Figure 123. Shown are data from the stationary FMCW over Hoop 5B before and after snow and oil was added to the top surface of the ice on January 7, 2015. Estimated location of ice surface set at ice depth of 0, estimated ice/water interface at approximately 60cm. Ice thickness possibly thinner in this hoop due to insulating effect of snow. After oil spill reflection of interface increases in amplitude by approximately a factor of 3. Red curves are traces from frequency sweeps from 0.5-2 GHz and from 2 GHz-0.5 GHz, and black curves are estimates of background incoherent noise from the complex FFT results.

4.2.4.2 Mobile FMCW

Figure 124 shows results from two profiles along the length of the tank, on November 24th (upper panel) and December 23rd (lower panel). The ice surface reflection was set to a depth of zero, and the direct airwave was at a travel-time of approximately -11 ns. On November 24th, the ice/water interface was estimated at ~7 ns, or about 47 cm depth, and had variations that were similar in space to those seen in the surface GPR results. On December 23rd, the ice/water interface was estimated at ~9 ns, or 61 cm depth. In the lower image near the center of the profile, the encapsulated oil in Hoops 3 and 4 can be seen (compare to surface radar figure 129).

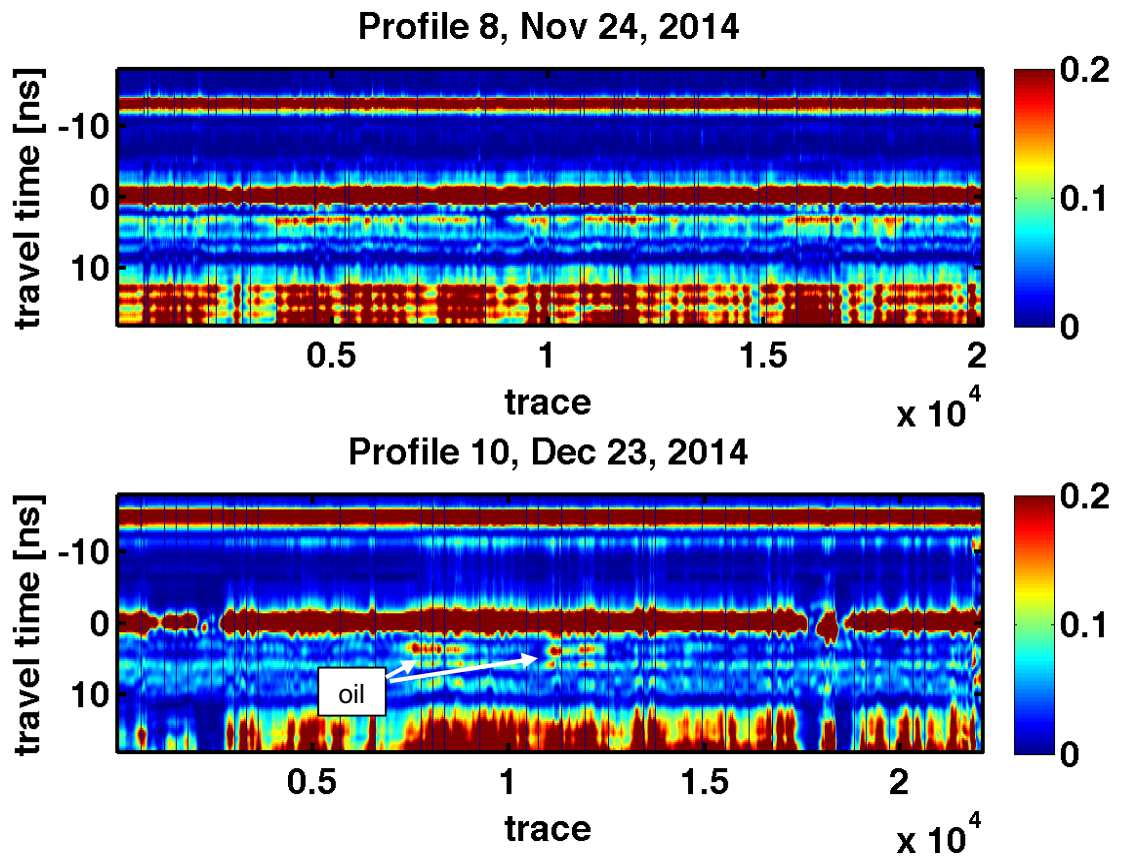


Figure 124. FMCW profile across length of tank, on November 24th and December 23rd. Ice surface reflection shown at a travel time of 0 ns. On November 24th (top panel), ice/water interface is estimated at approximately 7 ns (~47cm ice thickness), and on December 23rd the ice/water interface is estimated at ~9 ns (61cm ice thickness). Encapsulated oil is visible in hoops 3 and 4 from previous spills near the centre of the lower image. Signals below 10ns are noise.

This project was the first opportunity to test the FMCW prototype 3 in cold sea ice conditions with oil spills. Measurements were successfully made, which appear to have imaged the ice thickness and encapsulated oil in Hoops 3 and 4, during profile measurements with the system uncoupled from the ice surface and suspended in the air to simulate an airborne deployment. These are the first results with this prototype system that show promising results for imaging sea ice depth and encapsulated oil. The stationary FMCW system showed an increase by a factor of 3 in the ice/water interface after oil and snow addition at the ice surface in Hoop 5B as well. New software for processing the complex IQ mixed signal and extracting phase information was developed, along with hardware for remote local data logging and an improved 16-bit ADC.

While data was collected throughout the experiment with FMCW systems, as indicated earlier, the majority of the measurements were corrupted by radar system noise, environmental noise, and connection problems. Extensive effort was made with many different signal processing techniques (e.g. f-k filtering, processing in different frequency bands, wavelet de-noising). Many additional volunteer hours were used to try to resolve the noise problems, but unfortunately no major improvements were obtained. Phase information was studied in detail, but was unfortunately not interpretable.

4.2.5 GPR

GPR has previously proven to be effective in identifying oil underneath sea ice (Bradford et al, 2008) and although many of those results were successfully repeated here, some unintended consequences from the experiment design made signal interpretation difficult for several of the oil injections. Background noise levels in the bandwidth of the aerial GPR were higher than expected within the test basin, which necessitated stacking traces to reduce the noise. Additional stacking led to increased measurement and collection time, such that traces were collected every 6cm of carriage movement.

Relatively high ice sheet temperatures (Figure 125), especially during the first month of the experiment, had two impacts on the GPR signals: high surface scatter and high attenuation. These two effects resulted in the GPR on the above-ice carriage not being able to identify the ice/water interface on several profiles or over substantial sections of other profiles. In particular, a cooling system malfunction during November 17th - 24th resulted in warming of ice surface temperatures above intended values and that approached -7°C , beyond which sea ice conductivity rapidly increases (Morey et. al, 1982).

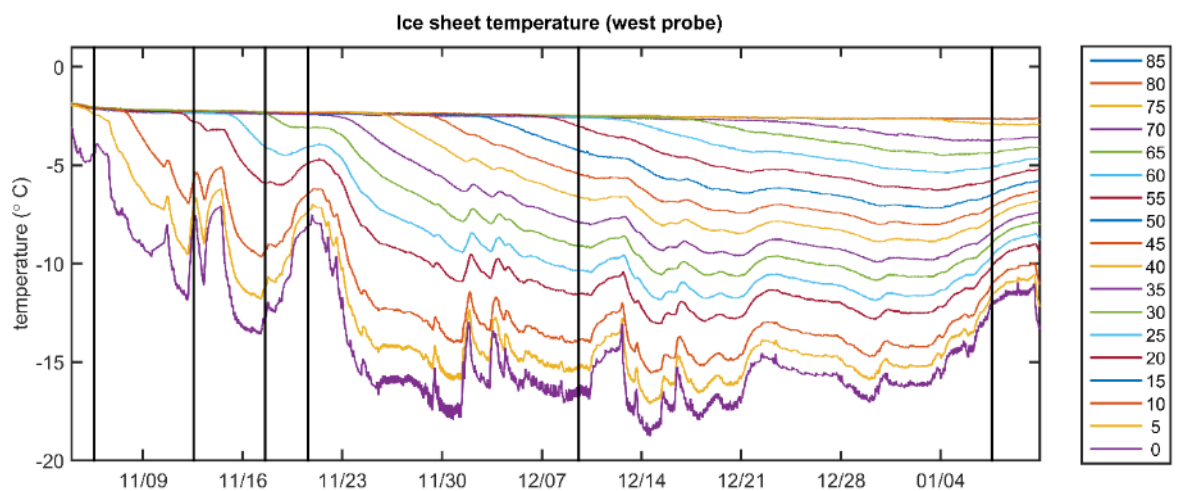


Figure 125. Ice sheet temperature profile from the West Probe thermistor string. Vertical black lines indicate injection dates for the six hoops. Note the two warming periods in November, particularly for November 16th- 24th. Ice surface temperatures during this time approached -7°C , and for injections in Hoops 1, 2 and 4, the full ice temperature profile was above -10°C .

As a precaution against oil spilling beyond the isolation hoop skirts for the injections into Hoops 3-6, insulation was placed directly on the ice surface for days-to-weeks prior to respective oil injections. The purpose of placing the insulation was to retard ice growth in the center of the cell end effectively create a small cavity under-ice that the oil would tend to migrate toward. Although hoop-specific surface temperatures were not collected, unexpectedly low radar penetration depths over those individual hoops immediately after insulation removal may be due to increased surface temperature, leading to greater brine volume near surface and higher surface scatter. The radar data presents evidence of this effect with increased reflection amplitudes where the insulation was recently removed.

Electrical anisotropy in ice growth in the ice sheet is identifiable over the course of many of the profiles, which exhibit as preferentially attenuated signal with polarization, similar to previous results (Babcock et al, 2015). Best results were obtained by summing two cross-polarized channels, which is how all of the GPR profiles are presented here.

Although the fixed boom height and mounting apparatus allowed for precise comparisons of the aerial sensors, the nearly constant height above the ice surface made interpretation difficult, as both instrument noise and ice sheet surfaces were recorded at constant times.

Two types of test basin profiles were collected with the aerial GPR: 1) weekly full basin profiles, across the full extent of the tank, and 2) shorter, single hoop profiles collected immediately preceding and following oil injections. In most cases, focused profiles were obtained daily for several days following injection, which allowed for comparison as the oil became encapsulated and the ice surface temperature decreased.

4.2.5.1 *Aerial GPR*

Note the use of the commercially available impulse radar in an airborne mode while of academic interest, is unlikely to result in an operational field system due to the lack of energy reaching the ice sheet and unwanted background noise. This type of system was designed to be used from the surface in an ice-coupled mode (where it has proven reliable over cold ice in many previous tests – validated here). While there have been notable successes (e.g. Svalbard 2008) in detecting oil on top of the ice from a helicopter, it is unreasonable to expect consistent and reliable detection of oil at depth in the ice from the air with the commercial GPR.

Hoop 1

For the oil injection into Hoop 1, the ice thickness of approximately 5 cm was on the order of the vertical resolution of the GPR, and the air/ice and ice/water interferences were not distinguishable. The ice temperature profile (from -8°C at the surface to -2°C at the base) resulted in high conductivity of the ice, contributing to the difficulty in distinguishing reflections beyond the initial air/ice interface. The ice was roughed to simulated slush ice; however, the signal return from inside and outside of the hoop was also not distinguishable.

Hoop 2

Similar results are seen in the signal response for the Hoop 2 injection as were observed for Hoop 1, although the ice thickness was approximately 20 cm at the time of the injection. There was no identifiable change in signal amplitude, surface roughness, or frequency when comparing the pre- and post-spill profiles, even with the post-spill profile occurring on the same day, before the loss of oil from the base of ice along the edge of the hoop skirt (Figure 126).

There were minor changes in the instantaneous phase of the signal in a portion of the cell, but not enough to contribute to an independent identification of the presence of oil. Since the injection occurred at the onset of a warming period in the ice sheet, it seems possible that the observed ice temperatures, again from -8°C at the surface to -2°C at the base, resulted in conductivity high enough to attenuate the signal before the base of ice reflection could be recorded.

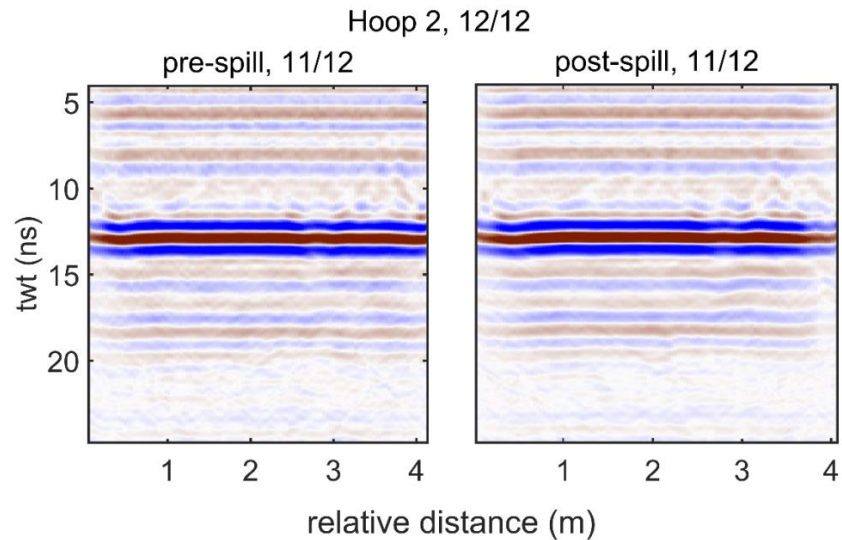


Figure 126. Pre and post-spill profiles over Hoop 2. The reflection from the air/ice interface (two-way time of ~13 ns) subsumes the base of ice reflection, and differences between the pre and post-spill profiles are not distinguishable, either in amplitude, frequency or phase.

Hoop 3

Although the ice sheet in Hoop 3 grew to ~30 cm at the time of the injection there continued to be no discernable, continuous reflections from the ice/water interface, or subsequently the ice/oil interface. The surface temperature of the ice was approximately -14°C, which should not have led to problematically high conductivity at the ice surface. The target thickness of oil at the base of the ice was 1 cm. Note that the ice coupled radar imaged a well-defined anomaly associated with the Hoop 3 injection, likely due to much lower signal to noise for the surface radar coupled with greater energy penetrating the ice which is inherent to this mode of operation.

Hoop 4

A cooling system defrost event beginning immediately prior to the Hoop 3 injection resulted in significant test basin warming, with ice surface temperatures above intended values from November 17th - 24th. The Hoop 4 injection, with a target thickness of 5 cm, occurred near the maximum recorded ice surface temperatures during this warming event, from -7°C to -8°C, which had a negative impact on the ability of the aerial GPR to record reflections below the air/ice interface. The post-spill profile did not show signal change beyond increased variability in the signal phase at the ice/oil interface, though this alone would not be sufficient to independently identify oil. Again, surface coupled radar identified a clear well-defined anomaly associated with this spill.

Hoop 5

The injection in Hoop 5 occurred when there was 50 cm of ice growth, and had a targeted release of 2 cm of oil at the base of the ice. The post-spill profile shows an increase in amplitude, an increase in the instantaneous frequency at the ice/oil interface and a significant change in phase. However, the base of ice reflection is not continuous across both of the profiles and is not far above the noise level in either case. The mid-sheet reflection layer (approximately 17 ns), possibly an artifact from the Nov 17th-24th warming period, is readily visible (Figure 127).

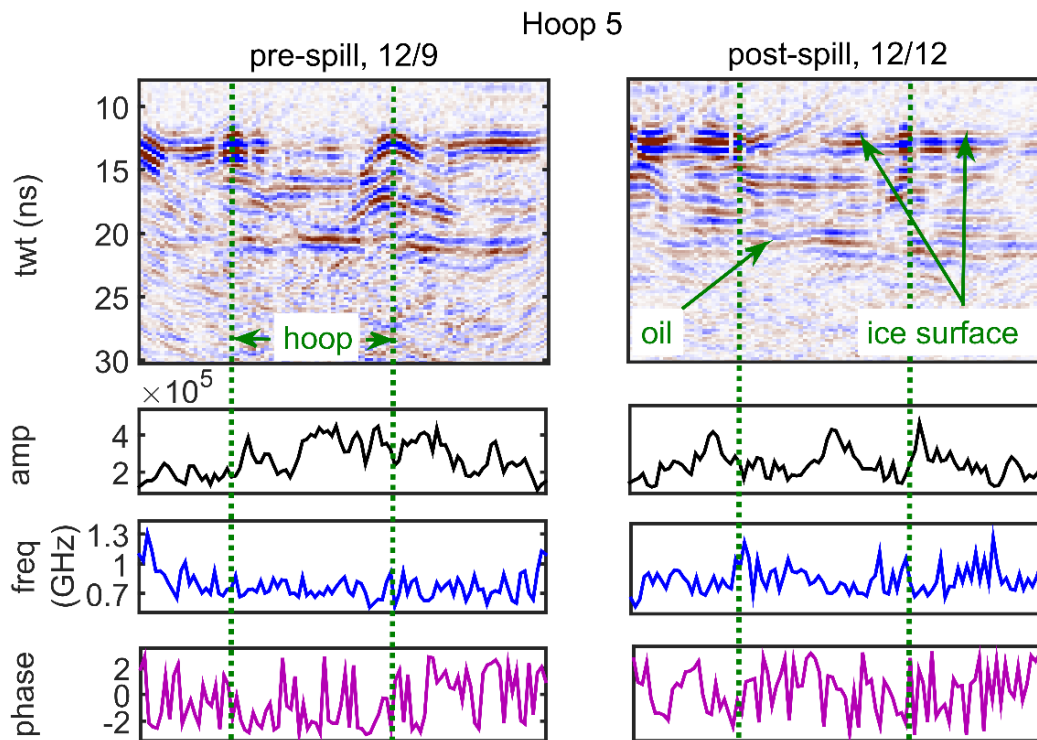


Figure 127. Pre- and post-spill profiles for the 2 cm oil injection into Hoop 5. The post-spill profile of the base of ice (two-way time of ~20 ns) shows a slight decrease in amplitude, an increase in the instantaneous frequency at the ice/oil interface and a significant change in phase, consistent with numerical models.

Hoop 6

For both the pre- and post-spill profiles on Hoop 6 there was a pile of snow adjacent to the east side of the hoop. With 70 cm of ice and the coldest ice sheet temperature profile, the differences between the ice/water interface in the pre-spill profile and the ice/oil interface in the post-spill profile are the most apparent of all of the spills. There are differences in signal amplitude, phase and frequency post-injection; in particular, the high amplitude reflection at the base of the ice extends farther to the east once oil is present (Figure 128). The amplitude and phase anomalies for the Hoop 6 spill are consistent with observations from the surface coupled radar.

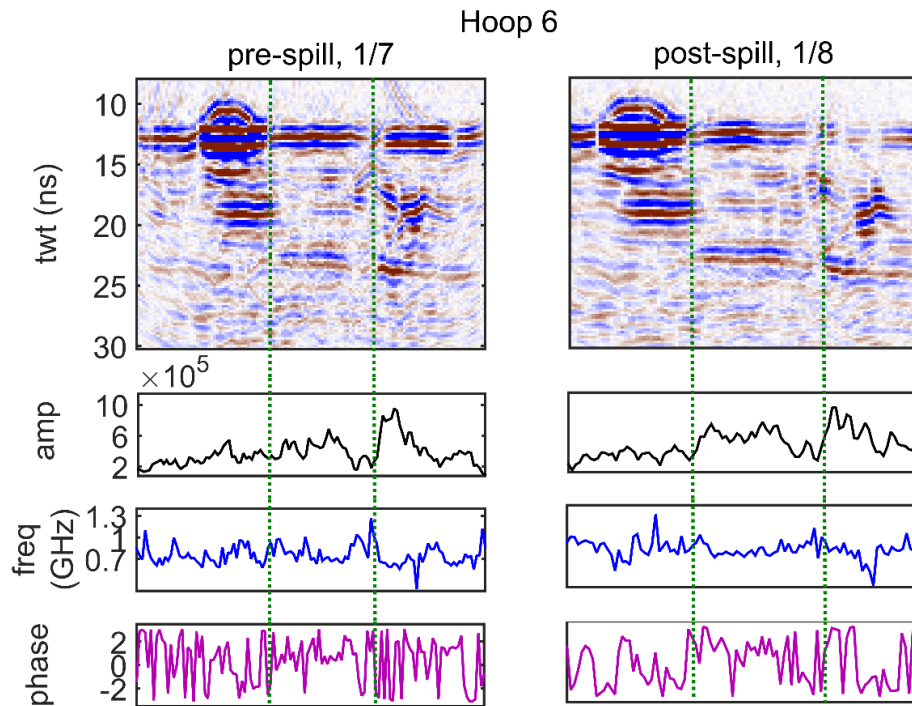


Figure 128. Pre and post-spill profiles for the injection in Hoop 6. At the base of the ice (~23 ns) there are differences in signal amplitude, phase and frequency post-injection; in particular, the high amplitude reflection at the base of the ice extends farther to the east once oil is present.

Full Basin Profiles

Full test basin profiles were collected approximately weekly throughout the experiment. The full profiles were typically collected on the day or two surrounding an injection. After the injection into Hoop 3 the scans were a week or more after injection dates due to software problems with the radar units. One benefit of this delay was that ice surface temperatures in Hoops 3-6 recovered to expected values, and radar penetration depths improved accordingly. Injected oil was most identifiable in the full tank profiles once it was encapsulated, especially in Hoops 3-5, with oil at depths of approximately 30 cm, 35 cm and 55 cm, respectively (Figure 129). Independent identification of the location of oil within the ice in field conditions, without some prior knowledge of ice structure and oil conditions, would be challenging given these changes in GPR response. For the profile taken on January 6th, with ice thickness varying between 55 – 70 cm (lesser in the Hoops 3-6 which had insulation placed on the ice surface during ice growth), the encapsulated spills in Hoops 3-5 are evident (Figure 130). Hoop 4 oil, in particular, which was targeted to be the thickest oil at 5 cm, is very evident. The signal from ice/water interface at the bottom of the sheet is not far above the background noise level.

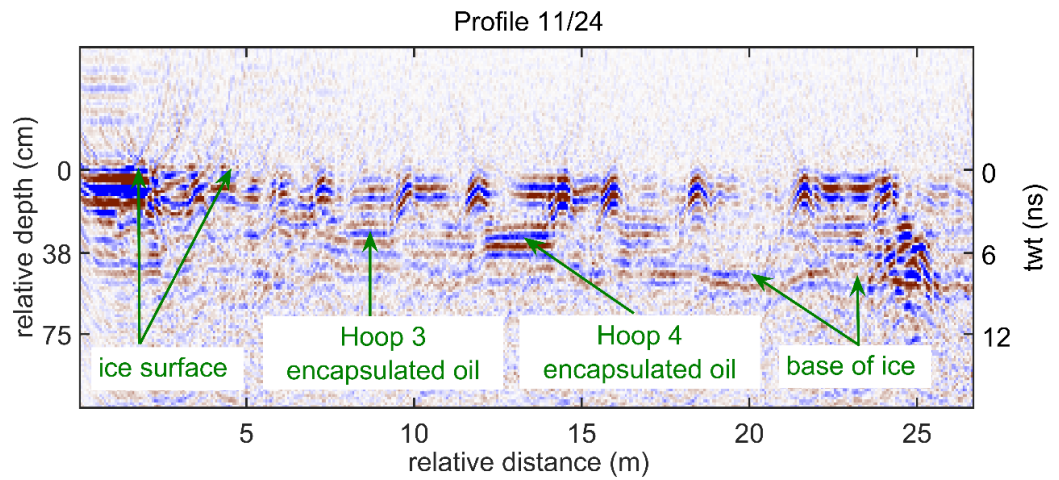


Figure 129. The full tank profile from November 24th, three days after the injection into Hoop 4. The encapsulated oil in that hoop is plainly visible, as is the majority of the base of ice reflection.

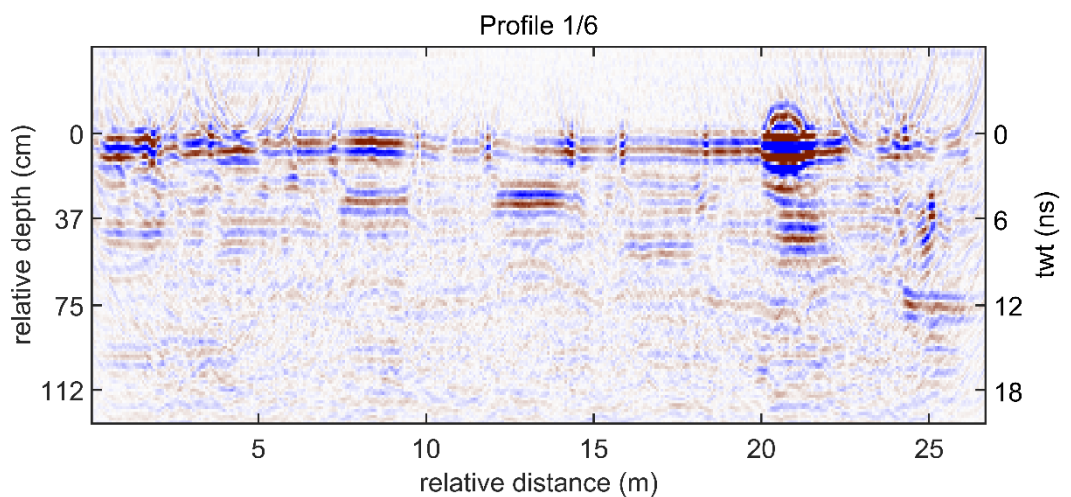


Figure 130. The full tank profile from January 6th, taken immediately prior to the injection into Hoop 6, shows the encapsulated oil in Hoops 3 (centered at 8 m) and 4 (centered at 14 m), with encapsulated oil also showing in Hoop 5 (centered at 17 m). The mound at 21m is a pile of snow placed near the eastern edge of Hoop 6. The base of ice reflection is visible in most areas at a depth of 60-75 cm, and is easier to identify in the full tank profile than in single-cell focused profiles.

4.2.5.2 Surface Based Measurements

Four time lapse, surface-based datasets were acquired to support the airborne radar tests. These were: 1) polarimetric ice coupled radar profiles with the commercial system to provide baseline measurements of the radar response to emplaced oil, 2) 3D polarimetric radar over a 2 m x 3.6 m area west of Hoop 6 with the 1GHz commercial system to measure cm scale ice roughness at the base of the ice, 3) expanding spread radar data with the 1GHz system to measure bulk ice velocity for depth conversion, and 4) multi-azimuth electrical resistivity data to measure DC electric conductivity and conductivity anisotropy to compare with radar derived values and to validate the electrical property model.

Ice coupled radar over the hoops

In previous controlled spill experiments conducted at CRREL (2004, 2011, 2012) and Svalbard (2006, 2008), the commercial pulsed radar in ground coupled mode proved to be effective in detecting oil spills at the ice/water interface, within the ice, and on the surface and cover by snow. The recent experiment was no exception, and for this reason ice-coupled profiles were acquired that spanned Hoops 2-6 on November 20th after the injection into Hoop 4, on December 11th after the Hoop 5 injection, and on January 10th after the Hoop 6 injection to provide a baseline response to aid in interpretation of the airborne radar data. Data was acquired with both the 1 GHz pulsed system and the 500 MHz pulsed system. The results presented here are from only the latter since this is similar to the airborne measurements. Note that on December 11th, the triggering system failed for the 500 MHz radar and so no ice coupled profile is available for that time. Additionally, an expanding spread radar profile was collected in the northeast portion of the tank near the time of each injection, which enabled propagation velocity measurements and the conversion of data from travel time to depth (Figure 131).

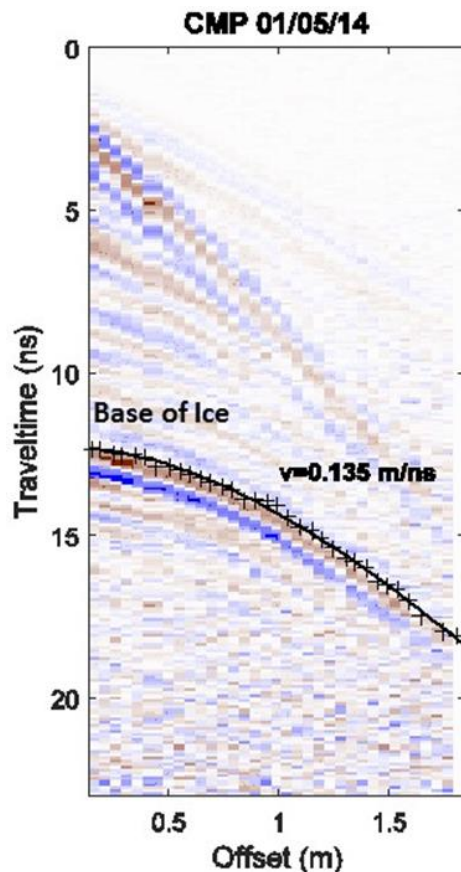


Figure 131. 1GHz radar expanding spread gather acquired on January 5, 2015. The base-of-ice reflection has a near offset arrival time of ~12 ns. By fitting a hyperbola to the travel times for this reflection, we can calculate the propagation velocity using the normal moveout equation. At this time the velocity is 0.135 m/ns.

Figures 132 and 133 present the data set acquired on January 10, 2015 and illustrate the main features evident in the ground-based profiles. Encapsulated oil injected into Hoops 3, 4, and 5 produce clear, well-defined reflections (Figure 132), while the spills in Hoops 4 and 5 (targeted for 5 cm and 2 cm, respectively) produce amplitude anomalies that are well above reflections due to natural variability in the ice (Figure 133). The thinner Hoop 3 injection (targeted for 1 cm) produces a clear reflection, but has an amplitude that is only slightly above the background reflections. These results are entirely consistent with the modelling results. The Hoop 6 injection

was not encapsulated and produced a major anomaly that was easily detectable (Figure 132). It had a reflection amplitude that is 1.6 times greater than the base-of-ice reflection (Figure 133) and is associated with a 57° phase rotation. While beyond the scope of this project, these characteristics make it possible to invert for oil layer thickness using full waveform inversion methods (Bradford et al., in press). Note that this approach can be used to measure encapsulated oil thickness as well.

Previous experiments demonstrated, and the present experiment confirms, that 500 MHz ground-coupled GPR is capable of detecting oil spills thinner than 1 cm. Spills of less than 1 cm produce reflections that are similar in amplitude to those produced by natural variations in the ice and may be difficult to identify under field conditions. Spills greater than 1 cm thick produce substantial anomalies that are easily differentiated from natural variations in the ice.

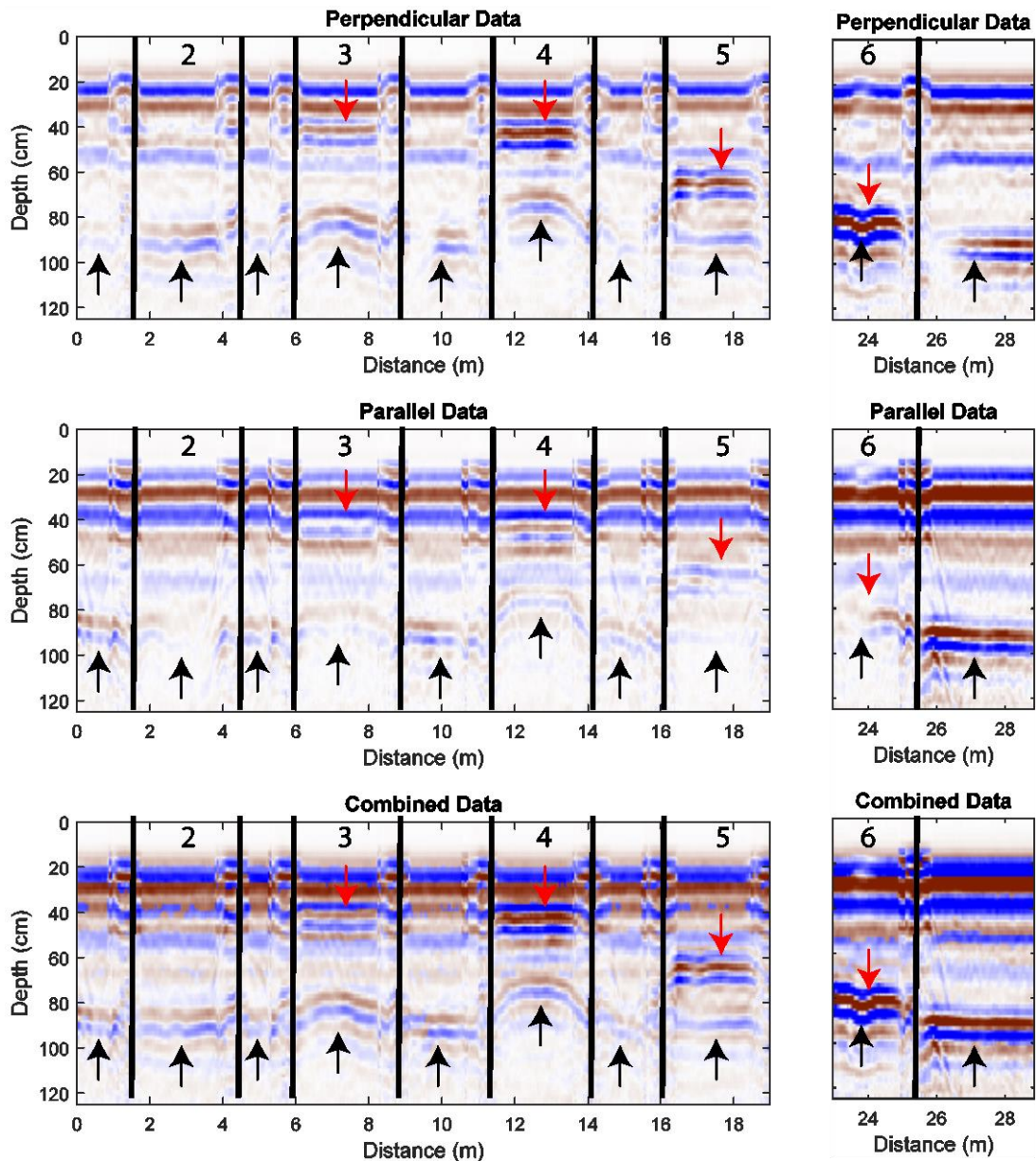


Figure 132. 500 MHz polarimetric GPR data acquired on January 10, 2015 after the Hoop 6 injection. Perpendicular polarization is aligned perpendicular to the long axis of the tank, parallel data are parallel to the tank axis;

combined data are computed by vector sum. Red arrows indicate encapsulated spill in Hoops 3, 4, 5, and oil at the base in Hoop 6. Black arrows indicate the base-of-ice reflection.

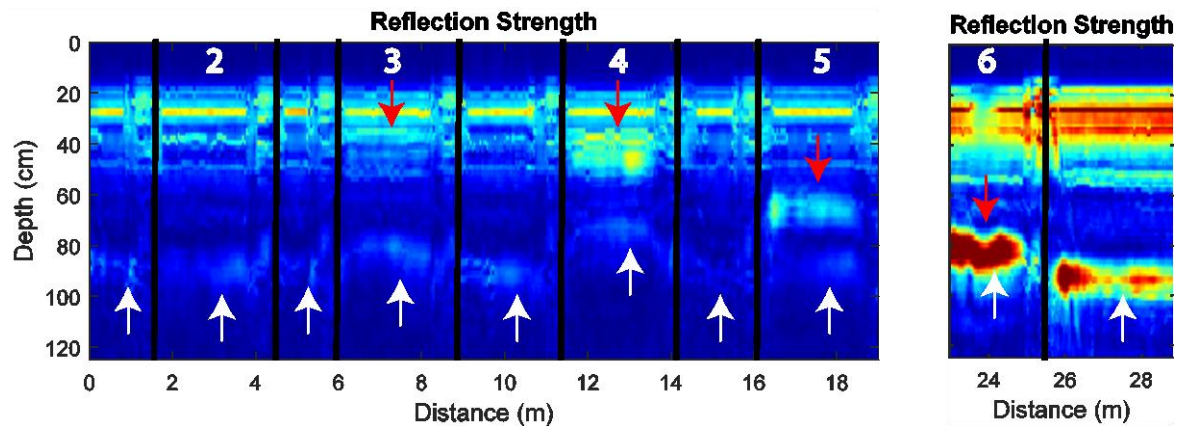


Figure 133. Plot of reflection strength for the profile acquired on January 10, 2015 and shown in Figure 132. The spill at the base of Hoop 6 and the encapsulated spills in Hoops 4 and 5 produce anomalies well above background, whereas the thinner Hoop 3 spill has an amplitude similar to natural variations in the ice. Red arrows indicate encapsulated spill in Hoops 3, 4, 5, and oil at the base in Hoop 6. White arrows indicate the base-of-ice reflection.

4.2.6 Narrowband Sonar

Hoop 1 Injection 1

Previous basin tests with narrow-beam sonars show the detection of oil beneath sea ice and the quantification of its thickness is possible using acoustic techniques (Wilkinson et al., 2014). Figure 134 shows the acoustic return from the 1 MHz transducer under Hoop 1. The blue line represents the water surface as seen during the calibration experiments. The red line shows the acoustic return from the ice bottom before the controlled release of oil. The black line denotes the acoustic return after the oil was injected. The difference between the pre-oil injection (dotted red line) and the post-oil injection return (black dotted line) should be the oil thickness. If correct, then the oil layer at the bottom of the ice is about a centimeter thick. This is at the minimum resolution of the system using one centimeter pulse widths.

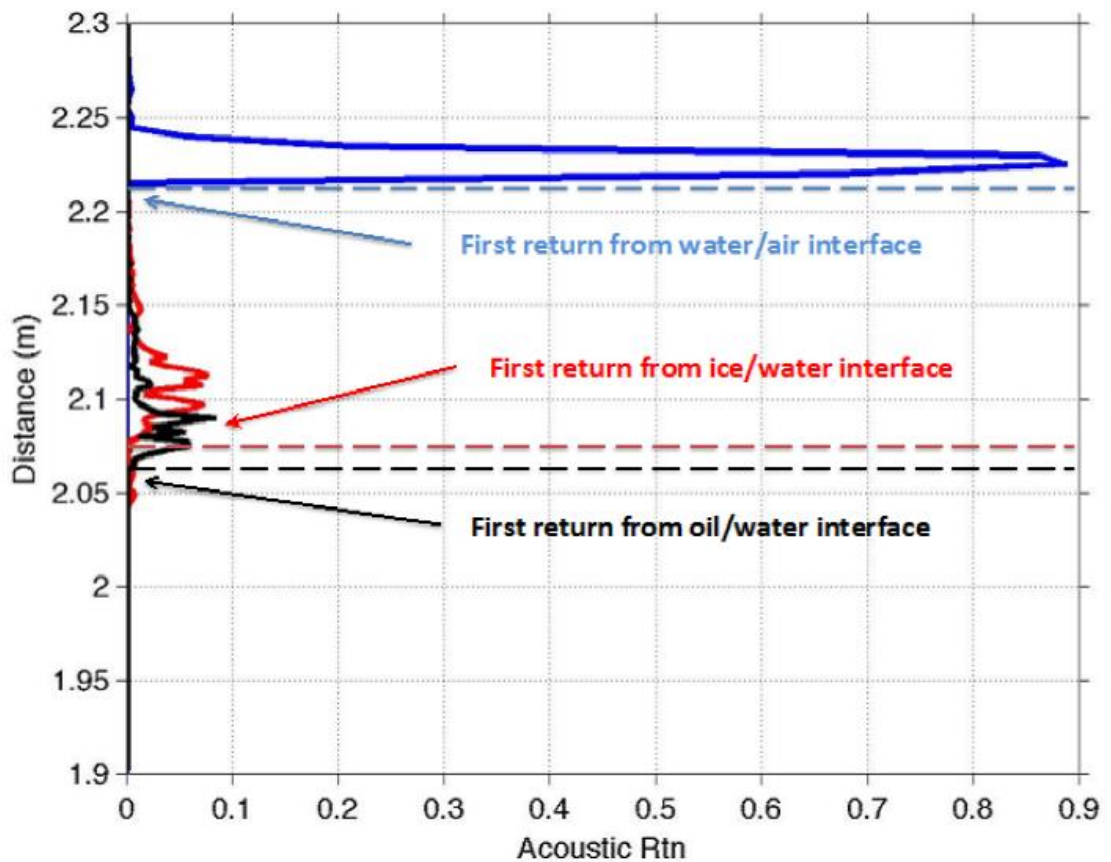


Figure 134: Acoustic returns from the 1 MHz transducer. Blue line: water surface (pre-ice formation), Red line: ice bottom (pre-oil injection), black line: oil bottom (post oil injection). Dashed lines denote the position of the first return from the interfaces. Note: traces are not corrected for the different sound speed of the various mediums.

Because it is likely that the frazil and ice blocks moved around during the introduction of the oil, this scenario is particularly challenging. As a result, it cannot be stated for certain that the difference in the acoustic signature between pre- and post-oil release is a result of oil located at the bottom of the ice, the result of the movement of the ice blocks giving a different acoustic signature, or a combination of both.

Notably, a peak return appeared in the 5 MHz transducer after the oil was introduced (see black circle in Figure 135 and Figure 136). This result is consistent with an increased acoustic return when the ice bottom is contaminated with oil. We see a similar outcome from the oil releases performed under the other hoops. This secondary evidence suggests that oil was indeed located above the transducers.

Pre-oil injection

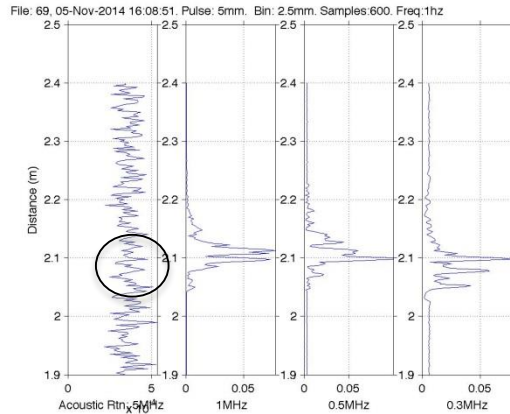


Figure 135. Pre-oil injection: Acoustic signature of the sea ice bottom about 20 minutes before the oil injection, as seen by the different transducers. Black circle highlights the absence of a return from the ice bottom in the 5 MHz transducer. Returns from 5 MHz, 1 MHz, 0.5 MHz, and 0.3 MHz transducers arranged left to right.

Post-oil injection

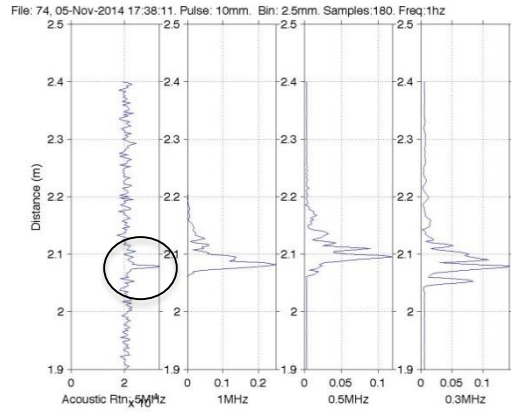


Figure 136. Post-oil injection: Acoustic signature of the oil located on the ice bottom, as seen by the different transducers. Black circle highlights the appearance of a peak in the 5 MHz after the oil has been released. Returns from 5 MHz, 1 MHz, 0.5 MHz, and 0.3 MHz transducers arranged left to right.

Hoop 1 Injection 2

The following results are based on three acoustic surveys. One before the oil injection occurred, one after the oil injection, and a moving survey of Hoop 1 on the day following the oil release. A summary is as follows:

1. Pre-oil injection: 04-Dec-2014 10:00:00
2. Oil introduced: 04-Dec-2014 10:37
3. Post-oil injection: 04-Dec-2014 11:00:00
4. Moving survey 05-Dec-2014 10:00:00
5. Figure 137 shows the raw data from the 300-second record of the four transducers after the oil was deployed. This figure shows that one can clearly identify the signal from both the ice bottom (oil/ice interface) and the bottom of the oil (water/oil interface) in all transducers other than the 5 MHz.
6. Figure 138 shows the average acoustic return from the 4 transducers. The blue line represents the return about 30 minutes before the oil was deployed. The black line displays the return after the oil was deployed. In all cases, other than the 5 MHz transducer, there is a clear return from the water/oil interface (first peak) and another return from the oil/ice interface (second peak). This second peak is located directly over the original ice bottom signal (in blue), which suggests that the sound speed of seawater and oil are very similar.

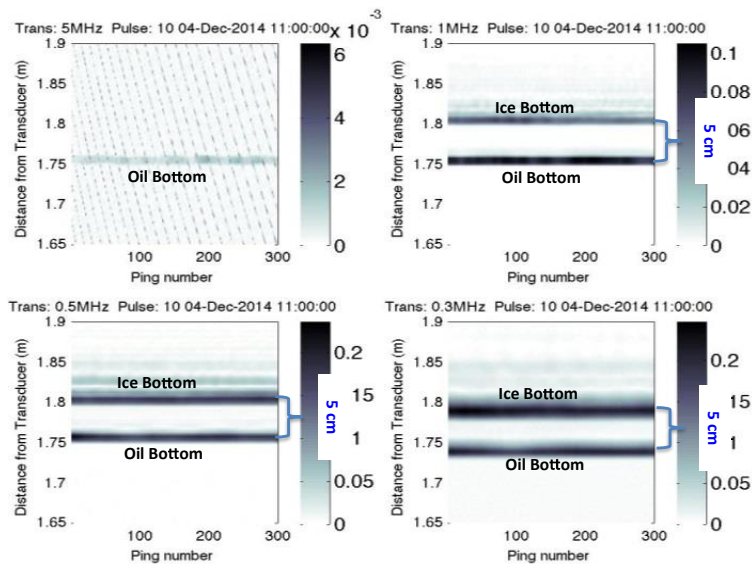


Figure 137. Plot of the raw acoustic signal over the 300-second record of the four transducers 30 minutes after the oil release. In all cases, other than the 5 MHz transducer, both the ice and the oil bottom can be clearly seen. The 5 MHz can only see the oil bottom.

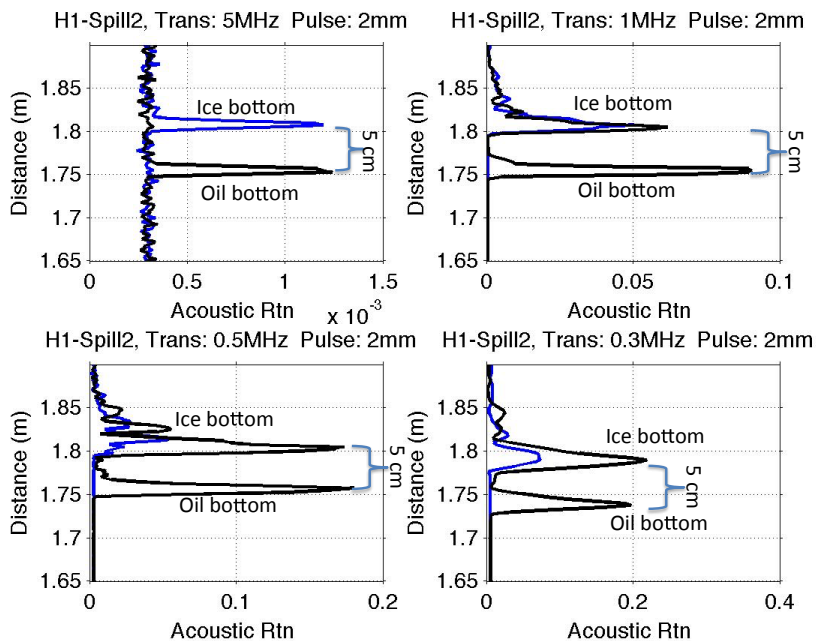


Figure 138. Plot of the average acoustic signal seen by the four transducers, both pre (blue line) and post (black line) oil deployment. In all cases, other than the 5 MHz transducer, both the ice bottom and the oil bottom can be clearly seen.

Based on the data within Figure 137 and Figure 138, the oil above the transducers was about 5 cm thick. The thickness of the oil corresponded to the distance between the ice/oil return and the water/oil return. The expected thickness resolution was 1 cm.

Importantly, a similar result is seen when the underwater carriage performed a complete scan under Hoop 1. As the platform moved under Hoop 1, all four transducers of the AQUAScat system recorded at 1 Hz (Figure 139). Both the undulating nature of the ice bottom, as well as the level spread of the oil, can be clearly seen. Because the ice bottom was not level, it is possible to see variability in the oil thickness across the hoop.

This is a significant result, and this output is similar to what would be expected from a system mounted on an autonomous underwater vehicle or remotely operated vehicle. It is also important to highlight that these results are the raw data and no processing has been applied to this data.

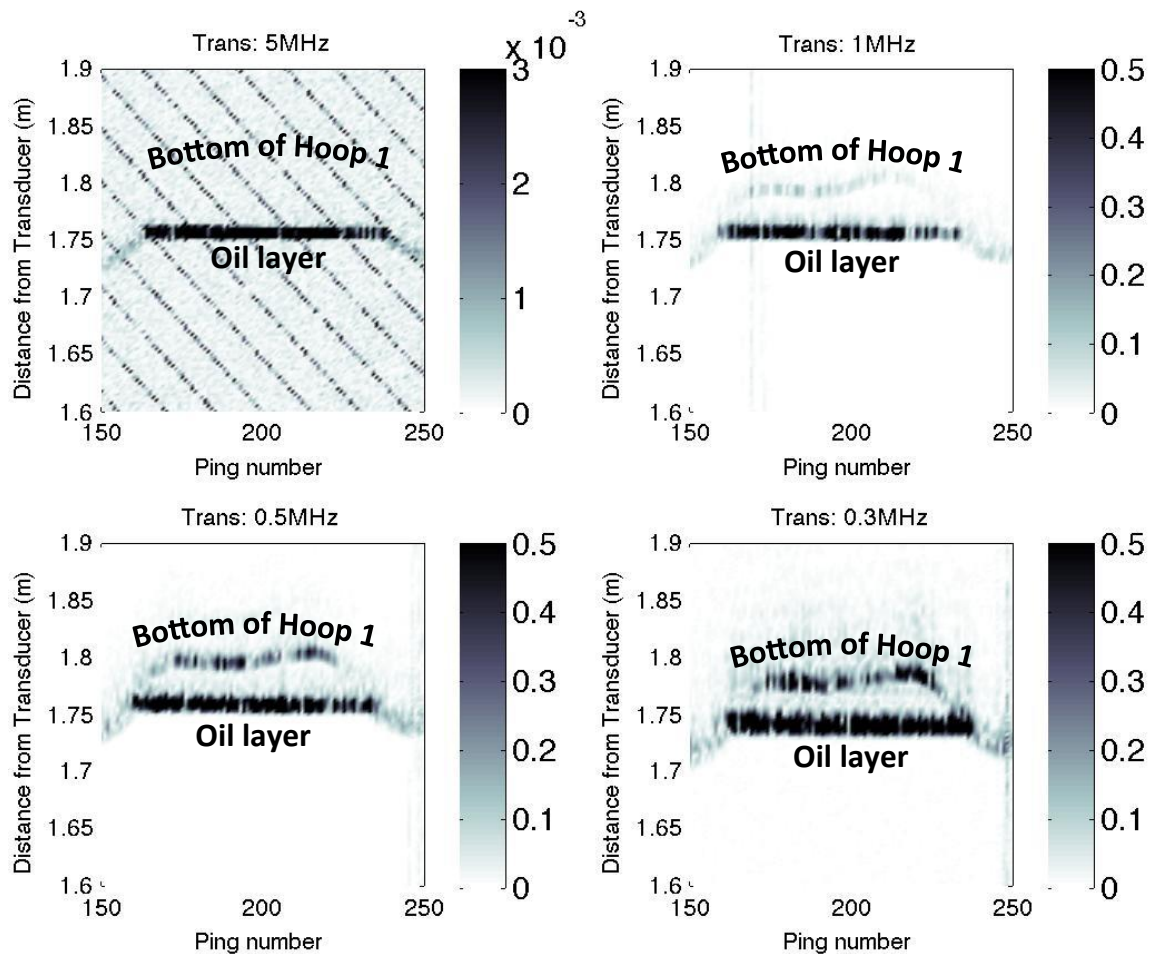


Figure 139. Plot of the raw acoustic signal from the four transducers during transit of Hoop 1. The transit was performed about a day after the oil release. In all cases, other than the 5 MHz transducer, both the ice and the oil bottom can be clearly seen. The 5 MHz can only detect the oil bottom.

Hoop 2

The AQUAScat system was activated approximately 10 minutes before the deployment of oil, and continued logging for about 50 minutes after the injection (total file length: 60 minutes). During this time, all transducers were activated and the system recorded data every second. A summary is as follows:

- 13:29 AQUAScat turned on
 - 5 MHz, 1 MHz, 0.5 MHz, 0.3 MHz transducers active

- Sampling frequency: 1 Hz (ping every second)
- Pulse length: 10 mm
- **13:39 Oil released under the ice**
- 14:29 AQUAScat stopped logging.

Figure 140 displays the raw data during this one-hour sampling period. The single return before the oil was deployed and the classic train-track dual return after the oil was injected are clearly visible.

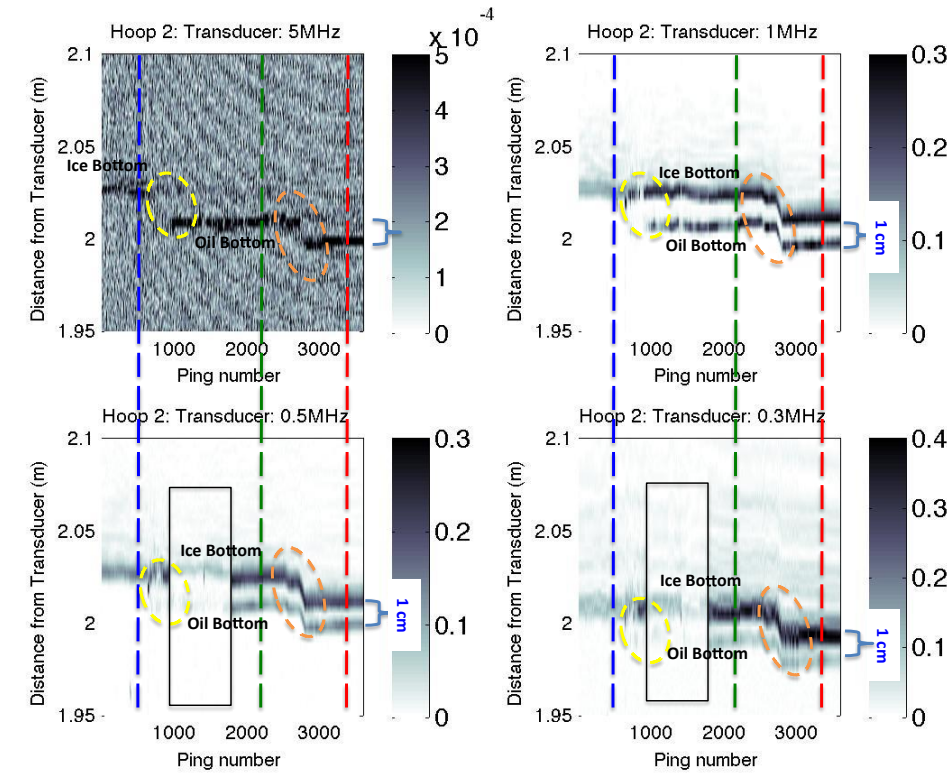


Figure 140. One hour time series displaying the raw output from the 5 MHz (top left), 1 MHz (top right), 0.5 MHz (bottom left), 0.3 MHz (bottom right) transducers. Main features are:

Blue dotted vertical line: Just before the oil was released. Single return from ice bottom.

Yellow circle: Release of the oil under the sea ice. Gradual increase in oil thickness, i.e. dual return.

Green dotted vertical line: About 25 minutes after the spill (see next figure).

Red dotted vertical line: About 45 minutes after the initial spill (see next figure).

Back rectangles: Time period the 0.5 MHz and 0.3 MHz channels experienced some interference, which reduced the amplitude of the return signal for this period.

Orange circle: Downward shift of 1-2 cm in the location of the water/oil and the oil/ice interface.

Figure 141 shows results of the average acoustic profile from the 1 MHz transducer. This figure displays the acoustic return before the oil was deployed (blue), 25 minutes after the oil was deployed (green), and 45 minutes after the oil was deployed (red). These plots relate the dotted lines of the same colour in the previous Figure 140.

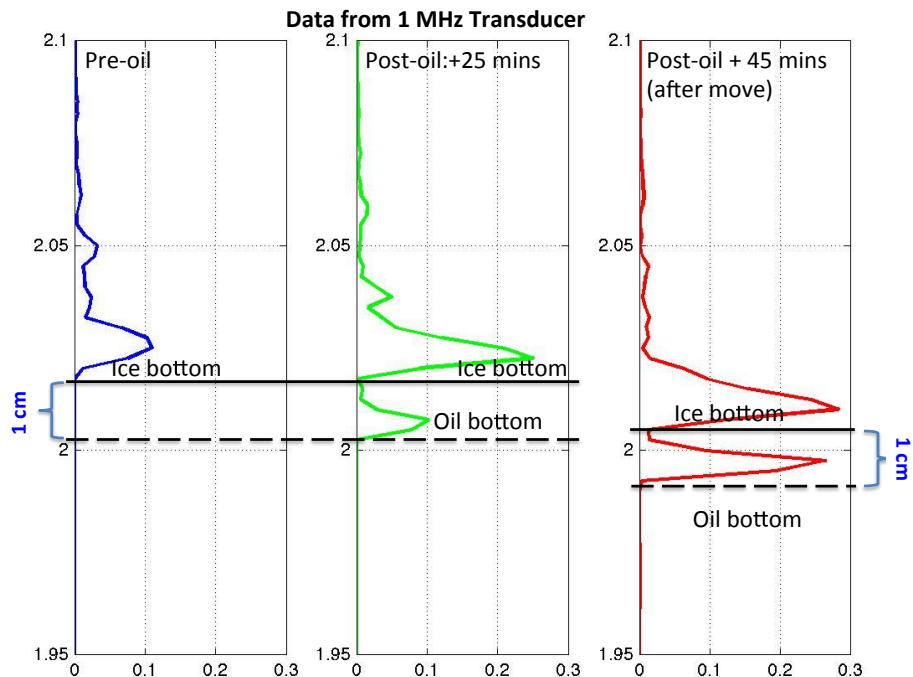


Figure 141: These profiles are from the 1 MHz transducer. This figure shows the acoustic return before the oil was deployed (blue), 25 minutes after the oil was deployed (green), and 45 minutes after the oil was deployed (red). Colour of the acoustic profiles relate to dotted lines in previous Figure 140.

The location of the ice bottom is clearly visible at about 2.01 m from the transducer, before the oil was injected. The amplitude of this return was about 0.1. After the oil was deployed (green) there was a larger return (0.27) at the same location at the ice bottom (the oil/ice interface), and a second return starting at about 2.00 m (the water/oil interface). Given the sound speed of oil and seawater, the oil thickness above the sonar of about 1 cm.

The red trace (far left) is the acoustic return 45 minutes after the oil was injected. The trace is almost identical to the green trace (taken 20 minutes earlier) except the whole plot is shifted downwards by about a centimetre. We do not have an explanation for the apparent downward shift in the signal.

Hoop 3

Due to a communication error within the cable connecting the Aquascats system to an external computer, data was not collected during the release of oil under Hoop 3; however, 15 continuous hourly measurements were collected about two days after the spill, from November 19th at 17:00 to the November 20th at 08:00. During this time all transducers were activated for a three-minute window at the start of each hour. A summary is as follows:

- **November 17 13:24 Oil released under the ice**
- November 19 17:00:00. AQUAscats programmed for hourly sampling
 - Total time elapsed since spill: 52 hours
 - 5 MHz, 1 MHz, 0.5 MHz, 0.3 MHz transducers active
 - Sampling frequency: 1 Hz (ping every second) for 3 minutes.
 - Pulse length: 10 mm
- November 20 08:00:00: Carriage moved away from being under Hoop 3.
 - Total time elapsed since oil injection: 67 hours

The following discussion is based upon the 15 hourly records that were obtained about two days after the oil release. Figure 142 shows the time series, from 17:00 on November 19th to 08:00 on the 20th, from each transducer. All transducers, other than the 5 MHz, saw a striped pattern to the acoustic time-series. This type of acoustic return was previously seen when ice began to form below the spilled oil. This process is known as the encapsulation of the oil. The 5 MHz system failed to penetrate through the ice and thus does have reflections from both the oil and ice.

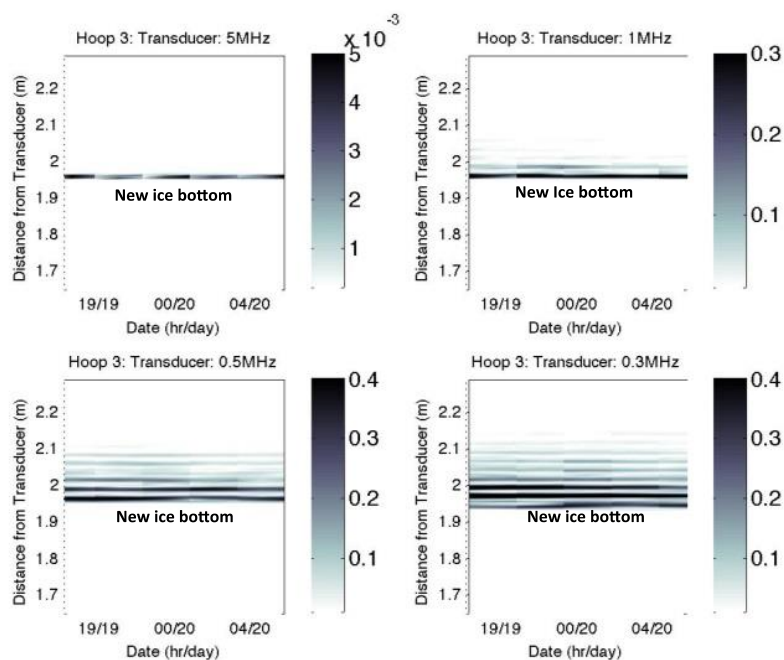


Figure 142. Time-series of acoustic returns under Hoop 3, from 17:00 on the November 19th to 08:00 on the November 20th. This figure displays the output from the 5 MHz (top left), 1 MHz (top right), 0.5 MHz (bottom left), 0.3MHz (bottom right) transducers.

Figure 143 clearly shows the striped acoustic return. The figure was obtained by calculating the average return for each transducer, over the combined 15-hour period. The series of peaks and troughs shown in Figure 143 are most likely due to a combination of the different reflection possibilities available to encapsulated oil (Figure 144).

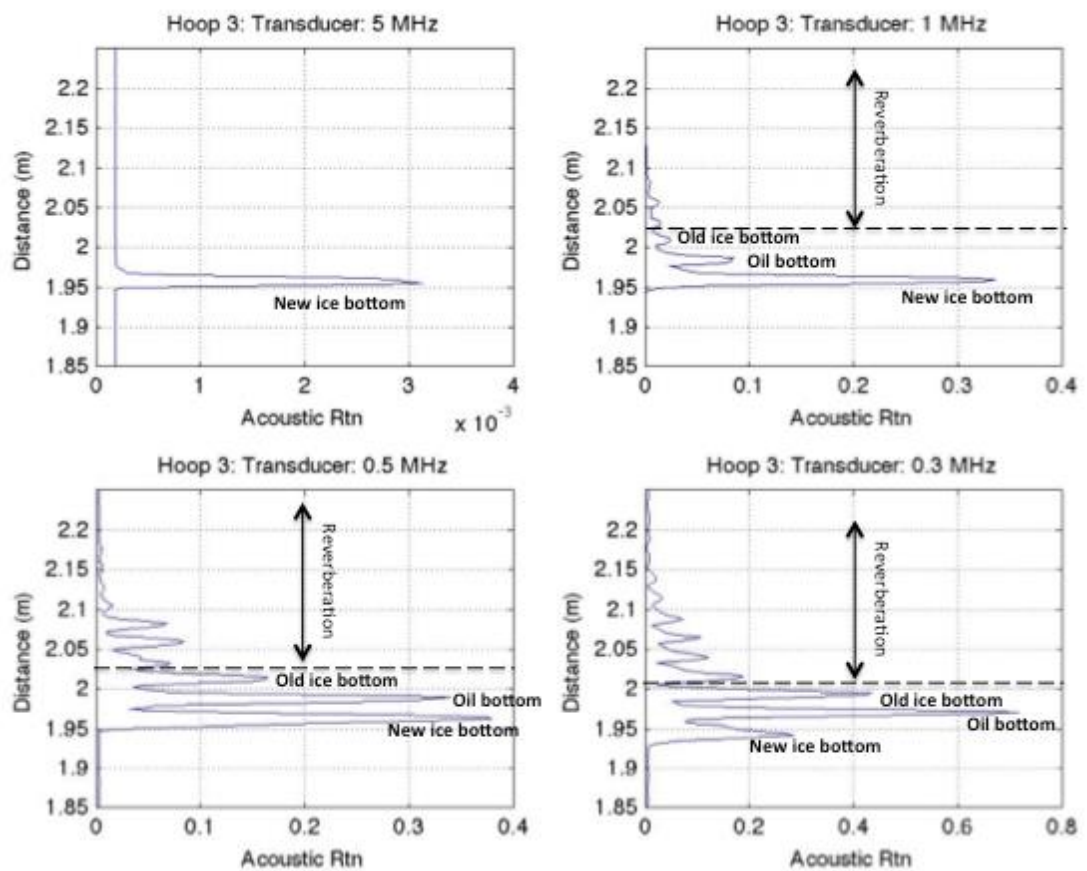


Figure 143. This figure displays the mean Acoustic return for the 5 MHz (top left), 1 MHz (top right), 0.5 MHz (bottom left), 0.3MHz (bottom right) transducers. Full time series can be seen in Figure 142.

If the ice/air interface is ignored, a 3-layer system can be assumed. The layers consisting of:

- Layer 1: newly formed sea ice layer that has grown below the oil,
- Layer 2: the oil layer itself, and
- Layer 3: the original sea ice that was present before the oil was released.

This 3-layer system provides the possibilities of numerous reflection points due to the acoustic impedance mismatch between seawater, sea ice, and oil. The schematic in Figure 144 summarizes some of the reflection possibilities for encapsulated oil.

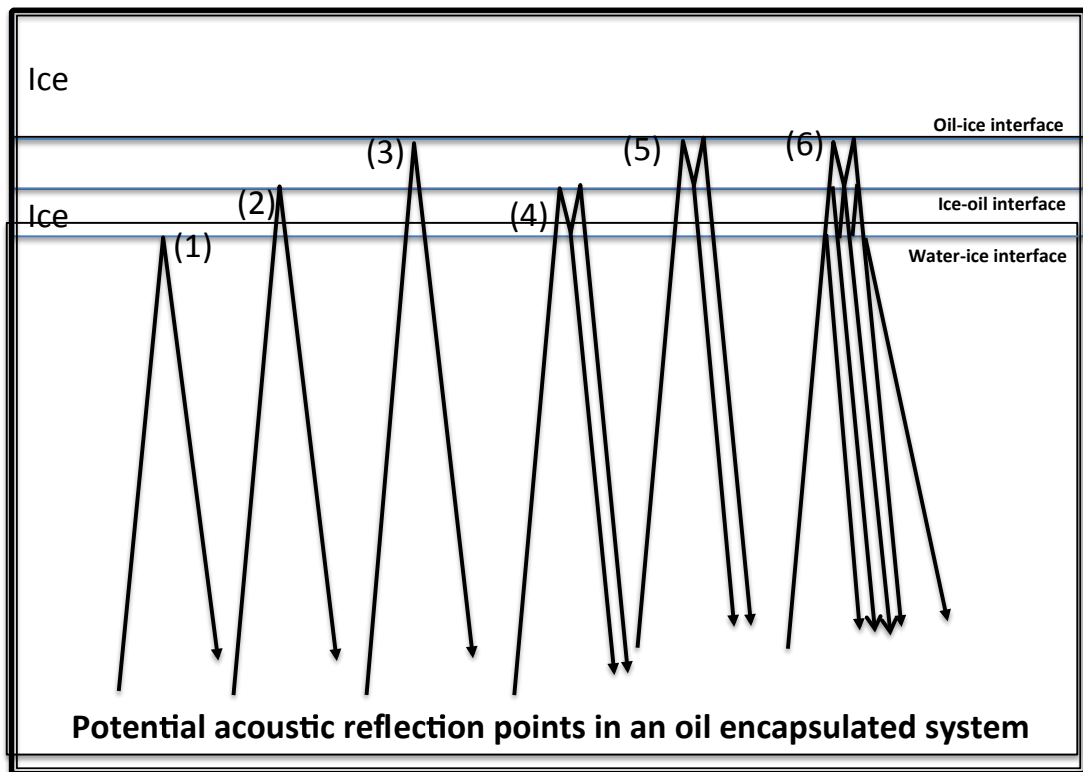


Figure 144 Graphic showing the potential acoustic reflection points for oil that encapsulated within sea ice.

These possibilities shown within Figure 144 are described in detail below:

- 1) Water/ice interface: The reflection from the bottom of the new ice that has formed below the oil.
- 2) Ice/oil interface: The reflection from the top of the new ice that has formed below the oil.
- 3) Oil/ice interface: The reflection from the bottom of the original sea ice that was present before the oil was released.
- 4) Internal reflections, new ice: The reverberation that is possible between the top and bottom of the ice that has formed below the oil, i.e. between the water/ice interface and the ice/oil interface.
- 5) Internal reflections, oil: The reverberation that is possible between the top and bottom of the oil layer, i.e. between the ice/oil interfaces and the oil/ice interface.
- 6) Combination of potential reflections: This shows the possible combinations of the above-mentioned reflection possibilities.

The combination of reflections from the different interfaces is the most likely reason there was a series of peaks and troughs in the 1 MHz, 0.5MHz and 0.3 MHz transducers. The lower frequency transducers have the most penetration and hence reflections. Multiple reflections are not possible within the 5 MHz due to the high attenuation rates at this frequency. The 5 MHz transducer just detects a reflection for the water/ice interface.

Figure 145 shows an example of the acoustic return from 0.3 MHz transducer. Each peak has been identified with a red line and Table 9 summarizes the location and distance between peaks. It is important to note that the sound speed was not altered to allow for difference in speed in the sea ice, oil and seawater.

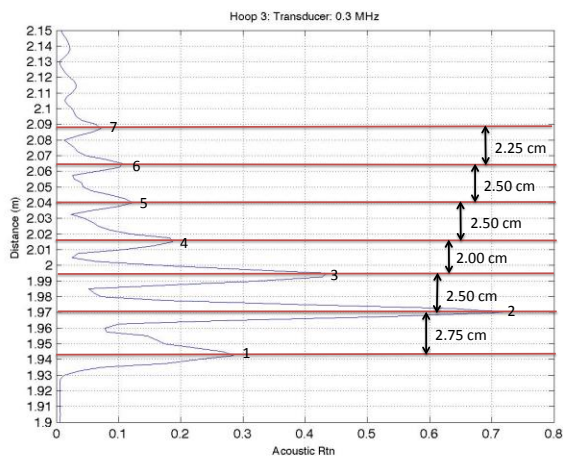


Figure 145 Average acoustic return, calculated from returns obtained between 17:00 on November 19th and 08:00 on November 20th, for the 0.3 MHz transducer. Each peak has been identified with a red line.

Table 9. Table showing the location and distance between each separate peak seen by the 0.3 MHz Transducer (see accompanying Figure 145).

Peak Number	Location of max peak (m)	Distance between peaks (m)
Peak 1	1.9425	
Peak 2	1.9700	0.02750 (P1-P2)
Peak 3	1.9950	0.02250 (P2-P3)
Peak 4	2.0150	0.02200 (P3-P4)
Peak 5	2.0400	0.02250 (P4-P5)
Peak 6	2.0650	0.02250 (P5-P6)
Peak 7	2.0875	0.02225 (P6-P7)

Hoop 4

The Hoop 4 release was imaged intensely for almost two weeks after the oil injection. As a result the AQUAscat was able to obtain hourly 3-minute snapshots from a few hours before the injection on November 20, 2014 11:00:00, through to 12 days after the injection December 1, 2014 10:00:00. A summary is as follows:

- AQUAscat programmed for hourly sampling
 - 5 MHz, 1 MHz, 0.5 MHz, 0.3 MHz transducers active
 - Sampling frequency: 1 Hz (ping every second) on the hour for 3 minutes.
 - Pulse length: 10 mm
- November 20th, 11:00:00. Pre-oil release survey
- **November 20th, 14:12:45. Oil released under the ice**
- Continuous hourly monitoring of acoustic returns
- December 1st, 10:00:00. Last hourly data under Hoop 4.

During this 12-day period, the sea ice grew about 10 cm, from 1.97 m above the transducers to 1.87 m (Figure 146). As a result, the experiment within this hoop represents an ideal opportunity to explore the encapsulation of oil and the acoustic signature during this process. It also allows the determination of the present limitations of the different transducer frequencies regarding the detection of encapsulated oil using acoustics.

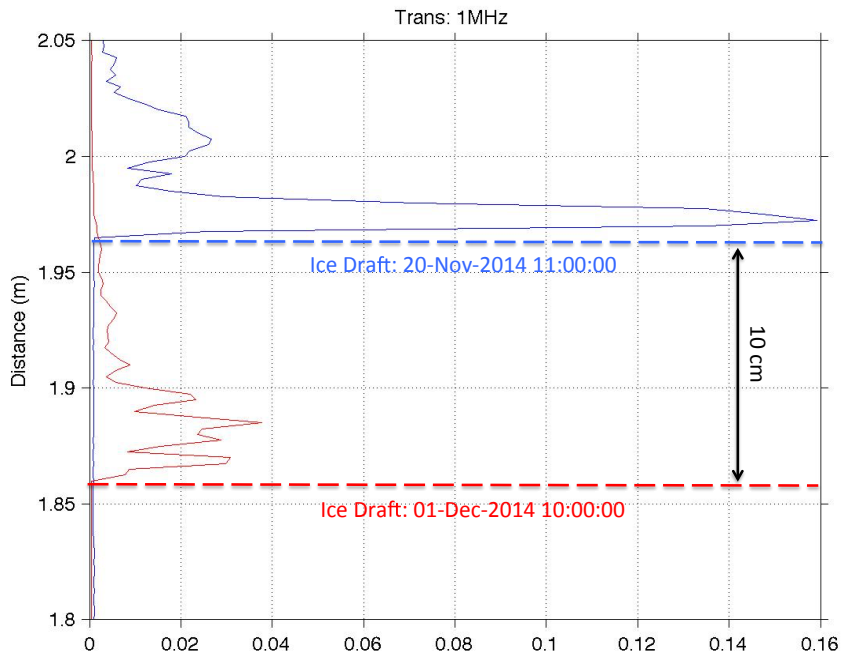
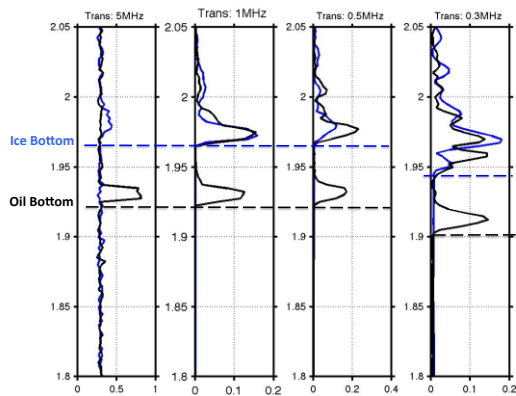


Figure 146. Ice draft as seen by the location of the bottom of the sea ice in the 1 MHz transducer. Blue dotted line represents the location of the water/ice interface on November 20th. Red dotted line represents location of the water/ice interface on December 1st.

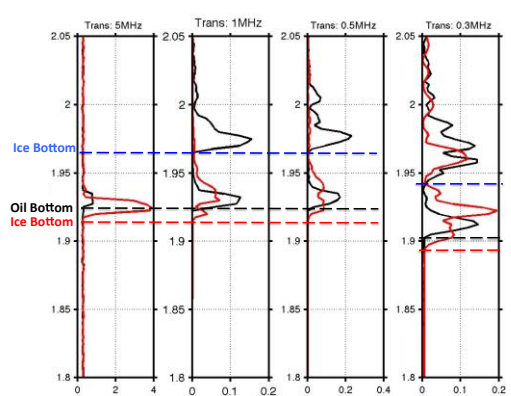
Oil Detection and Encapsulation

Figure 147 shows the acoustic return from Hoop 4 at various times over a seven-day period, from just before the oil was deployed, to when the oil began to be encapsulated (day 4), to a week after the release (Day 7). A more detailed description can be found below Figure 147.

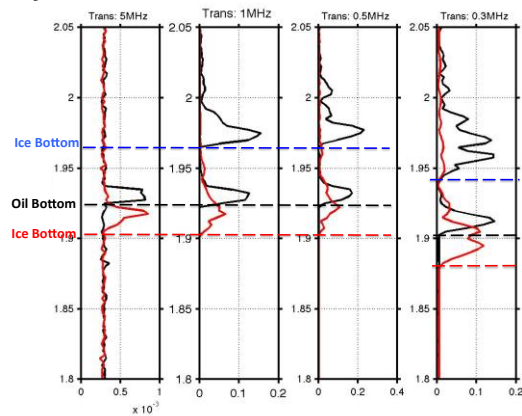
Day 0



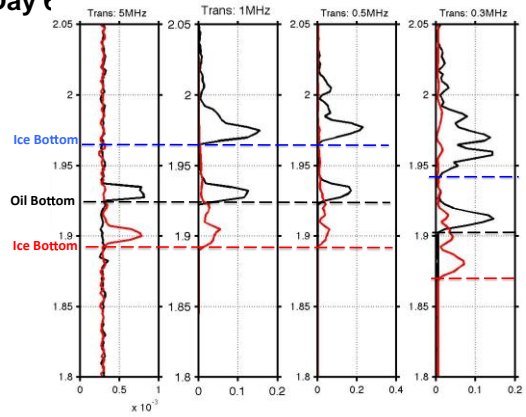
Day 4



Day 5



Day 6



Day 7

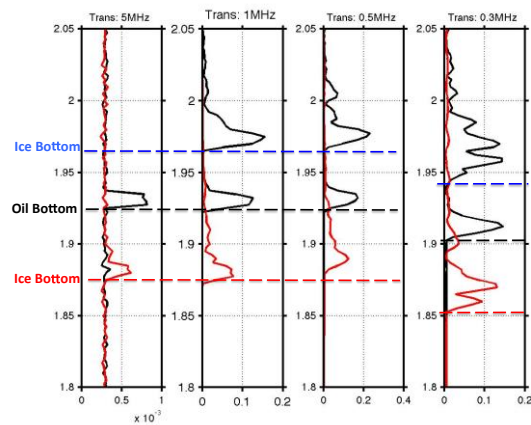


Figure 147. Acoustic returns under Hoop 4. Blue – ice bottom before oil injection, Black – return after release, Red – return on the sampling date.

Day 0: Oil was released under the ice at 12:45 pm. Before this release, the classic single-peak acoustic return from the ice bottom (blue trace) is observed; however, after the release, a two-peak return (black line) is detected. The first return (at 1.92 m) is the return from the bottom of the oil (water/oil interface), the second return (at 1.96 m) is from the ice bottom. The location of the ice bottom before (peak in blue line) and after the oil release (second peak in black line) is the same. This suggests that the oil and seawater have similar sound speeds.

Day 4: The first evidence of ice growth after the oil release occurred in Day 4. This can be seen by the first acoustic return in the red trace (Day 4: 102 hrs. after release), located slightly closer to the transducer head (about a centimeter) than the first acoustic return in the black trace (Day 0: 6 hrs. after release). This difference is due to ice forming below the oil layer, and therefore the sound hitting this “new” ice bottom first. From this figure, it looks like about 1 cm of ice has formed below the oil. This small amount of ice grown below the oil masks the acoustic from the original ice bottom from all transducers except the 0.3 MHz. The 0.3 MHz still obtains a clear return from the original ice bottom. Thus, as expected, the lower frequencies are able to penetrate the ice further.

The returns from the other transducers also showed noteworthy features. For example, the 5

MHz transducer showed a significant increase in acoustic return (peak height), whilst the 1 MHz and the 0.5MHz saw an increase in the width of the return peak. The increase in the width is particularly significant, as it suggests that we are receiving returns from the ice bottom (water/ice) and the ice top (ice/oil), of the ice that has grown below the oil. Taken together the resultant is a wider return to the acoustic reflection seen by the transducer.

Day 5: The ice that formed below the oil continued to grow during Day 5 and reached just over 2 cm below the location of the oil bottom (difference between the location of the red peak and black peak). Whilst there still was a slight increase in acoustic energy seen by the 0.3MHz transducer near the location of original ice bottom, it certainly is not as clear as in Day 4. This would suggest that the experimental conditions are near the limit of this system to detect oil encapsulated under sea ice through a clear return from the three interfaces involved, i.e. water/ice, ice/oil, and oil/ice. The Aquascat system is of a relatively low power and thus better signal penetration with a higher-powered instrument would be expected.

Day 6: The rate of ice growth increased, and the acoustic returns obtained during Day 6 suggest that the ice was located about 4 cm below the location of the oil bottom (difference between the location of the red peak and black peak). No clear evidence of the encapsulated oil can be seen in the acoustic return.

Day 7: The ice below the bottom of the oil was about 5 cm. No clear evidence of the encapsulated oil can be seen.

Figure 148 shows a summary of the acoustic returns seen by the four transducers for the period of November 21st to December 1st. During this time, about 12 cm of ice encapsulated the oil.

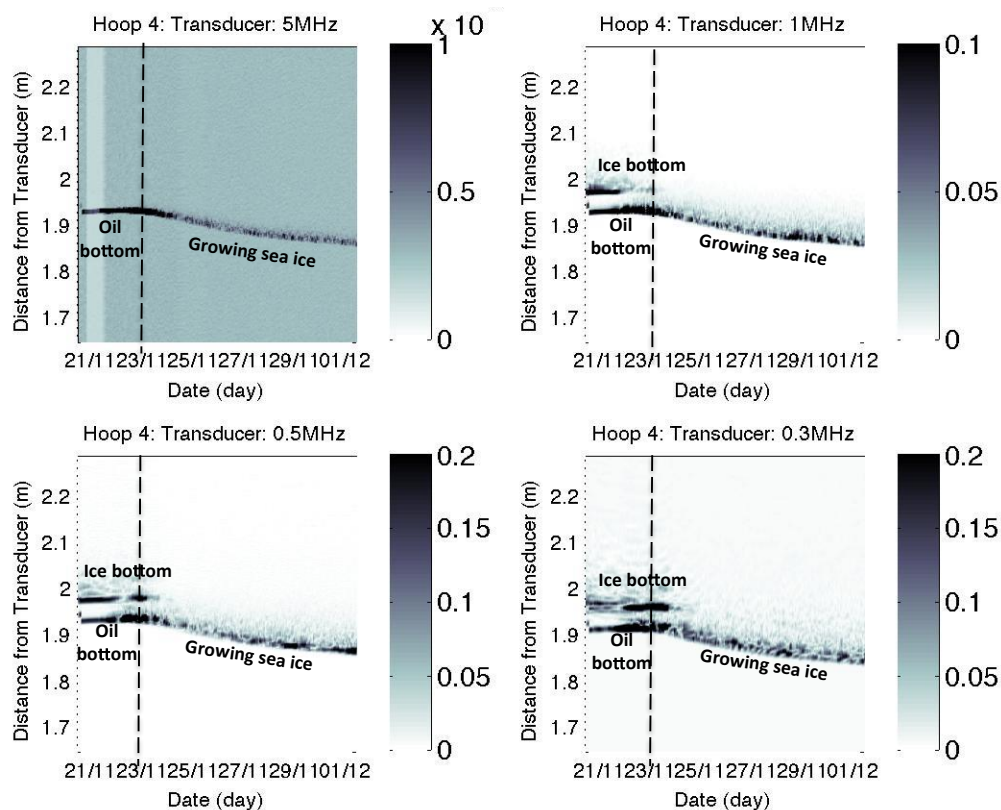


Figure 148. Time series of the raw acoustic returns from November 21st to December 1st. The black dotted line represents when the oil began to be encapsulated by the growing sea ice.

Hoop 5

The results from this particular hoop were mixed. High quality data was obtained just before and just after the oil release; however, beyond this time photographic evidence suggests that the resultant dataset was contaminated due to the continued release of bubbles from the instruments on the carriage. Consequently, results are shown before and after the injection occurred. A summary is as follows:

- AQUAScat programmed for hourly sampling
 - 5 MHz, 1 MHz, 0.5 MHz, 0.3 MHz transducers active
 - Sampling frequency: 1 Hz (ping every second) on the hour for 3 minutes.
 - Pulse length: 10 mm
- December 9th, 11:00:00. Pre-oil release survey
- **December 9th, 11:40:00. Oil released under the ice**
- December 9th, 12:00:00. Post-oil release survey
- Carriage parked under Hoop 5 during this time

For the Hoop 5 oil release, the underwater carriage was parked under the centre of the hoop. At 11:00 am, 40 minutes before the oil was injected, the acoustic returns were recorded from the four transducers. The blue line in Figure 149 shows the results before the oil release. Again, a single-peak acoustic return from the ice bottom is visible (blue trace). About 20 minutes after the oil release, a second survey was conducted. The results are also plotted in Figure 149. There clearly is a two-peak return (black line) after the oil release. The first return (at 1.65 m) is the return from the bottom of the oil (water/oil interface), the second return (at 1.71 m) is the oil/ice interface. The difference between the two returns, 6 cm, is the thickness of the oil located over the transducer.

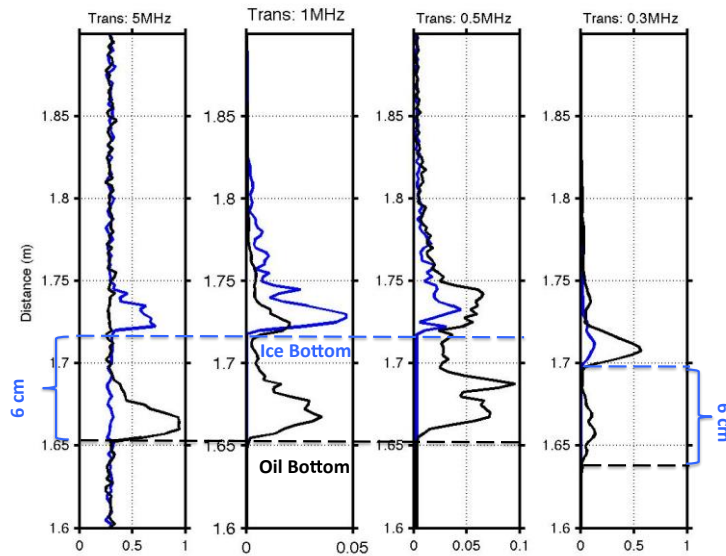


Figure 149. Blue trace shows the location of the ice bottom before the oil was deployed. The black line shows the location of the oil and ice bottom after the oil release. The difference between the two is the oil thickness, which is about 6 cm.

Hoop 6

The results from Hoop 6 are unique. This was because once the oil release had occurred in Hoop 6 the sea ice was allowed to warm. This allowed the vertical migration of the oil through the sea ice to occur. The net result was a reduction (over time) of the amount of oil under the ice. A summary is as follows:

- AQUAscat programmed for both hourly sampling as well as manual measurements:
 - 5 MHz, 1 MHz, 0.5 MHz, 0.3 MHz transducers active
 - Sampling frequency: 1 Hz (ping every second) on the hour for 3 minutes.
 - Pulse length: 10 mm (plus manual variations: 2.5 mm, 5 mm, 10 mm, 20 mm, and 40 mm.
- January 6th, 12:47:30. Pre-oil release survey
- **January 6th, 13:50: Oil released under the ice**
- January 6th, 14:48:50. Start Post-oil release survey
- January 8th, 10:26:29: Moving survey of oil
- February 9th, 12:00:00. Finish of Post-oil release survey

After the oil was released but before the ice was allowed to warm, a moving survey of the oil contained within Hoop 6 was performed. This was achieved by moving the carriage under the hoop, with the AQUAscat turned on. This kind of operation mimics that of an autonomous underwater vehicle. The results can be seen in Figure 150. The experiment was performed on January 8th at 10:26 am.

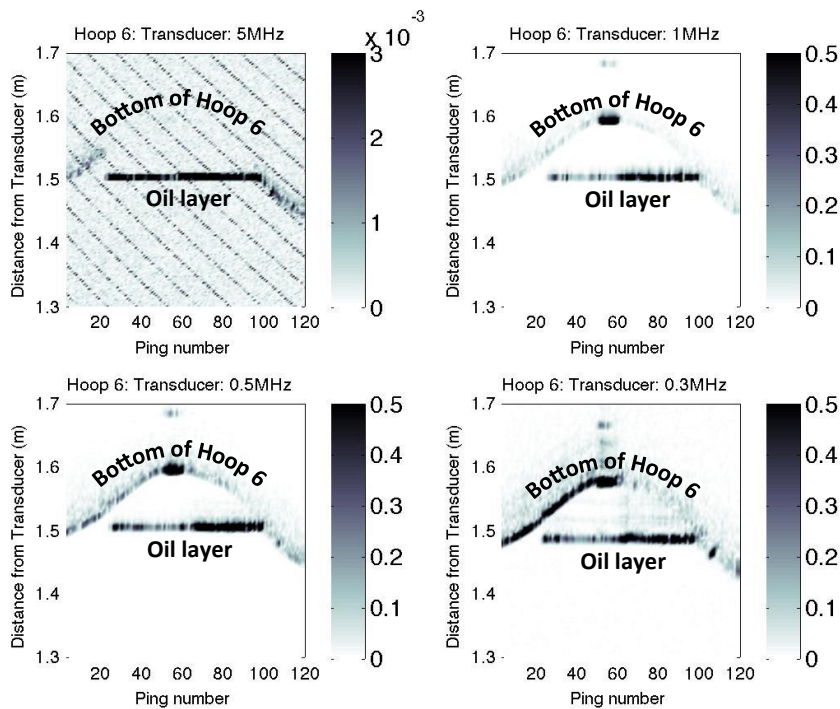


Figure 150. Raw acoustic returns from the moving trolley under Hoop 6. In all but the 5MHz both the ice bottom and the oil bottom can be clearly seen.

This figure shows the raw returns from the four transducers. In all but the 5 MHz transducer, a clear return from both the bottom of the oil (water/oil interface) as well as the bottom of the ice (oil/ice interface) was observed. Only the raw returns are shown in the figure and further processing could enhance the interfaces better.

Oil migration

In order to better understand the vertical migration of oil through sea ice, the temperature in the test basin room was raised to just above freezing. As sea ice warms, oil is able to migrate upward through the ice lattice to the ice surface. Figure 151 covers the period January 6th to February 9th. This includes the period before the oil was released, after the release, and the time the ice was warming up. Within this figure, the acoustic returns from both the ice bottom and the bottom of the oil are visible. The black dotted line represents the time oil began to migrate from the bottom of the ice to the surface. This occurred from the January 16th and continued until the recording finished on the February 9th. During this time, the oil under the sea ice thinned at a very consistent rate, reducing from about 9 cm to less than 2 cm.

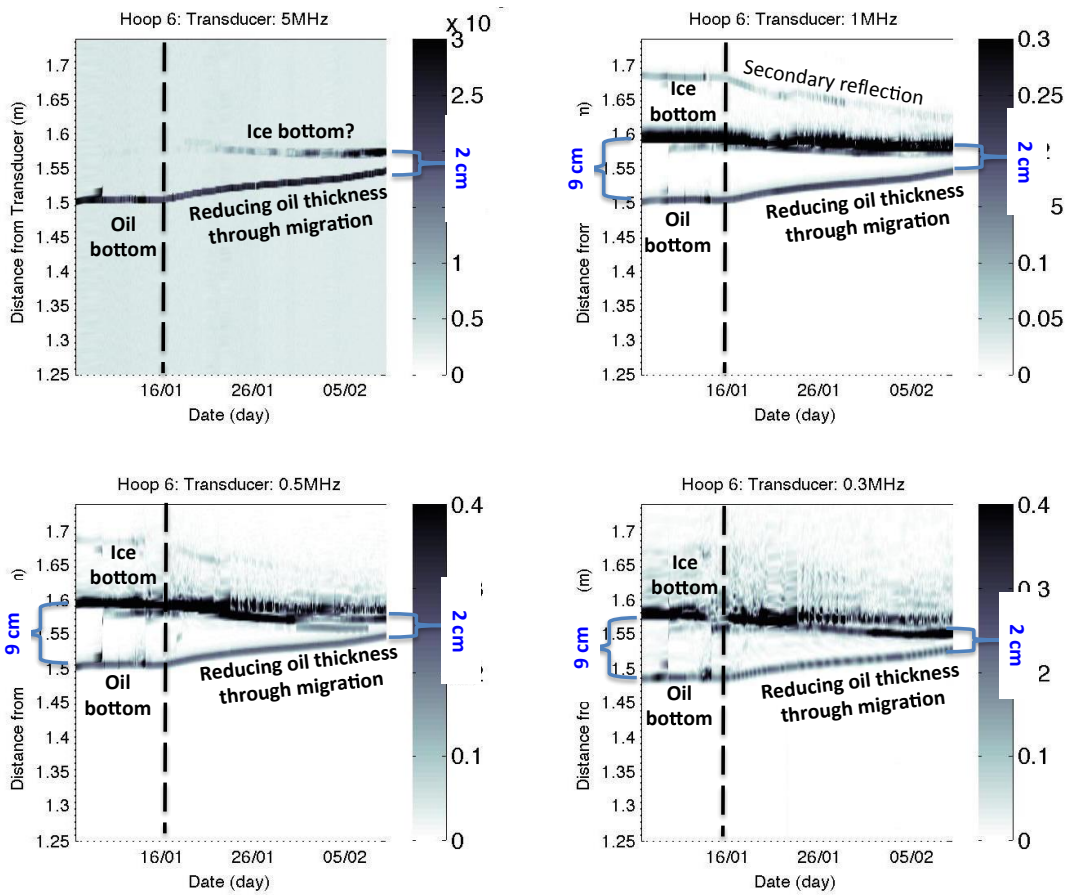
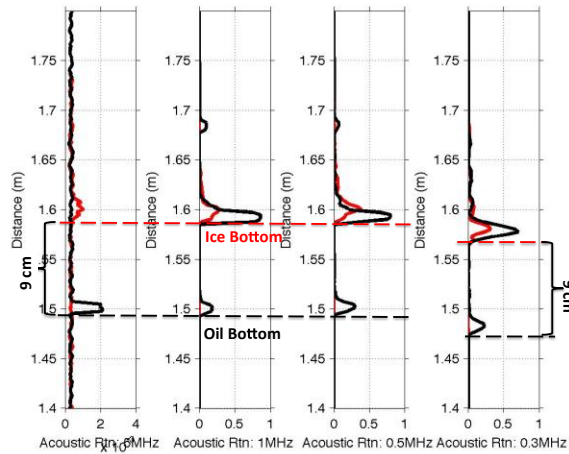


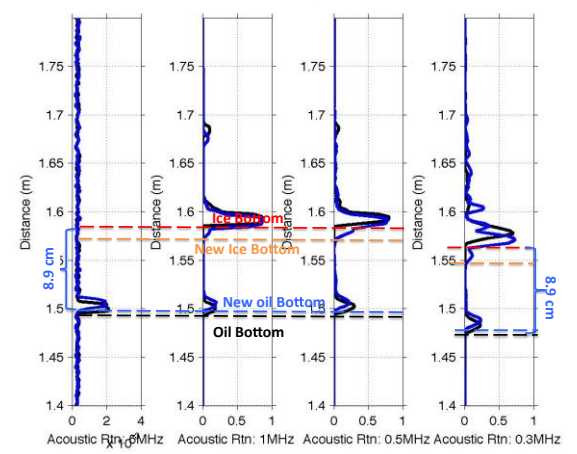
Figure 151. This figure shows the slow draining of oil under Hoop 6, from an initial thickness of about 9 cm to final thickness of around 2 cm. All transducers display this same retreat in oil thickness.

The reduction of oil thickness under Hoop 6 can be seen more clearly in Figure 152. This figure displays the acoustic return on the day of the injection (Day 0), 10 days after, 20 days after, 26 days after, and 34 days after the injection.

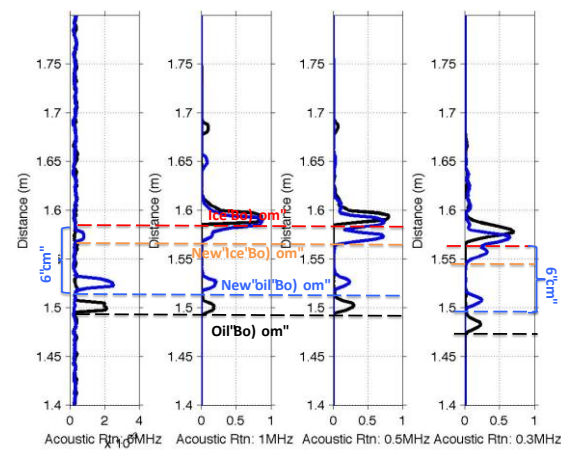
DAY 0: Red line: Pre-oil delivery: 06-Jan-2015 12:47:30
 Black line: Post-oil delivery: 06-Jan-2015 14:48:50



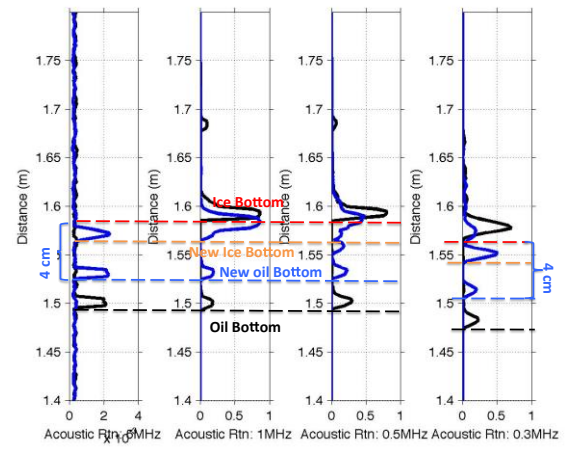
DAY 10: Black line: Post-oil delivery: 06-Jan-2015 14:48:50
 Blue line: Post-oil delivery: 16-Jan-2015 15:00:00



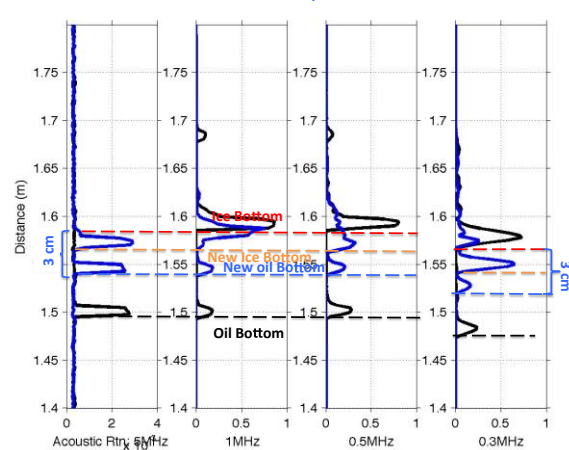
DAY 20: Black line: Post-oil delivery: 06-Jan-2015 14:48:50
 Blue line: Post-oil delivery: 26-Jan-2015 17:00:00



DAY 26: Black line: Post-oil delivery: 06-Jan-2015 14:48:50
 Blue line: Post-oil delivery: 01-Feb-2015 15:00:00



DAY 34: Black line: Post-oil delivery: 06-Jan-2015 14:48:50
 Blue line: Post-oil delivery: 09-Feb-2015 10:18:06



Top Left: Mean acoustic return before the oil release (in red) and after the oil release (in black).

Top Right: Mean acoustic return 10 days after the oil release. This plot shows the first stages of oil thickness reduction, about 0.1 cm. We also see the first stages of a new reflection just below the original ice bottom.

Middle Left: Mean acoustic return 20 days after the oil release. The oil thickness has reduced by about 3 cm. The reflection of the 'new' ice bottom has become stronger and can now be seen in the 5 MHz. Reflection from original ice bottom is still apparent.

Middle Right: Mean acoustic return 26 days after the oil release. The oil thickness reduced by about 5 cm. The reflection of the 'new' ice bottom has become more dominant.

Bottom Left: Mean acoustic return 34 days after the oil release. The oil thickness has reduced by about 7 cm and is only 2 cm thick. Still strong return by new ice bottom.

Figure 152. Mean acoustic return from the 1 MHz transducer over a 3 min recording cycle

One feature of the reduction of oil under Hoop 6 was the creation of a “new” ice bottom located just below the original ice bottom (orange line in Figure 152). This secondary bottom may in fact not be ice but could be due to a layer of brine that drained out of the warm sea ice, i.e. as the oil migrates upward, heavier brine moves downwards. This brine forms a new layer between the original ice bottom and the oil. Further investigation is needed to better understand this process.

4.2.7 *Broadband Sonar*

Hoop 1 – Injection 1

Injection 1 was performed under a layer of brash ice. The topography of the brash ice was rough so range from the instrument to the water/ice interface is poorly defined in comparison to a consolidated, columnar ice sheet. The acoustically inferred range to the surface varied from approximately 1.95-2.05 m, suggesting an ice thickness of 10-20 cm (prior to freezing the range was 2.15 m). Figure 153 includes normal incidence scattering results (envelopes and spectra) prior to and after the oil injection. Figure 153a shows that the envelopes of the low- and mid-frequency channels have multiple significant returns, suggesting that portions of the ice extended well below the other frazil/brash ice cover. The high-frequency channel appears less complicated, which could be a consequence of a relatively narrow (3.4°) beam width (hence the transducers could have been observing a smooth portion of the ice). Figure 153b includes the scattered spectrum prior to the oil injection. The spectra appear highly unstructured as a consequence of having a rough surface with protruding ice blocks. Figures 153c and 153d include the envelopes of the compressed pulse output and spectra following the oil injection. Just as before the injection, the low- and mid-frequency channels are highly irregular and difficult to interpret due to the roughness of the brash ice; however, the high-frequency channel envelope (Figure 153c) exhibits two dominant peaks that could be attributed to buoyant oil trapped below the ice although the frequency domain results remain complicated. These results suggest that, given the roughness of brash ice, high-frequency scattering techniques may be able to detect oil under smooth portions of brash ice but that verifying the presence of oil would require another technique capable of confirming its presence.

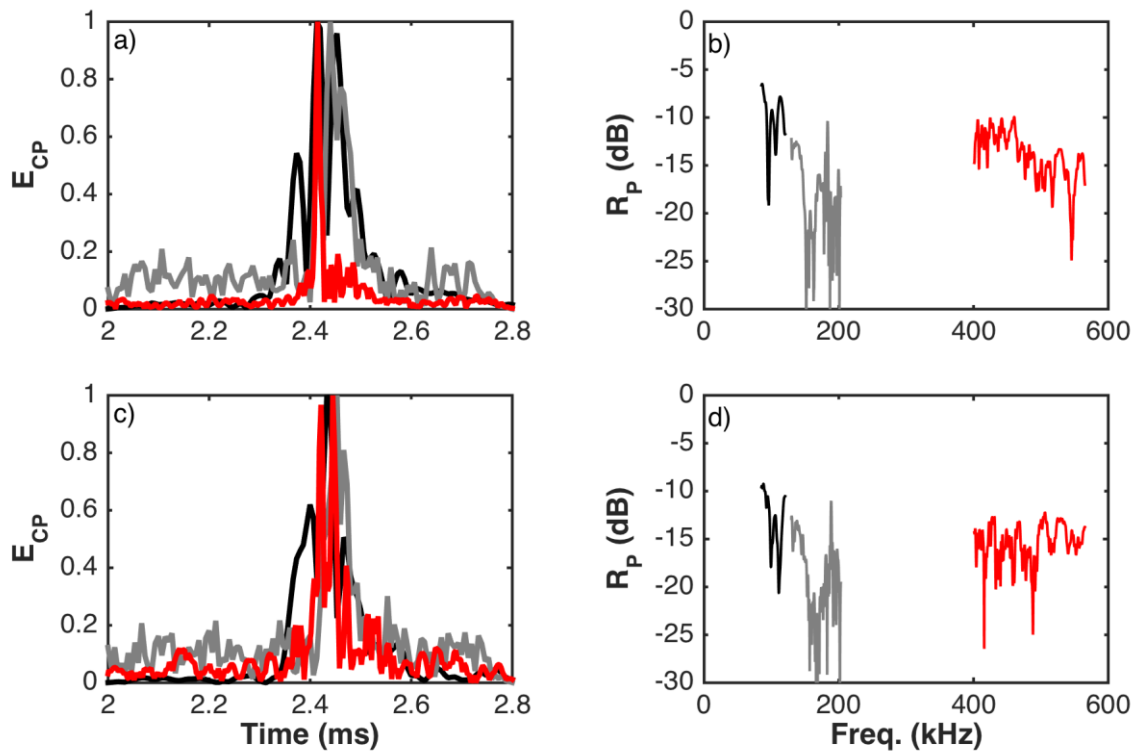


Figure 153. Hoop 1. Low-frequency channel (black), mid-frequency (gray), high-frequency (red). The mid-frequency channel was relatively noisy as a result of having improperly setup the channels. This was remedied before other injections.

Hoop 2

The injection under Hoop 2 was performed using a relatively small amount of oil with the intention of creating a thin layer of oil. Figure 154 includes the compressed-pulse output and spectra both prior to and within two hours following the oil injection. These results exclude the low-frequency channel due to noise problems that were solved before the oil injections. The lack of the low-frequency data does not affect the interpretation of the results. Figure 154a shows that the temporal domain results prior to the oil injection include a single peak associated with the water/ice interface. The scattered spectra (Figure 154b) from the water/ice interface is relatively low amplitude ($R < -10$ dB) and highly irregular. Results following the injection, however, are well structured and easier to interpret. In the temporal domain (Figure 154c) the mid-frequency channel includes a single peak while the high-frequency channel includes two clear peaks. The two peaks in the high-frequency channel are the result of the water/oil and oil/ice interfaces. Using a sound speed of oil of 1450 m/s, the oil layer is approximately 1 cm thick. The lack of two peaks in the mid-frequency channel is a result of the lower temporal (range) resolution of the channel, which is proportional to the bandwidth of the transmitted signal. In frequency-space, the mid-frequency channel does not reveal the presence of the oil layer because it is not resolved in the temporal domain. The high-frequency spectrum (Figure 154d), when compared to the pre-oil spectrum, appears highly structured with a clear null pattern attributed to the multiple interfaces. It is also noteworthy that amplitude of the frequency-spectra in the high-frequency channel increased by nearly 5 dB after the oil injection. These results demonstrate that higher-bandwidth signals increase the ability to resolve two interfaces although transmitting high frequency signals with more bandwidth can complicate the interpretation of the results (Bassett, 2014).

Following the injection, the oil migrated to the edges and outside of the hoop. This migration was attributed to a decrease in ice thickness near the edges of the hoop because of the containment skirts. Visual observations indicated that by the morning following the injection only small puddles of oil were scattered below the ice in the center of the hoop. The results presented in Figure 154 were obtained prior to and within two hours of the injection. Results obtained the following morning after that oil had migrated did not indicate the presence of the oil layer (i.e., only a signal peak attributed to the water/ice interface was present in the temporal domain data).

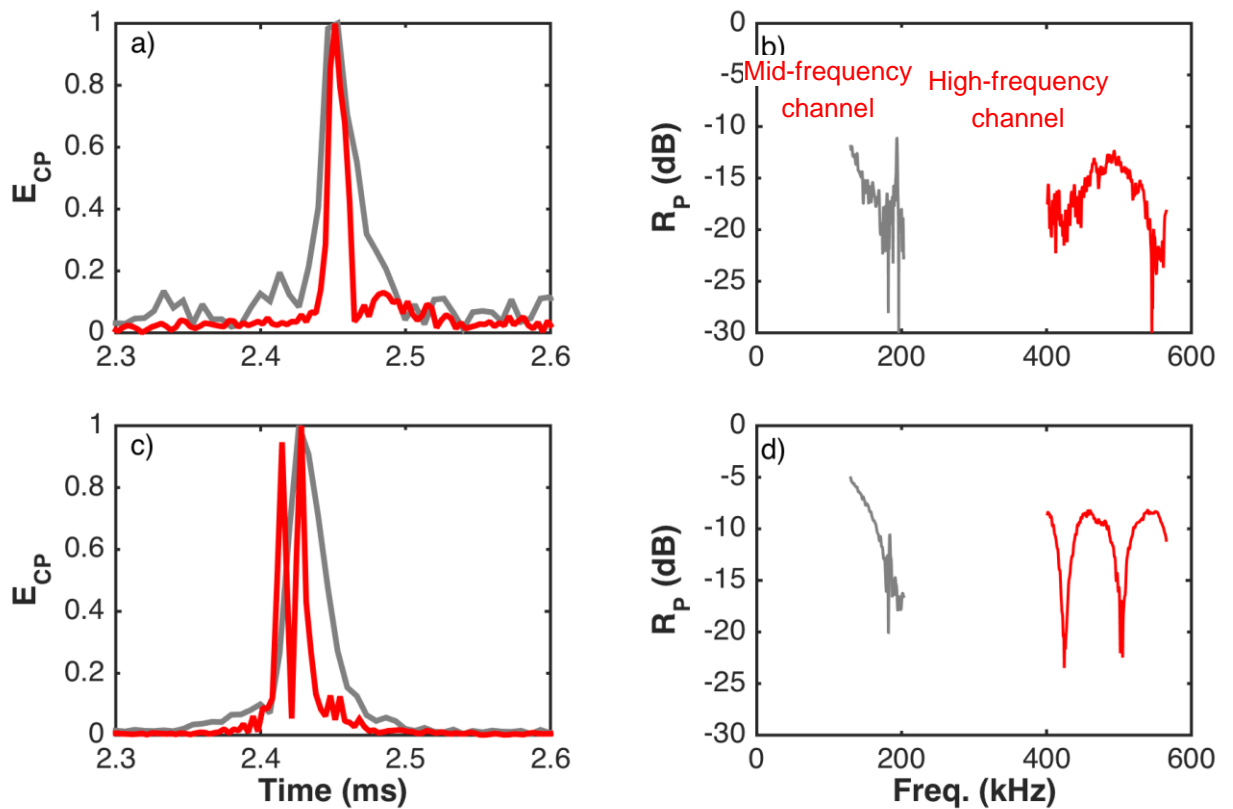


Figure 154. Hoop 2. Mid-frequency channel (gray), high-frequency channel (red). (a) E_{CP} prior to the oil injection. The single peak in both channels is a result of the water/ice interface. (b). The scattered spectrum prior to the injection. (c) Normalized E_{CP} less than two hours after the injection. The high-frequency channel resolves two peaks associated with the water/oil and oil/ice interfaces while the mid-frequency channel only resolves one interface due to its lower bandwidth. (d) The scattered spectrum in the high-frequency channel exhibits null patterns associated with the presence of an oil layer while the mid-frequency channel does not due to the lower bandwidth.

Hoop 3

The injection under Hoop 3 was similar to that under Hoop 2 although a larger quantity of oil was injected. Unfortunately, air was accidentally released under the hoop during the oil injection. Being a strong scatterer, the presence of the air layer under the ice makes it impossible to identify the presence of an oil layer. Figure 155 includes results for the compressed-pulse output and spectra

before and after the oil injection. Prior to the injection, the results are comparable to other ice-only measurements. That is, the temporal domain data suggest the presence of a single interface while the spectra are unstructured and difficult to interpret. Following the oil/air injection, the results (Figure 155c) still suggest the presence of a single interface. The spectra are consistent with a reflection coefficient of nearly 1 (0 dB), which is a clear indication of the presence of air under the ice.

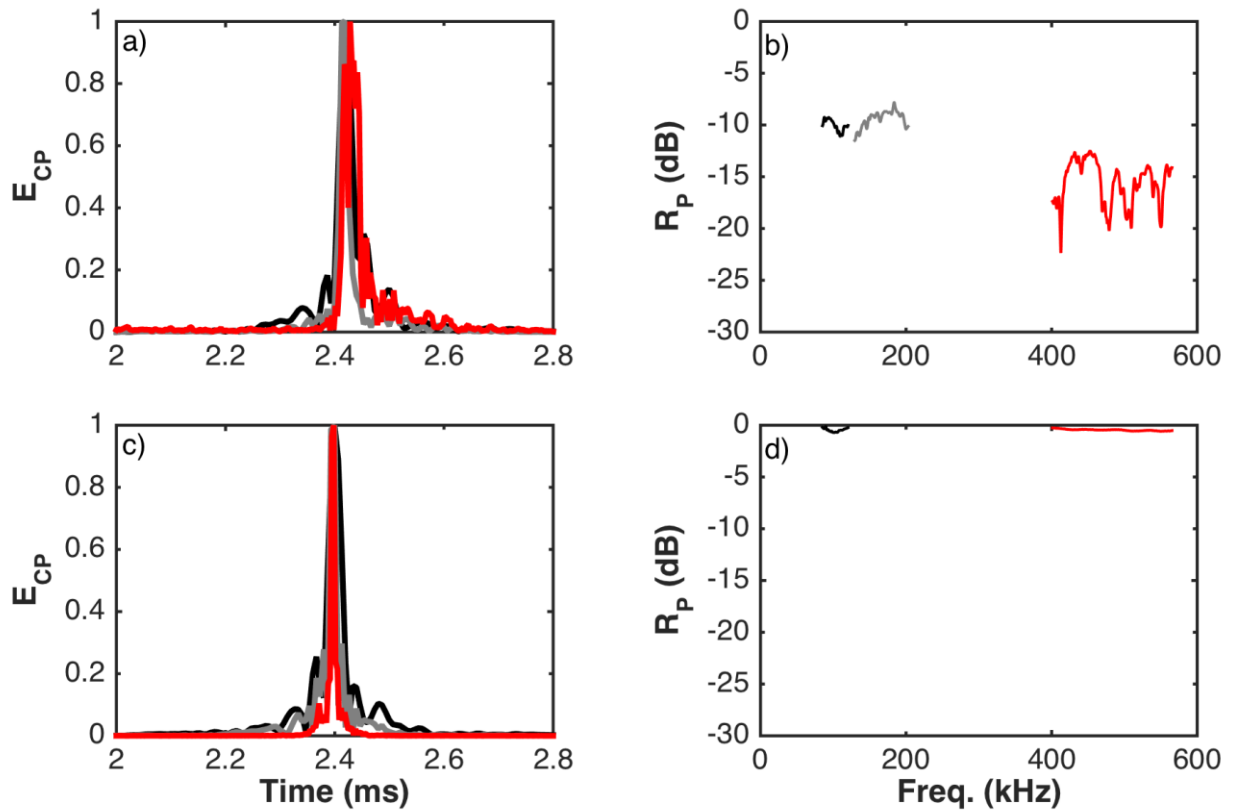


Figure 155. Hoop 3. Low-frequency channel (black), mid-frequency channel (gray), high-frequency channel (red). (a) Normalized E_{CP} prior to the oil injection. The single peak in both channels is a result of the water/ice interface. (b) The scattered spectrum prior to the injection. (c) E_{CP} immediately after the injection. Unlike other injections, a single interface was resolved due to the strong scattering from the air. (d) The scattered spectrum indicated a reflection coefficient of 1 (0 dB), clearly indicating the presence of the air.

Hoop 4 and 5

For simplicity, the results from Hoops 4 and 5 have been combined. They were the most successful injections of the experiment and, as a result, were analyzed in the greatest detail. Prior to presenting the results, it should be noted that Hoops 4 and 5 were analyzed, in part, by “mapping” under the injections with the cart moving at 3 m/min and the acoustic system sampling at a rate of 10 pings/second per channel. Because insulation had been placed over the ice of Hoops 3-6, the oil pooled under the center of the hoops. Near the edges where the ice was thicker, the oil layer was thinner, thus permitting an analysis of the performance of the system with multiple

oil thicknesses. In addition to presenting individual pings, this section includes a figure obtained while “mapping” under Hoop 5, the results of encapsulation, and describes a caveat to the interpretation of the encapsulation results.

Figure 156 includes compressed-pulse outputs and spectra for 200 pings obtained while transmitting under ice in addition to results for five inferred oil thicknesses obtained during a transect under Hoop 4. Figure 156a includes temporal domain results for a single ping under the ice prior to the oil injection. These results are again consistent with previous observations; a single peak is present and attributed to the water/ice interface. Figure 156g includes an average scattering spectrum derived from 200 pings during a transect between Hoops 4 and 5. As shown later, the average amplitude of scattering from the ice is lower than that observed under oil layers.

All subfigures in Figure 156 (excluding panels a and g) represent oil layers of different thicknesses. These results are consistent with the results from Hoop 2 prior to the oil migration out of the containment hoop. When the oil layer is sufficiently thick, all channels in the temporal domain can resolve it. The range resolutions for identifying oil layers using the different frequency transducers are 2.2 cm, 1.5 cm, 0.7 cm for the low-, mid-, and high-frequency channels, respectively. That is, a layer thinner than those respective resolutions will result in a single peak in the temporal domain; however, when the oil thickness exceeds those thicknesses, both interfaces can be clearly resolved. Note, these resolutions are a function of sound speed and, as a result, and temperature affect the range resolution though only by a relatively small amount. In the frequency domain, the results are all well-structured (they exhibit the expected null structure attributed to the two interfaces) in comparison to scattering from the ice alone. Just as the time delay between the returns from the interfaces in the temporal domain can be used to infer the oil thickness if the sound speed is known, the spacing between the nulls in frequency space can be used to infer the oil thickness. A decrease in the spacing between the nulls is indicative of a larger oil layer.

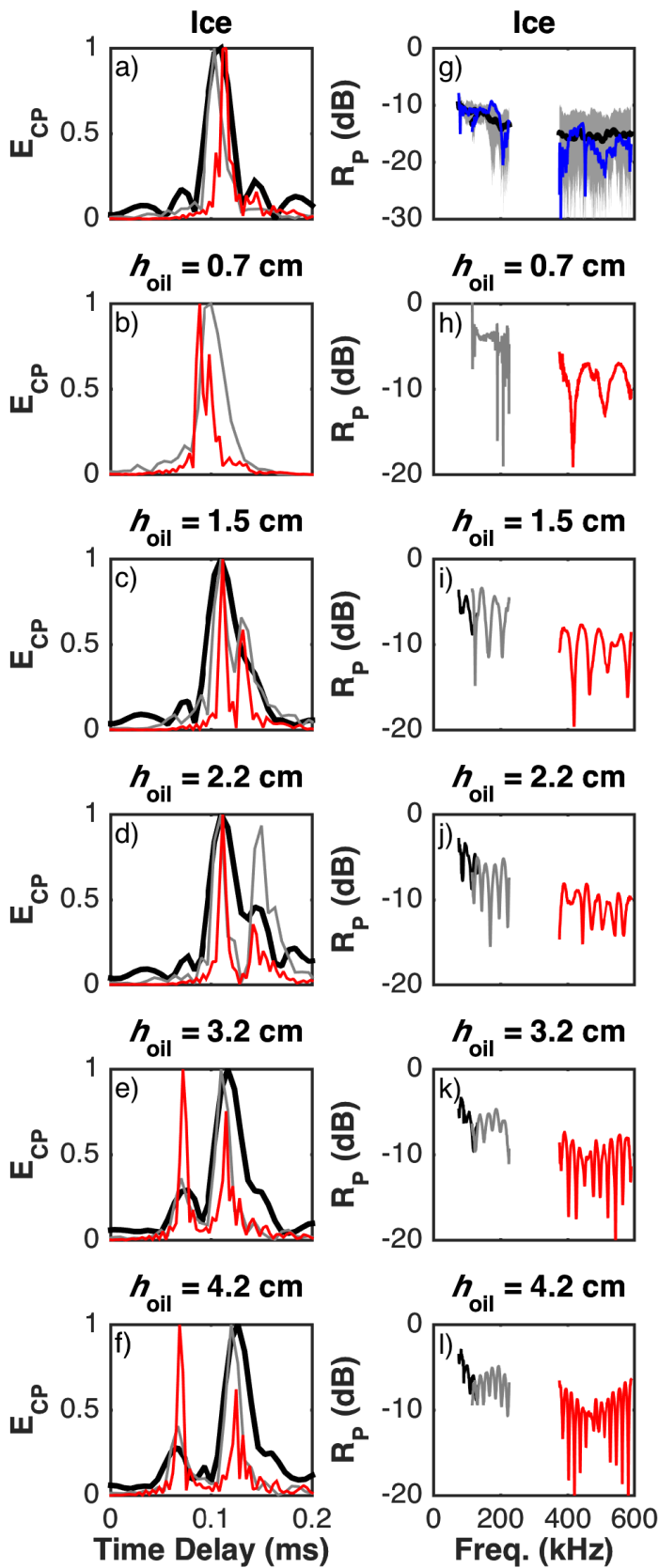


Figure 156. Hoops 4 and 5. Low-frequency channel (black), mid-frequency channel (gray), high-frequency channel (red). (a) Normalized E_{CP} for a single ping prior to the oil injection. (g) Scattering spectra from the ice obtained during a transect between Hoop 4 and 5. Two hundred pings (gray) are used to produce the average spectrum. The spectrum of a single ping is shown in blue. (b-f) E_{CP} for different oil thicknesses. Two peaks can be resolved when the oil layer is present and thicker than the range resolution of the channel. (h-l) Frequency spectra under different oil thicknesses. The predictable null structure observed under the oil layer can be used to estimate the thickness of the oil.

An example of the potential to map oil thicknesses based on observations from Hoop 4 is included in Figure 157. A contour of the compressed-pulse output from the high-frequency channel (Figure

157a) shows the presence of the oil layer while under the hoop; outside of the hoop, only a single layer is present. Due to the insulation, the thickness of the oil layer is constantly changing during the transect. Figure 157b includes a spectrogram for the individual pings as the cart transits under the hoop. While outside of the hoop, the spectra again appear unstructured while the observations under the hoop show a clear null structure that can be followed by eye as the oil thickness changes. Using the temporal and frequency domain data, the observations were inverted to estimate the oil thickness (Figure 157c). The results compare favorably suggesting that, at least under controlled conditions, algorithms for detecting oil layers and estimating their thickness could be automated.

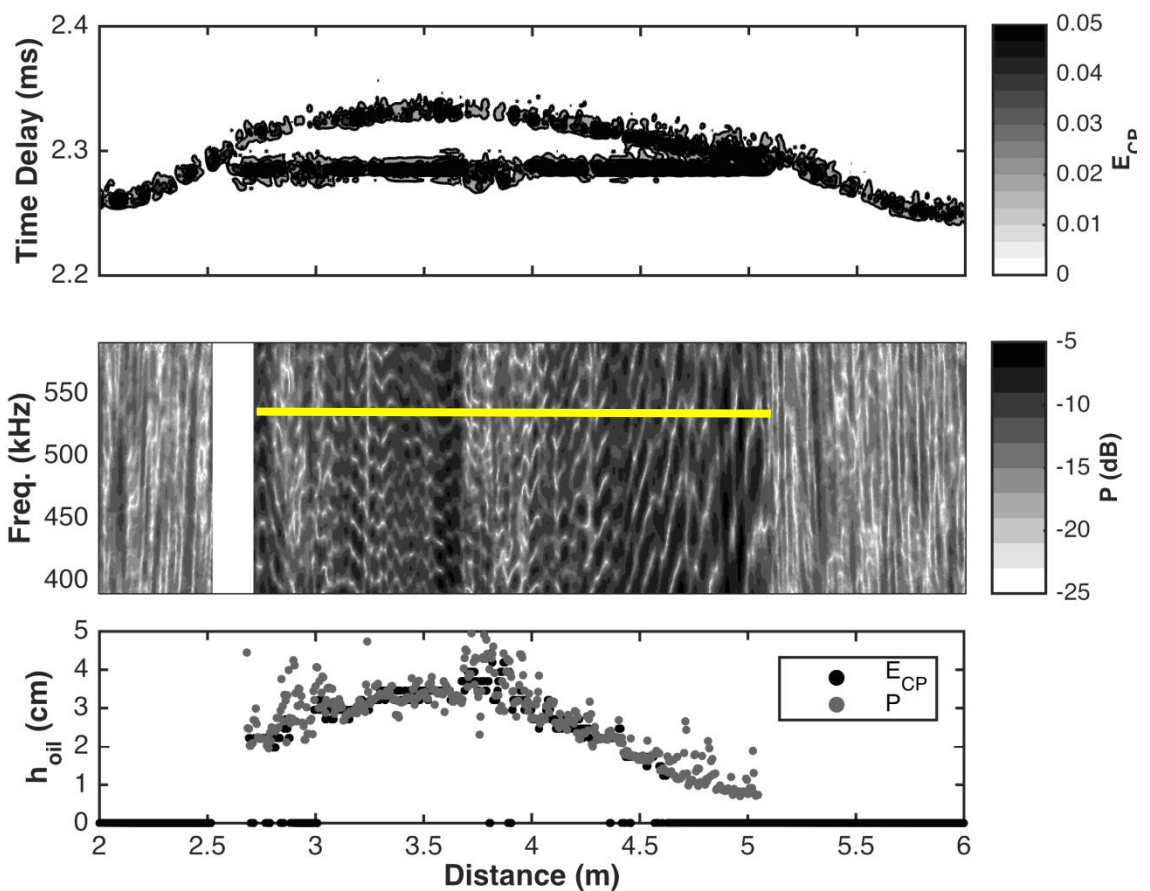


Figure 157. Hoop 4 spill map. (a) A contour of the compressed-pulse output from the high-frequency channel during a transect under Hoop 4 prior to encapsulation. The oil layer is clearly present while under the hoop. (b) A spectrogram. While outside of the hoop, the spectra are relatively unstructured. While under the hoop, the null structure associated with the two interfaces can be easily followed by eye (area of yellow line). (c) A comparison between the inferred oil thicknesses from the temporal and frequency domains.

The injections under both Hoops 4 and 5 were used to identify the potential of this system to detect encapsulated oil layers. Envelopes obtained using the low-frequency channel prior to and for 160 hours following the Hoop 4 injection are included in the top panel of Figure 158. Immediately below, a cartoon is provided to aid in the interpretation of the envelopes. Finally, the figure includes temporal domain results at regular intervals prior to and during encapsulation for the low- and mid-frequency channels. High-frequency results were not included because

encapsulation was not observed at any point, a fact that is attributed to a combination of increased scattering from and absorption in the skeletal layer at high frequencies. While the presence of the oil layer prior to encapsulation in the temporal domain can be inferred from the presence of two peaks (interfaces), encapsulation can be identified by searching either two or three peaks; given that under columnar ice alone only a single peak is present, any additional peak is indicative of another scatterer/interface. By acoustically inferring the ice growth, it was determined that oil could be detected with up to 7 cm of ice below it. This result, however, likely underestimates the true potential for detecting encapsulated oil because of the low power transmitted and high attenuation in the ice.

It should be noted that the sound speed of ice is about twice that of seawater or oil. This leads to what appears to be a crude oil layer that moves closer in time as shown in Figure 158. After the difference in sound speed is accounted for, the actual distance to oil layer remains constant.

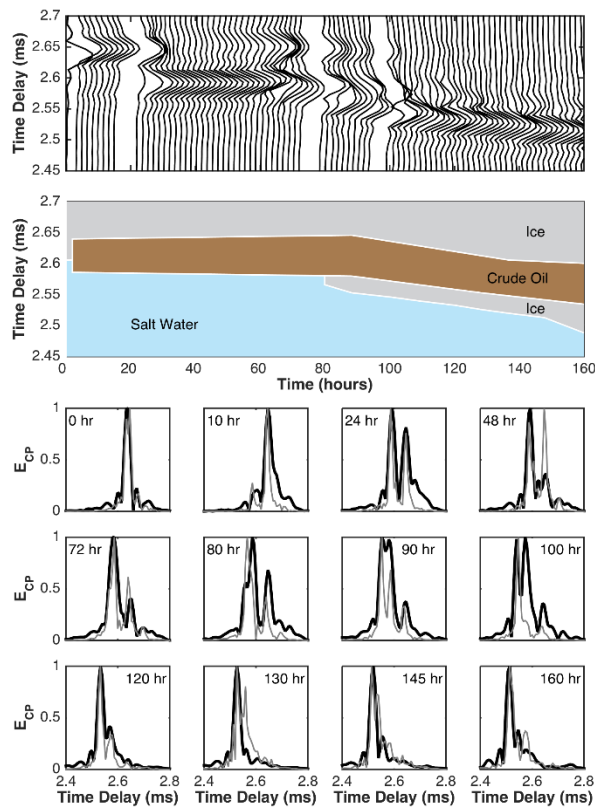


Figure 158. Encapsulation data from Hoop 5.

Figure 159 includes an image obtained December 12th under Hoop 4 using the video camera on the underwater carriage. The bottom interface clearly shows the outline of the various instruments present on the cart. Upon noticing this outline, the camera observed numerous bubbles floating towards the surface and that the cart and instruments were covered in bubbles, which were creating the bubble outlined image in the bottom of the hoop. The logical interpretation is that the bubbles floated to the ice interface where they had been interfering with scattering measurements. Given that bubbles scatter acoustics strongly, the high density of bubbles at the water/ice interface would effectively interfere with observations of encapsulation. Encapsulation results under Hoop 5 suffered from the same accumulation of bubbles at the ice interface and

thus provide no further insight into the potential for using broadband acoustics to detection encapsulation oil. Nonetheless, the results in the following section (Hoop 6) indicate that the signals can effectively observe scattering from the ice/air interface with much thicker ice layers, suggesting that the potential for detecting encapsulated oil was affected by the bubble accumulation.



Figure 159. Bubbles on under-ice surface, under Hoop 4. The high density of bubbles interfered with the acoustic scattering.

Hoop 6

The injection under Hoop 6, similar to Hoops 4 and 5, effectively demonstrated the effectiveness of broadband, acoustic scattering techniques at normal incidence for detecting layers of crude oil under congelation ice. The injection under Hoop 6 resulted in an oil layer (inferred acoustically at the center of the hoop) that was over 8 cm thick. Figure 160 includes the temporal- and frequency-domain results prior to and following the injection. Prior to the injection, the results are consistent with those from pre-injection observations from other hoops (Figures 160a and b). Likewise, following the injection, the results were consistent with the post-injection observations from Hoops 4 and 5. Given that the oil layer was thicker under Hoop 6, the time delay between peaks in the temporal domain was greater and the spacing of the nulls in frequency-space was smaller. Notably, Figure 160c includes a minor peak near 2.8 ms. This peak is associated with the ice/air interface, clearly indicating that the low-frequency channel is capable of penetrating through a relatively thick layer of ice; the acoustically inferred ice thickness prior to the oil injection was approximately 60 cm. Here, results in the temporal domain are presented in linear-space given the comparable amplitudes of the reflections from the water/oil and oil/ice interfaces. Nonetheless, analysis in log-space generally reveals a return from the ice/air interface, which was observed outside of hoops with ice thicknesses as large as 70 cm.

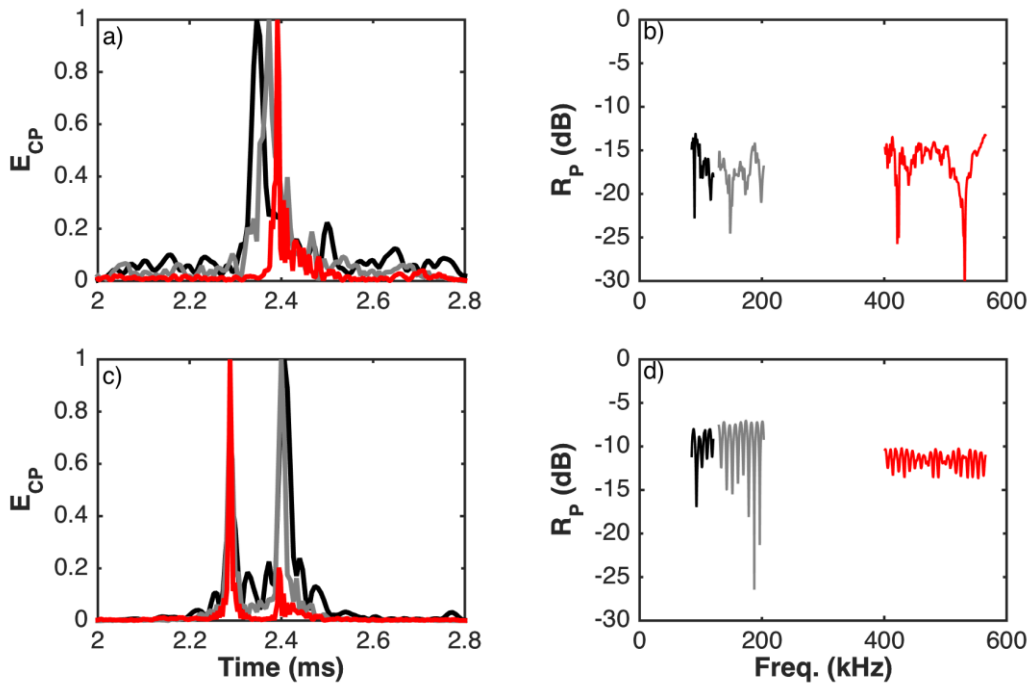


Figure 160. Hoop 6. Low-frequency channel (black), mid-frequency channel (gray), high-frequency channel (red). (a) Normalized E_{CP} prior to the oil injection. (b). The scattered spectrum prior to the injection. (c) Normalized E_{CP} after the injection. (d) The scattered spectrum showing the predictable null structure.

Following the injection in Hoop 6 the temperature in the facility was increased. The oil under Hoop 6 was continuously monitored during the melting period to observe any changes in the scattering from the oil beneath the ice. Figure 161 temporal (presented as a function of range assuming a sound speed of 1437 m/s) and frequency domain results from five different times during the melt out period. The first column of Figure 161 shows the results from January 7 at 13:00, prior to the melt out. As in Figure 160, the temporal domain results suggest an oil thickness of more than 8 cm. Rows 2-5 show the results for four other times; January 12th at 03:00, January 19th at 03:00, January 24th at 07:00, and January 30th at 09:00. Throughout this period the time distance between the peaks decreases, suggesting buoyant oil is migrating to the surface through the brine channels, which is consistent with photographic evidence. Beginning in the third row (January 19th) the results become increasingly complex; rather than two clear returns from the water/oil and oil/ice interfaces, additional returns are present. Without further evidence, it is only possible to speculate on the origin of these additional returns. They could be a result of multiple interface scattering, although under those circumstances, a proportional decrease in the amplitude would be expected with arrival, which does not occur in the results. It is also possible that the multiple returns could be a result of an additional interface being present. Such an interface could arise from water draining through from the ice that ends up being trapped between the oil salt water in the tank. Over time, the frequency spectra grow increasingly complex, reflecting the presence of the multiple returns present in the temporal-domain results.

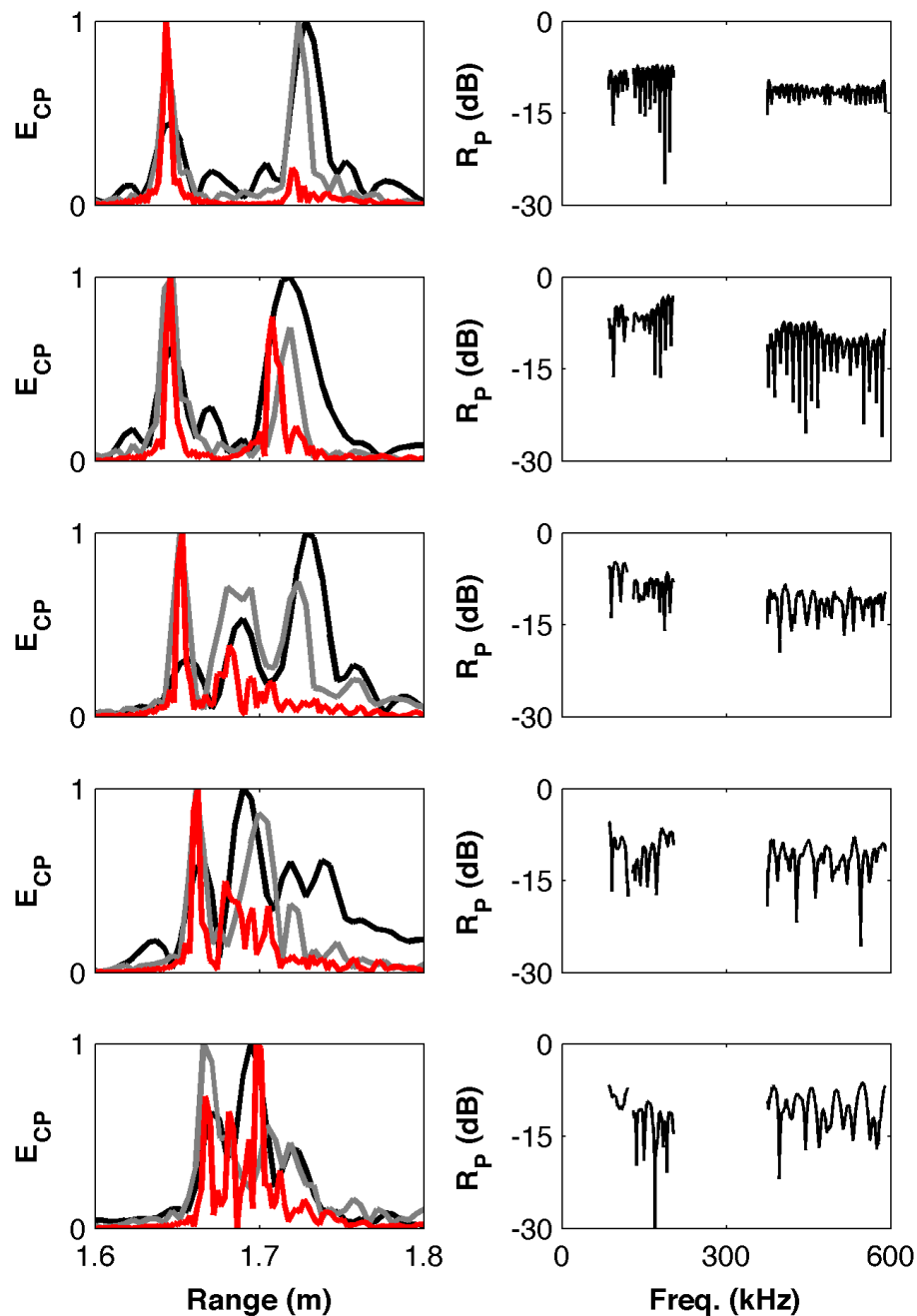


Figure 161. Temporal and frequency domain results from Hoop 6 while monitoring the melt-out stage. Column 1-5: January 7th at 1300; January 12th at 0300; January 19th at 0300; January 24th at 0700; January 30th at 0900. As time passes, the thickness of the oil layer decreases suggesting upward migration of the oil through the open channels. The increasing complexity (more than two peaks) of the returns in the temporal domain indicate either multiple scattering or the presence of additional interfaces such as a trapped water layer between the oil and ice. Without further evidence the origin of these additional returns is strictly speculation.

4.2.8 Multibeam Sonar

Because of the length of the isolation hoop skirt, the low angle of the Forward Looking Sonar (FLS) (30° from horizontal), and the thin ice conditions during the first injection, the FLS was only

able to image a portion of Hoop 1 (Figure 162). The surface observed with FLS seems very irregular and no apparent large patches of oil can be seen.

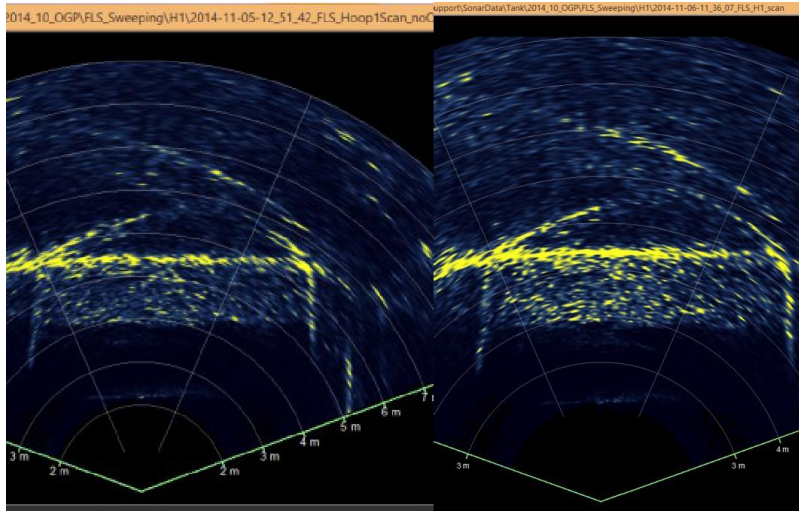


Figure 162. Before injection (left) and after injections (right)

Mixing of the ice during the injection created considerable uncertainty in the bathymetry of the slush-block ice mixture. The movement of the ice was likely the cause of small differences in bathymetry that were observed using the difference of surveys before and after the injection. The rough slush ice mixture showed no specular return that was characteristic of the flat ice in other hoops. There is some indication that oil may have been detected using the nadir beams (Figure 163).

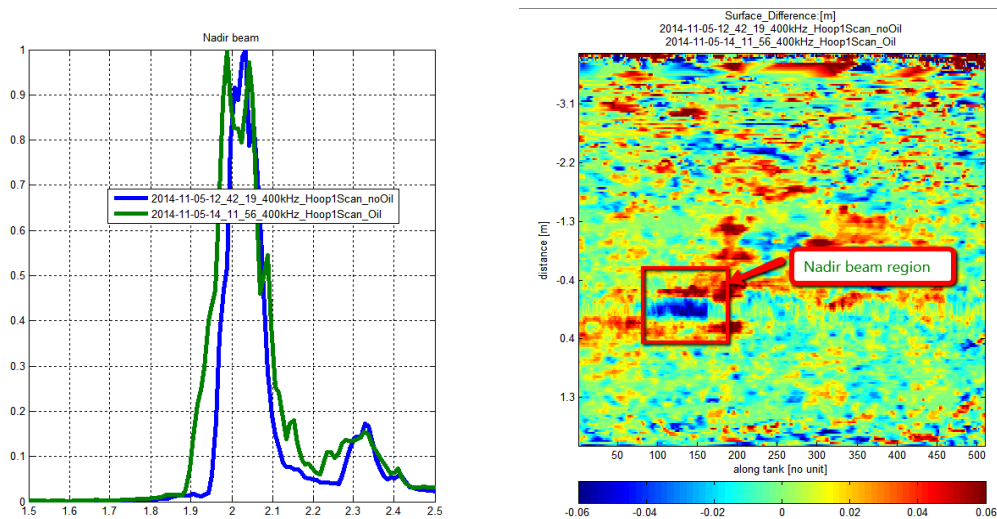


Figure 163. The nadir beam in the point (left) referenced by a surface difference map (right) showing possible double reflection from the oil and ice.

Hoop 1 – Injection 2

Because of the greater ice thickness, the FLS was able to image a greater portion of the hoop. However little difference was observed in the FLS signal after oil was injected (Figure 164).

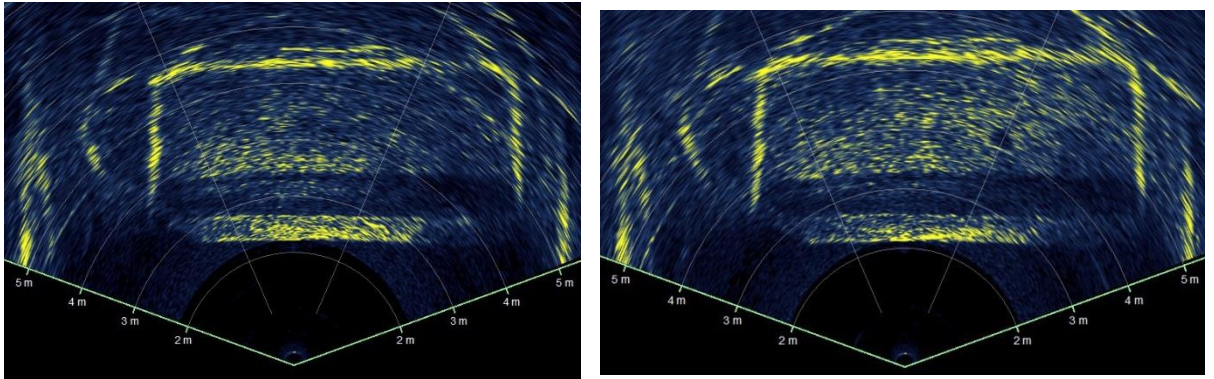


Figure 164. Before injection (left) and after injections (right).

The 200 and 400 kHz sonars were both able to detect the presence of oil through determining the change in the bathymetry, multiple reflections in the nadir beam, and a change in the bottom reflectance. The multiple reflections could be used to detect oil up to four days after the injection, but were not able to detect the oil eight days after the injection (Figure 165). Changes in the bottom reflectivity were observed after the injection of oil (Figure 166). The presence of oil provides a flatter surface that scatters the acoustics in a specular pattern. This scattering is greater than that observed for un-oiled sea ice. The acoustic return from the near nadir directions is greatly enhanced compared to flat sea ice.

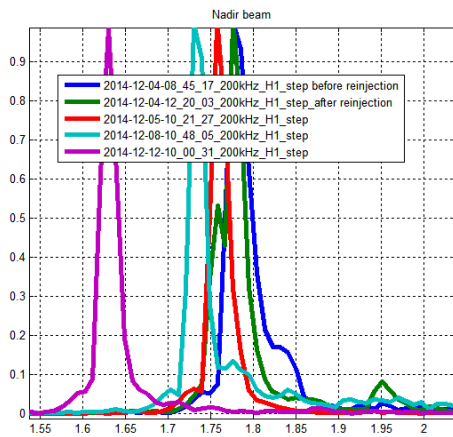


Figure 165. Nadir beam snippets at the same location over eight days.

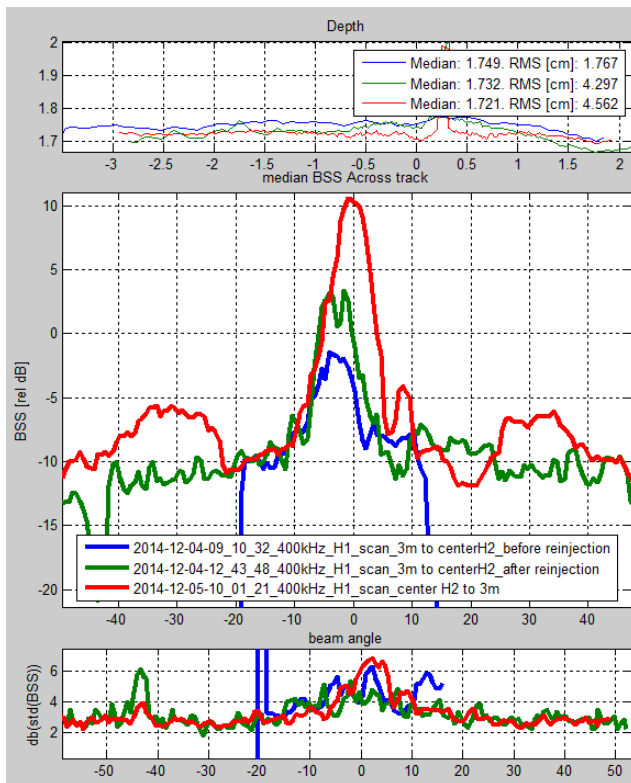


Figure 166. The equalized comparison of the Backscattered Angular Response (BAR) based on the relative intensity.

A multibeam sonar unit was operating during the second injection of oil into Hoop 1. A strange cloud-like phenomenon was observed (Figure 167) that the underwater video showed were oil droplets associated with the injection.

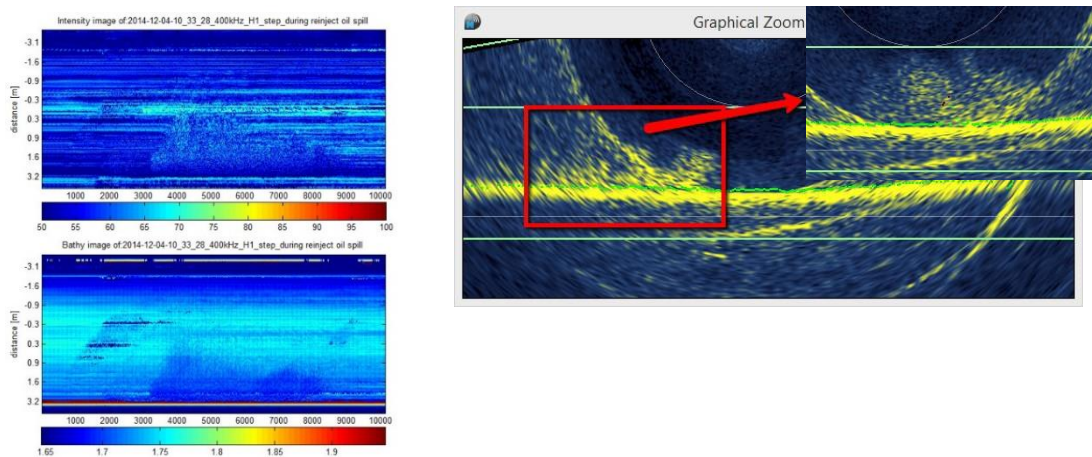


Figure 167. Multibeam data during the second injection into Hoop 1. Notice the cloud of returns away from the ice surface. This was found to be oil droplets in suspension during the injection.

Hoop 2

Most of the oil leaked out of this hoop within 24 hours of injection, which limited the oil detection capabilities. There was evidence of increased specular reflectance, indicating the presence of oil, in the 400 kHz data (Figure 168). The reflectance decreased back to an ice profile after a day. This suggests that the presence of the oil did not alter the bottom of the ice enough to have a lasting impact on the acoustic returns.

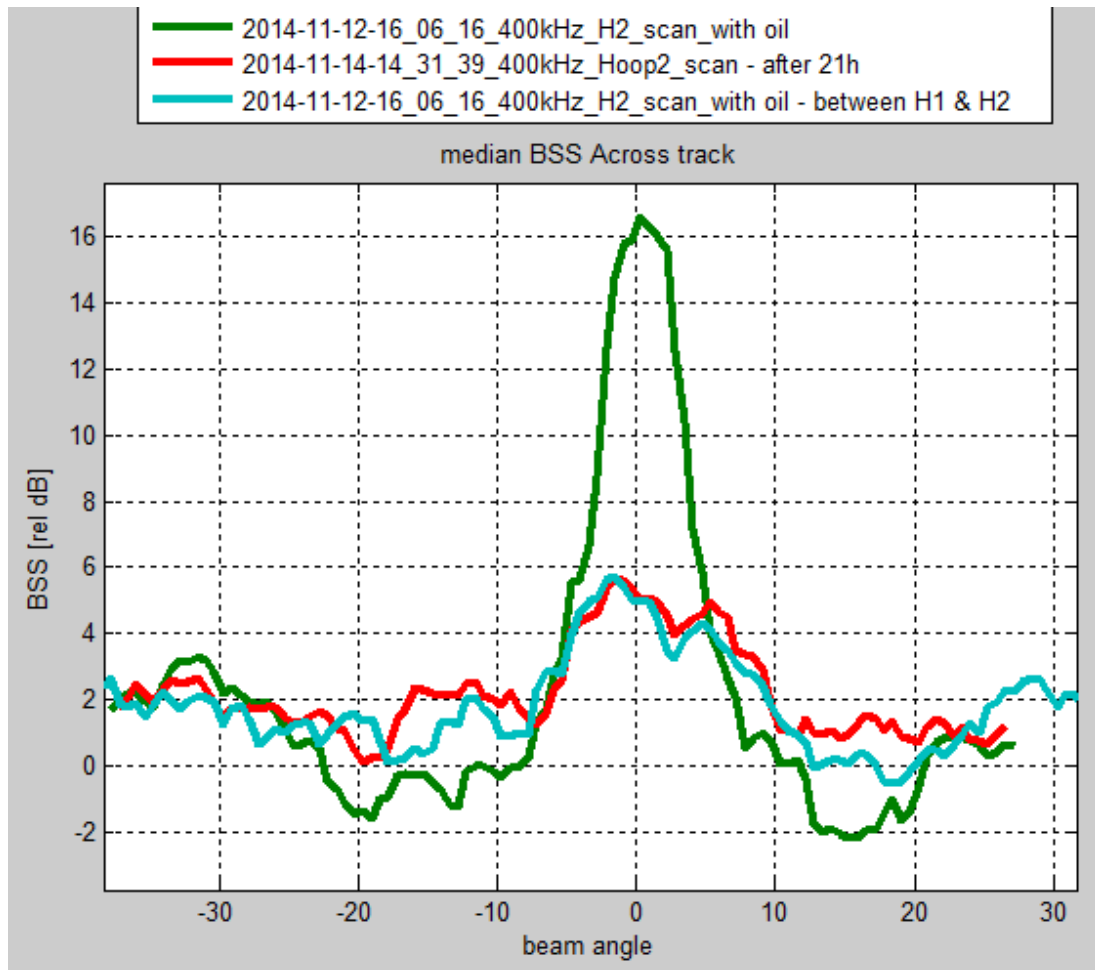


Figure 168. The change in bottom scattering strength associated with the presence of oil. The light blue line is a scan of clean ice just outside the hoop. The narrow hoop width limits the angular resolution of the pattern.

Hoop 3

What was believed to be fresh oil was evident in the FLS observations as a dark spot with low return (Figure 169). This was expected because at the angle of the detector most of the acoustic energy will scatter away from the sensor by a smooth surface. Later review of the injection video

showed that a large air bubble was injected into the hoop by accident, which could be responsible for the decreased signal observed.

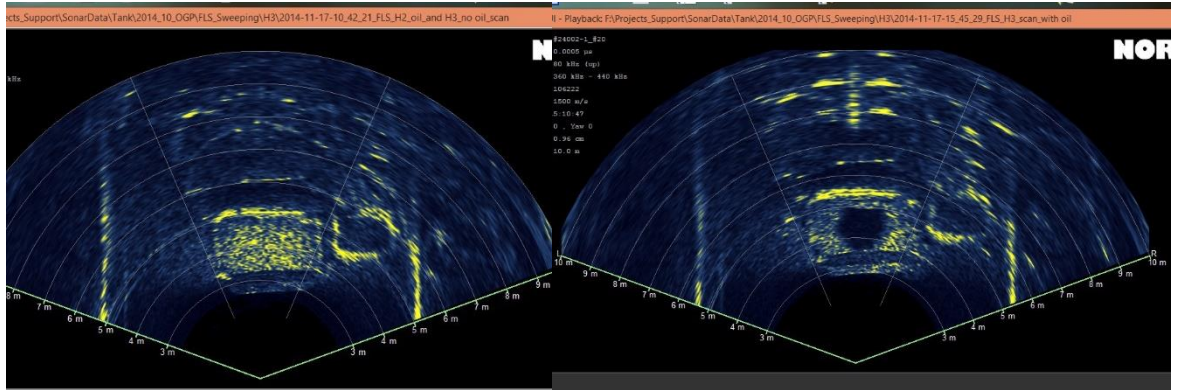


Figure 169. FLS observations before oil (left) and after oil injection (right).

The specular scattering produced high near-nadir returns with lower returns at larger angles in the multibeam data (Figure 170). This specular return pattern was observed at least through the first 48 hours. After that the oil was encapsulated and the angular pattern was that of ice.

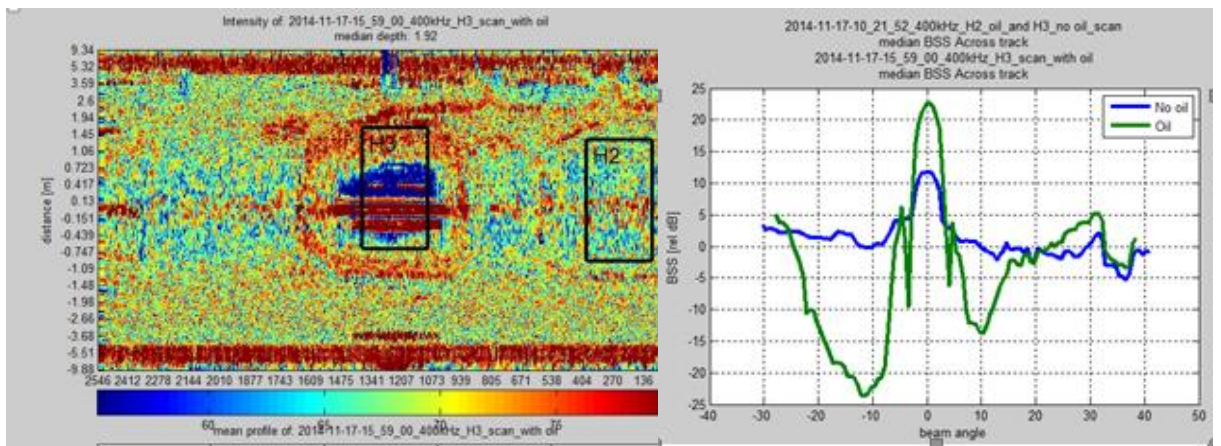


Figure 170. Map of acoustic return showing Hoops 2 and 3 after injection into Hoop 3 (left). The angular acoustic return is on the right. Scattering from the skirts of the hoop likely increase the scattering intensity observed at larger angles.

The oil thickness was not clearly evident in the nadir beam snips. It is likely that the oil thickness was near the minimum resolvable for this system.

Hoop 4

The FLS was not operated during the injection into Hoop 4. A firmware upgrade loaded during the experiment created issues and limited the data collected with the other multibeam units as well.

As occurred at the other hoops, the angular reflectance changed sharply after the injection of oil with increased returns from nadir and reduced returns at larger angles. The thickness of the fresh oil could be determined from the nadir beam (Figure 171).

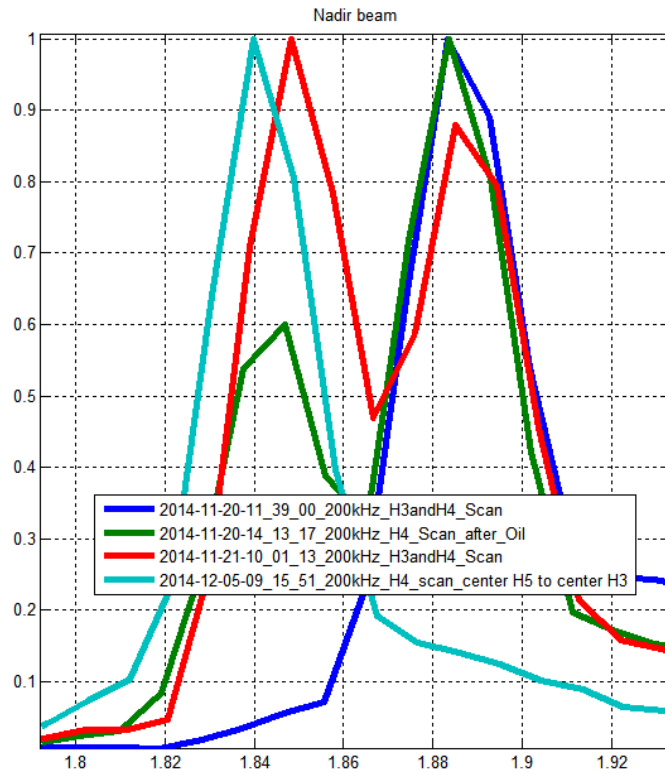


Figure 171. The nadir beam snippets from the 200 kHz unit show a double return associated with the oil layer that is observed 24 hours after injection. It is not observed two weeks later.

Hoop 5

The issues associated with the sonar firmware had not been fully cleared up by the injection into Hoop 5, so the data quality is questionable and was not analyzed further.

Hoop 6

Hoop 6 had longer containment skirts corresponding with thicker ice that made it difficult for the FLS to see past. A small dark area that is indicative of air is observed in the center of the hoop (Figure 172). Review of the injection video confirmed a small air bubble released during the oil injection.

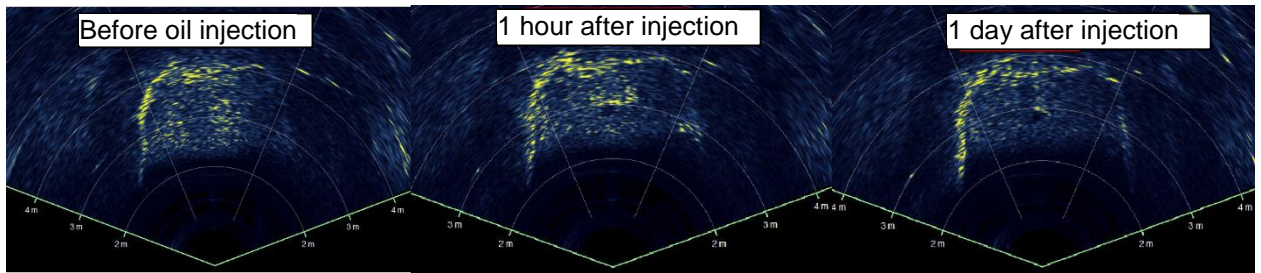


Figure 172. The FLS observations before, after, and one day after oil injection.

Enhanced backscatter in the nadir direction was observed. The reflection strength did not change appreciably off nadir as it had in other experiments. This may be because the longer hoop skirts created more signal at those angles.

The double reflection used to detect oil thickness was evident (Figure 173). The base of the oil layer was observed moving upward 2 cm over the two week period following the injection as the basin room warmed and melt ensued (Figure 174).

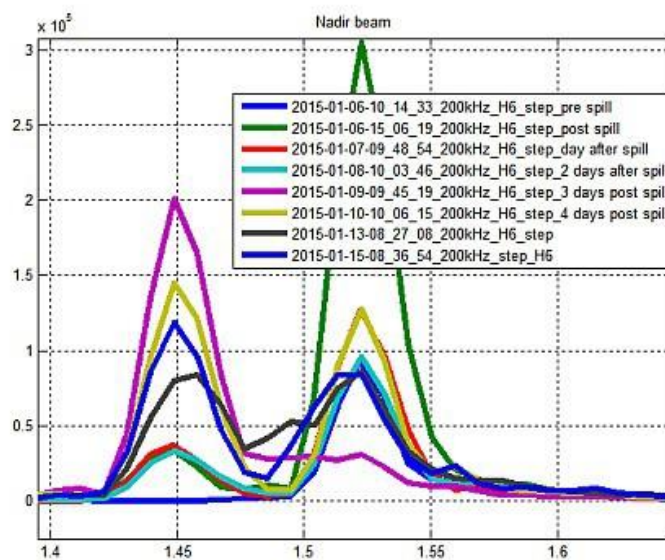


Figure 173. Nadir beam returns showing the oil and ice returns were detected over a nine day period. During this time the room temperature was elevated to stop ice growth and simulate sea ice melt condition. There was a change in the strength of the reflection from the oil surface that may be a result of oil weathering.

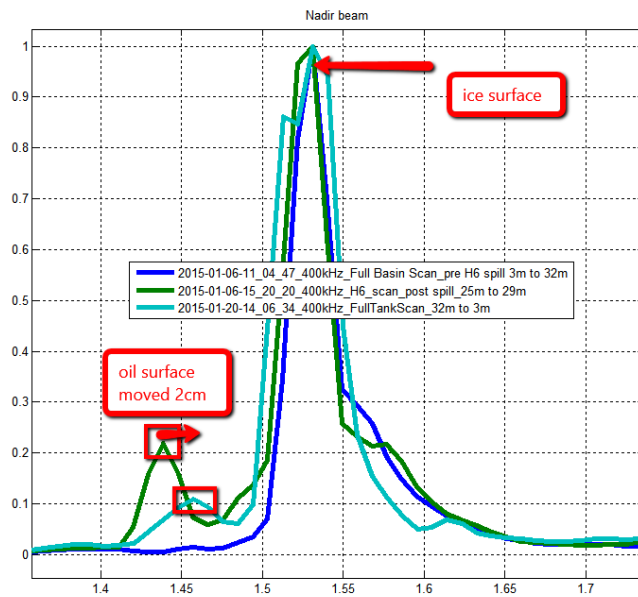


Figure 174. Signal from the oiled and clean ice surfaces was observed over time.

4.3 Modelling

4.3.1 Sea Ice Property Modelling

Field Observations and CRREL Tank Experiment

The freezing degree day CICE model allows for a comparison of field observation to the CRREL experiment. Ice growth rate and ice thickness are dependent on the amount of heat removed from the ocean, with the conductive flux through the ice cover describing the magnitude of this term. The relationship between the ice thickness and the freezing degree days or thawing degree days can be approximated by a square-root relationship (Figure 175).

There are potential differences between laboratory and natural conditions in the factors that control the growth rate: turbulent heat exchange at the surface or the longwave radiation budget may differ considerably in the open air and in the enclosed laboratory space. Hence, the growth history for the same number of freezing (or thawing) degree days may be different between artificial and natural sea ice. Fitting a square-root function (i.e., developing a freezing/thawing-degree day model) allows researchers to relate and compare sea ice grown in the tank with field observations.

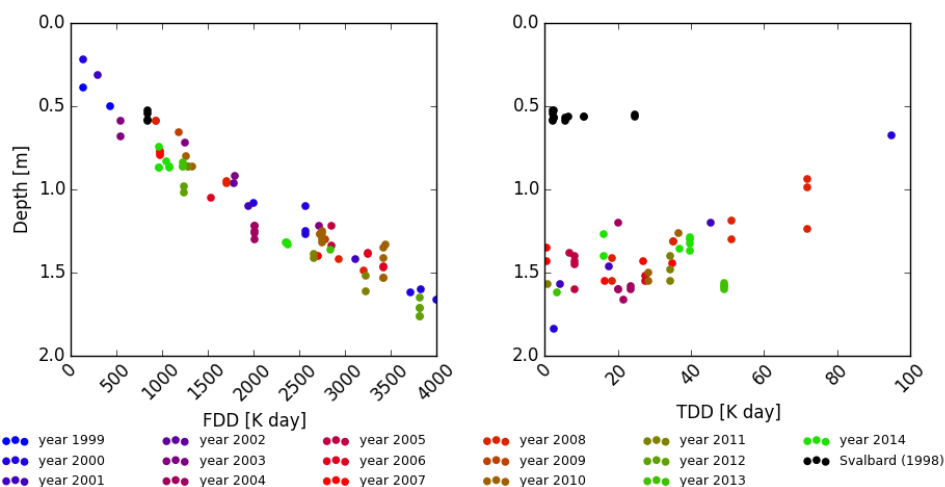


Figure 175. Ice core length as a function of the number of freezing or thawing degree days. Coloured data points represent ice cores collected at Barrow, black data points are ice cores collected in Svalbard.

In the early stages of the ice tank experiment, a few ice thickness measurements were collected to provide a first calibration of the model, which was later refined as the ice grew. This calibration step allowed the FDD/TDD approach to be applied to predict future ice growth and track the salinity evolution during the ice tank experiment.

Profiles and Statistics

During the growth season, interannual variability between the temperature and salinity profiles is larger for temperature than salinity. While the ice is cold (temperature below -5°C), the salinity profile in the ice interior remains near-constant. Due to the low permeability of the ice there is no convective overturning and freshwater flushing has not set in yet; absent these two key desalination mechanisms salinity remains stable. In contrast, temperature variations are imposed by changing air temperatures and the ice responds readily to these changes. Due to the variation in the seasonal meteorology, as well as climatology, outlier temperature profiles are more likely to be observed in the field (Figure 176).

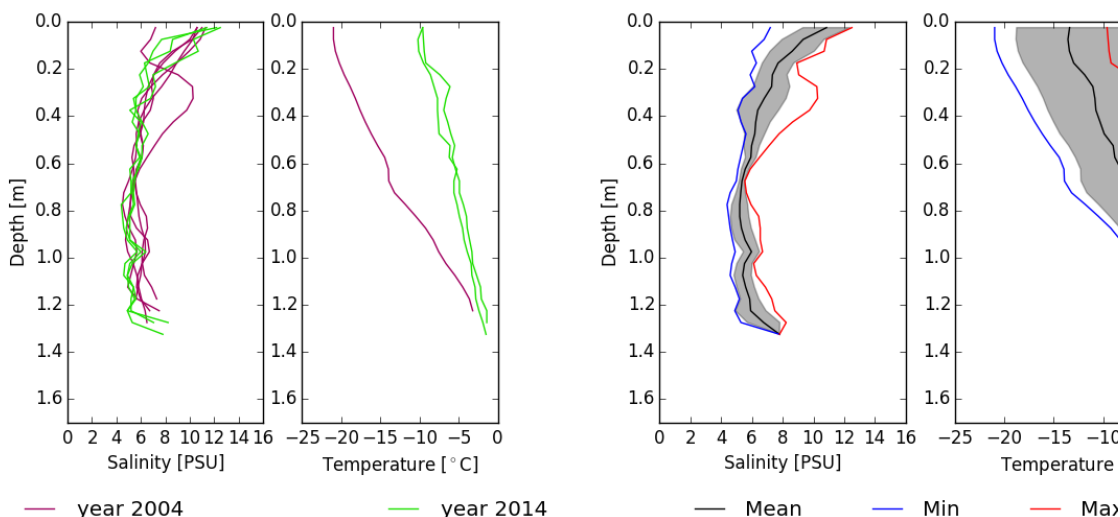


Figure 176. 2000 to 2500 K-days: temperature and salinity profiles (left) and corresponding statistical envelope (right)

For the FDD range of 3000-3500 K-days, in 2001, for which ice is much colder than in the other years, there was a disproportionate increase of the standard deviation. This observation is pertinent for other FDD/TDD intervals as well. Using the quartile (e.g., in a box plot) to describe the spread would have been more appropriate, but most of the groupings did not have enough members to provide meaningful statistics.

At greater depths in the ice cover, towards the ice bottom, salinity variations are in part due to thickness variations. Variations of the ice thickness over a few tens of meters can account up to 10% due to difference in snow cover. In our dataset, ice cores collected at a same sampling events are extracted less than 2 meters apart and their length is very similar. Large ice thickness differences between the samples are the results of temporal variations in the snow cover from a year to another and in between sampling events rather the expression of spatial variation. Also, natural variations and bottom roughness on the order of a few centimeters are a factor (Eicken et al., 2004). Furthermore, loss of brine from the highly permeable bottom layer immediately after sampling results in a bias with underestimated salinities in the bottom layers (Notz and Worster, 2008).

Brine Volume Fraction and Other Derived Properties

At thermodynamic equilibrium, temperature and salinity can be considered state variables of sea ice, controlling the volume fraction of the liquid phase. Thus, from measurements of temperature, salinity and sea ice density, or under the assumption of a constant air volume fraction - often neglected due to its small value ($\phi_a < 1\%$) - physical properties can be derived from ice property models (Petrich and Eicken, 2009; Cox & Weeks, 1983; Golden et al., 2007). Figure 177 shows the relationship between state variables and Figure 178 displays the statistical envelopes of the two state variables (salinity and temperature), the brine volume fraction ϕ_B , the sea ice electrical conductivity σ_{SI} , and the permeability k computed from the temperature and salinity profiles of the ice core belonging to the FDD group 2500 to 4000 K-days. Index b and si refer respectively to the brine and sea ice properties. The three physical properties are derived from equation (1), (3) and (5).

$$\phi_B = (1 - \phi_A) \frac{\rho_i S}{F_1(T) - \rho_i F_2(T)} \quad (1)$$

$F_1(T)$ and $F_2(T)$ are two empirical polynomial functions, based on the phase relations. They are described by Cox & Weeks (1986) for ice temperatures between -30°C and -2°C and by Leppäranta & Manninen (1988) for temperatures between -2°C and 0°C . With σ_B , the brine conductivity of sea ice, depending on the temperature and following Archie's law adapted to ice conditions at Barrow based on measurements by Jones et al. (2012), we arrive at:

$$\sigma_B = -T \cdot e^{0.5193 + 0.08755T} [mSm^{-1}] \quad (2)$$

$$\sigma_{SI} = \sigma_B \phi_B^2 [mSm^{-1}] \quad (3)$$

And ρ_i , the density of pure ice is given as:

$$\rho_i = 0.917 - 0.0001403T [gcm^{-3}] \quad (4)$$

Sea ice permeability, k , derived from the simplest hierarchical model, is described by (Golden et al. 2007):

$$k(\phi_B) = 3\phi_B^2 \times 10^{-8} [m^2] \quad (5)$$

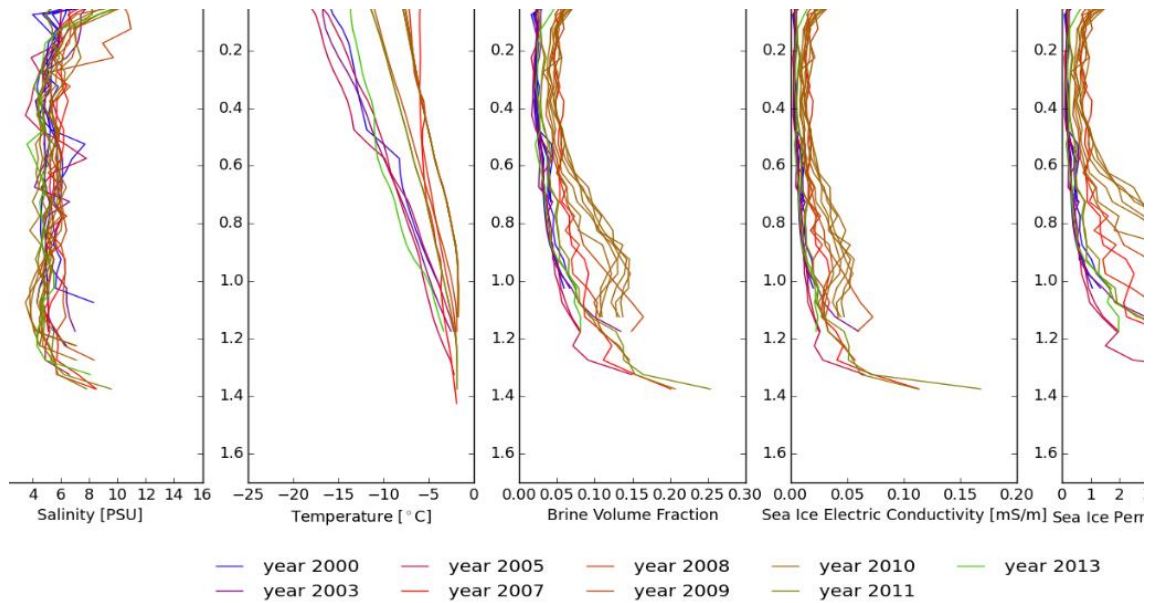


Figure 177. 2500 - 3000 K-days (growth season): relation between state variables (S, T) and the brine volume fraction and sea ice electric conductivity. As the electric conductivity is dependent on the brine volume fraction to the power of two, the shape of both profiles will be similar.

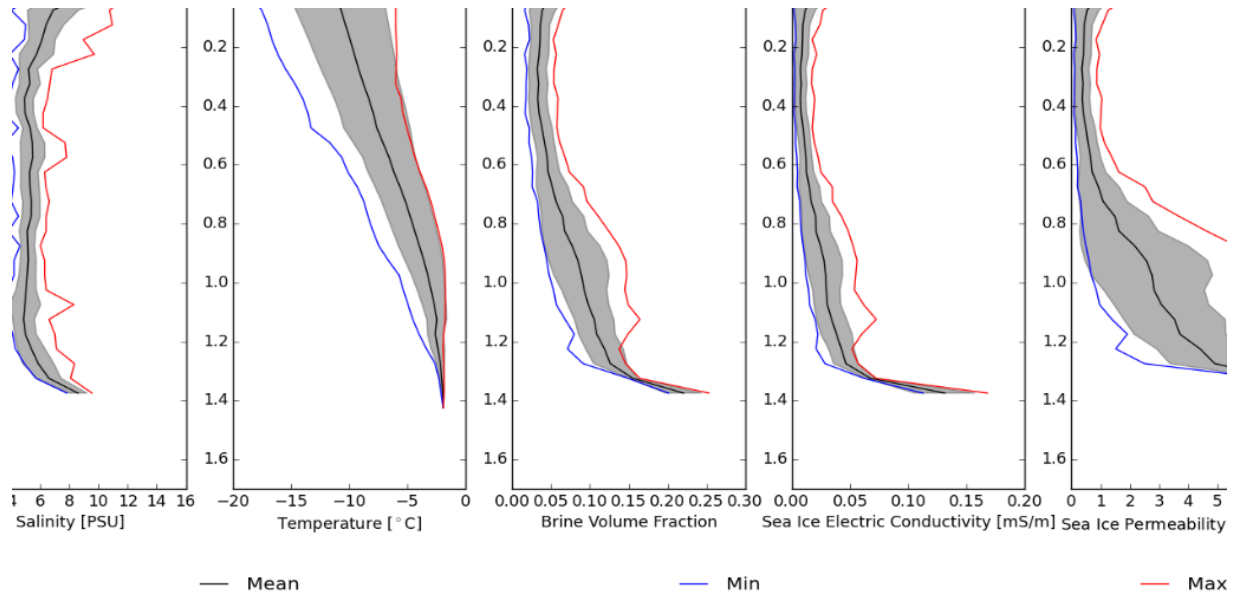


Figure 178. 2500 - 3000 K-days (growth season): statistical envelope for the state variables on the left (salinity and temperature), and the three derived physical properties on the right (brine volume fraction, sea ice electric conductivity, sea ice permeability).

Model Output

In brief, the CICE model was forced with 6-hr weather data from the National Climate Data Center, except for precipitation and humidity provided by the NCEP reanalysis model. Simulations were run for the period 1948-2013, with a focus on 1999 to 2013. Based on validation data with measured ice and snow thickness, a non-zero ocean-to-ice heat flux has to be specified to reproduce the full seasonal cycle. As a first step, a simple statistical approach is used to analyze the observations to determine the general trend of the model output. In order to simplify the comparison, only dates when an ice core has been collected in the field are used to compute the statistic of the model output. During the growth season, the model captures the trend of both salinity and temperature (Figure 179). As expected, salinity in the bottom layer is lower for observation data than simulations. Further work is required to validate and improve model output, and avoid peaks like the one visible at 1.1m depth.

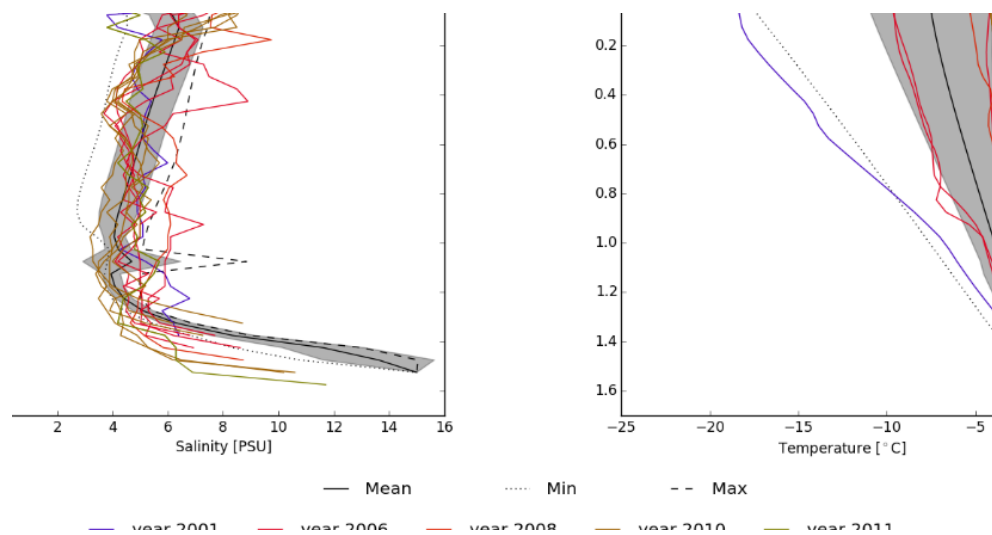


Figure 179. 3000-3500 K-days (growth season): model output is summarized in the grey statistical envelope and observations are displayed as colour profiles

During melt, significant deviations between observations and model output for ice temperature and salinity are observed, in particular near the ice surface where meltwater flushing is only partially captured by the CICE mushy-layer salinity module (Figure 180). Also, the model appears to overestimate the ice thinning rate due to melt.

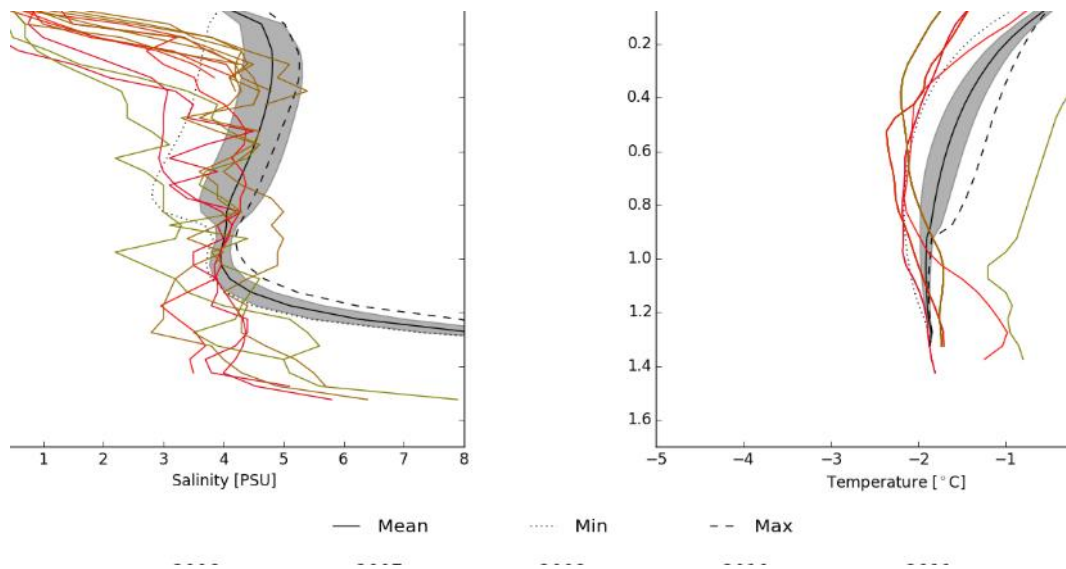


Figure 180. -25/-35 K-days (melt season): model output is summarized in the grey statistical envelop and observations are displayed in colour profiles

Currently, the model performs well to simulate the general trend and variation of the state variables of sea ice during the growth season. However, weather data and a minimum measurement of snow and ice thickness are required in order to tune the model and increase its accuracy.

The sea-ice property modelling provides the temperature, salinity, ice thickness, and other characteristics used as inputs to determine acoustical, optical, and electrical properties for sensor specific models. The output is provided as a function of time through the year to allow the sensor models to examine changes in performance through the life cycle of first year ice.

4.3.2 Acoustics Modelling

The results discussed here are based on data collected from Hoop 5. The model/data comparison is made in the temporal domain; the received sound intensity as a function of time are directly plotted against model predictions for both normal incidence as well as oblique incidence at 20 degrees. Data from before oil injection is compared to the model and the results are shown in Figure 181. For normal incidence (nadir), water/ice reflection dominates the initial arrival, ice volume scattering contributes to the “shoulder” portion of the arrival (2.6 – 2.7 ms, left panel), and ice/air reflection resulted in the second peak at about 2.7 ms in the left panel of Figure 181. Surprisingly, the roughness scattering at the water/ice interface is smaller than that of the ice volume scattering and was invisible in the data. At the oblique angle, however, ice volume scattering from the skeletal layer dominated all the received sound intensity, indicating the importance of the skeletal layer as a scatterer. Water/ice interface scattering yields good estimates of ice skeletal layer properties, such as its sound speed. Ice/air interface signal is good for inverting for ice bulk properties, such as sound speed.

Based on the excellent model/data comparison, a set of environmental parameters were derived and the results are given in Tables 10 and 11. The results indicate that the model can be effectively used to estimate difficult-to-measure environmental parameters.

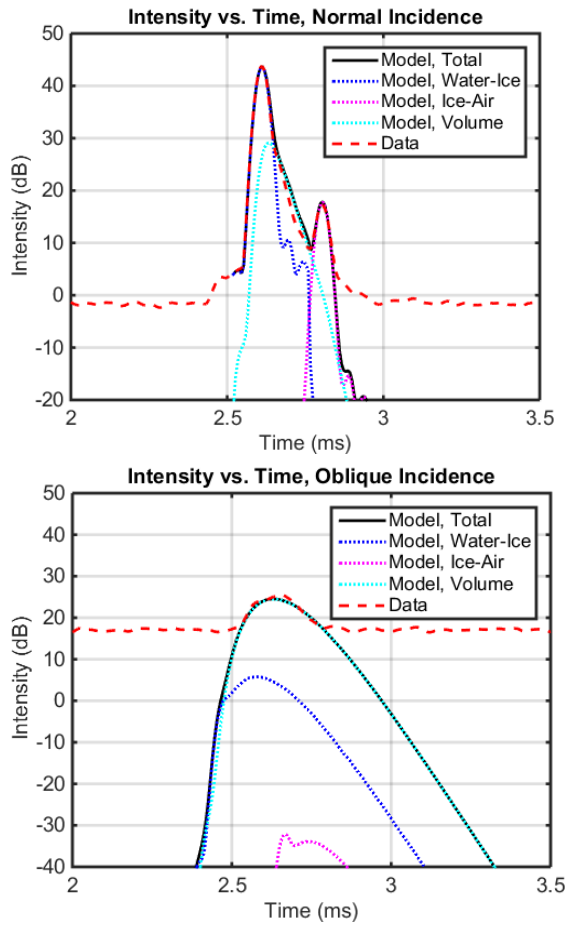


Figure 181. Model/data comparison for normal incidence (left) and at 20 degree oblique angle without oil layer (right).

Table 10. Model parameters. Input parameters are given in normal fonts, and inverted parameters from model are given in bold face.

$c_w = 1430$	Water sound speed (m/s)
$\rho_w = 1024$	Water density (kg/m ³)
$c_{ice_surf} = 1959$	Ice sound speed near water interface (m/s)
$c_{ice_bulk} = 2900$	Ice sound speed for bulk (m/s)
$\rho_{ice} = 920$	Ice density (kg/m ³)
$\delta_{ice} = 0.035$	Ice loss parameter
$\sigma_{ice} = 0.0013$	Ice volume scattering parameter
$\rho_{air} = 1.225$	Air density (kg/m ³)
$c_{air} = 331$	Air sound speed (m/s)

$w2_water_ice = 5 \cdot 10^{-6}$	Roughness spectral strength (meter units)
$\gamma2_water_ice = 3.5$	Roughness spectral exponent
$w2_ice_air = 5 \cdot 10^{-6}$	Roughness spectral strength (meter units)
$\gamma2_ice_air = 3.5$	Roughness spectral exponent

The following are model/data comparisons after a layer of oil is injected underneath the ice. Because the model predicts both reflection and scattering at both normal and oblique angles, the model parameters were highly constrained, yielding good estimates of ice parameters, such as attenuation coefficient and volume scattering strength. It was found that scattering away from normal incidence is dominated by ice volume heterogeneity (Figure 182). Oblique scattering with an oil layer increases by 10 dB as compared to that without an oil layer, possibly caused by the oil mixing into ice volume. This could be a good indicator of the ability of the sonar to detect oil presence at grazing angles.

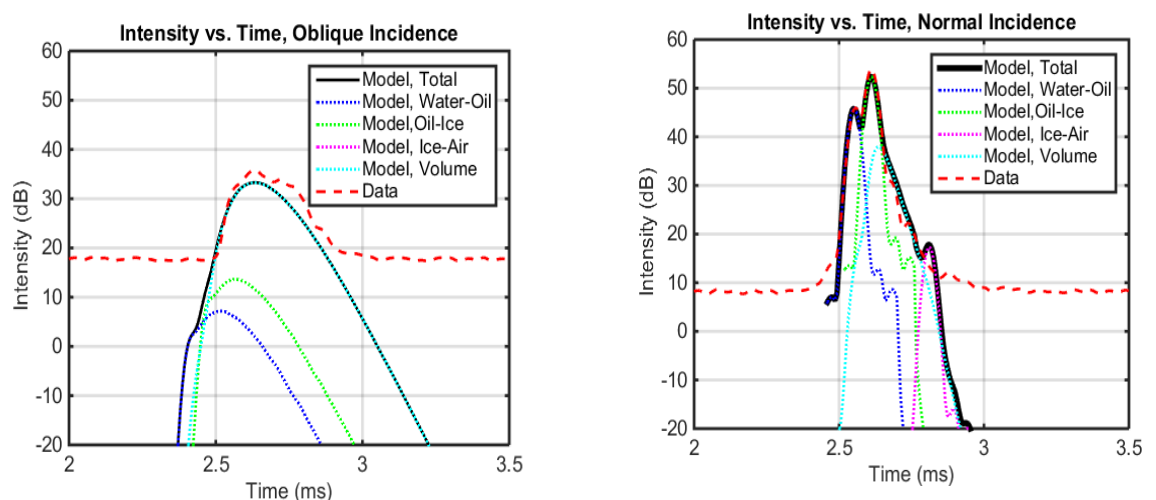


Figure 182. Model/data comparison for normal incidence (left) and at 20 degree oblique angle (right) with oil layer.

Table 11. Model parameters when oil layer is added. Input parameters are given in normal fonts, and inverted parameters from model are given in bold face.

$c_oil = 1500$	Oil sound speed for bulk (m/s)
$\rho_oil = 889$	Oil density (kg/m ³)
$\delta_oil = 0.001$	Oil loss parameter
$\sigma2_oil = 0.002$	Oil volume scattering parameter
$\sigma2_ice = 0.015$	Ice volume scattering parameter

Modelling Hypothetical Smooth Ice Scenarios

Scenario 1 - 2m D oil pool, October – July, Oil thickness (1, 2, 5, 10, and 15 cm), ice thickness below oil layer (1, 5, and 10 cm then monthly expected total ice thickness)

Scenario 2 - 200m D oil pool, October – July, Oil thickness (1, 2, 5, 10, and 15 cm), ice thickness below oil layer (1, 5, and 10 cm then monthly expected total ice thickness)

The model developed is based on general physical principles, hence a potential to be applied to a wide range of conditions which may be found in the Arctic environment; however, the model contains a set of parameters, and those parameters are either independently measured or determined by fitting to acoustics data collected in the CRREL indoor facility. It is useful to take the model and make predictions for the above scenarios; it is important to bear in mind, however, that when using the model predictions, there are inherent uncertainties associated with them due to unknown parameters, such as the scattering cross section of the mixture of oil and ice when new ice grown underneath the oil. Field data are eventually needed to truly validate the model.

When running the model for the specified Arctic scenarios, we made the following assumptions:

- The new ice grown underneath the oil layer is identical to that grown before oil injection.
- The oil/ice mixture remains the same condition after new ice layer is grown, hence, any ice structural change over time is not included (important to examine and verify in future).

The CRREL data were collected with the sonar systems mounted less than 2 m beneath the ice/oil. If the model runs used the same geometry, the results for the two specified scenarios would be identical because the sonar beam would have multiple “looks” of the ice/oil pool; however, anticipating real world conditions, the sonar is assumed to be ~10m beneath the ice. In this case, the 2 m diameter pool would be too small to allow the sonar to have more than a couple of independent samples of the pool, so a practical discrimination between with and without oil would be very difficult. For a pool of only 2 m in diameter, the sonar needs to be less than 5 m from the ice and the beam angle needs to be narrow (2-5 degrees).

Model Results: Oil Thickness

To address the oil thickness question posed in the field scenarios defined by the project, a 3-4 cm layer of oil from the CRREL test basin was studied extensively. The model demonstrated a 10 dB signal-to-noise as compared to no oil at these thicknesses. The thinnest layer of oil studied was about 2 cm, where the oil signal was clearly identifiable. The following assumption was made for model runs against oil layer thickness: the scattering acoustical cross section is proportional to oil layer thickness up to a maximum layer thickness of 10 cm, after which the cross section signal remains a constant. This assumption reasons that larger volumes of oil would provide more oil penetration into the ice skeletal layer, therefore enhancing scattering. It is also reasonable to assume that such enhancement would reach a limit where oil/ice mixture is saturated, and then the increase of scattering cross section would stop.

With the assumption, it is found that sound attenuation against oil layer thickness is negligible. Table 12 shows excess signal-to-noise as compared to when no oil is present.

Table 12. Signal: noise ratios for acoustically modeled oil thickness.

Oil layer thickness	1 cm	2 cm	5 cm	10 cm	15 cm
S/N (dB)	4	7	11	14	14

Model Results: Ice Layer Thickness after Oil Injection

Figure 183 shows model results for acoustic cross sections collected with a 20-degree backscatter incident angle under ice thicknesses of 1, 5, and 10 cm that theoretically have

developed under the oil layer. Knowing the difference in scattering oil and without oil is about 10 dB before the layer of new ice is grown underneath the oil, the model predicts that with 1 cm of new ice, detection remains practically the same as without new ice. When the new ice layer grows to 5 cm, the signal reduces by half, and detection is marginal. Finally, if the new ice layer is 10 cm, the model shows that signal from the oil is almost lost.

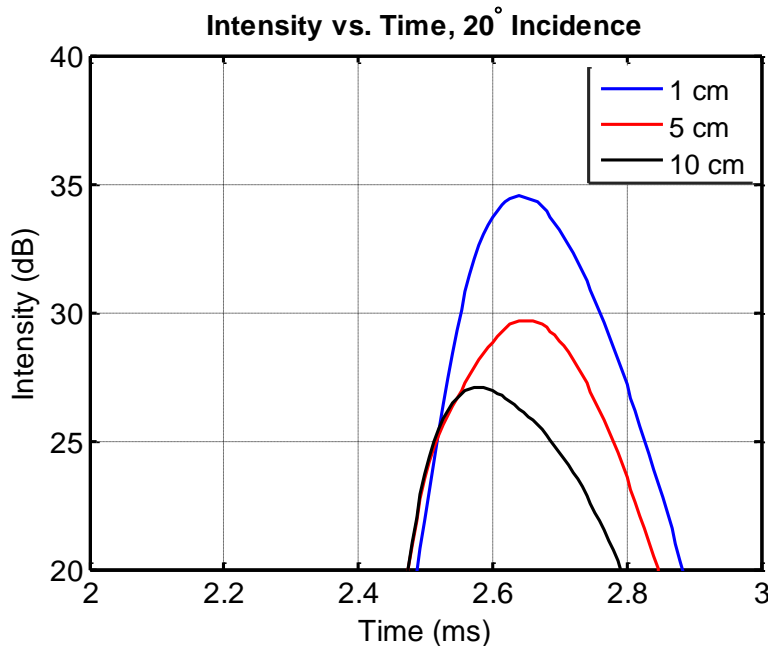


Figure 183. Modeled scattered intensity at a 20 degree incident angle for different thicknesses of ice grown after oil injection. In the absence of oil, the intensity is 25 dB.

Figures 184-186 show the scattered intensity at normal incidence (nadir). In this case, the scattering from the various interfaces dominates the signal, and the ice volume scattering does not show up as a detectable signal. At 1 cm, the ice/oil interface scattering dominates while the water/ice interface signal is smaller, though it arrives simultaneously, resulting in a large first peak. The oil/ice interface signature arrival (interface between oil and the old ice) also contributes significantly, but at a delayed time. In the absence of oil, the arrival has only a single peak from the water/ice interface. Thus, it can be inferred that the multiple arrivals in the scattered signal provide a clear detection signal. At 5 cm thickness, the multiple arrival structure persists. The reduced intensity is due attenuation of the ice/oil arrival. At 10 cm, three separate arrivals are found from water/ice, ice/oil, and oil/ice interfaces, respectively.

Although there is uncertainty in current model parameters, these quantitative model predictions help to draw the following broad conclusions:

- Applying acoustics signals in the 100-200 kHz range is an effective method to detect oil in ice from underneath sea ice.
- Combining normal and oblique angles in acoustic detection of oil in ice will provide more robust information about oil in and under sea ice.
- The normal incidence (nadir) provides a multiple arrival structure when oil is present due to multiple oil and ice layers and the resulting interfaces.

- Oblique scattering in these acoustical ranges effectively probes the ice volume heterogeneity. There is reason to believe that when oil penetrates into ice, the ice volume scattering strength will increase significantly.
- The current model can be broadened into wide-angle applications and adapted to other real Arctic conditions. To verify, it is important to find the opportunity to acquire field data from under Arctic ice.

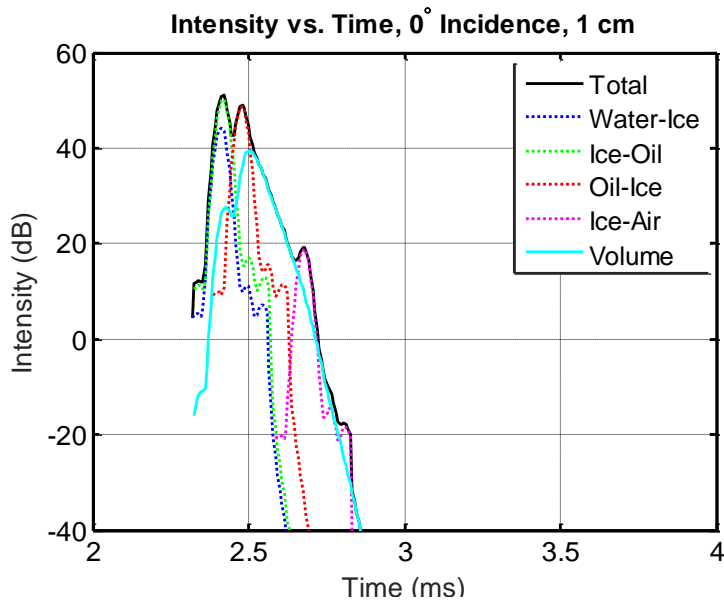


Figure 184. Model prediction for normal incidence (nadir) scattered intensity with 1 cm of new ice growth underneath a 4 cm oil layer.

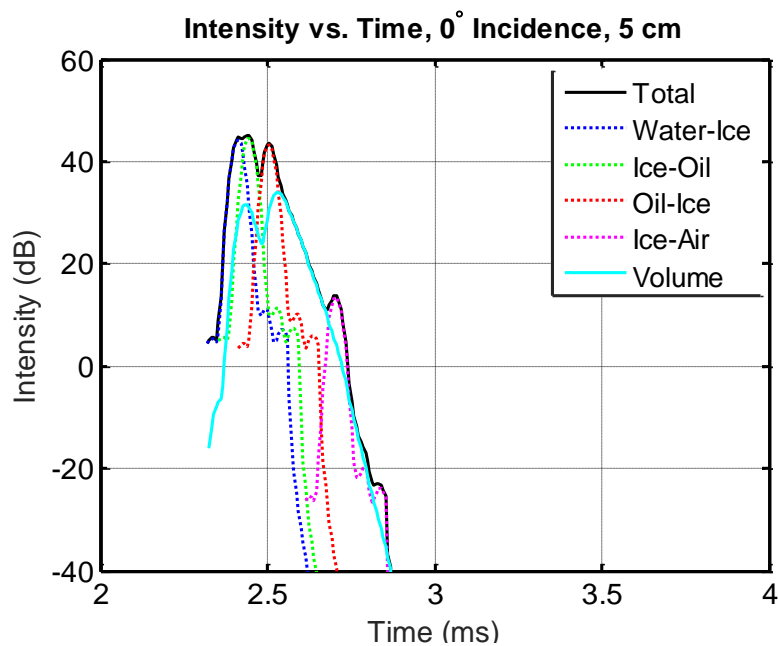


Figure 185. Model prediction for normal incidence (nadir) scattered intensity with 5 cm of new ice growth underneath a 4 cm oil layer.

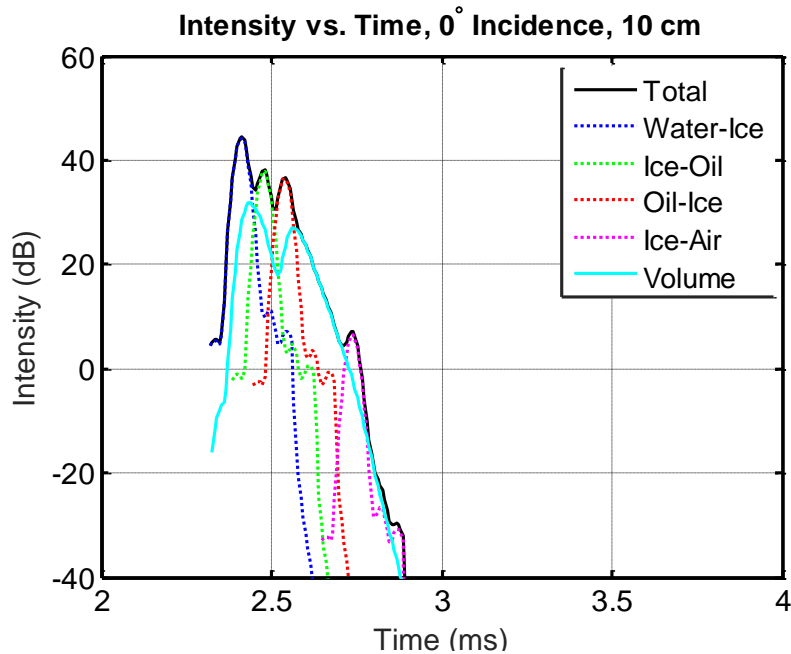


Figure 186. Model prediction for normal incidence (nadir) scattered intensity with 10 cm of new ice growth underneath a 4 cm oil layer.

4.3.3 Optical Modelling

Several possible approaches for optical modelling were considered for this project, based on different ways in which oil might be distributed in the ice. Laboratory results suggested that the ice albedo was affected by oil which rose upwards through brine channels, becoming irregularly distributed throughout the upper part of the ice. Measurements of transmitted light, on the other hand, were more strongly influenced by the layer of pooled oil encapsulated within during a significant fraction of the year, we opted to concentrate on transmitted light. In particular, we investigated the spatial variability of the signal below the ice to see whether ‘patches’ of oil (2 meters in diameter) would be obscured by ice growing beneath them or would remain visible as variations in the amount of light transmitted through the ice.

No measurements of the inherent optical properties of the specific oil used in the laboratory tests were available, so for our model we extrapolated the absorptivity of the oil from the complex refractive index for ‘Romashkino’ crude reported by Otremba (2000). These measurements extend from 350 nm to 750 nm; for higher wavelengths, we simply assumed that the absorptivity remained constant at the 750 nm value.

The Monte Carlo model used here was developed by Light et al. (2003). The model emits packets of photons from a virtual “sensor” and tracks their path through a specified domain until they are absorbed or escape; this “backwards” approach improves computational efficiency compared to a “forward” model where a majority of photons may not reach the virtual sensor. The domain in

this model consists of concentric cylinders divided into vertical layers, making it ideal for calculating radiative transfer through ice that contains isolated pools of oil.

Using this model, we can investigate the effect of ice thickness above and below a pool of oil, thickness of the oil pool itself, and the effect of snow on top of the ice. Each run of the Monte Carlo model gives results for a single wavelength of light. Most results reported below show what an upward-looking irradiance sensor 1 m below the ice would see as it made a transect across an oil pool 2 meters in diameter, for various initial thicknesses and post-spill ice growth. Post-spill ice thicknesses are based on expected monthly average thicknesses through the growth phase. A selected range of results are shown here.

The pool of oil absorbs most of the light driving the transmission toward zero directly below the oil (Figure 187). Because irradiance is modeled, there is some light coming from beyond the oil. Once the ice below the oil exceeds 25 cm, it is difficult to find evidence of the oil in the magnitude of the irradiance.

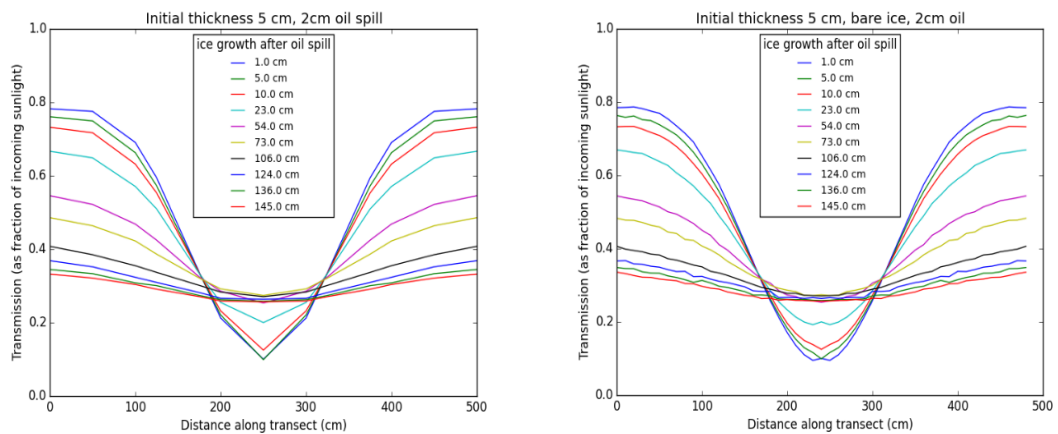


Figure 187. Bare ice with an initial thickness of 5 cm at the time of the spill, a 2 cm spill, and various amounts of ice growth. The version on the right was computed at higher spatial resolution.

The decrease in irradiance below the oil is still evident when starting with a greater initial ice thickness (Figure 188), although there is an expected decrease in brightness associated with losses in the ice. The transmission profile for ice that is a total of 140 cm thick is different depending on whether the oil layer is close to the surface or close to the bottom; if the layer is close to the bottom, there is a more marked difference between the oil spot and the ice around it. The larger the diameter the pool of oil, the more obvious it is (Figure 189) because less light is able to scatter below the pool of oil.

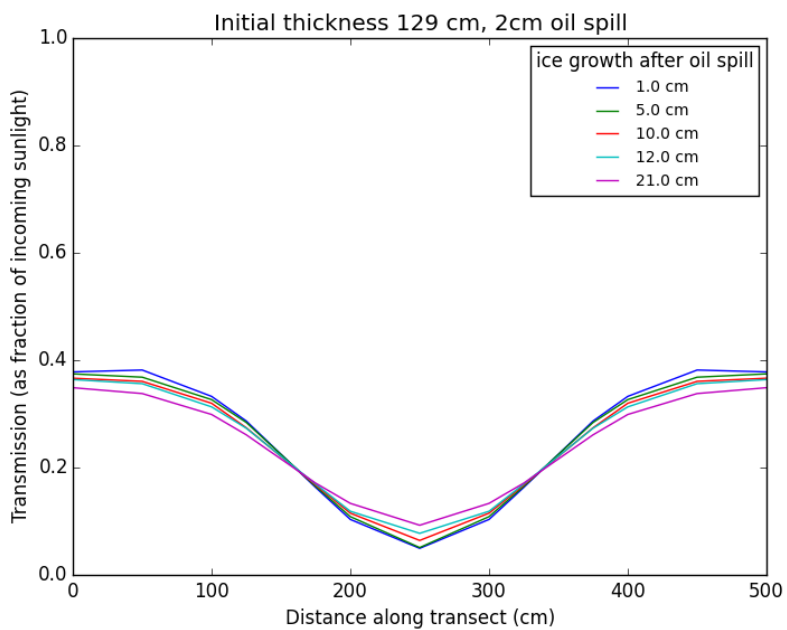


Figure 188. A 2 cm thick oil patch below 129 cm of ice with ice growth to 140 cm.

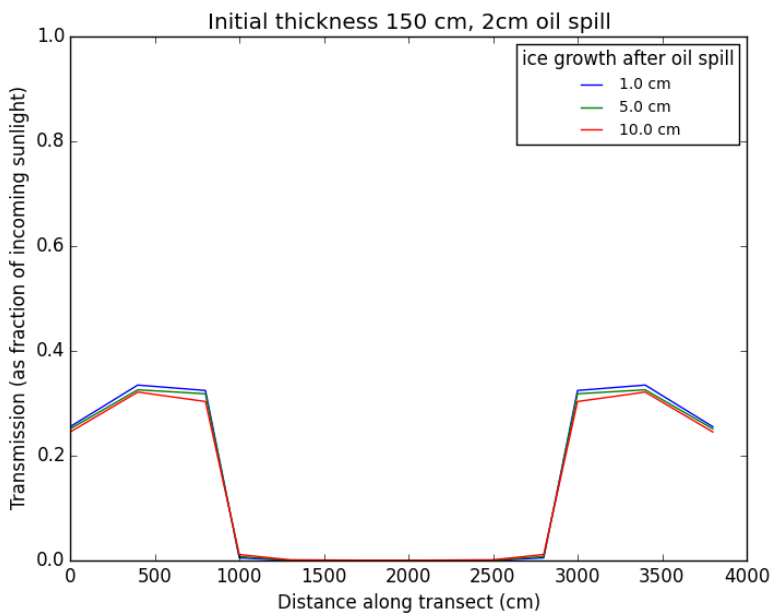


Figure 189. A 20 m diameter, 2 cm thick oil patch below 150 cm of ice with ice growth to 160 cm.

Ice with a 10-cm layer of oil looks very similar to that with a 2-cm layer (Figure 190). This suggests that modelling of oil 2 cm thick does well at predicting the effects on the light field of thicker pools of oil.

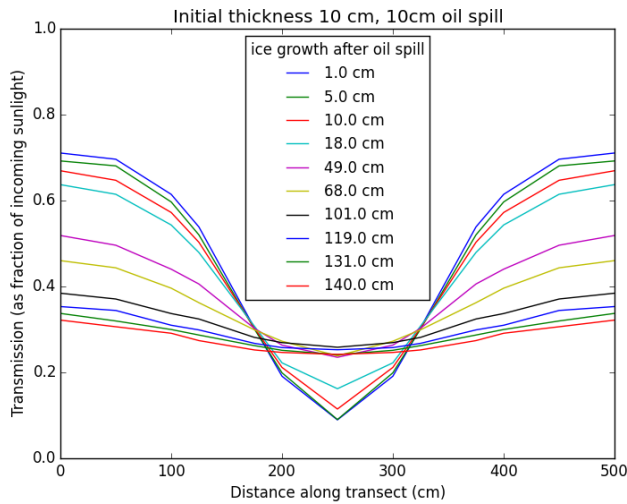


Figure 190. A 10 cm thick oil patch below thin ice with various encapsulation thicknesses.

Bare ice is a special case. More realistic scenarios include a drained surface layer or the presence of snow. The following results show ice with a 25 cm scattering layer. On clean sea ice such a scattering layer could be either weathered snow or “rotten” drained sea ice, which have similar optical properties; oil within the ice, however, would quickly rise up through a permeable drained layer, so if the oil remains encapsulated we can assume any scattering layer consists of snow. The top 5 cm highly scatters (100x the scattering coefficient of the interior ice) while the region between this top layer and the water level (the ‘freeboard’) moderately scatters. Saturated snow or ice below this level has the same scattering coefficient as normal ice. The light transmission with the scattering layer is lower than without, as expected; however, the oil patch is still readily visible for most ice thicknesses (Figure 191).

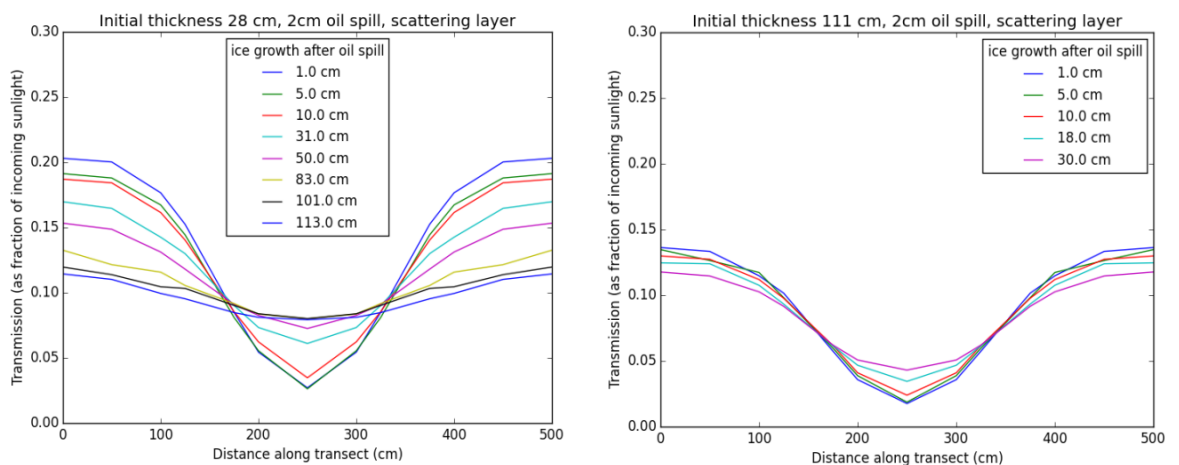


Figure 191. (Left) A 2 cm thick oil patch below 28 cm of ice with the ice surface conditions representative of weathered snow or rotten ice. (Right) The same oil and ice but with the oil below 111 cm of ice.

The results shown to this point are for light with a wavelength of 500 nm. Absorption and scattering in snow, ice, and oil are wavelength dependent. The maximum transmission through snow and ice tends to be between 450 and 550 nm, so it is at those wavelengths that the impact of oil is the greatest (Figure 192). The transmission spectra are all calculated for a point below the center of a 2-m oil pool, hence the low overall transmission. The transmission in the visible increases as the ice grows thicker, since light scatters into the sensor's field of view by the thick layer of ice. At longer wavelengths, however, the ice is more absorbent and thicker ice reduces transmission.

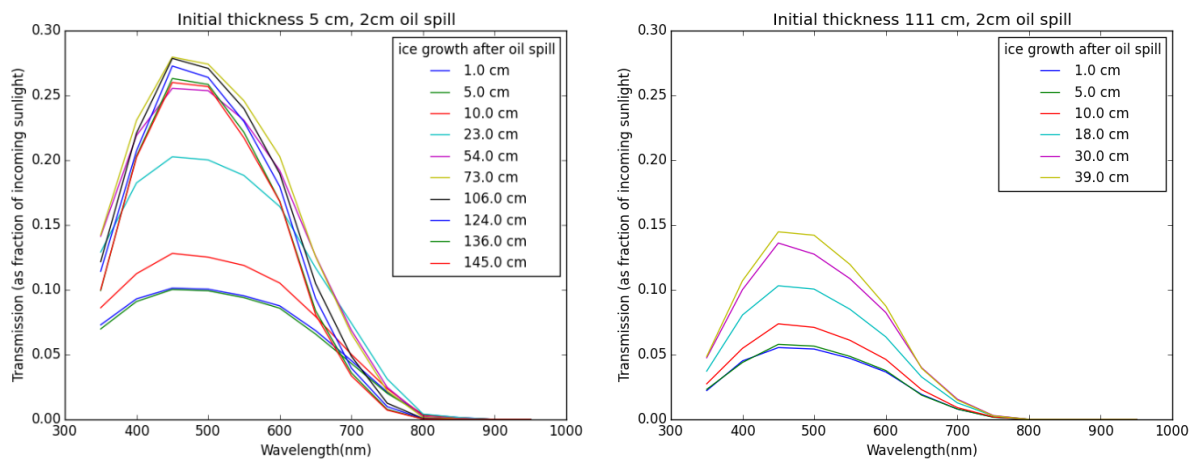


Figure 192. Transmission spectra for various ice thicknesses below a patch of oil at 5 cm depth (left) and 111 cm depth (right).

Attenuation by snow can also reduce the light field below the ice. Snow primarily scatters the light causing much of it to be reflected upward or absorbed by the snow. Oil attenuates light by absorption, but either scattering or absorption could lead to dark areas under the ice. A 25 cm thick patch of snow was modeled to compare to a similar size patch of oil (Figure 193). The snow does not attenuate the light to the same degree as the oil. Once over about 30 cm of ice growth occurs, there is enough scattering in the ice to reduce the difference in transmission between the snow and oil patches. The thickness of ice required to fill in the light field under an oil patch depends on the size of the oiled area.

Differences in the absorption characteristics of oil and snow/ice may allow spectral measurements to differentiate between the two.

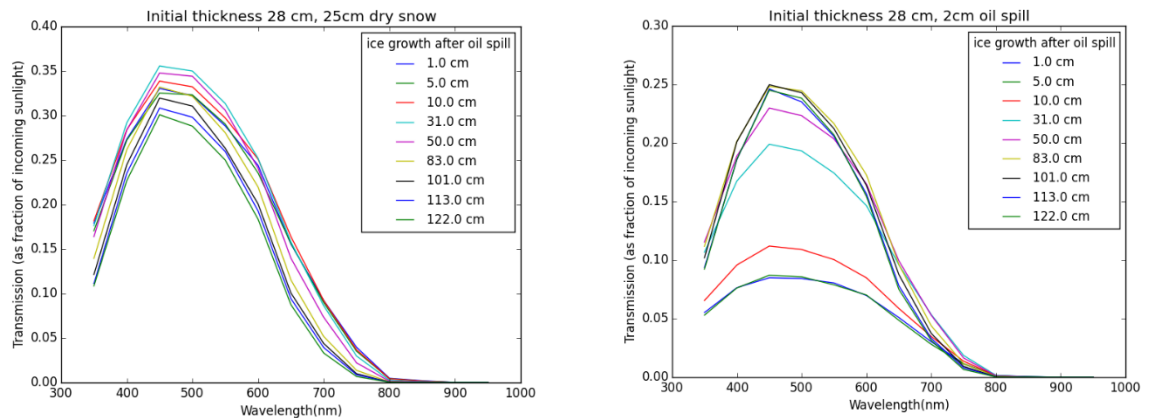


Figure 193. Transmission spectra for various ice thicknesses below a 2 m patch of dry snow on the surface (left) and a 2 cm thick patch of oil of the same size under 28 cm of ice (right).

4.4 Radar Modelling

4.4.1.1 Modelling Results: 1D Off-Ice Radar Modelling

Typical Response Characteristics

The first simulation is based on a simple ice model that produces no internal reflections, meaning that it has only smooth internal variations (Figure 194A). The ice thickness is comparable to what we might expect for first-year ice in mid-January. The purpose of this model is to illustrate the basic characteristics of the radar response to the oil trapped at the base of the ice. The oil thickness was allowed to vary from 0 to 20% of the total ice thickness, which is considered to be the magnitude of under-ice topographic variations in first-year ice. The radar response is plotted as a function of oil thickness. Figure 194B shows the simulated pulsed radar data. While the method of recording and displaying FMCW data differs from that of pulsed radar, the physical processes that govern the two types of radar are the same, and this pulsed radar model serves to illustrate the characteristics that can be expected to be observed with either type of model.

In Figure 194B, it is qualitatively clear that the radar response varies significantly with increasing oil thickness. Figure 194C shows the change in radar amplitude. When the oil thickness is below the conventional resolution of the radar (about 0.1 m in this case), the amplitude of the radar response varied significantly as a function of oil thickness. For very thin layers of oil (<0.02 m), a slight decrease in radar reflection amplitude is observed. Then as the oil thickness increases, the radar amplitude grows, reaching a maximum at $\frac{1}{4}$ the dominant wavelength of the radar signal. After this point, the amplitude decreases slightly then remains constant and is controlled at this point by the reflection coefficient between oil and seawater. The oil/seawater reflection coefficient is significantly higher than that for the sea ice/sea water interface, so the reflection amplitude remains at a level higher than the response with no oil. Additionally, there are significant variations in frequency content and phase of the reflected wavelet (Figures 194D and 194E). In combination, these attributes can provide an estimate of the oil layer thickness using, for example, the full waveform inversion approach described by Bradford et al. (in press). Above the conventional resolution limit, the reflection from the top and bottom of the oil layer can be detected and used to measure the oil thickness by dividing the velocity of signal propagation by the total travel time in the oil, then dividing by 2 to account for two-way travel time in the oil layer.

Test Basin Simulations

Simulations were run using the salinity and temperature profiles provided by the UAF team for spills in Hoops 2-6. The salinity and temperature profiles were developed for conditions outside of the test hoops. These properties differ in some important ways from those within the test hoops, and these differences result in models that are not directly comparable to the field data. In Hoop 2, the oil was not effectively contained within the skirt, so there is no comparison with the field data. In Hoops 3-6, foam was placed over the hoop to temporarily inhibit ice growth in an effort to create a topographic reservoir in which the oil would collect, decreasing the potential for migration outside the hoop. Placement of insulation on the ice alters the temperature profile, leading to warmer ice at the surface and an overall decrease in the temperature gradient through the ice. Additionally, thinner ice inherently has a different temperature profile than thicker ice. Despite the differences in model ice vs actual hoop conditions, the radar models produced results that are comparable to the field data, but with differences in travel time and total amplitude (because of different signal attenuation due to differing ice properties). These differences are most exaggerated in the Hoop 3 and 4 injections, where the ice was relatively thin. As well, various problems with the cooling system resulted in significant warming of the ice during the period just after injection 3 and surrounding injection 4 and may also have played a role.

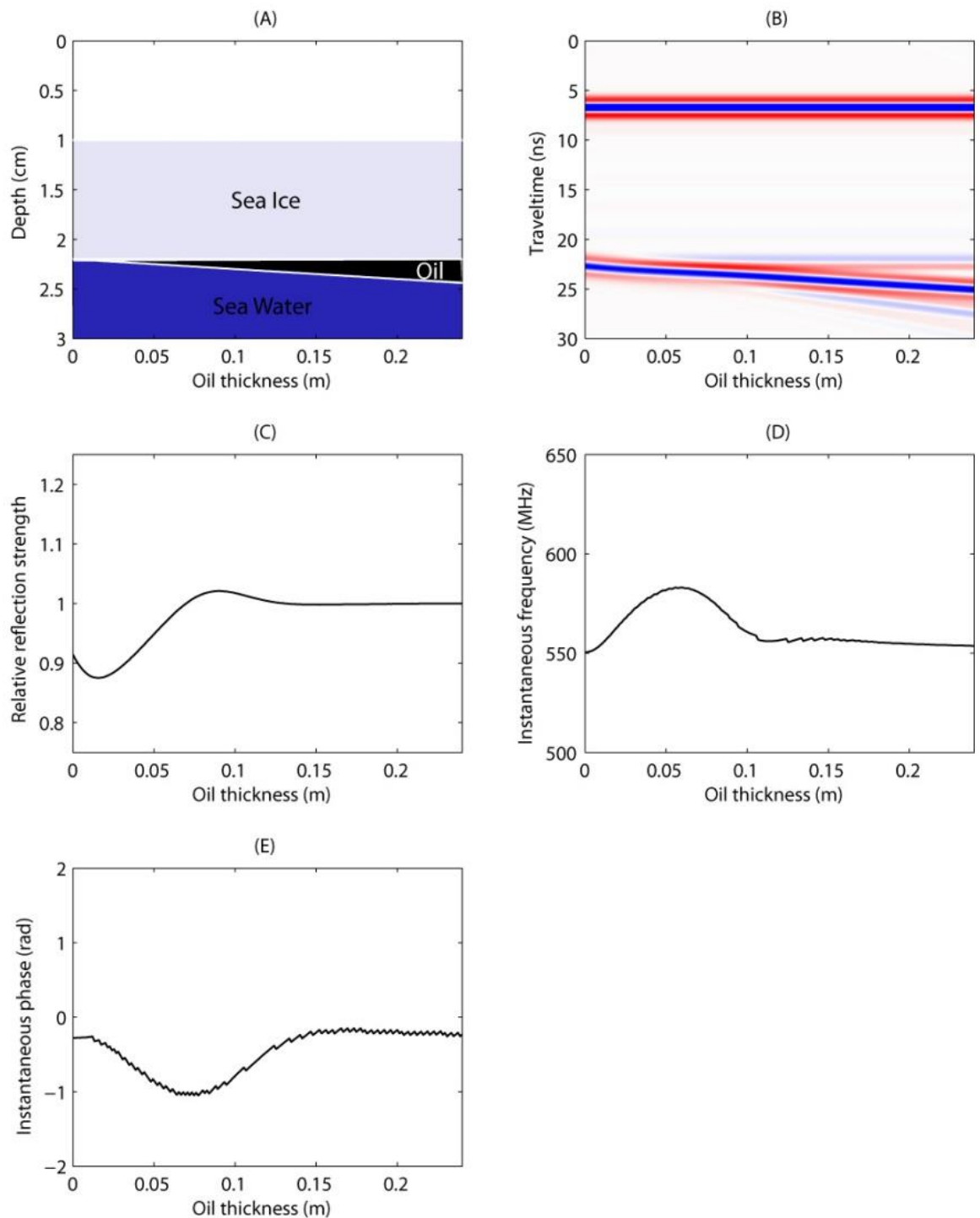


Figure 194. A) Simple sea ice model with oil spill at the base varying in thickness from 0 to 24 cm. B) Simulated pulse radar data for the model in A. C) Maximum reflection amplitude, D) instantaneous frequency and E) instantaneous phase as a function of oil layer thickness extracted from the data in B.

Figure 195 shows the before and after results for all injections for the FMCW radar, while Figure 196 shows the pulse radar results. For purposes of brevity, only the model data is shown, but attribute variations are highlighted within the text. In all cases, the base-of-ice reflection amplitude is second only to the ice surface reflection. All injections induced a phase shift and amplitude change for both FMCW and pulsed radar. Additionally, the relative changes for the FMCW and

pulsed radar are comparable. The Hoop 2 injection (2 cm of oil) produced a significant amplitude increase, while the Hoop 3 injection (1 cm of oil) produced a slight amplitude decrease. The Hoop 4 and Hoop 6 injections were both targeted for 5 cm of oil, and the radar amplitude increase is most marked for these two injections and is coupled with nearly a 180° phase rotation. The 2 cm spill in Hoop 5 produced a slight amplitude decrease. These general observations are consistent with what we observed in the ice-coupled pulsed radar laboratory data, which was the only data set in which it was possible to observe all hoops following injection 2.

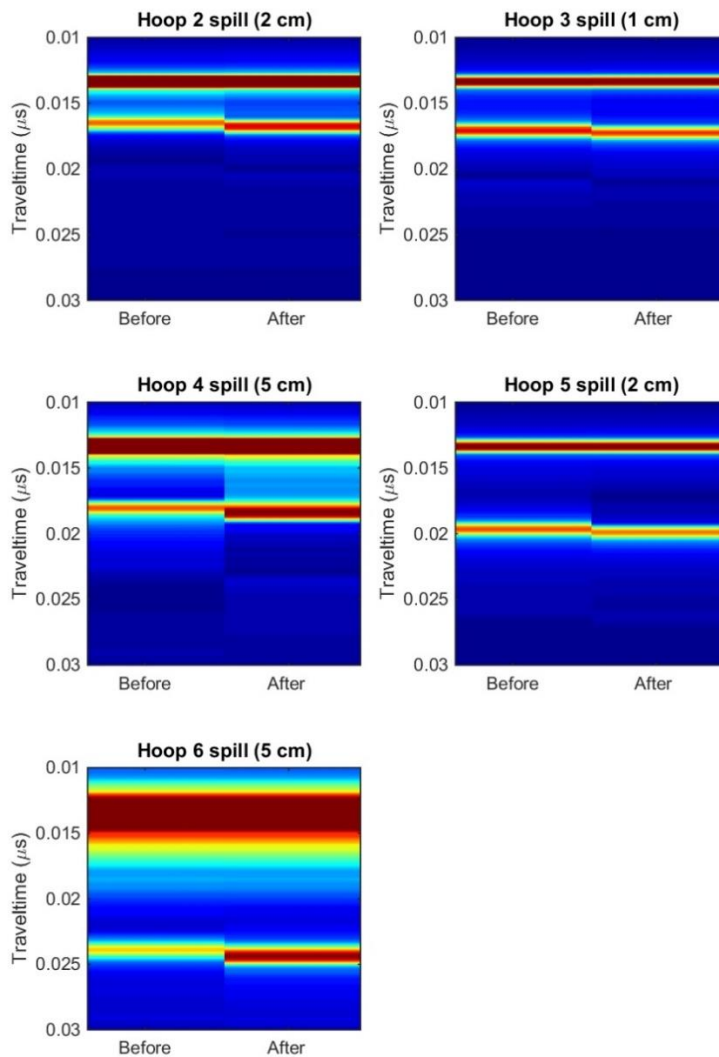


Figure 195. Before and after FMCW radar simulations for 5 injections in the test basin experiment.

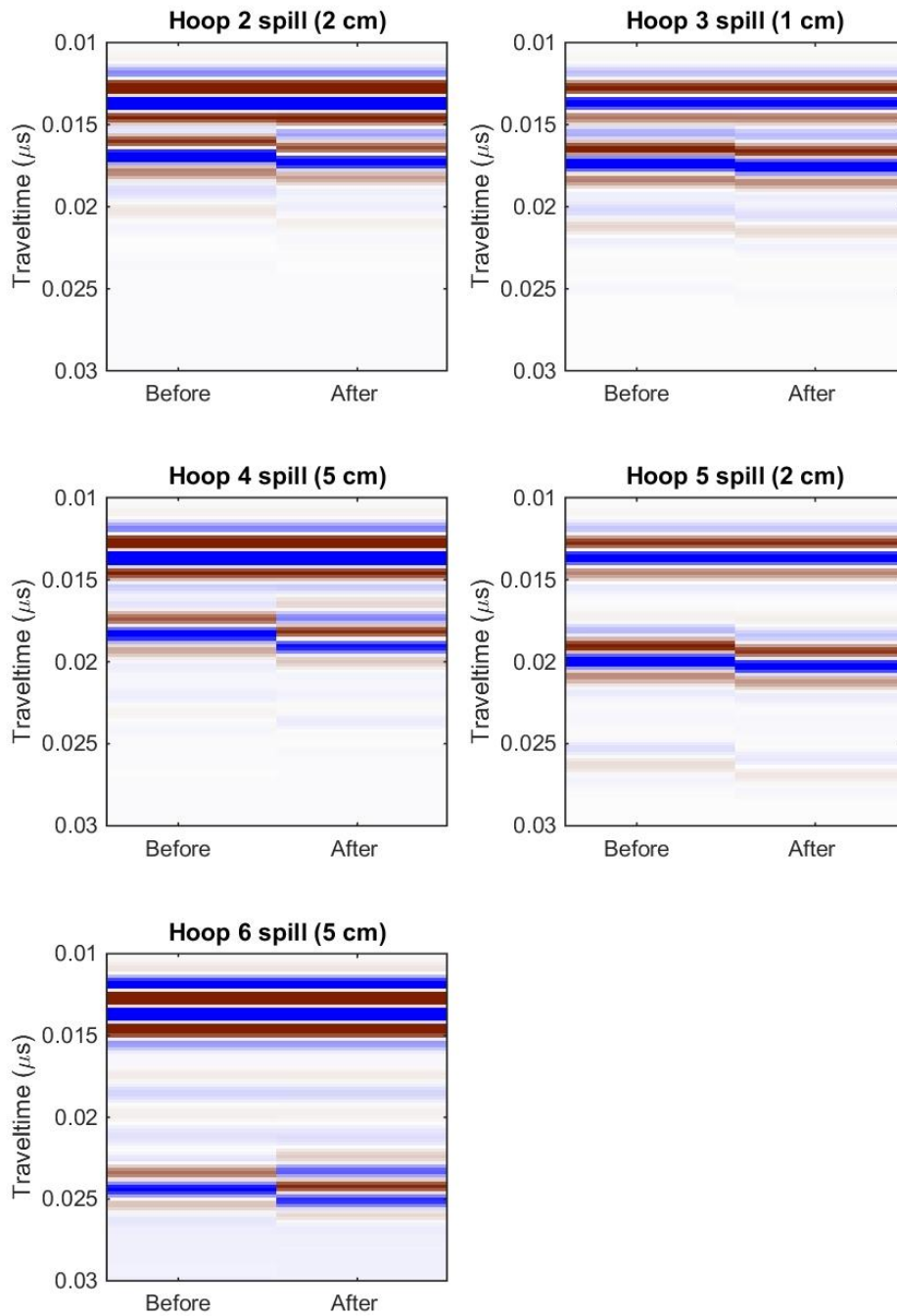


Figure 196. Before and after pulse radar simulations for 5 injections in the test basin experiment.

Next, the response to ice growth and the oil from each injection as it becomes encapsulated within the ice sheet was simulated. Figure 197 shows the results for the FMCW simulation and Figure 198 shows the results for the pulsed radar simulation. In all cases, the introduction of oil caused a substantial deviation of the radar response from background condition; the base-of-ice reflection increased in travel time, while the reflection from the encapsulated oil layer remained at approximately the same travel time. The encapsulated oil layers produced a clear reflection that was above the background reflectivity due to natural variations in the ice column. The encapsulated reflection amplitude tended to decrease as the ice column grew because as the ice grew colder around the oil, the permittivity contrast between the oil and the ice decreased, leading to a smaller reflection coefficient. The results of the simulation are comparable to the laboratory observations; however, the relative amplitude of the encapsulated oil reflection is higher in the laboratory data than in the simulations. Note that for the Hoop 2 scenario, the encapsulated oil is not well resolved from the ice surface reflection, but is still detectable.

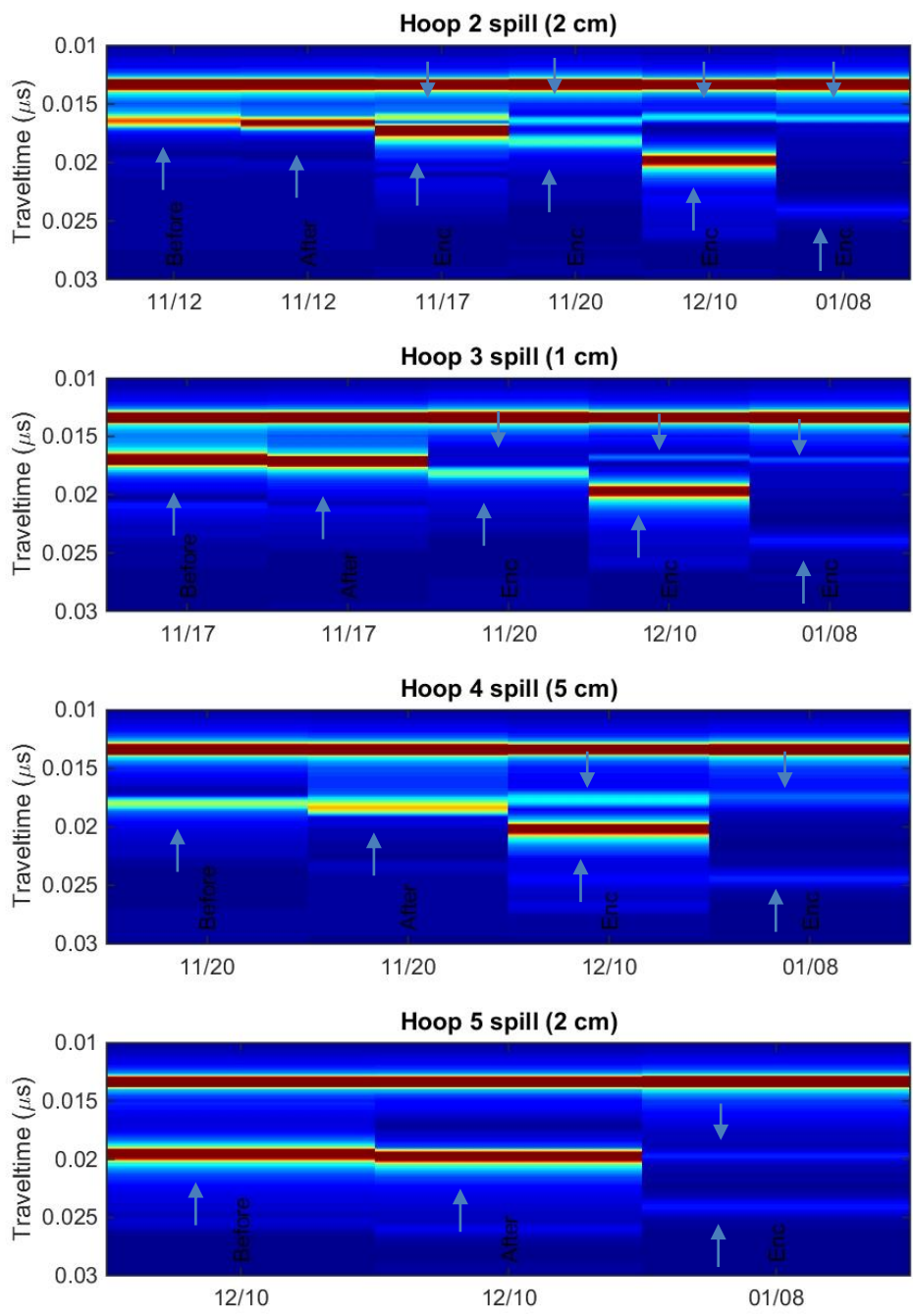


Figure 197. Simulations showing the evolution of the FMCW radar response for the injections into Hoops 2 – 5. Up arrows point to the base of ice and down arrows point to the encapsulated oil.

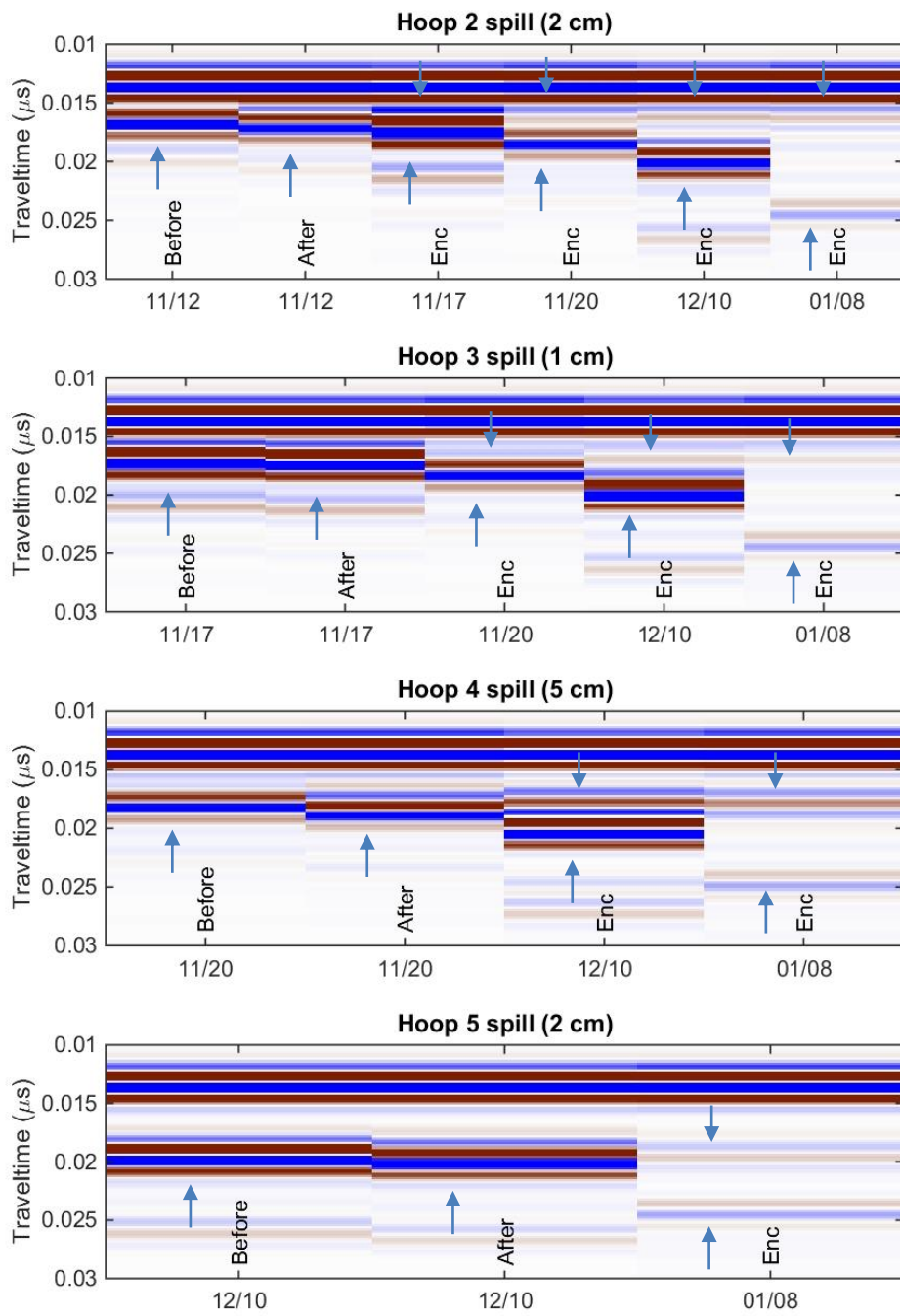


Figure 198. Simulations showing the evolution of the pulse radar response for the injections into Hoops 2 – 5. Up arrows point to the base of ice and down arrows point to the encapsulated oil.

Natural Ice Simulations

The results of the natural ice simulations are below. The models were run using the ice property models provided by the UAF team for typical first-year ice conditions on a monthly basis from November through June. For each spill scenario, a background model with no oil present in the system was run. Then for each month, spill thicknesses of 1 cm, 2 cm, 5 cm, 10 cm, and 15 cm were simulated. For each spill thickness, we modeled oil at the base of the ice, then with the oil encapsulated with 1 cm, 5 cm and 10 cm of ice beneath the oil, then with the full ice thickness for each subsequent month. Shown are the results for a January spill with 0, 1 cm and 2 cm of oil. These are representative of results for all other months, and for the thinnest spills called for in the project parameters. The thicker spills generally provide a greater response, so these thinnest spills define the lower limits of the radar detection. Plots for all model runs may be found in Appendix IV.

Figure 199 shows the FMCW model results and Figure 200 shows the results for pulsed radar. For both radars, introduction of 1 cm of oil at the base of the ice produced a small change in radar response. As this layer became encapsulated, the difference from background increased. The encapsulated oil layer can be observed through May; however, with just 1 cm of oil, the amplitude is comparable to reflections produced by natural variability in the ice. When the spill thickness increased to 2 cm of oil, the radar response over background increased notably. A clear and distinct response is observed from the encapsulated oil layer through April and can still be seen in May. With 2 cm of oil, the radar reflection amplitude is significantly above the amplitude of reflections produced by background variability in the ice. At greater oil thicknesses, the radar response became even more pronounced.

Note that base-of-ice reflection cannot be detected in May or June. In May, enough radar energy reaches encapsulated layers from spills up to February, but the systems cannot image the deeper reaches of the ice pack. Encapsulated spills in the shallow part of the ice pack, from a November or December spill are easily detected in May; however, no internal ice features can be imaged in June. Two factors influence the radar penetration: 1) warmer ice at the surface means greater surface scattering and less radar energy penetrating into the ice volume, and 2) a warmer ice pack corresponds to a higher brine concentration leading to greater radar signal attenuation – i.e. a shallower imaging potential.

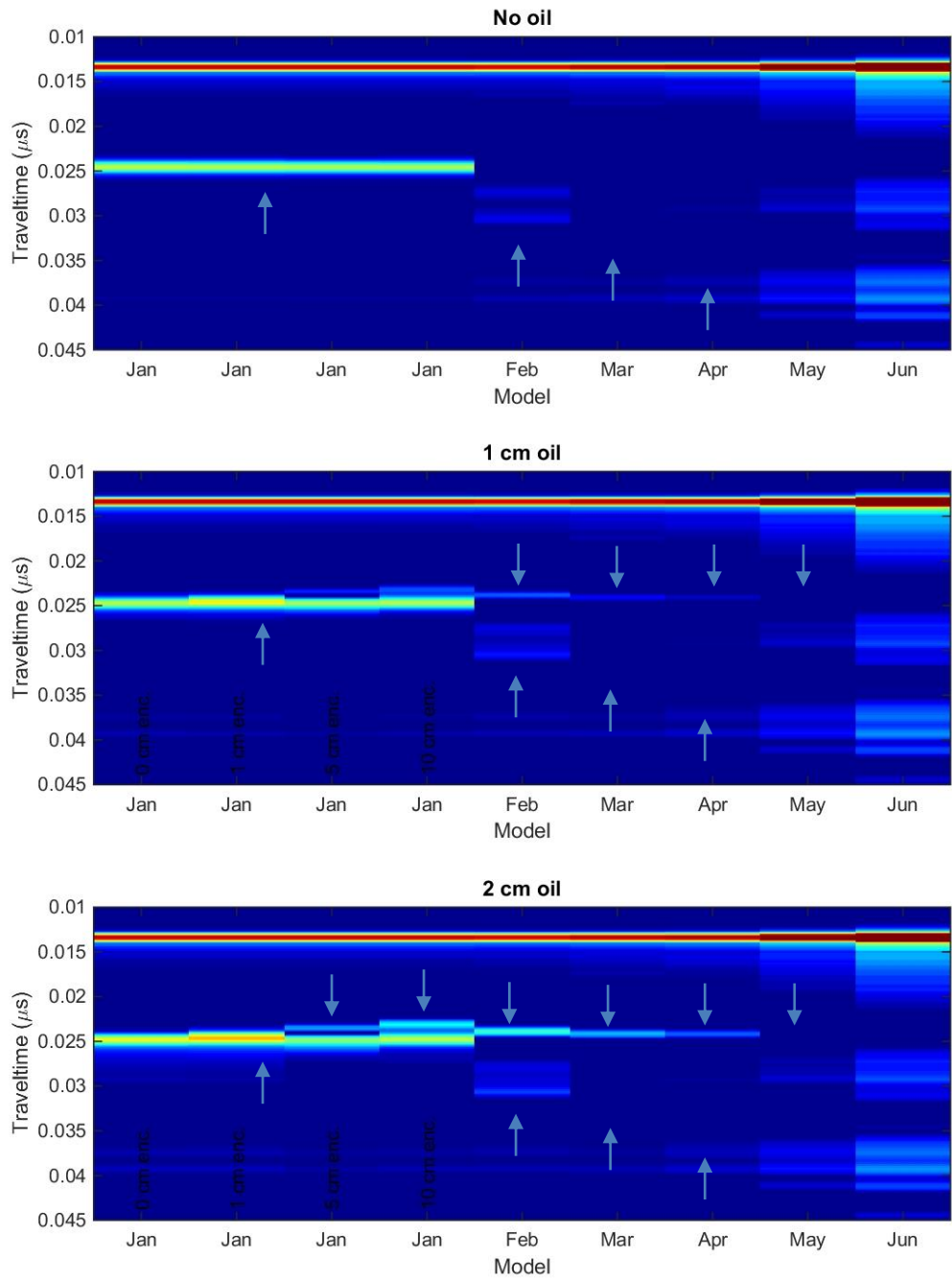


Figure 199. Evolution of the FMCW radar response to an oil spill in January. For comparison, oil spills of 0, 1, and 2 cm are shown. Up arrows point to the base of ice and down arrows point to the encapsulated oil.

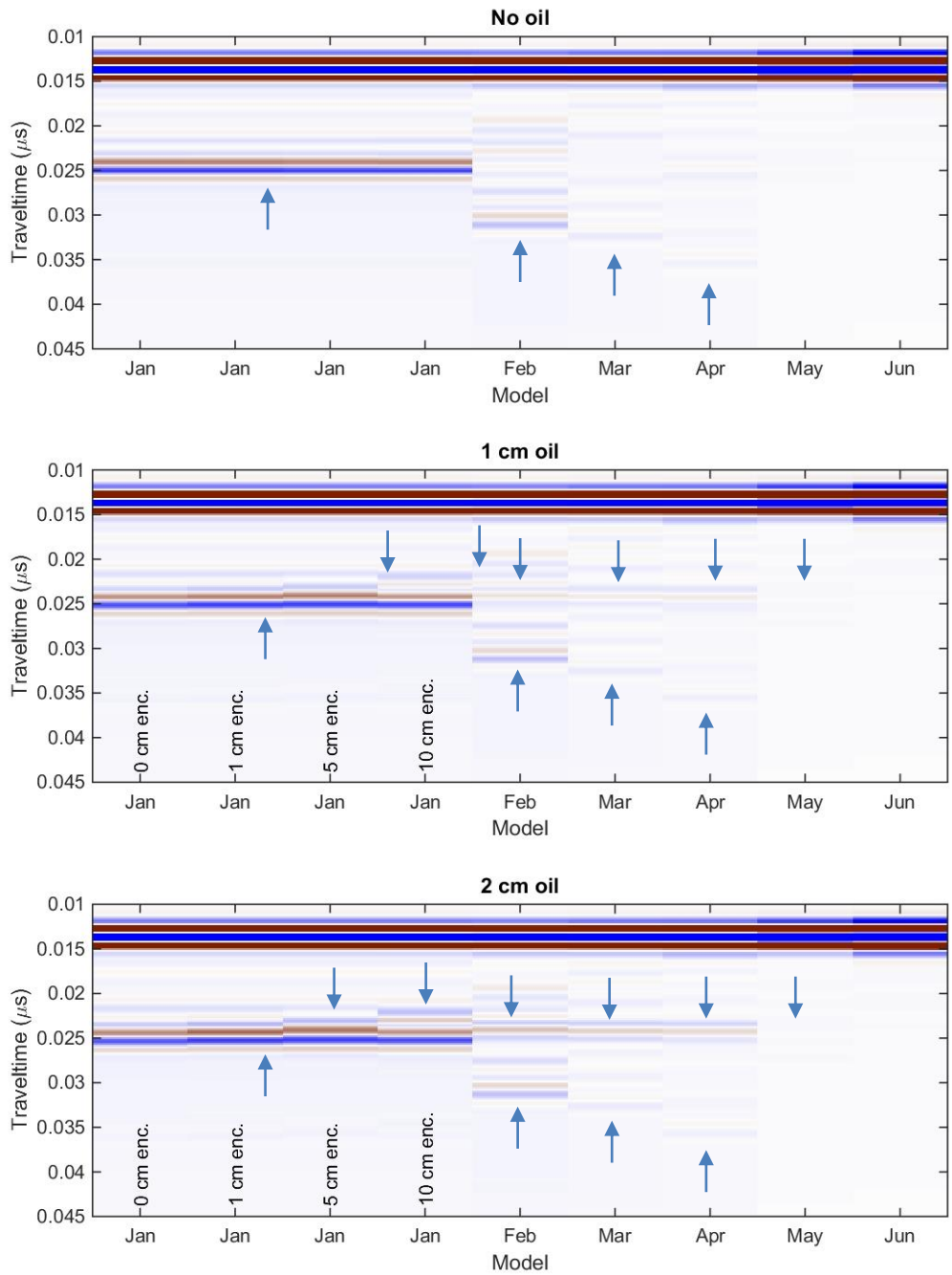


Figure 200. Evolution of the pulse radar response to an oil spill in January. For comparison, oil spills of 0, 1, and 2 cm are shown. Up arrows point to the base of ice and down arrows point to the encapsulated oil.

4.4.1.2 *Modelling Results: 2D Off-Ice Radar Modelling*

The purpose of these simulations is to evaluate the change in radar response with increasing flight height above the ice. In particular, how the radar footprint increasing as a function of height above the target impacts the radar systems' ability to identify a small scale spill. The project parameters dictate the evaluation of the response to a 2 m diameter pool and a 200 m diameter pool. The 200 m diameter pool is well above the radar footprint at any reasonable flight height, so the 1D model is an adequate representation for this case and was not further analyzed with the 2D model.

The response to a 2 m diameter pool was modeled using a 2D finite difference algorithm that operates using the exploding reflector principle. The exploding reflector principle states that the data recorded by a series of coincident sources and receivers at the surface is approximately equivalent to the data recorded as one way propagation by a line of receivers at the surface and an array of sources at all subsurface discontinuities. The sources have amplitude equal to the reflection coefficient at that point in the subsurface. This approach enables the simulation of an entire radar profile in a single model run, which greatly reduces the model run time, but at the cost of some reduced accuracy. This said, the model remains computationally intensive, and model runs are on the order of days, even for the small models simulated here.

Given the long run time, a single scenario was chosen for simulation – the January ice model with 5 cm of oil at the base of the ice. The model is 6 m long, with the 2 m oil pool placed in the center. Figure 201 shows the model electrical properties.

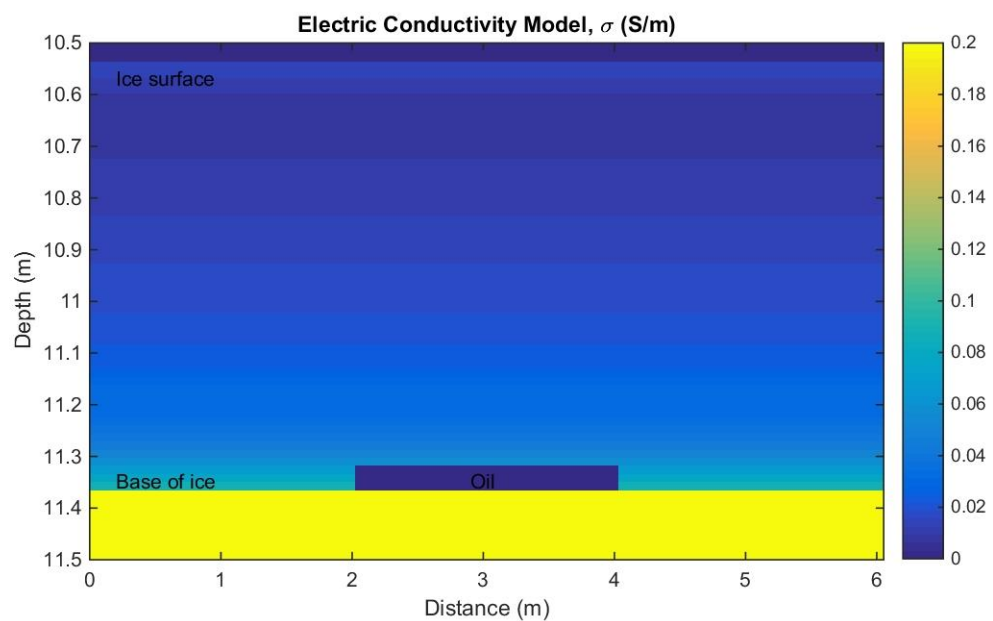
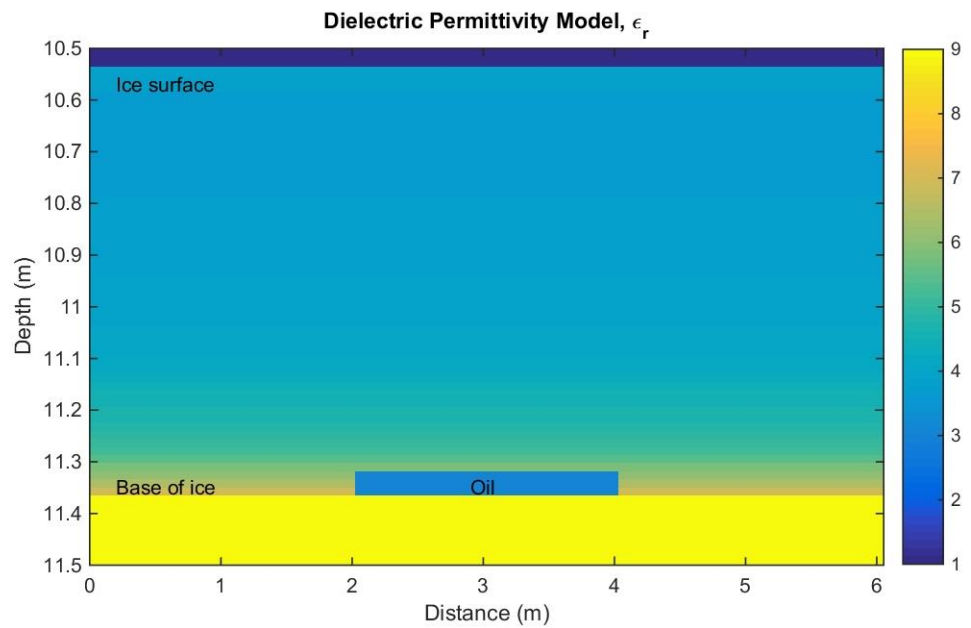


Figure 201. Ice electrical property models for the real world airborne radar simulation. Note that relative permittivity is clipped at 9 and conductivity at 0.2 S/m, even though the values for sea water are much higher (~87 & > 1 S/m respectively).

Pulsed Radar Model

For the pulsed radar, a 500 MHz Ricker wavelet was used as the source and is similar to the signal produced by our commercial radar system. This wavelet has a bandwidth from about 250 MHz to 1 GHz. The surface coupled radar response along with the responses at 2, 5, and 10 m heights are shown in Figure 202. At all elevations, there is a clear increase in amplitude associated with the oil pool. This is highlighted in the plotted reflection strength (Figure 203). This result is fully consistent with the observations of laboratory data acquired during the test basin experiment. For a more quantitative assessment, the reflection amplitude at the base of ice was extracted from each of the four models (Figure 204). For this model, the base of ice reflection amplitude over the oil spill was a factor of 2.1 larger than the background response where no oil was present. As the radar flight height increases, the amplitude increase becomes more laterally diffuse, as expected with an increasing radar footprint; however, even at the maximum model height of 10 m, the oil reflection amplitude was still 1.9 times greater than the background reflection. These results are encouraging and suggest that it will still be possible to detect relatively small pools from an airborne radar platform in a field scenario. A significant caveat here is that detection will require a flight path that passes within just a few meters of the pool. It must also be noted that this model does not include coherent noise due to scattering from the helicopter/airplane and that this noise is generally much higher in amplitude than the pulsed radar reflection from the base of ice.

FMCW Radar Model

The source for the FMCW simulation was a constant amplitude, linear sweep sine wave from 500 MHz to 1.7 GHz. Although the system deployed in the field sweeps to 3 GHz, little energy propagates through the ice above 1.7 GHz, and including the higher frequency would have significantly increased model run times. Figure 205 shows the simulated FMCW radar responses for surface coupled and heights of 2, 5, and 10 m above the ice. Scattering from the edges of the oil pool is not as prevalent as with the pulsed radar model. Figure 206 shows FMCW reflection amplitudes along the base of ice reflection. Again, for the surface-coupled radar, there was a factor of two increase in reflection amplitude over the oil pool. The peak amplitude actually increased slightly for heights of 2 m and 5 m, while at 10 m the amplitude is lower and diffused more laterally, as expected. There is a somewhat more complicated interference pattern produced for the FMCW radar than the pulsed radar near the edges of the oil pool. This is because of the slightly different bands of the two radars resulting in different resonant peaks. Note that this model does not correctly simulate the horn antennas utilized by the BSU field system, which tend to narrow the radar footprint and would sharpen the response to the oil pool at higher flight altitudes. Because of the improved directionality, this FMCW greatly reduces coherent noise generated by the helicopter or airplane. The modelling results suggest significant potential to detect an oil spill from an airborne platform for this spill scenario but as with the pulsed radar, the flight path would have to be within a few meters of the spill location.

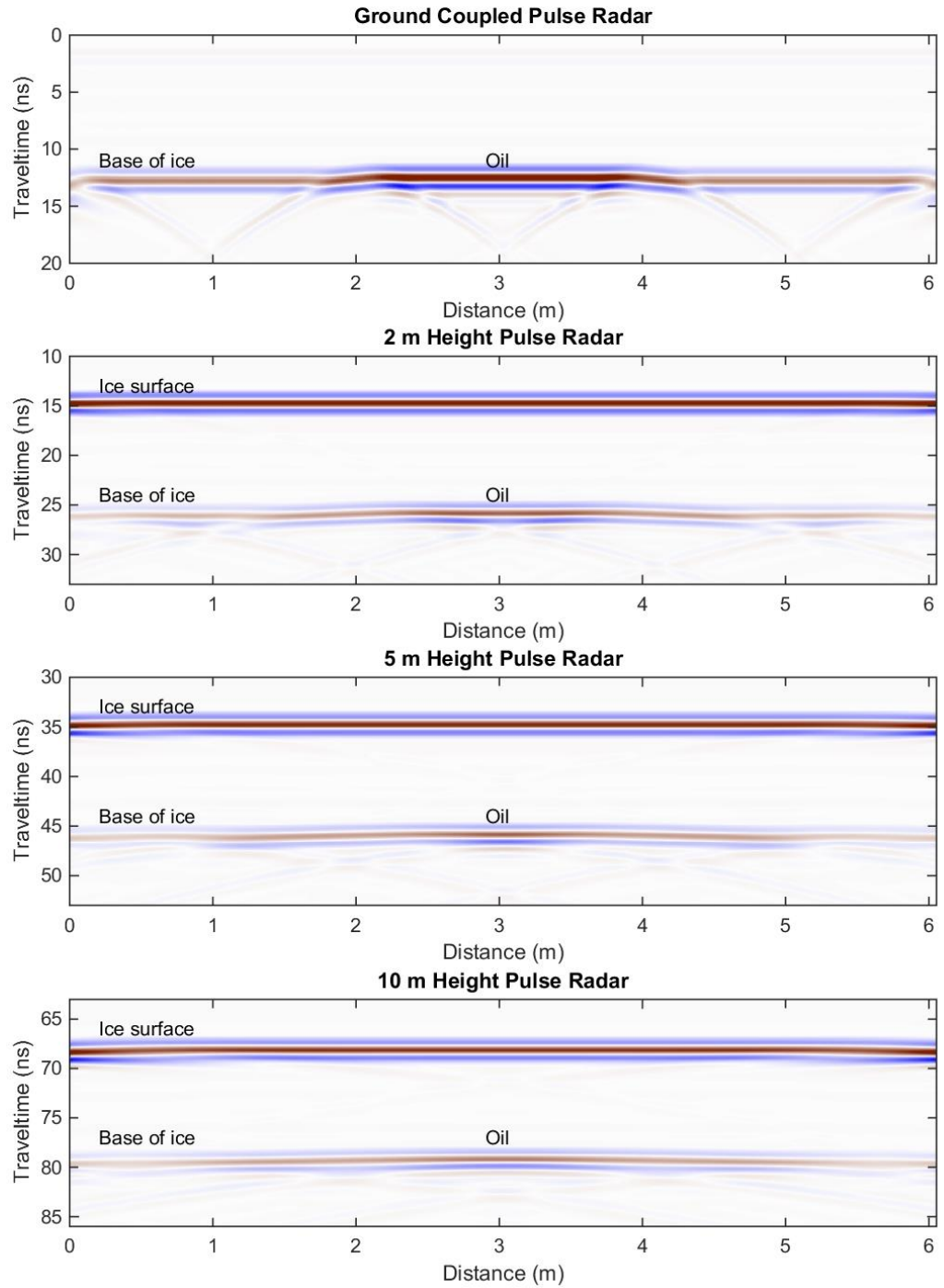


Figure 202. Pulsed radar model runs for the real world airborne radar simulation. The 2 m oil pool is simulated between meter 2 and 4 of the 6m long flight.

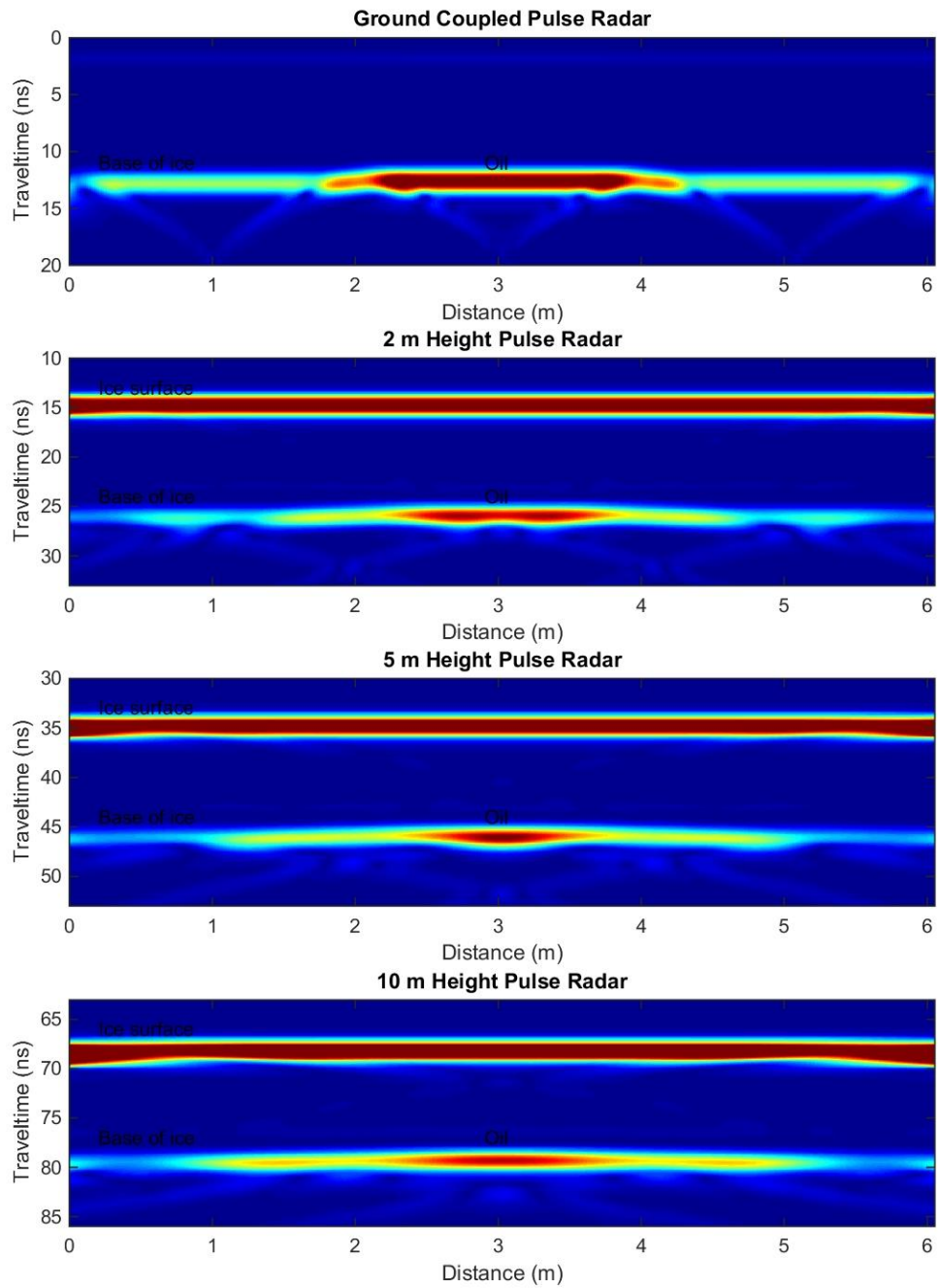


Figure 203. Reflection strength extracted from the simulated data shown in Figure 202. The 2 m oil pool is simulated between meter 2 and 4 of the 6m long flight. Note that the reflection amplitude becomes more laterally diffuse with increasing radar height above the ice.

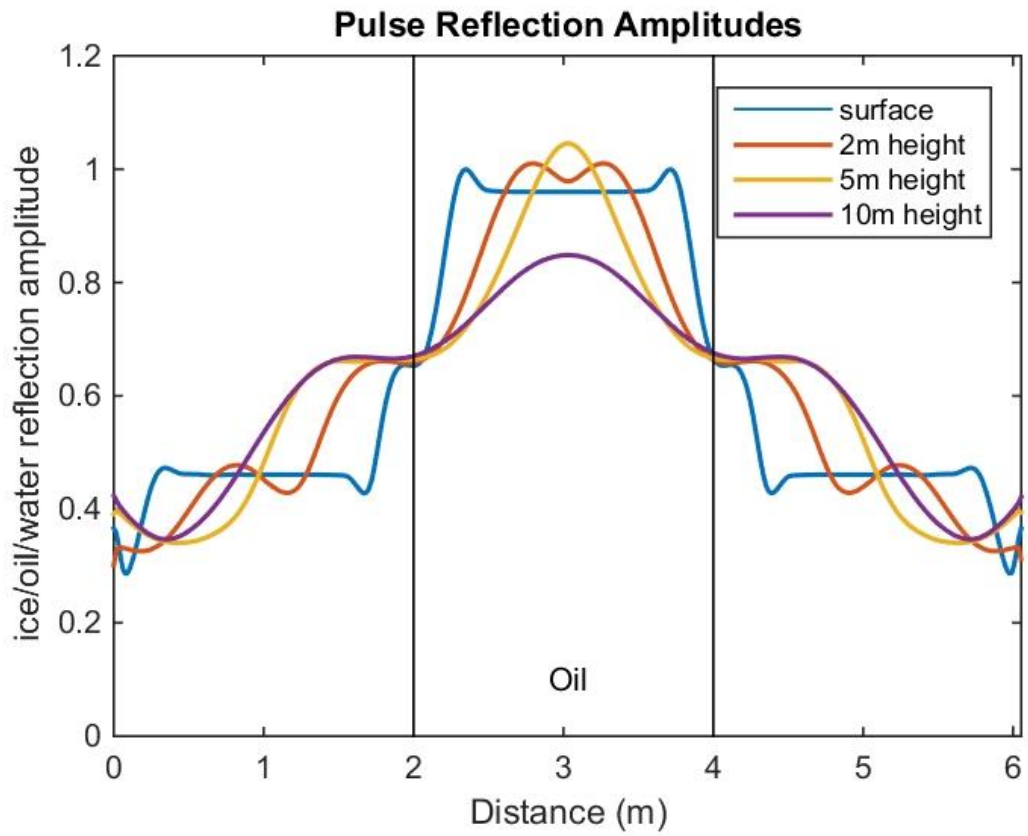


Figure 204. Amplitude along the base-of-ice reflection for the simulations shown in Figure 203. For the ground coupled radar, there is a factor of 2.1 increase in reflection amplitude over the oil. The response becomes more laterally diffuse with flight height, but remains significantly above the background at the maximum height of 10 m.

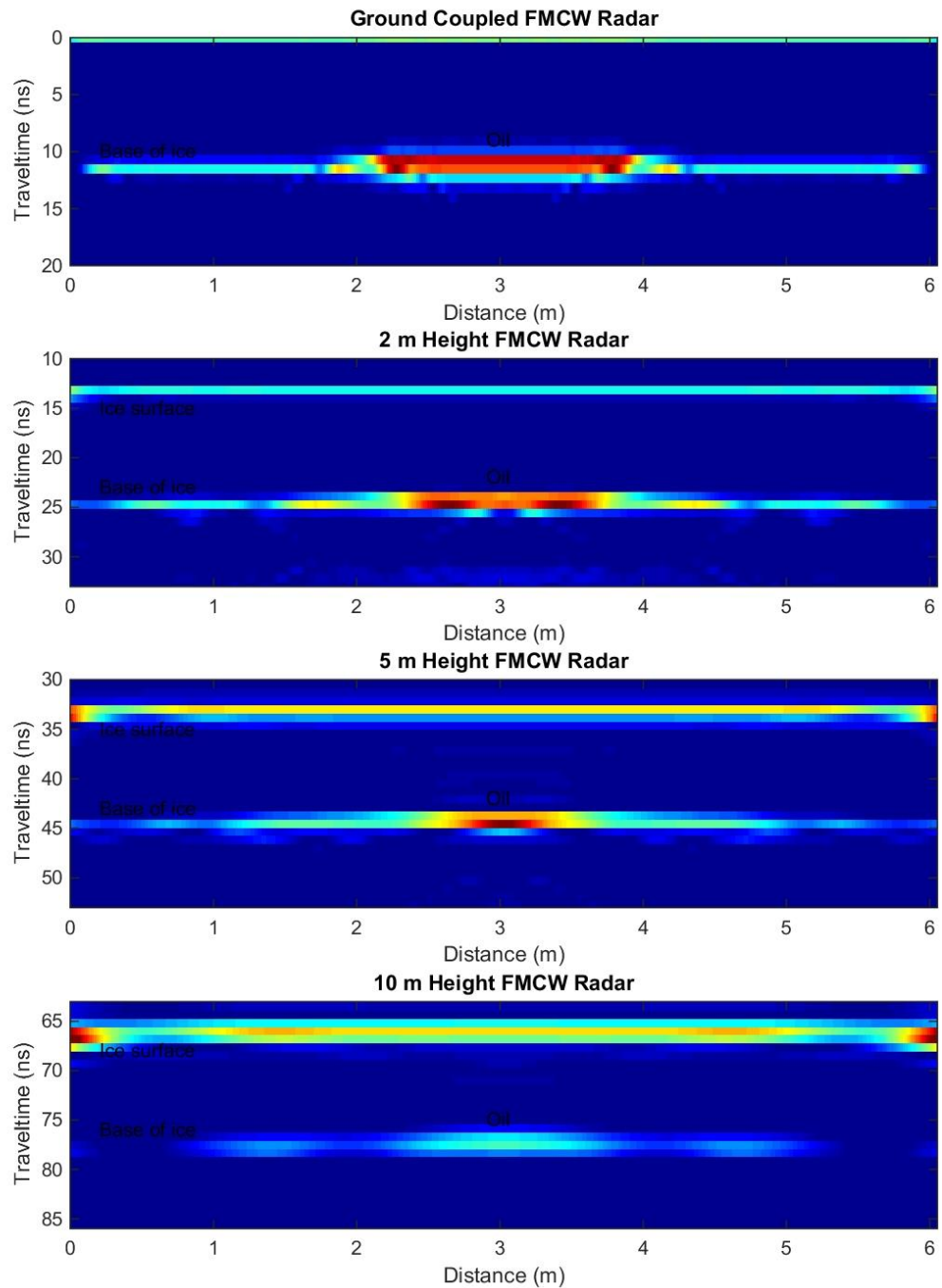


Figure 205. FMCW model data plots for the models shown in Figure 201. Compare to the pulse radar amplitude plot in Figure 203. The results are qualitatively similar.

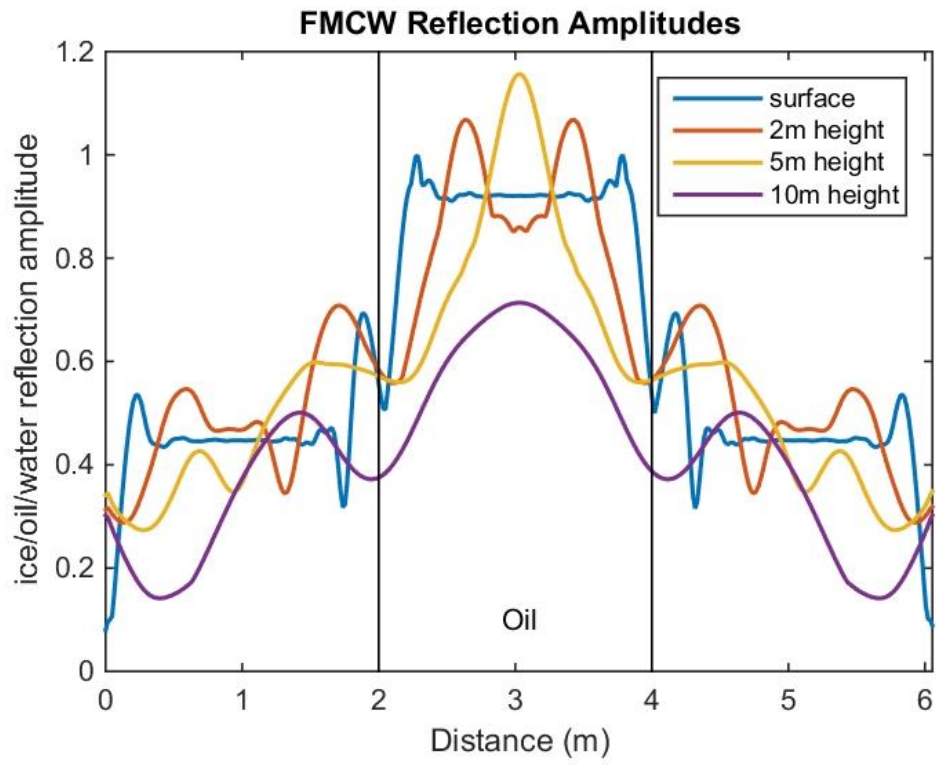


Figure 206. Amplitudes for the base-of-ice reflection from the FMCW radar. Compare to amplitudes for the pulsed radar in Figure 204.

5. DISCUSSION

5.1 General Comments

This section is primarily written by the Pegau, Garron, and Zabilansky based on the results presented earlier. The experiment was designed such that most of the equipment was operated by CRREL personnel rather than the instrument developers. There was a mechanism by which the data could be viewed remotely, but in some instances the lack of personnel on site limited the performance of the instruments. It also meant that the investigators were not fully aware of all the conditions in the tank. Some conditions, particularly bubbles under the ice, were not fully realized until after the experiment. This is mentioned because some of the interpretations in the results may conflict with the discussion below.

In general, the ice in the tank represents sea ice found in coastal areas in the presence of a weak current or in protected bays in the absence of a current. The largest observed difference in the ice structure is the absence of strong anisotropy within the horizontal plane due to c-axis alignment, which is absent in the tank as compared to samples from the field taken in regions with a weak current (such as coastal Alaska or coastal Siberia). This may mean there are minor differences in acoustic and electromagnetic properties, but not to a degree likely to impact oil detection or oil behavior in a significant fashion. The crystal structure of the basin ice was most notably different from pack ice in the lack of granular ice at the surface. The temperature and salinity characteristics of the ice are within expected values, so overall the ice is a good representative of natural level sea ice grown nearshore under quiescent conditions.

Working in an indoor environment allowed the environmental variables to be controlled and better regulate the conditions under which the oil was injected. However, there are limitations on many of the sensors imposed by being in a laboratory facility. Sensors were operated closer to the ice than would be used in the field. The short distance to the ice was mitigated by reducing power settings and this then required additional data processing to remove signal noise. As should be expected during any experiment of this length, issues cropped up with the instrumentation and basin cooling systems. Ways were found to fix problems and data continued to be collected. In the end, all types of instruments were able to demonstrate an ability to detect oil during some phase of the experiment.

5.2 Laboratory Performance

There were four primary types of experiments conducted during the project. The first injection was at the surface into a brash ice mixture. After that, all injections provided a layer of fresh oil under the ice. The oil then became encapsulated in the ice (with the exception of Hoop 6). The last experiment focused on migration of oil to the surface during melt.

The interpretation of the sensor performance is provided in Table (13). Some of the systems were potentially limited in their detection ability by the physical limitations of operating in the indoor facility, but this table provides a good indication of the overall capabilities of the different sensors.

5.2.1 Cameras

Optical cameras were used both above and below ice during regular operations to monitor the presence of oil, its distribution, movement through the ice, and to guide oil injections. From above, the ice must be clear of snow in order to visually detect oil. With the high spatial resolution of an

image, it was possible to detect small areas of oil within the brash ice from both above and below. With cameras beneath the ice, using the room lights, it was possible to monitor oil injections and determine which hoops had oil even after 30 cm of new ice grew below the oil. In the camera images, a pile of snow on the surface had a similar appearance to encapsulated oil. The experiment did not test the ability to use underwater lights in conjunction with underwater cameras to determine if encapsulated oil could be detected using lighting from below.

5.2.2 Thermal Infrared

Problems with the IR system chosen for this experiment restricted data collection during the ice growth phase of the experiment. The system was also inoperative during the experiment to determine if it could detect warm oil under sea ice. Two additional IR cameras were brought in for use during the melt phase to document the presence of oil, particularly after the oil was heated by an artificial sun. The ability to detect oil at the surface appears to depend on the amount of light and the air temperature. Oil in the ice that had been exposed to the artificial sun retained heat and remained visible in the thermal IR for several hours after the lighting was removed. The surface oil and ice had similar temperatures when room temperatures were cold and light levels low.

5.2.3 Radiometers

Radiometer results are similar to cameras. From above, the oil is easily detected when it is at the surface and not covered by snow. Oil encapsulated under a few centimeters of ice was not detectable in the albedo measurements. When the oil is on the surface, a simple band ratio using near infrared wavelengths appears to provide a means of discriminating oil from other objects.

From below, the presence of oil decreased the transmittance by three orders of magnitude, and the decrease remained constant through encapsulation and melt.

Table 13. Sensor performance during the laboratory experiments. A “yes” indicates the oil could be detected, “no” that is was not observed, “P” indicates there are still questions or the results were not consistent, and “N/A” is not applicable. In the encapsulated oil row, the number is the number of cm of ice below the oil layer.

Location	Airborne					On ice	Below ice											
	GPR	FMCW	Optical	FP	IR		GPR	Optical	FP	Narrowband	Narrowband	Narrowband	Narrowband	Broadband	Broadband	Broadband	Multibeam	Multibeam
	500 MHz	0.5-2 GHz	350-2500 nm	400-600 nm	7.5-13.5 μm	500 MHz	350-800 nm	400-600 nm	5 MHz	1 MHz	0.5 MHz	0.3 MHz	75-130 kHz	115-225 kHz	370-590 kHz	200 kHz	400 kHz	FLS
Oil and brash ice mixture	N	N	Y	Y	P	N/A	Y	N	Y	N	N	N	N	N	N	P	P	N
Fresh oil under ice	P	P	N	N	P	Y	Y	Y	Y	Y	Y	Y	Y	Y	Y	Y	Y	N
Encapsulated oil	Y	P	N	N	N	Y >3 0	Y >3 0	Y 6	N	N	Y 2	Y 5	Y 7	Y 7	N	Y 4	Y 4	N
Exposed oil on ice	P	P	Y	Y	Y	N/A	Y	N	N	N	N	N	N	N	N	N	N	N

5.2.4 Fluorescence Polarization

Like other optical sensors, the aerial FP sensor only detects oil at the surface. There was no indication of detection of oil a few centimeters below the surface. Below ice, the sensor detected small pockets of oil mixed in brash ice, fresh pools of oil, and could detect oil encapsulated by new ice up to six centimeters thick.

5.2.5 FMCW

The FMCW suffered from being a prototype system without a dedicated operator. The lack of an operator familiar with the system meant that there were issues with the electronics and interferences from other items in the tank that were not detected until the experiment was complete. These issues limit what can be determined about the capabilities of the system. The FMCW was able to detect encapsulated oil in some hoops (Figure 124), but did not detect the oil that was encapsulated under Hoops 1 and 5 at that time.

5.2.6 GPR

The surface-coupled GPR provided clear and consistent detection of encapsulated and fresh oil below the ice. The high signal to noise data is suitable for inversion using recently developed

waveform inversion methods. The unit was not used over Hoop 1 or during the melt phase, because of oil present at the surface that would contaminate the equipment.

Because of inadequate shielding, the aerial GPR data were heavily contaminated with coherent noise primarily from reflections from the boom that suspended the radar and the additional instrumentation mounted on the boom. Heavy manipulation of the data was required to extract the subsurface signal, but there were times that encapsulated oil and possibly oil at the base of the ice was detected. The results are generally consistent with previous experiments. The airborne GPR's ability to detect encapsulated oil still depends on the air temperature being below -10 C. Even when the ice is cold, it can be difficult to interpret the airborne GPR. For example, encapsulated oil is present in Hoop 1 in Figure 130 that was not identified during the analysis. The base of the ice is warmer, which causes more attenuation of the radar signal making oil detection near the base of the ice more difficult. The oil at the base of the ice could be identified when comparing before and after images, but would have been difficult to identify in the field.

5.2.7 Acoustics

All systems saw an increase in reflectivity in the nadir direction when oil was present. The structure of the skeletal layer of the ice is believed to be important to determine the changes in the acoustical return when oil is present.

The generation and shedding of small air bubbles by the underwater instruments reduced the sonar systems ability to detect encapsulated oil (discussed under problems encountered). The presence of large bubbles, such as those injected in hoops 3 and 6, had the largest impact on the acoustic signal making them easy to detect. This has implications in operational spill scenarios where gas will often accompany oil at the time of discharge.

5.2.7.1 Narrow Band, Single Beam Sonar

The narrow band, single beam sonar units were able to detect the presence of un-encapsulated oil under the ice. The 5 MHz unit was unable to penetrate the oil to determine thickness. Little difference in the ability to resolve oil thickness was observed among the frequencies. The 1, 0.5, and 0.3 MHz units were all able to measure the thickness up to 10 cm (Hoop 6). The ability to detect encapsulated oil increased as the frequency decreased with the 0.3 MHz unit able to detect oil with 5 cm of encapsulating ice.

5.2.7.2 Broad Band Sonar

The output of these systems had to be reduced to operate within the tank and therefore these results may not reflect the full capability of the systems. The broad band sonar did not detect small pockets of oil in the brash ice. The minimum detectable thickness of an oil layer increases with decreasing frequency, so the 500 kHz system was the best for penetrating oil and determining thickness. The ability to detect encapsulated oil increases with decreasing frequency so the unit with the 100 kHz central frequency could penetrate through the most ice. There is an indication that the 100 kHz unit could detect the ice/air interface through 60 cm of clean ice.

5.2.7.3 Multibeam Sonar

The surveys using the multibeam units under the brash ice suggest that they were able to detect one larger pocket of oil under the brash ice. The pockets of fresh oil associated with injections under solid ice were detectable using the upward-looking multibeam systems by the distinct angular reflectivity of fresh oil. Using the nadir beams, it was possible to determine thickness of the oil and encapsulation up to about 4 cm of ice. The FLS return was sensitive to the presence of large air bubbles, but it is not clear if it reliably detected fresh oil under the ice.

5.3 Expected Field Performance

Table 14 provides expected instrument performance on level (smooth) sea ice under field conditions. The year was broken into two parts: winter-spring when the majority of the ice is expected to be cold (<-10C) and snow covered and summer-fall when the snow would be thin to nonexistent and when the ice would be warm. It is assumed that it would not be safe to make surface measurements in the summer-fall period. Passive optical sensors (cameras and radiometers) are combined. Acoustic systems are also combined, although results are frequency-dependent. Fresh oil is considered to have less than 6 cm of encapsulating ice. This condition likely represents a time frame of 5-7 days after a spill, although encapsulation rates strongly depend on ice thickness and air temperature.

With all sensors, the ability to detect oil depends on the oil thickness, size of the patch of oil, and the distance from the sensor. When the oil is a small portion of the sensor footprint, it is more difficult to detect. Attenuation of the signal in air or water or ice also decreases detectability.

Table 14. The expected field performance in level first-year ice of instrumentation tested during this experiment, based on laboratory and modelling results. Sensors include Ground Penetrating Radar (GPR), Frequency Modulated Continuous Wave Radar (FMCW), Optical (cameras and radiometers), Fluorescence Polarization (FP), Thermal Infrared (IR), and Acoustic systems. The P (for possible) rating indicates that there are conditions that may allow the system to work, and others when it is expected to fail. A yellow P2 rating indicates that there is still insufficient data fully assess performance. N/A indicates that sensor application in this scenario is not relevant – e.g. using below ice sensors to detect exposed oil on the surface.

Location	Airborne					On ice ¹	Below ice		
Sensor	GPR	FMCW	Optical	FP	IR	GPR	Optical ⁴	FP	Acoustic
Fall-Winter-Spring									
Exposed oil on ice	Y	P2	Y	Y	P2 ³	Y	P2	N/A	N/A
Snow covered oil on ice	Y	P2	N	N	N	Y	P2	N	N
Fresh oil under ice or with up to 6 cm encapsulation)	P2	P2	N	N	N	Y	Y	Y	Y
Encapsulated oil (more than 6 cm new growth)	P	P2	N	N	N	Y	P ⁵	N	P2 ⁶
Summer ²									
Exposed oil on ice	P2	P2	Y	Y	Y	N/A	N/A	N/A	N/A

Notes to Table:

¹On-ice operations apply only to stable ice

² Snow covered oil on ice, oil beneath ice, or encapsulated oil is unlikely in summer

³ As long-wave IR detection depends on measurable temperature differences oil vs. ice related to solar input, there will be periods during the winter when detection is unlikely. Further testing is required to define the operating limits. .

⁴ The performance of optical systems is based on sufficient sunlight penetrating through the snow and ice.

⁵ The ability will depend on the thickness of ice below the oil and the width of the pool of oil.

⁶ The low signal to noise ratio in the tank environment prevented the sonar systems from operating at full power. In a field setting, acoustic systems may be able to detect oil that is encapsulated by more than 6 cm new ice.

5.3.1 GPR

The above-ice and on-ice results are generally consistent with other experiments and the modelling. The modelling suggests that oil can be detected using the system if the signal to noise can be maintained high enough. The usefulness of airborne GPR is currently limited by the ability to transmit sufficient power into the ice. The capability of airborne GPR to detect fresh oil at the bottom of the ice is marked as questionable in Table 14, because during this experiment there were times when oil was not detected. Ice-coupled GPRs can transmit sufficient power to detect fresh and encapsulated oil. Dual polarization GPR are necessary to overcome the anisotropic nature of the electrical properties of sea ice. Because of changes in the electrical properties of ice the GPR is limited to operating at cold temperatures.

5.3.2 FMCW

While modelling suggests that an airborne FMCW should be able to detect oil, this system has not performed well enough in the laboratory setting to evaluate its use in the field.

5.3.3 Optical

Passive optical systems require an adequate amount of sunlight. The need for light limits the system utility during much of the winter. Atmospheric conditions and the need for the oil to be exposed on the surface further limit above-ice systems. Below-ice systems depend on water clarity and the availability of sunlight. The model shows that the thickness of ice required to fill in the light field under an oil patch depends on the size of the oiled area. The larger the oil patch, the greater the encapsulation layer needed to fill in the light field. Radiometers and cameras are not affected as much as an irradiance sensor.

False positive signals in below-ice measurements may come from algae blooms and varying snow thicknesses. The auto gain feature in underwater cameras may lead to false brightening of pictures that mask the light lost due to absorption in oil.

5.3.4 Fluorescence

Fluorescence is detectable from above when oil is on the ice surface or from below when the oil is fresh. There are commercial airborne fluorosensors for spill response available, but they are typically used in specialized planes. We did not model the expected sensor performance in the field, but expect it to be the same as observed in the laboratory.

5.3.5 Acoustics

The acoustic modelling suggests that systems operating at 100-200 kHz are likely to be optimal for detection of oil in ice. A combination of the normal and oblique angles should provide more robust information about oil in and under ice. When oil thickness is greater than one centimeter,

data from these systems can be used to estimate the oil thickness. Under-ice melt ponds and false bottoms may provide false positive signals. The modelling is limited by a lack of understanding of the acoustic properties of the oil once it is encapsulated and verification of model results using field data.

Multibeam sonar provides a map of the under-ice topography that can be useful in determining likely locations for oil to accumulate. This information can be used by oil-spill models to determine the most-likely areas of oil deposition (Wilkinson et al. 2007).

5.4 Sensor Readiness

Each of the technologies are evaluated based on the Technical Readiness Levels (TRL) defined by the Arctic JIP (Table 15). Only the hardware and software criteria were considered. Since most of the sensors were not designed specifically to detect oil, the software is often the limiting component. Often, there is very mature software available, but it is not designed for detection of oil, so it requires training to interpret.

Table 15. Technical readiness level evaluation criteria used.

TRL	Development stage	Hardware development	Software development
0	Unproven idea/proposal	Paper concept. No analysis or testing has been performed.	Paper concept / basic flow diagram. No analysis or testing has been performed.
1	Concept demonstrated	Basic functionality demonstrated by analysis, reference to features shared with existing technology or through testing on individual subcomponents/subsystems. Shall show that the technology is likely to meet specified objectives with additional testing.	Basic functionality demonstrated by analysis and/or reference to features shared with existing software. Running code fragments used to demonstrate feasibility of proposed concepts.
2	Concept validated	Concept design or novel features of design validated through model or small scale testing in laboratory environment. Shall show that the technology can meet specified acceptance criteria with additional testing.	Pre-alpha (non feature-complete) version put through unit testing to verify that source code is fit for use. Threats to the existing code base from the embedding systems point of view identified and listed. External interfaces Identified.
3	New technology tested	Prototype built and functionality demonstrated through testing over a limited range of operating conditions. These tests can be done on a scaled version if scalable.	Functionality demonstrated through testing and debugging of first feature complete version (alpha version). Lifecycle issues with respect to platform bindings and upgrade challenges are addressed.
4	Technology qualified for first	Full-scale prototype built and technology qualified through testing	Factory acceptance test passed.

	use	in intended environment, simulated or actual. The new hardware is now ready for first use.	
5	Technology integration tested	Full-scale prototype built and integrated into intended operating system with full interface and functionality tests.	First user beta (open beta) version integrated into intended operational environment and system hardware with full interface and functionality tests. Site acceptance test passed.
6	Technology installed	Full-scale prototype built and integrated into intended operating system with full interface and functionality test programme in intended environment. The technology has shown acceptable performance and reliability over a period of time.	Release candidate (RC) version integrated into intended operational environment and system hardware with full interface and functionality tests. The software has shown acceptable performance and reliability over a period of time. Strategy for life cycle support in place.
7	Proven technology	The technology has successfully operated in an integrated system with acceptable performance within the predefined criteria.	Release candidate (RC) version integrated into intended operational environment and is ready for mass release.

5.4.1 GPR

Ground-based GPR is a mature technology with commercially available units, but the output takes specialized expertise to interpret. The technology is at TRL 6, and its applicability is limited by the ability to interpret the signal.

The concept of airborne GPR has been demonstrated, but it is limited by the ability to transmit enough energy into the ice. Modifications would be necessary if commercial systems were to be used for this purpose. The need for modifications prior to use puts these systems at a TRL 2.

5.4.2 FMCW

While modelling suggests that an airborne FMCW should be able to detect oil, this system has not performed well enough in the laboratory setting to evaluate its use in the field. The FMCW is at TRL 2; the prototype is built, but hasn't passed laboratory testing and the software is still designed for instrument developers.

5.4.3 Optical

Both cameras and radiometers are mature, commercially-available technologies that have been integrated into deployment systems both above and below water giving a TRL of 6 or 7. Some algorithm development may improve detection capabilities in both above and below water applications.

5.4.4 Fluorescence

There are commercial airborne fluorosensors for spill response available, but they are typically used in specialized planes. The underwater units have been tested in the laboratory environment and have mature software. The underwater units are TRL 5. The systems have been tested, but need to be integrated into deployment platforms to become TRL 6.

5.4.5 Acoustics

All three types of sonar units used during this test have commercially available versions. Most have been integrated into underwater platforms and used in Arctic conditions. Some testing occurred for detecting of oil in ice, and oil could be detected real time by a trained operator. Some software development would allow for unsupervised, automated detection of oil. The systems should be considered TRL 5 or 6.

5.5 Deployment Considerations

This report focuses on the performance of sensors that may be used for detecting spilled oil. The ability to search an area for oil also depends on the platform that the sensor is deployed on and the ability to transmit useful information back to the user.

Safety, survey speed, and capability to carry sensors depends on the platform selected. Airborne platforms include fixed-wing aircraft, helicopters, and a wide array of unmanned aerial vehicles (UAV). On the ice, there are a variety of snow machines. Below the ice, autonomous underwater vehicles (AUV) and remotely operated vehicles (ROV) are potential sensor platforms. Each of the platforms have advantages and disadvantages.

Larger aerial platforms generally have the greatest range (100s to 1000s of kilometers) and speed (50-100 of meters per second), which are important for covering large distances during a search. Fixed-wing aircraft are the fastest, tend to operate a bit higher, and can carry more than the others. Helicopters can operate closer to the ice and move slowly if necessary, invaluable in differentiating between oil and false targets like dirt on the ice. Unmanned aircraft reduce risk to personnel compared to manned aircraft. UAVs that are likely to be used have smaller payload capacity, range (10s of kilometers), and speed (10s of meters per second) than manned aircraft. Airborne systems have the advantage of transmitting data in real-time if the necessary infrastructure is in place.

On-ice surveys require personnel on the ice and represent considerable HSE risks especially in heavily ridged areas, rubble and on moving ice offshore. Survey efforts is likely to be in 10s of kilometers at 1-2 meters per second– more if a sensor, like a ground coupled GPR, can be towed behind a snow machine.

AUVs and ROVs have limited range (AUVs 10s -100s of kilometers, and ROVs in 10s to 100s of meters), and therefore need to be deployed near the survey area from a vessel or ice camp. ROVs have the ability to transmit data back in real time, allowing operators to adapt the survey as it develops. Currently, AUVs can transmit limited amounts of information acoustically or the data has to be collected at the end of the deployment, by which time the oiled ice may have drifted kilometers from its initial position when detected. Determining precise positioning for any systems under the ice requires additional equipment such as acoustic arrays.

The ability to provide data in real time is a key consideration for the transformation and integration of data products into actionable information. Data produced from remote sensing technologies

can range from simple to complex, but regardless of the complexity, the availability, and ease of data interpretation will ultimately determine if and how the products will be used. Data that are not provided in real time or must be post-processed have reduced utility during an active oil spill due to the inherent temporal delay. Bandwidth limitations may restrict the size of the data product that can be transmitted from the collection point to the decision makers, while simultaneously increasing the time it takes to deliver the product.

The utility of remote sensing systems depends on the speed of data delivery and product development. Oil detection products can be produced automated, semi-automated, and through post-processing of data. Automated processing (unsupervised processing) would likely include on-board processing of the data in close to real-time, formatted to the end user needs and the communication infrastructure to deliver that information to the end user without human intervention. Semi-automated processing (supervised processing) would achieve the same goal, but with human intervention as some point during the process. The semi-automated approach often requires a person with specialized training to interpret the data that returns. Post-processed data requires raw data are supplied for additional processing and interpretation prior to a product being available.

Most prototypical equipment produces data that, when processed, are interpretable by instrument developers or scientists. Products for a non-scientific audience require additional processing of the data into secondary and tertiary products. As systems mature, the automation of products improve; however, most systems are designed for other purposes and detection of oil requires additional software development.

Automated detection of oil was not a goal of the experiment reported here. Each of the tested sensors produced data products that were interpretable by the scientific audience for which they were intended and detected oil under various conditions. Data processing from the experiment was not required to meet near real-time data processing (less than two hours) standards. Nor were the data from different sensors integrated. An important next step in developing these technologies will be to identify the software improvements and data fusion required to provide useful products.

While the report focuses on the capabilities of the sensors, the appropriateness of a sensor suite also depends on the deployment platform and the ability to retrieve information.

5.6 Sensor Suite

This project confirms the overall conclusion of previous work including RS Phase 1: that no one sensor has the capability of detecting oil in all situations. In addition, some sensors may complement each other in terms of oil thickness resolution vs. area coverage or swath width. Future operational systems will likely employ suites of different sensors operating from various platforms under, on and above the ice surface to provide the means to detect oil in a range of ice environments at different times of the year. Particular sensors have different strengths and weaknesses, as evident in Tables (13 and 14). The selection of sensors also depend on the platform on which they are to be deployed; however, based on the performance of the sensors, their maturity, and integration into existing deployment systems, a number of possible sensor suites can be recommended.

5.6.1 *Oil on Ice*

The study results suggest that aerial sensors should include visible and thermal infrared imagers. Presently available radar technology provides the greatest opportunity for aerial mapping of oil on the ice surface or under snow, but requires future development to lead to an operational airborne tool to detect oil encapsulated within ice. Ground penetrating radar operating from the ice surface is an appropriate tool as long as there is a stable and safe working environment.

Currently, the optical systems including cameras, spectral radiometers, and laser fluorosensors along with IR detectors are the most fully developed technologies for airborne reconnaissance. All of these sensors are limited to detection of oil on the surface of bare ice. Introducing even a thin layer of snow over the oil, can reduce their capability to zero. All of these sensors can be mounted on fixed or rotary aircraft and, in many cases, are small enough to be mounted on unmanned aerial systems. For detection of oil at the surface, a minimum of a visible wavelength camera and a thermal IR camera should be used. An IR camera would help identify oil based on solar heating during the daytime and extend the capability into the dark to some extent. The laser fluorosensor and spectral radiometers are potential additions that can help identify oil from other dark objects. Other types of open water sensors, such as ultraviolet systems, may be of use, but remain untested for this application.

GPR is currently the only sensor that can detect oil on the ice surface buried under snow; however, data interpretation requires a well-trained operator.

5.6.2 *Oil under Ice*

From above the ice, the ice-coupled GPR is appropriate when the ice is cold enough for signal transmission and when a stable ice sheet is available to permit on-ice surveys. Again, data interpretation requires a well-trained operator.

Based on the results of this study, an effective underwater detection suite should have a low light camera, broadband and/or multibeam sonar, and possibly a spectral radiometer or FP. While the various sonar units had similar levels of performance, the multibeam type of sonar provides the added ability to create a 3D map of the underside of the ice that may help identify priority locations for oil to accumulate and narrow the search area (oil will naturally seek the highest spots in the under ice surface – thinnest ice). Because the false positives for the multibeam are most likely to occur in the spring when there is sufficient light, matching this system with a camera should provide coverage and positive identification. Cameras with the ice lit from above are the most versatile device tested and require the least skill to interpret the data. A multibeam sonar in the 200-400 kHz range seems to have a good combination of thickness resolution and penetration into the ice. The multibeam sonar would allow for mapping in the dark, but is best used before the oil is encapsulated. Under limited encapsulation, the nadir beam can be used to identify potential oil layers. At this time, a trained operator would need to interpret the multibeam sonar data. It is likely that software improvements and data processing algorithms could automate oil detection. A laser fluorosensor would be a useful addition to isolate potential false positive items (variations in snow depth or phytoplankton) in a camera image. The fluorosensor could also be used in the dark. These sensors can be deployed on ROVs or AUVs.

5.6.3 *Oil in Ice*

Two sensors demonstrated consistent capabilities for detecting oil with greater than six centimeters of encapsulating ice: the ice-coupled GPR and underwater cameras. The GPR requires cold ice and a trained operator for interpretation. Since airborne radars make similar

measurements, the lessons learned using the ice-coupled system can inform work with airborne systems. The underwater camera requires sufficient light from above and may not detect oil if the patch is small and the encapsulating ice is thick. Pictures are one of the easiest signals for untrained operators to interpret.

6. NEXT STEPS

These recommendations are meant to provide an indication of further research that would continue to develop our ability to detect and map oil in the ice environment. The recommendations are not made in an order of priority, because that order would change depending on the type of system to be further developed.

- Conduct blind tests where the operators are unaware of oil location – this could also be done by having a group that is unaware of the oil locations analyze the data.
- Evaluate capabilities of both long-wave and short wave infrared (FLIR and SWIR) systems at different times of the year.
- Redo encapsulated oil tests with acoustics. The shedding of bubbles during this experiment is likely to have limited the range that the acoustics systems could see into the ice. Outside of the areas with bubbles, the low-frequency, broadband systems were able to detect the ice/air interface through 60 cm of ice.
- Retest the FMCW. The system remains at the prototype stage and needs to be tested where any interference is removed and the ice is cold enough to allow the system to function properly. This will require a more user-friendly, real-time processing software system to identify problems in the field.
- Determine the capabilities of an underwater camera for detecting dark targets using a black target on the ice surface in the spring. Snow should be used around the target to determine the capability to discriminate between it and the target.
- Redo encapsulated oil tests with acoustics in a test setup that permits the sonar systems to transmit at full power.
- Determine the acoustical angular reflectivity of an oil layer. This can provide information about the best angle to detect oil and create the angular reflectivity function necessary for automated detection algorithms.
- Determine the capability of acoustically detecting oil thickness at incident angles other than nadir.
- Examine near infrared reflectivity for discrimination of oil and oil thickness determination. There has been some work in the field (e.g. Clark et al. 2010), but this seems to have the potential for simple, low-cost sensors that can discriminate oil from other substances.
- The shielding and source output (either energy level or focused transmission) to commercial GPR should be modified to improve the performance as an aerial sensor. This should be done working directly with the manufacturer.
- The acoustics model should be tested by checking the variables derived by the model by independent means and tested against field data.
- A critical limitation of the acoustic information is that they were not operated at realistic distances from the ice. Sub-footprint scale roughness needs to be included in the models and field measurements of acoustics and ice variability collected to determine potential limitations on detecting oil.
- The close proximity of the ice to sonar units limited the power they were able to transmit, so gaining additional range may allow for better penetration into the ice.
- Integrate sensors onto a platform and test under realistic Arctic conditions (weather, power, and communications).
- Other ice types should be investigated; i) undeformed, snow-covered, first year ice, ii) deformed, snow-covered, first year ice, iii) deformed, snow-free, first year ice, and iv) broken ice.

- Plan, permit and execute a deliberate oil injection in ice to test different systems in a field environment.

7. BIBLIOGRAPHY

- Babcock, E. L., J.H. Bradford, and C. Hall (2015), Electrical anisotropy in sea ice and a dual-polarization radar system to mitigate the effects of preferential attenuation in imaging sea ice, *Cold Reg. Sci. Technol.*, 118, 105-111.
- Bassett, C., A.C. Lavery, and T. Maksym (2014), Laboratory measurements of high-frequency, broadband acoustic scattering of growing sea ice and oil beneath sea ice, *Proc. Meet. Acoust.* (21), 1-8.
- Bassett, C., A. Lavery, T. Maksym, and J. Wilkinson (2015), Laboratory measurements of high-frequency, Acoustic Broadband Backscattering from Sea Ice and Crude Oil, *J. Acoust. Soc. Am.*, 137(1), EL32-EL38.
- Bello, J., A.G. Smirnov, and P. Toomey (2012), Development of a fluorescence polarization submersible instrument for the detection of submerged heavy oil spills, *Proceedings of Ocean Sensing and Monitoring IV*, (8372), doi:10.1117/12.919509.
- Bobra, A.M. and M.F. Fingas (1986), The behaviour and fate of Arctic oil spills, *Water Sci. Tech.*, 18(2), 13-23.
- Bradford, J.H., E.L. Babcock, H.P. Marshall, and D.F. Dickins (in press), Targeted reflection-waveform inversion of experimental ground-penetrating radar data for quantification of oil spills under sea ice, *Geophysics*.
- Bradford, J.H. and J.C. Deeds (2006), Ground-penetrating radar theory and application of thin-bed offset-dependent reflectivity, *Geophysics*, 71 (3), K47-K57, doi: 10.1190/1.2194524.
- Bradford, J.H., D. F. Dickins, and L. Liberty (2008), Locating oil spills under sea ice using ground-penetrating radar, *The Leading Edge*, 27(11), 1424-1435.
- Bradford, J.H., D.F. Dickins, and P.J. Brandvik (2010), Assessing the potential to detect oil spills in and under snow using ground-penetrating radar, *Geophysics*, 75(2), G1-G12.
- Bradford, J., H.P. Marshall, E. Babcock, and D. Dickins (2015), Targeted full-waveform inversion of ground-penetrating radar data for quantification of oil spills under sea ice, *OTC-25511-MS, Offshore Technology Conference*.
- Brown, C.E. (2011), Laser fluorosensors, In *Oil Spill Science and Technology: Prevention, Response, and Clean Up*, Edited by M. Fingas, Elsevier, Burlington, MA, USA, pp. 171-182.
- Chu, D. and T.K. Stanton (1998), Application of pulse compression techniques to broadband acoustic scattering by live individual zooplankton, *J. Acoust. Soc. Am.*, 104 (1), 39-55.
- Clark, R.N., G.A. Swayze, I. Leifer, K.E. Livo, R. Kokaly, T. Hoefen, S. Lundeen, M. Eastwood, R.O. Green, N. Pearson, C. Sarture, I. McCubbin, D. Roberts, E. Bradley, D. Steele, T. Rya, R. Dominguez, and the Airborne Visible/Infrared Imaging Spectrometer (AVIRIS) Team (2010), A method for quantitative mapping of thick oil spills using imaging spectroscopy, *USGS Open-File Report 2010-1167*, 54 pp.
- Clay, C.S. and H. Medwin (1977), *Acoustical oceanography: principles and applications*, Wiley, New York.
- Cox, G.F.N. and W.F. Weeks (1983), Equations for determining the gas and brine volumes in sea-ice samples, *Journal of Glaciology*, 29, 306-316.
- Cox, G.F.N. and W.F. Weeks (1986), Changes in the salinity and porosity of sea-ice samples during shipping and storage, *J. Glaciol.*, 32 (112), 371-375.
- Dick, R. and M. Fingas (1992), First results of airborne trials of a 64-channel laser fluorosensor for oil detection, *Arctic and Marine Oilspill Program*, 365-379.
- Dickins, D.F. (2005), New and innovative equipment and technologies for the remote sensing and surveillance of oil in and under ice, *Final Technical Report, contract number 1435-01-04-36285*, U.S. DOI Minerals Management Service, Washington, D.C., USA., 170 pp.
- Dickins, D.F. (2010), Project P5: Remote Sensing Summary Report, *SINTEF Oil-in-Ice final report No. 30*, Trondheim, 2010.
- Dickins, D.F. and Andersen, J.H. (2010), Evaluation of airborne remote sensing systems for oil in ice detection, *SINTEF Oil-in-Ice final report No. 28*, Trondheim, 2010.
- Dickins, D.F., P.J. Brandvik, L.G. Faksness, J. Bradford, and L. Liberty (2006), 2006 Svalbard experimental spill to study spill detection and oil behavior in ice, *Final Technical Report, contract number 1435-0106-CT-3925*, U.S. DOI Minerals Management Service, Washington, D.C., USA.

- Dickins, D.F., J. Bradford, and H.P. Marshall (2011), Detecting oil in sea ice using Ground-penetrating radar: Developing a new airborne system, *CRREL Field Test Report, prepared for Joint Industry Project Participants*. 36 pp.
- Dickins, D.F., J. Bradford, and L. Steinbronn (2008), Detection of oil on and under ice: Phase III evaluation of airborne radar system capabilities in selected Arctic spill scenarios, Boise State University, 55 pp.
- Dickins, D., I. Buist, and W. Pistruzak (1981), Dome Petroleum study of oil and gas under sea ice. *International Oil Spill Conference Proceedings, 1981(1)*, 183-189.
- Dickins, D.F., H.P. Marshall, and R. Hay (2012), Detecting oil in sea ice using Ground-penetrating radar: Developing a new airborne system, *2012 CRREL Test Report, prepared for Joint Industry Project Participants*. 30 pp.
- DiPerna, D.T. and T.K. Stanton (1991), Fresnel zone effects in the scattering of sound by cylinders of various lengths, *J. Acoust. Soc. Am.* (90), 3348-3355, <http://dx.doi.org/10.1121/1.401394>.
- Druckenmiller, M. L., H. Eicken, D. J. Pringle, C. C. Williams, and M. A. Johnson (2009), Towards an integrated coastal sea-ice observatory: System components and a case study at Barrow, Alaska, *Cold Reg. Sci. Technol.*, 56, 61–72, doi:10.1016/j.coldregions.2008.12.003.
- Eckart, C. (1953), The scattering of sound from the sea surface, *J. Acoust. Soc. Am.*, 25, 566-569, doi: 10.1121/1.1907128.
- Eicken, H. (2003), From the microscopic, to the macroscopic, to the regional scale: growth, microstructure and properties of sea ice, *Sea ice: An introduction to its physics, chemistry, biology and geology*, edited by Thomas, D. N. and G. S. Dieckmann, Wiley-Blackwell, Hoboken, USA, pp. 22-81.
- Eicken, H., T. C. Grenfell, D. K. Perovich, J. A. Richter-Menge, and K. Frey (2004), Hydraulic controls of summer Arctic pack ice albedo, *J. Geophys. Res.*, 109 (C08007), doi:10.1029/2003JC001989.
- Eicken, H., R. Gradinger, M. Kaufman, and C. Petrich (Aug 26, 2008, Updated 2014), Sea-ice core measurements (SIZONET, UCAR/NCAR -- CISL – ACADIS, doi:10.5065/D63X84KG.
- Francois, R.E. and G.R. Garrison (1982), Sound absorption based on ocean measurements: Part I: Pure water and magnesium sulfate contributions, *J. Acoust. Soc. Am.* 72, 896-907, [doi:10.1121/1.388170](https://doi.org/10.1121/1.388170).
- Francois, R.E. and G.R. Garrison (1982), Sound absorption based on ocean measurements: Part II: Boric acid contribution and equation for total absorption, *J. Acoust. Soc. Am.* (72), 1879-1890, doi:10.1121/1.388673.
- Fingas, M. and C.E. Brown (1997), Review of oil spill remote sensing, *Spill Science and Technology Bulletin*, 4, 199– 208.
- Fingas, M. and C.E. Brown (2000), A review of the status of advanced technologies for the detection of oil in and with ice, *Spill Sci. Tech. Bull.* 6(5/6), 295-302.
- Fingas, M. and C.E. Brown (2011), Introduction to spill modelling, In *Oil Spill Science and Technology: Prevention, Response, and Clean-up* edited by M. Fingas, Elsevier, New York, USA.
- Fingas, M. and C.E. Brown (2013a), Detection of oil in ice and snow, *J. Marine Sci. and Eng.*, 1, 10-20.
- Fingas, M. and C.E. Brown (2013b), Oil spill remote sensing, in *Earth System Monitoring*, edited by J. Orcutt. Springer, New York, pp. 337-388.
- Fingas, M.F. and B.P. Hollebone (2003), Review of behavior of oil in freezing environments, *Marine Pollution Bulletin*, 47, 333-340.
- Fricke, J. Robert (1993), Acoustic scattering from elemental Arctic ice features: numerical modelling results, *J. Acoust. Soc. Am.*, 93(4), 1784-1796.
- Gerland, S., and C. Haas (2004) Seasonal development of structure and optical surface properties of fast ice in Knogsfjorden, Svalbard, *Reports on Polar and Marine Research*, 492, 26-34.
- Gerland, S., J.G. Winther, J. B. Orbaek, and B. V. Ivanov (1999), Physical properties, spectral reflectance and thickness development of first year fast ice in Kongsfjorden, Svalbard, *Polar Res.*, 18(2), 275-282.
- Golden, K. M., H. Eicken, A. L. Heaton, J. Miner, D. J. Pringle, and J. Zhu (2007), Thermal evolution of permeability and microstructure in sea ice, *Geophys. Res. Lett.*, 34, L16501, doi:10.1029/2007GL030447.

- Grenfell, T.C. (1991), A radiative transfer model for sea ice with vertical structure variations, *J. Geophys. Res.*, (86), 16991-17001.
- Grenfell, T.C. and D.K. Perovich (2004), [Seasonal and spatial evolution of albedo in a snow-ice-land-ocean environment](#), *J. Geophys. Res. Oceans*, (109), C1.
- Grenfell, T.C. and D.K. Perovich (2008), [Incident spectral irradiance in the Arctic Basin during the summer and fall](#), *J. Geophys. Res.*, (113), D12117, doi:10.1029/JD009418.
- Hansen, K.A., M. Fitzpatrick, P.R. Herring, and M. VanHaverbeke (2009), Heavy oil detection (prototypes) – *Final Report, Report CG-D-08-09*, U.S. Coast Guard Research and Development Center, New London, Conn., USA.
- Harris, J. R., L. Wickert, T. Lynds, P. Behnia, R. Rainbird, E. Grunsky, R. McGregor, and E. Schetselaar (2011), Remote predictive mapping 3. optical remote sensing – a review for remote predictive geological mapping in northern Canada, **Geoscience Canada**, 38(2), 49-83.
- F. E. Hoge and R. N. Swift (1981), Airborne simultaneous spectroscopic detection of laser-induced water Raman backscatter and fluorescence from chlorophyll a and other naturally occurring pigments, *Appl. Opt.* 20, 3197-3205.
- Holt, B. and S. Digby (1985), Process and imagery of first-year fast sea ice during the melt season, *J. Geophys. Res.*, (90), C3, 5045-5062.
- Humpert, M. (2014), Arctic shipping: an analysis of the 2013 northern sea route season, *The Arctic Institute: Center for Circumpolar Studies*, 14 pp.
- Jackson, D.R., R. Odom, M.L. Boyd, and A.N. Ivakin (2010), A geoacoustic bottom interaction model (GABIM), *IEEE Journal of Oceanic Engineering*, 35, 603-617.
- Jackson, D. and M. Richardson (2007), High-frequency seafloor acoustics, Springer, New York, 616 pp.
- Jones, K. A., M. Ingham, and H. Eicken (2012), Modelling the anisotropic brine microstructure in first-year Arctic sea ice, *J. Geophys. Res.*, 117, C02005, doi:10.1029/2011JC007607.
- Karlsson, J., C. Petrich and H. Eicken (2011), Oil entrainment and migration in laboratory-grown saltwater ice, *Proceedings of the 21st Intl. Conf. Port and Ocean Eng. Under Arctic Conds.* Montreal, Canada.
- Lavery, A.C., D. Chu, and J.N. Moum (2010), Measurements of acoustic scattering from zooplankton and oceanic microstructure using a broadband echo sounder, *ICES J. Mar. Sci.*, (67), 379-394.
- Lavery, A.C. and T. Ross (2007), Acoustic scattering from double-diffusive microstructure, *J. Acoust. Soc. Am.*, (122), 1449-1462.
- Leppäranta, M. and T. Manninen (1988), The brine and gas content of sea ice with attention to low salinities and high temperatures, *Finnish Institute Marine Research Internal Report*, 88(2), Helsinki, Finland.
- Light, B., G.A. Maykut, and T.C. Grenfell (2003), Effects of temperature on the microstructure of first-year Arctic sea ice, *J. Geophys. Res.*, (108) C2, 3051, 10.1029/2001JC000887.
- Light, B., G.A. Maykut, and T. C. Grenfell (2004), A temperature-dependent, structural-optical model of first-year sea ice, *J. Geophys. Res.*, 109, C06013, doi: 10.1029/2003JC002164.
- Light, B., T.C. Greenfell, and D.K. Perovich (2008), Transmission and absorption of solar radiation by Arctic sea ice during the melt season, *J. Geophys. Res.*, 113, C03023, doi: 10.1029/2006JC003977.
- Liu, B., W. Zhu, and Y. Li (2015), Spectral characteristics analysis of oil film among sea ice, *IGARSS Proceedings, Geoscience and Remote Sensing Symposium*, 3450-3453.
- LOOKNorth (2014), Oil spill detection and modelling in the Hudson and Davis Straits, *Final Report R-13-087-1096 v2.0*, for Nunavut Planning Commission, Nunavut, Canada.
- Marshall, H.P. and G. Koh (2008), FMCW radars for snow research, *Cold Reg. Sci. Technol.*, 52, 118-131.
- Maksym, T., Singh, H., Bassett, C., Lavery, A., Freitag, L., Sonnichsen, F., and Wilkinson, J. (2014), Oil spill detection and mapping under Arctic sea ice using autonomous underwater vehicles, *Final Report BSEE Contract E12PC00053*, U.S. DOI, BSEE, Washington, D.C., USA.99 pp.
- Morey, R.M., A. Kovacs, and G.F.N. Cox (1984), Electromagnetic properties of sea ice, *Cold Reg. Sci. Technol.*, 9, 53-75.

- Norcor Engineering and Research Ltd. (1975), The interaction of crude oil with Arctic sea ice. *Prepared for the Department of Environment, Beaufort Sea Technical Report No. 27*, Victoria, BC, Canada.
- Notz, D., and M. G. Worster (2008), In situ measurements of the evolution of young sea ice, *J. Geophys. Res.*, 113, C03001, doi:10.1029/2007JC004333.
- Perovich, D.K. (1996), The optical properties of sea ice, *CRREL Monograph 96-1*, 31 pp.
- Petrenko, V.F. (1993), Electrical properties of ice. *CRREL Report 93(20)*, 81 pp.
- Petrich, C. and H. Eicken (2009), Growth, structure and properties of sea ice, in *Sea ice*, edited by Thomas, D. N. and G. S. Dieckmann, Wiley-Blackwell, Hoboken, USA, pp. 23-77.
- Petrich, C., J. Karlsson, and H. Eicken (2013), Porosity of growing sea ice and potential for oil entrainment, *Cold Reg. Sci. Technol.*, 87, 27-32.
- Potter, S., I. Buist, K. Trudel, D.F. Dickins, and E. Owens (2012,) Spill response in the Arctic offshore, *Final Report*, for American Petroleum Institute and the Joint Industry Programme on Oil Spill Recovery in Ice, 157 pp.
- Praks, J., M. Eskelined, J.Pulliainen, T. Pyhalahti, and M. Hallikainen (2004), Detection of oil pollution on sea ice with airborne and spaceborne spectrometer, *IGARSS Proceedings, Geoscience and Remote Sensing Symposium*, 273-276.
- Puestow, T., L. Parsons, I. Zakharov, N. Cater, P. Bobby, M. Fuglem, G. Parr, A. Jayasiri, S. Warren, and G. Warbanski (2013), Oil spill detection in low visibility and ice: surface remote sensing, *Final Report 5.1*, Joint Industry Programme to define the state-of-the-art for surface remote sensing technologies to monitor oil under varying conditions of ice and visibility, London, U.K.
- Rutledge, A.K. and D.S. Leonard (2001), Role of multibeam sonar in oil and gas exploration and development, *Offshore Technology Conference*.
- SL Ross Environmental Research Ltd., DF Dickins Associates LLC., and Envision Planning Solutions Inc. (2010), Beaufort Sea oil spills state of knowledge review and identification of key issues, Environmental Studies Research Funds Report No. 177. Calgary, Canada, 126 pp.
- Stanton, T. K., D. Chu, and O.H. Wiebe (1998), Sound scattering by several zooplankton groups. I. Experimental determination of dominant scattering mechanisms, *J. Acoust. Soc. Am.* (103), 225–235.
- Stanton, T.K., D. Chu, J.M. Jech, and J.D. Irish (2010), New broadband methods for resonance classification and high-resolution imagery of fish with swim bladders using a modified commercial broadband echo sounder, *ICES J. Mar. Sci.*, (67), 365-378.
- Stierle, A.P. and H. Eicken (2002), Sediment inclusions in Alaskan coastal sea ice: spatial distribution, interannual variability, and entrainment requirements, *Arctic, Antarctic, and Alpine Research*, 34 (4), 465-476, doi: 10.2307/1552205.
- Svejkovsky, J. and Muskat, J. (2009), Real-time detection of oil slick thickness patterns with a portable multispectral sensor." Final Report for U.S. Minerals Management Service Contract 0105CT39144, 37 pp.
- Svejkovsky, J., W. Lehr, J. Muskat, G. Graettinger, J. Mullin (2012), Operational utilization of aerial multispectral remote sensing during oil spill response: lessons learned during the deepwater horizon (MC-252) spill, *Photogrammetric Engineering and Remote Sensing* 78(10), 1089-1102.
- Thomas, D.N. and G.S. Dieckman (2010) *Sea Ice*, 2nd edn.
- Turin, G. (1960), An introduction to matched filters, *IRE transactions on Information theory*, 3(6), 311-329.
- Turner Designs (2012), Application note: crude oil, retrieved from *Turner Designs Inc.*, <http://www.turnerdesigns.com/t2/doc/appnotes/S-0079.pdf>.
- Untersteiner, N. (1968), Natural desalination and equilibrium salinity profile of perennial sea ice, *J. Geophys. Res.*, (73)4, 1251-1257.
- Wilkinson, J.P., P. Wadhams, and N.E. Hughs (2007), Modelling the spread of oil under fast sea ice using three-dimensional multibeam sonar data, *Geophys. Res. Lett.*, 34, L22506, doi:10.1029/2007GL031754.
- Wilkinson, J., T. Maksym, C. Bassett, A. Lavery, H. Singh, D. Chayes, P. Elosegui, P. Wadhams, K. Ulrick-Evers, and P. Jochmann (2014), Experiments on the detection and movement of oil spilled under sea ice, *Proceedings of the HYDRALAB IV Joint User Meeting*.

- Wilkinson, J., T. Maksym, and H. Singh (2013), Capabilities for detection of oil spill under sea ice from autonomous underwater vehicles, *Final Report 5.2*, 104 pp., Joint Industry Programme on oil spill detection and mapping in low visibility and ice: focus on undersea remote sensing, London, U.K.
- Wilkinson, J., T. Boyd, B. Hagen, T. Maksym, S. Pegau, C. Roman, H. Singh, and L. Zabilansky (2015), Detection and quantification of oil under sea ice: the view from below, *Cold Regions Science and Technology* 109, 9-17.
- Williams, K.L., G.R Garrison, and P.D. Mourad (1992), Experimental examination of growing and newly submerged sea ice including acoustic probing of the skeletal layer, *J. Acoust. Soc. Am.* 92(4), 2075-2092.
- Wozniak, B and J. Dera (2007), *Light absorption in sea water*. Springer. New York.

8. APPENDICES

Appendix I. Problems encountered

Several small problems with equipment occurred at different times of the experiment and we managed to work around those problems to continue collecting data. There were a few larger problems that affected the results that are worth highlighting to ensure they can be addressed in future experiments. Correction of these problems could expand the known capabilities to detect oil of the systems tested.

During December it was discovered that bubbles were forming on the underwater instruments. These would occasionally rise to the surface putting air pockets into the ice. This impacted the acoustic measurements and may have impacted measurements from above.

This problem was likely due to a bubbling system that was used to help maintain the tank free of ice and mix in the salt. This likely saturated the tank with air. As the ice sheet formed there was very limited air exchange possible so the gasses remained in suspension. As the temperature decreased, associated with brine rejection during ice formation, the gas saturation point in the tank was depressed further. The warm underwater instruments then caused the gas to come out of solution and form small bubbles on the instruments. These would then release and go up to the ice where they stayed. As we parked the sensors under the ice to study the encapsulation this caused there to be areas of bubble-covered ice (Figure a1). The air at the water/ice interface may have attenuated the acoustics and limited the detection of oil through encapsulation ice.

In the future it would be best to maintain a circulation that allows for gasses in solution to be exchanged with the atmosphere. Bubble buildup should also be monitored with the camera on the underwater carriage.



Figure a1. Bubbles rising from the instruments provide outlines of the instruments in the ice structure.

The airborne radar systems encountered an unexpected level of noise in their signal. The source of the noise was not isolated. Reflection from the boom, loosening electrical connections due to

moving the boom in and out, interference between radar systems mounted together, or combination of them could be the cause of the noise. Any source of major noise needs to be identified and mitigated prior to further experiments.

There was some oil that leaked out of the containment hoops. The containment skirts were cut to a length 15 cm longer than the ice thickness expected during the injection into each hoop. This was done to minimize interference with underwater instruments. The shortened skirts had a tendency to fold up in the corners as the ice growth neared the 15 cm point. The skirts either need to be longer or the bottom edge more heavily weighted to prevent oil from escaping. The addition of insulation to slow the ice growth and form a dome in the ice provided a good containment system. There were questions about the effect of the insulation on the ice properties. It appears that the temperature of the ice equalized with other areas of the tank within 12 to 24 hours of the insulation being removed.

The rising to the surface of small amounts of oil to the surface after the injections was unexpected, although it had been seen by Dickins (2005). This could be caused by changes in the ice growth at the boundaries of the containment hoops. After using the insulation to dome the bottom of the ice the oil still would come up along the edge of subsurface distribution.

Several additional sensors became available after the original proposal was submitted. To reduce interference from other active sensors, multiple scans of the tanks and hoops were made with various sensors on/off. This protocol successfully limited interferences from the other equipment, but consumed four times the amount of time than was originally allotted for this work. Future large-scale sensor experiments would benefit from budgeting for these extended scanning operations or restrict additional sensors being tested.

A modelling limitation is a lack of knowledge of the acoustic properties of encapsulated oil. It was simulated as a liquid layer. This seems consistent with the observations obtained from the cores, but not necessarily consistent with previous field experiments (see Figure 2-2 in Dickins et al. 2008). It is also possible that a change in the acoustics properties of the oil occurred as it was encapsulated. During this experiment ice temperatures remained above the pour point of the oil, but some of the components may have solidified. It is also possible that the ice structure penetrated through the oil creating a hybrid structure of oil and ice. We do not have the information needed to model the hybrid structure or a solidified layer of oil.

Appendix II. Sea ice properties comparison between the 2014 CRREL oil-in-ice experiment and first year Arctic sea ice

Project name: JIP, Remote Sensing of Oil in Ice
Title of report: Sea ice properties comparison between the 2014 CRREL oil-in-ice experiment and first year sea ice.
Authors: M. Oggier, H. Eicken
Date: September 3, 2014

Introduction

This report compares the sea ice properties of the ice grown in the CRREL tank during the experiment to ice properties representative of ice conditions in the North American Arctic (Barrow, AK, USA) and in the Archipelago of Svalbard (Kongsfjorden, Norway). The data and plots shown

in this report serve as reference to assess how representative the ice grown in the tank is of natural conditions.

Ice core data

Representative first year ice properties for Barrow and Svalbard have been computed from field observation data [cf. Sea ice properties modelling section]. For the CRREL experiment, data have been derived from ice-cores and in-situ temperature measurements performed during the experiment. For the following analysis, only cores extracted at the end of the growth season and before the beginning of the melt from the clean ice are considered. Ice thickness reached approximately 75cm with a variation of less than 5 centimeters (according to ice core data) observed throughout the tank. Sea ice bulk salinity was measured on cores cut into 5 cm thick segments and melted at room temperature in a sealed container. Two coring events have been considered:

- January 8: before the end of the growth season, 5 ice cores were extracted outside of the hoop along a transect from Hoop 1 to Hoop 5. (core named 20150108-oHX, X designates the number of the hoop in front of which the core is extracted)
- January 16: just after the refrigeration system had been turned off, cores were extracted near Hoop 6 (20150116A-D) and 6B (20150116-6B-OI)

Salinity and temperature profiles are discretized in 5-cm layer thickness, ranging from 2.5 cm depth to the full core length, rounded to the closest 5cm. Erroneous and missing data were replaced through linear interpolation between the two nearest points. Temperature profiles were measured with two thermistor strings throughout the water/ice/air layers.

Results

No granular sea ice was observed in any of the cores. Absence of this surface layer typically found in natural sea ice was expected as the water of the tank was cooled down without any agitation. In order to take in account the absence of this layer, which is typically more saline than the columnar sea ice, the top 10 centimeters of the salinity and temperature profile for Barrow data have been disregarded for the analysis. This adaptation concerns only data from Barrow, as the core stratigraphy is well known. Ice core observations from the field have been classified according to the degree days approach (see full report for details). The field-measurement dataset for which mean ice thickness comes closest to the thickness observed in the tank has been used. For comparison, 80 cm is the thickness reached by ice grown in mid-January at Barrow, AK, a location representative of oil and gas production and exploration areas in the Pacific Arctic sector.

In Figure 1 and 2, coloured curves display salinity and temperature profiles obtained during the CRREL tank experiments. The gray envelope in the background delimits the corresponding representative statistical value for Barrow for an equivalent ice thickness. The coring event of January 8 took place at the end of the growth period. Both salinity and temperature profiles are typical for young first-year sea ice, similar to those observed at Barrow. Mean value and spread of the salinity C-shaped curve coincide with naturally grown sea ice. The second coring event, on January 16, took place a few days after the cooling system had been turned off: the temperature profile in the ice had already had time to equilibrate with the warmer air temperature present in the cold room, whereas ice at Barrow experiences low surface temperatures for at least three more months. Decrease of the salinity at the top of the ice cover is the expression of the onset of surface melt, accompanied by desalination through drainage and meltwater flushing. The

presence of a higher salinity at the ice bottom indicates that bottom melt had not started yet, hence the salinity profile in the interior and bottom of the ice remains unaffected.

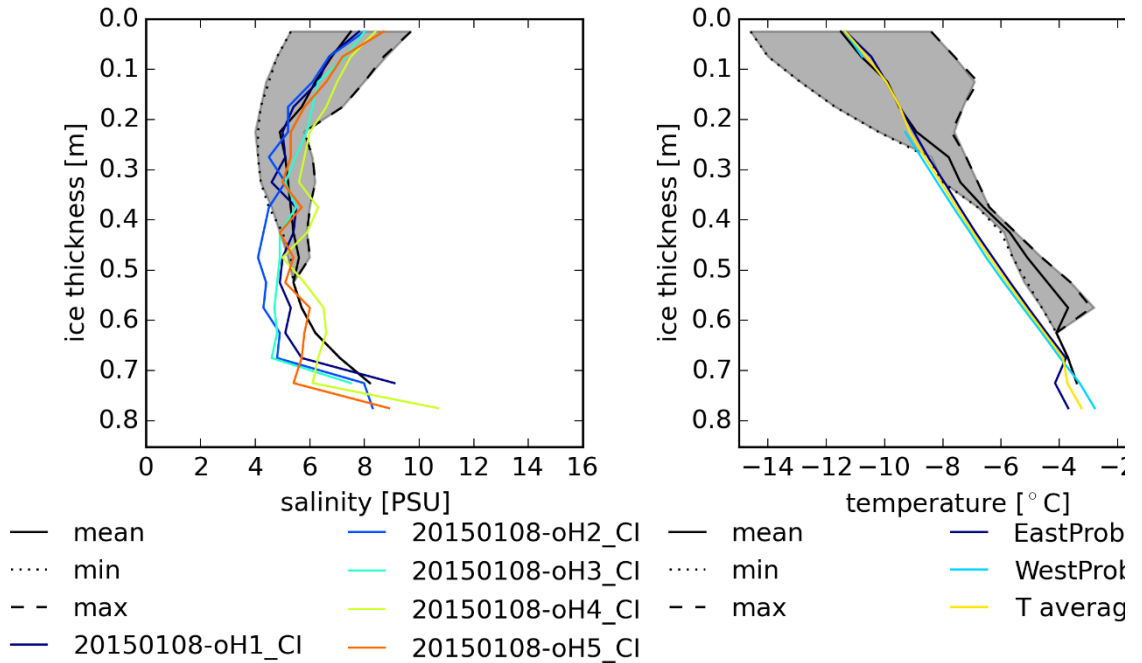


Figure 2 – At the end of the growth season 5 cores were extracted along a transect. Each salinity and temperature profile is displayed as a colour curve. The gray envelope corresponds to the representative statistical values for Barrow at equivalent ice thickness. Ranges in salinity and temperature correspond to conditions observed at Barrow in January.

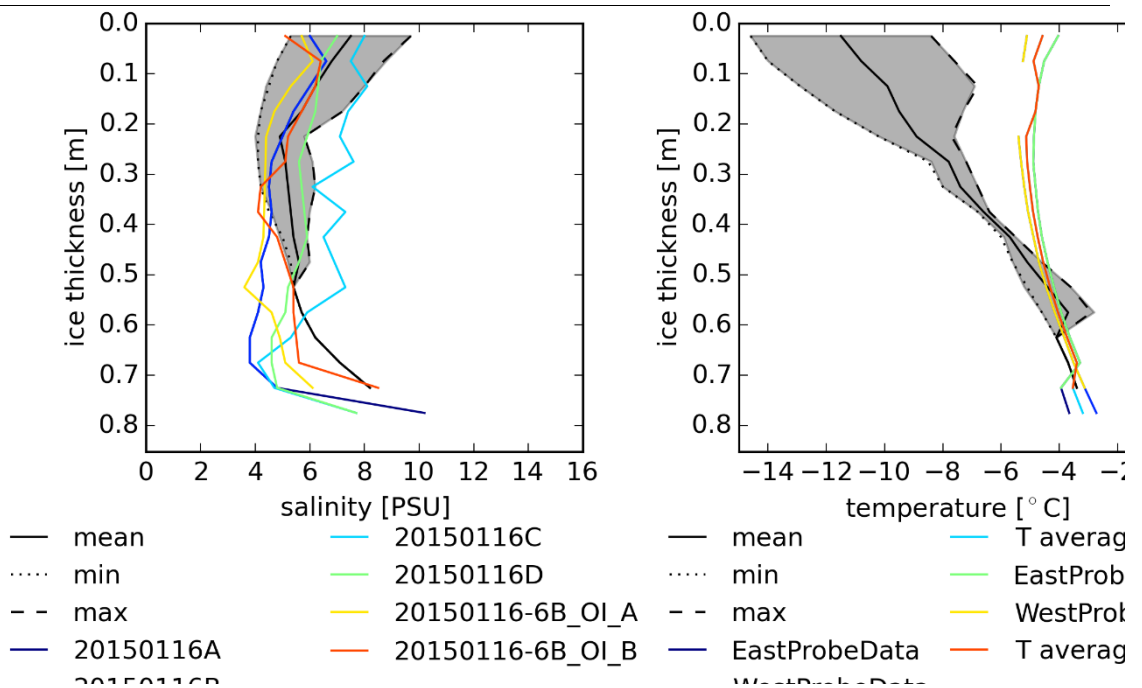


Figure 3 – A few days after the refrigeration was turned off, 5 cores were extracted along a transect. Each salinity and temperature profile is displayed as a colour curve. The gray envelope corresponds to the representative statistical values for Barrow at equivalent ice thickness (the top 10 cm of granular sea ice is not represented here). The range of salinity corresponds to conditions observed at Barrow in

January. The discrepancy in temperature data between representative field observations and the CRREL tank are explained by the fact that the ice had begun to warm due to shut-down of the cooling system for a few days prior to the sampling event.

Figure 3 and 4 compare salinity and temperature profiles to the representative values existing for Svalbard, compiled from ice cores extracted in May 1999 [Gerland, 1999]. Sea ice thickness reached an average of 0.6m this year, thinner than the ice growth in the tank. Disregarding the thickness, salinity profile of the CRREL experiment is similar both in value and shape as the one collected in the field. Large differences are visible in the temperature plot, which are explained by the climate in Svalbard, which is warmer than that simulated during the CRREL experiment.

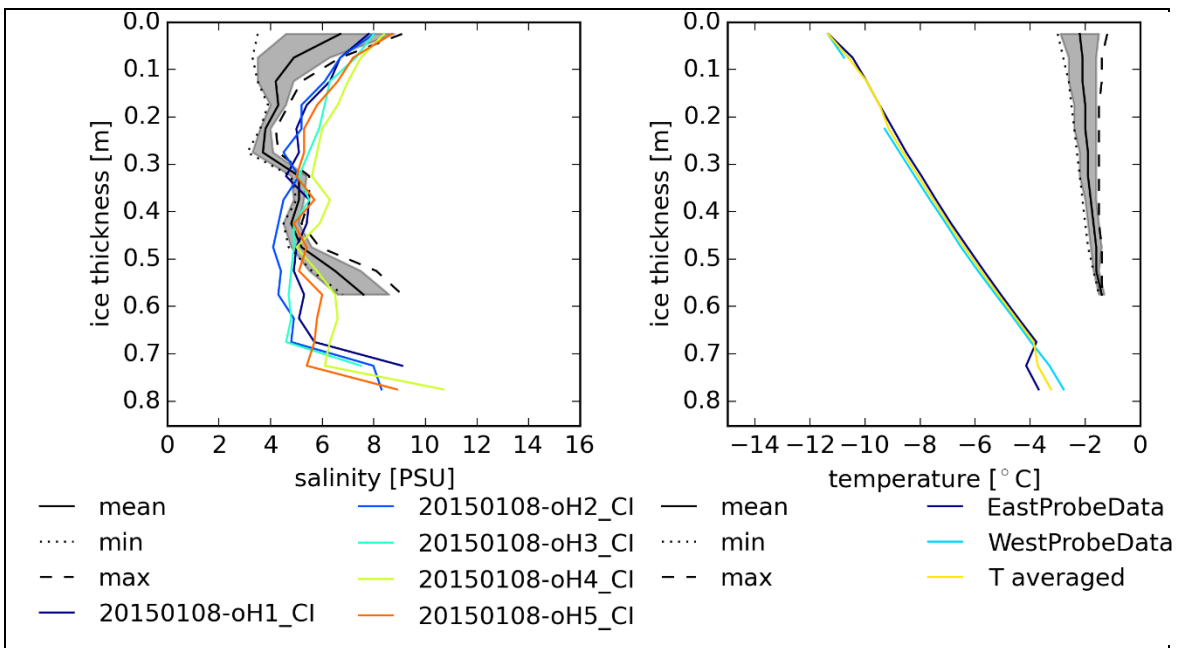


Figure 4 – At the end of the growth season 5 cores have been extracted along a transect. Each salinity and temperature profile is displayed as a colour curve. The gray envelope corresponds to the only representative data available for Svalbard.

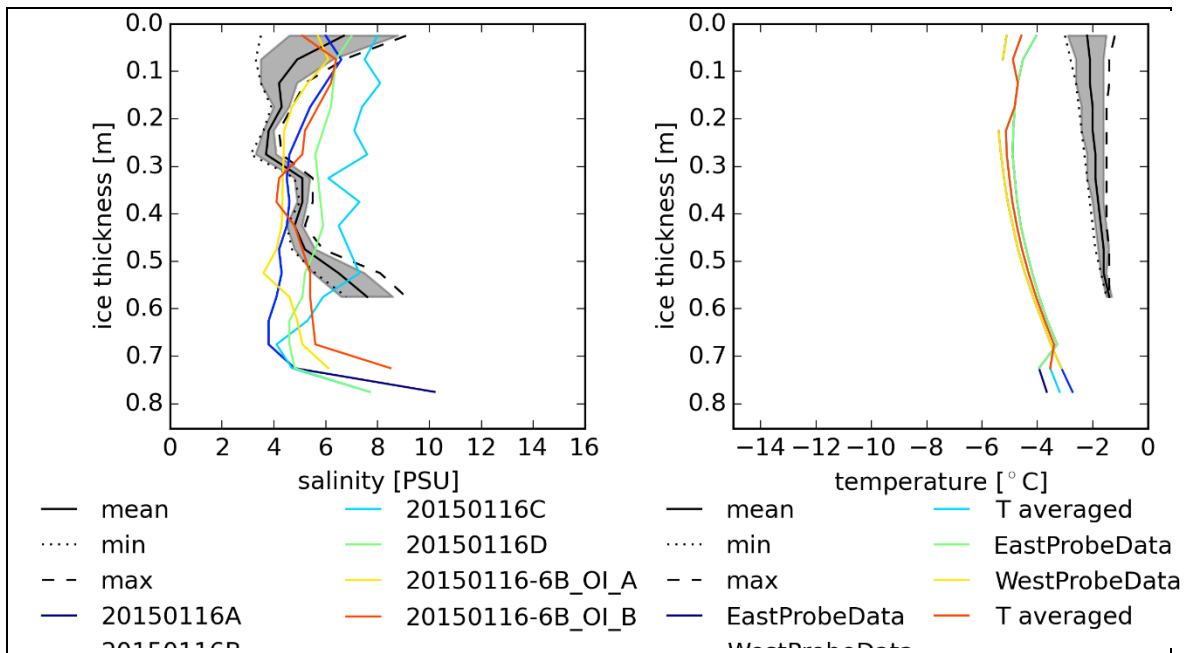


Figure 5 – A few days after the refrigeration was turn off, 5 cores have been extracted along a transect. Each salinity and temperature profile is displayed as a colour curve. The gray envelope corresponds to the only representative available for Svalbard.

Conclusion

Ice grown during the oil-in-ice experiment at CRREL is representative of ice growth under natural conditions in the North American Arctic. Salinity and temperature profiles of the artificial sea ice correlated closely with natural sea ice during mid-winter (mid-January).

Bibliography

Gerland, Sebastian, et al. "Physical properties, spectral reflectance and thickness development of first year fast ice in Kongsfjorden, Svalbard." *Polar Research* 18.2 (1999): 275-282.

Appendix III. Tabulation of first-year sea-ice properties representative of the annual cycle as relevant to 2014 CRREL oil-in-ice experiments

Project name: JIP, Remote Sensing of Oil in Ice
Title of report: Tabulation of first-year sea-ice properties representative of the annual cycle as relevant to 2014 CRREL oil-in-ice experiments
Authors: M. Oggier, H. Eicken, M. Jin
Date: November 4, 2014

Introduction

This report tabulates key first-year ice properties representative of ice conditions in the North American Arctic based on long-term measurements in undeformed sea ice at Barrow, AK. The data and plots shown in this report can serve as a reference to compare to the ice property evolution in CRREL oil-in-ice tank experiments. In addition, they support model simulations of ice properties relevant to oil-in-ice remote sensing by providing key property data on the physical state of the ice cover.

Background

Summary statistics of key sea-ice properties from field observations describing the state of sea ice, in particular temperature, bulk ice salinity and brine volume fraction, can serve as a benchmark to compare with property evolution of ice grown in the laboratory, specifically the 2014 CRREL oil-in-ice experiments. Observations made in the tank can hence potentially be extended to natural conditions for spills occurring in the field. Furthermore, a range of other physical properties, such as electrical conductivity or dielectric permittivity, can be computed from such data based on semi-empirical equations and porosity-property models. Seasonal and interannual variations are reflected by the temporal evolution of the mean and the variance. Finally, tabulations provide input data to run and validate models, as well as observe the impact of property variations on oil detection in ice.

Building on the analysis summarized in this report, the Community Ice Code (CICE) model, designed for fully coupled global climate models, is run in standalone mode, with an integrated module that includes ice salinity and temperature as prognostic variables. Hindcast simulations, forced with historical and reanalysis data, will be compared with observations to assess the performance of the model and its future use as a tool to predict regional ice variability in different Arctic regions. At the same time, the CICE model could also be used to track ice growth in the ice tank during the experiments,

Ice core data

Barrow

Data have been derived from ice-core and in-situ temperature measurements at the Mass Balance Station installed on homogeneous, undeformed landfast sea ice near Point Barrow from the 1999/2000 to the 2013/14 ice season (Eicken et al., 2014). While the position of the station varies slightly from year to year, observations are representative of first-year sea ice grown under quiet conditions in the North American Arctic. A typical annual cycle of ice growth and melt is displayed in **Figure 1**. Sampling dates depend on field work timing, which is scheduled to capture and follow the important changes in sea ice throughout the winter and spring: young first-year sea ice in January, mature sea ice in April and mid-May, desalination and melt through mid-June.

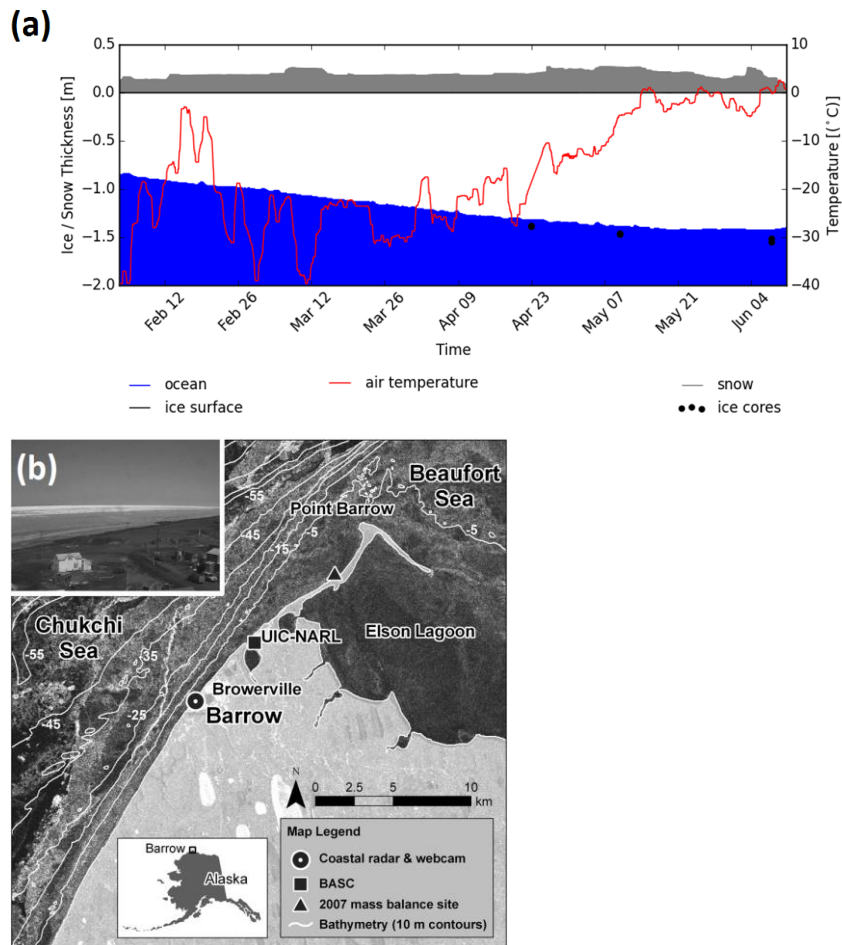


Figure 1 - (a) Typical profile of mostly level first-year ice at Barrow (data come from winter 2006) ; (b) Position of the MBS (Druckenmiller et al., 2009)

For a coring event, the sampling scheme consists of measuring the vertical temperature profile on one core with a probe thermometer inserted in a sequence of holes drilled at 5 or 10 cm intervals from the bottom. The sea ice bulk salinity profile is determined on adjacent cores, cut into 5 or 10 cm thickness segments, melted at room temperature in the laboratory in a sealed container. Salinity is measured with a conductivity probe. The number of cores collected for salinity measurements at each site varies from 1 to 3.

Temperature profiles recorded with an in-situ thermistor array at the mass balance station from 2006 through 2014 are used to supplement the ice-core measurements. The mass balance station is an automated site installed annually which provides 4-hourly measurements of temperature profiles, thickness information for ice and snow, sea-level measurements, temperature and relative humidity of the local atmosphere (2m above sea-level) (Druckenmiller et al., 2009). Temperature profiles are measured throughout the water/ice/snow/air at 10cm vertical intervals. Installation and removal dates are dependent on the time when the ice becomes securely landfast in the beginning of the calendar year and the melt advance and break-up in June.

Svalbard

The only ice core time series representative of oil and gas extraction regions in the Eurasian Arctic that we were able to locate was of ice cores retrieved at Kongsfjorden in Svalbard at the end of the growth season between May 5 and June 9, 1998 (Gerland et al., 1999). Each of the 10 coring events consists of two cores retrieved, one for temperature, and one for salinity profile measurement. This dataset is representative for thin first year sea ice (up to 80cm in thickness). Due to the lack of observations, no information on the interannual variability as well as ice conditions in early winter are available.

Data processing

First, each salinity and temperature profile is discretized with a 5-cm layer thickness, ranging from 2.5 cm depth to the full core length, rounded to the closest 5 cm. Erroneous and missing data are replaced by linear interpolation between the two nearest points.

Ice cores are typically grouped into different categories based on ice thickness, salinity curve shape, and seasonal stage. However, monthly groupings as performed by Dickins et al. (2008), do not provide meaningful results, since curve collections do not take into account the interannual variability in timing of the growth and melt season. Grouping by a given date and a given temporal spread around it, to aggregate cores from the same field campaign period (beginning January, April, early-May, ...) improve the result, but do not perform well in spring when desalination of the top layer is highly dependent on the number of days with surface thaw.

Hence, we have separated ice cores into different groups based on a degree-day approach. This index is defined as the difference between the daily average air temperature and a reference temperature. The latter was set to -1.8°C , the freezing point of sea water, rather than 0°C , to take into account sea ice thermodynamics. When the temperature falls below the reference, the index is positive and referred to as Positive Degree Days or Freezing Degree Days (FDD). The cumulative value of FDD calculated from the freeze up day to the coring date of a given core provides a measure of both the duration and severity of cooling during the ice season. Similarly, the cumulative thawing degree days (TDD) indicate the extent of potential melt that the ice sheet and the core extracted from it may have experienced. Furthermore, classifying the ice cores by FDDs and TDDs, rather than specific dates reduced interannual variations due to seasonal timing rather than genuine differences in ice properties (Figure 2).

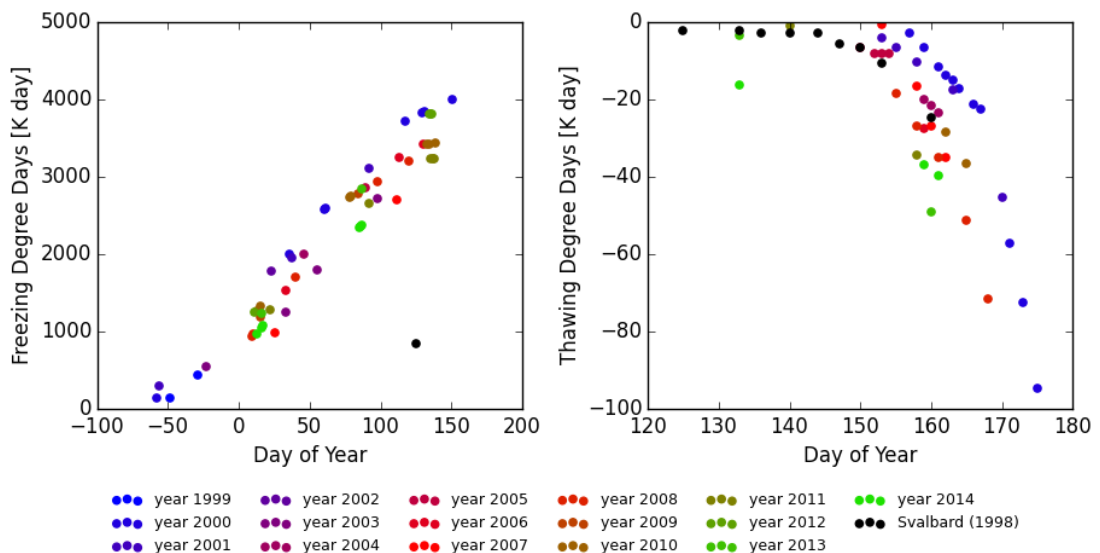


Figure 2 - Interannual variability and long-term change as shown in ice growth/melt conditions: for the same day of the year, the number of freezing degree days has decreased steadily. Each point describes a date when one or several ice cores have been sampled. Coloured data points represent ice cores collected at Barrow, black data points are ice cores collected in Svalbard.

Finally, mean and standard deviation are computed for each group. The resulting statistical envelope is a measure of the spread of sea ice properties. Salinity and temperature data for observations at Barrow are gathered in Figures 1 and 2 for the ice growth period, whereas Figures 3 and 4 display salinity and temperature for the melt season (Thawing Degree Days).

Discussion

Field observations and CRREL tank experiment

The freezing degree day model allows for a comparison of field observation to the CRREL experiment. Ice growth rate and ice thickness are dependent on the amount of heat removed from the ocean, with the conductive flux through the ice cover describing the magnitude of this term. The relationship between the ice thickness and the freezing degree days or thawing degree days can be approximated by a square root relationship (Figure 3).

There are potential differences between laboratory and natural conditions in the factors that control the growth rate: turbulent heat exchange at the surface or the longwave radiation budget may differ considerably in the open air and in the enclosed lab space. Hence, the growth history for the same number of freezing (or thawing) degree days may be different between artificial and natural sea ice. Fitting a square root function (i.e., developing a freezing/thawing-degree day model) will allow us to relate and compare sea ice grown in the tank with field observations.

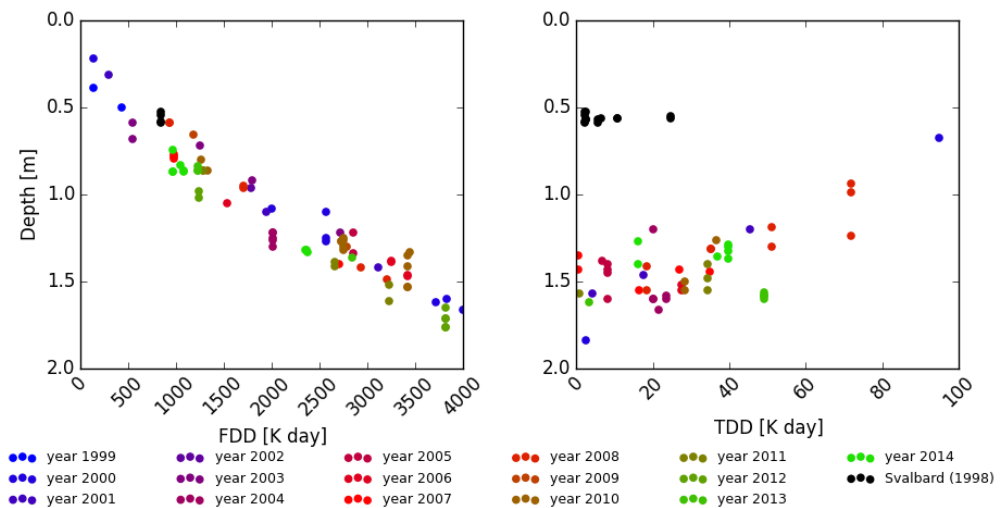


Figure 3 - Ice core length as a function of the number of freezing or thawing degree days. Coloured data points represent ice cores collected at Barrow, black data points are ice cores collected in Svalbard.

In the early stage of the ice tank experiment, a few ice thickness measurements are enough to provide a first calibration of the model, which will be later refined as the ice grows. Then, the FDD/TDD approach can be applied to predict future ice growth and track the salinity evolution during the ice tank experiments.

Profiles and statistics

During the growth season, interannual variability between the profiles is larger for temperature than salinity. While the ice is cold (temperature below -5°C), the salinity profile in the ice interior remains near-constant. Due to the low permeability of the ice there is no convective overturning and freshwater flushing has not set in yet; absent these two key desalination mechanisms salinity remains stable. In contrast, temperature variations are imposed by changing air temperatures and the ice responds readily to these changes. Due to the variation in the seasonal meteorology, as well as climatology, outlier temperature profiles are more likely to be observed (Figure 4).

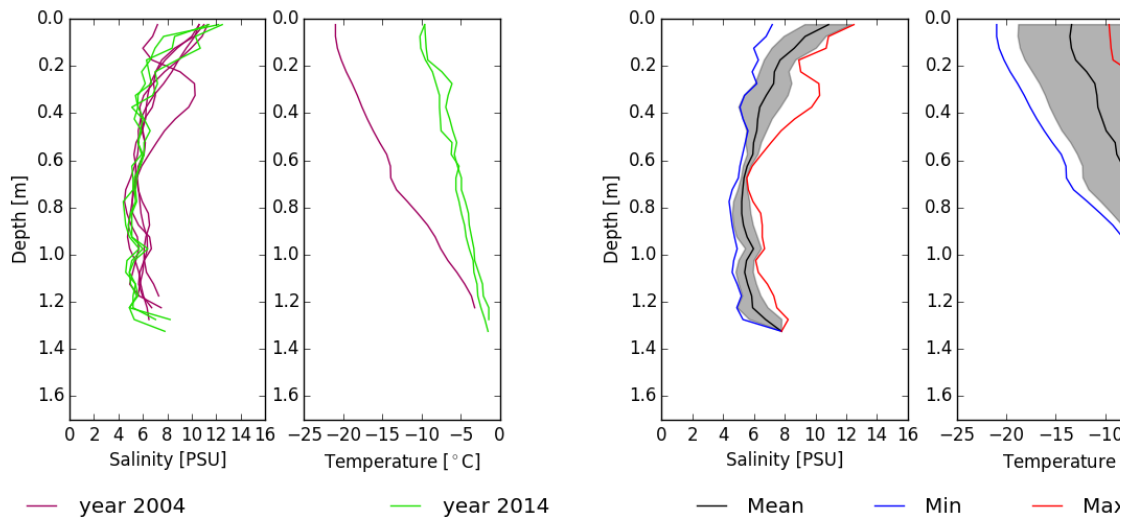


Figure 4 - 2000 to 2500 K-days: temperature and salinity profiles (left) and corresponding statistical envelope (right)

For the FDD range of 3000-3500 K-days, in 2001, for which ice is much colder than in the other years, with a disproportionate increase of the standard deviation. This observation is pertinent for other FDD/TDD intervals as well. Using the quartile (e.g., in a box plot) to describe the spread would have been more appropriate, but most of the groupings do not have enough members to provide meaningful statistics.

At greater depths in the cover, towards the ice bottom, salinity variations are in part due to thickness variations. Thus, ice thickness may vary somewhat due to snow cover variations. Also, natural variations and bottom roughness on the order of a few centimeters are a factor (Eicken et al., 2004). Furthermore, loss of brine from the highly permeable bottom layer immediately after sampling results in a bias with underestimated salinities in the bottom layers (Notz and Worster, 2008).

Brine volume fraction and other derived properties

At thermodynamic equilibrium, temperature and salinity can be considered state variables of sea ice, controlling the volume fraction of the liquid phase. Thus, from measurements of temperature, salinity and sea ice density, or under the assumption of a constant air volume fraction - often neglected due to its small value ($\phi_a < 1\%$) - physical properties can be derived from ice property models (Petrich and Eicken, 2009; Cox & Weeks, 1983; Golden et al., 2007)(Figure 5). Figure 6 displays the statistical envelopes of the two state variables (salinity and temperature), the brine volume fraction ϕ_B , the sea ice electrical conductivity σ_{si} , and the permeability k computed from the temperature and salinity profiles of the ice core belonging to the FDD group 2500 to 4000 K-days. Index b and si refer respectively to the brine and sea ice properties. The three physical properties are derived from equation (1), (3) and (5).

$$\phi_B = (1 - \phi_A) \frac{\rho_i S}{F_1(T) - \rho_i F_2(T)} \quad (1)$$

$F_1(T)$ and $F_2(T)$ are two empirical polynomial functions, based on the phase relations. They are described by Cox & Weeks (1986) for ice temperatures between -30°C and -2°C and by Leppäranta & Manninen (1988) for temperatures between -2°C and 0°C . With σ_B , the brine conductivity of sea ice, depending on the temperature and following Archie's law adapted to ice conditions at Barrow based on measurements by Jones et al. (2012), we arrive at:

$$\sigma_B = -T \cdot e^{0.5193 + 0.08755T} [\text{mSm}^{-1}] \quad (2)$$

$$\sigma_{SI} = \sigma_B \phi_B^2 [\text{mSm}^{-1}] \quad (3)$$

And ρ_i , the density of pure ice is given as:

$$\rho_i = 0.917 - 0.0001403T [\text{gcm}^{-3}] \quad (4)$$

Sea ice permeability, k , derived from the simplest hierarchical model, is described by (Golden et al. 2007):

$$k(\phi_B) = 3\phi_B^2 \times 10^{-8} [\text{m}^2] \quad (5)$$

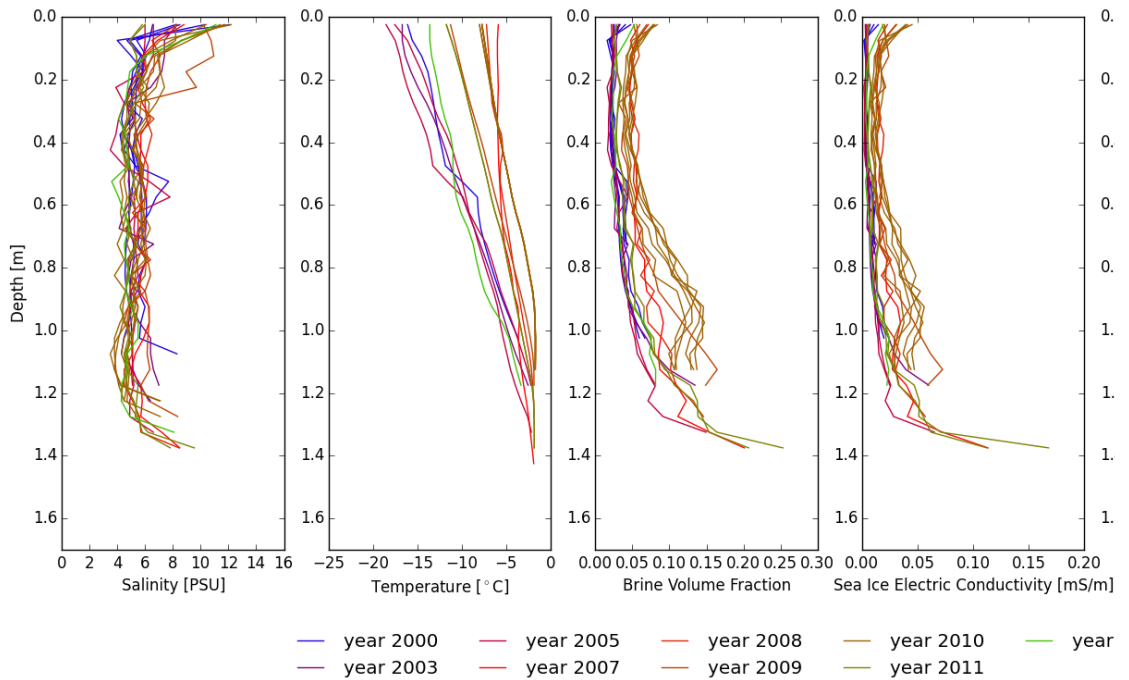


Figure 56 - 2500 - 3000 K-days (growth season): relation between state variables (S, T) and the brine volume fraction and sea ice electric conductivity. As the electric conductivity is dependent on the brine volume fraction to the power of two, the shape of both profiles will be similar.

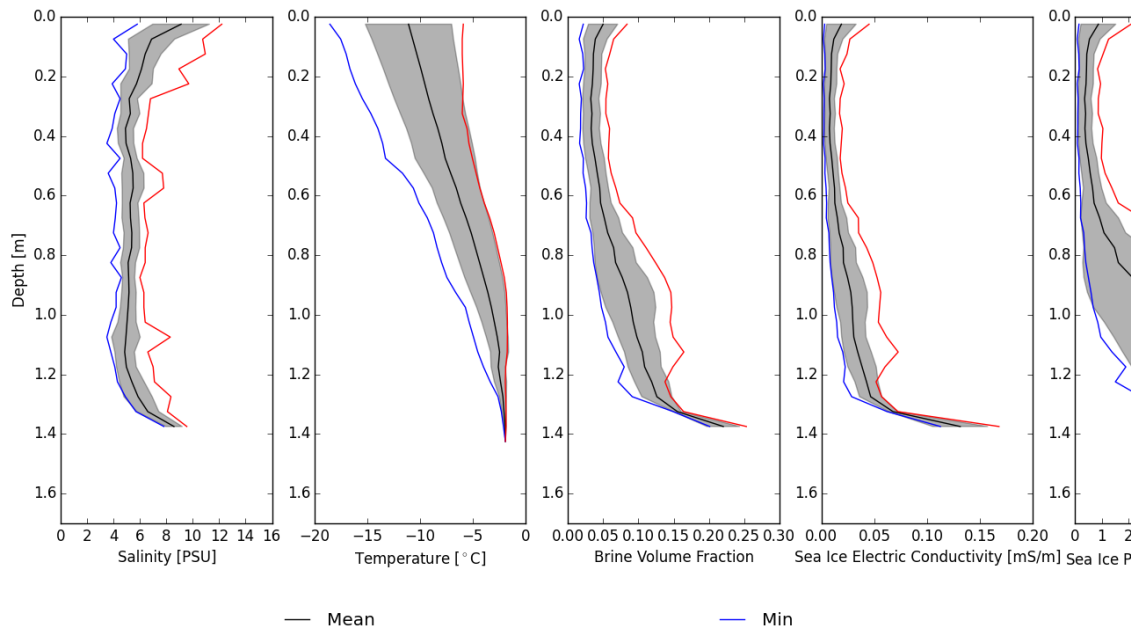


Figure 6 - 2500 - 3000 K-days (growth season): statistical envelope for the state variables on the left (salinity and temperature), and the three derived physical properties on the right (brine volume fraction, sea ice electric conductivity, sea ice permeability).

Model output

In brief, the CICE model was forced with 6-hr weather data from the National Climate Data Center, except for precipitation and humidity provided by the NCEP reanalysis model. Simulations were run for the period 1948-2013, with a focus on 1999 to 2013. Based on validation data with measured ice and snow thickness, a non-zero ocean-to-ice heat flux has to be specified to reproduce the full seasonal cycle. As a first step, a simple statistical approach is used to analyze the observations to determine the general trend of the model output. In order to simplify the comparison, only dates when an ice core has been collected in the field are used to compute the statistic of the model output. During the growth season, the model captures the trend of both salinity and temperature (Figure 7). As expected, salinity in the bottom layer is lower for observation data than simulations. Further work is required to validate and improve model output, and avoid peaks like the one visible at 1.1m depth.

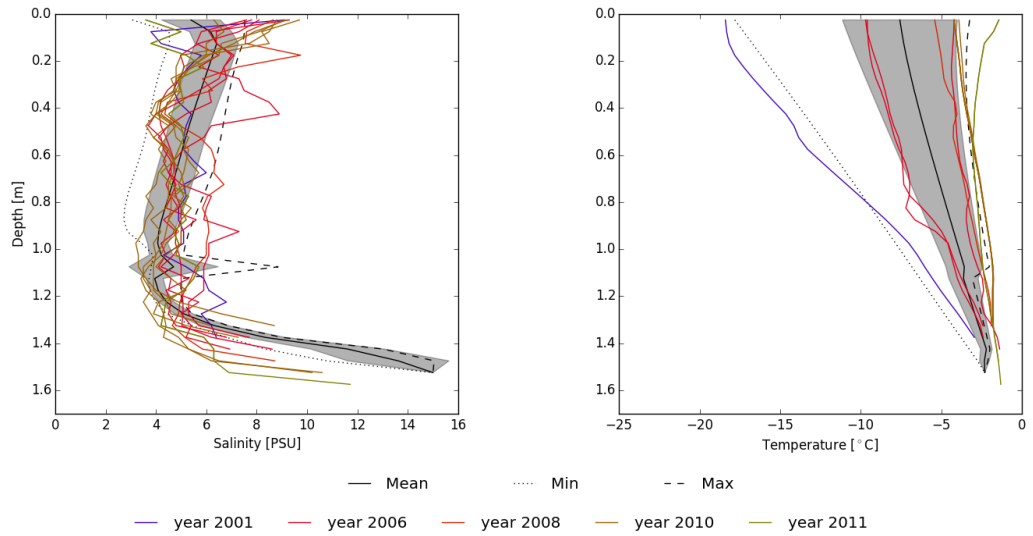


Figure 7 - 3000-3500 K-days (growth season): model output is summarized in the grey statistical envelope and observations are displayed as colour profiles

During melt, significant deviations between observations and model output for ice temperature and salinity are observed, in particular near the ice surface where meltwater flushing is only partially captured by the CICE mushy-layer salinity module (Figure 8). Also, the model appears to overestimate the ice thinning rate due to melt.

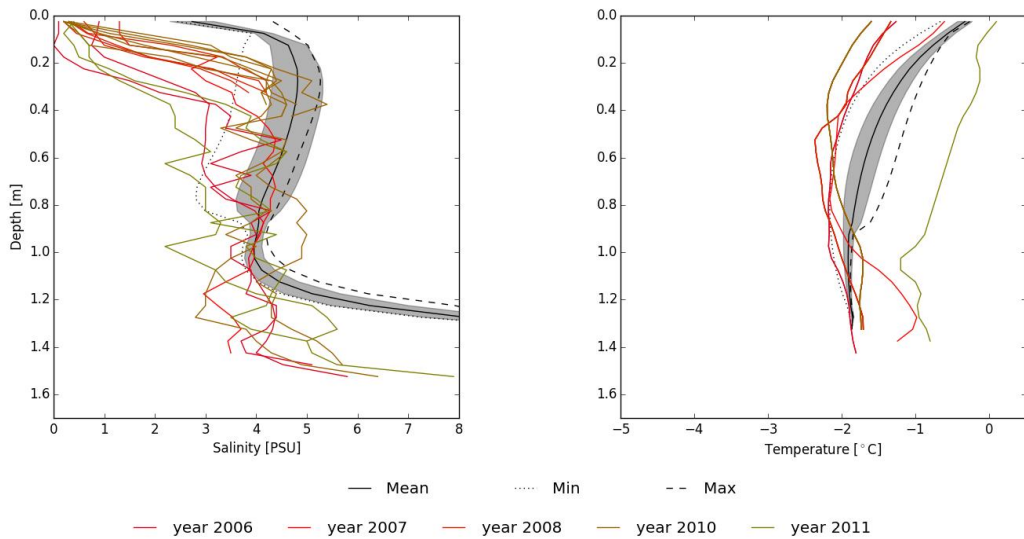


Figure 8 - -25/-35 K-days (melt season): model output is summarized in the grey statistical envelope and observations are displayed in colour profiles

Currently, the model performs well to simulate the general trend and variation of the state variables of sea ice during the growth season. However, weather data and a minimum measurement of snow and ice thickness are required in order to tune the model and increase its accuracy.

Bibliography

- Cox, G.F.N. and Weeks, W. F. *Equations for determining the gas and brine volumes in sea-ice samples.* Journal of Glaciology, 29:306–316, 1983
- Dickins. D, DF Dickins and Associates, Bradford J. and Steinbronn L. (2008) *Detection of Oil on and Under Ice: Phase III Evaluation of Airborne Radar System Capabilities in Selected Arctic Spill Scenarios* *Detection of Oil on and Under Ice: Phase III Evaluation of Airborne Radar System Capabilities in Selected Arctic Spill Scenarios.* Boise State University, 55 pp.
- Druckenmiller, M. L., H. Eicken, D. J. Pringle, C. C. Williams, and M. A. Johnson (2009), Towards an integrated coastal sea-ice observatory: System components and a case study at Barrow, Alaska, Cold Reg. Sci. Technol., 56, 61–72, doi:10.1016/j.coldregions.2008.12.003
- Eicken, H., T. C. Grenfell, D. K. Perovich, J. A. Richter-Menge, K. Frey (2004) Hydraulic controls of summer Arctic pack ice albedo. J. Geophys. Res., 109(C08007):doi:10.1029/2003JC001989
- Eicken, H., R. Gradinger, M. Kaufman, C. Petrich. (Aug 26, 2008, Updated 2014). Sea-ice core measurements (SIZONET). UCAR/NCAR -- CISL -- ACADIS. <http://dx.doi.org/10.5065/D63X84KG>
- Gerland, S., J.-G. Winther, J. B. Orbaek, B. V. Ivanov (1999), Physical properties, spectral reflectance and thickness development of first year fast ice in Kongsfjorden, Svalbard, Polar Res., 18(2), 275-282.
- Golden, K. M., H. Eicken, A. L. Heaton, J. Miner, D. J. Pringle, and J. Zhu (2007), Thermal evolution of permeability and microstructure in sea ice, Geophys. Res. Lett., 34, L16501, doi:10.1029/2007GL030447.
- Jones, K. A., M. Ingham, and H. Eicken (2012), Modelling the anisotropic brine microstructure in first-year Arctic sea ice, J. Geophys. Res., 117, C02005, doi:10.1029/2011JC007607
- Leppäranta, M., Manninen, T., 1988. *The brine and gas content of sea ice with attention to low salinities and high temperatures.* Finnish Institute Marine Research Internal Report, 88-2. Helsinki
- Notz, D., and M. G. Worster (2008), In situ measurements of the evolution of young sea ice, J. Geophys. Res., 113, C03001, doi:10.1029/2007JC004333
- Petrich, C. and H. Eicken (2009) Growth, structure and properties of sea ice, in Thomas, D. N. and G. S. Dieckmann (eds.) *Sea ice*, Wiley-Blackwell, pp. 23-77

Barrow

Table 1 - Representative ice salinity profiles varying by range of FDD for ice growth. N_c is the number of cores used to compute the statistic for a given range at a given depth.

Range [K day]	0 - 500			500 - 1000			1000 - 1500			1500 - 02000			2000 - 2500			2500 - 3000			3000 - 3500			3500 - 4000		
	S	Std	N_c	S	Std	N_c	S	Std	N_c	S	Std	N_c	S	Std	N_c	S	Std	N_c	S	Std	N_c	S	Std	N_c
Depth [cm]	[PSU]	Dev		[PSU]	Dev		[PSU]	Dev		[PSU]	Dev		[PSU]	Dev		[PSU]	Dev		[PSU]	Dev		[PSU]	Dev	
2.5	8.1	1.4	3	11.1	2.7	5	10.7	2.7	10	11.8	0.3	6	10.8	1.5	8	9.4	2.2	23	7.8	2	13	7.3	1.5	7
7.5	5.6	1.1	3	8.1	1.8	5	8.1	2	10	7.2	2.4	6	9.3	1.4	8	7.5	2.4	23	6.6	1.4	13	6.5	2.6	7
12.5	6.1	0.5	3	6.3	1.7	5	6.6	1.4	10	6.2	1.3	6	8.6	1.4	8	6.9	1.8	23	6.1	1.4	13	6.0	0.8	7
17.5	6.4	0.8	3	5.1	1.9	5	6.3	1.4	10	6.5	1.1	6	7.7	1.0	8	6.4	1.5	23	6.2	1.2	13	6.0	0.6	7
22.5	6.2	0.1	2	5.6	1.2	5	6.3	1	10	6.9	1.6	6	7.3	1.0	8	6.2	1.7	23	5.8	0.7	13	6.0	0.8	7
27.5	6.1	0.4	2	5.4	1.1	5	5.8	0.8	10	6.3	1.5	6	7.3	1.2	8	5.8	1.7	23	5.4	0.9	13	5.8	0.8	7
32.5	6.4		1	5.4	0.8	5	5.7	0.7	10	6.3	2	6	6.8	1.4	8	5.7	1.2	23	5.3	0.8	13	5.0	0.9	7
37.5	9.7		1	5.4	0.8	5	5.6	0.9	10	6.2	1.3	6	6.4	1.4	8	5.2	1.1	23	5.0	1.2	13	5.1	0.6	7
42.5				5.3	0.7	5	5.5	0.8	10	5.7	0.7	6	6.3	0.9	8	5.3	1	23	4.7	1.3	13	4.8	0.4	7
47.5				5.2	0.5	5	5.5	0.5	10	5.8	0.5	6	6.2	0.7	8	5.4	0.6	22	4.7	0.6	13	4.7	0.4	7
52.5				5.1	0.6	5	5.5	0.6	10	5.9	0.9	6	6.0	0.5	8	5.5	0.8	22	4.8	0.6	13	4.7	0.5	7
57.5				5.1	0.5	5	5.4	0.5	10	5.5	0.6	6	5.9	0.3	8	5.7	1.3	22	4.8	0.5	13	5.1	0.3	7
62.5				4.9	0.3	4	5.6	0.8	10	5.5	0.6	6	5.6	0.3	8	5.4	0.6	22	4.9	0.5	13	5.1	0.3	7
67.5				5.0	0.5	4	5.6	0.9	9	5.6	0.7	6	5.4	0.2	8	5.3	0.6	22	4.9	0.7	13	5.2	0.2	7
72.5				5.3	0.7	4	5	0.5	8	5.3	0.7	6	5.3	0.3	8	5.5	0.7	22	4.9	0.6	13	5.1	0.5	7
77.5				7.1	0.5	3	5.3	0.6	8	5.8	0.5	6	5.2	0.5	8	5.4	0.7	20	5.0	0.7	13	5.0	0.4	7
82.5				8.2		1	6.4	0.3	7	5.2	0.5	6	5.2	0.6	8	5.1	0.6	20	4.9	0.6	13	4.5	0.3	6
87.5										5.1	0.4	6	5.3	0.6	8	5.2	0.5	20	4.9	0.7	13	4.7	0.4	6
92.5										5.6	0.8	5	5.6	0.7	8	5.3	0.8	20	5.0	0.9	13	5.1	0.6	6
97.5										4.9	0.6	3	6.0	0.5	8	5.1	0.6	19	4.8	0.8	13	5.0	0.4	6
102.5										5.5	0.1	3	5.5	0.5	8	5.1	0.7	19	4.6	0.7	13	5.0	0.7	6
107.5										7.6	0.7	2	5.4	0.6	8	5.0	1.1	19	4.6	0.9	13	4.8	0.6	6
112.5													5.6	0.6	8	5.0	0.9	17	4.8	0.9	13	4.7	0.6	6
117.5													5.9	0.6	8	5.4	1.8	17	4.8	0.8	13	4.6	0.6	6
122.5													5.9	1.0	6	5.4	0.9	14	4.8	0.8	13	4.5	0.6	6
127.5													6.8	1.1	4	5.9	1.1	9	4.8	0.7	13	4.6	0.6	6
132.5													7.8		1	6.6	0.8	6	5.3	1.2	13	4.7	0.7	6
137.5																8.6	0.6	4	6	1.0	11	4.8	1.0	6
142.5																			6.4	1.1	7	4.7	0.8	6
147.5																			6.8	1.0	5	4.6	0.8	6
152.5																			9.2	1.7	3	5.4	2.3	6
157.5																			11.7		1	6.0	2.5	6
162.5																						6.1	2.3	4
167.5																						8.4	1.8	3
172.5																						10.6		1

Table 2 - Representative ice temperature profiles varying by range of FDD for ice growth. N_c is the number of cores used to compute the statistic for a given range at a given depth. No temperature data are available for range 500 to 1000 K-days.

Range [K-day]	0 to 500			500 to 1000			1000 to 1500			1500 to 02000			2000 - 2500			2500 to 3000			3000 to 3500			3500 to 4000		
	T [°C]	Std Dev	N_c	T [°C]	Std Dev	N_c	T [°C]	Std Dev	N_c	T [°C]	Std Dev	N_c	T [°C]	Std Dev	N_c	T [°C]	Std Dev	N_c	T [°C]	Std Dev	N_c	T [°C]	Std Dev	N_c
2.5	-9.8	4.9	3				-13.4	3.3	7	-17.2	2.4	5	-13.4	5.4	3	-11.1	4	17	-5.9	4.5	12	-6.1	2.1	3
7.5	-9.2	4.7	3				-13.2	3.6	7	-16.6	2.5	5	-13.6	5.3	3	-10.7	3.7	17	-5.9	4.4	12	-6.1	2.1	3
12.5	-8.0	4.4	3				-12.4	3.5	7	-15.8	2.5	5	-13.4	5.2	3	-10.3	3.6	17	-5.9	4.3	12	-6.2	2.1	3
17.5	-6.9	4.0	3				-11.4	3.2	7	-14.9	2.4	5	-13.0	5.1	3	-9.9	3.4	17	-5.8	4.2	12	-6.2	2.2	3
22.5	-7.0	2.5	2				-10.3	3	7	-14.3	2.3	5	-11.9	5.5	3	-9.5	3.3	17	-5.7	4.0	12	-6.3	2.2	3
27.5	-4.8	1.6	2				-9.4	2.8	7	-13.3	2.3	5	-11.0	5.6	3	-9.2	3.1	17	-5.6	3.9	12	-6.2	2.2	3
32.5	-4.4		1				-8.7	2.9	7	-12.2	2.3	5	-10.8	5.2	3	-8.8	3.0	17	-5.5	3.7	12	-6.0	2.2	3
37.5	-3.7		1				-7.8	2.8	7	-11.2	2.4	5	-10.7	4.9	3	-8.3	2.9	17	-5.3	3.5	12	-5.9	2.1	3
42.5							-7.0	2.9	7	-10.4	2.5	5	-10.3	4.7	3	-7.9	2.8	17	-5.2	3.4	12	-5.8	2.1	3
47.5							-6.3	3.1	7	-9.8	2.4	5	-9.9	4.5	3	-7.6	2.8	17	-5.1	3.3	12	-5.7	2	3
52.5							-5.5	3.0	7	-8.8	2.3	5	-9.0	4.5	3	-7.1	2.5	17	-4.9	3.2	12	-5.6	1.9	3
57.5							-4.8	2.8	7	-8.0	2.5	5	-8.8	4.0	3	-6.5	2.2	17	-4.8	3	12	-5.5	1.9	3
62.5							-4.2	2.4	7	-7.3	2.6	5	-8.2	4.1	3	-6.1	2.2	17	-4.6	2.9	12	-5.4	1.8	3
67.5							-3.5	1.9	7	-6.4	2.7	5	-8.1	4.1	3	-5.6	2.1	17	-4.4	2.7	12	-5.5	1.7	3
72.5							-3.2	1.5	5	-5.6	2.5	5	-7.9	3.8	3	-5.1	2.0	17	-4.2	2.6	12	-5.5	1.6	3
77.5							-3.1	0.8	3	-4.9	2.3	5	-7.1	3.3	3	-4.7	1.9	17	-4.0	2.4	12	-5.4	1.6	3
82.5							-2.5	0.7	3	-4.4	2.1	5	-6.5	2.9	3	-4.3	1.8	17	-3.9	2.2	12	-5.2	1.6	3
87.5										-4.1	2.0	5	-5.9	2.4	3	-3.9	1.8	17	-3.6	2.0	12	-5.1	1.5	3
92.5										-5.8	0.7	2	-5.4	2.0	3	-3.5	1.6	17	-3.3	1.7	12	-4.9	1.4	3
97.5										-5.0	0.6	2	-4.9	1.9	3	-3.2	1.4	17	-3.1	1.5	12	-4.7	1.2	3
102.5										-4.2	0.5	2	-4.4	1.6	3	-2.9	1.2	17	-2.9	1.4	12	-4.4	1.0	3
107.5										-3.6	0.3	2	-3.8	1.2	3	-2.6	1.0	16	-2.8	1.3	12	-4.2	0.8	3
112.5													-3.2	1.0	3	-2.4	0.8	16	-2.6	1.1	12	-4.1	0.8	3
117.5													-2.8	0.6	3	-2.5	0.7	10	-2.5	1.0	12	-3.9	0.7	3
122.5													-2.3	0.7	3	-2.4	0.6	5	-2.4	0.8	12	-3.8	0.6	3
127.5													-1.6	0.2	2	-2.2	0.3	5	-2.2	0.6	12	-3.6	0.6	3
132.5													-1.5		1	-2.0	0.2	4	-2.1	0.5	12	-3.5	0.6	3
137.5																-1.9	0.1	3	-2.0	0.5	5	-3.3	0.5	3
142.5																-1.9		1	-1.5	0.1	3	-3.1	0.4	3
147.5																			-1.5	0.0	2	-2.9	0.3	3
152.5																			-1.4		1	-2.7	0.2	3
157.5																			-1.3		1	-2.5	0.2	3
162.5																						-2.2		1

Table 3 - Representative ice salinity profiles varying by range of TDD for ice melt. N_c is the number of cores used to compute the statistic for a given range at a given depth. *: only the top of the ice cores of -15 to -10 K-days have been collected

Range [K day]	0 to -5			-5 to -10			-10 to -15*			-15 to -25			-25 to -35			-35 to -50			-50 to -100		
	S [PSU]	Std Dev	N_c	S [PSU]	Std Dev	N_c	S [PSU]	Std Dev	N_c	S [PSU]	Std Dev	N_c	S [PSU]	Std Dev	N_c	S [PSU]	Std Dev	N_c	S [PSU]	Std Dev	N_c
2.5	3.3	1.7	6	1.0	0.5	6	0.6	0.3	3	0.9	0.8	17	0.4	0.3	15	0.5	0.4	7	1.0	0.7	8
7.5	4.8	1.8	6	2.5	0.6	6	1.2	0.3	3	1.6	0.9	17	0.8	0.4	15	0.6	0.4	7	0.9	0.7	8
12.5	5.1	1.6	6	3.6	0.7	6	2.2	0.3	3	2.3	1.1	17	1.4	0.9	15	0.8	0.6	7	1.5	0.8	8
17.5	4.9	1.4	6	4.4	0.9	6	3.2	0.4	3	3.1	1.1	17	2.3	1.2	15	1.3	0.9	7	2.2	0.8	8
22.5	5.3	0.9	6	4.1	0.6	6	4.0	0.3	3	3.5	1.0	17	2.9	1.2	15	2.1	1.1	7	2.9	0.8	8
27.5	5.2	0.5	6	4.6	0.7	6	4.0	0.4	3	3.7	0.8	17	3.5	1.2	15	2.7	1.0	7	3.1	0.7	8
32.5	5.3	0.7	6	4.4	0.6	6	4.2	0.4	3	3.9	0.6	17	3.7	0.9	14	3.1	1.1	7	3.2	0.8	8
37.5	5.1	0.3	6	4.9	0.6	6	4.4	0.4	3	4.0	0.6	17	4.0	0.9	11	3.3	0.9	7	3.3	0.7	8
42.5	5.1	0.3	6	4.7	0.2	6	4.7	0.4	2	4.2	0.5	16	3.8	0.7	9	3.7	0.8	7	3.3	0.8	7
47.5	5.2	0.3	5	4.9	0.5	6	5.1		1	4.4	0.6	14	3.4	0.5	7	3.7	0.9	7	3.4	1.0	7
52.5	5.2	0.3	5	4.7	0.5	6	5.2		1	4.5	0.6	14	3.9	0.7	7	3.8	0.5	6	3.5	1.0	7
57.5	4.8	0.4	5	4.7	0.4	5	5.2		1	4.5	0.6	12	4.0	0.7	7	4.1	0.3	6	3.2	0.6	6
62.5	4.6	0.5	5	4.7	0.8	5	5.1		1	4.6	0.7	12	3.6	0.8	7	4.1	0.3	6	3.1	0.5	6
67.5	4.3	0.4	5	4.8	0.6	5				4.5	0.5	12	3.6	0.5	7	4.0	0.4	6	3.1	0.6	5
72.5	4.4	0.4	5	4.4	0.6	5				4.6	0.5	12	3.6	0.5	7	4.0	0.3	6	3.0	0.6	5
77.5	4.6	0.3	5	4.3	0.8	5				4.5	0.4	12	3.8	0.6	7	3.9	0.5	6	2.8	0.6	5
82.5	4.5	0.3	5	4.4	0.7	5				4.4	0.5	12	4.2	0.6	7	3.6	0.6	6	2.7	0.7	5
87.5	4.1	0.4	5	4.3	0.7	5				4.4	0.6	12	3.9	0.5	7	3.6	0.2	6	2.7	0.7	5
92.5	4.1	0.4	5	3.9	0.6	5				4.3	0.5	12	4.0	0.6	7	3.6	0.5	6	3.0	0.7	5
97.5	4.1	0.5	5	3.9	0.5	5				4.3	0.4	12	3.8	0.7	7	3.6	0.6	6	3.1	0.6	4
102.5	3.9	0.5	5	4.1	0.6	5				4.1	0.4	12	3.8	0.6	7	3.3	0.5	6	2.9	0.6	3
107.5	3.9	0.5	5	3.8	0.3	5				4.1	0.5	12	3.9	0.5	7	3.3	0.7	6	2.5	0.4	3
112.5	4.3	0.7	5	3.9	0.0	5				4.2	0.5	12	3.8	0.4	7	3.1	0.5	6	2.1	0.5	3
117.5	4.3	0.4	5	4.5	0.6	5				4.1	0.5	12	3.8	0.6	7	3.0	0.5	6	2.3	0.4	3
122.5	4.4	0.8	5	4.9	0.5	5				4.1	0.4	11	4.1	0.7	7	2.7	0.7	6	2.8	0.7	2
127.5	4.7	1.7	5	5.3	0.8	5				4.1	0.4	10	4.0	0.8	7	2.9	1.1	5	1.6		1
132.5	6.3	3.5	5	6.8	2.6	5				4.2	0.6	10	4.3	0.6	7	4.3	0.3	2			
137.5	5.3	1.2	4	8.4	2.9	5				4.3	0.9	10	4.4	0.7	7						
142.5	7.1	3.9	4	8.4	2.9	3				4.4	0.9	8	4.4	0.7	6						
147.5	6.2	0.6	3	4.5		1				4.4	1.0	7	5.2	0.4	5						
152.5	9.7	1.9	3	6.2		1				4.8	1.8	7	6.7	0.9	3						
157.5	13.8		1	7.7		1				3.9	0.4	5									
162.5										3.6		1									

Table 4 - Representative ice temperature profiles varying by range of TDD for ice melt. N_c is the number of cores used to compute the statistic for a given range at a given depth. Maximal depth for FDD range -10 to -15 K-days is only 65 cm, as only the top of the core was retrieved during the coring. *: only the top of the ice cores of -15 to -10 K-days have been collected

Range [K day]	0 to -5			-5 to -10			-10 to -15*			-15 to -25			-25 to -35			-35 to -50			-50 to -100		
	T	Std	N_c	T	Std	N_c	T	Std	N_c	T	Std	N_c	T	Std	N_c	T	Std	N_c	T	Std	N_c
Depth [cm]	[°C]	Dev		[°C]	Dev		[°C]	Dev		[°C]	Dev		[°C]	Dev		[°C]	Dev		[°C]	Dev	
2.5	-1.9	1.4	6	-0.3	0.5	6	-0.2	0.2	3	-0.4	0.6	14	-1.3	0.5	14	-0.9	0.1	4	0.3	0.5	8
7.5	-2.1	1.3	6	-0.7	0.4	6	-0.4	0.2	3	-0.5	0.6	14	-1.4	0.5	14	-1.0	0.2	4	0.0	0.3	8
12.5	-2.2	1.2	6	-1.0	0.3	6	-0.6	0.2	3	-0.7	0.6	14	-1.5	0.5	14	-1.0	0.4	4	-0.3	0.1	8
17.5	-2.4	1.1	6	-1.1	0.3	6	-0.8	0.2	3	-0.8	0.7	14	-1.6	0.5	14	-1.1	0.4	4	-0.4	0.1	8
22.5	-2.5	1.0	6	-1.3	0.3	6	-1.0	0.2	3	-1.0	0.7	14	-1.7	0.5	14	-1.2	0.4	4	-0.5	0.2	8
27.5	-2.6	0.9	6	-1.5	0.3	6	-1.2	0.2	3	-1.1	0.7	14	-1.8	0.5	14	-1.3	0.4	4	-0.6	0.2	8
32.5	-2.7	0.8	6	-1.6	0.3	6	-1.3	0.2	3	-1.2	0.6	14	-1.9	0.5	14	-1.4	0.4	4	-0.7	0.2	8
37.5	-2.8	0.8	6	-1.7	0.3	6	-1.4	0.1	3	-1.3	0.6	14	-1.9	0.5	14	-1.4	0.4	4	-0.8	0.2	8
42.5	-2.8	0.8	6	-1.8	0.3	6	-1.5	0.1	3	-1.4	0.6	14	-2.0	0.5	14	-1.5	0.5	4	-0.9	0.2	8
47.5	-2.8	0.7	6	-1.9	0.3	6	-1.6	0.1	3	-1.5	0.6	14	-2.0	0.5	14	-1.6	0.5	4	-1.1	0.1	7
52.5	-2.8	0.6	6	-2.0	0.2	6	-1.8	0.0	3	-1.7	0.6	13	-2.1	0.5	14	-1.6	0.6	4	-1.3	0.1	7
57.5	-2.9	0.6	6	-2.0	0.2	5	-1.9	0.1	3	-1.7	0.6	12	-2.1	0.4	14	-1.6	0.6	4	-1.3	0.1	6
62.5	-2.8	0.5	6	-2.1	0.2	5	-2.0	0.1	3	-1.7	0.6	11	-2.1	0.4	14	-1.6	0.6	4	-1.3	0.1	6
67.5	-2.8	0.4	6	-2.1	0.2	5	-2.0	0.1	2	-1.7	0.6	11	-2.1	0.4	14	-1.6	0.6	4	-1.3	0.1	6
72.5	-2.7	0.4	6	-2.1	0.2	5				-1.7	0.6	10	-2.0	0.4	14	-1.6	0.5	4	-1.3	0.1	5
77.5	-2.7	0.4	5	-2.1	0.1	5				-1.7	0.6	10	-2.0	0.4	14	-1.7	0.5	4	-1.3	0.1	5
82.5	-2.6	0.4	5	-2.1	0.0	5				-1.7	0.6	10	-2.0	0.4	14	-1.6	0.4	4	-1.3	0.1	5
87.5	-2.5	0.3	5	-2.1	0.1	5				-1.7	0.5	10	-1.9	0.3	14	-1.6	0.4	4	-1.2	0.1	5
92.5	-2.4	0.3	5	-2.1	0.2	5				-1.7	0.5	9	-1.9	0.3	14	-1.6	0.4	4	-1.2	0.2	5
97.5	-2.4	0.3	5	-2.0	0.2	5				-1.7	0.4	9	-1.9	0.3	14	-1.5	0.5	4	-1.2	0.2	5
102.5	-2.3	0.3	5	-1.9	0.1	5				-1.7	0.4	9	-1.8	0.2	14	-1.4	0.5	4	-1.3	0.0	2
107.5	-2.2	0.2	5	-1.8	0.1	5				-1.6	0.4	9	-1.8	0.2	14	-1.4	0.4	4	-1.3	0.0	2
112.5	-2.1	0.2	5	-1.8	0.2	5				-1.6	0.3	9	-1.7	0.3	14	-1.4	0.4	4	-1.2	0.0	2
117.5	-2.0	0.2	5	-1.7	0.2	5				-1.5	0.3	9	-1.7	0.3	14	-1.3	0.5	4			
122.5	-1.9	0.1	5	-1.7	0.1	5				-1.5	0.3	8	-1.7	0.3	14	-1.6	0.1	3			
127.5	-1.8	0.1	5	-1.7	0.1	5				-1.4	0.3	8	-1.6	0.3	14	-1.5	0.1	3			
132.5	-1.8	0.1	4	-1.7	0.1	5				-1.4	0.2	8	-1.6	0.3	14						
137.5	-1.7	0.2	3	-1.6	0.1	4				-1.3	0.3	5	-1.4	0.4	4						
142.5	-1.6	0.2	2	-1.5	0.1	3				-1.4	0.3	4	-1.8	0.0	2						
147.5	-1.7	0.4	2	-1.4		1				-1.2	0.3	3									
152.5	-1.6	0.4	2							-1.0	0.2	3									

Svalbard

Table 5 - Representative ice salinity and temperature profiles varying by range of degree day for ice melt. N_c is the number of core used to compute the statistic for a given range at a given depth.

Range [K day]	Salinity [PSU]									Temperature [°C]								
	0 to -10			-10 to -20			-20 to -30			0 to -10			-10 to -20			-20 to -30		
	S	Std	N_c	S	Std	N_c	S	Std	N_c	T	Std	N_c	T	Std	N_c	T	Std	N_c
Depth [cm]	[PSU]	Dev		[PSU]	Dev		[PSU]	Dev		[°C]	Dev		[°C]	Dev		[°C]	Dev	
2.5	7.5	1.6	4	3.5		1	0.8		1	-2.4	0.5	4	-1.2		1	0.0		1
7.5	5.3	1.4	4	3.6		1	3.6		1	-2.3	0.4	4	-1.4		1	-0.6		1
12.5	4.4	0.7	4	3.5		1	3.3		1	-2.2	0.4	4	-1.4		1	-0.8		1
17.5	4.3	0.2	4	3.9		1	3.2		1	-2.2	0.3	4	-1.5		1	-0.9		1
22.5	3.9	0.2	4	3.7		1	2.9		1	-2.1	0.3	4	-1.5		1	-1.1		1
27.5	3.7	0.5	4	3.7		1	3.6		1	-2.0	0.3	4	-1.5		1	-1.2		1
32.5	5.2	0.3	4	5.0		1	3.5		1	-2.0	0.2	4	-1.5		1	-1.1		1
37.5	5.1	0.2	4	5.0		1	4.3		1	-1.9	0.2	4	-1.5		1	-1.3		1
42.5	4.9	0.3	4	4.5		1	4.2		1	-1.8	0.2	4	-1.5		1	-1.3		1
47.5	5.3	0.4	4	4.7		1	4.0		1	-1.7	0.2	4				-1.4		1
52.5	6.5	1.2	3	5.8		1	5.1		1	-1.5	0.1	3				-1.4		1
57.5	7.6		1							-1.5	0.1	2						

Core excluded from analysis

The core BRW_CS-20050328 was grouped into the 2500-3000 K-days class; however its core length of 1.22 did not match with the average core length of this group (1.4m). The much reduced core length was likely due to removal of the ice cover in early winter as a result of a break-out event, with ice disproportionately thinner. The core was eliminated from the analysis.

List of half cores

Top cores have been collected at several occasions to study surface desalination processes. For this purpose, only the top half meter was extracted.

BRW_CS-20000510
BRW_CS-20000301A
BRW_CS-20000301B
BRW_CS-20000607
BRW_CS-20000609
BRW_CS-20000610
BRW_CS-20000611
BRW_CS-20000612
BRW_CS-20000614
BRW_CS-20000615
BRW_CS-20000619
BRW_CS-20000621
BRW_CS-20080606A
BRW_CS-20080606B
BRW_CS-20080606C
BRW_CS-20080606D
BRW_CS-20090325B
BRW_CS-20100604
BRW_CS-20100607
BRW_CS-20100611C
BRW_CS-20100611D
BRW_CS-20100611E
BRW_CS-20100611F
BRW_CS-201006

Appendix IV. Radar modelling runs not presented in the main report.

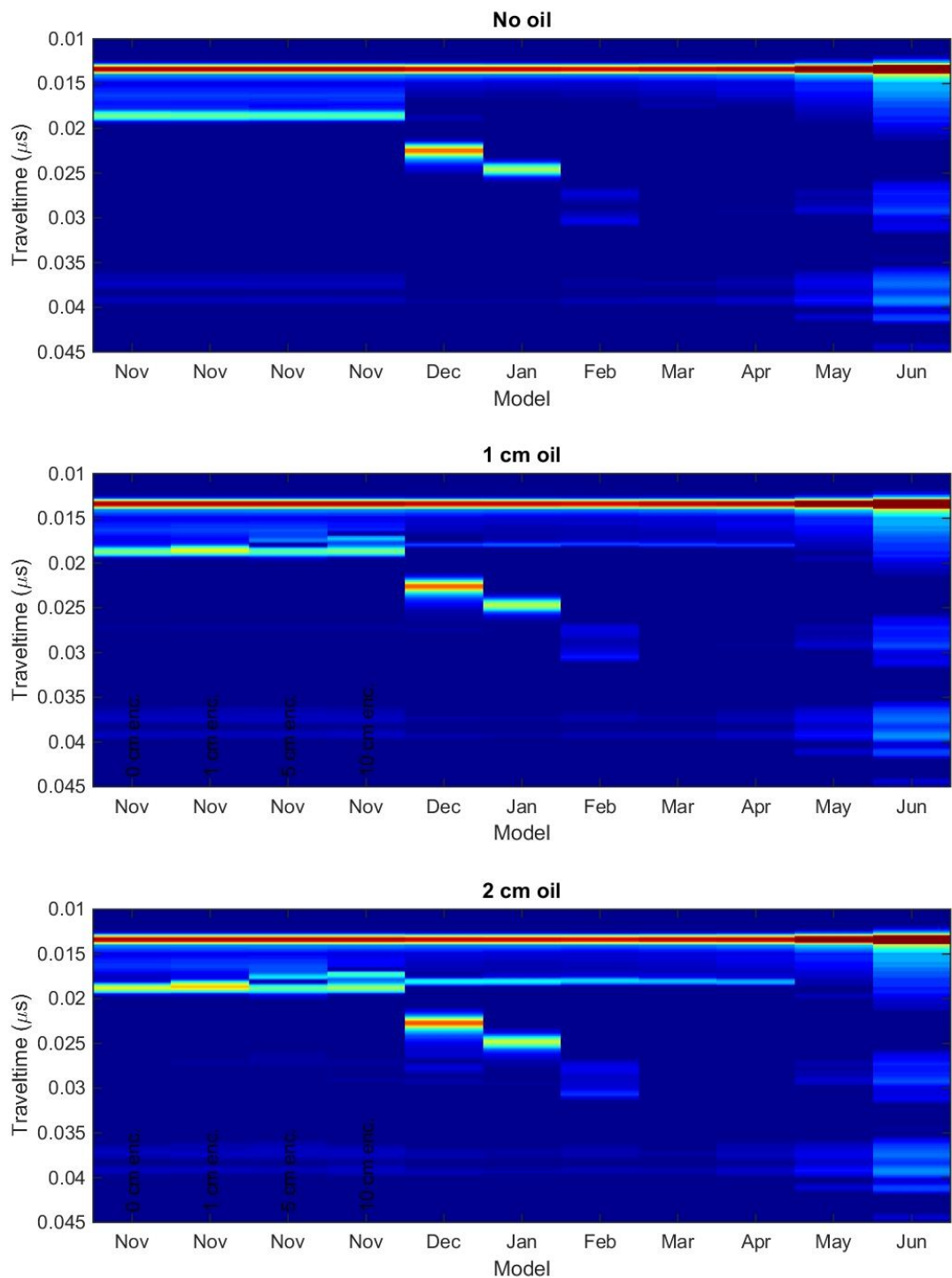


Figure MG1. Evolution of the FMCW radar response to an oil spill in November with oil spills of 0, 1 cm and 2 cm thickness.

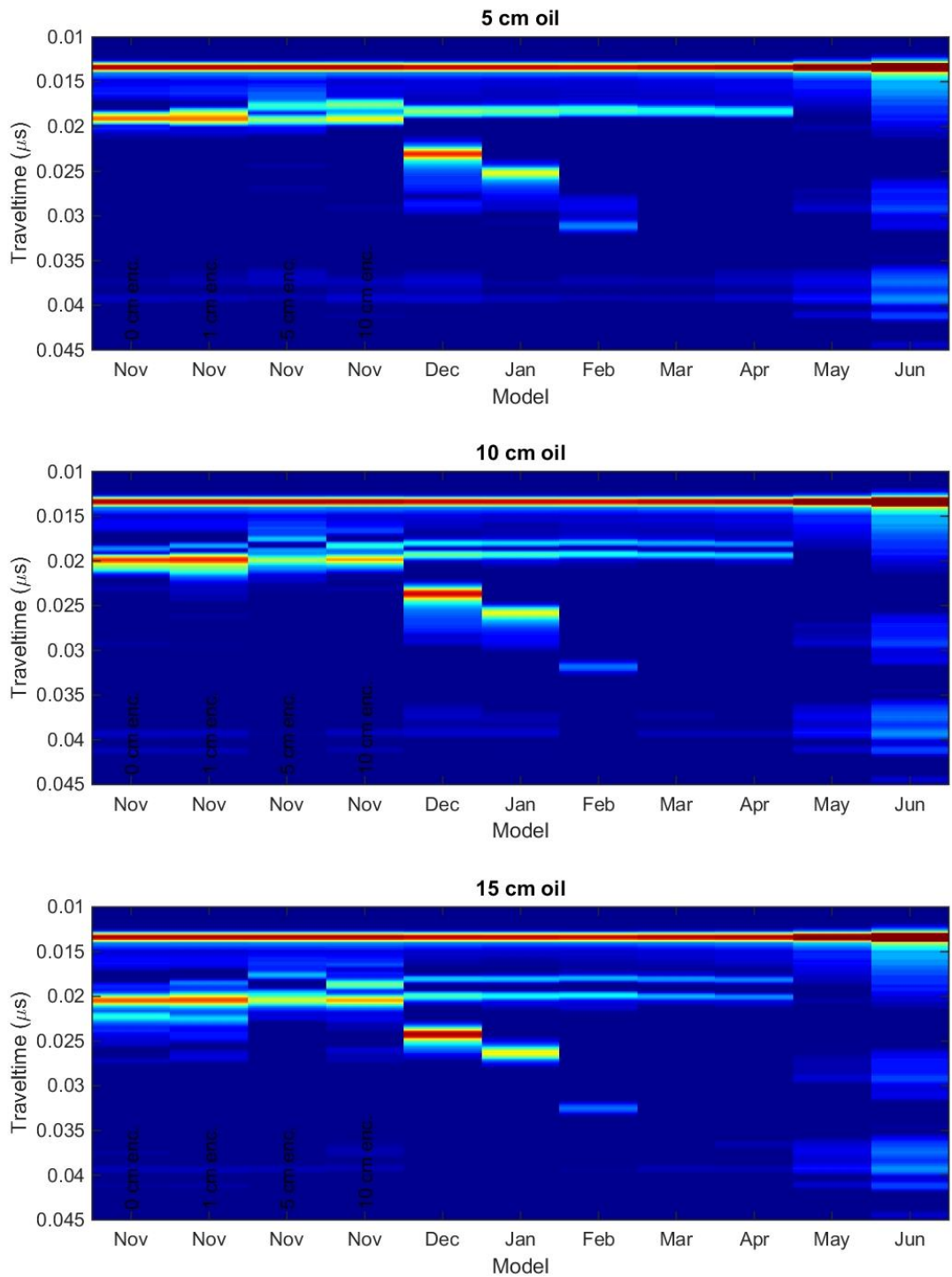


Figure MG2. Evolution of the FMCW radar response to an oil spill in November with oil spills of 5 cm, 10 cm, and 15 cm thickness.

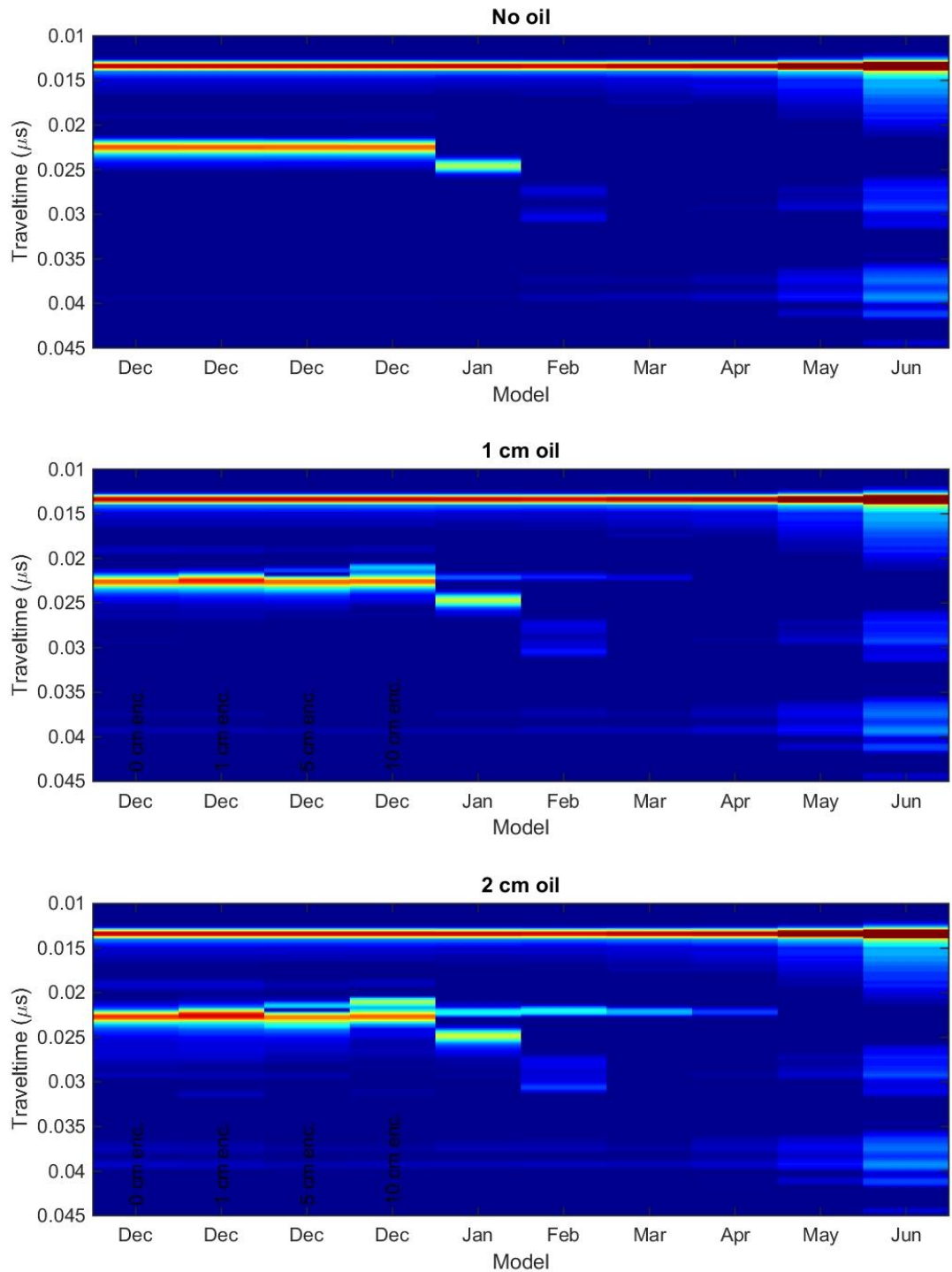


Figure MG3. Evolution of the FMCW radar response to an oil spill in December with oil spills of 0, 1 cm and 2 cm thickness.

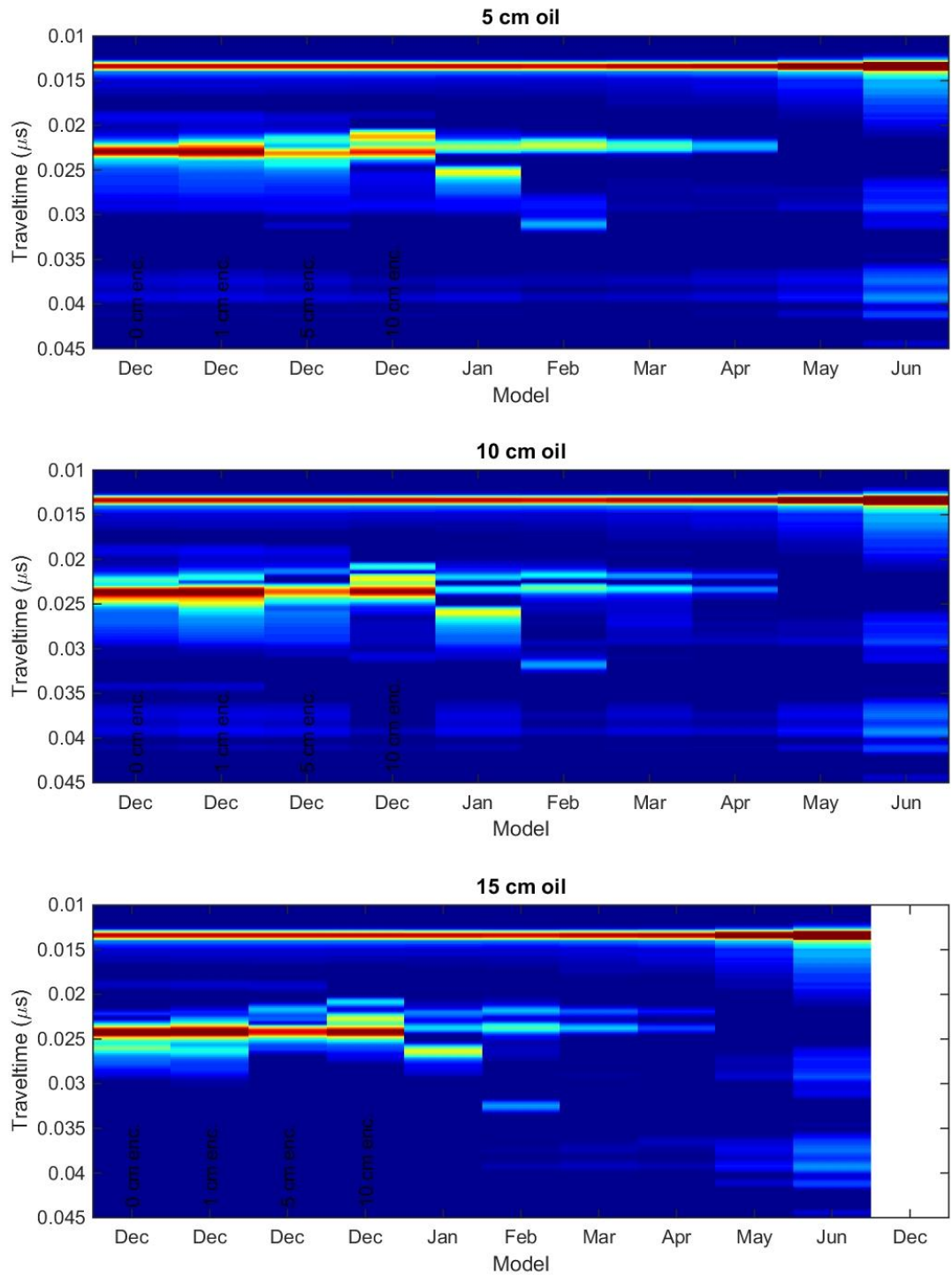


Figure MG4. Evolution of the FMCW radar response to an oil spill in December with oil spills of 5 cm, 10 cm, and 15 cm thickness.

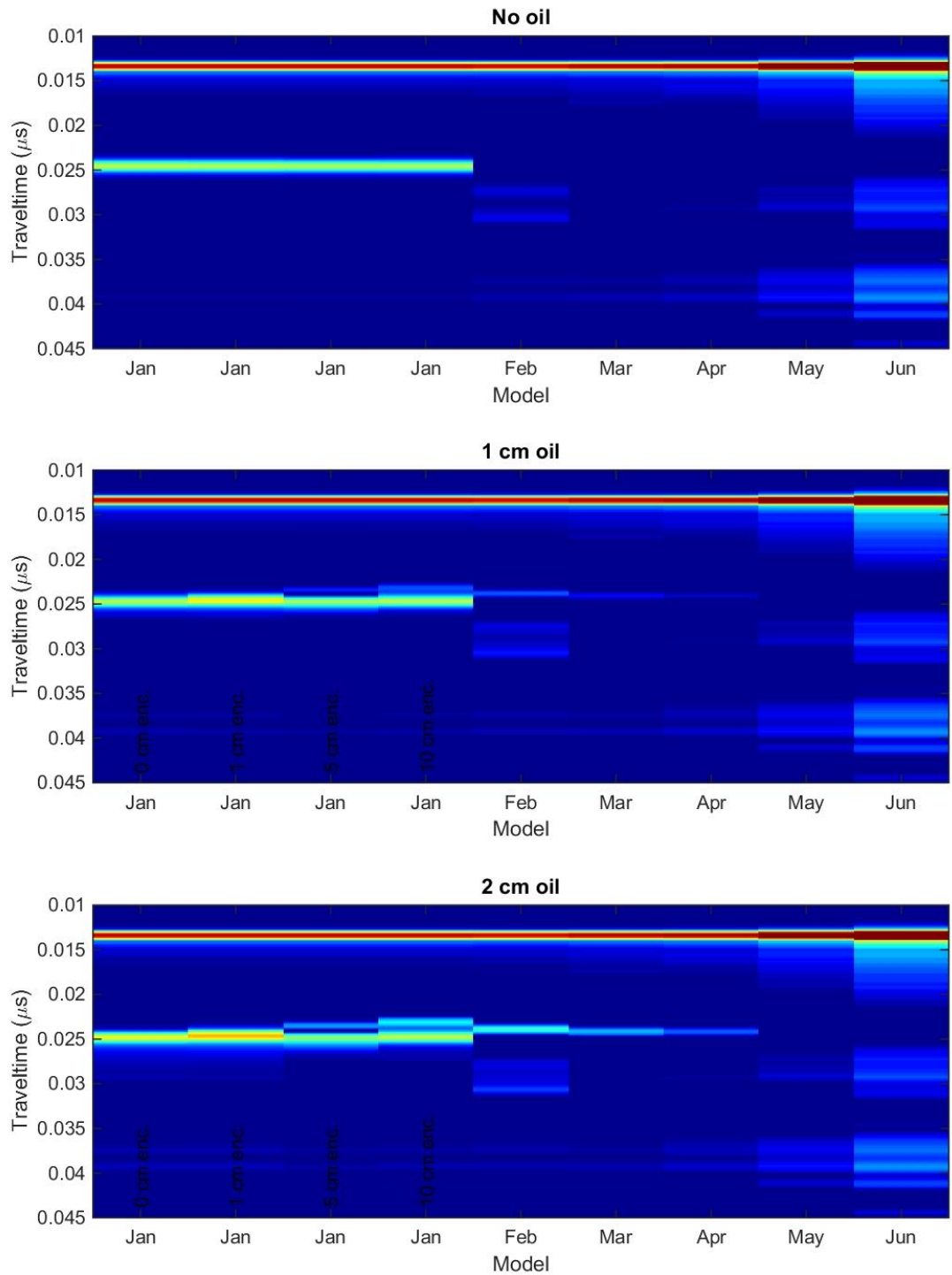


Figure MG5. Evolution of the FMCW radar response to an oil spill in January with oil spills of 0, 1 cm and 2 cm thickness.

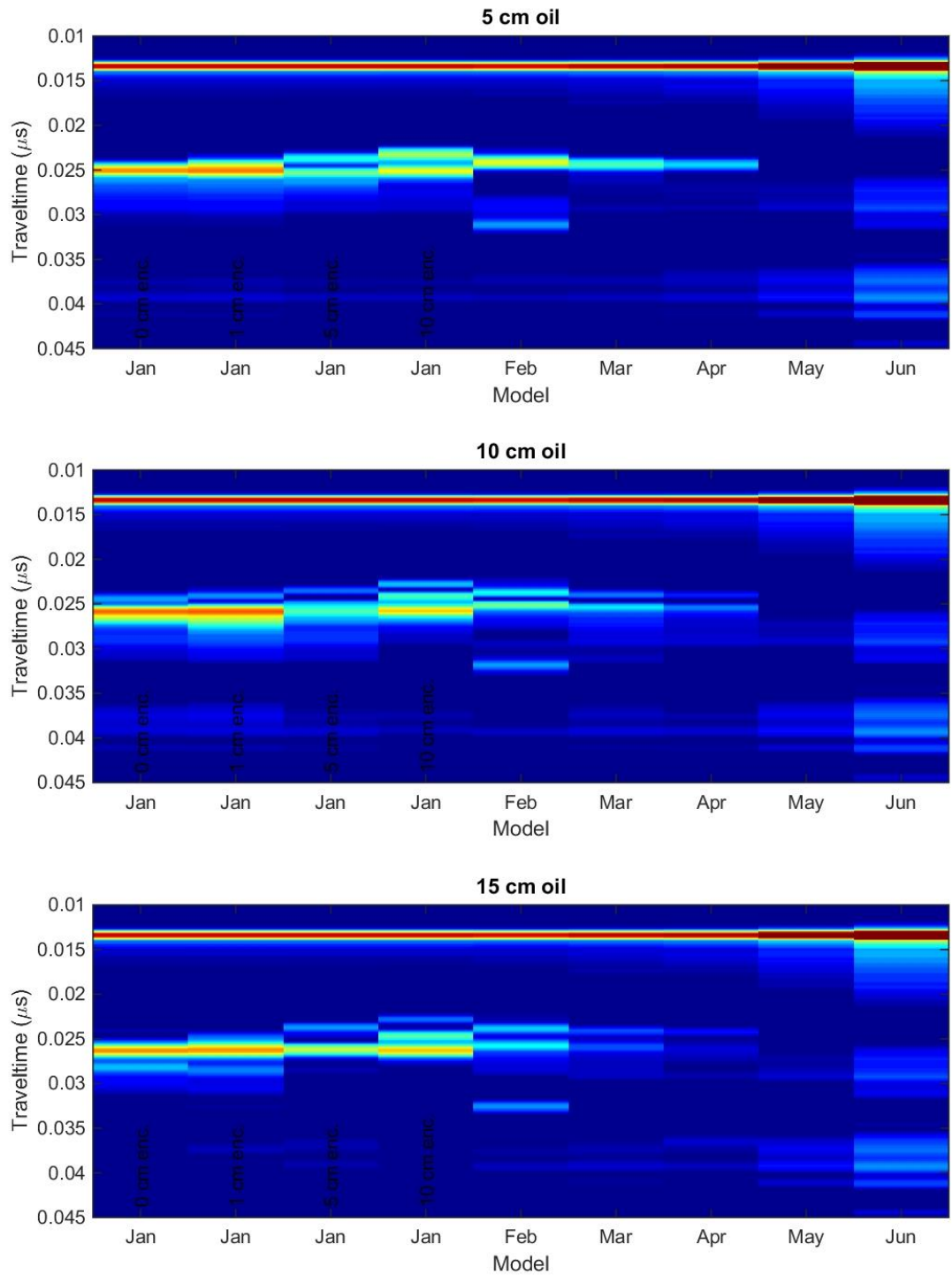


Figure MG6. Evolution of the FMCW radar response to an oil spill in January with oil spills of 5 cm, 10 cm, and 15 cm thickness.

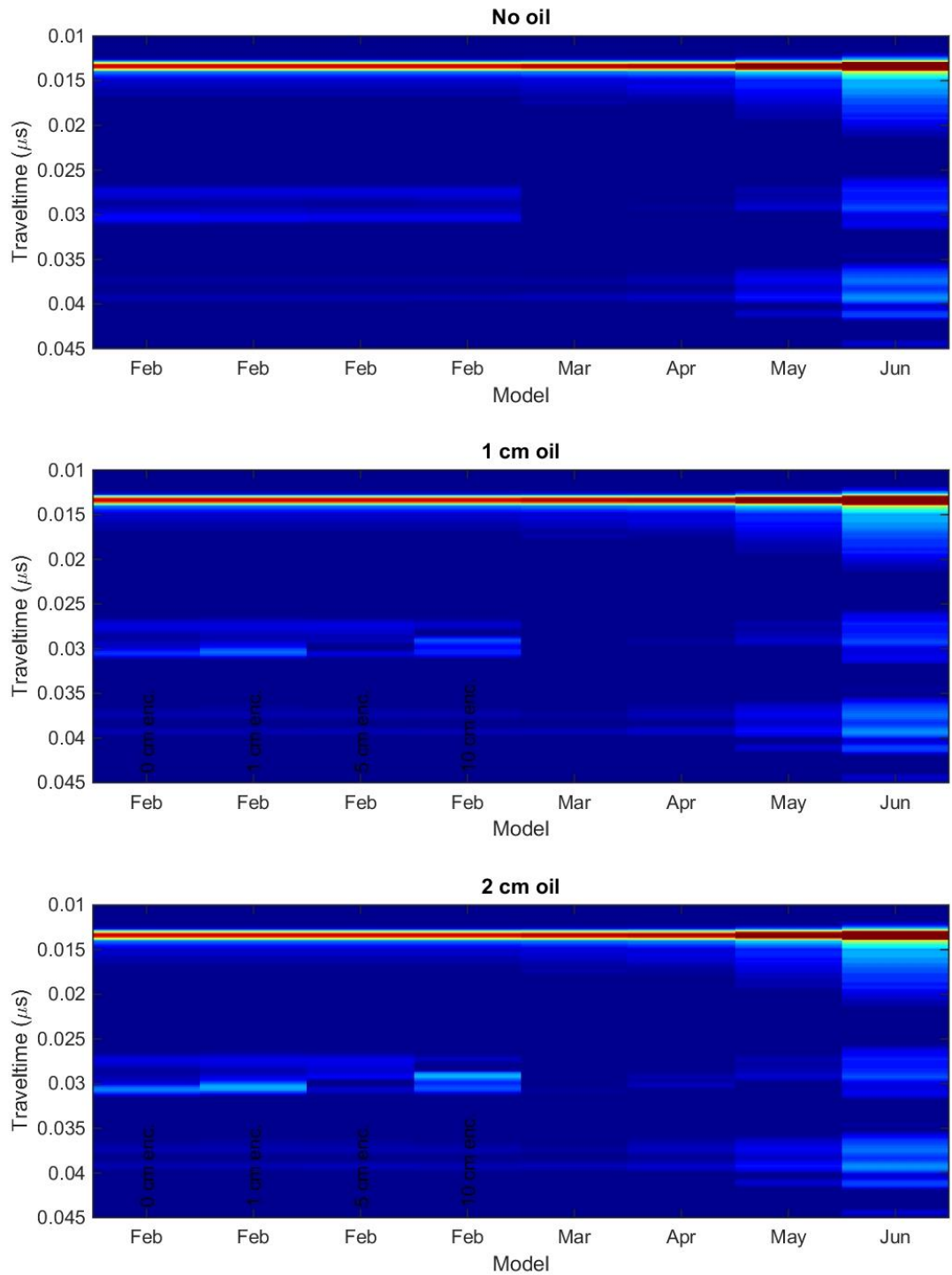


Figure MG7. Evolution of the FMCW radar response to an oil spill in February with oil spills of 0, 1 cm and 2 cm thickness.

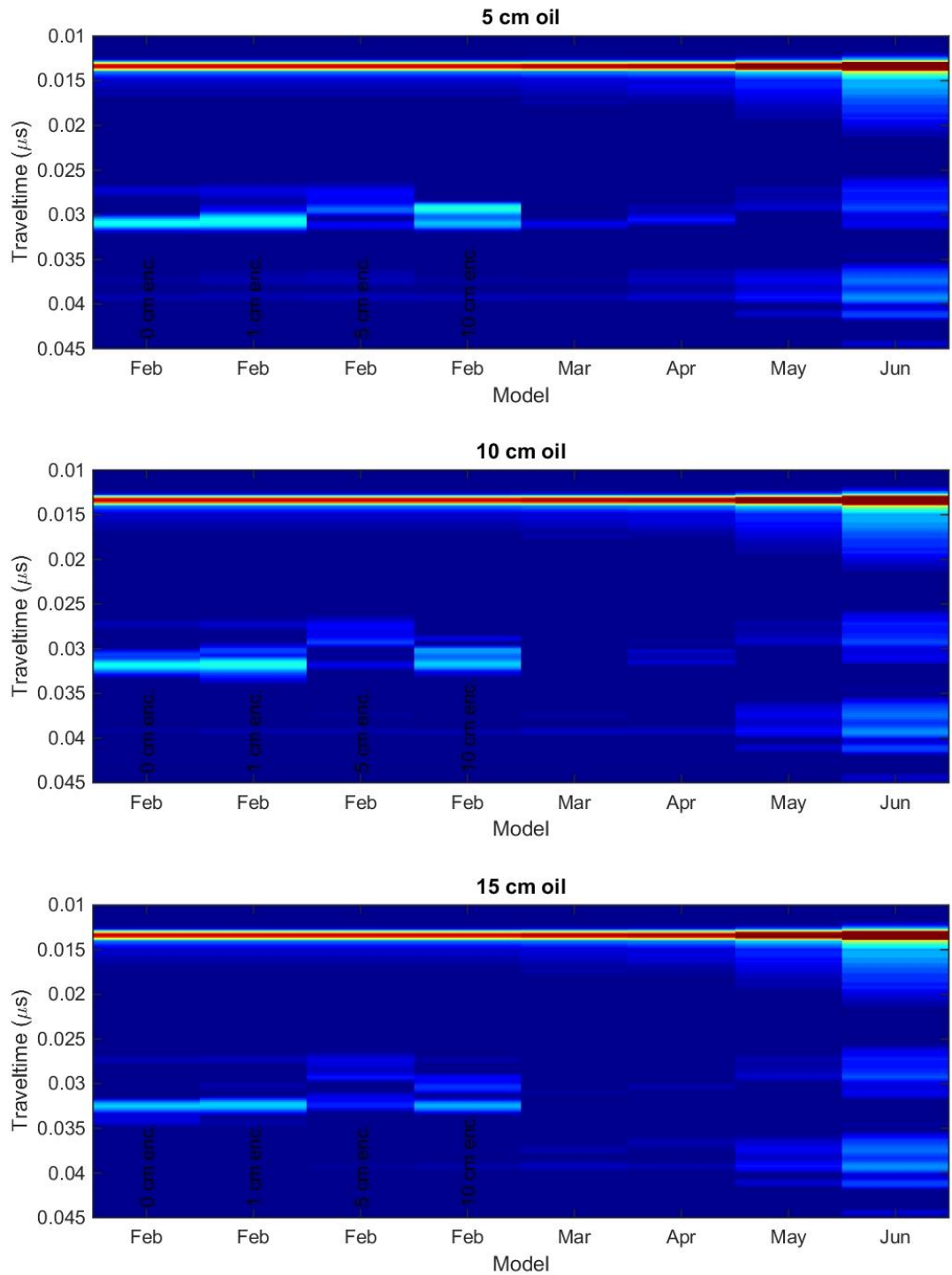


Figure MG8. Evolution of the FMCW radar response to an oil spill in February with oil spills of 5 cm, 10 cm, and 15 cm thickness.

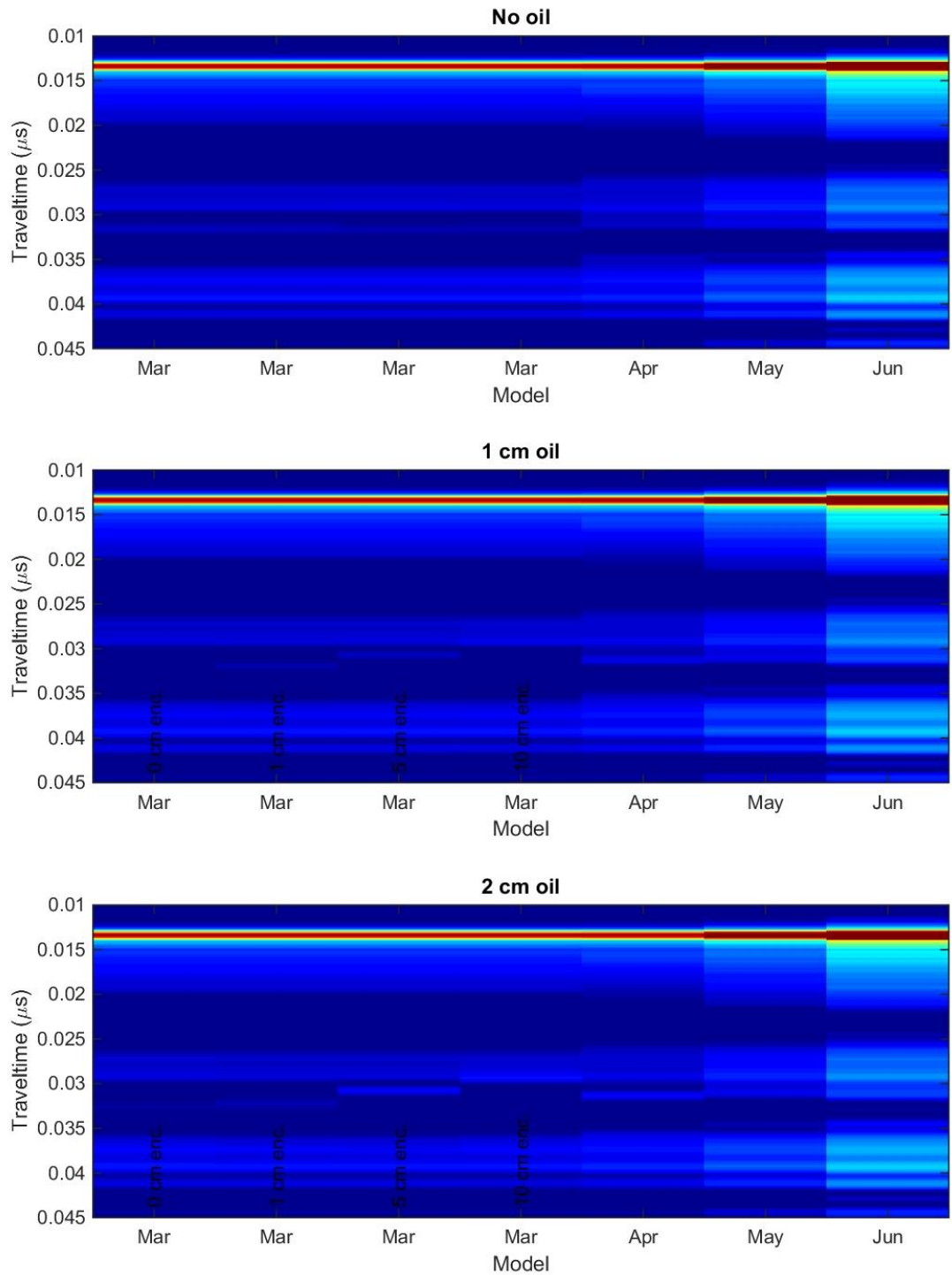


Figure MG9. Evolution of the FMCW radar response to an oil spill in March with oil spills of 0, 1 cm and 2 cm thickness.

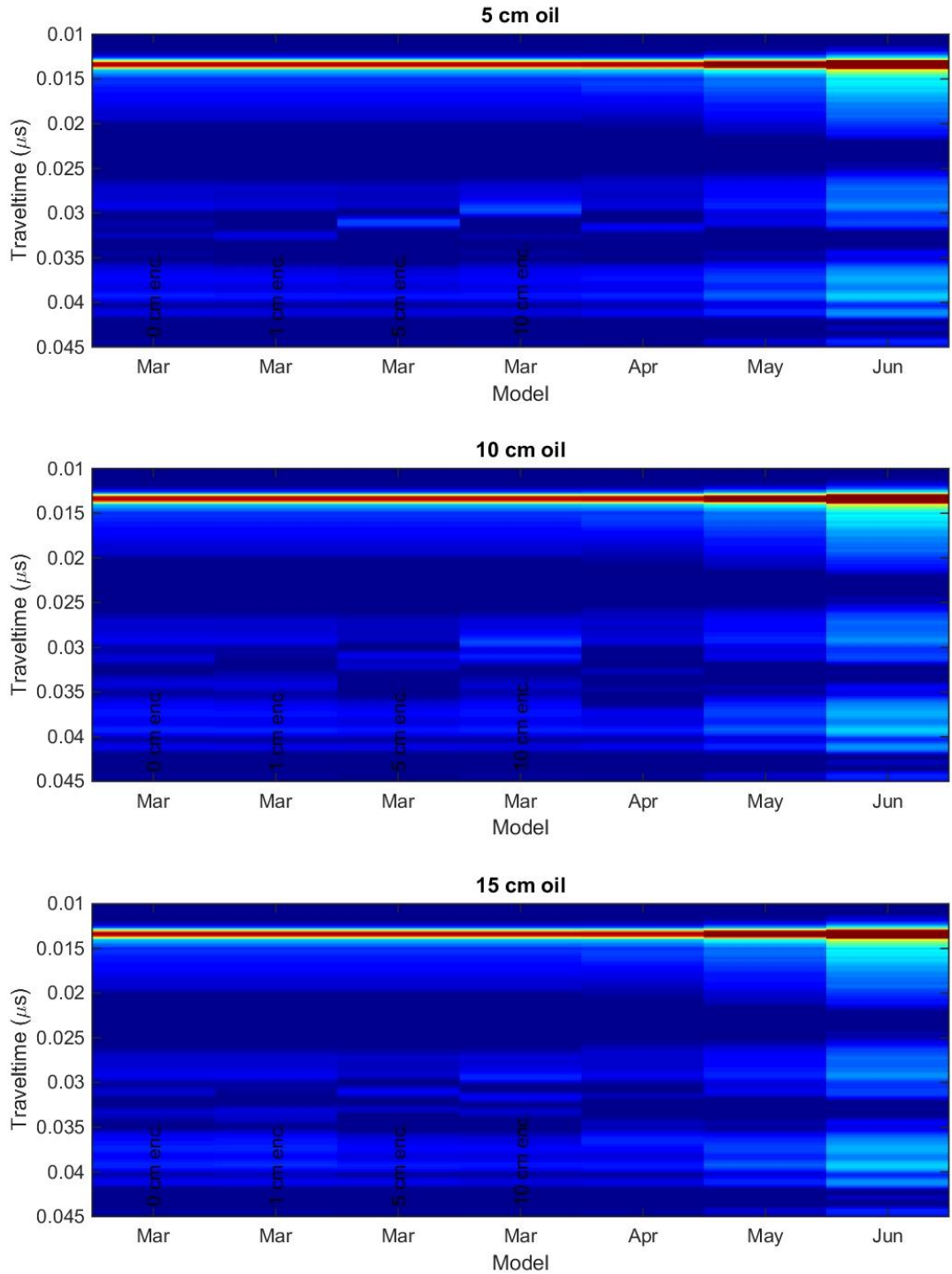


Figure MG10. Evolution of the FMCW radar response to an oil spill in March with oil spills of 5 cm, 10 cm, and 15 cm thickness.

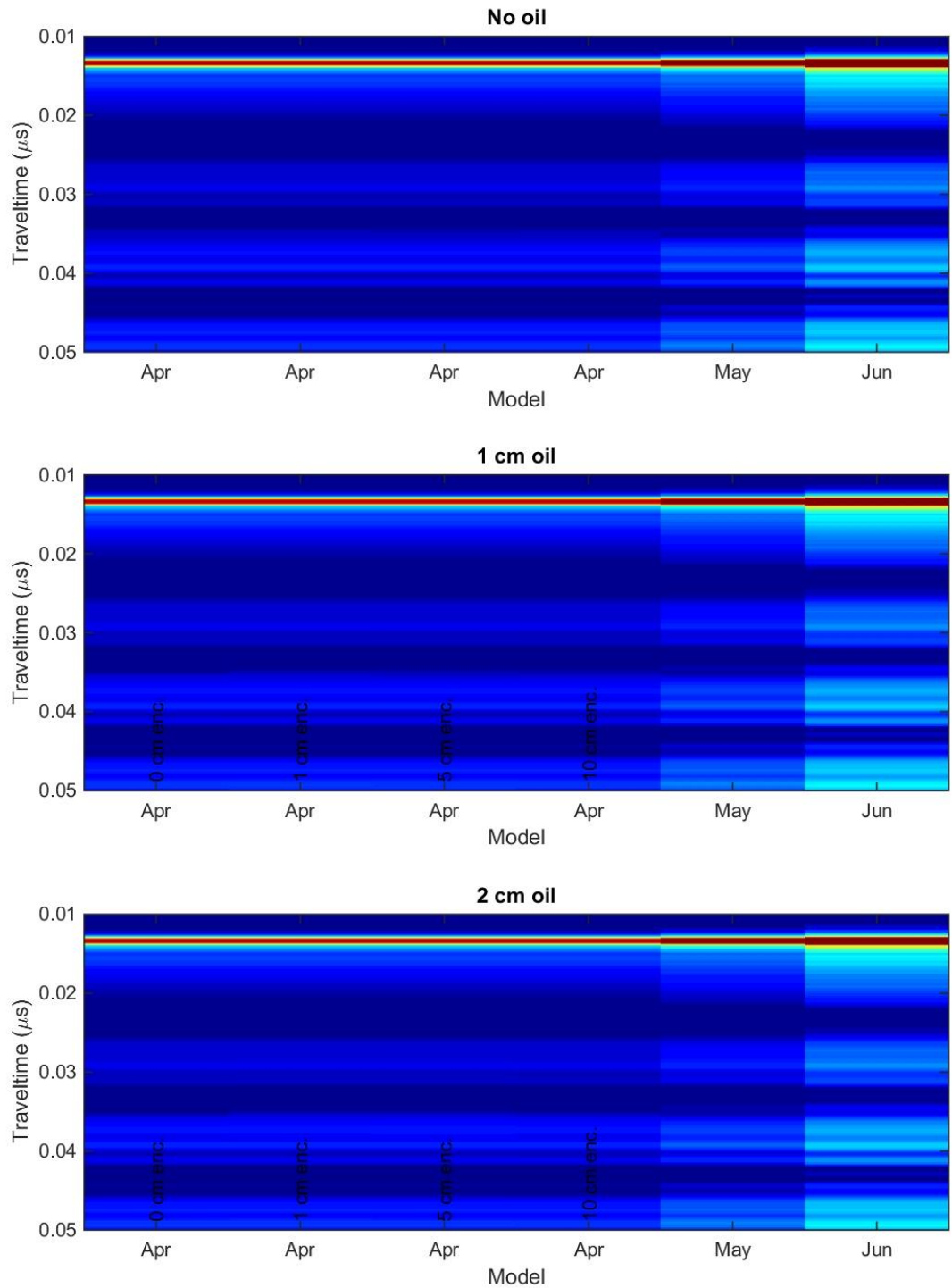


Figure MG11. Evolution of the FMCW radar response to an oil spill in April with oil spills of 0, 1 cm and 2 cm thickness.

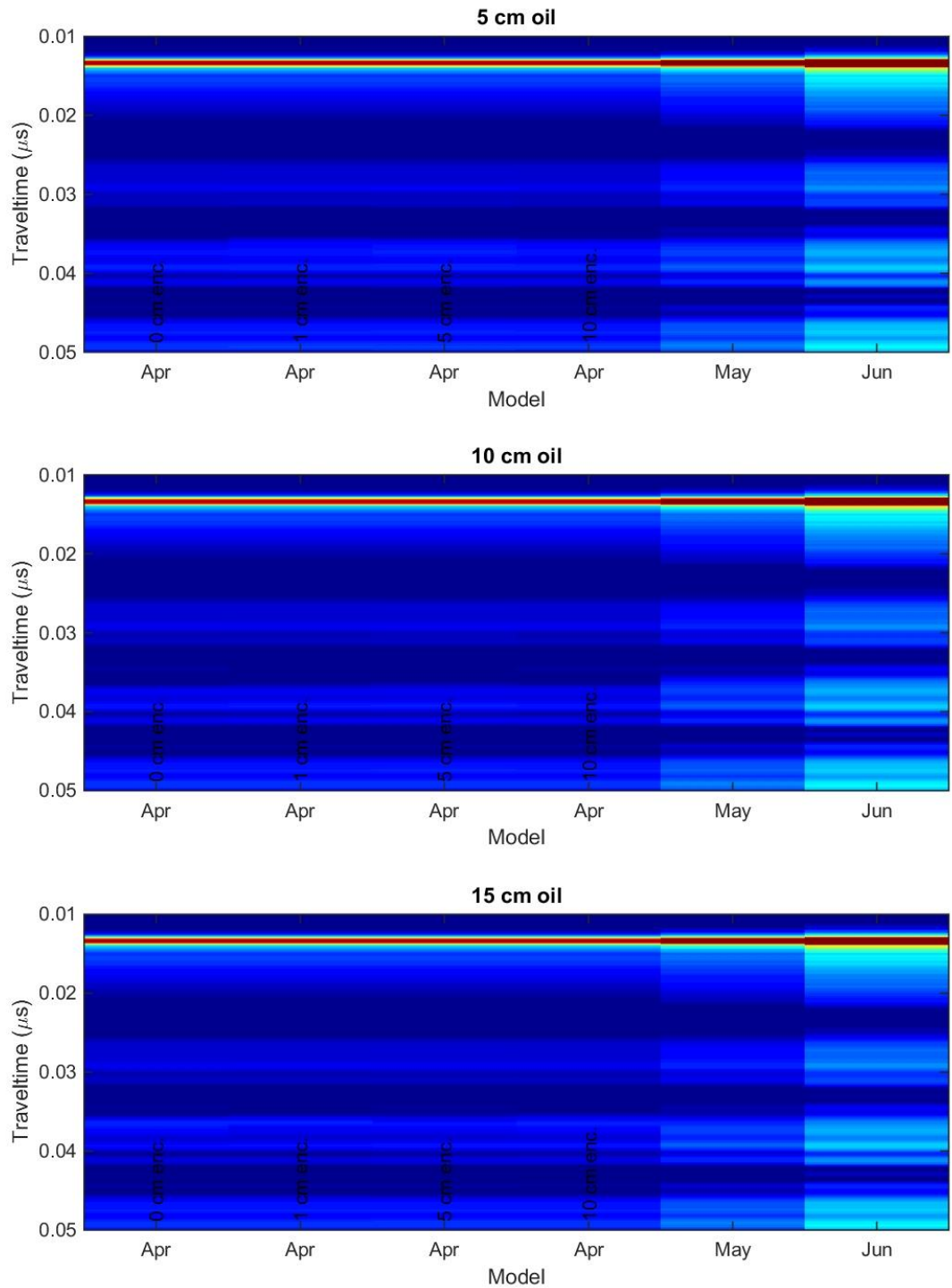


Figure MG12. Evolution of the FMCW radar response to an oil spill in April with oil spills of 5 cm, 10 cm, and 15 cm thickness.

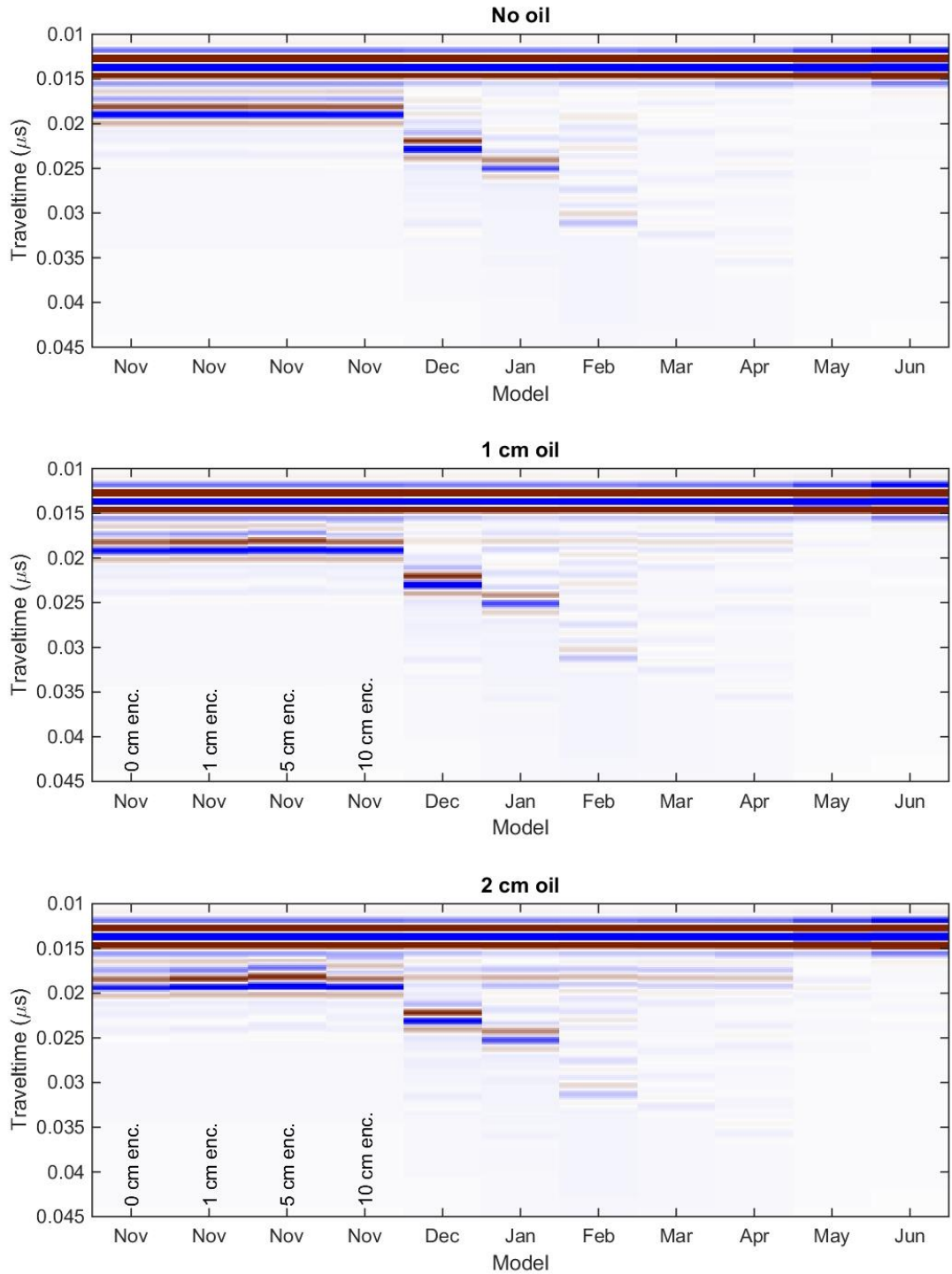


Figure MG13. Evolution of the pulsed GPR response to an oil spill in November with oil spills of 0, 1 cm and 2 cm thickness.

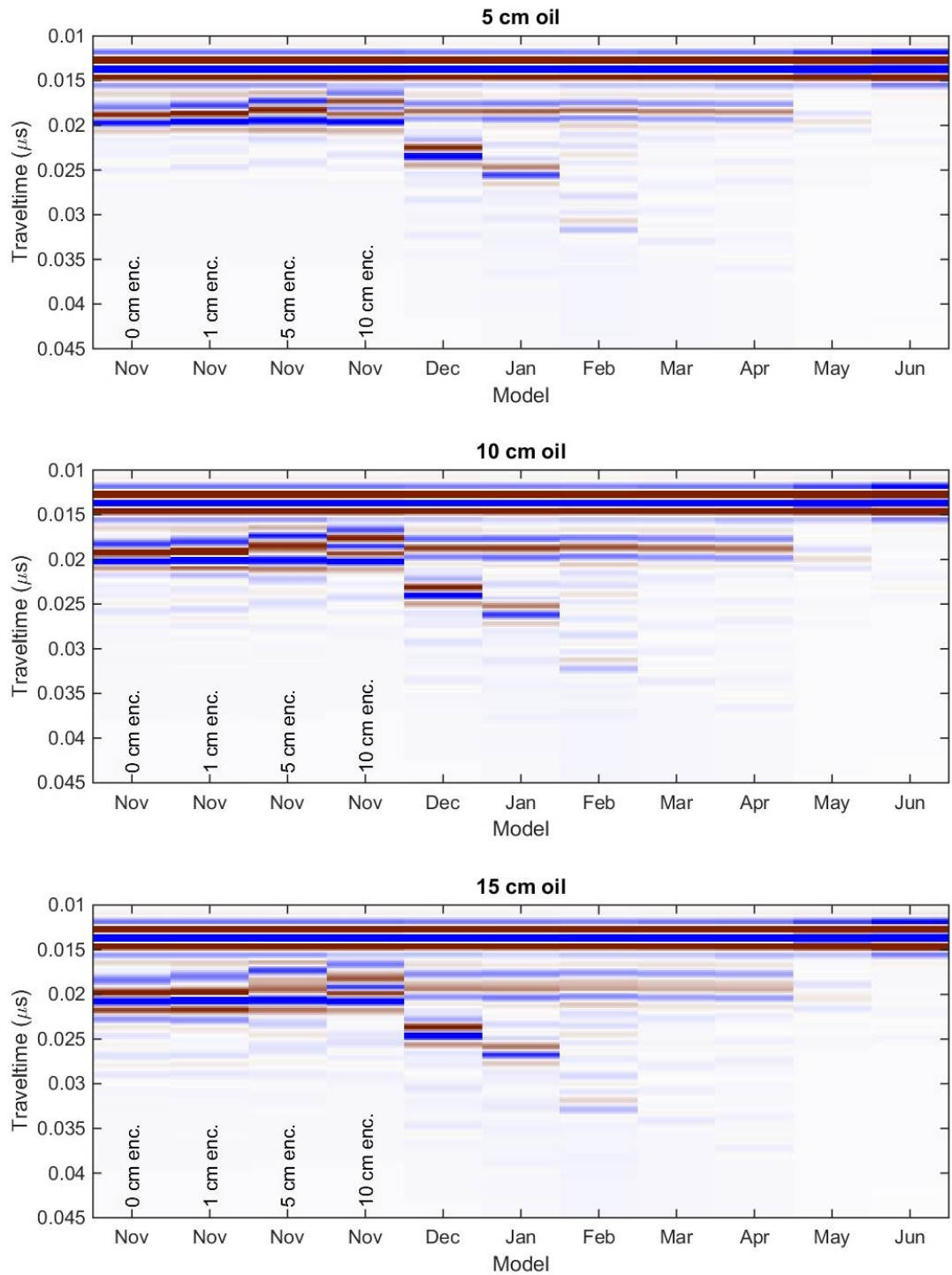


Figure MG14. Evolution of the pulsed GPR response to an oil spill in November with oil spills of 5 cm, 10 cm and 15 cm thickness.

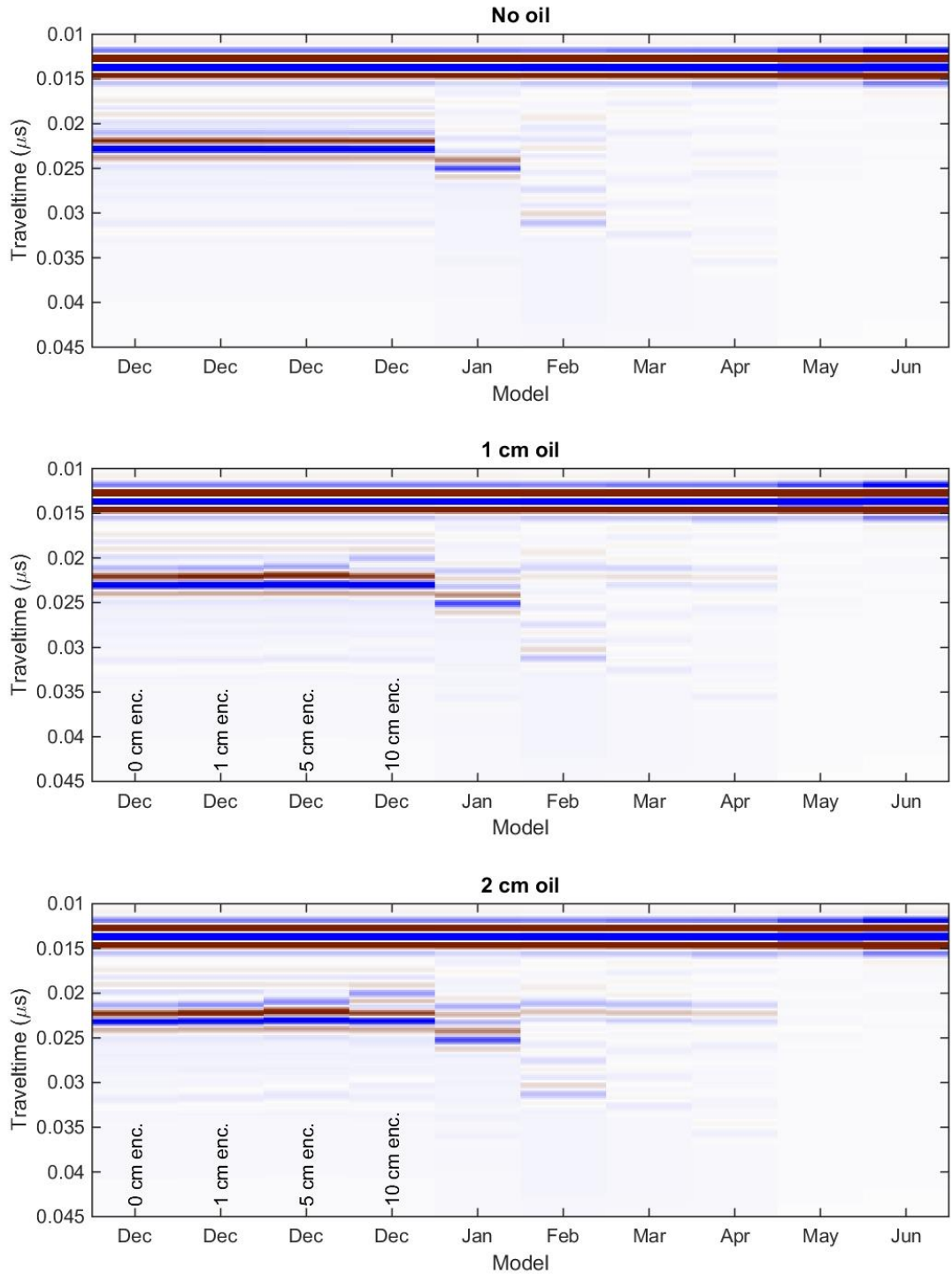


Figure MG15. Evolution of the pulsed GPR response to an oil spill in December with oil spills of 0, 1 cm and 2 cm thickness.

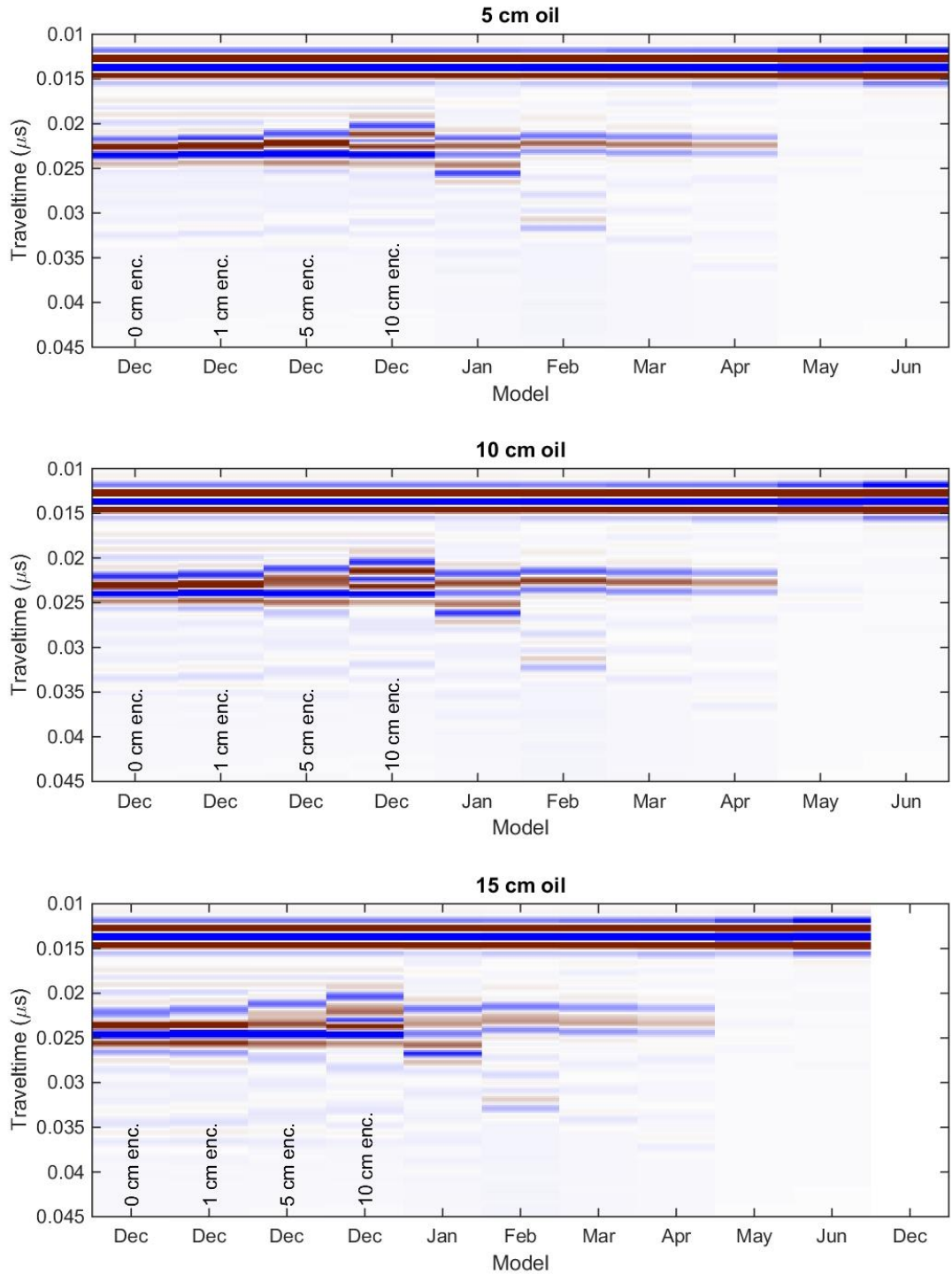


Figure MG16. Evolution of the pulsed GPR response to an oil spill in December with oil spills of 5 cm, 10 cm and 15 cm thickness.

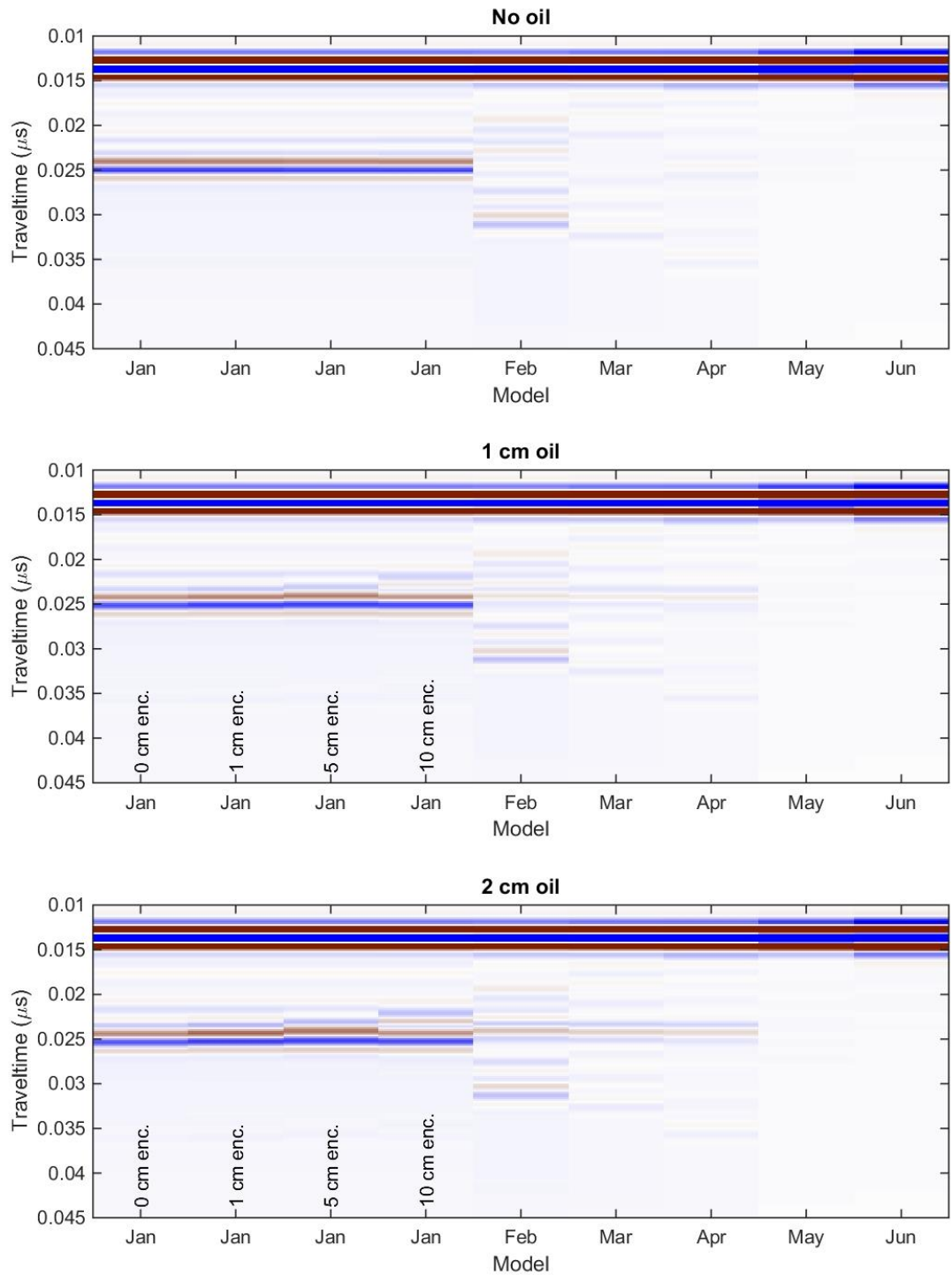


Figure MG17. Evolution of the pulsed GPR response to an oil spill in January with oil spills of 0, 1 cm and 2 cm thickness.

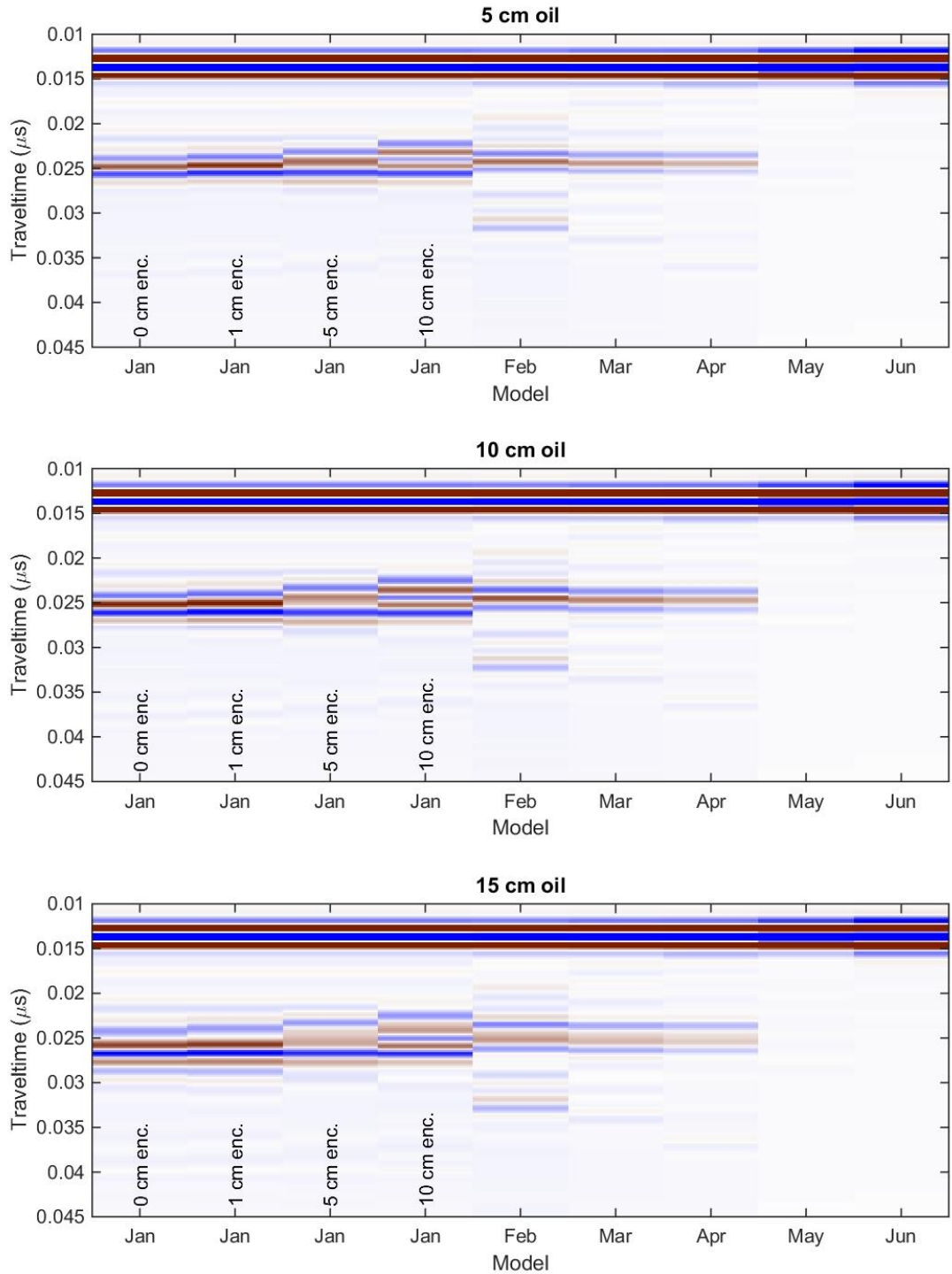


Figure MG18. Evolution of the pulsed GPR response to an oil spill in January with oil spills of 5 cm, 10 cm and 15 cm thickness.

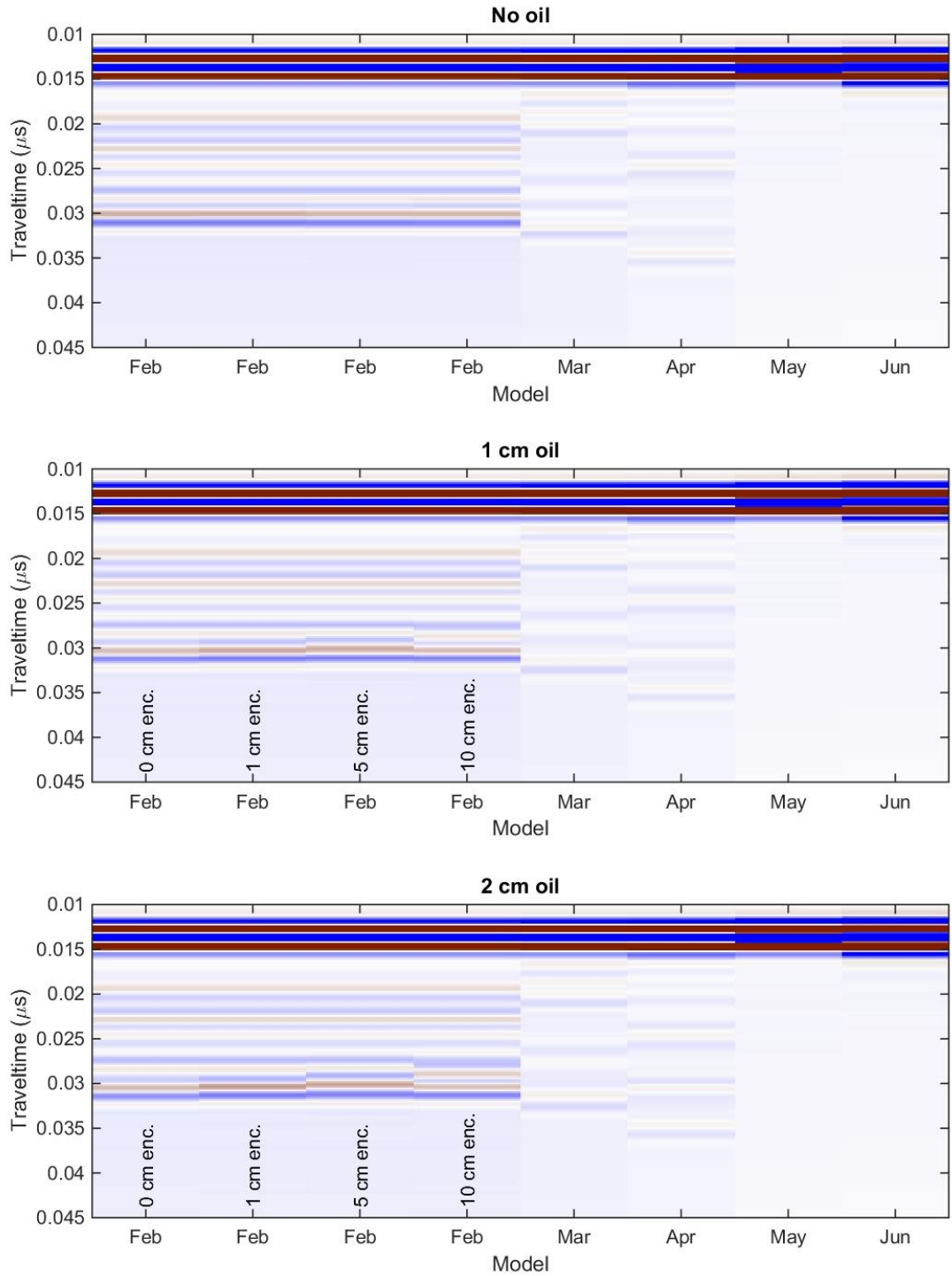


Figure MG19. Evolution of the pulsed GPR response to an oil spill in February with oil spills of 0, 1 cm and 2 cm thickness.

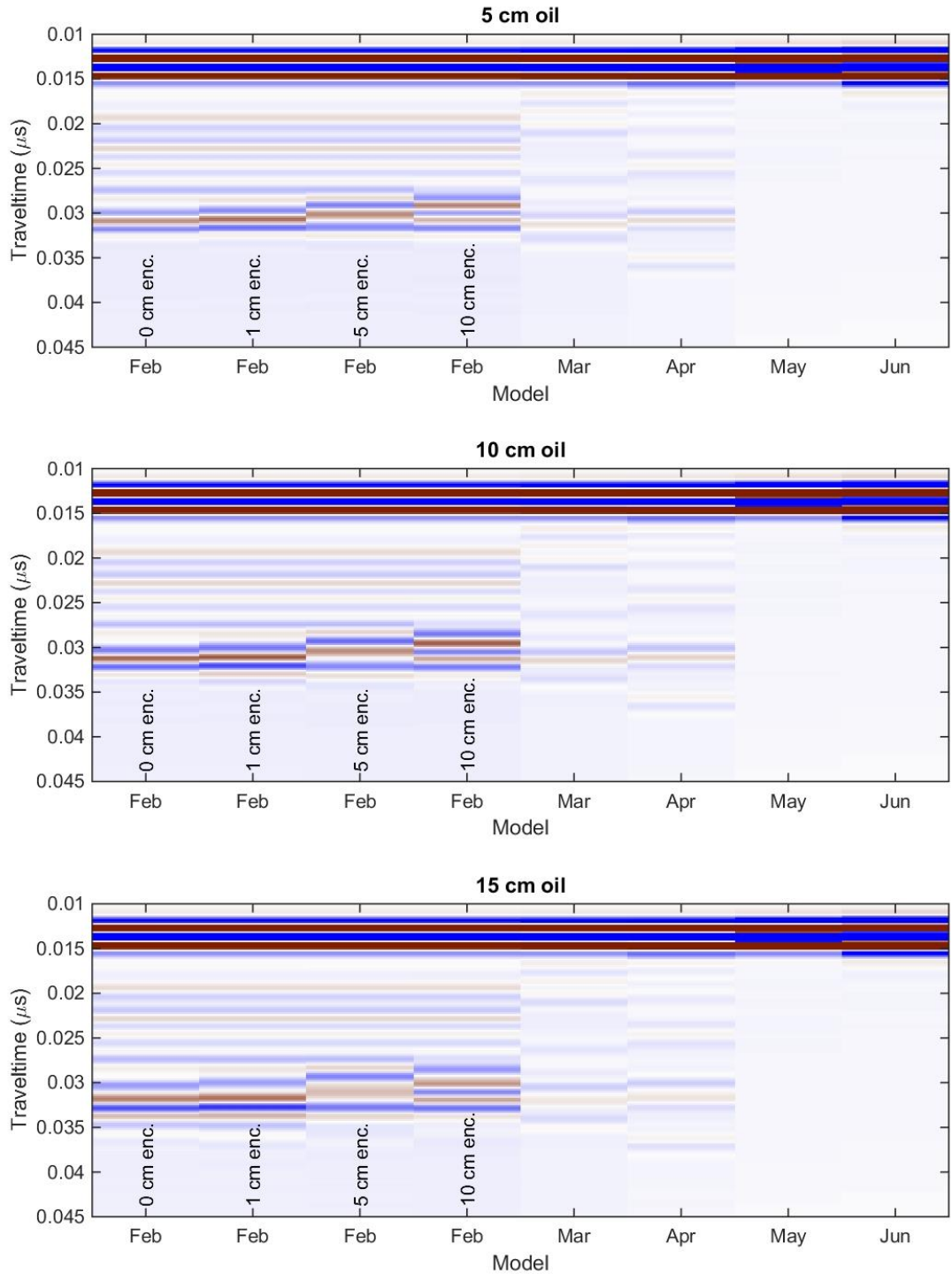


Figure MG20. Evolution of the pulsed GPR response to an oil spill in February with oil spills of 5 cm, 10 cm and 15 cm thickness.

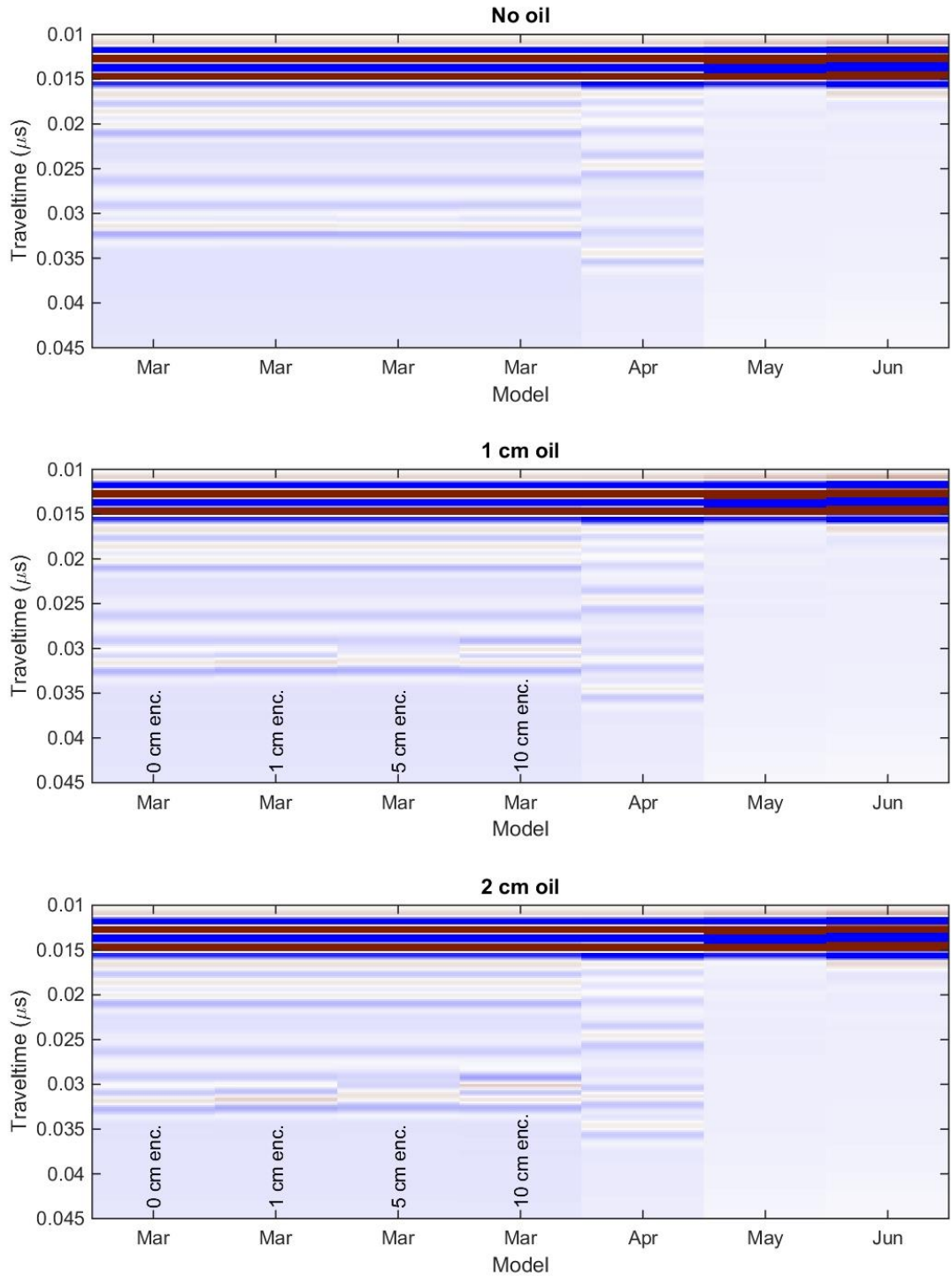


Figure MG21. Evolution of the pulsed GPR response to an oil spill in March with oil spills of 0, 1 cm and 2 cm thickness.

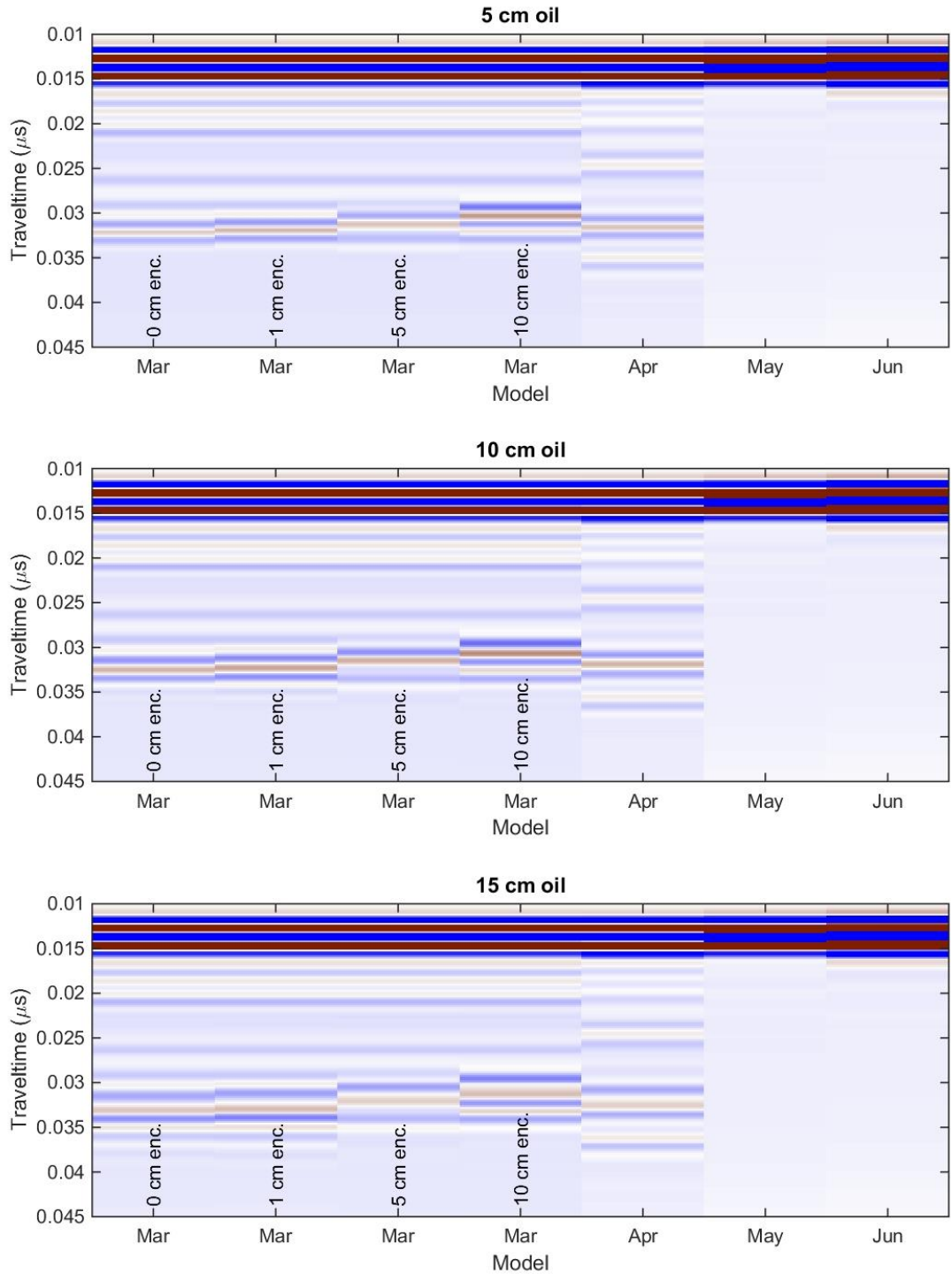


Figure MG22. Evolution of the pulsed GPR response to an oil spill in March with oil spills of 5 cm, 10 cm and 15 cm thickness.

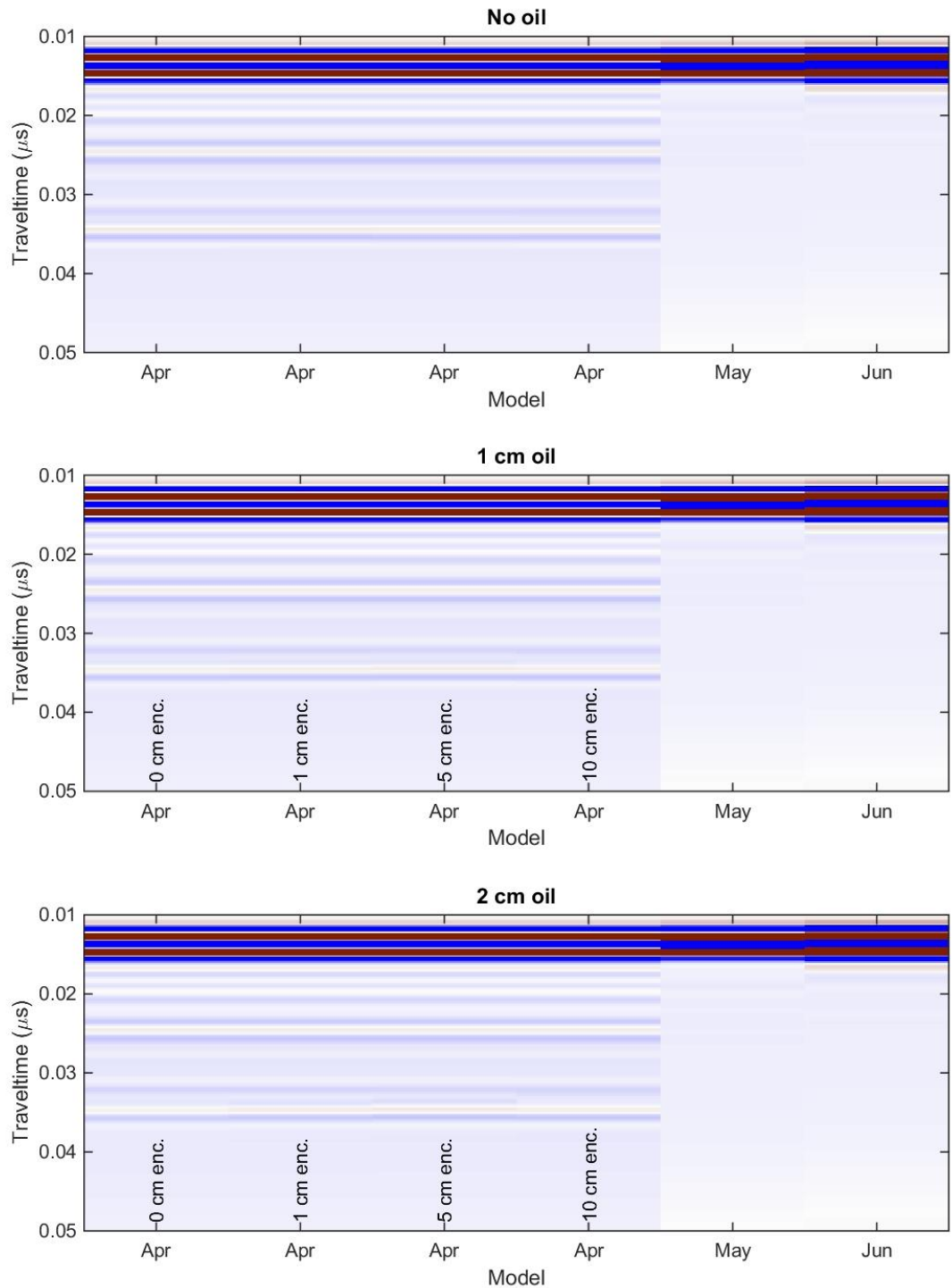


Figure MG23. Evolution of the pulsed GPR response to an oil spill in April with oil spills of 0, 1 cm and 2 cm thickness.

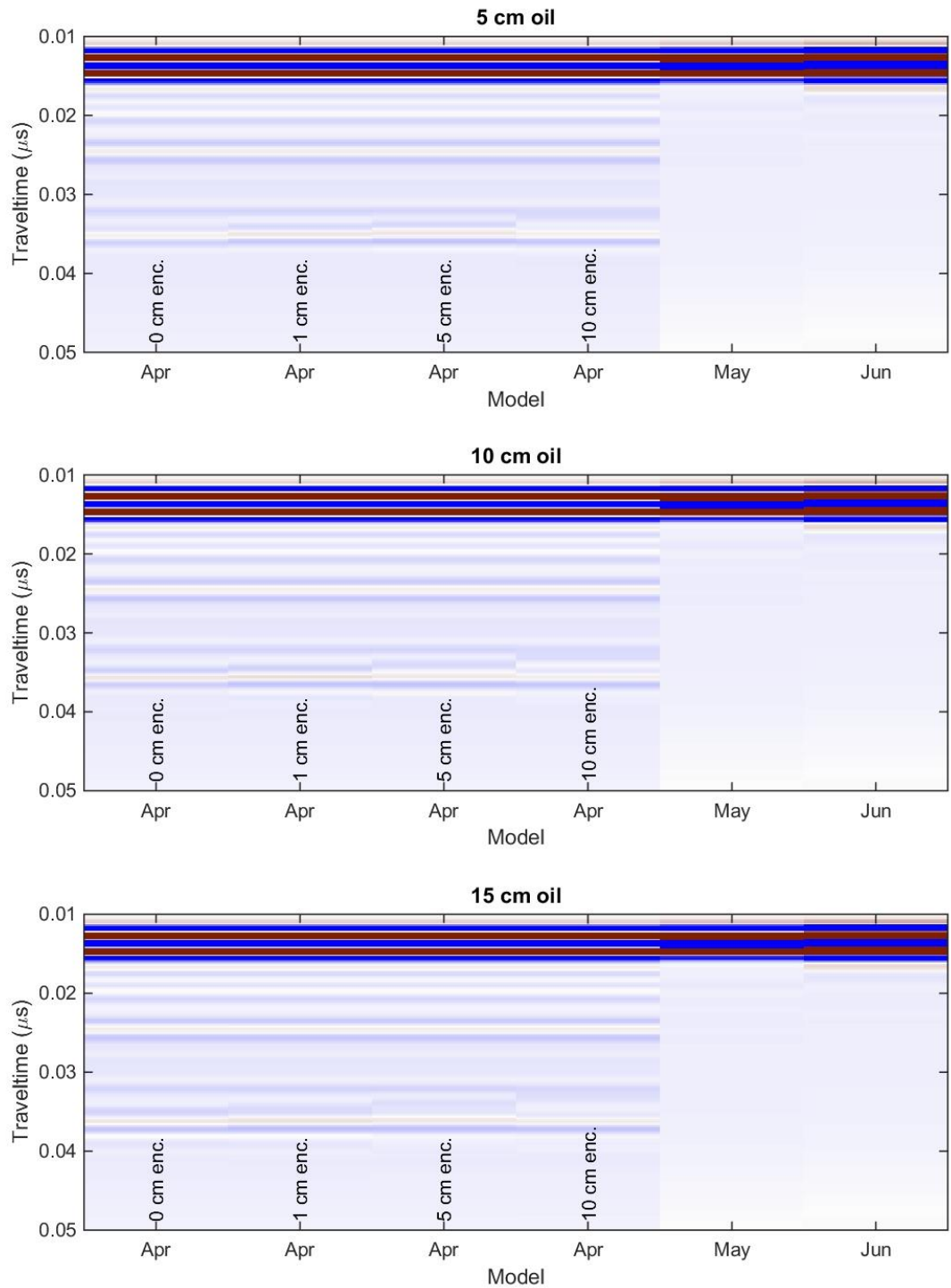


Figure MG24. Evolution of the pulsed GPR response to an oil spill in April with oil spills of 5 cm, 10 cm and 15 cm thickness.

Appendix V. Surface GPR data not presented in the main report

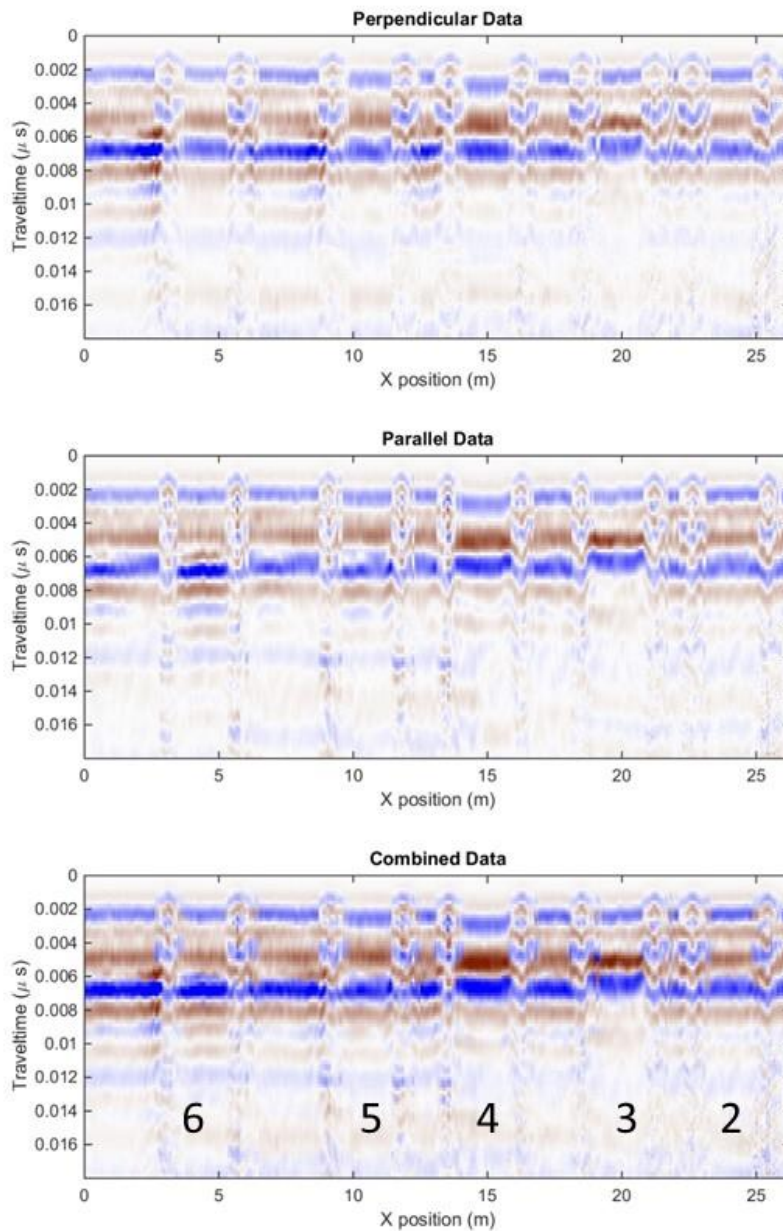


Figure GS1. 500 MHz surface coupled GPR acquired on 11/19 after the cell 3 and 4 spills. Note the phase and amplitude anomalies at the base of ice (0.006-0.007 μ s) in cells 3 and 4.

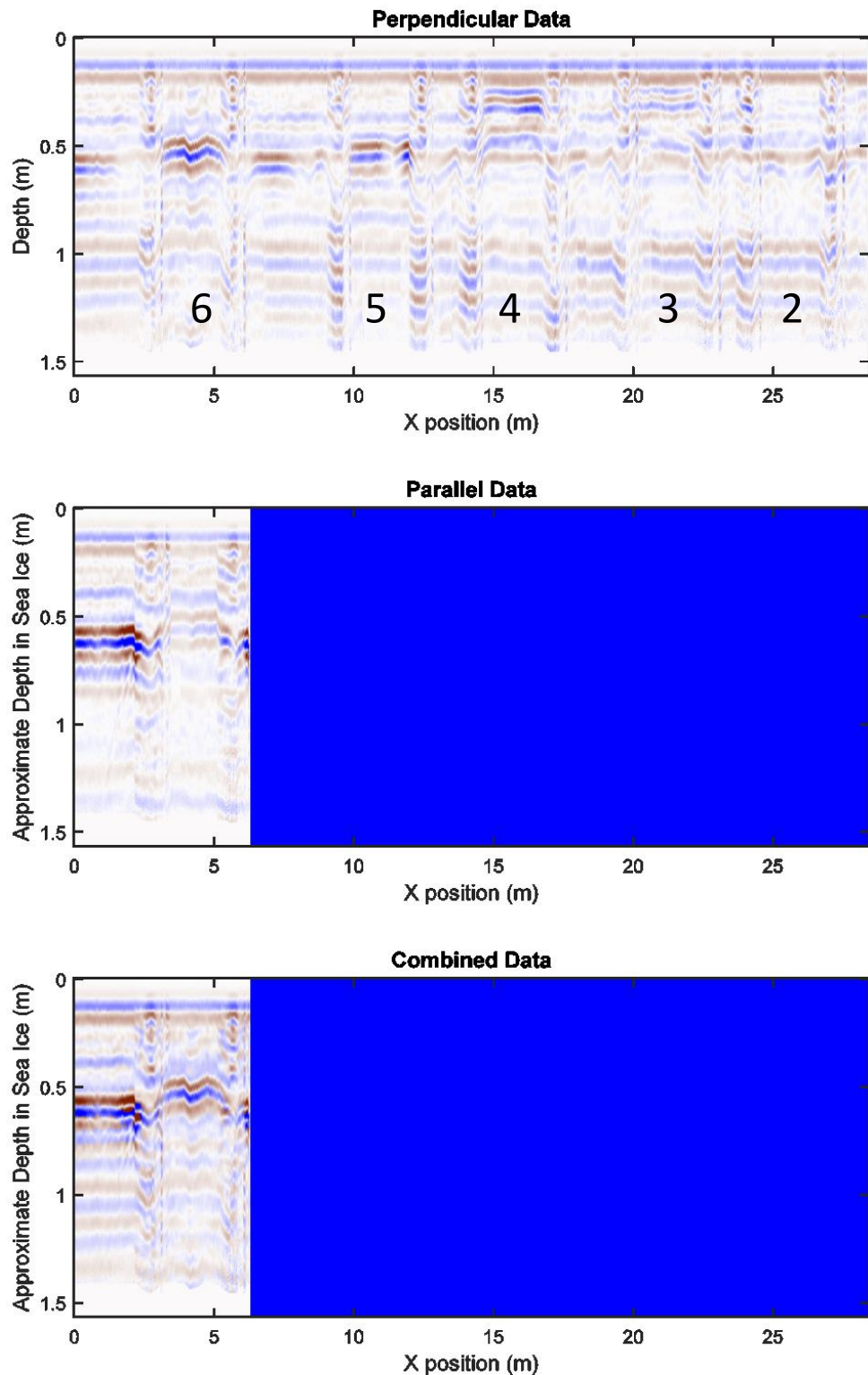


Figure GS2. 500 MHz surface GPR acquired on 12/11 after the cell 5 spill. The parallel data channel failed just after traversing cell 6. Base of ice is clear in perpendicular channel at a depth of ~0.6 cm. Cell 5 shows a nearly 90 degree phase reversal and slight amplitude increase. The encapsulate spills in cells 3 and 4 are clearly imaged at a depth of ~ 35 cm.

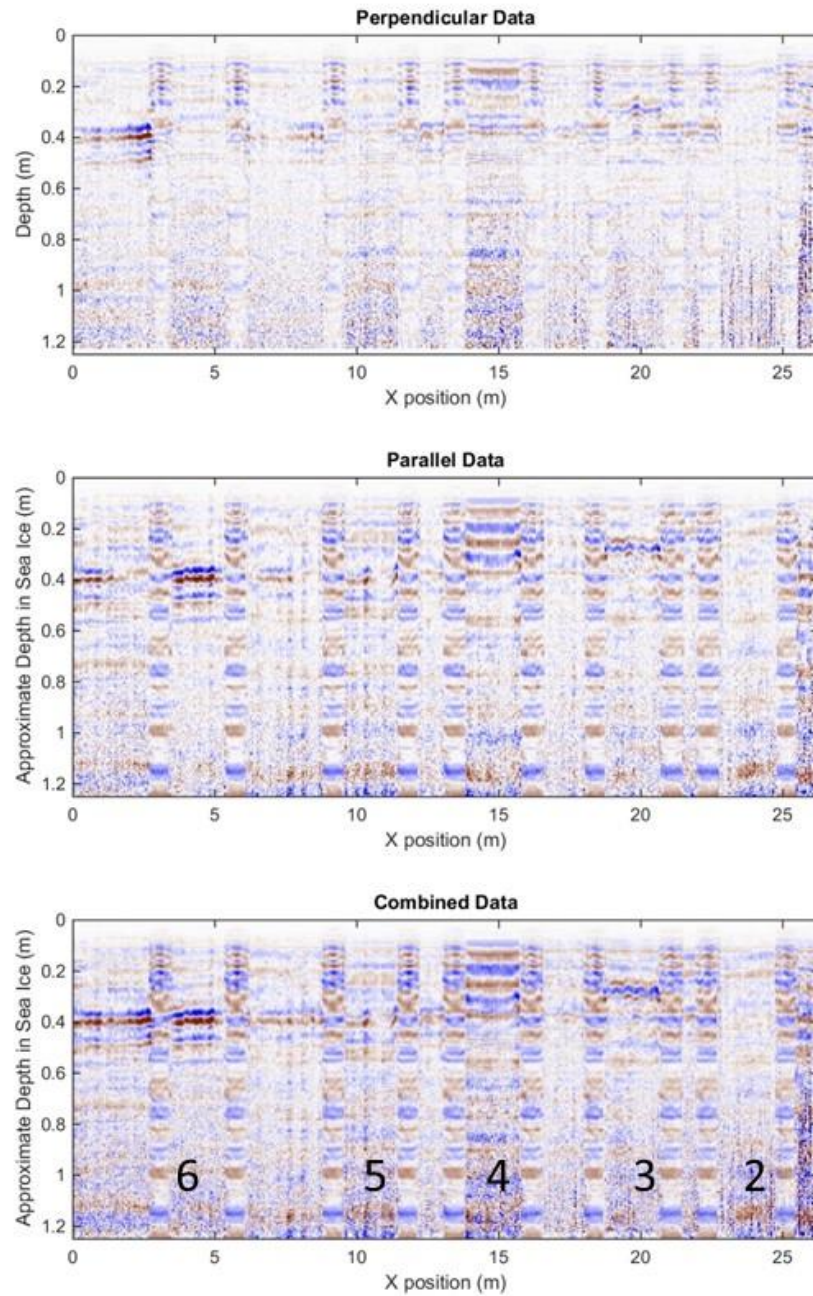


Figure GS3. 1GHz profile acquired on 11/19 after the cell 3 and 4 spills. Base of ice is imaged from 0 – 21 m but has low signal to noise. Warm ice due insulation on the surface affects the surface coupling of the radar as seen in cell 4. The cell 3 base of ice/top of oil surface is irregular, likely due to migration of the oil through brine channels when the ice was warmer.

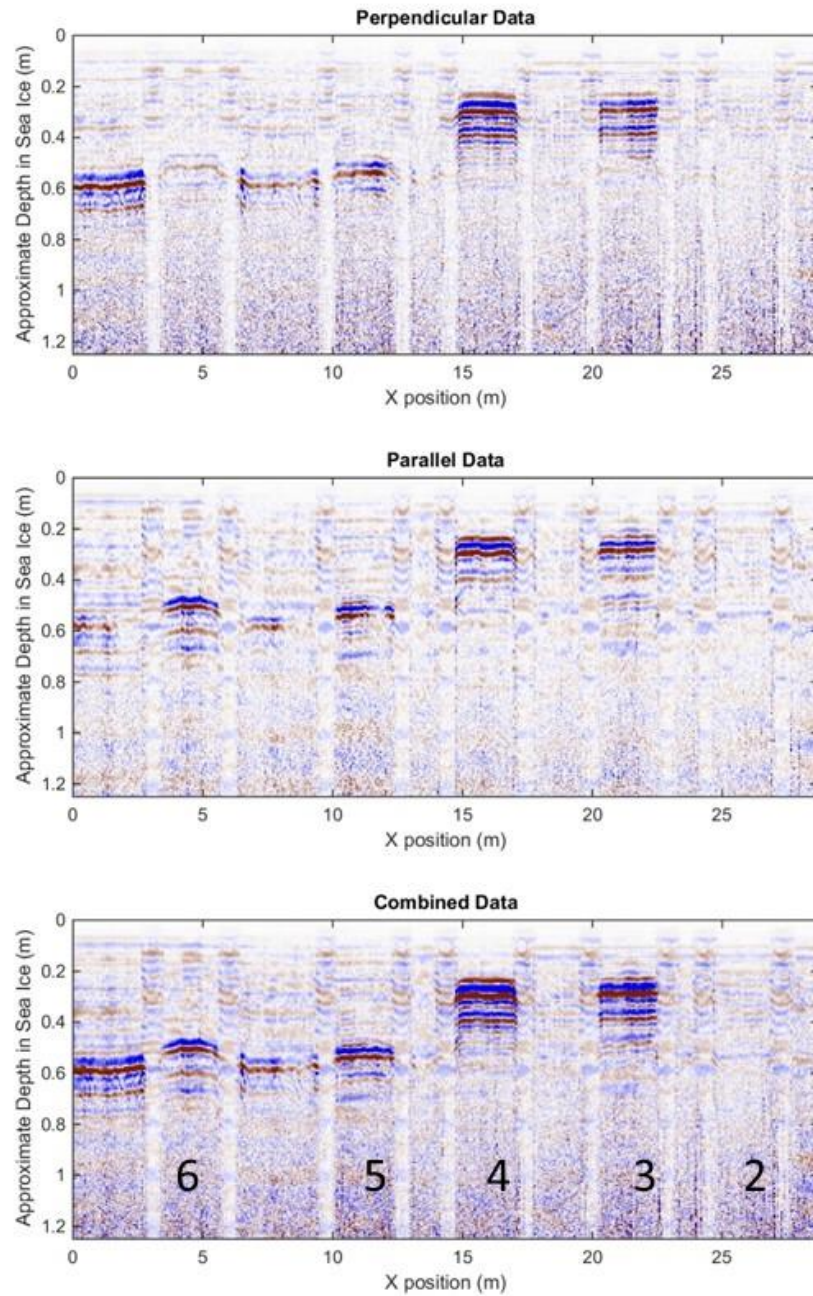


Figure GS4. 1GHz surface GPR data acquired on 12/10 after the cell 5 spill. Base of ice is imaged clearly from 0 m to 15 m. The cell 5 spill is primarily evident as a phase rotation at the base of ice reflection. The encapsulated spills in 3 and 4 are clearly evident. Multiple scattering in the oil layer of 3 and 4 likely obscures the base of ice in 3 and 4.

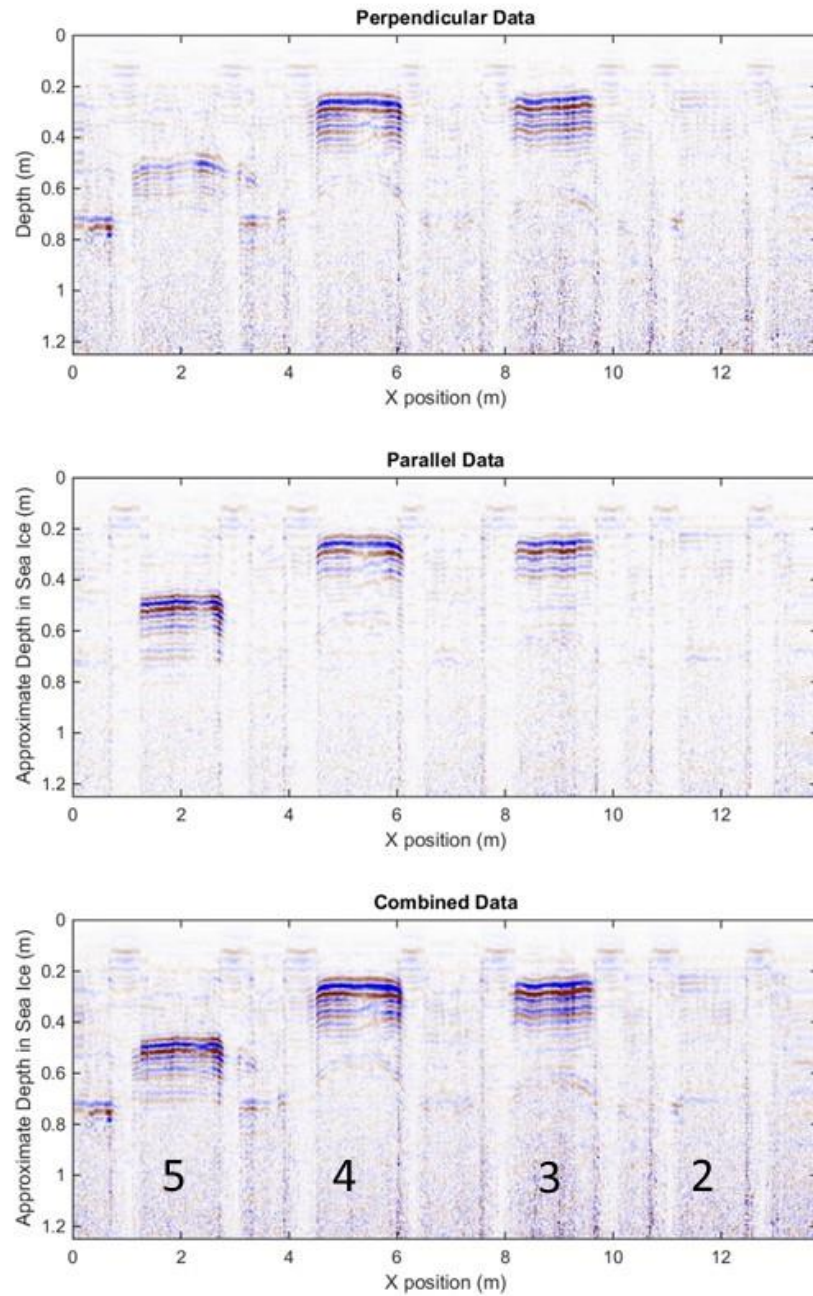


Figure GS5. 1 GHz profile acquired on 01/05 before the cell 6 spill. Base of ice imaged from 0 to 11 m but is weak and highly irregular with roughly 20 cm variation – it is thinnest under cells 3 and 4. Encapsulated spills in cells 3, 4, and 5 are clearly imaged.

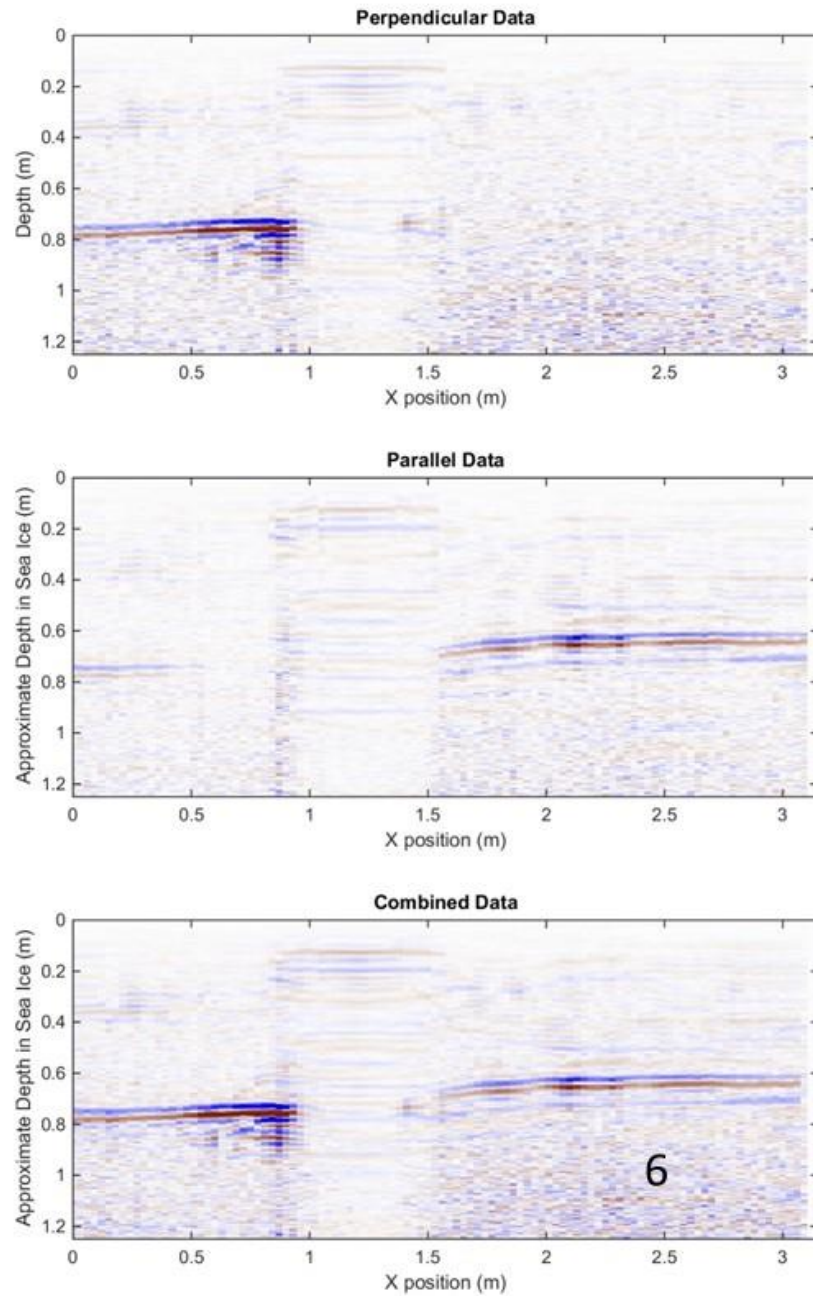


Figure GS6. 1GHz profile over cell 6 and the adjacent ice to the west prior to the cell 6 spill. Base of ice is clearly imaged and consistent in amplitude and phase, with the exception of near the containment skirt due to containment skirt interference.

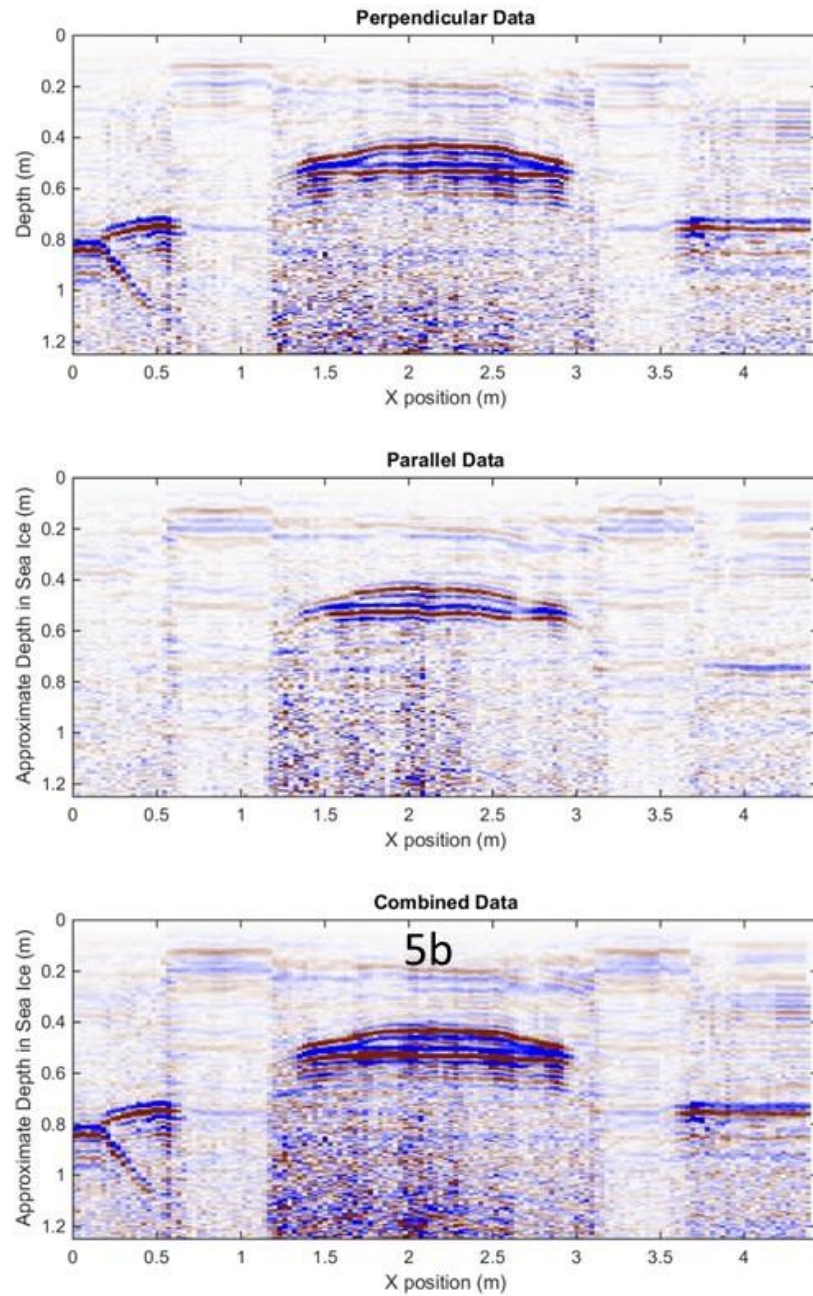


Figure GS7. 1GHz profile acquired across cell 5b on 01/05. Both the top and bottom of the encapsulated spill from early December are clearly imaged, with the top appearing as a domed surface and the base appearing as a horizontal reflector.

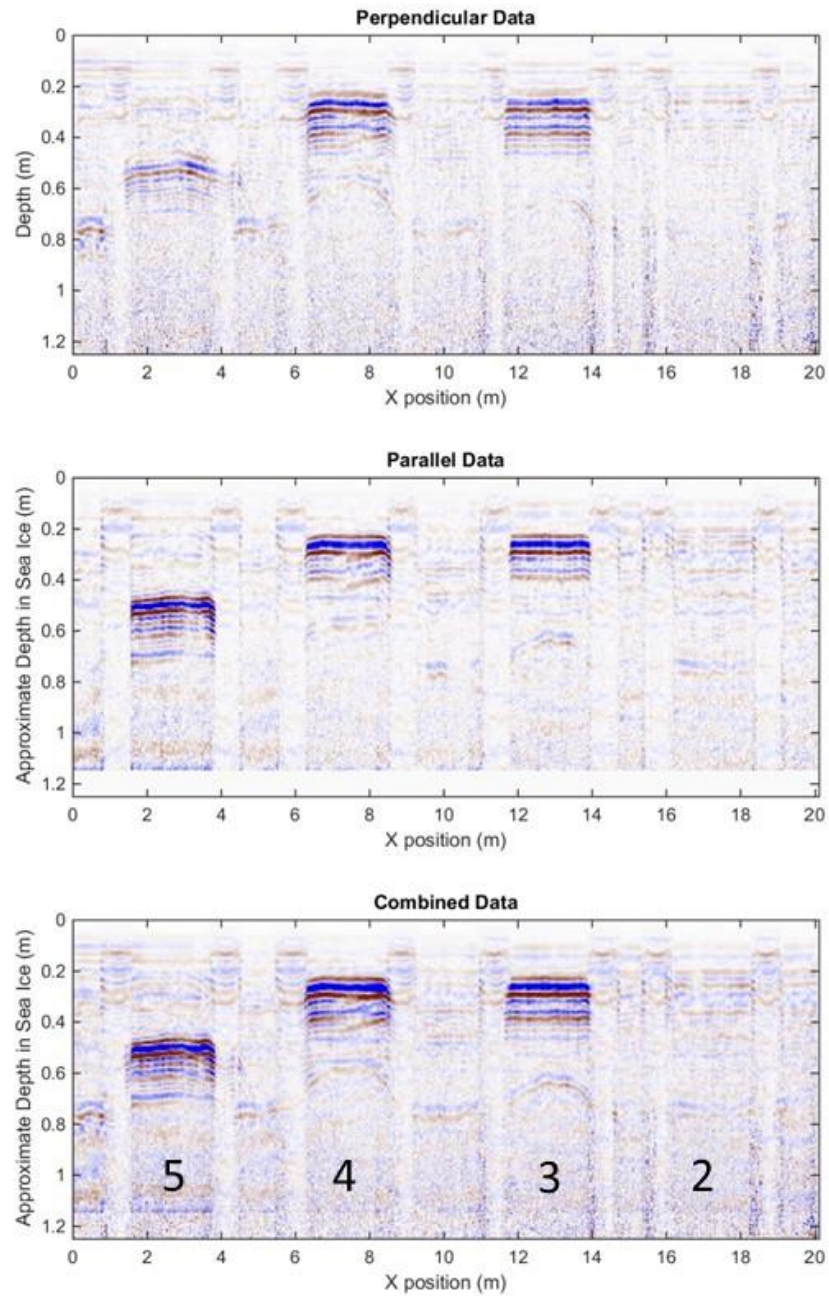


Figure GS8. 1GHz surface GPR profile acquired on 01/10. The base of ice is imaged as a weak, variable reflector from less than 0.6 m depth (cell 4) to nearly 0.8 m depth (west of cell 5). Encapsulated spills in cells 3, 4, and 5 are clearly imaged.

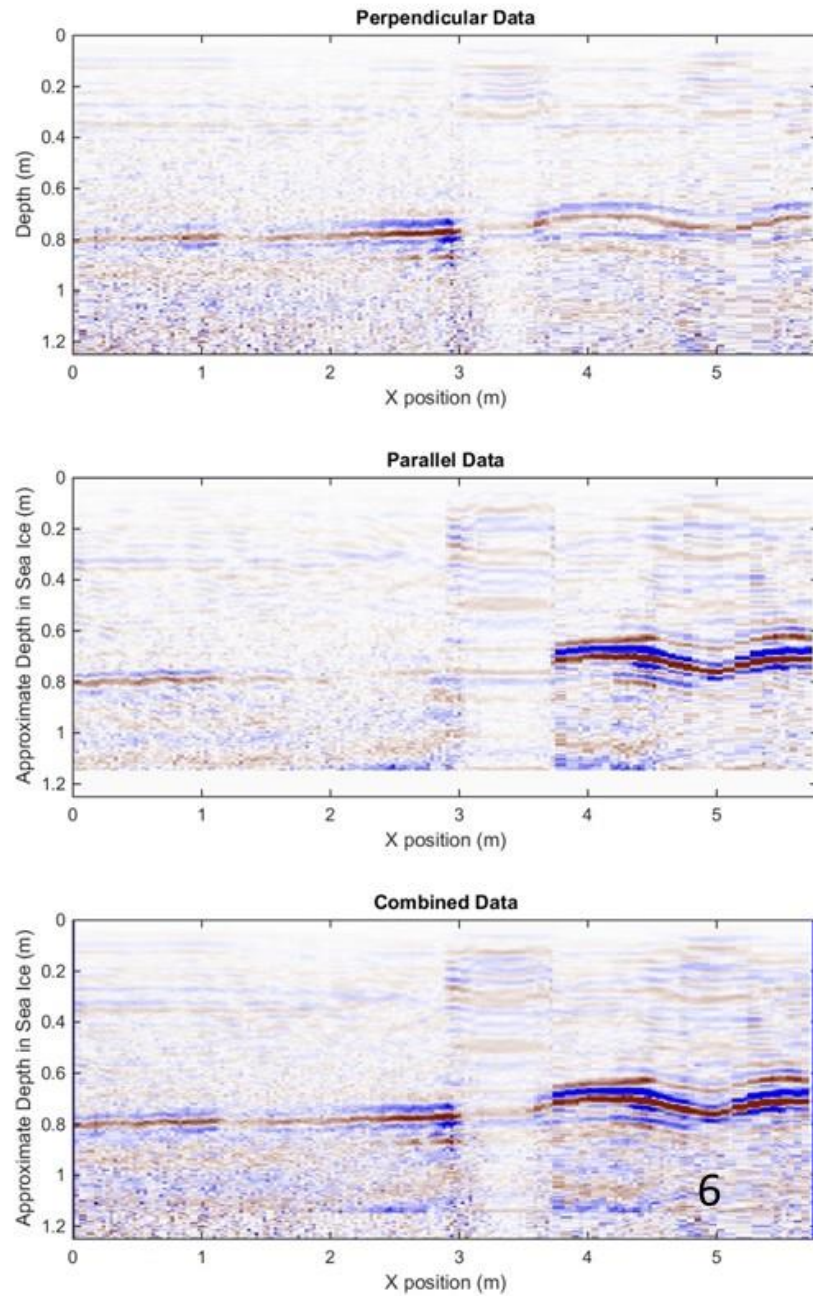


Figure GS9. 1GHz surface GPR profile acquired over cell 6 on 01/10 after the cell 6 spill. Major amplitude and phase anomalies are introduced by the spill. Compare to Figure GS6.

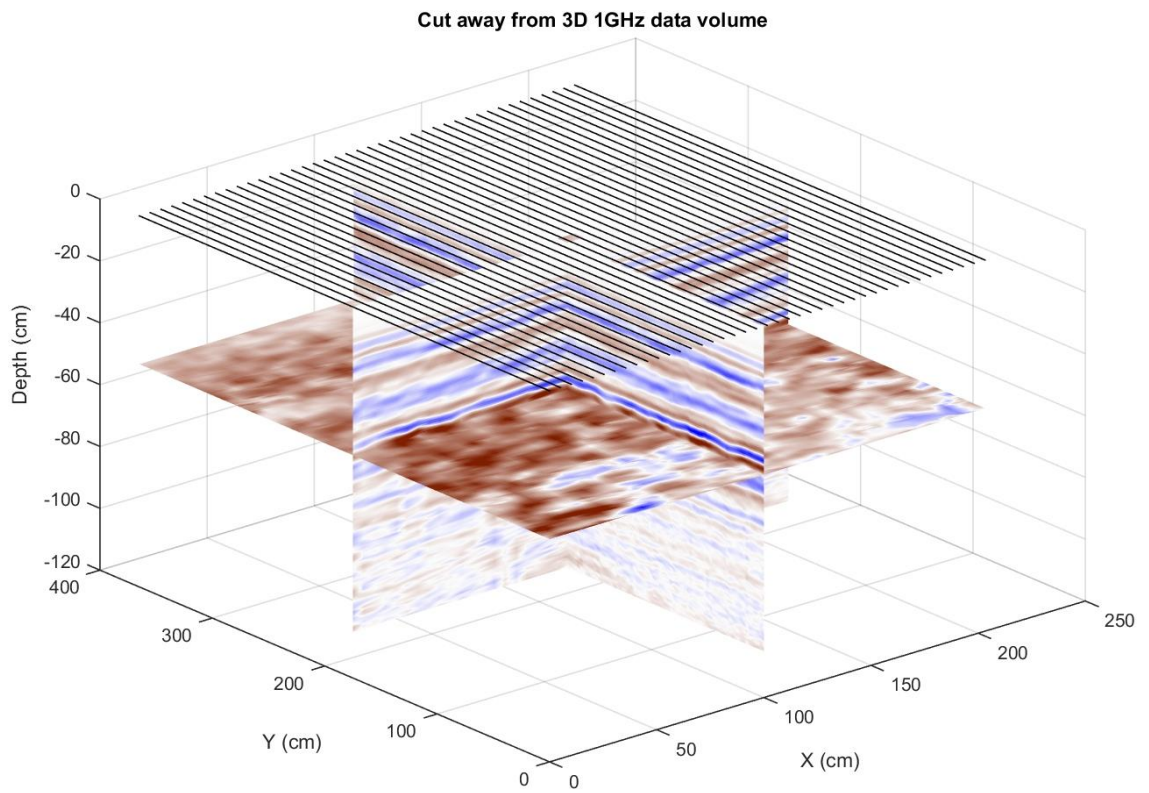


Figure GS10. 3D 1GHz data volume acquired on 11/18. The horizontal slice is just below the base of ice reflection.

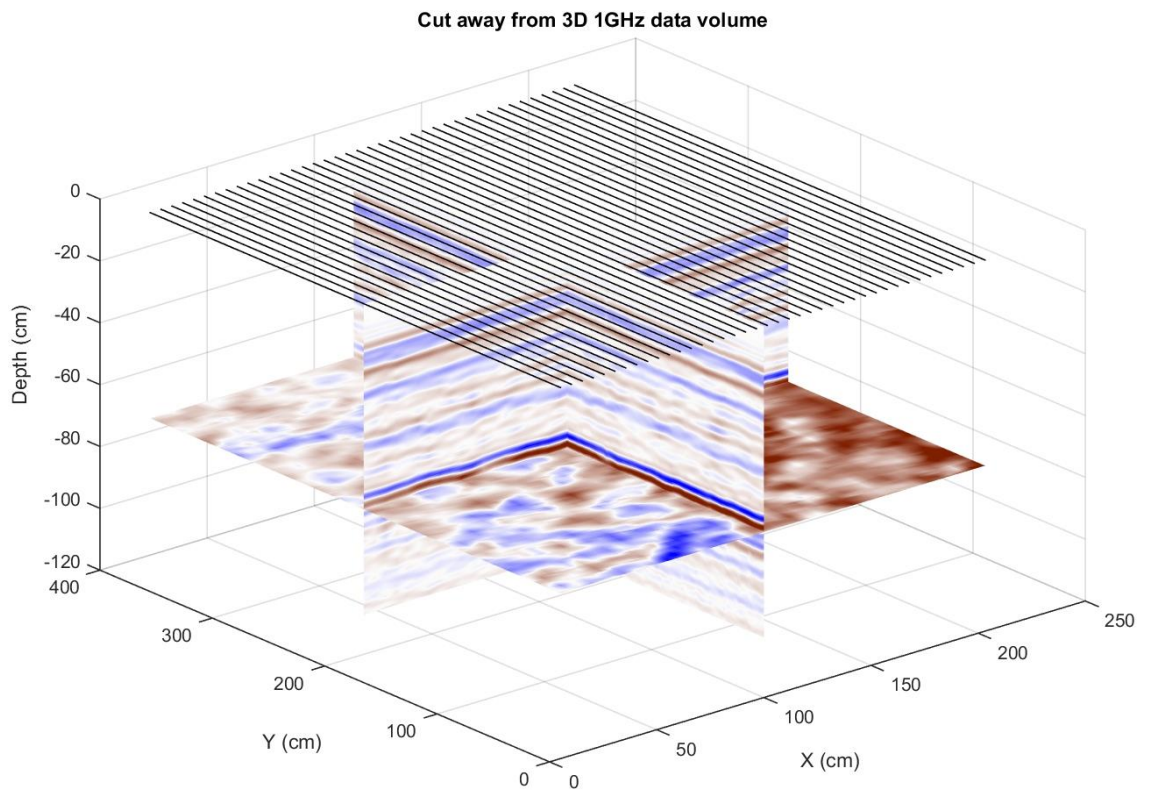


Figure GS11. 3D 1GHz data volume acquired on 12/10. The horizontal slice is just below the base of ice reflection.

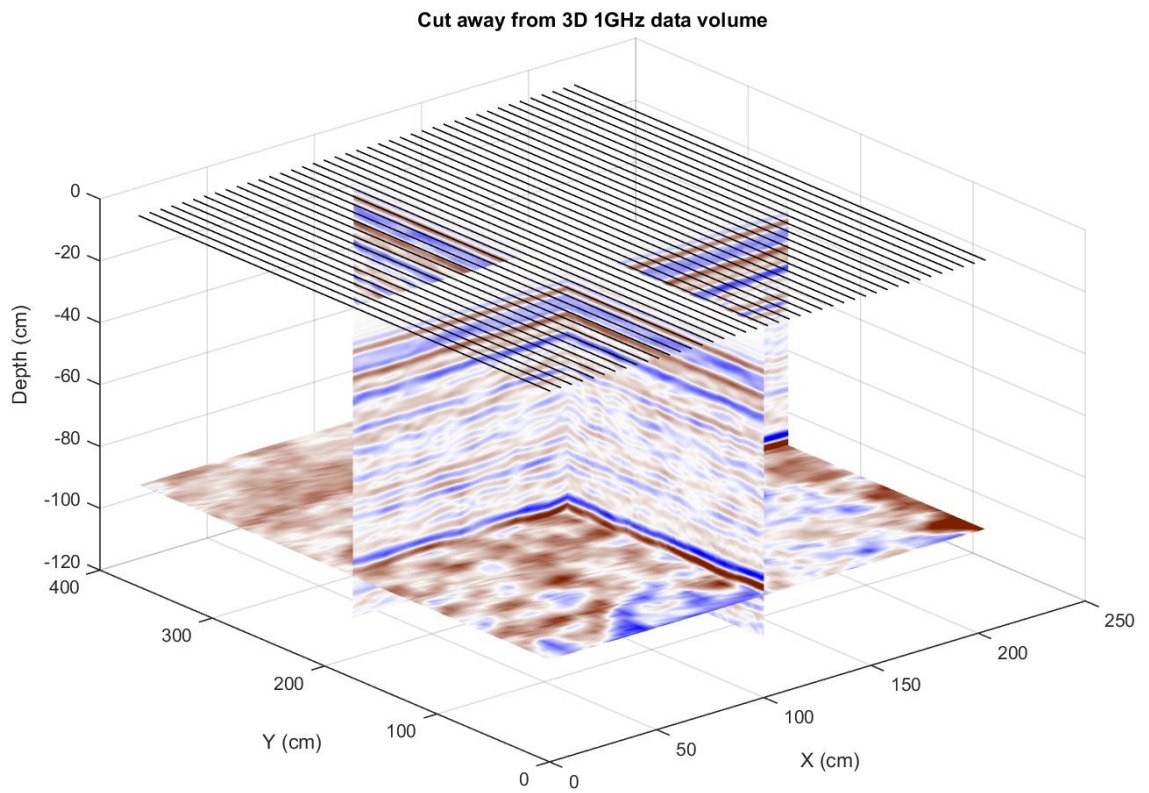


Figure GS12. 3D 1GHz data volume acquired on 01/10. The horizontal slice is just below the base of ice reflection.

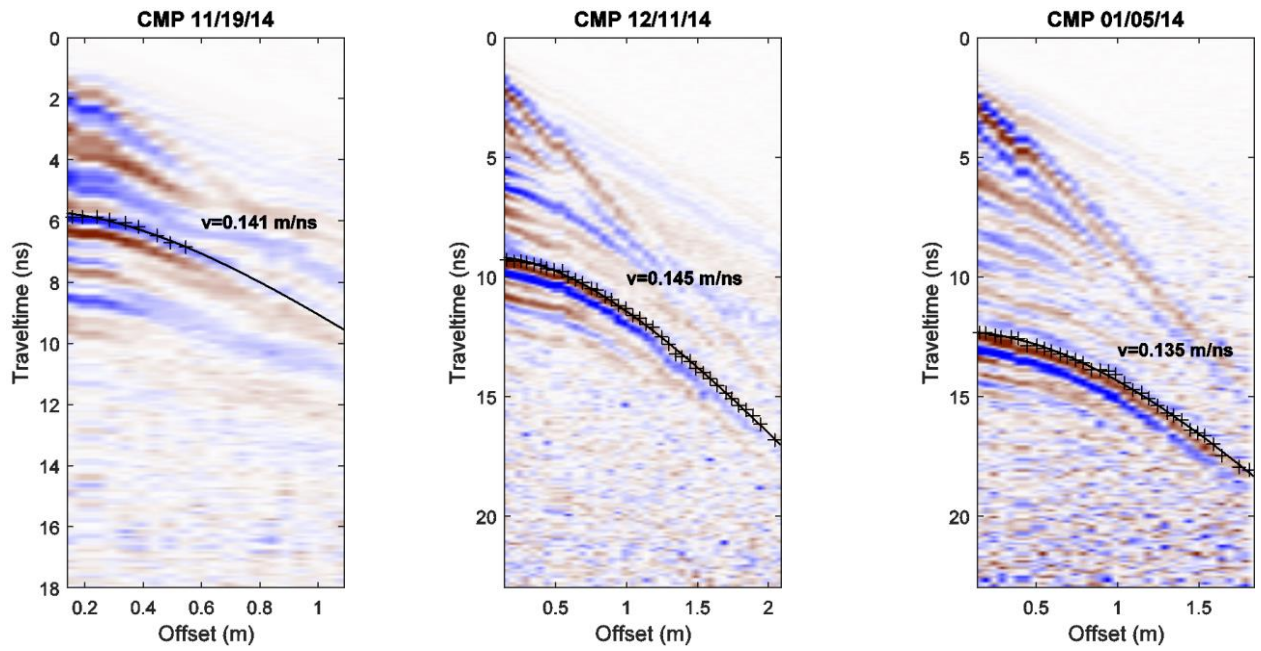


Figure GS13. Common midpoint (CMP) or expanding spread gathers acquired throughout the survey to measure radar velocity within the icepack. Base of ice reflection picks along with the travel time curve fit and velocity are shown. On 11/19, we only used offsets to 0.5 m because of interference from surface coupled waves.

Appendix VI. Additional aerial GPR plots

All figures are the combined polarizations collected with the aerial 500 MHz GPR. Of note, the ice surface comes in a varying two-way travel times from the antenna in different profiles because of small variations in boom attachment height. For the Hoop 1 and full long-axis tank profiles the antenna footprint starts immediately inside Hoop 1.

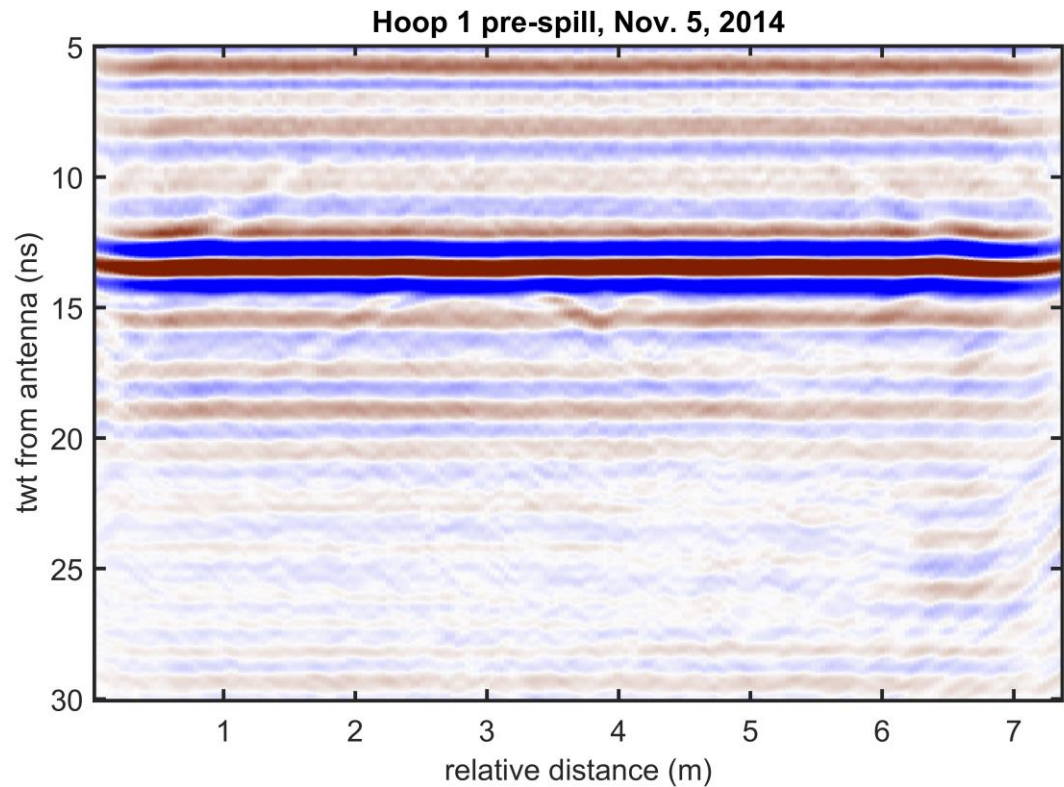


Figure AG1. The pre-spill profile over Hoop 1 starts just within the hoop and crosses outside of the hoop at 3 m relative distance. The pre-spill profile does not show a difference in response at the ice surface within the hoop compared to the clear ice outside of the hoop, although the ice surface within the hoop was disturbed in order to mimic grease ice. The nominal ice thickness was 5 cm of ice, and the air/ice and ice/water reflections are not distinguishable.

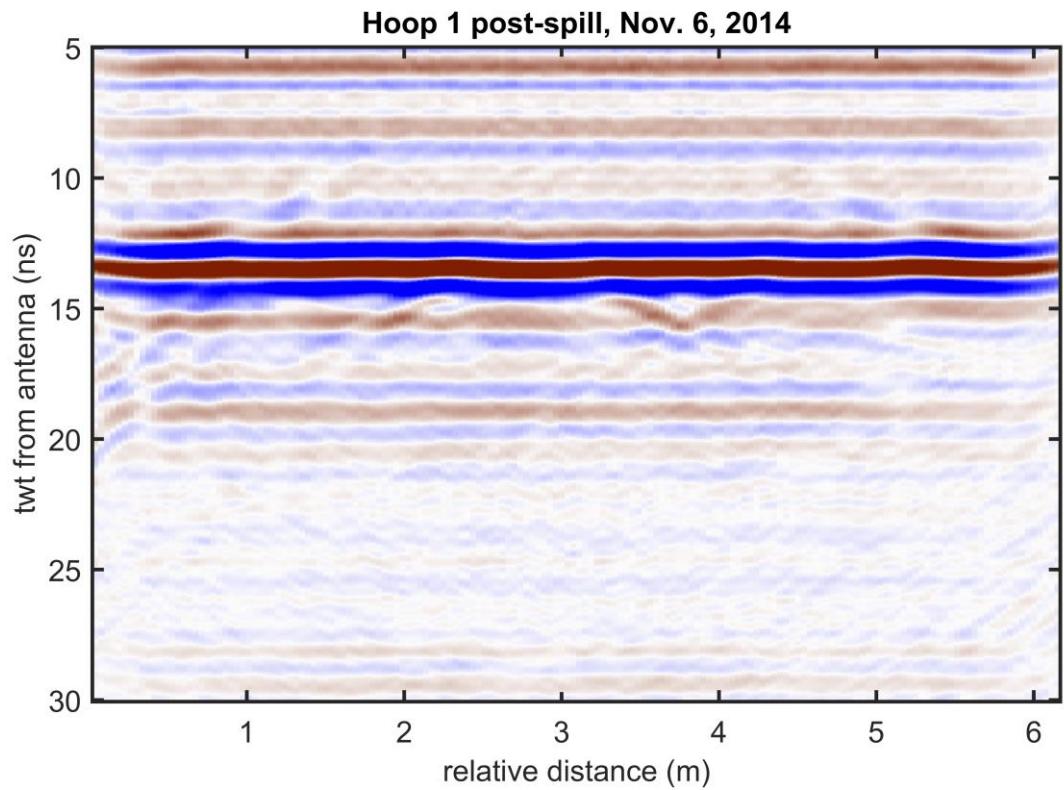


Figure AG2. The post-spill profile for the Hoop 1 spill also does not show a difference in response at the ice surface within the hoop, over grease ice, compared to outside the hoop. It also does not show a difference in response when compared with the pre-spill profile taken the previous day.

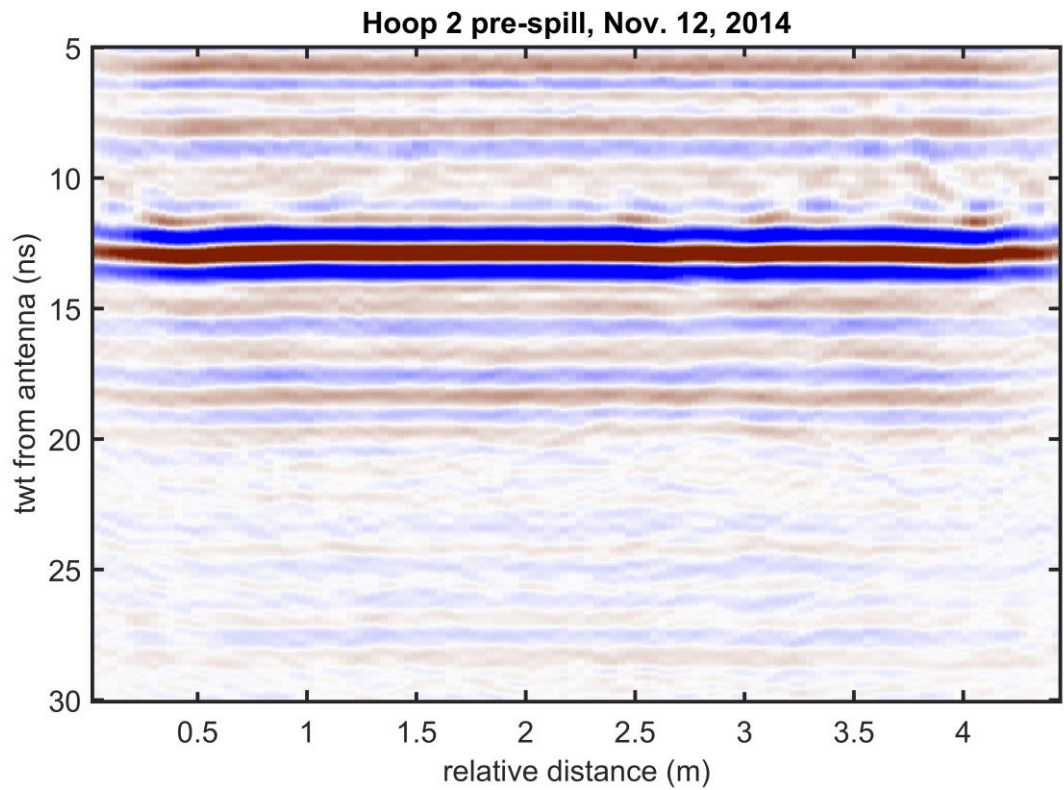


Figure AG3. The pre-spill profile for the Hoop 2 injection occurred over 20 cm of ice, and the air/ice and ice/water reflections are not distinguishable. Warm ice surface temperatures during this period caused higher than intended conductivity and may have contributed to the signal attenuation.

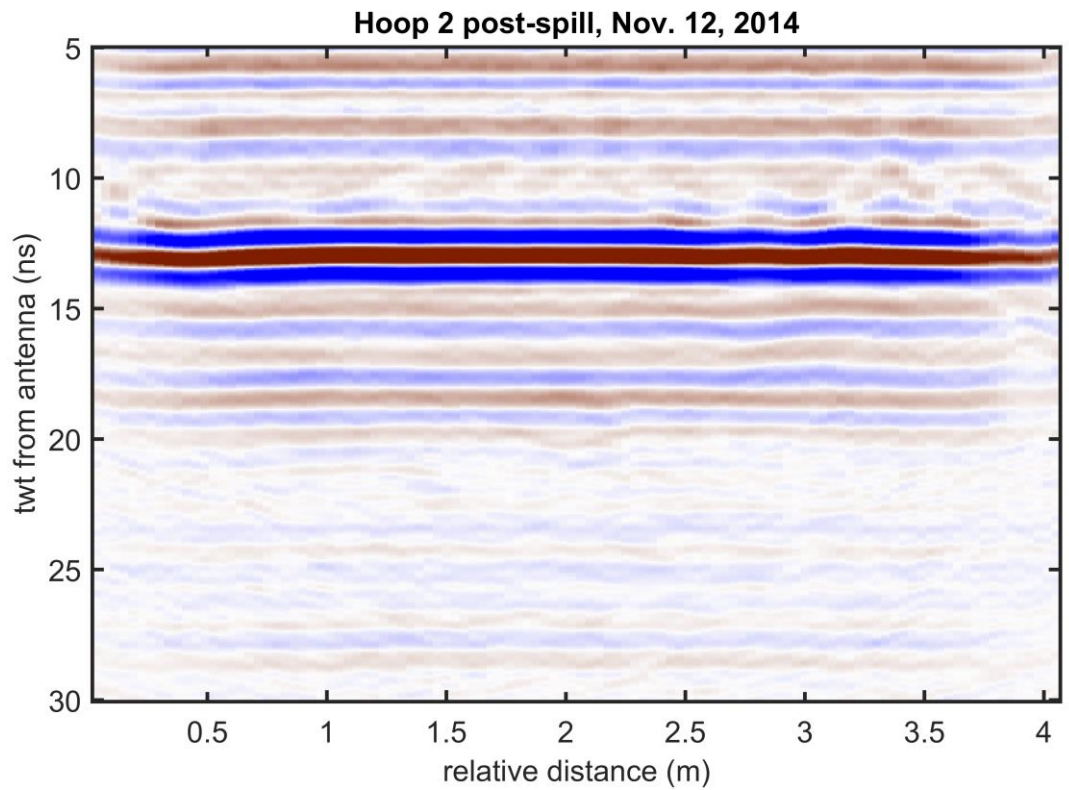


Figure AG4. The post-spill profile for the Hoop 2 spill does not have a distinguishable change in reflection characteristics from the pre-spill profile.

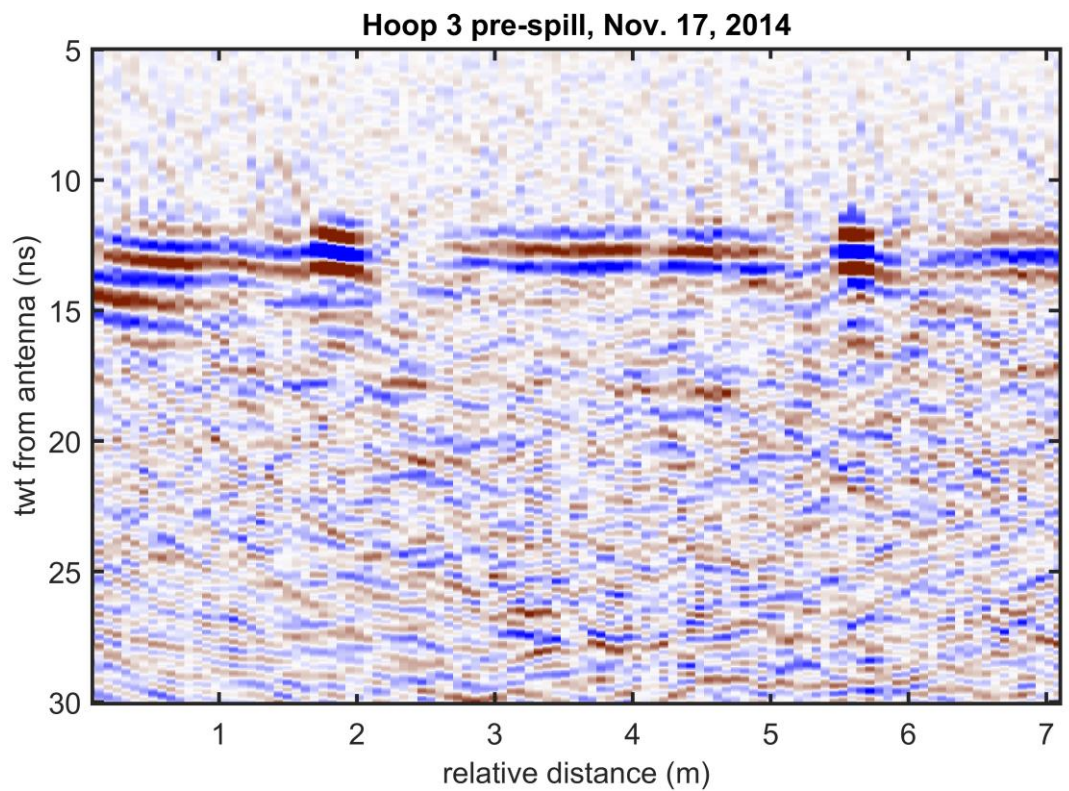


Figure AG5. The pre-spill profile over Hoop 3 also occurred with warmer than intended ice sheet temperatures, with the ice surface reaching $-8\text{ }^{\circ}\text{C}$. The nominal ice thickness was 35 cm. The ice/water interface may be intermittently visible at $\sim 17\text{ ns}$ two-way travel time, but it certainly not identifiable across the length of the profile.

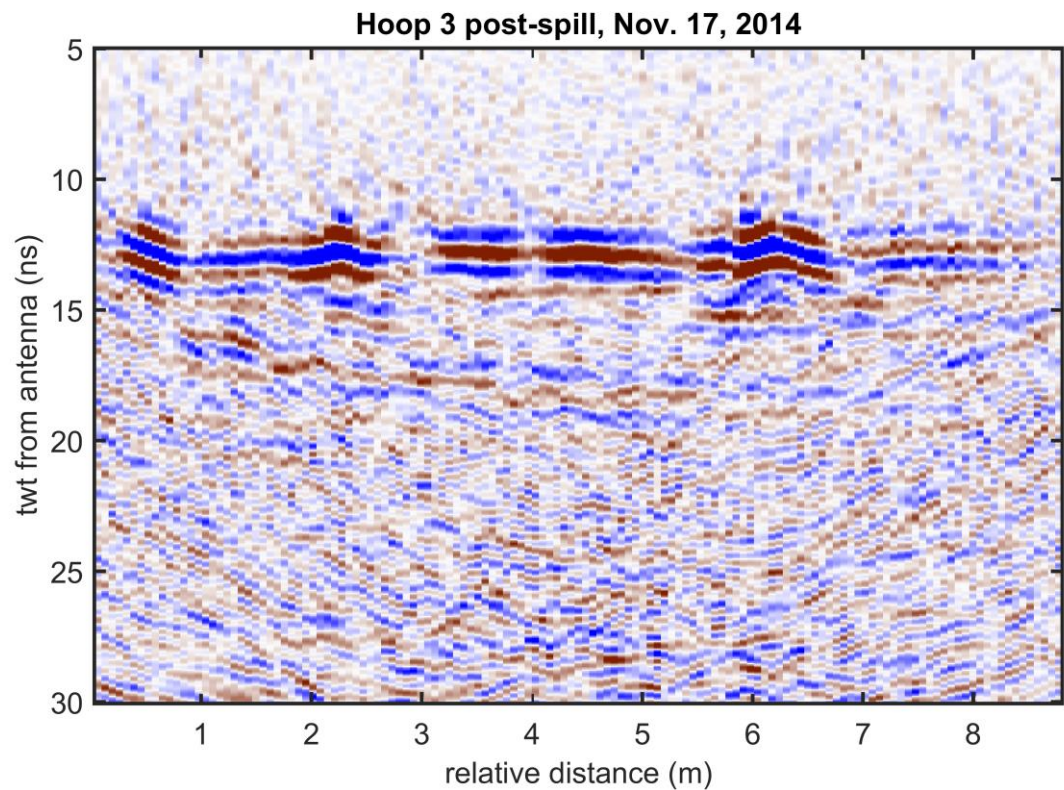


Figure AG6. The post-spill profile for Hoop 3 may show a slightly more continuous signal along the ice/water interfaced compared with the pre-spill profile. However, the interface that appears at the reasonable two-way travel time of 17 ns within the hoop seems to rise to unreasonably short travel times, given the 35 cm ice thickness, outside of the hoop. Since the ice sheet experienced warmer than intended temperatures and high conductivity it is difficult to interpret signal below the ice surface as an oil/water or ice/water interface.

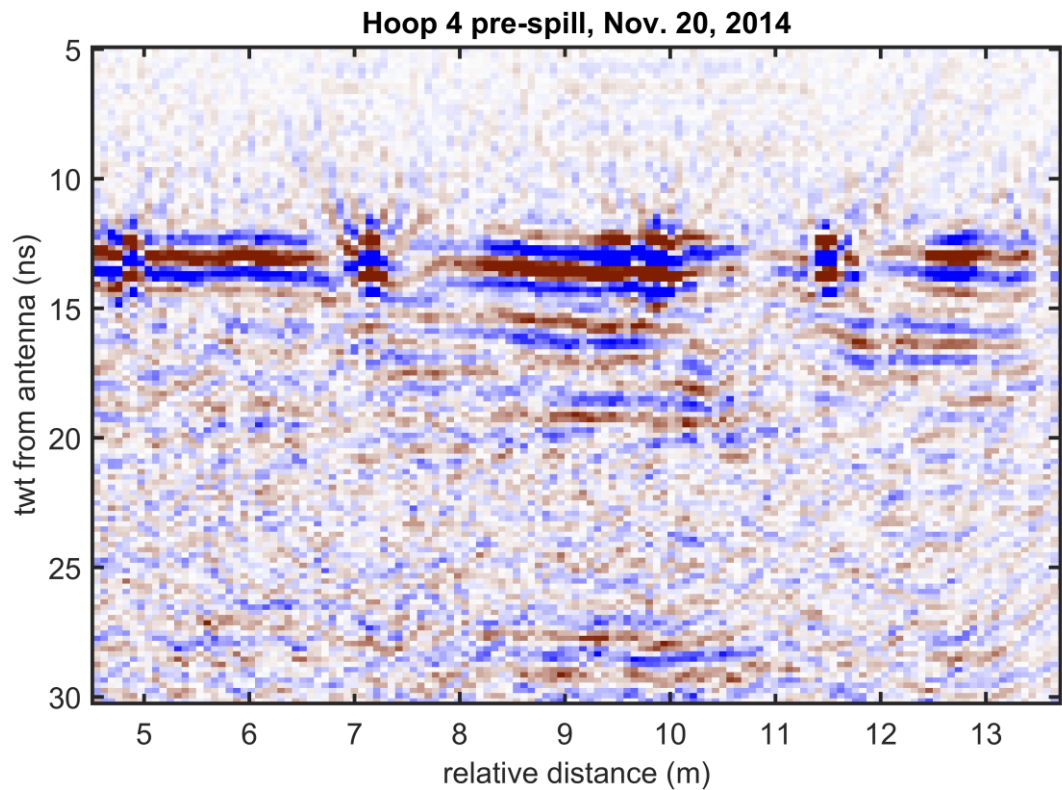


Figure AG7. The pre-spill profile over Hoop 4 begins just inside of Hoop 3 and ends at the beginning of Hoop 5, centered over Hoop 4. The pre-spill profile shows a mid-sheet reflective layer at 16 ns in both Hoop 4 and Hoop 5, which may have been a result of the previous warming period and higher than intended ice sheet temperatures. There is not a continuous reflection from the ice/water interface across the profile, but at relative profile distances of 9 – 10 m there is signal that is reasonable for 35 cm of ice.

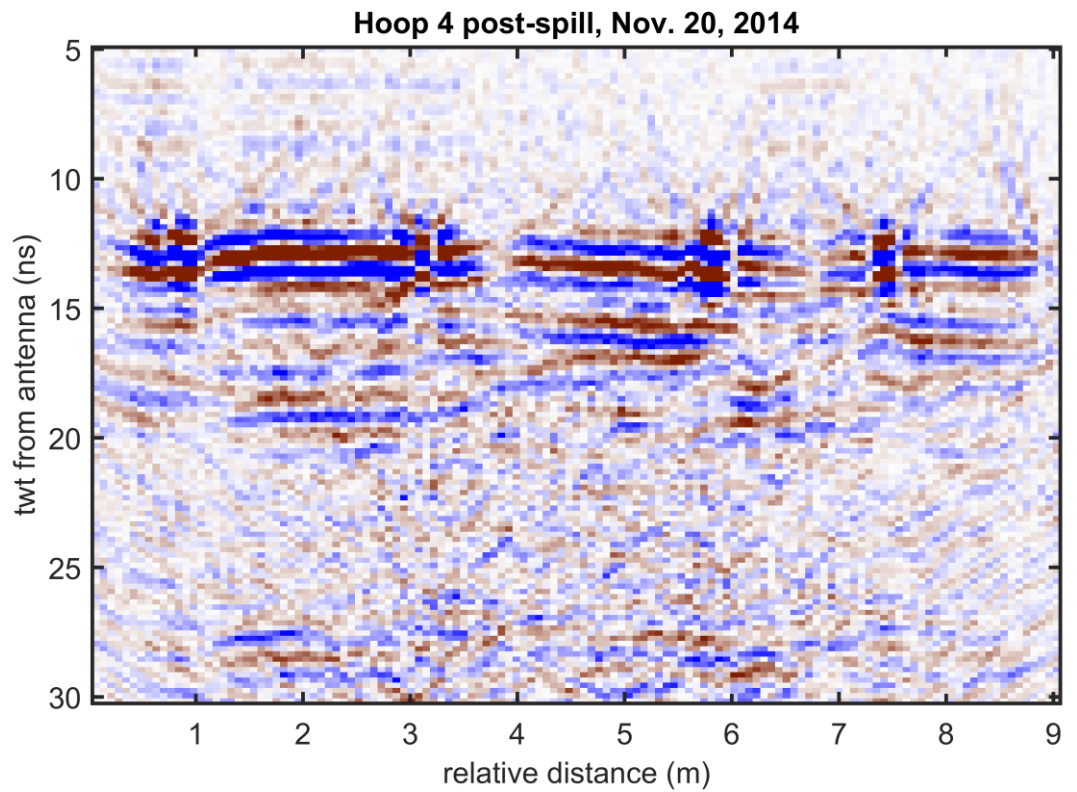


Figure AG8. For the Hoop 4 post-spill profile the reflection from the base of the ice is more continuous than in the pre-spill profile; however, it is still discontinuous enough that drawing conclusions about whether it is ice/water or ice/oil is difficult. Most of the signal below the mid-sheet reflection under Hoop 4 was attenuated.

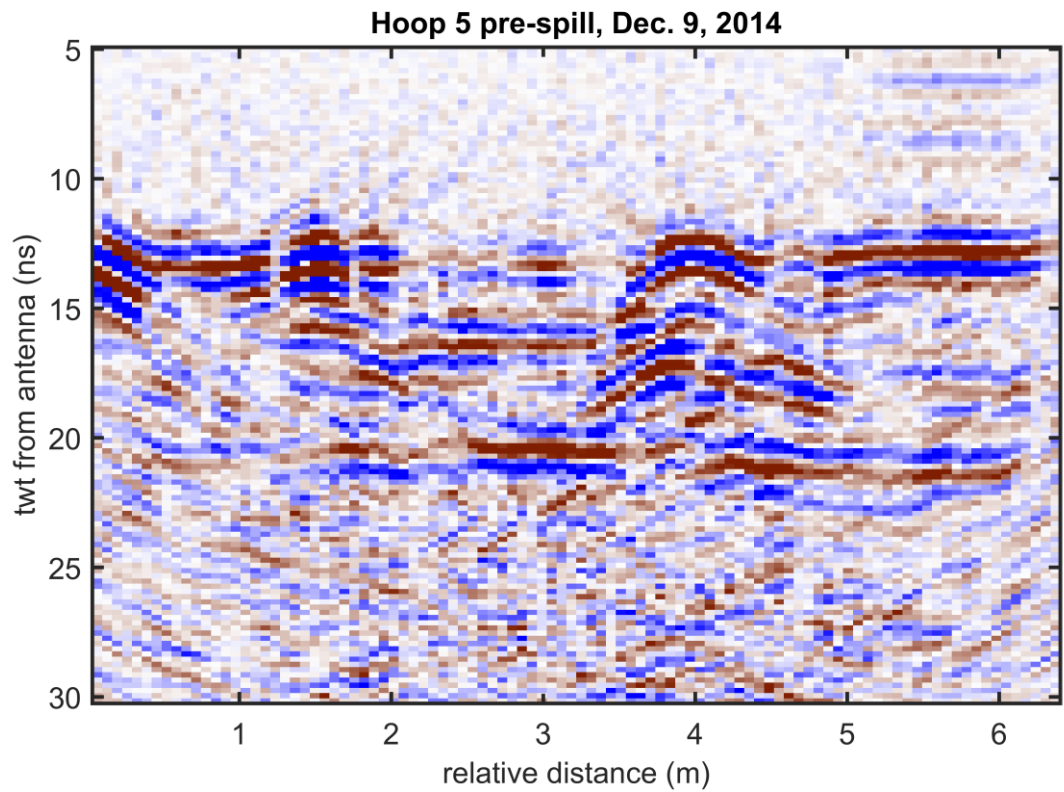


Figure AG9. The pre-spill profile over Hoop 5 displays the same mid-sheet layer visible, perhaps an effect from the warming period. The base of ice reflection is not uniform across the extent of the profile, but is visible in places at a relative two-way travel time of 19 ns for the 50 cm ice sheet.

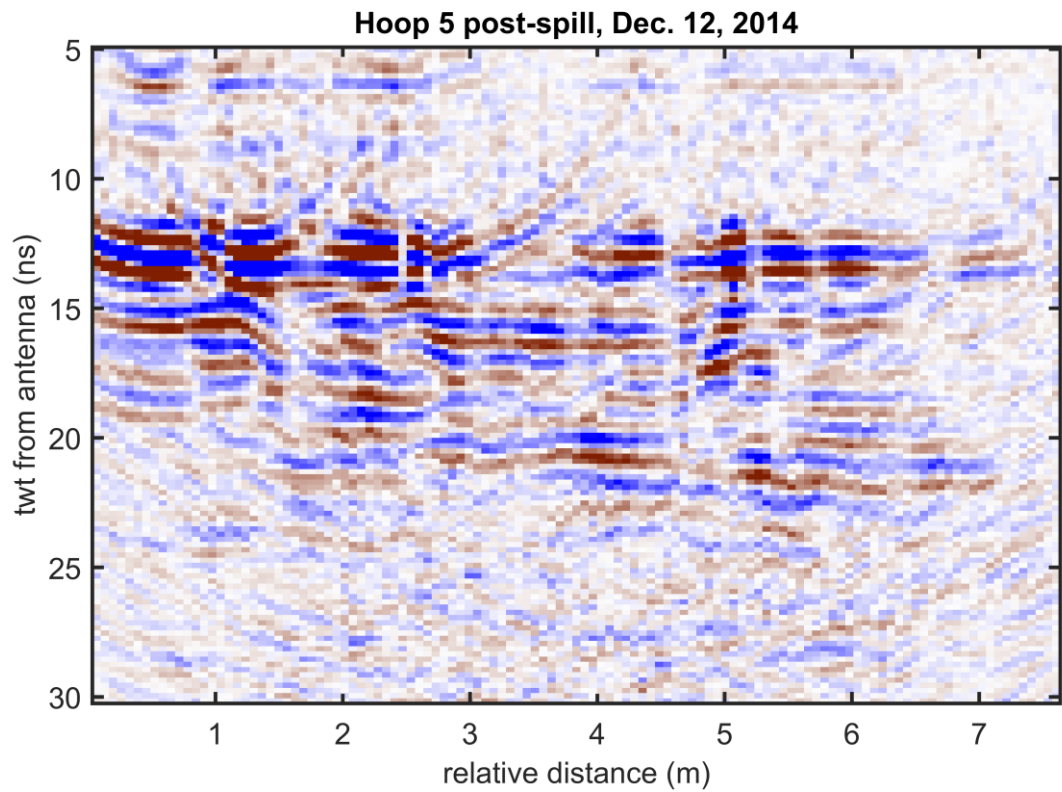


Figure AG10. The oil from the Hoop 5 injection is identifiable in the post-spill profile as a more continuous reflection across the base of the Hoop 5 ice. Along with the signal being more continuous, the amplitude decreased and the instantaneous frequency increased which is consistent with the modeled behavior for an oil layer of 2 cm thickness at the base of the ice (see Aerial GPR and Modelling report sections).

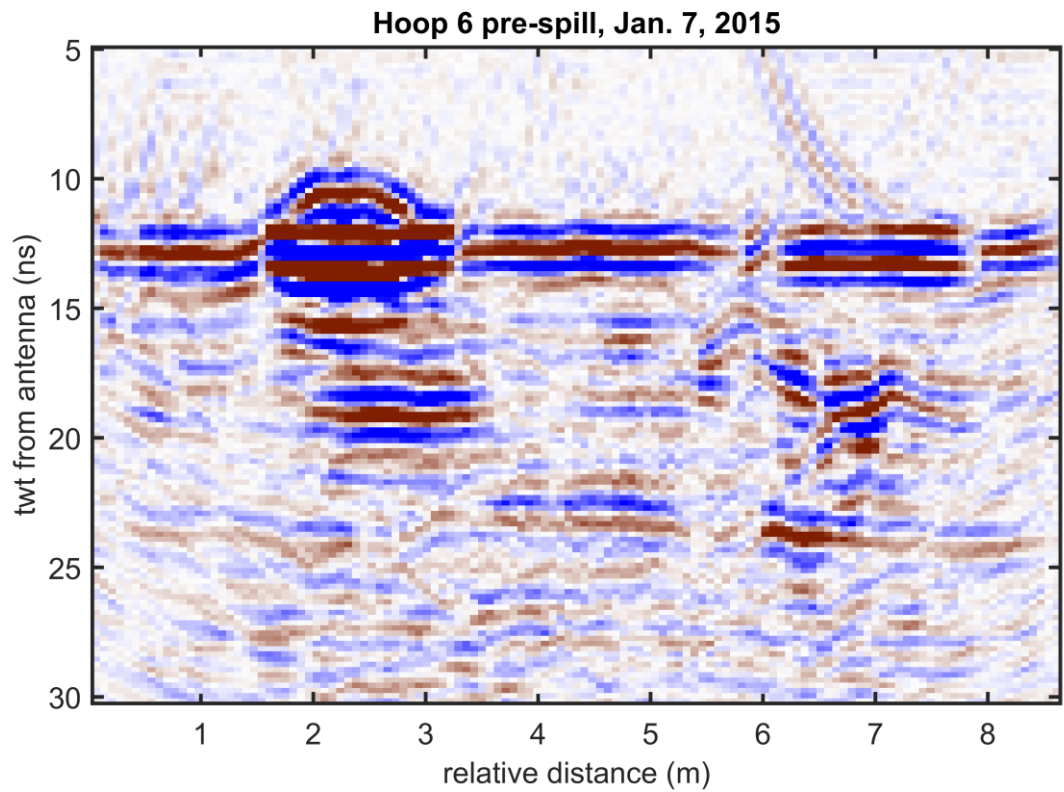


Figure AG11. A mound of snow is readily visible on the ice surface at 2 – 3 m of relative distance in the Hoop 6 pre-spill profile. The base of ice reflection is visible in sections of the profile. The mid-sheet reflection mainly below the snow pile may be a multiple from the snow and ice surface.

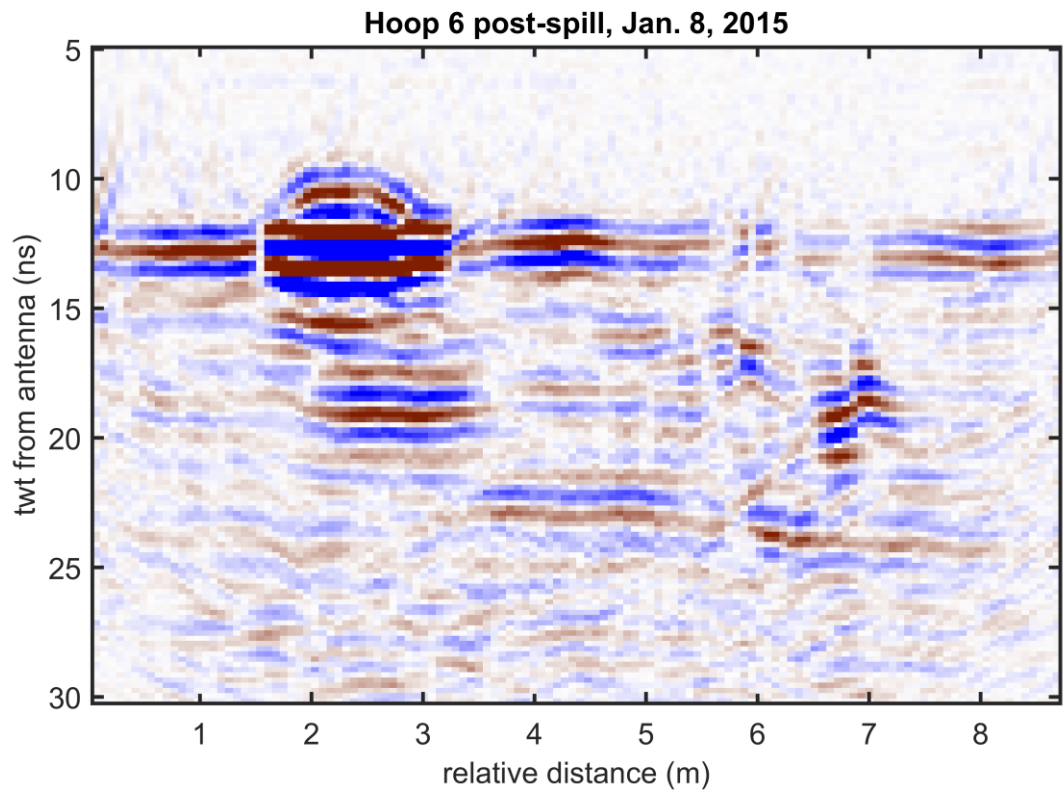


Figure AG12. The post-spill profile for the Hoop 6 injection shows extension of the base of ice reflection across more of the hoop base, with a notable increase in amplitude. Although this was the thickest ice sheet for any of the spills the oil is most easily identified post-spill for the Hoop 6 injection.

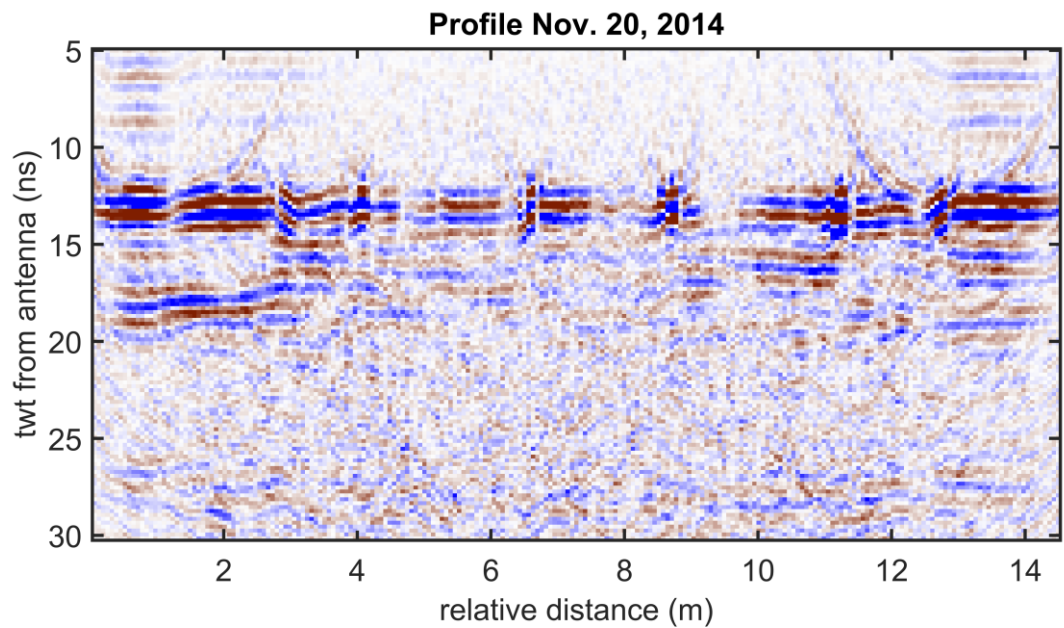


Figure AG13. The November 20th long profile did not cover the full tank extent, but ran from the center of Hoop 2 to the center of Hoop 5. The ice surface is visible for the first several meters along the tank at approximately 17 - 18 ns. Hoop skirt edges are visible as irregularities along the air/ice interface. There is also a mid-sheet reflective layer present at 15 – 16 ns, in particular below Hoop 4 at 10 m relative distance. Note that this profile was taken prior to the Hoop 4 injection on the same day.

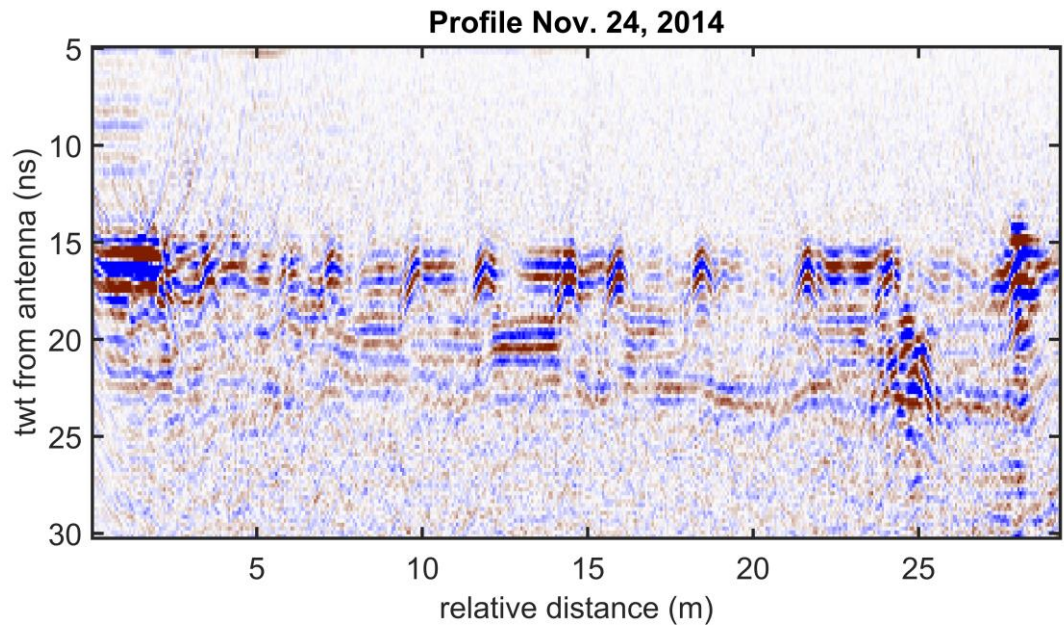


Figure AG14. The November 24th profile ran for the full long axis of the basin. Encapsulated oil is plainly visible in Hoop 4 at approximately 12-15 m relative distance and 20 ns two-way travel time. The base of ice reflection is mainly present at 22 – 23 ns. There is mid-sheet noise at 25 m distance as well as a strong reflection at the end of the profile, perhaps from equipment on the ice surface at the back of the basin. High amplitude reflections at the ice surface for the first few meters of the profile may be caused by warm ice conditions at the edge of the room near the carriage door.

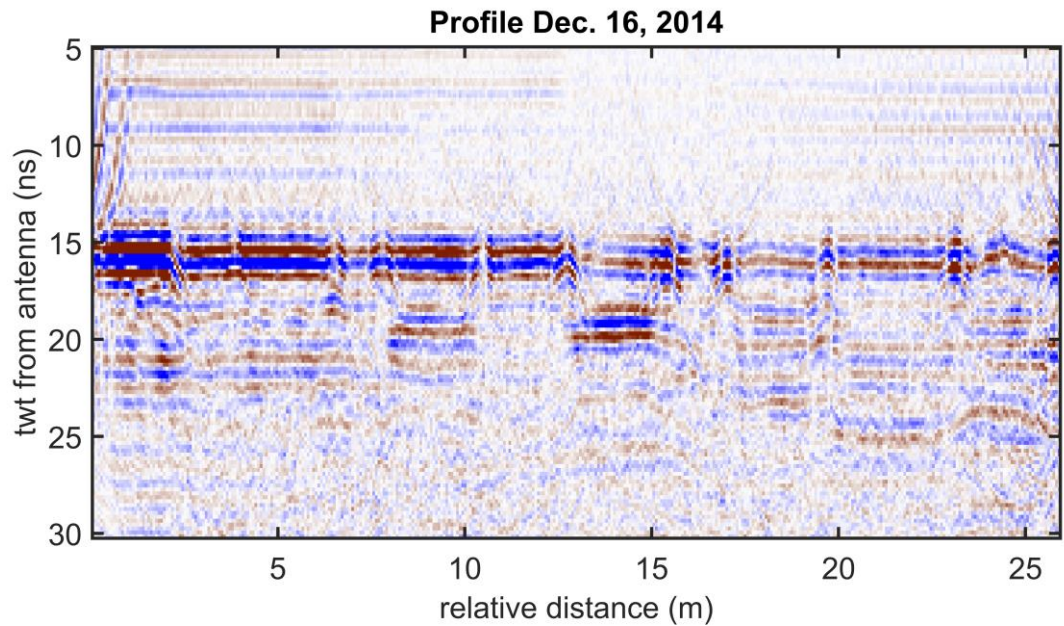


Figure AG15. The December 16th profile was taken several days following the injection into Hoop 5 on December 9th. While the encapsulated spills into Hoops 3 and 4 are plainly visible, it is difficult to distinguish signal from Hoop 5 oil. The ice at the time of the profile was approximately 55 cm thick and the base of ice is intermittently visible at 23 – 24 ns. The reflection at approximately 22 ns from 0 – 8 m distance is likely background noise and not the base of ice reflection.

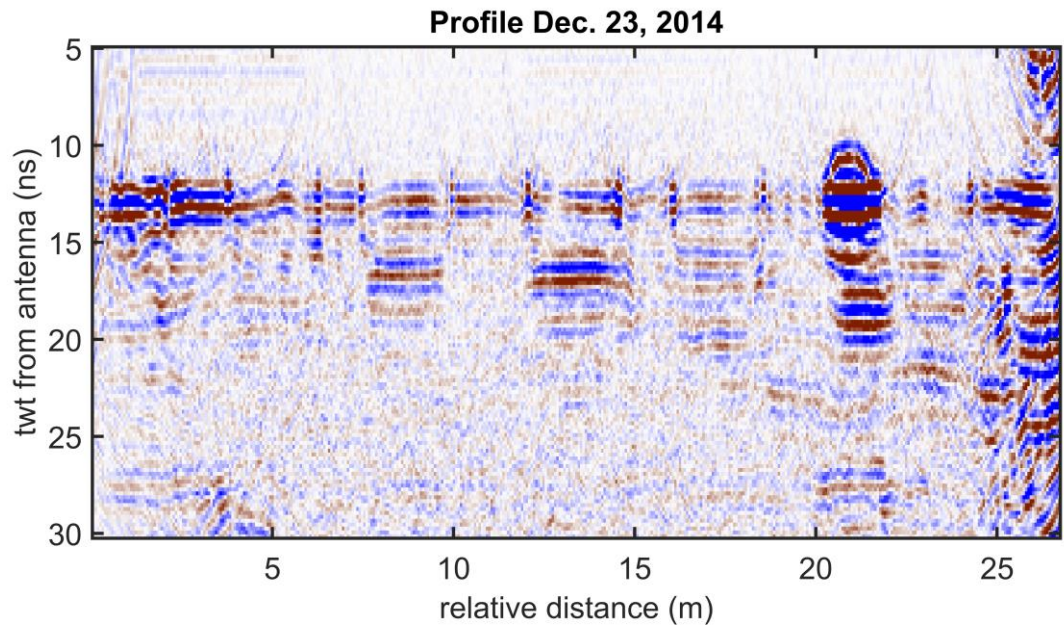


Figure AG16. The encapsulated spills in Hoops 3 and 4 are again plainly visible in the December 23rd profile. Snow on the ice surface is visible as a hump between Hoops 5 and 6. Strong end-of-tank reflections from on-ice equipment saturate the last few meters of the profile.

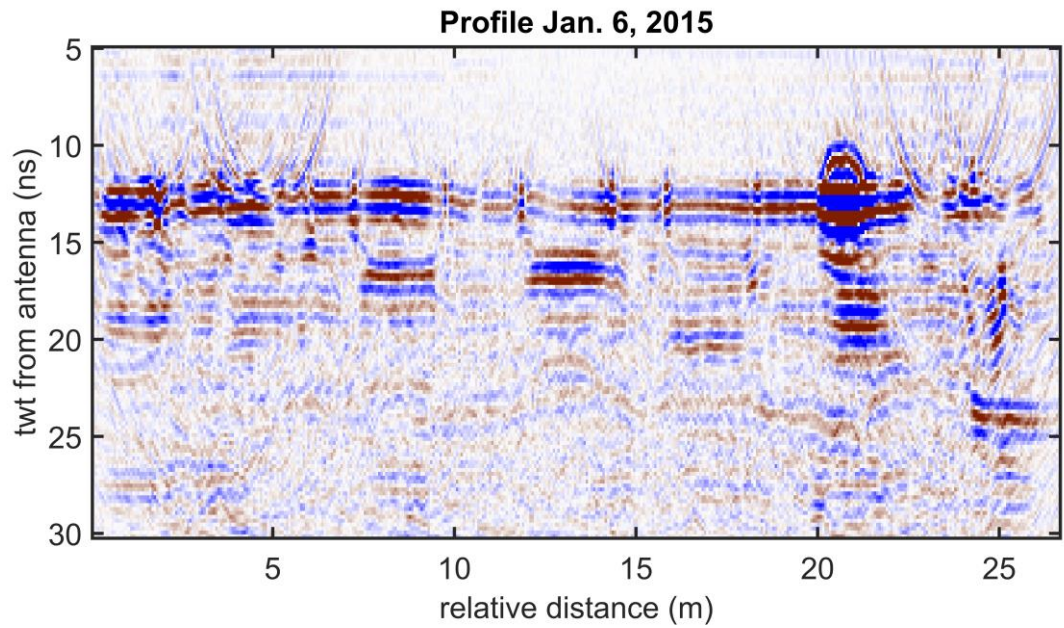
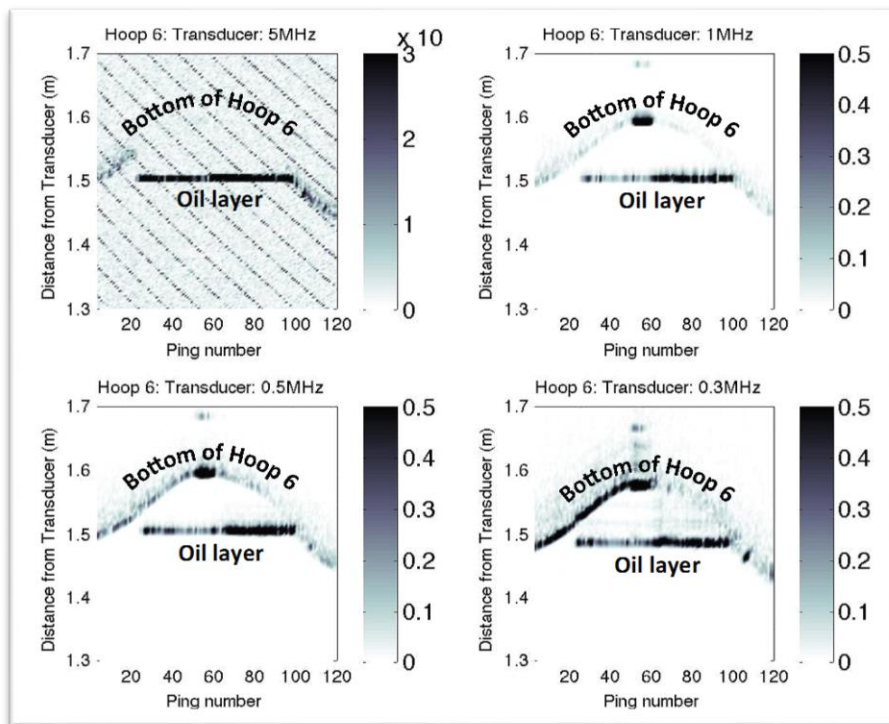


Figure AG17. The January 6th profile was collected prior to the injection into Hoop 6. The base of ice reflection is generally interpretable at 23 – 24 ns, although it is not far above the background noise level. Encapsulated oil is plainly visible in Hoops 3 and 4, and is possibly visible in Hoop 5.

Oil Detection Under Sea Ice

Single-beam narrowband sonar



Raw data from the 4 transducers of the Aquascat system showing oil lying within Hoop 6

By

J. Wilkinson

Polar Ocean Services Ltd

Single-beam narrowband sonar

J. Wilkinson

Polar Ocean Services Ltd

Active acoustics offer the possibility to detect oil that is contained underneath the ice, as well

as oil encapsulated within the ice itself. Importantly active acoustic techniques also provide the opportunity to monitor the thickness of this oil layer.

The effectiveness of this technique is dependent on the acoustic impedance mismatch of the four mediums involved, air, sea ice, oil, and seawater. This mismatch allows the location of the interfaces to be identified, i.e. air-ice, oil-ice, oil-seawater, and oil-ice interfaces. From this information the location and thickness of the oil within or under the sea ice can be established.

The role of Polar Ocean Services Ltd lies within Sub-Task 1.3.1: Single-beam narrowband sonar. The aim of this task is to detect oil under or within sea ice, and to better understand the returned acoustic signal both from sea ice and also from oil contaminated sea ice. This was achieved through the use of the Aquascat system.

Key Results:

- The single-beam narrowband sonar was **able to detect oil under all Hoops**.
- The single-beam narrowband sonar was **able to detect encapsulated oil** up to an ice thickness of around 5 cm below the oil.
- **Low frequency** transducers are best suited to the **detection of encapsulated oil**. Detection of oil encapsulated under thicker ice is likely with a more powerful sonar, see next steps section below.
- The single-beam narrowband sonar was able to continuously **monitor the thickness of oil** that was contained under the sea ice.
- The single-beam narrowband sonar was able to **monitor the reduction of oil thickness** due to the oil migrating up through the warming sea ice.
- Significantly **more acoustic energy is reflected** by the ice bottom when oil is present under the sea ice.
- The clear identification of oil was possible with **very limited processing of the data**.

Note: All data displayed in this report, unless otherwise stated, is in its raw format.

No filtering or enhancement. The reason is to show the reader the ease or difficulty to identify oil under or encapsulated within the ice.

Next steps: Based on the detailed analysis of the data gathered it is our opinion that additional investment would be fruitful in the following areas:

- **Better detection of encapsulated oil:** Our results suggest the detection of oil located under sea ice is indeed possible with acoustics. However the detection of oil encapsulated within the ice with the present acoustic system was limited to about 5 cm of new ice forming below the oil. It is clear that it is not the acoustic technique that is limiting the detection of encapsulated oil, but rather it was the power of the present system that was a limiting factor. New experiments should be performed with a more powerful sonar system. We have initiated discussions with the manufacturer who have confirmed that this is indeed possible.
- **Influence of grazing angle:** The tests we have performed have shown the clear ability to detect oil with a single beam sonar looking vertically upwards. However an acoustic system should have the ability to look at a range of angles to detect oil. Additional tests to understand

the influence of various grazing angle on the detection of oil should be performed. The mounting of a single-beam sonar on a rotating platform would enable us to better quantify the acoustic returns at different angles.

- **Automatic detection of oil:** The ability to unambiguously determine the acoustic return from oil and sea ice is clear. An obvious next step is the development of automatic oil detection algorithms. Development of algorithms to automatically detect an oil signature from acoustic returns is needed for 'smart' autonomous detection systems for autonomous underwater vehicles or remotely operated vehicles. The data we have collected could be utilised for this task.
- **Blind test:** Determine the ability to detect oil under a blind test, i.e. detection of oil when there is no visible evidence of oil within or under a continuous sheet of sea ice. This would provide the ability to test both the detection equipment as well as the time taken to process the data to produce a positive or negative result.

Description of the AQUAscat 1000

The following information has been compiled from the AQUAscat 1000 User Manual (AQUAscat1000 Manual V5.0.pdf) and from the website of the manufacturer, the Aquatec Group ([www. http://www.aquatecgroup.com](http://www.aquatecgroup.com)). The User Manual is classified as COMMERCIAL IN CONFIDENCE, however we have received authorization for the publication of the following information regarding this system (email 25 April 2015: Andy Smerdon, Managing Director).

The AQUAscat1000 is a commercially available Acoustic Backscatter System that is manufactured by the Aquatec Group, UK. It was designed as a high frequency acoustic device for sediment concentrations and sizing. However it has a broad use from the detection of zooplankton in the water column through to precision altimetry, dredge plumes, and turbulence. We used the system for the detection of oil under sea ice.

For our test regime the AQUAscat 1000 has advantages over other single-beam, narrowband sonar systems due to:

- the AQUAscat 1000 has been designed to acquire large quantities of data over extended periods of time,
- the system is a high fidelity system and thus can resolve thin layers with low noise (from 2½ millimetres upwards),
- the system can drive up to four transducers at a range of frequencies (300 kHz to 5 MHz) ,
- the Aquascat records the full echogram profile, so multiple interfaces can be resolved and the returned echogram compared to theoretical predictions,
- the sonar is compact, low power, and relatively inexpensive enabling it to be deployed easily on AUVs or similar platforms.

Possibly the most important attribute of the AQUAscat 1000 for our tests is that it can be powered remotely and therefore we can monitor output in real-time. This can be achieved by running an additional cable to the system.



Figure 1: Illustration showing the AQUAscat 1000. The black cylinder is the subsea housing that contains the electronics and batteries and the blue cabling runs to the 4 transducers. (adapted from : <http://www.aquatecgroup.com/index.php/aquascats-p-menu>).

Operation of the AQUAscat 1000

The AQUAscat transmits pulses of high frequency sound on up to four transducers, each of which may operate at a different frequency. It measures the returned sound at discrete spatial intervals programmable from 2½ millimetres to 4 centimetres.

We have chosen a range of frequencies based on results of previous oil in ice experiments. These experiments showed that these frequencies will capture the practical range of penetration depths into the ice (so that encapsulated oil can be detected), while balancing differing range resolution and practical range limitations for use on AUVs and ROVS. The frequencies chosen were:

- v. 5.0 MHz
- vi. 1.0 MHz

- vii. 0.5 MHz
- viii. 0.3 MHz,

The 0.3 MHz transducer is custom made at our request to enable it be compared to the lower frequency broadband systems, (see WHOI). These frequencies have been chosen because of their resolution properties (i.e. 5 MHz), through to their ice penetrating properties (i.e. 0.3 MHz). We are recording the full echogram profile so multiple interfaces can be resolved, and the returned echogram compared to theoretical predictions.

Aquascat Parameters: Set during experiment

Parameter	Channel 1	Channel 2	Channel 3	Channel 4
Samples to average	1	1	1	1
No of Bins	256	256	256	256
Beam Width	3	0.9	3.75	2.4
Power Level	0	0	0	0
Profile Rate	1 Hz	1 Hz	1 Hz	1 Hz
Transducer Frequency	0.3 MHz	5 MHz	0.5MHz	1MHz
Gain	0	0	0	0
Transducer Radius	0.025 m	0.052 m	0.012 m	0.009 m
Ping rate (second)	1	1	1	1

Table 1: Parameters that remained constant during the experiment.

Aquascat Parameters: Could be varied during experiment.

Parameter	Channel 1	Channel 2	Channel 3	Channel 4
Ping length (2.5, 5, 10, 20, & 40 mm are possible)	Generally 10 mm	Generally 10 mm	Generally 10 mm	Generally 10 mm
Number of Pings in a file (fully changeable)	180 seconds, but user changeable.	180 seconds, but user changeable	180 seconds, but user changeable	180 seconds, but user changeable

Table 2: Parameters that the user controlled during the experiment.

Mounting/deployment approach

The AQUAscat system was located over two regions of the trolley. The transducers (0.3MHz, 0.5 MHz, 1 MHz, and 5 MHz) are located in the centre of the trolley (red circle in accompanying Figure 2), whilst the electronics pod was located near the side of the trolley (yellow circle in accompanying Figure 2). A 200 ft. cable connected the base unit to a laptop. The laptop was situated in the 'warm' room that is adjacent to the tank.

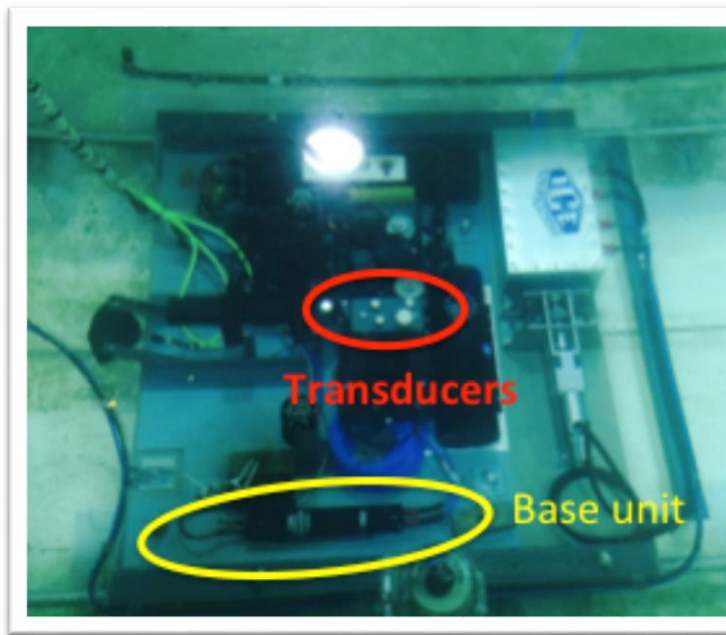


Figure 2a (above): Example of the mounting of the four transducers. A similar system was used on the trolley.

Figure 2b (left): Layout of the Aquascat on the trolley. The Base unit was placed near the side of the trolley, whilst the transducers were placed near the centre of the trolley.

Description of the measurement approach

Our sampling strategy involves (a) user-controlled (stationary), (b) user-controlled (moving trolley) and (c) autonomous measurements (stationary trolley). These sampling strategies are described below.

(a) User-controlled measurements (stationary)

This sampling strategy was performed when the trolley was stationary under an area of interest i.e. the oil spill. The sampling regime was entered and controlled from the Aquascat software on the PC. We performed 5 back-to-back logging runs. These are:

- (6) 3 minute run, all Transducers active with pulse length 2.5 mm.
- (7) 3 minute run, all Transducers active with pulse length 5 mm.
- (8) 3 minute run, all Transducers active with pulse length 10 mm.
- (9) 3 minute run, all Transducers active with pulse length 20 mm.
- (10) 3 minute run, all Transducers active with pulse length 40 mm.

The aim of this sampling strategy was to better understand the influence of pulse length of the detection of oil.

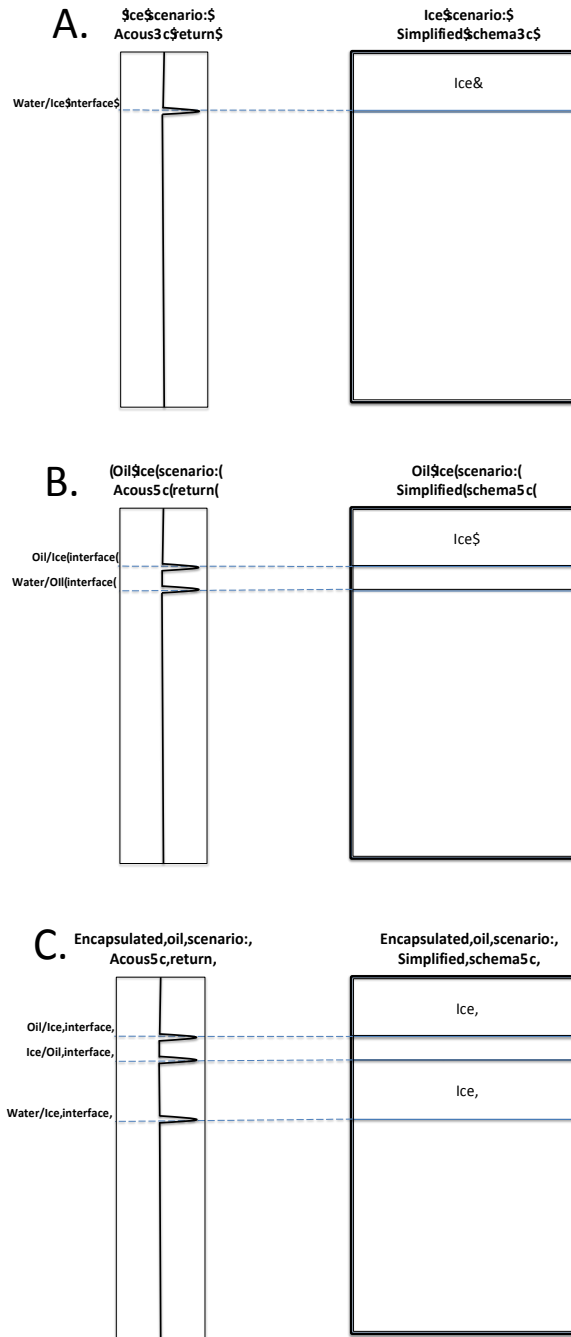
(b) User-controlled measurements (moving)

It was not practical to perform the five different pulse lengths runs when the trolley was moving. Therefore we set the pulse length to 10 mm for all four transducers during moving event.

(c) Autonomous measurements (stationary)

When the trolley is parked and not in use, i.e. outside working hours, we set the sampling regime to automatically perform readings every few hours. With this regime selected we cannot perform runs at different pulse lengths, therefore we set the pulse length to 10 mm for all four transducers. Due to a communication problem (see section below) we set the system to run on the hour for 5 minutes.

How can we detect oil under sea ice using acoustics?



Sea ice is typically a strong reflector of sound because of the acoustic impedance contrast between seawater and the ice bottom (see Figure 3 A.). If there is oil present under the sea ice there is also a somewhat weaker acoustic impedance contrast between oil and seawater. These impedance differences can be exploited with active sonar to detect the presence or absence of oil spills under sea ice, via detection of acoustic reflections from the water/oil and oil/ice interfaces (see Figure 3 B.). With a multilayer system of seawater, oil, and ice, some acoustic energy is reflected from the first interface, whilst the remainder is transmitted across the interface into the overlying medium (the encapsulated oil). From there it will continue on to the next interface whereby some acoustic energy will be reflected and the remainder transmitted and so on (see Figure 3 C.).

A profiling sonar, like the Aquascats system (i.e. one that records the return waveform for each transmitted pulse), should be able to detect an acoustic return first from the oil-water interface (surface of the oil), and then some time later detect a second return from the oil-ice interface (surface of the ice). The time difference (related to distance through the sound speed of each medium), between the returns from each of the interfaces is a measurement of the thickness of the oil layer.

Figure 3. Schematic showing three possible oil under ice scenarios (right) and the approximate acoustic return (left). These are:

(A) Ice only: Acoustic return from the ice bottom.

(B) Oil-Ice: First acoustic return from the water-oil interface and the second return from the oil-ice interface.

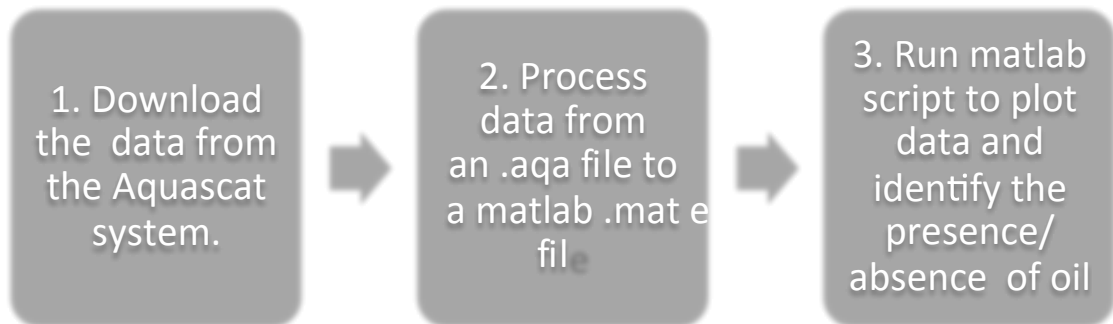
(C) Encapsulated oil: First acoustic return from the water-ice interface, the second return from

the oil-ice interface and the third return from the ice-oil interface.

Note: This cartoon does not take into account differences in sound speed, scattering or absorption properties of each medium.

Data Processing:

The data processing of the Aquascats data was a simple 3-step process.



Step 1: Download data from the Aquascat unit

Step 2: Run custom MATLAB script to change the Aquascat data from a priority ‘.aqa’ file to a MATLAB based ‘.mat’ file.

Step 3: Run another custom MATLAB script to plot data. The exact script used depends on whether the dataset is from (1) a moving trolley or (2) a stationary trolley. These are explained below:

Processing for a moving trolley:

No filtering or additional processing of data required. Raw data was collected at one reading per second, and displayed in the report. This raw data was adequate for our needs to detect oil. Examples of the raw data from a moving trolley under Hoop 1 and Hoop 6 can be seen below.

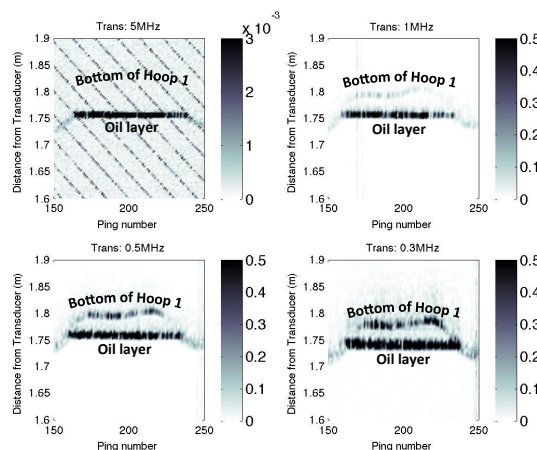


Figure 4 Raw data from the Aquascat system showing oil lying under Hoop 1.

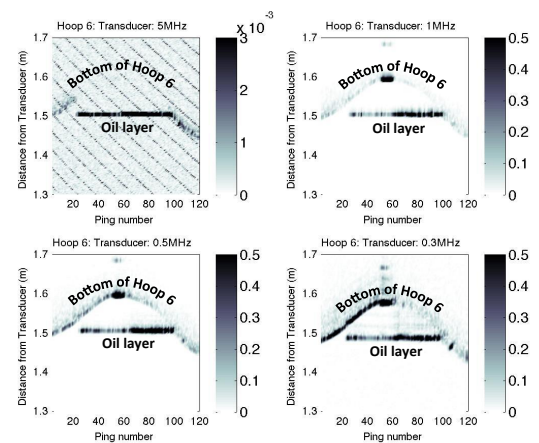


Figure 5 Raw data from the Aquascat system showing oil lying under Hoop 6.

Processing for a stationary trolley:

No filtering, some processing of data. Raw data was collected at one reading per second over a set period of time, usually over a three-minute period. The data processing involved calculating the average return from these measurements. Example of the raw data set and the processed dataset that delivers the resultant average return can be seen below.

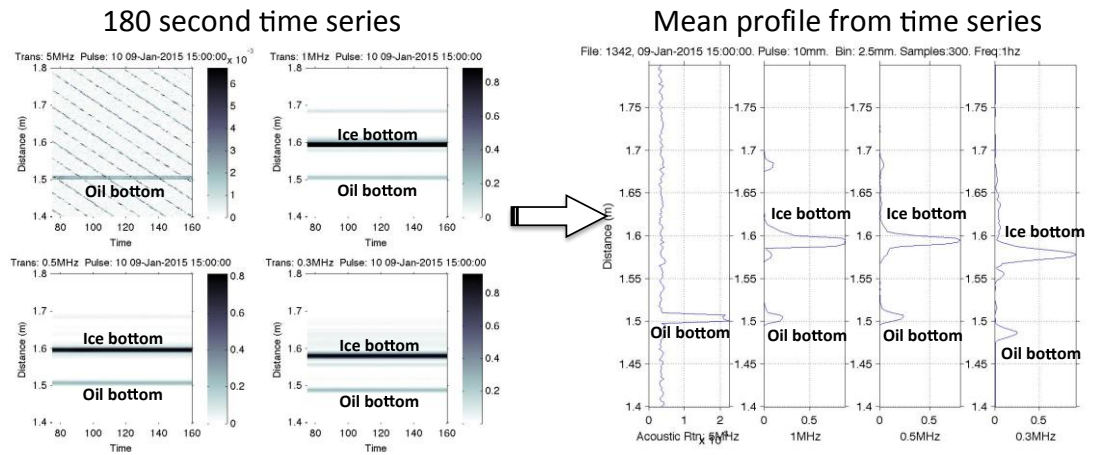


Figure 6: Left: Raw time series of data showing the acoustic returns over the logging period of 180 seconds. The oil bottom and ice bottom can clearly be seen. Right: Processed data showing the calculated average return from the measurements made over 180 seconds.

Communication issues:

As the experiments progressed the communication with the AQUAscatter system became troublesome. Upon investigation this problem was identified as the 200 ft. communication cable running between the PC and the trolley. A cable, especially of this length, is not normally used with the system but is needed for these experiments as it allows the user to control the sampling strategy in real time. It is essential for sampling strategy (a) user-controlled (stationary) and (b) user-controlled (moving trolley).

As a result of this problem and in order not to miss any data we set the system to record in autonomous mode (sampling strategy (c) autonomous measurements: stationary trolley) until a new cable arrived. The new cable was shipped to CRREL (5 December). Whilst extremely disappointing this issue did not influence results as the sampling strategy (a) is mainly aimed at encapsulated oil, which occurred after 9 December.

Calibration

In order to better understand the sonar return from the sea ice bottom and the spilled crude oil there was a need to calibrate the sonars under calm conditions. We performed our calibrations when the water in the tank was fully quiescent (no ice). To ensure these conditions remained during these tests all other activity in the tank ceased.

The tests stepped through the five different pulse lengths. These were 2.5 mm, 5 mm, 10 mm, 20 mm and 40 mm. Each of these five calibration tests were performed over a 300 second period, with all transducers active (5 MHz, 1 MHz, 0.5 MHz, 0.1MHz). The results are shown below.

Results: Pulse length: 2.5 mm.

Date/Time: 03-Nov-2014 12:12:44
 Bin size: 5 mm.

of Samples: 300.
 Sampling Frequency: 1Hz
 Transducers: All 4 transducers (5 MHz, 1MHz, 0.5 MHz, 0.3 MHz)
 File number: 13

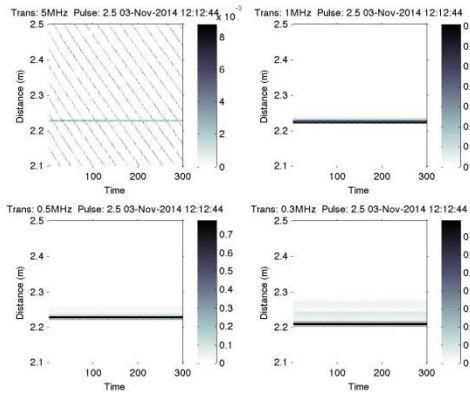


Figure 7. A 300 second record of the acoustic return (every second) from a 2.5 mm pulse.

Top left: 5 MHz; Top right: 1 MHz,
 Bottom left: 0.5 MHz; Bottom right: 0.3 MHz.

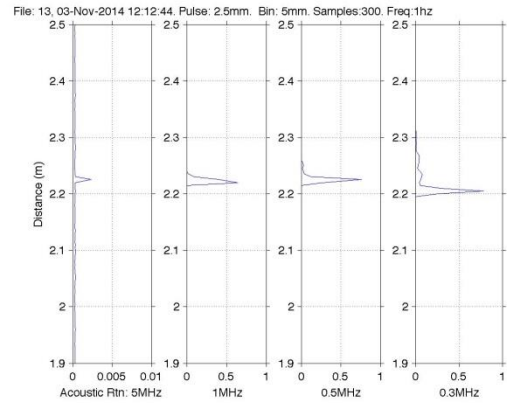


Figure 8. Average acoustic return calculated from the 300 second record for a 2.5 mm pulse.

From left to right we have the return from 5 MHz, 1 MHz, 0.5 MHz, and 0.3 MHz.

Transducer	Strength of First return	Distance to water surface (First return)	Strength of Maximum return	Distance to water surface (Maximum return)
5 MHz	0.002364	2.225 m	0.002364	2.225 m
1 MHz	0.643100	2.220 m	0.643100	2.220 m
0.5 MHz	0.265580	2.220 m	0.760300	2.225 m
0.3 MHz	0.261170	2.200 m	0.785880	2.205 m

Table 3. Summary of the acoustic characteristics of the water surface as seen by each of the four transducers. First return is defined as the first acoustic that is above the background level. Maximum return is defined as the maximum acoustic return.

Note: The slight difference in the distance to the water surface for each transducer is due to differences in the mounting height of each transducer on the trolley.

Results: Pulse length: 5 mm.

Date/Time: 03-Nov-2014 11:46:47
 Bin size: 5 mm.
 # of Samples: 300.
 Sampling Frequency: 1Hz
 Transducers: All 4 transducers (5 MHz, 1MHz, 0.5 MHz, 0.3 MHz)
 File number: 9

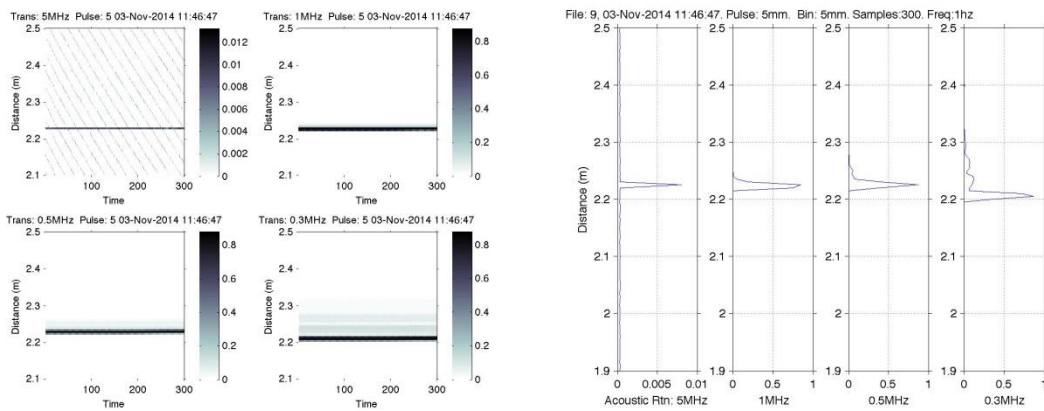


Figure 9. A 300 second record of the acoustic return (every second) from a 5 mm pulse.

Top left: 5 MHz; Top right: 1 MHz,
 Bottom left: 0.5 MHz; Bottom right: 0.3 MHz.

Figure 10. Average acoustic return calculated from the 300 second record for a 5 mm pulse.

From left to right we have the return from 5 MHz, 1 MHz, 0.5 MHz, and 0.3 MHz.

Transducer	Strength of First return	Distance to water surface (First return)	Strength of Maximum return	Distance to water surface (Maximum return)
5 MHz	0.0080519	2.225 m	0.0080519	2.225 m
1 MHz	0.747900	2.220 m	0.8453800	2.225 m
0.5 MHz	0.370520	2.220 m	0.8724900	2.225 m
0.3 MHz	0.349860	2.200 m	0.8701500	2.205 m

Table 4. Summary of the acoustic characteristics of the water surface as seen by each of the four transducers. First return is defined as the first acoustic that is above the background level. Maximum return is defined as the maximum acoustic return.

Note: The slight difference in the distance to the water surface for each transducer is due to differences in the mounting height of each transducer on the trolley.

Results: Pulse length: 10 mm.
 Date/Time: 03-Nov-2014 11:54:44
 Bin size: 5 mm.
 # of Samples: 300.
 Sampling Frequency: 1Hz
 Transducers: All 4 transducers (5 MHz, 1MHz, 0.5 MHz, 0.3 MHz)
 File number: 10

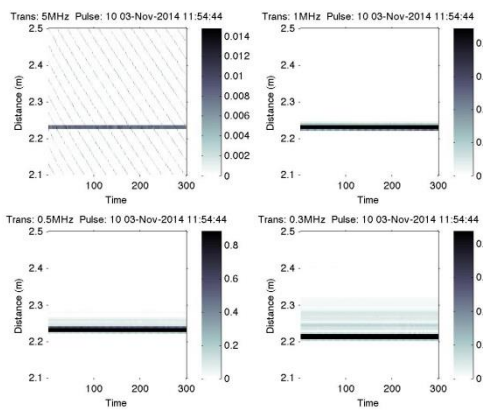


Figure 11. A 300 second record of the acoustic return (every second) from a 10 mm pulse.

Top left: 5 MHz; Top right: 1 MHz,
 Bottom left: 0.5 MHz; Bottom right: 0.3 MHz.

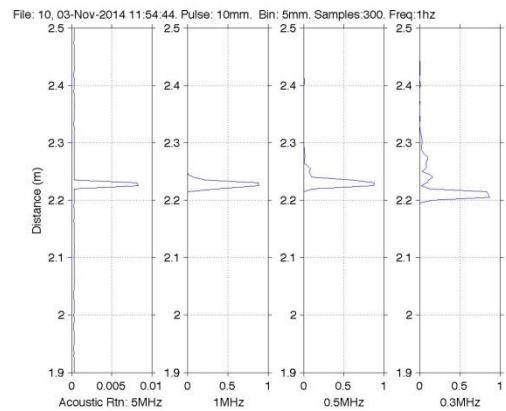


Figure 12. Average acoustic return calculated from the 300 second record for a 10 mm pulse.

From left to right we have the return from 5 MHz, 1 MHz, 0.5 MHz, and 0.3 MHz.

Transducer	Strength of First return	Distance to water surface (First return)	Strength of Maximum return	Distance to water surface (Maximum return)
5 MHz	0.0083274	2.225 m	0.0083274	2.225 m
1 MHz	0.3663800	2.220 m	0.8887500	2.225 m
0.5 MHz	0.1098700	2.220 m	0.8828000	2.230 m
0.3 MHz	0.1587200	2.200 m	0.8675500	2.205 m

Table 5. Summary of the acoustic characteristics of the water surface as seen by each of the four transducers. First return is defined as the first acoustic that is above the background level. Maximum return is defined as the maximum acoustic return.

Note: The slight difference in the distance to the water surface for each transducer is due to differences in the mounting height of each transducer on the trolley.

Results: Pulse length: 20 mm.

Date/Time: 03-Nov-2014 12:00:26
 Bin size: 5 mm.
 # of Samples: 300.
 Sampling Frequency: 1Hz
 Transducers: All 4 transducers (5 MHz, 1MHz, 0.5 MHz, 0.3 MHz)
 File number: 10

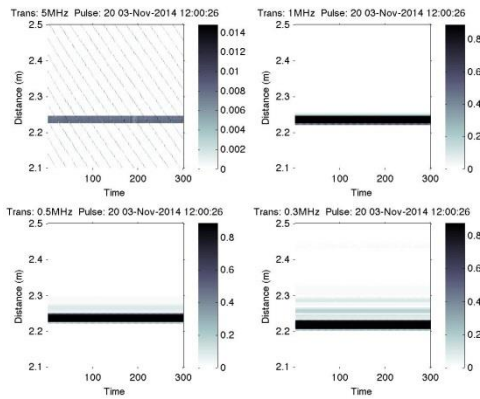


Figure 13. A 300 second record of the acoustic return (every second) from a 20 mm pulse.

Top left: 5 MHz; Top right: 1 MHz,
 Bottom left: 0.5 MHz; Bottom right: 0.3 MHz.

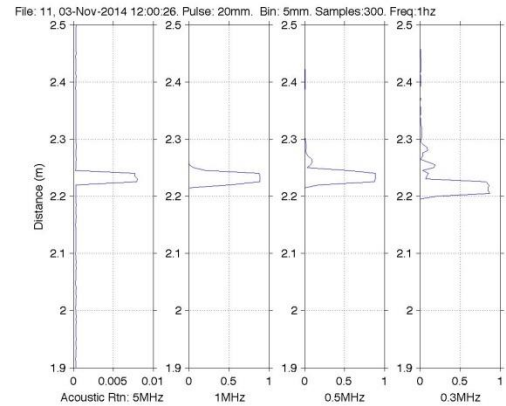


Figure 14. Average acoustic return calculated from the 300 second record for a 20 mm pulse.

From left to right we have the return from 5 MHz, 1 MHz, 0.5 MHz, and 0.3 MHz.

Transducer	Strength of First return	Distance to water surface (First return)	Strength of Maximum return	Distance to water surface (Maximum return)
5 MHz	0.0079097	2.225 m	0.0080457	2.230 m
1 MHz	0.5016800	2.220 m	0.8889100	2.235 m
0.5 MHz	0.1725400	2.220 m	0.8861100	2.235 m
0.3 MHz	0.2100300	2.200 m	0.8707900	2.205 m

Table 6. Summary of the acoustic characteristics of the water surface as seen by each of the four transducers. First return is defined as the first acoustic that is above the background level. Maximum return is defined as the maximum acoustic return.

Note: The slight difference in the distance to the water surface for each transducer is due to differences in the mounting height of each transducer on the trolley.

Results: Pulse length: 40 mm.
 Date/Time: 03-Nov-2014 12:06:45
 Bin size: 5 mm.
 # of Samples: 300.
 Sampling Frequency: 1Hz
 Transducers: All 4 transducers (5 MHz, 1MHz, 0.5 MHz, 0.3 MHz)
 File number: 10

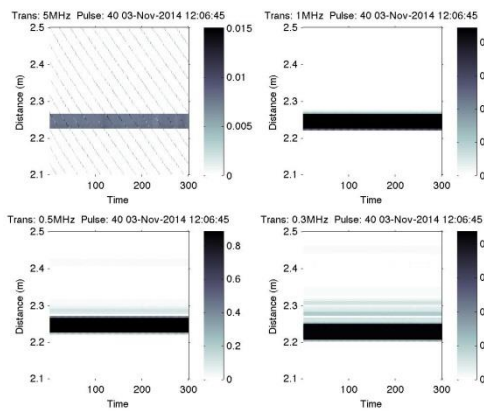


Figure 15. A 300 second record of the acoustic return (every second) from a 40 mm pulse.

Top left: 5 MHz; Top right: 1 MHz,
 Bottom left: 0.5 MHz; Bottom right: 0.3 MHz.

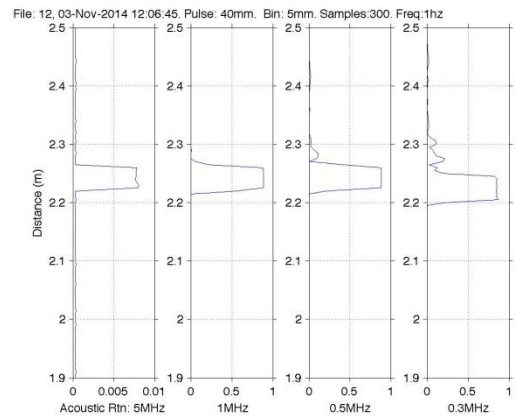


Figure 16. Average acoustic return calculated from the 300 second record for a 40 mm pulse.

From left to right we have the return from 5 MHz, 1 MHz, 0.5 MHz, and 0.3 MHz.

Transducer	Strength of First return	Distance to water surface (First return)	Strength of Maximum return	Distance to water surface (Maximum return)
5 MHz	0.0079922	2.225 m	0.0080955	2.230 m
1 MHz	0.5508400	2.220 m	0.8889500	2.235 m
0.5 MHz	0.2010600	2.220 m	0.8862600	2.240 m
0.3 MHz	0.2310800	2.200 m	0.8716600	2.205 m

Table 7. Summary of the acoustic characteristics of the water surface as seen by each of the four transducers. First return is defined as the first acoustic that is above the background level. Maximum return is defined as the maximum acoustic return.

Note: The slight difference in the distance to the water surface for each transducer is due to differences in the mounting height of each transducer on the trolley.

Impact of sea ice on acoustic return

An example of the impact of sea ice on the acoustic return can be seen in the figures below. These measurements were obtained in the same location as our calibration runs, but about two days afterwards. During this time a thin layer of sea ice formed above the transducers.

Whilst the bin size has been reduced from 5 mm to 2.5 mm for these measurements, we can see the significant differences a few centimetres of sea ice can make to the acoustic return. The main points are:

- Almost total attenuation/scattering of the 5 MHz signal.
- Reduction in the strength of the returned signal by an order of magnitude in the 1 MHz, 0.5 MHz and 0.3 MHz transducers.

Results: Pulse length: 10 mm.

Date/Time: 05-Nov-2014 11:46:24
Bin size: **2.5 mm.**
of Samples: 180.
Sampling Freq: 1Hz
Transducers: All 4 transducers (5 MHz, 1MHz, 0.5 MHz, 0.3 MHz)
File number: 63

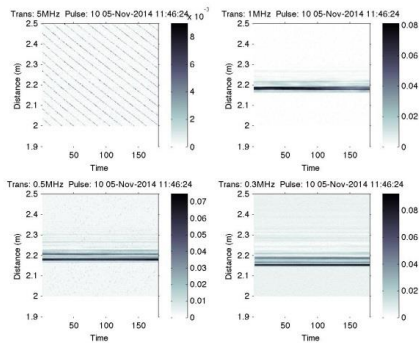


Figure 17. A 180 second record of the acoustic return (every second) from a 10 mm pulse.

Top left: 5 MHz; Top right: 1 MHz,
 Bottom left: 0.5 MHz; Bottom right: 0.3 MHz.

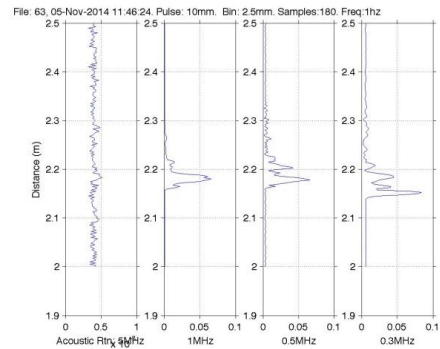


Figure 18. Average acoustic return calculated from the 180 second record for a 10 mm pulse.

From left to right we have the return from 5 MHz, 1 MHz, 0.5 MHz, and 0.3 MHz.

Transducer	Strength of First return	Distance to water surface (First return)	Strength of Maximum return	Distance to water surface (Maximum return)
5 MHz	N/A	N/A	N/A	N/A
1 MHz	0.00516820	2.1600 m	0.06622100	2.1800 m
0.5 MHz	0.00655260	2.1625 m	0.06593100	2.1775 m
0.3 MHz	0.00606570	2.0000 m	0.08405500	2.1525m

Table 8. Summary of the acoustic characteristics of the water surface as seen by each of the four transducers. First return is defined as the first acoustic that is above the background level. Maximum return is defined as the maximum acoustic return.

Main Discussion point:

- Significant acoustic energy reflected at the water/air interface; water surface.
- The presence of sea ice reduces the amount of returned acoustic energy
- The acoustic return from water/air interface by the 5 MHz transducer was about two orders of magnitude lower than the other transducers. This is to be expected, as at this high frequency there is significant attenuation/ absorption within the water column.
- When mounting the transducer heads on the trolley there will be slight differences in their vertical position. These offsets have been calculated based on the distance from the transducer to water/air interface. The following table displays these differences relative to the 5 MHz transducer.

Transducer	Vertical offset between transducers: relative to the 5 MHz Transducer (Positive value indicates the transducer is mounted closer to water surface)
5 MHz	~ 0.0 cm
1 MHz	~ 0.0 cm
0.5 MHz	~ - 0.5 cm
0.3 MHz	~ + 2.0 cm

Table 9. Table showing the mounting offset for each transducer relative to the 5 MHz transducer. Results based on location of water surface during calibration tests.

- Both the 0.5 MHz and 0.3 MHz transducers displayed some acoustic returns after the main return had passed. See black circles in Figure 19. These effects were not seen in the 5 MHz or the 1 MHz. The beam-width for the 5 MHz, 1 MHz, 0.5 MHz and 0.3 MHz are 0.9°, 2.4°, 3.75°, and 3° respectively. These beam widths relate to a footprint at the water surface (approx. distance 2.22 m away) of around 0.03 m, 0.09 m, 0.15 m, and 0.12 m. As the sides of the tank (or other scattering possibilities), were well beyond these distances it suggests that these additional returns are an artefact of side-lobes from the main acoustic signal. This shows the importance of knowing the characteristics of your transducer before the interpretation of an acoustic signal is performed. For example, for our project the acoustic return from a side-lobe could be wrongly interpreted as a return from an oil layer within the ice.

Main experiment: Detection of Oil spilled under sea ice

A total of 7 spills were performed under sea ice within the 6 Hoops (two spills were performed in Hoop 1). The times, ice conditions and oil characteristics are summarized in table 10.

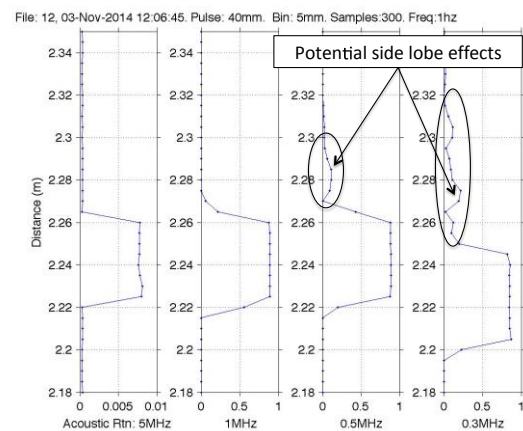


Figure 19. Figure showing possible side-lobe effects (black circle) within the 0.5 MHz and 0.3 MHz transducers. These effects are not seen within the 5 MHz and 1 MHz transducers.

Hoop ID	Injection Date Start Time	Ice Thickness seen by sonar (cm)	Injection Amount (l)	Estimated Oil Thickness (cm)	Oil Thickness seen by sonar (cm)
1	5-Nov-14 16:37	15	90	0.5	1
1 (2nd spill)	4-Dec-14 10:37	42	360	2	5
2	12-Nov-14 13:39	13	150	2	1
3	17-Nov-14 13:24	27	75	1	2
4	20-Nov-14 12:45	27	375	5	4
5	9-Dec-14 11:40	51	150	2	6
6	6-Jan-15 13:50	63	300	4	9

Table 10. Injection conditions in Hoops 1 to 6. Ice thickness is estimated from the range to the broadband sonar plus an estimated freeboard height. The curvature of the ice bottom in hoops 3-6 can lead to difference of ± 2 cm. *Note: We have assumed a sound speed of 1500 m/s for the duration of the experiment. We have not accounted for possible differences in sound speed due to changes in the water properties or the different scattering or absorption properties of each medium.*

In the following sections we provide a detailed analysis of the main oil detection results of the single beam sonar. We describe each Hoop separately.

Hoop 1

Spill 1: Frazil/Brash ice

Oil spill date/time: 5-Nov-14 16:37

Oil located on bottom of ice

Hoop 1- Spill 1: Frazil/Brash ice

Oil spill date/time: 5-Nov-14 16:37

Ice conditions:

The ice conditions comprised of a mixture of frazil ice crystals and broken ice blocks from the initial ice cover. Whilst the ice cover was in an unconsolidated state the mixture of ice types meant the ice bottom topography was quite rough.

Ice Draft: ~15 cm (water surface @ 2.22 m, ice bottom at 2.07 m)

Oil Spill:

The oil was released from below the ice cover via a pressurised hose. The underwater camera also revealed that the pressure of the hose redistributed the frazil and brash ice within the Hoop during the release process. As a result it is likely that the shape of ice-bottom topography would be different at the start to that of the end of the oil release process. The oil was initially located under the frazil/brash mixture, but over a short period of time it migrated up to the water/ice surface.

Summary of results

- Oil layer detected: Results suggest an oil layer of about 1 cm below the frazil/brash mixture.
- Secondary confirmation achieved via a 'new' peak appearing in the 5 MHz transducer after oil release.

Description	Detect ice bottom				Detect oil at bottom of ice				Detect oil thickness				Detect encapsulated oil			
	5 MHz z	1 MHz z	0.5 MHz z	0.3 MHz z	5 MHz z	1 MHz z	0.5 MHz z	0.3 MHz z	5 MHz z	1 MHz z	0.5 MHz z	0.3 MHz z	5 MHz z	1 MHz z	0.5 MHz z	0.3 MHz z
Pre oil release	X	✓	✓	✓	---	---	---	---	---	---	---	---	---	---	---	---
Post spill release	X	✓	✓	✓	✓	✓	✓	✓	X	✓	✓	✓	---	---	---	---
After oil encapsulation	---	---	---	---	---	---	---	---	---	---	---	---	---	---	---	---

Grey: Not applicable to the data gathered.

Green: Success

Red: Failure

Amber: Success, but with caveats.

Results

Previous tests with narrow-beam sonars have shown the detection of oil beneath sea ice, and the quantification of its thickness is indeed possible using acoustic techniques (Wilkinson et al., 2014). Figure 20 shows the acoustic return from the 1 MHz transducer under Hoop 1. The blue line represents the water surface as seen during the Calibration experiments. The red line shows the acoustic return from the ice bottom before the controlled release of oil. The black line denotes the acoustic return after the oil was spilled. The difference between the pre-oil spill (dotted red line) and the post-oil spill return (black dotted line) should be the oil thickness. If correct then the oil layer at the bottom of the ice is about a centimetre thick.

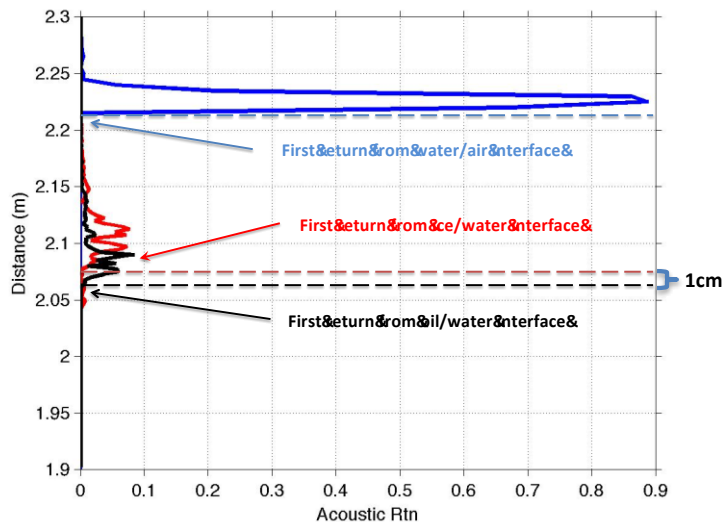


Figure 20: Acoustic returns from the 1 MHz transducer. Blue line: water surface (pre-ice formation), Red line: ice bottom (pre-oil spill), black line (post oil spill). Note: traces are not corrected for the different sound speed of the various mediums.

Because it is likely that the frazil and ice blocks moved around during the introduction of the oil this scenario is particularly challenging. As a result we cannot say for certain that the difference in the acoustic signature between pre and post oil release is a result of oil located at the bottom of the ice, the result of the movement of the ice blocks giving a different acoustic signature or a combination of both.

Interestingly we see an appearance of a peak return in the 5 MHz transducer after the oil was introduced (see black circle in Figure 21 and Figure 22). This result is consistent with an increase acoustic return when the ice bottom is contaminated with oil. We see a similar outcome in the oil releases performed under the other Hoops. This secondary evidence suggests that oil was indeed located above the transducers.

Pre-oil spill

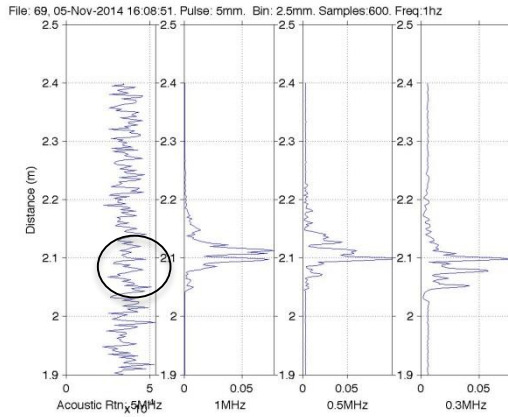


Figure 21. Pre-oil spill: Acoustic signature of the sea ice bottom about 20 minutes before the oil injection, as seen by the different transducers. Black circle shows the absence of a return from the ice bottom in the 5 MHz transducer.

From left to right we have the return from 5 MHz, 1 MHz, 0.5 MHz, and 0.3 MHz.

Post-oil spill

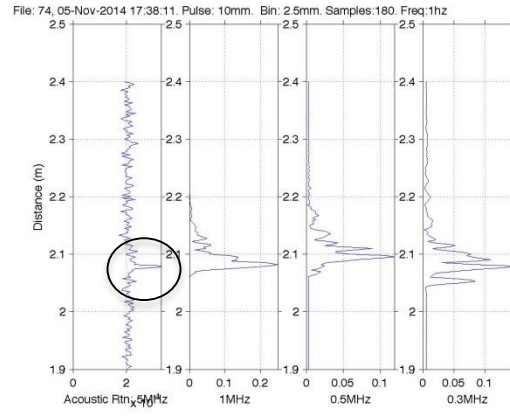


Figure 22. Post-oil spill: Acoustic signature of the oil located on the ice bottom, as seen by the different transducers. Black circle: Notice the appearance of a peak in the 5 MHz has returned. Once the oil has been released.

From left to right we have the return from 5 MHz, 1 MHz, 0.5 MHz, and 0.3 MHz.

Hoop 1- Spill 2

Solid ice sheet

Oil spill date/time: 4-Dec-14 10:37

Oil located on bottom of ice

Hoop 1- Spill 2: Solid ice sheet

Oil spill date/time: 4-Dec-14 10:37

Ice conditions:

The ice conditions comprised of continuous ice cover. Due to the subsequent ice growth (of about a month) no evidence of the frazil and broken ice blocks that made up the initial ice cover was evident. Ice bottom was essentially level.

Ice Draft: 42 cm (water surface @ 2.22 m, ice bottom at 1.8 m)

Oil Spill:

The oil was released from below the ice cover via a pressurised hose.

Summary of results from Hoop 1 Spill 2

- Oil layer detected during both stationary and moving transits.
- Oil thickness of about 5 cm was determined during both stationary and moving transits.
- Both the undulating nature of the ice bottom and the levelling effect of the oil surface covering the sea ice can be seen during the transit of the trolley under Hoop 1.
- More of acoustic energy is reflected when the sea ice bottom is contaminated with oil.
- The 5 MHz transducer could not see through the oil to the ice bottom.

Description	Detect ice bottom				Detect oil at bottom of ice				Detect oil thickness				Detect encapsulated oil			
	5 MHz	1 MHz	0.5 MHz	0.3 MHz	5 MHz	1 MHz	0.5 MHz	0.3 MHz	5 MHz	1 MHz	0.5 MHz	0.3 MHz	5 MHz	1 MHz	0.5 MHz	0.3 MHz
Pre oil release	✓	✓	✓	✓	---	---	---	---	---	---	---	---	---	---	---	---
Post spill release	✓	✓	✓	✓	✓	✓	✓	✓	X	✓	✓	✓	---	---	---	---
After oil encapsulation	---	---	---	---	---	---	---	---	---	---	---	---	---	---	---	---

Grey: Not applicable to the data gathered.
 Green: Success
 Red: Failure
 Amber: Success, but with caveats.

Results:

The following results are based on three acoustic surveys. One before the oil spill occurred, one after the oil spill, and a moving survey of Hoop 1 on the day following the oil release. A summary is as follows:

1. Pre-oil spill: 04-Dec-2014 10:00:00
Oil introduced: 04-Dec-2014 10:37
2. Post-oil spill: 04-Dec-2014 11:00:00
3. Moving survey 05-Dec-2014 10:00:00

The pre and post oil spill dataset is the result of a three-minute recording that was processed to provide average acoustic return for this period. The exception is the moving survey, which is a visualisation of the raw data only.

The raw data from the 300-second record of the four transducers, after the oil was deployed, can be seen in Figure 23. This figure shows that one can clearly identify the signal from both the ice bottom (oil-ice interface) and the bottom of the oil (water-oil interface) in all transducers other than the 5 MHz.

Figure 24 shows the average acoustic return from the 4 transducers. The blue line represents the return about 30 minutes before the oil was deployed. The black line displays the return after the oil was deployed. In all cases, other than the 5 MHz transducer, there is a clear return from the water-oil interface (first peak), and another return from the oil-ice interface (second peak). This second peak is located directly over the original ice bottom signal (in blue), which suggests that the sound-speed of seawater and oil are very similar.

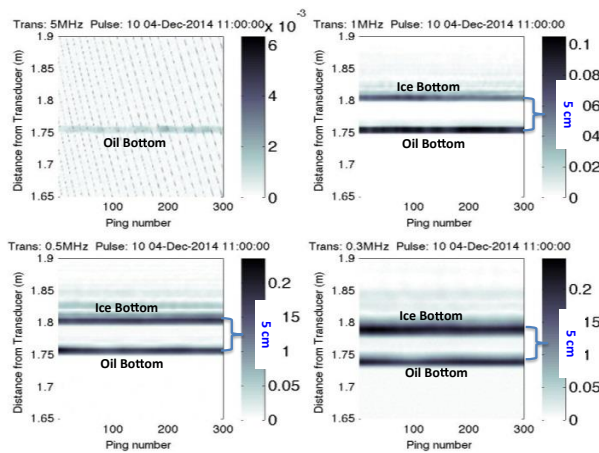


Figure 23. Plot of the raw acoustic signal over the 300 second record of the four transducers 30 minutes after the oil release. In all cases, other than the 5 MHz transducer, both the ice and the oil bottom can be clearly seen. The 5 MHz can only see the oil bottom.

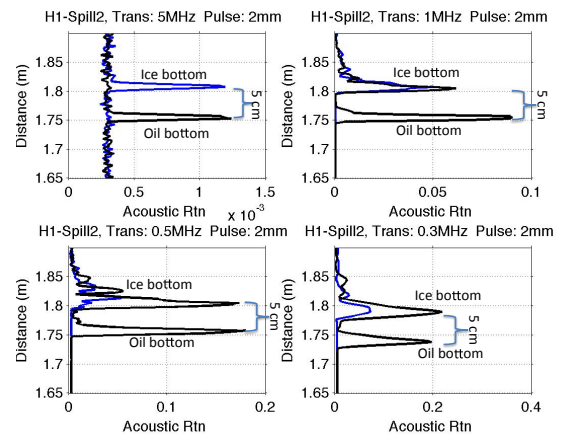


Figure 24. Plot of the average acoustic signal seen by the four transducers, both pre (blue line) and post (black line) oil deployment. In all cases, other than the 5 MHz transducer, both the ice bottom and the oil bottom can be clearly seen.

Based on the data within Figure 23 and Figure 24 we can see that the oil above the transducers is about 5 cm thick. The thickness of the oil corresponds to the distance between the ice-oil return and the water-oil return.

Importantly we see a similar result when the trolley performed a complete scan under Hoop 1. As the trolley moved under Hoop 1 all four transducers of the AQUAscat system recorded at 1 Hz. The results can be seen in Figure 25. Both the undulating nature of the ice bottom as well as the level spread of the oil can be clearly seen.

This is a significant result and this output is similar to what would be expected from a system mounted on an Autonomous underwater vehicle or remotely operated vehicle. It is also important to remember that this is the raw data and no processing has been applied to this data.

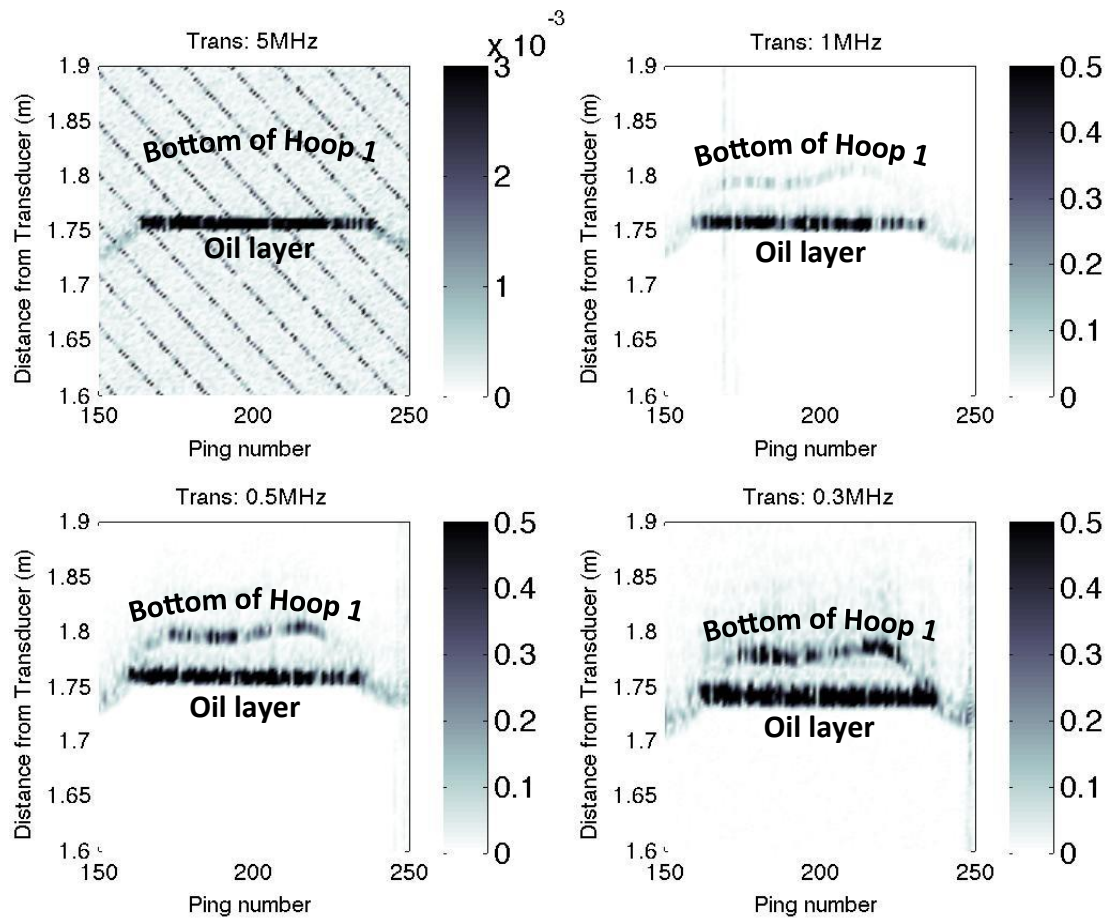


Figure 25. Plot of the raw acoustic signal from the four transducers during transit of Hoop 1. The transit was performed about a day after the oil release. In all cases, other than the 5 MHz transducer, both the ice and the oil bottom can be clearly seen. The 5 MHz can only see the oil bottom.

Hoop 2

Solid ice sheet

Oil spill date/time: 12-Nov-14 13:39

Oil located on bottom of ice

Hoop 2: Solid ice sheet

Oil spill date/time: 12-Nov-14 13:39

Ice conditions:

The ice conditions comprised of continuous ice cover. Due to the subsequent ice growth (of about a month), the no evidence of the frazil and broken ice blocks that made up the initial ice cover was evident. Ice bottom was essentially level.

Ice Draft: ~15 cm (as seen by sonar)

Oil Spill:

The oil was released from below the ice cover via a pressurised hose.

Summary of results from Hoop 2

- Oil layer below sea ice detected
- Oil thickness was about 1 cm
- More of acoustic energy is reflected when the sea ice bottom is contaminated with oil.
- The 5 MHz transducer did not see through the oil to the ice bottom.

Description	Detect ice bottom				Detect oil at bottom of ice				Detect oil thickness				Detect encapsulated oil			
	5 MHz	1 MHz	0.5 MHz	0.3 MHz	5 MHz	1 MHz	0.5 MHz	0.3 MHz	5 MHz	1 MHz	0.5 MHz	0.3 MHz	5 MHz	1 MHz	0.5 MHz	0.3 MHz
Pre oil release	✓	✓	✓	✓	---	---	---	---	---	---	---	---	---	---	---	---
Post spill release	✓	✓	✓	✓	✓	✓	✓	✓	X	✓	✓	✓	---	---	---	---
After oil encapsulation	---	---	---	---	---	---	---	---	---	---	---	---	---	---	---	---

Grey: Not applicable to the data gathered.

Green: Success

Red: Failure

Amber: Success, but with caveats.

Results:

The AQUAscat system was activated about 10 minutes before the deployment of oil, and continued logging for about 50 minutes after the spill (total file length 60 minutes). During this time all transducers were activated and the system recorded data every second. A summary is as follows:

- 13:29 AQUAscat turned on
 - 5 MHz, 1 MHz, 0.5 MHz, 0.3 MHz transducers active
 - Sampling frequency: 1 Hz (ping every second)
 - Pulse length: 10 mm
- **13:39 Oil released under the ice**
- 14:29 AQUAscat stopped logging.

Figure 26 displays the raw data during this one-hour period. Importantly this figure clearly shows the single return before the oil was deployed and the classic train-track dual return after the oil was injected.

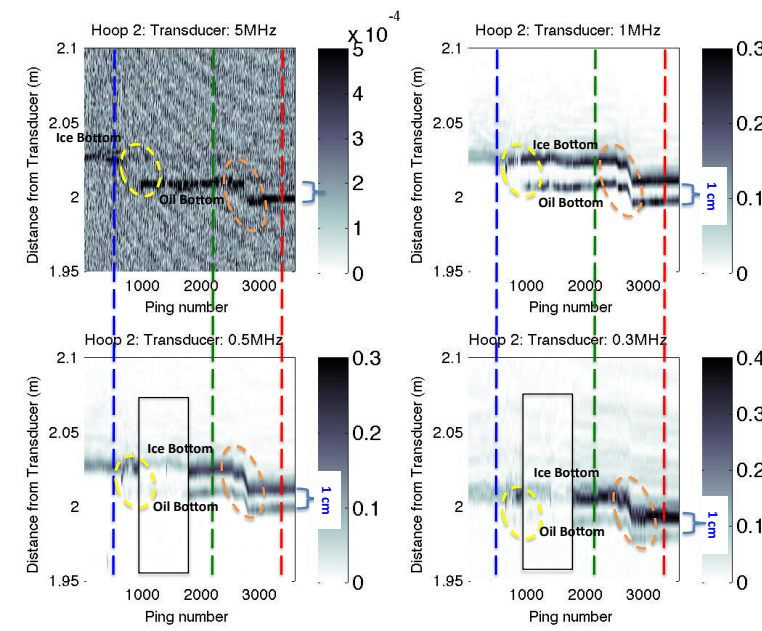


Figure 26. One hour time series displaying the raw output from the 5 MHz (top left), 1 MHz (top right), 0.5 MHz (bottom left), 0.3 MHz (bottom right) transducers. Main features are:

Blue dotted vertical line: Just before the oil was released. Single return from ice bottom

Yellow circle: Release of the oil under the sea ice. Gradual increase in oil thickness, i.e. dual return.

Green dotted vertical line: About 25 minutes after the spill (see next figure).

Red dotted vertical line: About 45 minutes after the initial spill (see next figure).

Back rectangles: Time period the 0.5 MHz and 0.3 MHz channels experienced some interference, which reduced the amplitude of the return signal for this period.

Orange circle: Downward shift of 1-2 cm in the location of the water-oil and the oil-ice interface.

Figure 27 shows results of the average acoustic profile from the 1 MHz transducer. This figure displays the acoustic return before the oil was deployed (blue), 25 minutes after the oil was deployed (green), and 45 minutes after the oil was deployed (red). These plots relate the dotted lines of the same colour in the previous Figure 26.

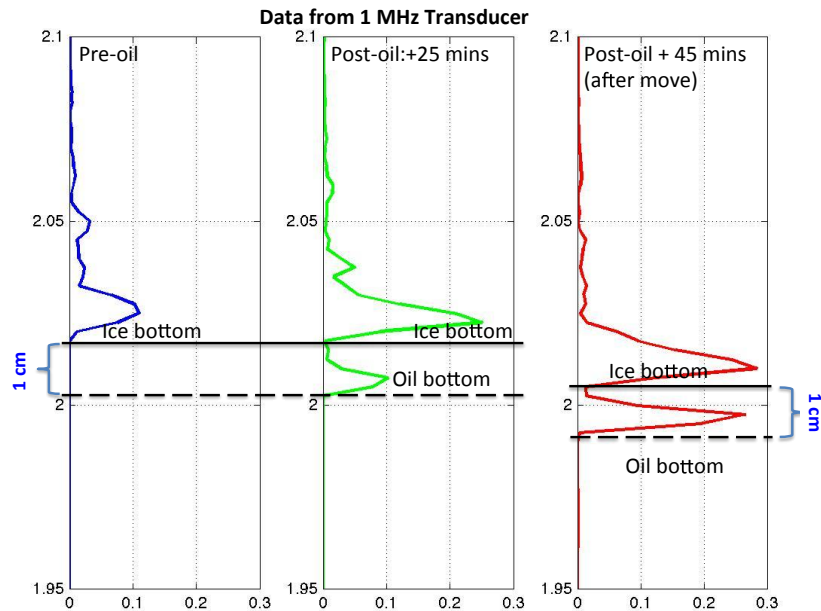


Figure 27: These profiles are from the 1 MHz transducer. This figure shows the acoustic return before the oil was deployed (blue), 25 minutes after the oil was deployed (red), and 45 minutes after the oil was deployed. Colour of the acoustic profiles relate to dotted lines in previous Figure 26.

Stepping through this figure we can clearly see the location of the ice bottom, at about 2.01 m from the transducer, before the oil was spilled. The amplitude of this return is about 0.1. After the oil was deployed (green) we see a larger return (0.27) at the same location at the ice bottom (the oil-ice interface), and a second return starting at about 2.00 m (the water-oil interface). If one assumes the same sound speed for oil and seawater we have an oil thickness above the sonar of about 1 cm.

The red trace (far left) is the acoustic return 45 minutes after the oil was spilt. The trace is almost identical to the green trace (taken 20 minutes earlier) except the whole plot is shifted downwards by about a centimetre.

Hoop 3

Solid ice sheet

Oil spill date/time: 17-Nov-14 13:24

Oil located on bottom of ice

Hoop 3: Solid ice sheet

Oil spill date/time: 17-Nov-14 13:24

Ice conditions:

The ice conditions comprised of continuous ice cover.

Ice Draft: ~ 27 cm (as seen by sonar)

Oil Spill:

The oil was released from below the ice cover via a pressurised hose.

Summary of results from Hoop 3

- Results suggest oil was encapsulated.
- Encapsulated oil layer detected by 1 MHz, 0.5 MHz, and 0.3MHz transducers.
- Encapsulated oil thickness above transducers was about 2 cm.
- The 0.3MHz transducer could see the encapsulated oil the greatest distance into the ice. This was about 5 cm.
- The 5 MHz transducer could see ice bottom, but not encapsulated oil.
- More of acoustic energy from the low frequency transducers entered the system.

Description	Detect ice bottom				Detect oil at bottom of ice				Detect oil thickness				Detect encapsulated oil			
	5 MHz	1 MHz	0.5 MHz	0.3 MHz	5 MHz	1 MHz	0.5 MHz	0.3 MHz	5 MHz	1 MHz	0.5 MHz	0.3 MHz	5 MHz	1 MHz	0.5 MHz	0.3 MHz
Pre oil release	---	---	---	---	---	---	---	---	---	---	---	---	---	---	---	---
Post spill release	---	---	---	---	---	---	---	---	---	---	---	---	---	---	---	---
After oil encapsulation	✓	✓	✓	✓	---	---	---	---	X	✓	✓	✓	X	✓	✓	✓

Grey: Not applicable to the data gathered.

Green: Success

Red: Failure

Amber: Success, but with caveats.

Results:

Due to a communication error within the cable connecting the AQUAscat system (see page 11 for more details) we were not able to collect data during the release of oil under Hoop 3. We did however collect 15 continuous hourly data snapshots about two days after the spill, from 19th November at 17:00 to the 20th November at 08:00. During this time all transducers were activated for a three-minute window at the start of each hour. A summary is as follows:

- **17-November 13:24 Oil released under the ice**
- 19-November 17:00:00. AQUAscat programmed for hourly sampling
 - Total time elapsed since spill: 52 hours
 - 5 MHz, 1 MHz, 0.5 MHz, 0.3 MHz transducers active
 - Sampling frequency: 1 Hz (ping every second) for 3 minutes.
 - Pulse length: 10 mm
- 20-November 08:00:00: Trolley moved away from being under Hoop 3.
 - Total time elapsed since spill: 67 hours

The following discussion is based upon the 15 hourly records that were obtained about two days after the oil release. Figure 28 shows this time series, from 17:00 on the 19th to 08:00 on the 20th, from each transducer. Interestingly all transducers, other than the 5 MHz, see a stripped pattern to the acoustic time-series. We have previously seen this type of acoustic return when ice begins to form below the spilled oil. This process is known as the encapsulation of the oil.

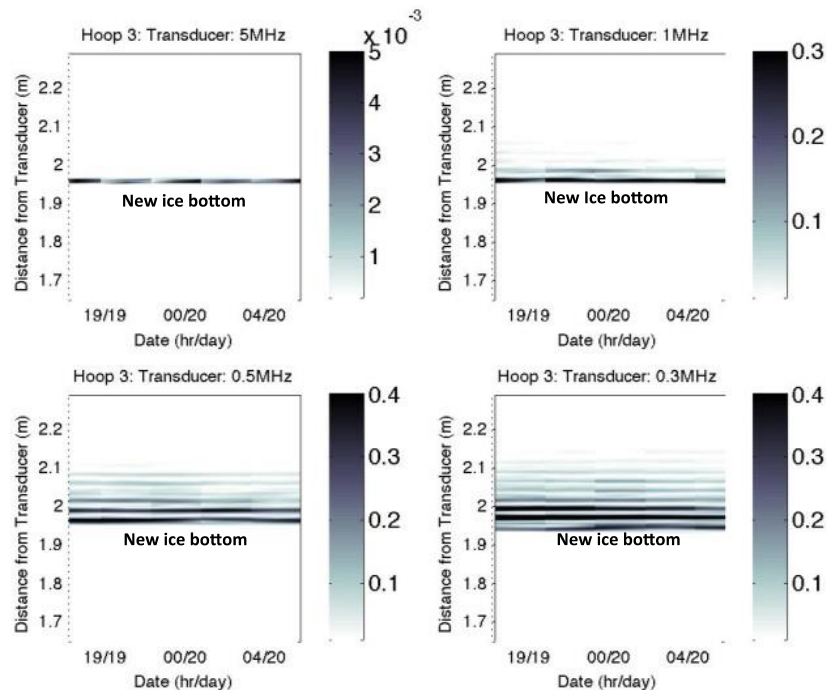


Figure 28. Time-series of acoustic returns under Hoop 3, from 17:00 on the 19th November to 08:00 on the 20th November. This figure displays the output from the 5 MHz (top left), 1 MHz (top right), 0.5 MHz (bottom left), 0.3MHz (bottom right) transducers.

The acoustic return that generates this stripped pattern can be seen more clearly in Figure 29. The figure was obtained by calculating the average return, for each transducer, over the combined 15 hours period. The series of peaks and troughs shown in Figure 29 is most likely due to a combination of the different reflection possibilities available to encapsulated oil.

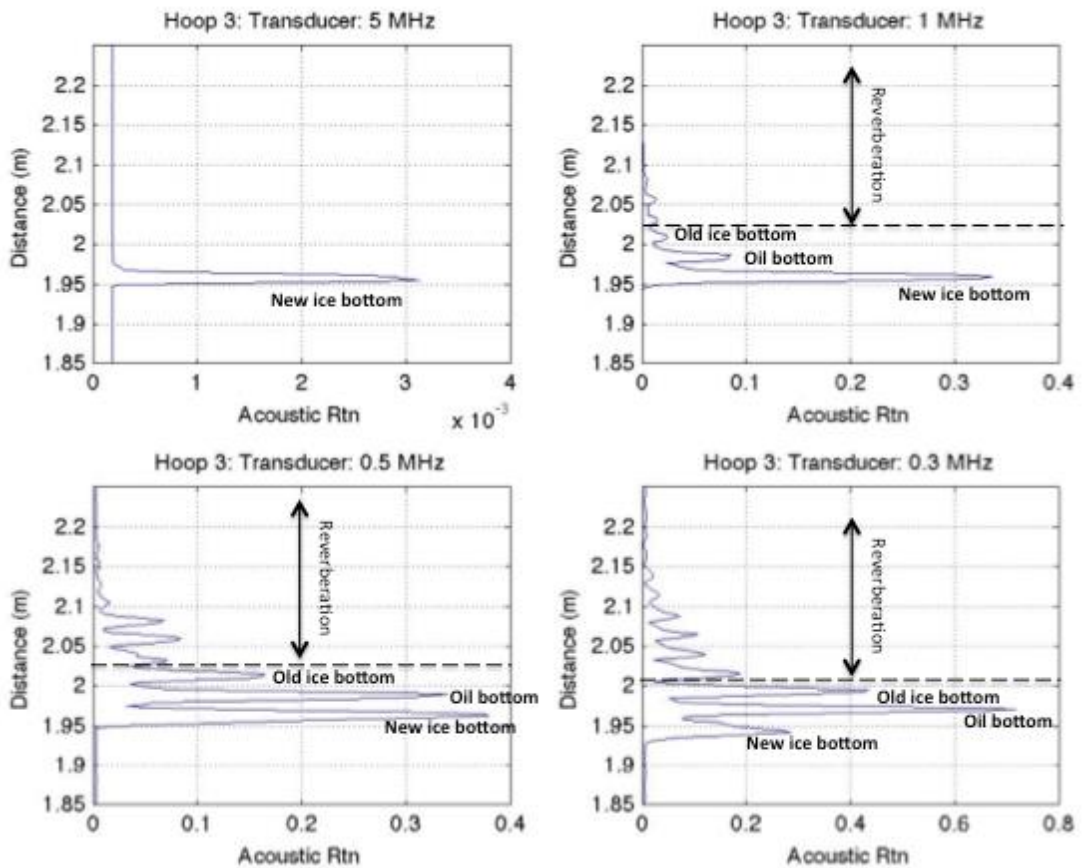


Figure 29. This figure displays the mean Acoustic return for the 5 MHz (top left), 1 MHz (top right), 0.5 MHz (bottom left), 0.3MHz (bottom right) transducers. Full time series can be seen in Figure 28.

If we ignore the ice-air interface we can assume we have a 3-layer system. The layers being:

- Layer 1: newly formed sea ice layer which has grown below the oil,
- Layer2: the oil layer itself, and
- Layer 3: the original sea ice that was present before the oil was released.

This 3-layer system provides the possibilities of numerous reflection points due to the acoustic impedance mismatch between seawater, sea ice and oil. The schematic in Figure 30 summarizes some of the reflection possibilities for encapsulated oil.

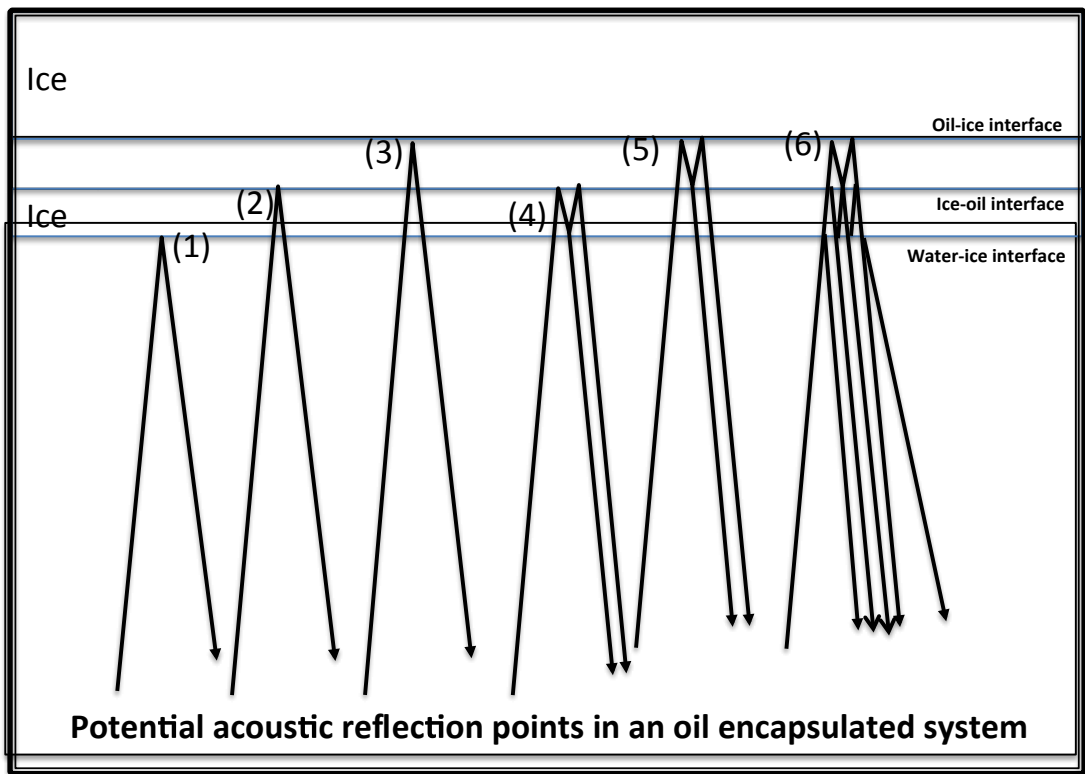


Figure 30 Cartoon showing the potential acoustic reflection points for oil that encapsulated within sea ice

These possibilities shown within Figure 30 are described in detail below:

- 7) Water-ice interface: The reflection from the bottom of the new ice that has formed below the oil.
- 8) Ice-oil interface: The reflection from the top of the new ice that has formed below the oil.
- 9) Oil-ice interface: The reflection from the bottom of the original sea ice that was present before the oil was released.
- 10) Internal reflections, new ice: The reverberation that is possible between the top and bottom of the ice that has formed below the oil, i.e. between the water-ice interface and the ice-oil interface.
- 11) Internal reflections, oil: The reverberation that is possible between the top and bottom of the oil layer i.e. between the ice-oil interfaces and the oil-ice interface.
- 12) Combination of potential reflections: This shows the possible combinations of the above mentioned reflection possibilities.

The combination of reflections from the different interfaces is the most likely reason why we see a series of peaks and troughs in the 1 MHz, 0.5MHz and 0.3 MHz transducers. The lower frequency transducers have the most penetration and hence reflections. Multiple reflections are not possible within the 5 MHz due to the high attenuation rates at this frequency. The 5 MHz transducer just sees a reflection for the water-ice interface.

Figure 31 shows an example of the acoustic return from 0.3 MHz transducer. Each peak has been identified with a red line and the location and distance between peaks are summarised in

Table 11. It is important to remember that the sound speed has not been altered to allow for difference in speed in the sea ice, oil and seawater.

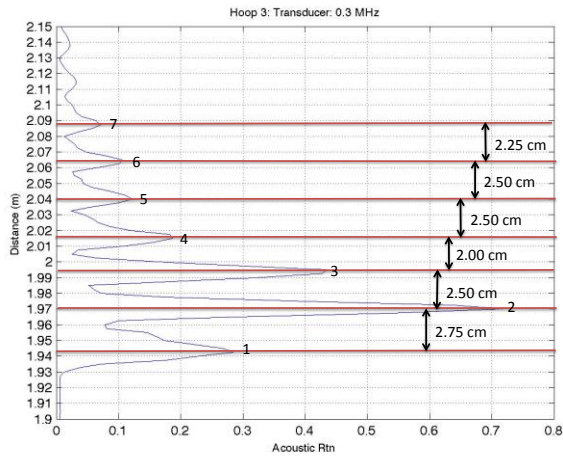


Figure 31 Average acoustic return, calculated from returns obtained between 17:00 on the 19th November and 08:00 on the 20th November, for the 0.3 MHz transducer. Each peak has been identified with a read line.

Peak Number	Location of max peak (m)	Distance between peaks (m)
Peak 1	1.9425	
Peak 2	1.9700	0.02750 (P1-P2)
Peak 3	1.9950	0.02250 (P2-P3)
Peak 4	2.0150	0.02200 (P3-P4)
Peak 5	2.0400	0.02250 (P4-P5)
Peak 6	2.0650	0.02250 (P5-P6)
Peak 7	2.0875	0.02225 (P6-P7)

Table 11. Table showing the location and distance between each separate peak seen by the 0.3 MHz Transducer (see accompanying Figure 31).

Hoop 4

Solid ice sheet

Oil spill date/time: 20-Nov-14 12:45

Oil located on bottom of ice

Oil encapsulation

Hoop 4: Solid ice sheet

Oil spill date/time: 20-Nov-14 12:45

Ice conditions:

The ice conditions comprised of continuous ice cover.

Ice Draft: ~ 27 cm (as seen by sonar)

Oil Spill:

The oil was released from below the ice cover via a pressurised hose. The deployment occurred in a number of stages.

Summary of results from Hoop 4

- Oil layer detected
- Oil thickness above transducers was about 4 cm.
- More of acoustic energy is reflected when the sea ice bottom is contaminated with oil.
- The 5 MHz transducer did not see through the oil to the ice bottom.
- Only the 0.3 MHz transducer could detect encapsulated oil through 5 cm of ice.

Description	Detect ice bottom				Detect oil at bottom of ice				Detect oil thickness				Detect encapsulated oil			
	5 MHz	1 MHz	0.5 MHz	0.3 MHz	5 MHz	1 MHz	0.5 MHz	0.3 MHz	5 MHz	1 MHz	0.5 MHz	0.3 MHz	5 MHz	1 MHz	0.5 MHz	0.3 MHz
Pre oil release	✓	✓	✓	✓	---	---	---	---	---	---	---	---	---	---	---	---
Post spill release	X	✓	✓	✓	✓	✓	✓	✓	X	✓	✓	✓	---	---	---	---
After oil encapsulation	X	✓	✓	✓	✓	✓	✓	✓	X	✓	✓	✓	X	✓	✓	✓

Grey: Not applicable to the data gathered.
 Green: Success
 Red: Failure
 Amber: Success, but with caveats.

Results:

The Hoop 4 release was particularly interesting as this Hoop was followed for almost two weeks. As a result the AQUAscatter was able to obtain hourly 3 minute snapshots from a couple of hours before the spill on 20-Nov-2014 11:00:00, through to 12 days after the spill 01-Dec-2014 10:00:00. A summary is as follows:

- AQUAscatter programmed for hourly sampling
 - 5 MHz, 1 MHz, 0.5 MHz, 0.3 MHz transducers active
 - Sampling frequency: 1 Hz (ping every second) on the hour for 3 minutes.
 - Pulse length: 10 mm
- 20-November, 11:00:00. Pre-oil release survey
- **20-November, 14 12:45. Oil released under the ice**
- Continuous hourly monitoring of acoustic returns
- 01-December, 10:00:00. Last hourly data under Hoop 3.

During this 12-day period the sea ice grew about 10 cm, from 1.97 m above the transducers to 1.87 m (see Figure 32). As a result the experiment within this Hoop represents an ideal opportunity to explore the encapsulation of oil and the acoustic signature during this process. It also allows us to determine the present limitations of the different transducer frequencies regarding the detection of encapsulated oil using acoustics.

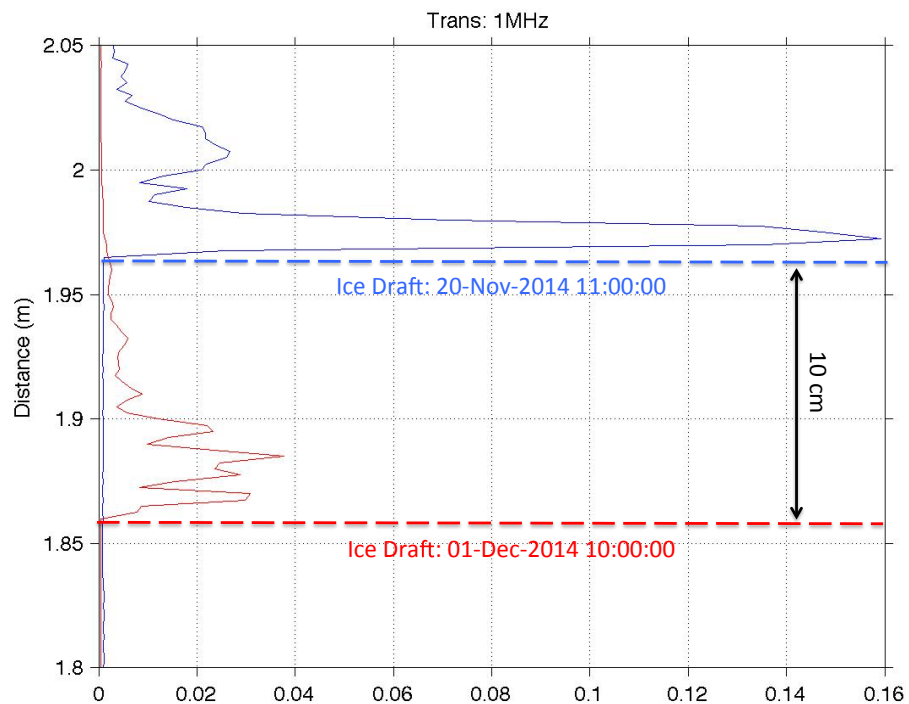
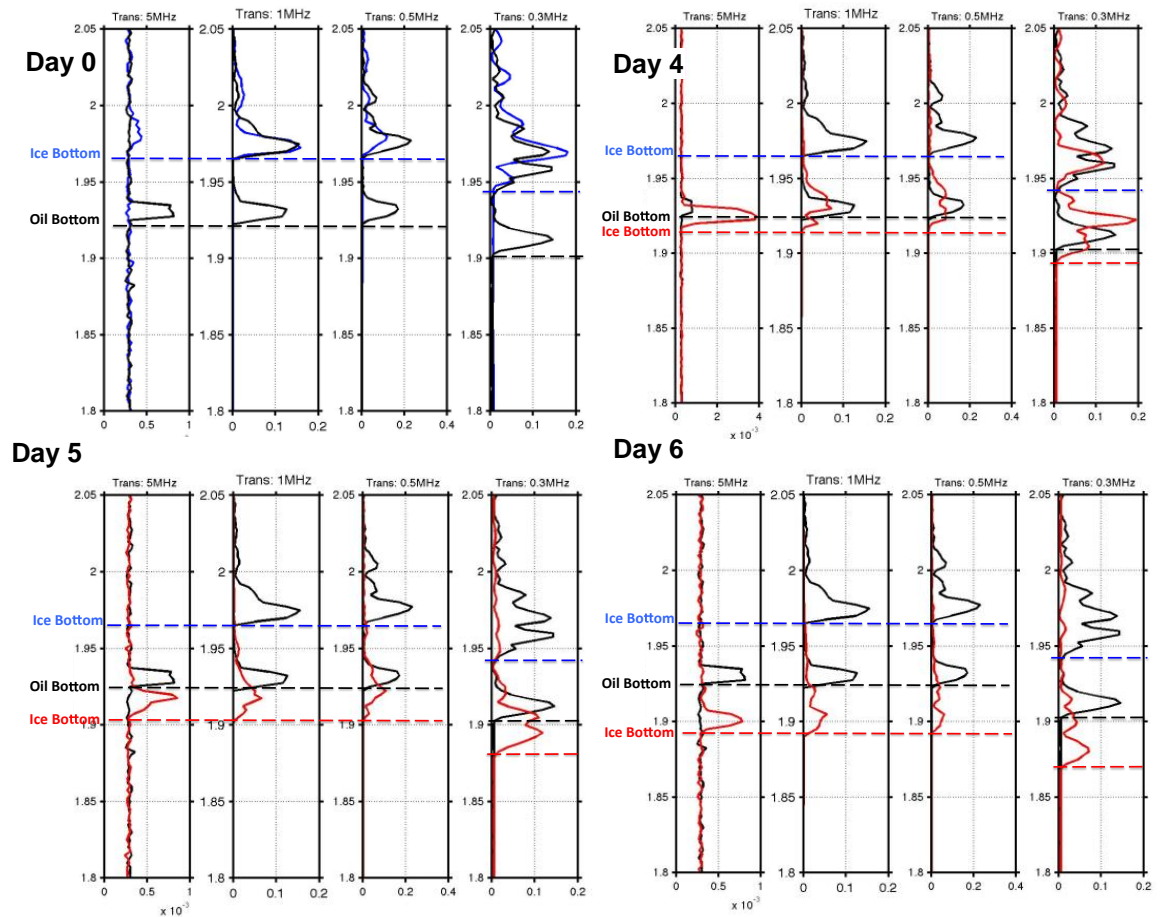


Figure 32. Ice draft as seen by the location of the bottom of the sea ice in the 1 MHz transducer. Blue dotted line represents the location of the water-ice interface on 20 November. Red dotted line represents location of the water-ice interface on 20 November.

Oil detection and encapsulation.

The following figure (Figure 33) shows the acoustic return from Hoop 4 at various times over a seven-day period. From just before the oil was deployed, to when the oil began to be encapsulated (day 4), to a week after the release (Day 7). A more detailed description can be found below Figure 33.



Day 0

Day 4

Day 5

Day 6

Day 7

Figure 33. Acoustic returns under Hoop 4

Top Right (Day 0). Blue trace shows the location of the ice bottom before the oil was deployed. The black line shows the location of the oil and ice bottom 6 hours after release.

Top Left (Day 4). The black line shows the location of the oil and ice bottom 6 hours after release. Red trace acoustic return from 102 hrs (Day 4: 24 Nov 18:00) after release.

Top Left (Day 5). The black line shows the location of the oil and ice bottom 6 hours after release. Red trace acoustic return from 126 hrs (Day 4: 25 Nov 18:00) after release.

Top Left (Day 6). The black line shows the location of the oil and ice bottom 6 hours after release. Red trace acoustic return from 150 hrs (Day 4: 26 Nov 18:00) after release.

Top Left (Day 7). The black line shows the location of the oil and ice bottom 6 hours after release. Red trace

acoustic return from 174 hrs (Day 4: 27 Nov 18:00) after release.

Detailed description of Figure 33.

Day 0: Oil was released under the ice at 12:45 pm. Before this release, the classic single-peak acoustic return from the ice bottom (blue trace) is observed; however, after the release, a two-peak return (black line) is detected. The first return (at 1.92 m) is the return from the bottom of the oil (water/oil interface), the second return (at 1.96 m) is from the ice bottom. The location of the ice bottom before (peak in blue line) and after the oil release (second peak in black line) is the same. This suggests that the oil and seawater have similar sound speeds.

Day 4: The first evidence of ice growth after the oil release occurred in Day 4. This can be seen by the first acoustic return in the red trace (Day 4: 102 hrs. after release), located slightly closer to the transducer head (about a centimeter) than the first acoustic return in the black trace (Day 0: 6 hrs. after release). This difference is due to ice forming below the oil layer, and therefore the sound hitting this “new” ice bottom first. From this figure, it looks like about 1 cm of ice has formed below the oil. This small amount of ice grown below the oil masks the acoustic from the original ice bottom from all transducers except the 0.3 MHz. The 0.3 MHz still obtains a clear return from the original ice bottom. Thus, as expected, the lower frequencies are able to penetrate the ice further.

The returns from the other transducers also showed noteworthy features. For example, the 5 MHz transducer showed a significant increase in acoustic return (peak height), whilst the 1 MHz and the 0.5MHz saw an increase in the width of the return peak. The increase in the width is particularly significant, as it suggests that we are receiving returns from the ice bottom (water/ice) and the ice top (ice/oil), of the ice that has grown below the oil. Taken together the resultant is a wider return to the acoustic reflection seen by the transducer.

Day 5: The ice that formed below the oil continued to grow during Day 5 and reached just over 2 cm below the location of the oil bottom (difference between the location of the red peak and black peak). Whilst there still was a slight increase in acoustic energy seen by the 0.3MHz transducer near the location of original ice bottom, it certainly is not as clear as in Day 4. This would suggest that the experimental conditions are near the limit of this system to detect oil encapsulated under sea ice through a clear return from the three interfaces involved, i.e. water/ice, ice/oil, and oil/ice. The AQUAscat system is of a relatively low power and thus better signal penetration with a higher-powered instrument would be expected.

Day 6: The rate of ice growth increased, and the acoustic returns obtained during Day 6 suggest that the ice was located about 4 cm below the location of the oil bottom (difference between the location of the red peak and black peak). No clear evidence of the encapsulated oil can be seen in the acoustic return.

Day 7: The ice below the bottom of the oil was about 5 cm. No clear evidence of the encapsulated oil can be seen.

A summary of the acoustic returns seen by the four transducers for the period of 21 November to 1 December can be seen in the figure below. During this time the oil was completely encapsulated by about 12 cm of ice.

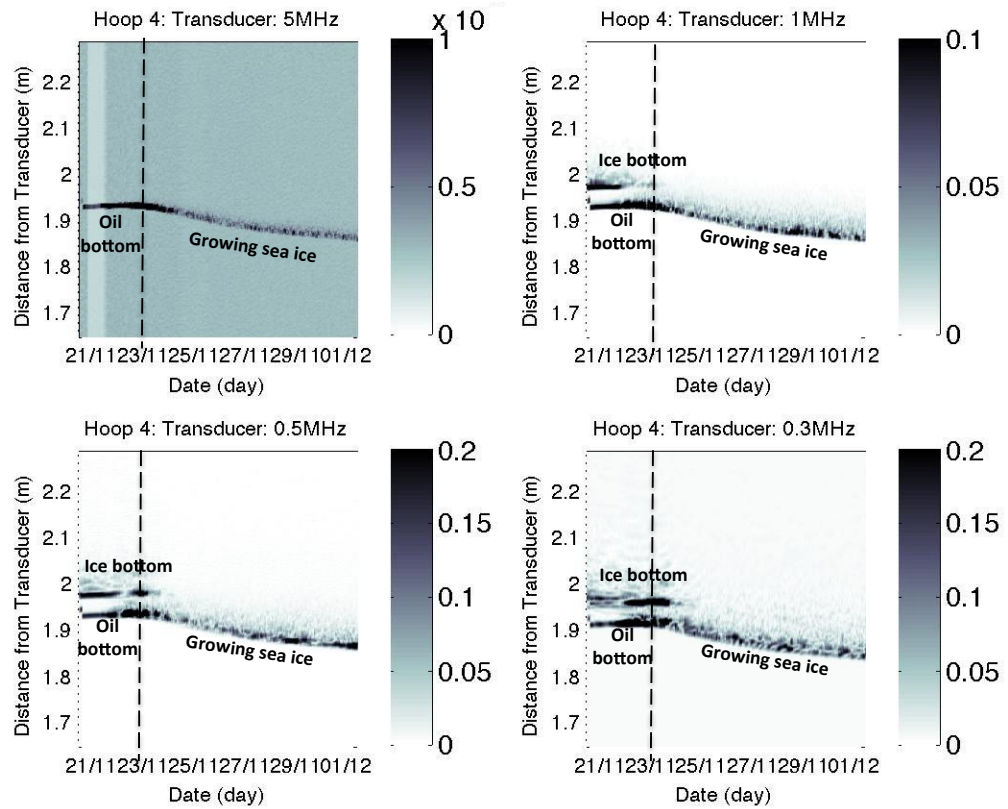


Figure 34 Time series of the raw acoustic returns from 21 November to 1 December. The black dotted line represents when the oil began to be encapsulated by the growing sea ice.

Hoop 5

Solid ice sheet

Oil spill date/time: 9-Dec-14 11:40

Oil located on bottom of ice

Hoop 5: Solid ice sheet

Oil spill date/time: 9-Dec-14 11:40

Ice conditions:

The ice conditions comprised of continuous ice cover.

Ice Draft: ~ 51 cm (as seen by sonar)

Oil Spill:

The oil was released from below the ice cover via a pressurised hose.

Summary of results from Hoop 5

- Oil layer detected
- Oil thickness above transducers was about 6 cm
- The 5 MHz transducer did not see through the oil to the ice bottom.

Description	Detect ice bottom				Detect oil at bottom of ice				Detect oil thickness				Detect encapsulated oil			
	5 MHz	1 MHz	0.5 MHz	0.3 MHz	5 MHz	1 MHz	0.5 MHz	0.3 MHz	5 MHz	1 MHz	0.5 MHz	0.3 MHz	5 MHz	1 MHz	0.5 MHz	0.3 MHz
Pre oil release	✓	✓	✓	✓	---	---	---	---	---	---	---	---	---	---	---	---
Post spill release	X	✓	✓	✓	✓	✓	✓	✓	X	✓	✓	✓	---	---	---	---
After oil encapsulation	---	---	---	---	---	---	---	---	---	---	---	---	---	---	---	---

Grey: Not applicable to the data gathered.

Green: Success

Red: Failure

Amber: Success, but with caveats.

Results:

The results from this particular hoop were mixed. High quality data was obtained just before and just after the oil release, however beyond this time photographic evidence suggests that the resultant dataset was contaminated due to the continued release of air trapped within the trolley. Consequently we show results just before and after the spill occurred. A summary is as follows:

- AQUAscot programmed for hourly sampling
 - 5 MHz, 1 MHz, 0.5 MHz, 0.3 MHz transducers active
 - Sampling frequency: 1 Hz (ping every second) on the hour for 3 minutes.
 - Pulse length: 10 mm
- 09-December, 11:00:00. Pre-oil release survey
- **09-December, 11:40:00. Oil released under the ice**
- 09-December, 12:00:00. Post-oil release survey
- Trolley parked under Hoop 5 during this time

For the Hoop 5 oil release the trolley was parked under the centre of the hoop. At 11:00, 40 minutes before the oil was spilled, we recorded the acoustic return from the four transducers. The blue line in Figure 35 shows the results before this release. Again we see a single-peak acoustic return from the ice bottom (blue trace). About 20 minutes after the release a second survey was conducted. The results are also plotted in Figure 35. Here we clearly see a two-peak return (black line). The first return (at 1.65 m) is the return from the bottom of the oil (water-oil interface), the second return (at 1.71 m) is difference between the two, 6 cm, is the thickness of the oil located under the transducer.

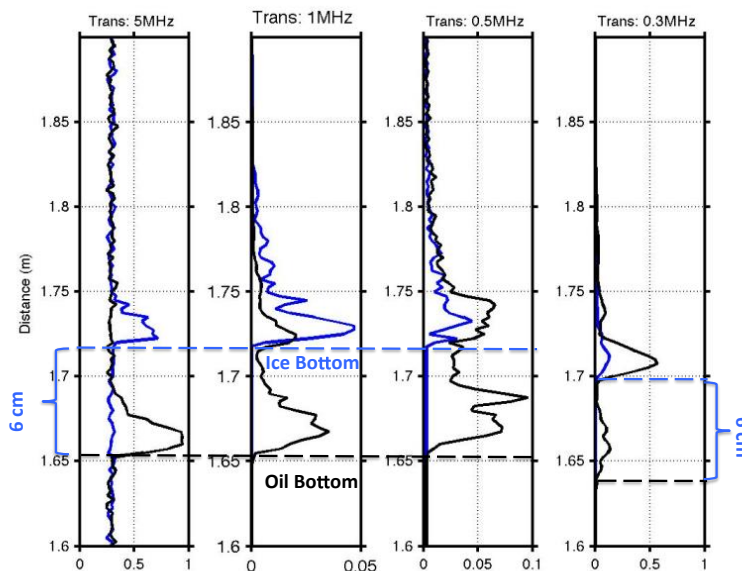


Figure 35 Blue trace shows the location of the ice bottom before the oil was deployed. The black line shows the location of the oil and ice bottom after the oil release. The difference between the two is the oil thickness, which is about 6 cm.

Hoop 6

Solid ice sheet

Oil spill date/time: 6-Jan-15 13:50

Oil located on bottom of ice
Vertical Oil migration through the ice

Hoop 6: Solid ice sheet

Oil spill date/time: 6-Jan-15 13:50

Ice conditions:

The ice conditions comprised of continuous ice cover.

Ice Draft: ~ 63 cm (as seen by sonar)

Oil Spill:

The oil was released from below the ice cover via a pressurised hose.

Summary of results from Hoop 6

- Oil layer detected
- Oil thickness above transducers was initially 9 cm, but reduced to 2 cm due to the upward migration of the oil.
- The reduction of oil thickness was continuously monitored during the oil migration phase.
- The 5 MHz transducer detected the ice bottom and oil thickness once oil migration began.

Description	Detect ice bottom				Detect oil at bottom of ice				Detect oil thickness				Detect encapsulated oil			
	5 MHz	1 MHz	0.5 MHz	0.3 MHz	5 MHz	1 MHz	0.5 MHz	0.3 MHz	5 MHz	1 MHz	0.5 MHz	0.3 MHz	5 MHz	1 MHz	0.5 MHz	0.3 MHz
Pre oil release	✓	✓	✓	✓	---	---	---	---	---	---	---	---	---	---	---	---
Post spill release	✓	✓	✓	✓	✓	✓	✓	✓	✓	✓	✓	✓	---	---	---	---
After oil encapsulation	---	---	---	---	---	---	---	---	---	---	---	---	---	---	---	---

Grey: Not applicable to the data gathered.

Green: Success

Red: Failure

Amber: Success, but with caveats.

Results:

The results from Hoop 6 are unique. This was because once the oil release had occurred the sea ice was allowed to warm. This allowed the vertical migration of the oil through the sea ices to occur. The net result was a reduction (over time) of the amount of oil under the ice. A summary is as follows:

- AQUAscat programmed for both hourly sampling as well as manual measurements:
 - 5 MHz, 1 MHz, 0.5 MHz, 0.3 MHz transducers active
 - Sampling frequency: 1 Hz (ping every second) on the hour for 3 minutes.
 - Pulse length: 10 mm (plus manual variations: 2.5 mm, 5 mm, 10 mm, 20 mm, and 40 mm).
- 06-January, 12:47:30. Pre-oil release survey
- **06-January, 13:50: Oil released under the ice**
- 06-January, 14:48:50. Start Post-oil release survey
- 08-January, 10:26:29: Moving survey of oil
- 09-February, 12:00:00. Finish of Post-oil release survey

After the oil was released but before the ice was allowed to warm a moving survey of the oil contained within Hoop 6 was performed. This was achieved by moving the trolley under the hoop, with the AQUAscat turned on. This kind of operation mimics that of an autonomous underwater vehicle. The results can be seen in Figure 36. The experiment was performed on 08-January at 10:26.

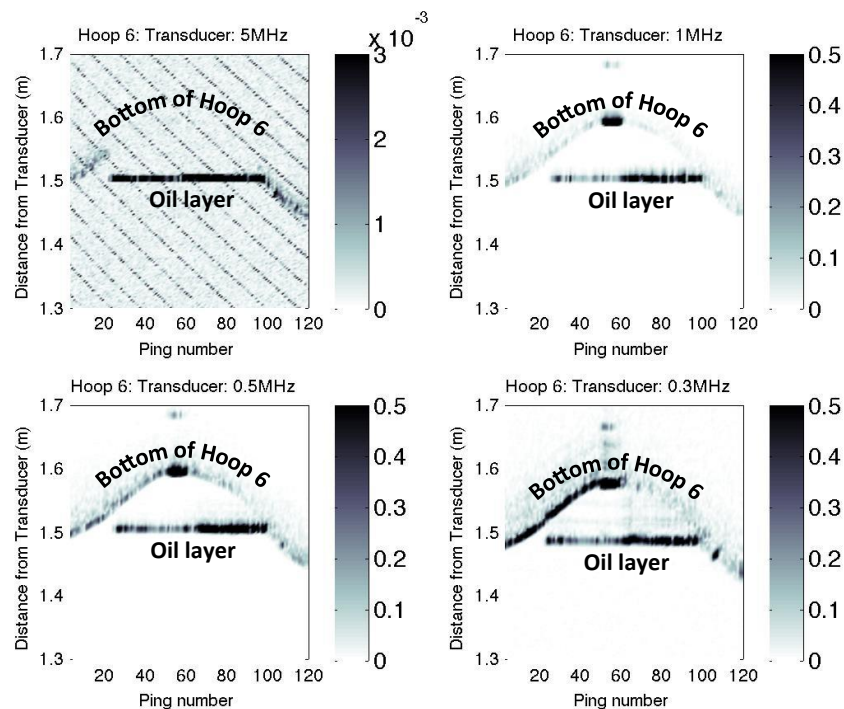


Figure 36. Raw acoustic returns from the moving trolley under Hoop 6. In all but the 5MHz both the ice bottom and the oil bottom can be clearly seen.

This figure shows the raw returns from the four transducers. In all but the 5 MHz transducer a clear return from both the bottom of the oil (water-oil interface) as well as the bottom of the ice (oil-ice interface). Only the raw returns are shown in the figure and further processing could enhance the interfaces better.

Oil migration

In order to better understand the vertical migration of oil through sea ice the freezer room was turned off and the room was allowed to warm naturally. As sea ice warms oil is able to migrate upwards, through the ice lattice, to the ice surface. Figure 37 covers the period 6 January 12:47:30 to 9 February 10:18:06. This includes the period before the oil was released, after the release, and the time the ice was warming up. Within this figure we can see the acoustic returns from both the ice bottom and the bottom of the oil. The black dotted line represents the time oil began to migrate from the bottom of the ice to the surface. This occurred from the 16th January and continued until the recording finished on the 9th February. During this time the oil under the sea ice thinned at a very consistent rate, reducing from about 9 cm to less than 2 cm.

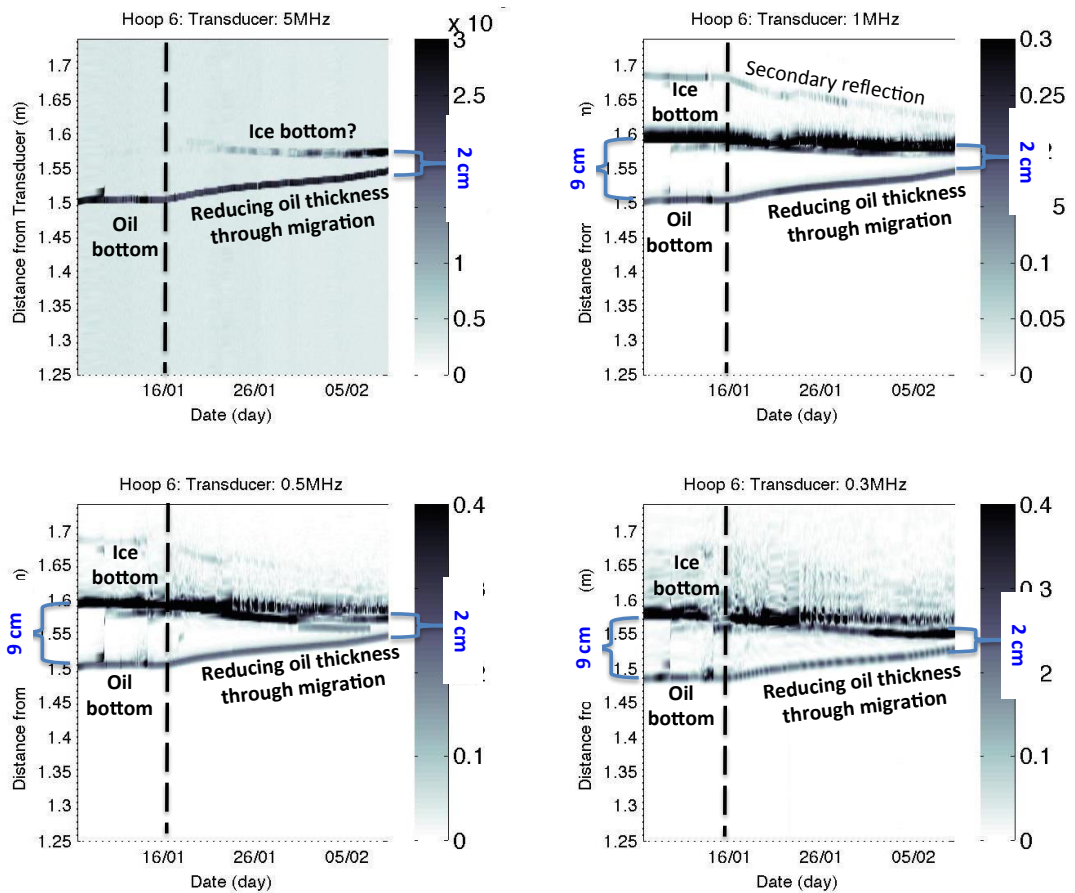
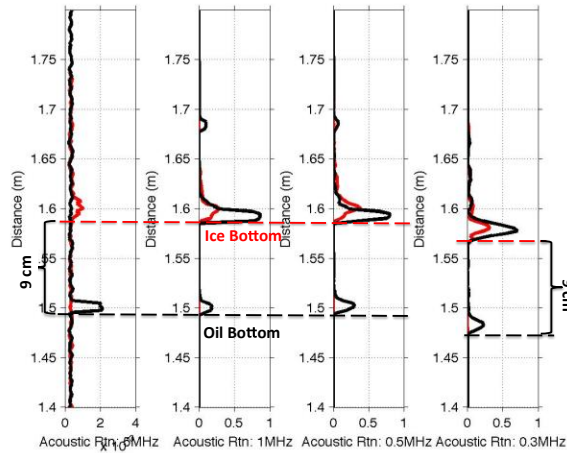


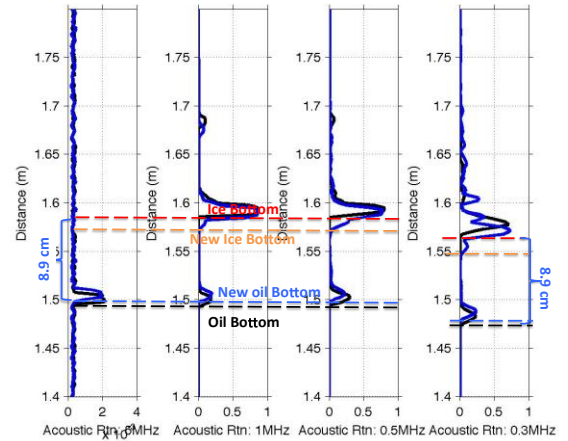
Figure 37. This figure shows the slow draining of oil under Hoop 6, from an initial thickness of about 9 cm to final thickness of around 2 cm. All transducers display this same retreat in oil thickness.

The reduction of oil thickness under Hoop 6 can be seen more clearly in Figure 38. This figure displays the acoustic return on the day of the spill (Day 0), 10 days after the spill, 20 days after the spill, 26 days after the spill and 34 days after the spill.

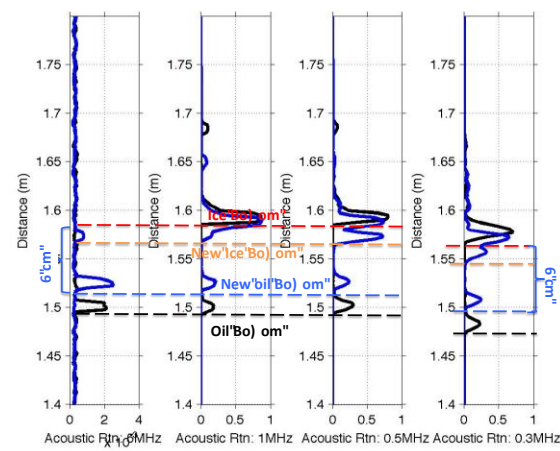
DAY 0: Red line: Pre-oil delivery: 06-Jan-2015 12:47:30
 Black line: Post-oil delivery: 06-Jan-2015 14:48:50



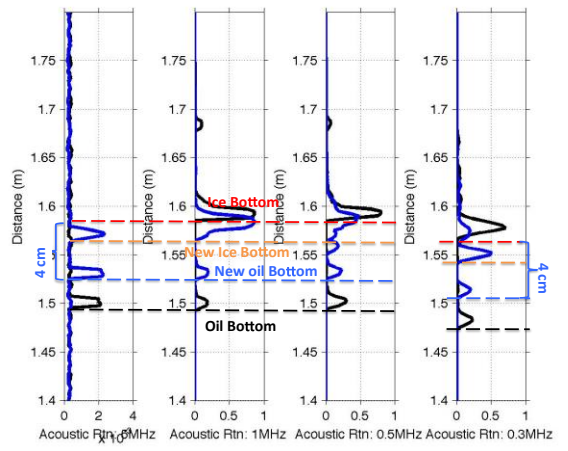
DAY 10: Black line: Post-oil delivery: 06-Jan-2015 14:48:50
 Blue line: Post-oil delivery: 16-Jan-2015 15:00:00



DAY 20: Black line: Post-oil delivery: 06-Jan-2015 14:48:50
 Blue line: Post-oil delivery: 26-Jan-2015 17:00:00



DAY 26: Black line: Post-oil delivery: 06-Jan-2015 14:48:50
 Blue line: Post-oil delivery: 01-Feb-2015 15:00:00



DAY 34: Black line: Post-oil delivery: 06-Jan-2015 14:48:50
 Blue line: Post-oil delivery: 09-Feb-2015 10:18:06



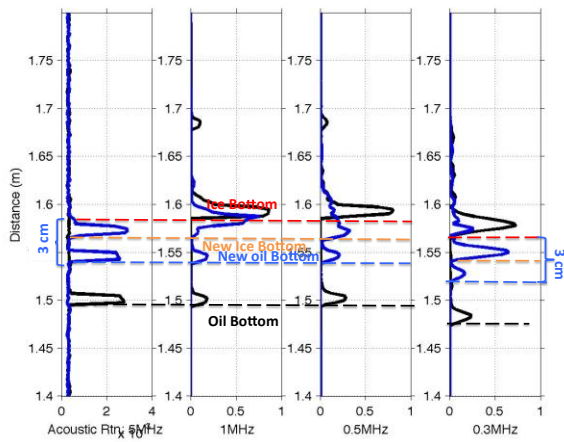
Figure 38. Mean acoustic return from the 1 MHz transducer over a 3 min recording cycle.

Top Left: Mean acoustic return before the oil release (in red) and after the oil release (in black).

Top Right: Mean acoustic return 10 days after the oil release. This plot shows the first stages of oil thickness reduction, about 0.1 cm. We also see the first stages of a new reflection just below the original ice bottom.

Middle Left: Mean acoustic return 20 days after the oil release. The oil thickness has reduced by about 3 cm. The reflection of the 'new' ice bottom has become stronger and can now be seen in the 5 MHz. Reflection from original ice bottom is still apparent,

Middle Right: Mean acoustic return 26 days after the



oil release. The oil thickness reduced by about 5 cm. The reflection of the 'new' ice bottom has become more dominant.

Bottom Left: Mean acoustic return 34 days after the oil release. The oil thickness has reduced by about 7 cm and is only 2 cm thick. Still strong return by new ice bottom.

One interesting feature of the reduction of oil under Hoop 6 was the creation of what we call a 'new' ice bottom located just below the original ice bottom (orange line in Figure 38). This secondary bottom may in fact not be ice but could be due to a layer of brine that has drained out of the warm sea ice, i.e. as the oil migrates upward, heavier brine moves downwards. This brine forms a new layer between the original ice bottom and the oil. Further investigation is needed to better understand this process.

Appendix VIII. Health and Human Safety Plan

US Army Corps of Engineers Engineer Research and Development Center
Cold Regions Research and Engineering Laboratory Hanover, New Hampshire

Health and Safety Plan

EVALUATION OF REMOTE SENSING TECHNOLOGIES TO DETECT OIL IN AND UNDER ICE

6 June 2014 - (Revised August 12, 2014)

Prepared by:
Leonard Zabilansky, P.E.
Ice Engineering Facility Manager and Civil Engineer

Evaluation of Remote Sensing Technologies to Detect Oil In and Under Ice

Reference COE and CRREL Safety SOP's Safety SOP

EM 385-1-1 September 2008

CR 200-1-1 ERDC Environmental Assessment of Activities, 24 April 2014

CRREL Ammonia Emergency Response Plan (RV-Z-8)

CRREL Emergency response plan (RV-Z-6).

Hot Work Permit (RV-Z-11)

Lock Out- Tag Out (RV-Z-13)

Prepared by: Leonard Zabilansky-IEF Manager Date

Reviewed by: Byron Young-Environmental Date

Reviewed By: Colin O'Connor-Safety Officer Date

Reviewed by: Jared Oren-ERB Supervisor Date

GLOSSARY OF TERMS

Abbreviation	Definition
AED	Automated External Defibrillator
ANS	Alaska North Slope C
COE	Corp of Engineers
CPR	Cardiopulmonary Resuscitation
CRREL	Cold Regions Research and Engineering Laboratory
SEMO	Safety and Management Office
CRZ	Contamination Reduction Zone
CZ	Control Zone
DPW	Department of Public Works
EM-SOP	Engineering Manual SOP
EPA	Environmental Protection Agency
EZ	Exclusion zone
GRF	Geophysical Research Facility
HASP	Health and Safety Plan
HSM	Health and Safety Manager
HSS	Health and Safety Specialist
IEF	Ice Engineering Facility
JHA	Job Hazard Analysis
LEL	Lower Explosive Limit
MSDS	Material Safety Data Sheets
NHDES	New Hampshire Department of Environmental Services
OSHA	Occupational Safety Health Agency
PFD	Personal flotation device
PMP	project management plan
PPE	Personal protective equipment
SSO	Site Safety Officer
SZ	Support Zone
TCLP	Toxic Characteristic and Leaching Properties
TIAC	Technical Information Analysis Center
WZ	Work Zone

GENERAL

1.1. PROJECT OVERVIEW

The project is an integrated research programme to examine and to validate the detection capability of a wide range of under, above, and on-ice remote sensing technologies in a carefully controlled laboratory setting. Laboratory investigations will take place in the Test Basin at the Cold Regions Research and Laboratory (CRREL), a unique facility consisting of a large test basin housed in a temperature-controlled environmental which allows artificial ice sheets, and corresponding environmental conditions, to be created. In addition to replicating Arctic temperature conditions, other weather events frequently encountered, including snow and fog, can also be replicated in the testing facility.

In general, the testing effort will involve the creation of an ~80cm thick artificial sea ice sheet in the Test Basin. Containment hoops with vertical curtains will be frozen into the ice to confine the crude oil as it is injected under the ice at different intervals during the two month ice growth period. The oil migration through the ice will be monitored during the one month melt out phase. A suite of sensors including underwater, surface and aerial instruments will be mounted to the underwater, main or personnel carriages in the Test Basin. The ice will be cored to characterize the crystal structure of the ice and migration of the oil through the test. Generally, the test methodology is similar to previous remote sensing of oil spills in sea ice tests conducted at CRREL in 2004, but with a different hoop configuration. To create the different test scenarios the tank surface will be subdivided into 15 different test areas with the hoops as shown in Figure A.1. The primary test hoops are along the centerline of the tank and common to all the sensors to facilitate direct comparisons of the different sensing technologies. To allow for ice coring during the decay phase, hoops corresponding to the primary hoops designate by subscript "a" will be subjected to similar conditions as the primary hoops. Supplemental hoops used for fixed instrumentation or other environmental consideration are designated with a subscript "b" with the oil being injected approximately the same time as hoops with the corresponding digit. Figure A.2 is from a previous test in the Test Basin conducted by Dickins (2005). The ice thickness at the time of the injection and the nominal oil thickness for the respective hoops are listed in Table A1.

During the experiment, the ice growth, ice property evolution, and oil weathering will be continuously monitored.

1.2. MAIN RISKS

Three main risks have been identified and focused on. The risk, techniques to mitigate the risk, and any required certification are described below.

1.2.1. Spills associated with injection of oil: The tank area will be subdivided into individual test cells using rectangular containment hoops as shown in Figure A.2. Oil will be injected under the ice within the respective test cell using a variable speed lobe pump and an injection wand inserted through an access hole outside the containment hoop. The amount of oil that will be injected into the hoops varies with experiment, and ranges from 10 to 375 liters (2.5 to 100 US gallons) to a total of 1160 liters (300 US gallons). The schedule for the oil injections are a function of ice thickness and nominal oil thickness are listed in Table A1. Potential oil spills are associated with the movement of the oil tote,

leaks in the hoses, and post oil injections. To minimize the potential of an oil spill associated with moving the oil, a 330 US gallon tote of oil will be placed in as secondary containment on the main carriage in the basin. The tote will remain on the carriage for successive injections and moved to the injection site to minimize hose length, decreasing potential leak sources. The bottom of the oil tote has a valve with cam-lock connection. When oil is not being injected the valve will be secured. The suction hose from the tote to the suction side of the pump will have isolation valves that can be secured if the lobe pump needs to be serviced. A spring loaded valve on the oil suction will be manually held open during the pumping process. Following the oil injection the oil will be flushed from the pump and the injection hose using water drawn from the tank. The discharge water from the flushing operation will be injected into the injection cell. During the injection process, the oil will be kept in a closed system from the tote to under the ice with no threat of exposure. Level C PPE will be used when the line needs to be opened. The carriage will be parked in a room above freezing to avoid freezing the hoses.

1.2.2. Air quality degradation during melt out. During the majority of the test, the oil will be sealed under the ice and isolated from the tank area. During the melt out phase, it is anticipated the oil will migrate up the brine channels and gasses will be released above the ice. The air quality will be monitored and if the levels rise, access to the tank will be limited and respirators will be used by personnel in the tank. If the level becomes excessive, the room will be ventilated.

1.2.3. Cable entanglement: The underwater carriage will traverse the 140 ft. tank originating at the prep tank at the east end of the main tank. The underwater carriage has a bundle of cables for carriage power and control and a second bundle for the sensors on the platform. The cables will be deployed and recovered manually. To minimize entanglement, access to the prep tank area will be limited during carriage deployment and recovery, and the cables will be stored on a vertical rack with pins spaced approximately 3' apart horizontally near the top. Approximately 10' of cable can be stored per wrap. A further concern is cable recovery while the carriage is backing. An underwater a Pan-Tilt-Zoom (PTZ) camera will be mounted on the carriage with real-time display during the recovery operation. Near open water, PFD will be worn.

The Health and safety plan (HASP) represents the minimum health and safety and emergency response activities associated with the evaluation of remote sensing technologies to detect oil in and under ice. As a US ARMY Corps of Engineers (COE) laboratory, all activities associated with the research effort will be in accordance with the COE Emergency Management Standard Operating Procedures (EM-SOP), COE Safety Hand book EM 385-1-1 September 2008, CR 200-1-1 ERDC Environmental Assessment of Activities, 24 April 2014, and the CRREL Ammonia

Emergency Response Plan (RV-Z-8), CRREL Emergency response plan (RV-Z-6), Hot Work Permit (RV-Z-11 and EM385-1-1), Lock Out- Tag Out (RV-Z-13 and EM385-1-1), and where appropriate, in accordance with a Ladder Safety and Fall protection plan, amongst others. All other hazardous activities should be performed IAW CRREL SOPs and EM 385-1-1 under the oversight of the site safety officer Zabilansky.

ASSIGNMENT OF HASP RESPONSIBILITY

HEALTH AND SAFETY MANAGER (HSM)

Leonard Zabilansky, principle investigator, shall ensure that a safety and occupational health plan is developed, in accordance with the Safety and Occupational Health reference Document contained in the USACE Business Manual EM 385-1-1, and incorporated into each Project Management Plan (PMP).

HEALTH AND SAFTY SPECIALIST (HSS)

Colin O'Connor is the CRREL HSS and will determine the acceptable health and safety training required for individuals before they may work at the test site. Training on respirator protection and fire safety should be completed prior to the start of project testing.

SITE SAFETY OFFICER (SSO)

The site safety officer Leonard Zabilansky is responsible for oversight of the HASP and determination of imminent safety hazard, emergency situation, or other potentially dangerous situations. Alternate: Seth Campbell.

HAZARD ASSESSMENT

HAZARDOUS MATERIAL DESCRIPTION/CHARACTERIZATION

Oil that contains benzene will be injected under the ice. Anhydrous ammonia is used in the closed loop refrigeration system in the Test Basin which may leak during the tests. Detailed information of the hazardous materials and compounds used or released in the test basin are listed in the Material Safety Data Sheets (MSDS) in Appendix E. They address health hazards, chemical characteristics, protection, exposure limits, and first aid procedures.

DEGREE OF HAZARD

On-site hazards may include, but are not limited to, both physical and chemical hazards. Physical hazards include slips, trips and falls, exposure to cold, mechanical hazards, open water hazards, electrical hazards, and fire. A hazard analysis will be performed by the onsite HSO prior to testing.

3.1.1. Chemicals

- Liquid Hydrocarbons: Alaska North Slope (ANS) (MSDS in Appendix E). According to available product safety information, respiratory protection is not needed, as the evaporation rate of the oil is negligible, resulting in the off-gassing of little, if any, vapors, but level will be monitored.
- Benzene: A component in the ANS. It is not expected to be off-gassed due to cold temperatures. However, it will still be monitored.
- Anhydrous ammonia refrigerant (MSDS in the Appendix E). Ammonia is used in the closed loop refrigeration system with the potential of a leak.

3.1.2. Physical Hazards See Job Hazard Analysis (JHA) In Appendix B

3.1.3. Confined Space – N/A (Test Basin is not considered a confined space)

3.1.4. Dispensing flammable and combustible liquids-general

- Flammable liquid dispensing systems shall be electrically bonded and grounded to prevent any static charge.
- Flammable or combustible liquids shall be drawn from, or transferred into, vessels, containers, tanks within a building or outside only through a closed pipe system, from safety cans, by means of a device drawing through the top, or from a container,

or portable tanks, by gravity or pump, through an approved self-closing valve. Transfer by means of air pressure on the container or portable tanks is prohibited.

TRAINING REQUIREMENTS

BASIC TRAINING REQUIRED

All personnel participating in the project will be trained prior to project commencing on the contents of this HASP, the JHA, and the MSDSs for hazardous chemicals that they could be exposed to, and all emergency procedures. Employees operating equipment (i.e. saw, chainsaw, augers) will be trained by the SSO on proper operation according to manufacturer guidelines. All personnel must review the safety plan and sign that they understand and will comply.

SAFETY BRIEFINGS

A safety briefing will be performed by an on-site senior member in charge (e.g. SSO) prior to ice cutting, injecting oil under the ice and other activities deemed high risk.

SAFETY AUDITS

Safety audits will be conducted on an as needed basis by the SSO to assist site personnel in conducting activities safely.

FIRST AID AND CPR

In the event of medical/traumatic emergency in IEF Test Basin during this project, staff will contact emergency response (911) via telephone and perform immediate first response care, up to their level of training if it is safe to do so, until emergency care arrives. Specific hazards which might lead to an emergency and hazard mitigating strategies are discussed in the JHA (Appendix B).

EMERGENCY MEDICAL TREATMENT

Standard emergency procedures for medical emergency will be followed by calling 911.

Provisions for emergency medical treatment shall be integrated with the overall Site Emergency Plan (SOP RV-Z-6) and following shall be available:

- Phone, located at the southwest corner in the Test Basin Room near rear exit door.
- First aid kits in compliance with OSHA requirements and emergency first aid stations in the immediate work vicinity.
- AED's are located on the wall in the lobby by the security office and in the TIAC Break Room. AED's are self-explanatory and will guide user on what to do upon opening. Dial 911 before using any AED.
- Eye wash stations are located in the shop area outside the Test Basin.
- Conspicuously posted phone numbers and procedures for contacting ambulance services, fire department, police, and medical facility near the Telephone within the Test Basin Room.
- Maps and directions to medical facilities.

Contact information for CRREL, emergency rescue, and the local hospital are listed in Appendix C.

SITE CONTROL MEASURES

The purpose of the site control measures discussed in this section is to maintain order at the site and to minimize chemical and physical hazards to on-site personnel, visitors, and the public.

Site control zones (CZ) will include an exclusion zone (EZ), a contamination reduction zone (CRZ), and a support zone (SZ). In addition, temporary activity-specific work zones (WZs) will be established at specific locations.

The measures described in this section will be utilized when deemed necessary and/or appropriate in accordance with the site specific procedures described in Appendix A.

Site Control Zone (CZ)

The Test Basin area is defined as the CZ.

Exclusion Zone (EZ)

The EZ is the containment hoop as the surface will be contaminated as the oil migrated through the ice.

Work Zone (WZ)

Temporary activity-specific WZs shall be established when the oil is injected and will include the section of the walkway along the tank to and including the containment hoop. Each specific WZ shall be established and marked by safety rope or tape as appropriate.

ATEX Zones

We are not expecting any ATEX (explosive atmospheres) in the workplace, but we will be using an ITX M40 to monitor LEL to identify any buildup of potentially explosive levels. If explosive conditions are present, test will be stopped and re-evaluated. The room will be immediately evacuated and the room will be ventilated. Cell phone use in the work area is restricted during critical tasks (i.e. crane operation and fuel injection) due to risk management concerns over distractions, which will also minimize ignition risks.

PERSONNEL DECONTAMINATION

When the oil is being managed, personnel decontamination areas will be established on-site. Personnel will decontaminate and/or dispose of soiled protective clothing (i.e., disposable boots and gloves, etc.)

EQUIPMENT DECONTAMINATION AREA

To prevent off-site transport of contamination, equipment will be decontaminated at a fixed temporary decontamination area. Equipment will be pressure washed and wiped down prior to storage. Decontamination liquids will be collected and disposed.

SITE VISITORS

Visitors and test participants are required to report to the CRREL personnel prior to accessing the Test Basin. Visitors must sign in and out daily for the duration of their approved visit. All site visitors will receive a safety briefing prior to entering the test area

PERSONAL PROTECTIVE EQUIPMENT

GENERAL

Personal protective equipment (PPE) for general operations will be consistent with the requirements of 29 CFR 1910 Subpart I, "Personal Protective Equipment." Protection may be upgraded or downgraded, as deemed appropriate by the SSO and verified by the HSM.7.2.

Signage will be posted that clearly states when such PPE as hard hats, hearing protection and fall protection will be required. Fall protection will be worn when working above 4 ft. (1.2 m) or more. Full harness fall protection with double, self-arresting lanyards will be used in such cases. All personnel who may be required to use such equipment must be trained in its correct use. In addition, tie-off points need to be provided that can hold a 5000 lb. load. Use of fall protection needs to be specified for any man-riding equipment that raises personnel above a drop of 1.2 m or greater.

ANTICIPATED LEVELS OF PROTECTION

All participants in the WZ will wear level D protection as defined below.

Basic Level D personal protective clothing and equipment:

- Eye protection (safety glasses, goggles).
- Hardhat (when overhead hazards exist).
- Steel toe, steel shank boots.
- Noise protection - as warranted.
- Fall-arrest system (life line, safety belt, tie-off point) when working above 2 metres height.
- PFD to be worn when working within 1 meter of the tank that has open water or unsafe ice.
- Cold weather clothing and work gloves as warranted.

When working during oil activities, all participants will wear level D protection as defined above plus:

- Disposable Tyvek coveralls.
 - Oil resistance gloves (neoprene, nitrile).
- If action levels in section 8 are exceeded, and based on evaluation of the conditions, if Level C or B respiratory protection is deemed necessary, work activities will be halted and the HSM will be contacted immediately before upgrading the levels of protection. Level C will consist of all PPE required in Level D above plus:
- Respiratory protection (Half / Full Face Mask with Organic Vapor Cartridges rated for oil and mist environments).

AIR MONITORING

Atmospheric conditions will be monitored during oil activities to determine the possible need to upgrade the personal protection of on-site workers. Both fixed and mobile sensors with proven past abilities to operate at cold temperatures will be used during the experiment. During oil activities an Industrial Scientific M40 4-Gas meter will take direct reading for H₂S, LEL, O₂ and CO. Benzene, H₂S and LEL will be used as indicators initially to determine if ventilation is necessary or if there is a buildup. Other compounds, including CH₄, SO₂, NO_x, COV, and BTEX may be monitored if necessary, i.e. if a buildup is detected in Benzene, H₂S or LEL. Gastec tubes will be used to take Benzene readings during regular intervals (every 30 minutes to 2 hours) to establish levels. CRREL SEMO will provide instructions on how monitor atmospheric conditions.

<u>Instrument</u>	<u>Action Level</u>	<u>Protection/Action</u>
Industrial Scientific	Oxygen < 19.5% O ₂	Halt work, leave area, ventilate
M-40 4-Gas Meter	H ₂ S >5 ppm, LEL >10%	atmospheric

Gastec Tubes	DetectorBenzene Greater than 0.5 ppm	Don Respiratory protection (as a minimum half mask respirator with Organic vapor cartridge)
Wall Ammonia Sensor	mountedAmmonia great than 25 ppm	Halt work, Evacuate the cold room, Contact DPW, return only after Room is cleared by DPW

*In the event action levels are exceeded personnel will execute action and notify CRREL personnel

DECONTAMINATION PROCEDURES

The SSO shall determine the level of decontamination necessary based on the evaluation of specific work activities and the potential degree of contamination encountered.

EQUIPMENT

Equipment will be decontaminated within the decontamination area using a hot water pressure washer and wiping down. Hazardous waste will be disposed of in accordance with COE and State of NH policy.

PERSONNEL

Decontamination of personnel in Level D will consist of:

- Removal and disposal of coveralls.
- Removal and disposal of gloves.
- Washing boots or other non-disposable protective equipment (i.e., hard hat, safety glasses/goggles, etc.) suspected of being contaminated using soap solution followed by potable or distilled water rinse.

Decontamination of personnel using Level C protective equipment will consist of the same as above, plus:

- Removal, cleaning, and storage of respiratory equipment.

CONTAMINATION PREVENTION

One of the most important aspects of decontamination is the prevention of contamination. Good contamination prevention should minimize worker exposure and help ensure valid sample results by precluding cross-contamination. Procedures for contamination avoidance include:

Personnel

- Know the limitations of all PPE being used.
- Do not walk through areas of obvious or known contamination.
- Do not handle or touch contaminated materials directly. Do not sit or lean on potentially contaminated surfaces.
- Make sure all PPE has no cuts or tears prior to donning.
- Fasten all closures on suits, covering with tape, if necessary.
- Take particular care to protect any skin injuries.
- Do not carry cigarettes, gum, food, or candy into contaminated areas.
- Do not smoke, eat, or drink in contaminated areas.

Sampling/Monitoring

- Cover instruments with clear plastic, leaving openings for sampling ports, sensor points.
- Bag sample containers prior to placement of sample material into containers.

General

- If contaminated tools are to be placed on non-contaminated equipment for transport to the decontamination pad, use plastic to keep the non-contaminated equipment clean.

DISPOSAL PROCEDURES

Discarded materials, waste materials, or other field equipment and supplies shall be handled in such a way as to preclude the potential for spreading contamination, creating a sanitary hazard, or causing litter to be left on site. Thought and preparation beforehand can eliminate unnecessary generation and inappropriate management of hazardous waste during the course of the project.

Waste oil, water with waste oil or any contaminated waste derived from the waste crude oil will be handled and disposed per NHDES Hazardous Waste Rules Env-HW, EPA 40 CFR Hazardous waste rules and Regulation No. 200 Environmental Quality U.S. ARMY ENGINEER RESEARCH AND DEVELOPMENT CENTER (ERDC) DISPOSAL OF HAZARDOUS WASTE. To dispose of a known hazardous waste, an MSDS/SDS and generator knowledge or a lab analysis also known as Toxic Characteristic and Leaching Properties (TCLP) are required. Representative samples of the recovered oil and oiled waste will be sent to independent laboratory (Eastern Analytical Laboratory) for characterization and required disposal procedures. The form 1930 needs to be filled out and completed before turn in for disposal to the lab hazardous waste point of contact (John Hebert). The oil waste will be disposed by a certified hazardous waste disposal company. Additional information regarding the hazardous waste program for both NHDES and EPA are as follows:

<http://des.nh.gov/organization/divisions/waste/hwcb/>

<http://www.epa.gov/osw/laws-regs/regs-haz.htm>

Potentially contaminated materials, e.g., clothing, gloves, etc., will be bagged or drummed with appropriate labeling affixed as regulated, and segregated for proper disposal.

Non-contaminated materials shall be collected, bagged, and disposed of as normal domestic waste.

GENERAL SAFE WORK PRACTICES AND COMMUNICATIONS

SAFETY EQUIPMENT

Basic emergency and first aid equipment will be available in or near the Test Basin. This shall include communications equipment, first aid kit, emergency eye wash, fire extinguishers, and other safety-related equipment. AEDs are located in TIAC Break Room, second floor in the building adjacent to the Test Basin. Location will be noted in safety briefing.

COMMUNICATIONS

Telephones – Either land line or cellular telephone will be used for communication with emergency support services/facilities.

Hand Signals - Hand signals will be used by the entire in the event verbal communication is lost.

Signal Meaning

Hand gripping throat Out of air; can't breathe

Grip partner's wrist Leave area immediately; no debate

Hands on top of head Need assistance

Thumbs up OK; I'm all right; I understand

Thumbs down No; negative

SAFE WORK PRACTICES

The following safe work practices will be implemented during site operations:

- Only properly trained and equipped personnel will be allowed to work in potentially contaminated areas.
- The number of personnel and equipment in the sampling areas will be kept to a minimum, consistent with safe site operations.
- At least two personnel must be present – no working alone.
- Running is prohibited.
- Texting or use of cellular phones during critical operations (such as crane usage and oil injection) is prohibited.
- Workers shall not exit until soiled equipment and clothing have been removed and decontaminated or properly disposed of.
- Eating, drinking, chewing gum or tobacco, smoking, or any practice that increases the probability of hand-to-mouth transfer, ingestion, and inhalation of potentially contaminated materials is prohibited.
- As necessary, personnel will thoroughly wash their hands and faces upon leaving the investigation areas.
- Contact with potentially contaminated materials and surfaces shall be avoided. Personnel shall comply with contamination control measures.
- Personnel with facial hair or other face piece seal obstructions will not be permitted to work where respirators are required.
- Work shall only be conducted if adequate illumination is provided.
- During the oil injection process and when the oil has migrated through the ice, all sources of ignition (including cell phones) will be prohibited and 2 fire extinguishers will be maintained on hand at each exit of the test basin.
- Good housekeeping practices will be followed; i.e. management of extension cord, hoses, proper disposal of sorbent pads, etc.

SAFETY MONITORING

Monitoring will include any near-misses or incidents of not following safety procedures outlined this plan. Safety performance will include reporting accident free hours. Reported

near-misses will be tracked, and a recorder on a safety board will be located in the instrumentation corridor.

SAFETY MEETINGS

Prior to Injecting Oil

Toolbox talks and safety briefing will occur prior to injecting oil to review the procedures and safeguards. During these meetings it will be made clear that all personnel have the right to halt work if they observe an unsafe action or situation.

Post oil injection

Following oil injection, personnel will review lessons learned and discuss improvements to the procedure.

EMERGENCY PREPAREDNESS

EMERGENCY COORDINATOR

The Site Emergency Coordinator shall be the senior research team member who will implement the emergency action plan as outlined (29 CFR 1910.38). The following six items are typically more applicable to operating facilities, and will be implemented to the extent possible when applicable.

- Emergency escape procedures and routes.
- Procedures for those remaining for critical operations.
- Procedures to account for employees after evacuation.
- Rescue and medical duties.
- Preferred means of reporting fires and emergencies.
- Names, job titles, or departments to contact for additional information of duties.

These items will be discussed during each site orientation meeting conducted on-site by the SSO.

EMERGENCY SERVICES CONTACTS

The Emergency Coordinator shall verify appropriate emergency contacts and make contact with these before beginning work on-site as appropriate. The Emergency Coordinator will inform the emergency contacts about the nature and duration of work expected on the site and the type of contaminants and possible health or safety effects of emergencies involving these contaminants. Also at this time, the Emergency Coordinator and the emergency response contacts shall make arrangements to handle any emergencies that might be anticipated.

Site specific emergency phone numbers are provided in Appendix C.

IMPLEMENTATION

The Emergency Coordinator shall implement the emergency action procedures whenever conditions at the site warrant such action. The Emergency Coordinator will be responsible for coordinating the evacuation, emergency treatment, and emergency transport of site personnel as necessary, and for notification of emergency response units and the appropriate management staff. The following conditions may require implementation of emergency action procedures:

- Fire or explosion on-site.
- Serious personal injury.
- Release of hazardous materials, including gases or vapors at levels greater than the maximum use concentrations of respirators.

The Emergency Coordinator shall verify appropriate emergency contacts and make contact with these before beginning work on-site as appropriate. The Emergency Coordinator will inform the emergency contacts about the nature and duration of work expected on the site and the type of contaminants and possible health or safety effects of emergencies involving these contaminants. Also at this time, the Emergency Coordinator and the emergency response contacts shall make arrangements to handle any emergencies that might be anticipated.

FIRE OR EXPLOSION

When oil is being injected under the ice or the oil has migrated through the ice, all sources of ignition will be prohibited and 2 fire extinguishers will be maintained on hand at each exit of the test basin.

If an actual fire or explosion has taken place, emergency steps will include 1) evacuation of work area, and 2) notification CRREL Security and the fire department and other appropriate emergency response groups if necessary.

ANHYDROUS AMMONIA REFRIGERANT LEAK

An ammonia detector is installed in the Test Basin and with the read out display above the personnel door from the IEF Shop. In the event there is a leak of the closed loop anhydrous ammonia refrigeration system and the concentration exceeds 25 ppm, an alarm is broadcasted over the CRREL Refrigeration radio to alert the refrigeration staff that is available 24/7. If the concentration exceeds the 25 ppm, all personnel will evacuate the Test Basin and wait for guidance from Refrigeration staff.

An important property of ammonia is its pungent odor. The threshold concentration at which ammonia is detectable varies from person to person; however, ammonia can be usually detected at concentrations in the range of 5 ppm to 50 ppm. Concentrations above about 100 ppm are

uncomfortable to most people; concentrations in the range of 300 to 500 ppm will cause people to leave the area immediately.

If personnel working in the test area smell ammonia below the 25 ppm concentrations they should contact CRREL refrigeration personnel at extension 4755 to allow the leak to be repaired before triggering the alarm.

PERSONAL INJURY

Emergency first aid will be administered on-site as appropriate. Then, the individual will be decontaminated if possible, depending on the severity of the injury, and transported to the nearest medical facility if needed.

OVERT CHEMICAL EXPOSURE

Typical response procedures include:

SKIN CONTACT: Use copious amounts of soap and water. Wash/rinse affected area thoroughly, and then provide appropriate medical attention. Eye wash will be provided on-site and eyes should be rinsed for 15 minutes upon chemical contamination.

INHALATION: Move to fresh air and/or, if necessary, decontaminate/transport to hospital.

INGESTION: Decontaminate and transport to emergency medical facility.

PUNCTURE WOUND OR LACERATION: Decontaminate and transport to emergency medical facility. The SSO will provide medical data sheets to medical personnel as requested.

COLD EXPOSURE

Persons working in the Test Basin when it is below freezing may be subject to frostbite. Ambient temperatures in the Test Basin cold room will be maintained at or below -20°F (-29°F). Extreme cold for even a short time may cause severe injury to the surface of the body, or result in profound generalized cooling of the body core, resulting in coma and death. Areas of the body which have high surface area-to-volume ratio such as fingers, toes, ears, are the most susceptible. Accidents due to cold exposure such as cold surface risks by contact cooling (intentional or accidental); with bare skin can lead to severe burning in a very short period of time.

Local injury resulting from cold is included in the generic term frostbite. There are several degrees of damage. Frostbite of the extremities can be categorized into:

- Frost nip or incipient frostbite: Characterized by suddenly blanching or whitening of skin.
- Superficial frostbite: Skin has a waxy or white appearance and is firm to the touch, but tissue beneath is resilient.
- Deep frostbite: Tissues are cold, pale, and solid; extremely serious injury.

Prevention of frostbite is vital. In order to reduce the risk, personnel will keep extremities warm by wearing insulated clothing as part of one's protective gear during extremely cold conditions. Personnel will check for symptoms of frostbite at every break, and check coworkers exposed skin frequently during cold room work. Personnel will be briefed on the dangers and ways to prevent frostbite.

To administer first aid for frostbite, personnel will be brought to a warm space to rewarm the affected areas quickly in water between 39°C and 41°C (102°F to 105°F), and warm drinks, not including coffee, tea, or alcohol will be given to the injured person. The frozen parts will be kept in warm water or covered with warm clothes for 30 minutes and the injured area will be elevated and protected from injury. Blisters will not be broken, and sterile, soft, dry material will be used cover the injured areas.

After thawing, the personnel try to move the injured areas a little, but no more than can be done alone (without help). Rubbing, using ice, snow or gasoline (or anything cold), heat lamps or hot water bottles or the use of a hot stove on the affected body part will all be avoided.

Systemic hypothermia is caused by exposure to freezing or rapidly dropping temperature. Its symptoms are usually exhibited in five stages: 1) shivering; 2) apathy, listlessness, sleepiness, and (sometimes) rapid cooling of the body to less than 95°F; 3) unconsciousness, glassy stare, slow pulse, and slow respiratory rate; 4) freezing of the extremities; and, finally, 5) death.

Effects arising from cold exposure will be minimized by providing workers with insulated clothing when working in below freezing temperatures. Personnel who are cold or become wet will be excused to returned to warm area and everyone will be encouraged to limit the time in the cold room the less than 3 hours with a 10 minute break per hour.

ACCIDENT INVESTIGATIONS AND REPORTING

All accidents or injuries, however slight, resulting from testing programme must be reported to the project manager, safety office and appropriate supervisor within 24 hours. A determination will be made for further investigation and or other actions.

ACCESS AUTHORIZATIONS

Personnel authorized to enter the Test Basin while activities are being conducted must be authorized by the lead CRREL project personnel.

RECORDKEEPING

The following records and reports will be established and kept as appropriate.

- Safety Observations (suggestions as to how to improve safety, safety statistics i.e. number of personnel, accident free hours, near-misses, unsafe observations)
- Accident/Incident Reports
- Daily Sign In/Sign Out Log
- Air Monitoring Records
- Material Safety Data Sheets
- Respirator Fit Test Records
- Respirator Inspection Records

Appendix A. OIL CONTAINMENT HOOP LAYOUT IN THE TEST BASIN

TS (Thermistor String) 5cm from 10 above water surface to 1 m below.
 10cm spacing to bottom
 SP Sound Propagation cage supplied by WHOI
 ACT Acoustic Calibration Targets (location defined by others)
 CT Inserted in ice when holes available (Don Perovich)

Hoop Size:
 Hoop 1: 3m x 6m (LxW)
 Hoop 2-6: 3m x 2.5m
 'a' Hoops 1.5m x 1.5m
 'b' Hoops 2.5m x 1.5m

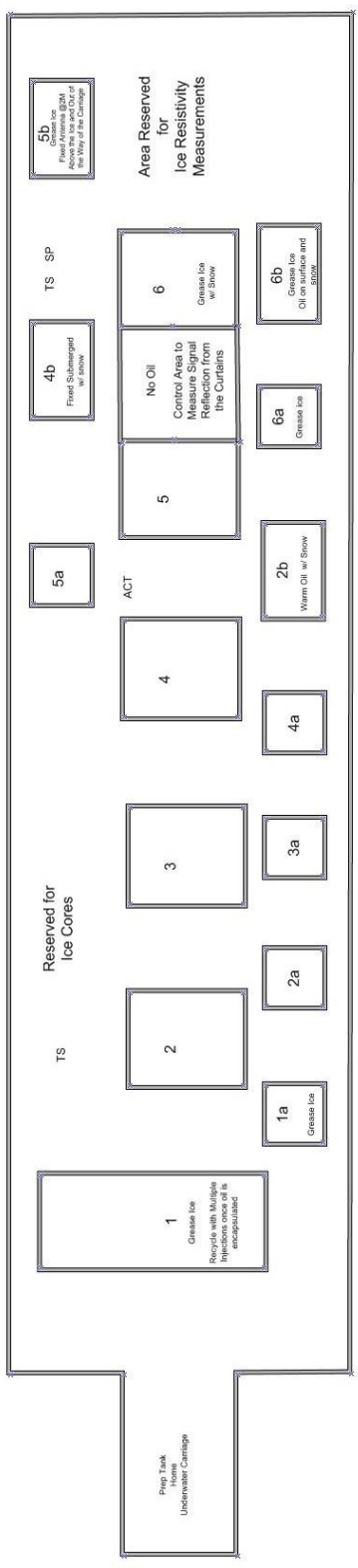


Figure A.1. Layout of the Test Areas defined by the containment hoops. Hoops 1-6 are primary hoops along the centerline of the tank. The hoops designated with an “a” subscript will receive oil injections and be used for destructive testing during melt out. Hoops with “b” subscript are supplemental hoops and will be injected with oil with the corresponding primary hoop. See Table A1 for details on thickness at injection and nominal thickness of oil.

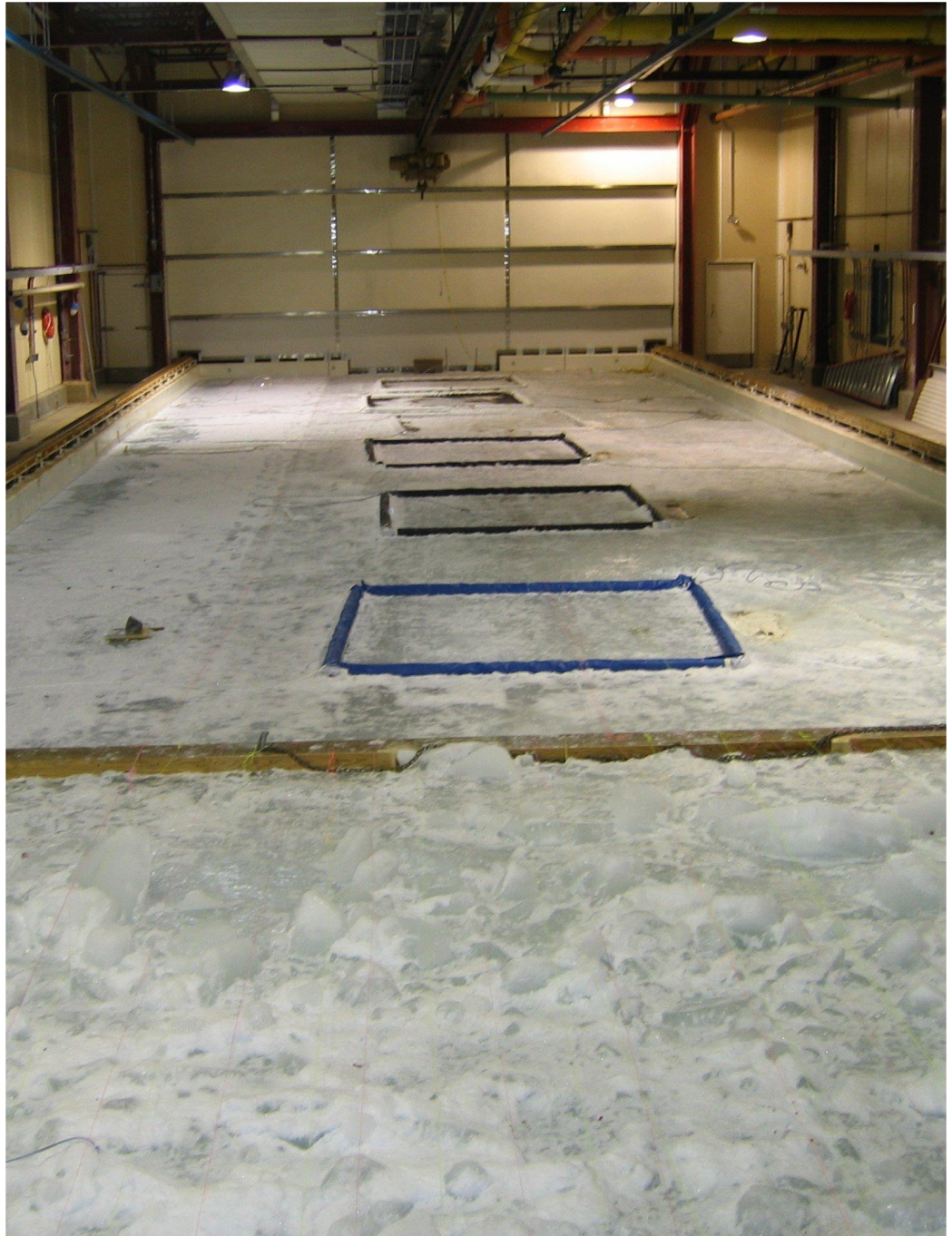


Figure A.2. Confinement hoops used in the Test Basin for the previous Remote Sensing Test from Dickens (2005). The current project will utilize the hoop configuration in Figure A.1.

Table A1. Oil injection schedule as function of ice thickness and corresponding nominal ice thickness (PFD)

Oil Confinement Hoop Configuration CRREL Basin								
Updated		5/10/2014						
Hoop ID	Dimension (L x W)	Curtain Depth	Surface Ice @ Freeze up	Ice Thickness @ Oil Injection	Nominal Oil Thick	Oil Injection Method	Snow	Remarks
	m	cm		cm	cm			
1	3 x 6	100	grease	5cm Frazil+	0.5	Spray on Surface and mixed		Test multi-beam system. Start with grease ice spray oil in surface and mix. See Recycle of Hoop 1
2	3x2.5	35	columnar	20-25	2	single		Thin ice with oil and anticipate encapsulation.
3	3x2.5	50	columnar	35-40	1	single		Mid-thickness ice with thin layer of oil and anticipate encapsulation. Compare with 3,4,and 4b.
4	3x2.5	50	columnar	35-40	5	stair step		Mid-thickness ice with thick layer of oil and anticipate encapsulation. Compare with 3,4,and 4b.
5	3x2.5	70	columnar	55-60	2	single		Thicker ice and anticipate encapsulation of the oil layer. Compare with 2 and 5b.
6	3x2.5	100	grease	80	5	stair step	Snow in steps stay thru melt out	Thick ice and thick layer of oil prior to melt out.
"a" Designated a control hoop that corresponds with primary hoop "Duplicating" oil and ice conditions. Ice will be used for destructive testing during melt out phase.								
1a	1.5x1.5	100	grease	5cm Frazil+	0.5	Spray on surface and mixed		Will have multiple injections like Hoop1. See Recycle of Hoop 1
2a	1.5x1.5	35	columnar	20	2	single		Thin ice with oil and anticipate encapsulation.
3a	1.5x1.5	50	columnar	35	1	single		Mid-thickness ice with thin layer of oil and anticipate encapsulation. Compare with 3,4,and 4b.
4a	1.5x1.5	50	columnar	35	5	stair step		Mid-thickness ice with thick layer of oil and anticipate encapsulation. Compare with 3,4,and 4b.
5a	1.5x1.5	70	columnar	55	2	single		Thicker ice and anticipate encapsulation of the oil layer. Compare with 2 and 5b.
6a	1.5x1.5	100	grease	80	5	le injection	Snow in steps stay thru melt out	Thick ice and thick layer as in Hoop 6 of oil prior to melt out. Considering the oil injection is not being monitored, all the oil will be injected as one injection. will inject Final thickness of oil 1 t

Appendix B. JOB HAZARD ANALYSIS (JHA)

The following table lists basic or generic tasks necessary for the conducted in the Test Basin at CRREL. Hazards associated with the tasks are listed with preventive measures to be followed by affected personnel.

Task Hazard Prevention

TASK	HAZARDS	PREVENTION/CONTROL
1) Materials handling, general set-up	<p>a) Lifting material(s) (muscle strains, back injuries)</p> <p>b) Forklift operations (objects striking)</p> <p>c) Crane(s) operations (objects striking)</p> <p>e) Hand/power tools (muscle strains, pinch points, electrocution)</p>	<p>a) Use proper lifting techniques; lift with your legs, not your back; get help for heavy loads, use mechanical devices (i.e., fork lift, cranes).</p> <p>b) Follow acceptable safe practices for operators. Forklifts will only be operated by CRREL employees trained to operate that specific truck. Mark off areas where Forklifts will be used to restrict other traffic and pedestrians. Use a Ground Guide or a spotter. All forklifts must be examined at least daily before being used. Seatbelts will be utilized at all times while operating a forklift. A vehicle that is damaged, defective or otherwise unsafe must be removed from service.</p> <p>c) Do not stand under raised loads. Do not exceed capacity of crane. Cranes will be operated only by CRREL employees trained to operate that specific crane. Mark off areas where cranes will be lifting restrict pedestrians. All lifting hardware will be inspected at least daily before being used. Any lifting hardware that is damaged, defective or otherwise unsafe must be removed from service.</p> <p>e) Use correct tool for the job, use correct PPE and proper body positioning when handling tools. Inspect all power tools to ensure no frayed or exposed wires exist, equipment is grounded and insulated and GFI's extension cords etc. are functioning properly.</p>
2) Hoop assembly and placement into tank (set-up)	<p>a) Rigging from work boat or crane (falls)</p> <p>b) Cable handling (pinch points)</p> <p>c) Positioning bridges (objects striking)</p> <p>d) Positioning boom equipment. (objects striking)</p>	<p>a) Personnel on work boat MUST wear PFD's. Evenly distribute weight and do not overload. Life preservers are in place as needed.</p> <p>b) Wear hand protection during rigging.</p> <p>c) Have appropriate lines of continual communication.</p> <p>d) No one permitted under heavy loads...</p>
3) Oil transfer	<p>a) Spilled oil/deck area (slip/fall hazard)</p> <p>b) Pressurized equipment/pumps/hoses/lines (pressure release, objects striking)</p>	<p>a) Clean spills on deck/bridges immediately. Utilize spill equipment, as required.</p> <p>b) Inspect all equipment prior to use. Do not use damaged equipment. Replace cracked hoses, broken gauges prior to pressurization. Inspect for leaks. Use adequate PPE (hard hat, gloves, and face shield).</p>

4) Carriage(s) operation positioning and movement	a) Carriage movement (objects striking, falls)	<p>a) Carriage will only be operated by CRREL employees with experience to operate the carriage. See appendix D. Personnel are not permitted on/ or off the carriages while in motion or on the motor platform while in operation.</p> <p>b) All guard rails must be in place and secured while working on moving carriage.</p> <p>c) Carriage operator will ensure that all personnel in the area are aware of any operations before commencing. Continued and open communications with carriage operator is mandatory. Area around the carriage will be restricted and secured prior to any movement.</p>
5) Oil addition to test tank	<p>a) Splashing/spraying oils while transferring to Test Tank. [Slips/falls, exposure (skin/eyes), exposure (inhalation)]</p> <p>b) Pressure release (object striking, pinch points)</p>	<p>a) Wear appropriate PPE (protective clothes, goggles/face shield, nitrile gloves). Air sample base line tests will be taken. Appropriate respirators will be worn as required. Technician will keep bridge/deck as oil-free as possible.</p> <p>b) Utilization of damaged hoses for faulty equipment is prohibited. Check all piping, hoses, hose connections, etc. prior to use. Bleed pressure prior to disconnect. Wear PPE to include protective clothes, goggles/face shield, hard hat, and nitrile gloves.</p>
6) Refrigeration leak	a) Exposure to anhydrous ammonia in the event of an event of leak	<p>a) Smell ammonia- notify CRREL personnel.</p> <p>b) Ammonia alarm sounds level exceeds 25ppm – evacuate the room.</p>
7) Ice and Water Safety	<p>a) Slips, Trips, and Falls.</p> <p>b) Access to the ice cover</p>	<p>a) Traction devices are mandatory to be worn at all times when working on ice in the test basin. The walking surfaces around the tank must be kept clear of oil, snow and ice buildup and will be scratched or sanded as needed. Work areas must remain clear and free of clutter. Ensure equipment, cords, hoses and materials are positioned in a manner to reduce congestion, trip hazards, and ensure accessibility.</p> <p>b) Personnel will work from the carriages when the ice is less than 4"thick and the room is below freezing. During the warm up period, access to the ice will be determined by CRREL personnel. PFD's are required whenever there is a drowning hazard. EM 385-1-1</p>

8) Electrical	a) Electrical shock	a) Inspect all electric tools, lights, cords and other equipment for damage or wear prior to use. <u>Do not use damaged equipment.</u> Report any discrepancies immediately. Tape electrical connections to reduce migration of water at connections. GFCI's are required for all electric tools and lighting.
9) Removal of oil from test tank	a) Oil exposure (skin/eye contact) b) Falls, slips c) Sorbent boom sweeping.	a) Wear protective clothing, goggles/face shields and chemical resistant gloves. b) When moving oil from the water with high pressure hose streams, avoid direct contact of oil with water stream. Clean any splashed oil from the deck with absorbent pads.
10) Health Management	a) Frostbite b) Hypothermia c) Noise d) Soft Tissue Injuries (Back, Shoulder, Arm, Knee, etc.)	a) Protect exposed skin from cold/wind. Watch co-workers for signs of frostbite. Immediately move any affected personnel to warm, indoor area for evaluation and treatment. b) Dress according to conditions as the test tank will be refrigerated to -20F. c) Hearing protection is required when noise levels reach 82 dBA. During high noise activities, such as tool or equipment operations, or over 100 dBA, double hearing protection will be used. As a general rule, if employees are required to raise their voice to be heard above operating equipment in normal conversation then hearing protection should be used. Personnel operating and working in the vicinity of chainsaws and augers will wear double hearing protection. d) Work activities will use mechanical lifting/carrying devices whenever possible. If not possible, personnel must exercise proper lifting techniques. Seek assistance for awkward and large loads or loads greater than 50 pounds. Do pre-job stretching and warm-up, use proper SIM techniques, take breaks as necessary and re-energize.

11) Environmental Management	a) Spill Prevention and Response	a) Transfer recovered product to portable storage tanks for long- term storage. Thoroughly clean and wrap equipment to prevent dripping during transport. ALL equipment must be completely decontaminated and inspected prior to being stored. Report all spills/leaks immediately to CRREL Facility personnel. For small spills, API Tier 1 measures apply, for spills >100 kg API Tier 2 applies.
12) Cables	a) instrumentation cables from underwater carriage	a) Cables from the underwater carriage will be staged in the prep tank (east end) of the test basin. Cable managed to avoid tangling during deployment and recovery. All cables that present a trip hazard shall be adequately marked
12) GPR Instrumentation *	a) Noise b) Electrical Hazard	a) 500-1000 Mhz will require hearing protection b) See item 8
13) Frequency-Modulated Continuous Wave (FMCW) *	a) Noise b) Electrical hazard	a) hearing protection b) see item 8
14) Passive optical *	a) Electric shock	b) see item 8
15) Visible light- spectral radiance *	a) Humans humans sensitive to 390-700 nm, Excessive exposure to the lowest wavelengths of UV light, also called UV-C, (180-290 nm) can cause damage to the Cornea as well as the Lens. The mid UV wavelengths, also called UV-B, (290-320 nm) can cause damage to the Lens as well as cause welders eye (feels like sand in the eye); Blue light (380-480 nm) can cause damage to the Retina, Infrared light can cause damage to both the lens and cornea as well as the retina b) Electrical hazard	a) eye protection appropriate to widest range of applications b) see item 8
16) Thermal infrared *	a) Damage vision b) Electrical Hazard	a) Eye protection b) see item 8
17) Laser-fluorosensors *	a) Damage vision b) Electrical Hazard	a) Eye protection b) see item 8
18) Micro-CT scanners *	a) noise	
19) Acoustic – sonar	a) Noise b) Electrical Hazard	a) Hearing protection b) see item 8
* Reviewed and adjusted when sensors have been defined		

Appendix C. EMERGENCY TELEPHONE NUMBERS

EMERGENCY CONTACTS

SITE LOCATION: US Army Corps of Engineers, Cold Regions Research Engineering Laboratory, 72 Lyme Road, Hanover, New Hampshire, 03755. See attached map.

CRREL Emergency Telephone Numbers

Name	Title	Organization	Telephone #
Emergency/ Security			911
Security Office	Security	CRREL	603-646-4800
Byron Young	Environmental	CRREL	603-646-4602
Colin O'Connor	Safety Officer	CRREL	603-646-4860
Leonard Zabilansky	IEF Manager	CRREL	603-646-4319
Jared Oren	ERB Supervisor	CRREL	603-646-4458
Andre St. Louis	FE Supervisor	CRREL	603-646-4105

POLICE DEPARTMENT: Hanover Police Department, 46 Lyme Rd., Hanover, NH, Phone 911 (emergency) or 603-643-2222

FIRE DEPARTMENT: Hanover Fire Department, 46 Lyme Rd., Hanover, NH, Phone 911 (emergency) or 603-643-3424

AMBULANCE: Fire Department – Phone 911

HOSPITALS: Alice Peck Day Memorial (APD) (occupational health injuries)

125 Mascoma Street, Lebanon, NH. 03766 Phone 603-448-3121

Dartmouth Hitchcock Medical Center (DHMC)

1 Medical Center Dr., Lebanon, NH 03766 (603) 650-5000

POISON CONTROL CENTER: S/A Hospital above

HAZARDOUS WASTE DISPOSAL/CLEAN-UP CONTRACTORS:

Tradebe Treatment and Recycling of Bridgeport (203) 334-1666 or (888-276-0887)

North Country Environmental Services (800)479-5299

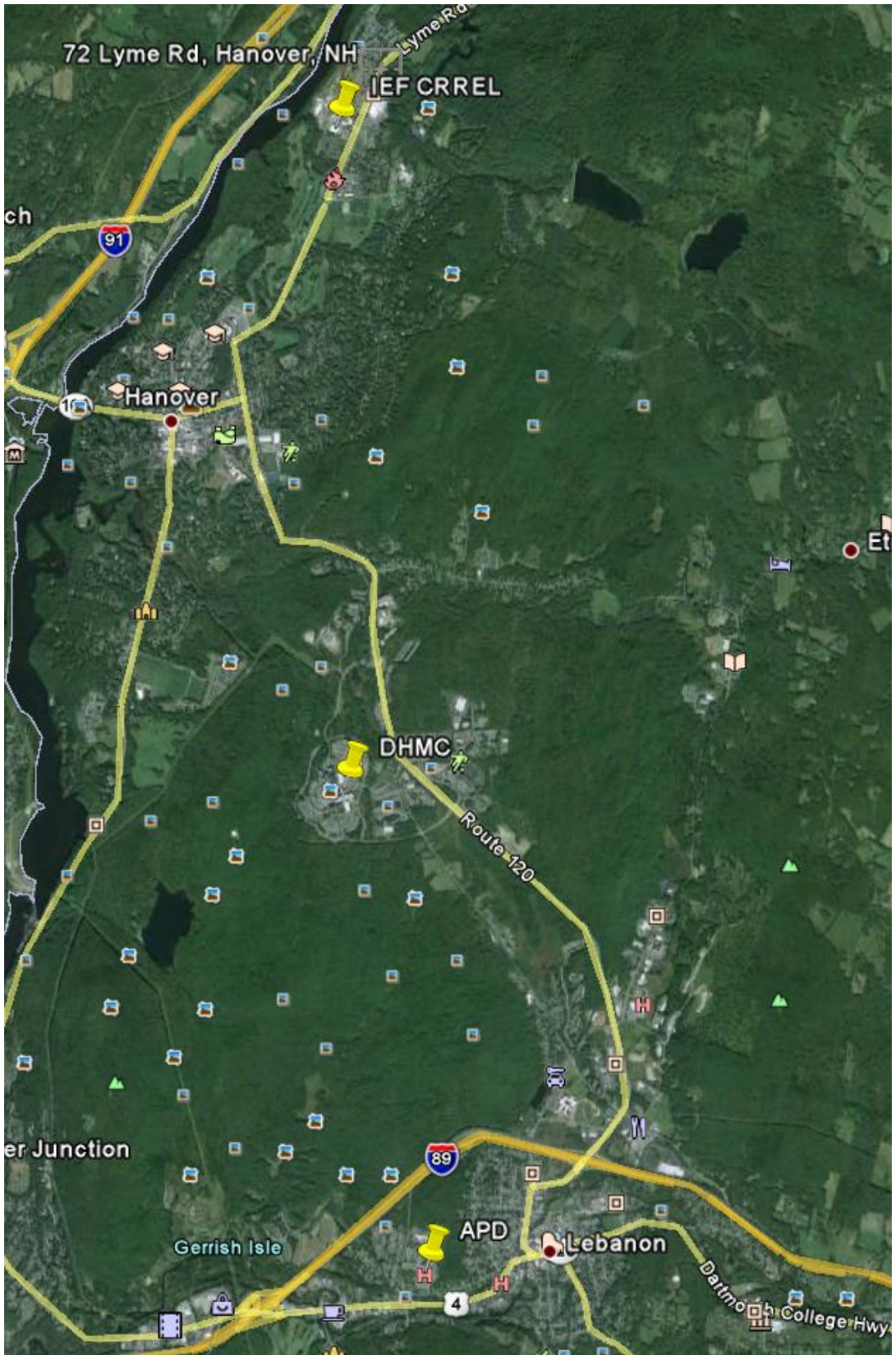
Clean Harbors

(800)645-8265

JIP Programme Manager: Joseph Mullin (301)-898-0044, Cell (301) 606-8060

JIP Executive Committee Chair: Jennifer Wyatt (403)-234-5194, Cell: 403 990
4674

Route to Hospitals



Appendix D. QUALIFIED EQUIPMENT OPERATORS

Fork lift operators

- Bill Burch
- John Hebert (Trainer)

Crane Operators

- Troy Arnold
- Bill Burch (Trainer)
- Seth Campbell
- Ben Winn
- Jesse Stanley (Trainer)
- Leonard Zabilansky (Trainer)

Main Carriage Operators

- Seth Campbell
- Ben Winn
- Jesse Stanley (Trainer)
- Leonard Zabilansky

Personnel Carriage Operators

- Troy Arnold
- Bill Burch
- Seth Campbell
- Ben Winn
- Jesse Stanley (Trainer)
- Leonard Zabilansky (Trainer)

Underwater Carriage

- Troy Arnold
- Seth Campbell
- Ben Winn (Trainer)
- Jesse Stanley (Trainer)
- Leonard Zabilansky

Appendix E. MATERIAL SAFETY DATA SHEETS

ANS oil

Benzene

Anhydrous Ammonia

